Universidad Autónoma de Madrid

Doctoral Thesis

On the Physics of Exciton-Polariton Condensates: from Fundamental Phenomena to Emergent Applications

Author:
Carlos Antón

Supervisor:
Prof. Luis Viña

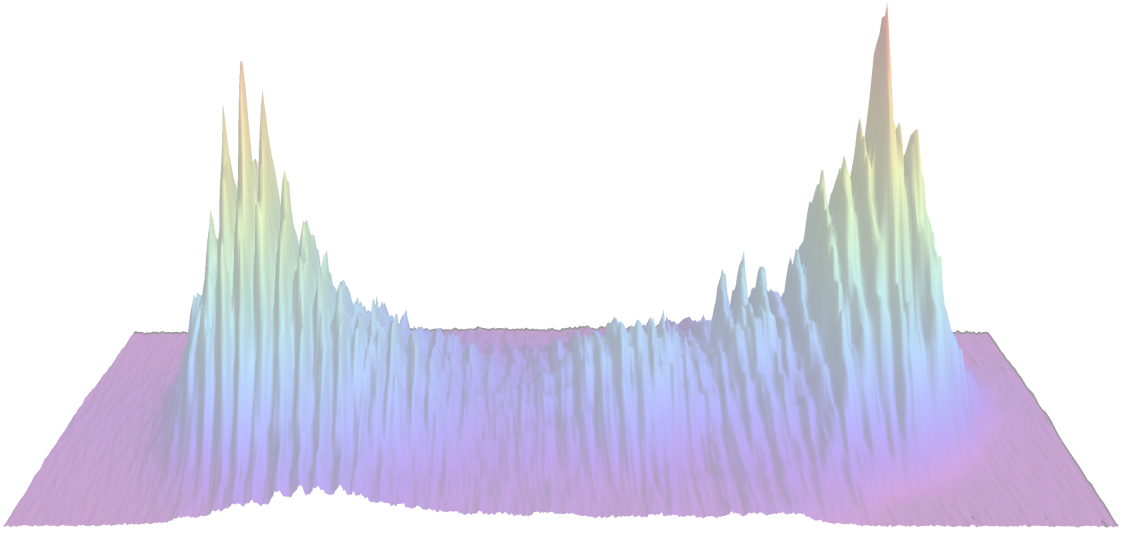

A thesis submitted in fulfilment of the requirements
for the degree of Doctor of Philosophy
in the

Departamento de Física de Materiales

February 2015

Cover background image: from Fig. 7.3(a) in Chapter 7, momentum distribution $n(\mathbf{k})$, at 35 ps after a pulsed excitation, showing two pairs of ballistic condensates propagating at $k_x = \mp 1.6$ μm^{-1}, respectively. The conspicuous interference pattern of the polariton PL intensity evidences the remote coherence between propagating polaritons that are spatially separated.

To my family

And now, I said, let me show in a figure how far our nature is enlightened or unenlightened: –Behold! human beings living in a underground den, which has a mouth open towards the light and reaching all along the den; here they have been from their childhood, and have their legs and necks chained so that they cannot move, and can only see before them, being prevented by the chains from turning round their heads. Above and behind them a fire is blazing at a distance, and between the fire and the prisoners there is a raised way; and you will see, if you look, a low wall built along the way, like the screen which marionette players have in front of them, over which they show the puppets.

I see.

And do you see, I said, men passing along the wall carrying all sorts of vessels, and statues and figures of animals made of wood and stone and various materials, which appear over the wall? Some of them are talking, others silent.

You have shown me a strange image, and they are strange prisoners.

Like ourselves, I replied; and they see only their own shadows, or the shadows of one another, which the fire throws on the opposite wall of the cave?

(...)

And if they were able to converse with one another, would they not suppose that they were naming what was actually before them?

Very true.

And suppose further that the prison had an echo which came from the other side, would they not be sure to fancy when one of the passers-by spoke that the voice which they heard came from the passing shadow?

No question, he replied.

To them, I said, the truth would be literally nothing but the shadows of the images.

That is certain.

And now look again, and see what will naturally follow it' the prisoners are released and disabused of their error. At first, when any of them is liberated and compelled suddenly to stand up and turn his neck round and walk and look towards the light, he will suffer sharp pains; the glare will distress him, and he will be unable to see the realities of which in his former state he had seen the shadows; and then conceive some one saying to him, that what he saw before was an illusion, but that now, when he is approaching nearer to being and his eye is turned towards more real existence, he has a clearer vision, -what will be his reply? And you may further imagine that his instructor is pointing to the objects as they pass and requiring him to name them, -will he not be perplexed? Will he not fancy that the shadows which he formerly saw are truer than the objects which are now shown to him?

Far truer.

Plato, *"The Republic"*, Book VII, (360 B.C.E).

Translated by Benjamin Jowett.

UNIVERSIDAD AUTÓNOMA DE MADRID

Introduction

Facultad de Ciencias
Departamento de Física de Materiales

Doctor of Philosophy

On the Physics of Exciton-Polariton Condensates: from Fundamental Phenomena to Emergent Applications

by Carlos Antón

The boom of the Computer Age, triggered by the start of the Digital Revolution in the past century, has definitely changed our society today. Part of this change has been starred by semiconductor materials, whose dimensions can be miniaturized and their electrical and optical properties can be controlled at will. Among the many technological successes occurred during the past 100 years in semiconductor physics, it is worthwhile to mention the invention of the dynamically tunable conductance of a germanium-based transistor [1, 2], demonstrated by J. Bardeen and W. Brattain in the group of W. Shockley in *Bell Laboratories* [3]. Unprecedented techniques in sample growth, controlled miniaturization and final optimization of the speed of semiconductor based devices were also achieved in this mythical center. Nowadays, the transistor, constituting a fundamental component in computers, has reached minimum sizes in the order of tens of nanometers and increased its processing speed up to GHz regime [4, 5].

This year 2015 has been proclaimed the "*International Year of Light and Light-based Technologies*". Light plays a key role as an intercross branch of knowledge, with a crucial importance in our daily lives. It is fair to say that the present century will depend as much on photonics as the 20th century did on electronics. In the context of our Computer Age, the need for further pushing the limits of the modulation speed in electronics and the seek of new routes for constructing and expanding the worldwide telecommunications have produced the appearance of hybrid electro-optic technologies, which try to profit from the best qualities of semiconductor electronics and photonics.

Nowadays silicon is the key material used in the actual electronic components. Nevertheless, silicon-based computer CPUs are reaching the physical limits for the amount of information to be transferred and processed. The limited bandwidth of the electronic-signals modulation imposes the necessity of exploring new technological alternatives that, in addition, should solve the problems of heat dissipation in the present transistors.

The research on optoelectronics presents the best alternative for the next impulse of our Information Era, even though there are still many challenges to be addressed before photon-based transistors become a reality [6]. There have been many advances in silicon photonics [7], notwithstanding this material posses an indirect band-gap, and thus requires phononic assistance (exchange of momentum through vibrations of the system) in optical transitions. This property of its band structure negatively biases the optical efficiency of the material for its use in optoelectronics.

III-V compounds, with a direct band gap, have been one of the choices during the last decades to develop optoelectronics. For example, it is notable to mention the realization of the first semiconductor laser at the beginning of 1960s [8], constituted from forward biased $GaAs$ $p-n$ junctions. The appearance of nano-structured semiconductor materials took place after developing more complex crystal growth techniques: molecular beam epitaxy (MBE) or metalorganic vapor phase epitaxy (MOVPE). Layered structures combining $GaAs$ and $AlAs$ or the alloy $Al_xGa_{1-x}As$ opened the door to a new generation of engineered materials whose optical and electrical properties can be designed with those growth techniques. The choice for these materials is based on the similarity of their lattice constant. This significantly reduces the inter-layer strain and permits the growth of high quality layers whose thickness can be also reduced up to tens of nanometers.

The technological pursuit was directed to create efficient lasing nanostructured materials, known as Vertical Cavity Surface Emitting Lasers (VCSELs), demonstrated in 1979 [9]. The efforts in research aimed to lower the VCSEL lasing threshold and to force single mode emission; as a result, semiconductor microcavities (MCs) were created, inaugurating a second generation of advanced engineered-materials. MC structures are composed by a planar emitting active medium surrounded by two high quality mirrors, the so-called distributed Bragg reflectors (DBRs), which are composed by many thick layers of semiconductors. Nowadays, there are many applications of optical MCs in technology, for example, III-V semiconductors MCs are used to control the laser emission spectra in long-distance data transmission through optical fibers. MCs also permit the narrowing of the laser spot-size that is necessary in the read/write processes of CD, DVD and blue-ray players.

The quest for thresholdless lasers [10] improved the quality of the DBR-mirrors, so that now cavity-photons can be kept between the mirrors for times long enough to be absorbed and emitted by the active media, a quantum well (QW), many times creating excitons. In such conditions, the oscillation between the photon- and the exciton-state renders a new quasi-particle called exciton-polaritons [11]. The properties of polaritons combine the ones of its constituents, and so, on the one hand polaritons possess strong dipole-dipole and Coulomb interactions from its excitonic part. This makes polaritons suffer strong nonlinear phenomena, such as parametric scattering. On the other hand, from its photonic part, polaritons have a mass which is five orders of magnitude lighter than that of electrons in vacuum. The light polariton mass renders a macroscopic de Broglie wavelength that becomes comparable to the polariton inter-particle distance — in the micrometer scale —

at temperatures up to 300 K. In this framework of solid state physics, new quantum many-body phenomena can be explored using simple experimental apparatus.

Particles with an integer spin are classified as bosons and they can constitute a single state composed by a macroscopic number of them [12] in a well-known phenomenon called Bose-Einstein condensation (BEC). The experimental demonstration of this effect was firstly accomplished in cold atom gases by the group of C. E. Wieman and E. A. Cornell [13] and a few months later by the group of W. Ketterle [14]. Atomic BECs, apart from their interest in fundamental physics, have proven their potential for practical applications as, for example, interferometric devices with high precision measurements for gravimeters, accelerometers, etc [15–19].

Polaritons condensates, as a real alternative candidate in solid-state physics to atomic-BECs, were demonstrated by several groups 10 years ago [20–22] They display very attractive, flexible qualities such as high-temperature of condensation [23] and the possibility to achieve condensation through electrical injection [24, 25], among many others.

The difference of polariton condensates when compared to BEC atomic gases, is that polaritons have a finite lifetime, and that they recombine and are emitted outwards the MC. This fact conditions the theoretical formalism in which polariton are described, given the impossibility to define a "temperature" of the system, and instead of having a thermodynamic equilibrium polaritons are said to constitute "out-of-equilibrium" BEC condensates — we will discuss these differences in the first part of this thesis. However, the photonic emission of the polaritons after their annihilation presents an unprecedented advantage in the experimental measurements when compared with those performed in atomic BECs or superfluid helium. The wavefunction of the emitted photons is an exact copy of the intra-cavity polariton wavefunction and thus the optical measurements performed on these photons bestow full information about, for example, the polariton dynamics and their coherence.

The manipulation of the condensed polariton flow has revealed its superfluid behavior [26–28]. Recent progresses augur the appearance of a new generation of optoelectronic devices based on MC-polaritons in the next years [29–45], some of them discussed in this thesis [46–48].

Abstract

THIS PhD thesis is devoted to the study of exciton-polariton condensates in semiconductor MCs. Here these gases made of exciton-photon mixtures are optically excited, both resonantly and non-resonantly, and imaged in real and momentum spaces by means of optical setups. The possibility to measure the polariton coherence and phase properties, together with their emission energy and dynamics, allows for the full characterization of the polariton macroscopic wavefunctions. Thanks to their photonic character, polaritons can be manipulated at will through all-optical excitation and constitute promising building-blocks for the realization of polariton-based semiconductor chips.

The thesis is divided in four parts comprising the following Chapters.

Part I describes the physics background underlying the creation of polariton condensates. The interactions between cavity photons and semiconductor quasi-particles, excitons, involved in the formation of polaritons are described from a classical, semiclassical and quantum points of view in Chapter 1. Special attention is given to light propagation in MCs and its interaction with the dipole moment of QW excitons that form polaritons. High bosonic densities and liquid Helium temperatures enable polaritons to condense into a single coherent state out-of-equilibrium, whose basic properties are discussed in Chapter 2 and contrasted with those of other types of BECs.

We present in Part II a detailed description of the samples, Chapter 3, and experimental procedures, Chapter 4, used for excitation and detection of the samples emission. We also describe the experimental methodology used for the data analysis in the different parts of this thesis.

Part III is devoted to the study of four fundamental phenomena in polariton condensates: the optical parametric oscillator (OPO) regime, the quantized rotation of superfluid polaritons, the coherence dynamics of polariton in momentum space and the polariton spin textures induced by the spin Hall effect in quasi-1D systems for which the energy relaxation plays an important role.

The occurrence of topological defects in polariton superfluids in the OPO regime has been demonstrated in the last years in the group hosting this PhD work [28, 49]. These studies reported the observation of metastable persistent polariton superflows sustaining a quantized angular momentum, m, after applying a 2-ps laser pulse carrying a vortex state. A gain response in the condensate lasts for tens of picoseconds during which no dissipation of the circulating currents is detected. Angular momentum was also transferred directly into the steady state, which acquired permanent rotation for as long as the vortex remains within the condensate. Although there are similarities with rotating trapped atomic gases, non-equilibrium systems show a richer phenomenology. In Chapter 5, the deterministic behavior of both the onset and dynamics of vortex-antivortex

pairs generated by perturbing the system with a pulsed probe is explained in terms of local supercurrents [50, 51]. Simulations elucidate the reason why topological defects form in pairs and can be detected by direct visualizations in multishot OPO experiments.

Chapter 6 studies the polariton OPO dynamics in a 40 μm-$\varnothing$ pillar MC using a *pump + probe* excitation scheme, that differs from common resonant excitation [29, 52–54]. A long-lived (1 ns) OPO polariton signal is ignited and we observe a transient behavior, characterized by a collective oscillation of the condensed OPO polaritons in the pillar. Thereafter, they reach a quasi-steady state displaying a ring-like emission pattern, due to repulsive interaction with the exciton population in the center of the pillar. We study the full dynamics of the creation and decay of this OPO condensate in real and momentum-space. The interpretation of the experimental measurements of the spatial emission dynamics is supported by theoretical simulations using the two-dimensional (2D) coupled Gross-Pitaevskii (GP) equations for excitons and photons [55].

Exciton-polariton BECs, due to their dual wave-particle nature, share many properties with classical waves as, for instance, interference phenomena, which are crucial to gain insight into their ondulatory character. In Chapter 7 we show that the use of momentum-space optical interferometry, which avoids any spatial overlap between two parts of a macroscopic quantum state, presents a unique way to study coherence phenomena in polariton condensates. We address a longstanding question in quantum mechanics: "*Do two components of a condensate, which have never seen each other, possess a definitive phase?*" [56]. A positive answer to this question is experimentally obtained for light-matter condensates [57], created under precise symmetry conditions, in semiconductor MCs, taking advantage of the direct relation between the angle of emission and the in-plane momentum of polaritons.

In Chapter 8, we investigate optically the spin transport by propagating polariton condensates along macroscopic distances in a quasi-one-dimensional (1D) MC ridge. Under circularly polarized, non-resonant excitation, a sinusoidal precession of the spin in real space is observed, whose phase depends on the emission energy. Through polarization- and time-resolved spectroscopy, we demonstrate that the power and the degree of polarization of the excitation determines the polariton condensate spin textures. The experimental results are compared with simulations of the polariton condensate dynamics based on a generalized GP equation, modified to account for incoherent pumping, decay and energy relaxation within the condensate [58].

Part IV is devoted to the implementation and optimization of polariton devices in quasi-1D MCs. Such systems, which can be reconfigured on the fly, pave the way to widespread applications in the control of quantum fluidic circuits [39, 41, 42].

Many theoretical works [31, 32, 35, 59, 60] anticipate promising perspectives for the implementation and development of polariton circuits in 1D geometries, where the polariton flow can be guided, gated and trapped in many practical ways. After the seminal studies of E. Wertz

and coworkers [36, 40, 61], on the propagation, manipulation and amplification of macroscopically extended polariton condensates, an intense research for probing the practical properties of 1D polariton circuits has thriven, such as the realization of a double-barrier resonant tunneling diode and the implementation of an Mach–Zehnder interferometer with all-optical phase modulation [44, 45].

In a different way, T. Gao and coworkers developed a polariton condensate transistor switch in a quasi-1D MC ridge through non-resonant optical excitation of a MC ridge with two beams [43]. In this device, polaritons are formed at the source, from where they are ballistically ejected towards the edge of the ridge (collector), relaxing their energy in presence of the excitonic reservoir. The polariton propagation can be gated using a 20 times weaker second beam (gate) to switch ON and OFF the flux of polaritons, and therefore, the formation of the trapped collector state. In the first part of Chapter 9 we present a time-resolved study of the logic ON/OFF operation of this polariton condensate transistor switch. The experimental results are interpreted in the light of simulations based on the generalized GP equation, including incoherent pumping, decay, and energy relaxation within the condensate [46].

Following these studies in the second part of Chapter 9 we present a time-resolved study of energy relaxation and trapping dynamics of polariton condensates in a semiconductor MC ridge. In these experiments, the combination of the two non-resonant, pulsed laser sources gives rise to profuse quantum phenomena where the repulsive potentials created by the lasers allow the modulation and control of the polariton flow. We analyze in detail the dependence of the dynamics on the power of both lasers and determine the optimum conditions for realizing an all-optical polariton condensate transistor switch [62].

Chapter 10 addresses an important aspect of the polariton condensate transistor switch: the operation speed of the device by means of excitonic gating. We present a time-resolved photoluminescence (PL) study in real and momentum space of the switch. A study of the device operation dependence on the power of the pulsed gate beam obtains a satisfactory compromise for the ON-OFF signal ratio and switching time of the order of 0.3 and ∼50 ps, respectively. The opposite transition is governed by the long-lived gate excitons, consequently, the OFF-ON switching time is ∼200 ps, limiting the overall operation speed of the device to ∼3 GHz [48].

Further studies on the spin-based polariton transistor switch have been performed in collaboration with the group of Prof. P. Savvidis. Nevertheless, for the sake of limiting the extension of the thesis, we do not include these results here.

In Chapter 11, an approach for the implementation of a logic AND gate is performed under two pulsed, spatially separated and delayed excitation-beams, tuned to the bare exciton mode. In this scheme, we study the dynamics of polariton condensate wave trains that propagate along a quasi-1D waveguide. Through the application of tunable potential barriers the propagating polaritons can be reflected and multiple reflections used to confine and store an initially propagating state.

Energy-relaxation processes allow the delayed relaxation into a long-living coherent ground state. Aside from the potential routing of polariton condensate signals, the system forms an AND-type logic gate compatible with incoherent inputs [47].

Resumen

Esta tesis está dedicada al estudio de condensados de polaritones excitónicos en microcavidades (MCs) semiconductoras. Estos gases compuestos por la mezcla de excitones y fotones se excitan ópticamente, tanto resonantemente como no-resonantemente, y la distribución de la emisión de dichos condensados se reconstruye tanto en el espacio real como en el espacio de momentos mediante sistemas experimentales ópticos. La posibilidad de medir la fase y las propiedades de coherencia de los polaritones, junto con su energía de emisión y su dinámina, permite la caracterización completa de la función de onda macroscópica de los polaritones. Gracias a su carácter fotónico, los polaritones pueden ser manipulados a voluntad mediante excitación puramente óptica y constituyen "bloques de construcción fundamentales" en la realización de dispositivos semiconductores basados en polaritones.

Esta tesis se divide en cuatro partes, comprendiendo los Capítulos siguientes.

La Parte I describe la base fundamental de la física subyacente en la creación de los condensados de polaritones. Las interacciones entre los fotones de la cavidad y las cuasi-partículas de los semiconductores, llamadas excitones, que participan en la formación de polaritones, se describen desde puntos de vista clásicos, semiclásicos y cuánticos en el Capítulo 1. Se presta atención especial a la propagación de la luz en las MCs semiconductoras y a su interacción con el momento dipolar de los excitones de pozo cuántico que da lugar a la formación de polaritones. La obtención de una alta densidad bosónica y el uso de bajas temperaturas de helio líquido permiten que los polaritones condensen en un único estado coherente fuera-de-equilibrio, cuyas propiedades básicas se discuten en el Capítulo 2 y se contrastan con las de otros tipos de condensados de Bose-Einstein.

En la Parte II se presenta una descripción detallada de las muestras de MCs semiconductoras empleadas en los experimentos, Capítulo 3, los procedimientos experimentales usados para la excitación y detección de la emisión de las muestras, Capítulo 4. También se describe la metodología experimental utilizada para el análisis de datos en las diferentes partes de esta tesis.

La Parte III se dedica al estudio de cuatro fenómenos fundamentales en condensados de polaritones: el régimen del oscilador paramétrico óptico (OPO), la rotación cuantificada de polaritones superfluidos, la dinámica de coherencia de polaritones en espacio de momentos y las texturas del "spin" de los polaritones inducidas por el efecto spin-Hall óptico en sistemas cuasi-1D en los que la relajación de energía juega un papel importante.

La aparición de defectos topológicos en superfluidos de polaritones en el régimen OPO se ha estudiado en los últimos años en el grupo anfitrión de este trabajo de doctorado [28, 49]. Estos estudios demostraron la observación de superfluidos persistentes meta-estables de polaritones, capaces de mantener un momento angular cuantizado, m, después de su excitación con un pulso láser de 2-ps de duración llevando consigo un vórtice de luz con momento angular m. La respuesta

de ganancia del condensado dura decenas de picosegundos, período durante el cual no se detecta ninguna disipación de las corrientes circulantes de polaritones. El momento angular también se pudo transferir directamente al estado estacionario de los polaritones, que adquieren una rotación permanente durante el tiempo que el vórtice se matiene en el condensado. A pesar de que hay similitudes con sistemas formados por gases atómicos confinados y en rotación, los sistemas de no-equilibrio de polaritones muestran una fenomenología más rica. En el Capítulo 5, el comportamiento determinista de la formación y la dinámica de pares de vórtices-antivórtices, generados por perturbaciones del sistema con haces pulsados de luz láser ("pruebas"), se explica en términos de supercorrientes locales de polaritones [50, 51]. Las simulaciones llevadas a cabo en este trabajo elucidan los motivos por los cuales los defectos topológicos se forman en parejas y explican por qué dichos pares de vórtice-antivórtice pueden ser detectados mediante una visualización directa en experimentos de OPO con disparos múltiples del láser de "prueba".

El Capítulo 6 estudia la dinámica de polaritones OPO en una MC con forma de pilar cuyo diámetro es 40 μm-$\varnothing$. Se ha empleado en la excitación un esquema de *bombeo + prueba*, que difiere de la excitación resonante comúnmente empleada [29, 52–54]. Se logra encender una señal de polaritones OPO de gran duración (1 ns) y se observa un comportamiento transitorio caracterizado por una oscilación colectiva de los polaritones OPO condensados en el pilar. A continuación de dicho periodo transitorio, los polaritones alcanzan un estado cuasi-estacionario mostrando una distribución de la emisión en forma de anillo, debido a la repulsión excitónica localizada en el centro del pilar. Estudiamos en detalle la dinámica completa de la creación y decaimiento de este condensado OPO tanto en el espacio real como en el de momentos. La interpretación de las medidas experimentales de la dinámica de emisión se apoya en simulaciones teóricas que emplean las ecuaciones de Gross-Pitaevskii (GP) en dos dimensiones para excitones y fotones [55].

Los condensados de Bose-Einstein de polaritones excitónicos, debido a su naturaleza dual onda-corpúsculo, comparten muchas propiedades con ondas clásicas como, por ejemplo, fenómenos de interferencia, los cuales son cruciales para comprender mejor su carácter ondulatorio. En el Capítulo 7 mostramos que el uso de la interferometría óptica en el espacio de momentos, sin que exista ningún solapamiento espacial entre dos partes de un estado cuántico macroscópico, presenta una manera única para estudiar los fenómenos de coherencia en los condensados polaritones. En este Capítulo abordamos a una pregunta de larga data en la mecánica cuántica: "*¿Poseen una fase definida dos componentes de un condensado que jamás se han visto el uno al otro?*" [56]. Obtenemos experimentalmente una respuesta positiva a esta pregunta en el caso de condensados de luz-materia (polaritones), que se han creado bajo condiciones precisas de simetría, en MCs semiconductoras, aprovechando la relación directa entre el ángulo de emisión de los fotones y la proyección del momento de los polaritones en el plano de la MC [57].

En el Capítulo 8 investigamos ópticamente el transporte de "spin" en condensados de polaritones propagantes a lo largo de distancias macroscópicas en MCs cuasi unidimensionales (1D).

Mediante excitación no resonante con luz láser polarizada circularmente, se observa una precesión sinusoidal del spin de los polaritones en el espacio real, siendo la fase de dicha oscilación dependiente de la energía de emisión de los polaritones. A través de espectroscopia resuelta en polarización y en tiempo, se demuestra que la potencia y el grado de polarización de la excitación determinan las texturas de spin de los condensados polaritónicos. Los resultados experimentales se comparan con simulaciones de la dinámica de condensados de polaritones basadas en una ecuación de GP generalizada, la cual ha sido modificada para dar cuenta del bombeo incoherente, el decaimiento de los polaritones y su relajación de energía dentro del condensado [58].

La Parte IV está dedicada a la implementación y optimización de dispositivos de polaritones en MCs cuasi-1D. Estos sistemas, que pueden ser re-configurados con facilidad, abren un camino para obtener aplicaciones dedicadas al control de circuitos de fluidos cuánticos [39, 41, 42].

Existen muchos trabajos teóricos que anticipan perspectivas prometedoras para la aplicación y desarrollo de circuitos polaritones en geometrías 1D [31, 32, 35, 59, 60], donde el flujo de polaritones puede ser guiado, controlado y atrapado en diversas formas prácticas. Los estudios seminales de E. Wertz y sus colaboradores [36, 40, 61], sobre la propagación, manipulación y amplificación de condensados de polaritones extendidos microscópicamente, han provocado una investigación intensa para indagar en las propiedades prácticas de los circuitos de polaritones 1D, dando lugar a trabajos tales como la realización de un diodo-túnel resonante con doble barrera y la implementación de un interferómetro de Mach-Zehnder, donde la modulación de la fase de los polaritones en dicho interferómetro se realiza mediante excitación óptica [44, 45].

De una manera diferente, T. Gao y sus colaboradores desarrollaron un transistor-interruptor de polaritones condensados en una MC con una estructura cuasi-1D MC, mediante la excitación con dos haces de luz láser no resonantes [43]. En este dispositivo, los polaritones se forman en la fuente, desde donde son expulsados balísticamente hacia el borde de la estructura 1D (colector), relajando su energía en presencia de un reservorio de excitones. La propagación de los polaritones puede ser controlada empleando un haz láser secundario (puerta), el cual tiene una intensidad 20 veces más débil que la de la fuente, pero siendo capaz de cambiar el estado del transistor entre ON y OFF (encendido y apagado, respectivamente) bloqueando el flujo de polaritones hacia el colector, y por lo tanto, condicionando la formación del estado de colector atrapado. En la primera parte del Capítulo 9 se presenta un estudio resuelto en tiempo del funcionamiento de la lógica operacional ON/OFF de este transistor-interruptor de polaritones condensados. Los resultados experimentales se interpretan a la luz de las simulaciones basadas en la ecuación GP generalizada, incluyendo bombeo incoherente, el decaimiento de los polaritones y su relajación de la energía dentro del condensado [46].

A raíz de estos estudios, en la segunda parte del Capítulo 9 presentamos un minucioso estudio resuelto en tiempo de la relajación de energía de los polaritones y de la captura dinámica de dichos condensados en la MC semiconductora 1D. En estos experimentos, la combinación de dos

fuentes de luz láser no resonantes y pulsadas da lugar a fenómenos cuánticos donde los potenciales excitónicos repulsivos (creados por dichos láseres) permiten la modulación y el control del flujo de los polaritones propagantes en la estructura. Analizamos con detalle la dependencia de la dinámica polaritónica con la potencia de excitación de ambos láseres y determinamos las condiciones óptimas para la realización del transistor-interruptor óptico de polaritones condensados [62].

El Capítulo 10 aborda un aspecto importante del transistor-interruptor de polaritones condensados: la velocidad de operación del dispositivo por medio del control excitónico de la puerta. Presentamos un estudio de la fotoluminiscencia resuelta en tiempo en el espacio real y de momentos del interruptor. El estudio de la dependencia de operación del dispositivo con la potencia de excitación del haz de puerta pulsado nos ha permitido obtener el compromiso satisfactorio del cociente entre las señales de ON-OFF del orden de 0.3 y el tiempo de conmutación de $\sim$ 50 ps. La transición opuesta OFF-ON está condicionada por el largo tiempo de vida de los excitones en la puerta, en consecuencia, el tiempo de conmutación de dicha transición OFF-ON es de $\sim$ 200 ps, lo que limita la velocidad total del funcionamiento del dispositivo a $\sim$ 3 GHz [48].

Se han realizado otros estudios, en colaboración con el grupo del Prof. P. Savvidis, sobre un transistor-interruptor de polaritones basado en el spin de los polaritones. Sin embargo, en aras de limitar la extensión de la tesis, no incluimos aquí estos resultados.

En el Capítulo 11, un nuevo enfoque para la implementación de una puerta lógica tipo AND (conjunción) se realiza bajo excitación con dos haces de luz láser pulsada, separados espacialmente y retrasados temporalmente, cuya energía además ha sido sintonizada a la del modo excitónico. En este esquema, se estudia la dinámica de trenes de ondas de polaritones condensados que se propagan a lo largo de una guía de onda cuasi-1D. A través de la aplicación de barreras de potencial sintonizables, los polaritones al propagarse sufren reflexiones y estas múltiples reflexiones se emplean para confinar y almacenar un estado polaritónico inicialmente propagante. Los procesos de relajación de energía que experimentan los polaritones permiten la relajación retardada en un estado de baja energía con un largo tiempo de vida. Aparte de la capacidad para re-direccionar la propagación de los polaritones, este sistema constituye una puerta lógica tipo AND compatible con entradas de excitación incoherentes [47].

Dear Reader, in first place, thank you for reading this book, we hope that you enjoy it as much as we did planning, performing and analyzing the experiments that it compiles. Here we give you some brief indications for a comfortable reading of this thesis.

The different Sections (and corresponding lower sub-levels of organization) on each Chapter will be referred in the text with the symbol § and the corresponding linked reference number (see also the list of Contents for a detailed organization of the book). We highly recommend to follow the Nomenclature, where three different categories index and describe the Abbreviations, Physical Constants and Symbols used along this book, indicating the page where they appear for the first time.

Many of the experimental figures showing the dynamics of polariton condensates in the different Chapters are accompanied by external links to the websites where the videos of such figures are permanently available. We strongly suggest to consult those videos in order to gain insight in the time-resolved phenomena (when demanded by the reader). Most of the references of this thesis are hyperlinked to their publication websites in order to ease a faster access of the reader to the cited work.

Please, take your seat and fasten your seat belt.

Acknowledgements

All the achievements described in this PhD thesis would not have been possible without the help of great people to whom I am immensely indebted. I would like to first acknowledge my advisor, Prof. Luis Viña, who trusted in me to make this work. I am grateful for all his efforts done along these years, providing all the available tools for carrying out our research in the best possible way, and for careful guiding me with his clever scientific advice.

I have benefited during these years from positive interactions with the highly qualified research team SemicUAM, at the Departamento de Física de Materiales, Universidad Autónoma de Madrid. When performing the experiments, I had the pleasure to learn from Prof. José Manuel Calleja, Prof. Maria Dolores Martín, Dr. Guilherme Tosi and Dr. Jorge Cuadra. The success of our group work is also greatly due to the theoretical support provided by Prof. Carlos Tejedor, along with help and fruitful discussions with Prof. Francesca Marchetti, Andrei Berceanu, Dr. Alejandro González, Dr. Elena del Valle, and Dr. Fabrice Laussy (Fabrice, thank you so much for helping me out with my LaTeX problems). This thesis would not have been possible without the help of my outstanding international collaborators. Thanks goes to Prof. Pavlos Savvidis and Dr. Peter Eldridge; the interaction and collaboration with these researchers gave rise to many of the experimental results described here. I am specially indebted with Dr. Tim Liew and S. Morina, at the University of Singapore, for collaborating with us and contributing with his always wonderful theoretical simulations.

Very special thanks goes to my profesor and friend Dr. José Luis Brun, who established my connection with Prof. Luis Viña. José Luis trusted in my potential when I met him in my 2^{nd} Physics course in Universidad de Zaragoza. He showed me the doors to a new academic life in Madrid. I am indebted not only for teaching me top-quality Classical Mechanics with clever and exciting ideas [63], but also for constant advise and support (I hope to meet you again in Paris again very soon, last time we missed the front of the Saint Denis Cathedral).

Since 2005, my academic tutor and friend, Dr. José Barquillas, was very supportive, a great advisor and above all, he was and is an outstanding friend. His infinite patience to teach me concepts on electronics (where I was a blockhead) certainly have had a direct, positive effect on the conceptualization of many of the ideas described in this thesis. Your enthusiasm and dedication in teaching are worthy of admiration.

The fact that polaritons emerged as a hot topic in the last years strongly resides on the high-quality samples grown by MBE. I acknowledge Dr. Aristide Lemaître and Prof. Jacqueline Bloch at the Laboratoire de Photonique et de Nanostructures (Marcoussis, France), Prof. Zacharias Hatzopoulos, Dr. Georgios Konstantinidis, Dr. Georgios Deligeorgis and Prof. Pavlos Savvidis (again) at the Institute of Electronic Structure and Laser (FORTH, Heraklion, Greece) for providing the

last-generation samples used to obtain the results presented here. I also greatly acknowledge the friendly and stimulating work environment found during my 6-months stay in the Quantum Dots group leaded by Prof. Pascale Senellart at the Laboratoire de Photonique et de Nanostructures (Marcoussis, France), my next destination. The constant enlightenment from Prof. Pascale Senellart, the support and help from Prof. Loïc Lanco, Dr. Simone Portalupi, Dr. Niccolo Somaschi, Dr. Daniel Lanzillotti-Kimura, Valerian Giesz, Lorenzo de Santis, and Justin Demory culminated in great scientific results, fascinating knowledge and new experimental expertise in a very short (but intense) time. Merci and grazie to all of you.

I would also like to thank all the new fellas I have met in different parts of the world thanks to the fantastic and inspiring conferences that I have attended in recent years. Elena, Max, Maria, Paco, Gabriele, Francesco, and many others, I hope to see you soon, wherever it is!

Talking about new friendships along these years, I would like to mention my Italian friends, Dr. Daniele Candini, Davide Montalegni and Davide Denina, siete splendidi. Thank you so much for your always kind hospitality and thank you for the endless anecdotes that we have lived together, including the hospital stay in La Spezia... All my gratitude is with my good friend Vicente Sanchez de la Blanca, thank you for all these years of friendship and great music.

And last but not least, I want to acknowledge too my friends from "La Mesa": Dr. Juan Carlos Lagomacini, Prof. José Luis Plaza, Dr. Jorge Cuadra, Dr. Guilherme Tosi, Dr. Dipankar Sarkar and Christoph Lingg. Thank you my friends for the wonderful days in the laboratory, the canteen and all the nice moments together.

This PhD Thesis will (hopefully) receive the International Mention thanks to the positive reports that I obtained from the two following researcher post-Docs: Dr. Niccoló Somaschi and Dr. Maksym Sich, to whom I am gratefully indebted. Thank you.

Finally, many funding sources, including Spanish MEC (MAT2008-01555, MAT2011-22997, QOIT-CSD2006-00019) and CAM (S-2009/ESP-1503), European "Clermont4" (235114), Spinoptronics (237252), INDEX (289968) and ESF-RNP POLATOM, allowed for the availability of top-class experimental setups and spreading results in international conferences. I am also grateful to the IMDEA-Nanoscience and the UAM for financial support at the early stages of my thesis and I specially acknowledge an FPI and FPU scholarship from the Spanish Ministry of Science and Innovation, which supported the work presented here. Thanks to the FPU program I could benefit from a 6-months stay in the group of Prof. Pascale Senellart.

Esta Tesis va dedicada muy especialmente, con todo mi cariño y respeto, para mis padres, Luis Antonio y Ana María, a los cuales les debo todo lo que tengo. Mamá, Papá, muchas gracias por vuestra ayuda y paciencia, y por los valores y la educación que me habéis inculcado. No habría llegado hasta aquí sin vuestro apoyo incondicional y sin vuestro amor.

A mi hermana mayor, Dra. Isabel Antón-Solanas, quién abrió senda en la familia con el camino del Doctorado, y a mi hermana Ana, la última de los tres hermanos en llevar a cabo este excitante camino investigador (ánimo) en *GSK Human Performance Lab*.

Finalmente, mis agradecimientos van para Jennifer, tu cariño, tu paciencia y tu apoyo han sido una pieza clave para acabar este trabajo, muchas gracias por acompañarme en este viaje, y los que tengan que venir.

List of Publications

- G. Tosi, F. M. Marchetti, D. Sanvitto, C. Antón, M. H. Szymanska, A. Berceanu, C. Tejedor, L. Marrucci, A. Lemaître, J. Bloch, L. Viña, *"Onset and dynamics of vortex-antivortex pairs in polariton OPO superfluids"*, Physical Review Letters **107**, 036401 (2011).

- C. Adrados, T. C. H. Liew, A. Amo, M. D. Martín, D. Sanvitto, C. Antón, E. Giacobino, A. Kavokin, A. Bramati, and L. Viña, *"Motion of Spin Polariton Bullets in Semiconductor Microcavities"*, Physical Review Letters **107**, 14640 2 (2011).

- R. Spano, J. Cuadra, C. A. Lingg, M. D. Martín, G. Tosi, C. Antón, D. Sanvitto, L. Viña, P.R. Eastham, M. van der Poel, and J. Hvam, *"Coherence properties of 2D and 1D exciton-polariton OPO condensates"*, New Journal Physics **14**, 075018 (2012).

- C. Antón, G. Tosi, M. D. Martín, L. Viña, A. Lemaître and J. Bloch, *"Role of supercurrents on vortices formation in polariton condensates"*, Optics Express **20**, 16366 (2012).

- M. D. Martín, C. Antón, L. Viña, B. Pietka, and M. Potemski, *"Recombination dynamics of excitons and exciton complexes in single quantum dots"*, Europhysics Letters **100**, 67006 (2012).

- C. Antón, T. C. H. Liew, G. Tosi, M. D. Martín, T. Gao, Z. Hatzopoulos, P. S. Eldridge, P. G. Savvidis, and L. Viña, *"Dynamics of a polariton condensate transistor switch"*, Applied Physics Letters **101**, 261116 (2012).

- C. Antón, T. C. H. Liew, G. Tosi, M. D. Martín, T. Gao, Z. Hatzopoulos, P. S. Eldridge, P. G. Savvidis, and L. Viña, *"Energy relaxation of exciton-polariton condensates in quasi-one-dimensional microcavities"*, Physical Review B **88**, 035313 (2013).

- C. Antón, T. C. H. Liew, J. Cuadra, M. D. Martín, P. S. Eldridge, Z. Hatzopoulos, G. Stavrinidis, P. G. Savvidis, and L. Viña, *"Quantum reflections and shunting of polariton condensate wave trains: Implementation of a logic AND gate"*, Physical Review B **88**, 245307 (2013).

- C. Antón, T. C. H. Liew, D. Sarkar, M. D. Martín, Z. Hatzopoulos, P. S. Eldridge, P. G. Savvidis, and L. Viña, *"Operation speed of polariton condensate switches gated by excitons"*, Physical Review B **89**, 235312 (2014).

- C. Antón, G. Tosi, M. D. Martín, Z. Hatzopoulos, G. Konstantinidis, P. S. Eldridge, P. G. Savvidis, C. Tejedor, and L. Viña, *"Quantum coherence in momentum space of light-matter condensates"*, Physical Review B **90**, 081407(R) (2014).

- C. Antón, D. Solnyshkov, G. Tosi, M. D. Martín, Z. Hatzopoulos, P. G. Savvidis, G. Malpuech, and L. Viña, *"Ignition and formation dynamics of a polariton condensate on a semiconductor microcavity pillar"*, Physical Review B **90**, 155311 (2014).

- C. Antón, S. Morina, T. Gao, P. S. Eldridge, T. C. H. Liew, M. D. Martín, Z. Hatzopoulos, P. G. Savvidis, I. A. Shelykh, and L. Viña, *"Optical control of spin textures in quasi-one-dimensional polariton condensates"*, Physical Review B **91**, 075305 (2015).

Oral presentations

- July 29-August 3, 2012, Zurich (Switzerland). 31st International Conference on the Physics of Semiconductors. *"Topological defects in polariton condensates created by Gaussian probe beams"*

- September 9-14, 2012, Cambridge (United Kingdom). POLATOM Network Conference, (presented by **L. Viña**). *"Topological defects and confinement effects on exciton-polariton condensates"*

- December 14, 2012, Miraflores de la Sierra (Spain). XV Jornada de Jóvenes Científicos del Instituto de Ciencia de Materiales Nicolás Cabrera. *"Dynamics of a polariton condensate transistor switch"*

- May 27-31, 2013, Crete (Greece). 14th Conference on Physics of Light-Matter Coupling in Nanostructures (presented by **L. Viña**). *"Dynamics of a polariton condensate transistor switch"*

- July 17-18, 2013, Valencia (Spain). XXXIV Meeting of the Real Sociedad Española de Física - Symposium "Electronic Properties of Semiconductors, Graphene and Novel Two Dimensional Layered Materials". *"Momentum space interferences as an evidence of remote quantum coherence of condensates"*

- July 1-5, 2013, Wroclaw (Poland). 20th International Conference on Electronic Properties of Two-Dimensional Systems and 16th International Conference on Modulated Semiconductor Structures (presented by **L. Viña**). *"Implementation of an AND gate with Bose-Einstein polariton condensates"*

- September 9-13, 2013 Rome (Italy). 13th Conference on Optics of excitons in Confined Systems (presented by **M. D. Martín**). *"Realization of an AND gate with Bose-Einstein exciton-polariton condensates"*

- September 9-13, 2013 Rome (Italy). 13th Conference on Optics of excitons in Confined Systems. *"Energy relaxation and trapping dynamics of polariton condensates in quasi-1D microcavities"*

- December 19, 2013, Miraflores de la Sierra (Spain). XVI Jornada de Jóvenes Científicos del Instituto de Ciencia de Materiales Nicolás Cabrera. *"Quantum coherence of light-matter condensates that have never seen each other"*

- August 10-15, 2014, Austin (United States of America). 32nd International Conference on the Physics of Semiconductors. *"Momentum space interferences as an evidence of remote quantum coherence of condensates"*

- August 10-15, 2014, Austin (United States of America). 32nd International Conference on the Physics of Semiconductors (presented by **L. Viña**). *"Quantum ping-pong and shunting of polariton condensate wave trains: Implementation of a logic AND gate"*

- November 19, 2014, Madrid (Spain). IFIMAC's Seminar. *"Quantum coherence in momentum space of light-matter condensates"*

- December 4 2014, Madrid (Spain). ICMM-CSIC Seminar (presented by **L. Viña**). *"Optical Manipulation of Polariton Condensates on a Chip"*

- February 3-8, 2014, Medellin (Colombia). 16th Conference on Physics of Light-Matter Coupling in Nanostructures (presented by **L. Viña**). *"Optical Manipulation of Polariton Condensates on a Chip"*

Contents

List of Figures

List of Tables

Nomenclature

Abbreviations

0D 110
Zero-dimensional.

1D xi
One-dimensional.

2D xi
Two-dimensional.

3D 4
Three-dimensional.

Al 3
Aluminium.

AlAs viii
Aluminium arsenide.

$Al_xGa_{1-x}As$ viii
Aluminium gallium arsenide with x $(1-x)$ concentration of Al (Ga).

AND xii
Basic digital logic gate that implements logical conjunction.

As 3
Arsenic.

AV 55
Antivortex.

BEC ix
Bose-Einstein condensation/condensate.

BKT 48
Berezinskii-Kosterlitz-Thouless.

CB 5
Conduction Band.

CCD 94
Charge-coupled device.

Cd 23
Cadmium.

CdTe 23
Cadmium Telluride.

cGPE 59
Complex Gross-Pitaevskii equation.

CNOT 169
Controlled NOT gate.

CQED 31
Cavity Quantum-ElectroDynamics.

cw 56
Continuous-wave.

DBR viii
Distributed Bragg Reflector.

FFT 105
Fast Fourier Transform.

FP 13
Fabry-Pérot.

FWHM 16
Full Width at Half Maximum.

Ga 3
Gallium.

GaAs viii
Gallium arsenide.

GaN 23
Gallium nitride.

GP xi
Gross-Pitaevskii.

He 78
Helium.

HH 78
Heavy hole, see equation (3.0).

iFFT 105
Inverse Fast Fourier Transform.

LBO 93
Lithium Triborate (LiB_3O_5).

LG 103
Laguerre-Gauss.

LH 78
Light hole, see equation (3.0).

LPB 25
Lower polariton branch.

MBE viii
Molecular beam epitaxy.

MC viii
Microcavity.

MCP 97
Micro-channel plate.

MOVPE viii
Metalorganic vapor phase epitaxy.

MPB 79
Medium Polariton Branch.

N 23
Nitrogen.

Ne 78
Neon.

NOT 228
Logic gate that implements logical negation operation.

ODLRO 47
Off-diagonal long-range order.

OPA 57
Optical parametric amplification.

OPO x
Optical parametric oscillator.

PL xii
Photoluminescence.

QD 167
Quantum Dot.

QW viii
Quantum well.

Rb 47
Rubidium.

RRS 60
Resonant Rayleigh scattering.

SCR 3
Strong Coupling Regime.

SEM 80
Scanning Electron Microscopy.

S-O 32
Spin-Orbit (coupling).

Te 23
Tellurium.

TE 82
Transverse electric mode.

TM 82
Transverse magnetic mode.

TMM 13
Transfer Matrix Method.

TOPO 57
Triggered optical parametric oscillator.

UPB 25
Upper polariton branch.

V 55
Vortex.

VB 5
Valence Band.

VCSEL viii
Vertical Cavity Surface-Emitting Laser.

WCR 24
Weak Coupling Regime.

WP 136
Wave Packet.

ZnO 55
Zinc oxide.

Physical Constants

ϵ_0 10
Permittivity of free space, its value is $\epsilon_0 = 8.854187817 \times 10^{-12}$ F/m, see equation (1.8).

μ_0 10
Permeability of free space, its value is $\mu_0 = 4\pi \times 10^{-7}$ V s/(A m), see equation (1.8).

μ_B 155
Bohr magneton $\mu_B = 5.7883818066 \times 10^{-5}$ eV T^{-1}.

a_B 9
Bohr radius, see equation (1.4).

c 10
Speed of light in vacuum, its value is $c = 2.99792458 \times 10^8$ m/s, see equation (1.10).

e 8
Electric charge carried by a single electron $e = 1.602176565 \times 10^{-19}$ C, see equation (1.3).

$\hbar$ 7
Reduced Planck constant $\hbar = h/(2\pi) = 6.58211928(15) \times 10^{-16}$ eV s.

k_B 35
Boltzmann constant $k_B = 8.6173324 \times 10^{-5}$ eV K^{-1}, see equation (2.1).

m_e 162
Free electron mass, its value is $m_e = 0.510998910 \times 10^6$ eV/c^2.

Symbols

$\varnothing$ xi
Diameter.

α 59
Polariton repulsive interaction coupling constant, see equation (2.36).

$\alpha_{1/2}$ 159
Interaction strength between polaritons with parallel/antiparallel spins, see equation (8.2).

β 63
Phenomenological coefficient whose value is chosen to describe the exciton reservoir decay into the polariton condensate, see equation (2.40).

Δ 4
High symmetry line inside the Brillouin zone.

$\Delta_{\mathrm{TM,TE}}$ 84
Energy splitting between the TE and TM modes in a MC, see equation (3.2).

Δ_p 60
Effective pump detuning, see equation (2.37).

δ 14
Phase acquired by the beam while propagating inside FP medium, see equation (1.21).

$\delta^{(2)}(\mathrm{r})$ 50
2D Dirac delta function.

ϵ 8
Electric permittivity, see equation (1.3).

ϵ_B 21
Normalized background dielectric constant, see equation (1.33).

ϵ_i 35
ith energy level, see equation (2.1).

Γ 4
High symmetry point at the center of the Brillouin zone.

Γ 59
Polariton decay rate, see equation (2.36).

Γ_A 66
Decay rate of active excitons, see equation (2.44).

Γ_D 66
Decay rate of dark excitons, see equation (2.46).

Γ_I 66
Decay rate of inactive excitons, see equation (2.45).

Γ_{NL} 159
Nonlinear loss corresponding to polaritons scattering out of the condensate, see equation (8.2).

Γ_R 63
Rate at which excitons decay, see equation (2.40).

Γ_x 22
Exciton radiative broadening describing the exciton radiative lifetime, see equation (1.35).

γ_c 23
Cavity photon lifetime, see equation (1.36).

κ 141
Difference between the k_x values of two counter-propagating polaritons overlapping and interfering in real space.

Λ 4
High symmetry line inside the Brillouin zone.

λ_0 14
Wavelength of a electromagnetic wave in the vacuum, see equation (1.21).

λ_T 37
de Broglie wavelength, which reflects the average quantum size of the particles conforming the gas at temperature T, and V is the volume of the gas, see equation (2.7).

μ 10
Magnetic permeability, see equation (1.8).

μ_c 35
Chemical potential, see equation (2.1).

μ_{eh} 9
Electron-hole reduced effective mass $\mu_{eh} = \frac{m_e m_h}{m_e + m_h}$, see equation (1.5).

ν, ν' 68
Phenomenological parameters determining the strength of the polariton energy relaxation, see equation (2.47).

ϖ 50
Vorticity, see equation (2.34).

ρ 161
Parameter fitted to the experimental results, which relates the condensation rates for $\sigma^{+/-}$-polarized polaritons from the excitonic reservoir, $W_- = \rho W_+$.

ρ_e 9
Charge density.

Σ 4
High symmetry line inside the Brillouin zone.

ς 29
Hopfield coefficient, see equation (1.52).

$\sigma^{+/-}$ 34
Right-/left-hand circularly polarized detection (or light excitation, depending on the context), see equation (1.57).

$\tau_{fast(slow)}$ 194
Energy fast (slow) decay time at the source, see Chapter 9.

$\Phi_{e(h)}$ 8
Electron (hole) wave function in band structure theory.

$\phi(\mathbf{k})$ 4
Bloch-like solution in a periodical potential.

χ 29
Hopfield coefficient, see equation (1.52).

$\Psi_1^{coh}(k_x)$ 138
Coherent state formed by the two left-propagating polariton condensates (spatially separated by a distance d) in $\mathbf{k}$-space, see equation (7.3).

ψ 59
Polariton wavefunction, see equation (2.36).

ψ_σ 159
Spinor polariton wavefunction, where $\sigma = \pm$ denotes the two circular polarizations of polaritons, see equation (8.2).

$\psi_{1,2}^{A,B}$ 137
Propagating polariton wave packets, where the superscript (A, B) refers to the excitation beam and the subscript 1(2) is for WPs initially moving to the left (right), *i.e.* with $k_x < 0$ ($k_x > 0$).

Ω_R 23
Rabi splitting, see equation (1.38).

$\overrightarrow{\Omega}_k$ 155
In-plane MC vector proportional to the effective magnetic field $\overrightarrow{H}_{\text{eff}} = \frac{\hbar}{\mu_B g}\overrightarrow{\Omega}_k$.

$\Omega_{x(y)}$ 155
Component of the in-plane vector $\overrightarrow{\Omega}_k$, see equation (8.1).

ω 14
Wave frequency of a electromagnetic wave, see equation (1.21).

ω_{LT} 21
Wave frequency accounting for the longitudinal-transverse splitting, see equation (1.33).

A 136
Laser beam impinging on the ridge and creating two propagating polariton condensates (see also B), used in Chapters 7 and 11.

$A_{i(r)}$ 14
Incident (reflected) amplitude into the interface in a FP interferometer, see equation (1.19).

$A_{L(R)}$ 233
Left- (right-) propagating polariton condensate created by the A laser beam, used in Chapter 11.

$A^{+/-}(z)$ 11
Scalar, positive/negative propagating electric field, see equation (1.11).

a 4
GaAs lattice parameter, 0.565 nm.

$\hat{a}_{\mathbf{p}}/\hat{a}_{\mathbf{p}}^{\dagger}$ 42
Operator annihilating/creating a particle in the single-particle state with momentum $\mathbf{p}$ in the second quantization picture, see equation (2.8).

$\mathbf{B}$ 10
Magnetic induction field.

B 11
Scalar magnetic field, see equation (1.11).

B 136
Laser beam impinging on the ridge and creating two propagating polariton condensates (see also A), used in Chapters 7 and 11.

$B_{L(R)}$ 233
Left- (right-) propagating polariton condensate created by the B laser beam, used in Chapter 11.

b 4
$GaAs$ lattice parameter in reciprocal space, ~ 11 nm^{-1}.

$\hat{b}_{\mathbf{p}}/\hat{b}^{\dagger}_{\mathbf{p}}$ 43
Quasi-particle annihilation/creation operator related to the single-particle operators through the Bogoliubov transformations, see equation (2.16).

C 170
Collector, region at the edge of the ridge.

$\hat{C}/\hat{C}^{\dagger}$ 28
Photon annihilation/creation operator, see equation (1.45).

$\mathscr{C}_A$ 237
Quasi-static, trapped polariton condensate formed at the border of the ridge under $(B, A) = (0, 1)$ excitation conditions, used in Chapter 11.

$\mathscr{C}_{A-B}$ 239
Quasi-static, trapped polariton condensate formed between A and B repulsive potentials, used in Chapter 11.

$\mathscr{C}_{B\wedge A}$ 232
Quasi-static, trapped polariton condensate formed at the border of the ridge under $(B, A) = (1, 1)$ excitation, used in Chapter 11.

$\mathscr{C}_C$ 170
Condensate trapped at C.

$\mathscr{C}_{S-G}$ 170
Condensate trapped between S and G.

c_s 42
Speed of sound, defined as $c_s = \sqrt{\frac{gN}{mV}}$ in the weakly-interacting Bose gas, see equation (2.13).

$\mathbf{D}$ 10
Electric displacement.

D 63
Reservoir spatial diffusion coefficient, see equation (2.40).

$\mathscr{D}^{P}$ 189
Experimental line as a guide to the eye that marks the horizon discontinuity between propagating polaritons and noise along the ridge.

$\mathscr{D}^{S-P}$ 190
Experimental line as a guide to the eye that marks the horizon discontinuity between the PL at S and the propagating polaritons along the ridge.

d 138
Spatial distance between two polariton WPs propagating in the same direction at the same speed overlapping and interfering in momentum space (sometimes also dubbed d_{AB}), see equation (7.5).

d_{12} 140
Spatial distance between the two polariton WPs ψ_1^B and ψ_2^A stopped at the exciton barriers A and B, respectively.

$\mathbf{E}$ 9
Electric field.

E 11
Scalar electric field, see equation (1.11).

E 6
Energy.

E_0 42
Ground state energy in the weakly-interacting Bose gas, see equation (2.10).

E_B 9
Binding energy of the ground exciton state, see equation (1.6).

$\hat{E}_{LP}$ 59
Operator representing the parabolic dispersion of the lower polariton branch, see equation (2.36).

$E_{e(h)}$ 7
Electron (hole) ground state energy in band structure theory.

E_{gap} 5
Energy difference between the maximum of the valence band and the minimum of the conduction band.

$\mathbf{F}_d$ 63
Drag force exerted by a defect on a flowing quantum fluid, see equation (2.38).

G 170
Gate.

G_σ 161
Constant representing the strength of forward scattering processes between excitons in the reservoir and in the condensate, $\sigma = \pm$ denotes the two circular polarizations of polaritons, see equation (8.4).

g 42
Interaction coupling constant in a weakly-interacting Bose gas, see equation (2.9).

$g_{R/I/D}$ 65
Strengths of interaction with the active (R), inactive (I) and dark (D) hot exciton states, respectively, see equation (2.43).

g 155
Electron g-factor.

$\mathbf{H}$ 9
Magnetic field.

$\mathcal{H}$ 3
Hamiltonian of a semiconductor crystal, see equation (1.1).

$\mathcal{H}_e$ 3
Hamiltonian for the *valence electrons* with the ions frozen in their equilibrium positions, see equation (1.1).

$\mathcal{H}_{e-h}$ 8
Hamiltonian accounting for electron-hole Coulomb interactions.

$\mathcal{H}_{e-ions}$ 3
Hamiltonian describing changes in the electronic energy as a result of the displacements of the ions from their equilibrium positions, see equation (1.1).

$\mathcal{H}_{e-ph}$ 21
Hamiltonian accounting for the electron-photon interactions, see equation (1.30).

$\mathcal{H}_{ions}$ 3
Hamiltonian describing the interaction between atomic nuclei and cores electrons, see equation (1.1).

$\overrightarrow{H}_{\mathbf{eff}}$ 155
Effective magnetic field accounting for the optical Spin Hall effect.

$\mathcal{I}$ 25
Imaginary part of a complex function, see equation (1.41).

$I\left(\mathscr{C}_C\left[\mathscr{C}_{S-G}\right]\right)$ 192
Emission intensity of the condensate trapped at the collector [between source and gate], see Chapter 9.

$I\left(S\right)$ 192
Emission intensity at the source position, see Chapter 9.

$\mathbf{J}$ 9
Current density.

K 4
High symmetry point on the surface of the Brillouin zone.

$\mathbf{k}$ 4
Momentum space vector.

k 10
Scalar value of the wave vector of a electromagnetic wave in a media with refractive index n, $k = k_0 n$.

k_0 10
Scalar value of the wave-vector of a electromagnetic wave (whose wavelength is λ_0) in vacuum $k_0 = 2\pi/\lambda_0$.

L 4
High symmetry point on the surface of the Brillouin zone.

$\hat{L}/\hat{L}^\dagger$ 28
Lower polariton annihilation/creation operator, see equation (1.49).

L_c 13
Thickness of a medium in a FP interferometer.

L_{DBR} 23
DBR effective length, see equation (1.36).

$\mathbf{M}$ 9
Magnetic polarization per unit volume.

m x
Quantized angular momentum.

m^* 7
Effective mass given by $m^* = \hbar^2 / \left(\frac{\partial^2 E}{\partial k^2}\right)$.

$m_{e(h)}$ 8
Electron (hole) effective mass, see equation (1.3).

m_P 59
Polariton effective mass.

N 36
Total number of particles in a BEC, see equation (2.3).

$N(\mathbf{r}, t)$ 63
Incoherent reservoir of excitons, see equation (2.39).

N_0 36
Number of particles in the ground state of a BEC, see equation (2.3).

$N_{A/I/D}$ 65
Density distributions of active (A), inactive (I) and dark excitons (D), respectively, see equation (2.43).

N_T 36
Number of particles out of the BEC (thermal component of the gas), see equation (2.4).

n 10
Refractive index, see equation (1.10).

n_{12} 141
Condensate formed by the spatial overlap between ψ_2^A and ψ_1^B at $x = 0$.

$n_1^{coh}(k_x)$ 138
Density of the order parameter $\Psi_1^{coh}(k_x)$ in $\mathbf{k}$-space, see equation (7.4).

$n_{C(X)}$ 28
Number of photons (excitons) in the second quantization picture, see equation (1.46).

n_i 35
Distribution of particles in thermal equilibrium at the ith energy level, see equation (2.1).

$n_j^{A,B}$ 137
Density of the propagating polariton WPs, given by $n_j^{A,B} = (\psi_j^{A,B})^\dagger \psi_j^{A,B}$, where $j = 1, 2$.

P 9
Electric polarization per unit volume.

P 42
Pressure of a weakly-interacting Bose gas, see equation (2.11).

P 59
Pumping rate from the reservoir, see equation (2.36).

$P_{A(B)}$ 136
Pump power of excitation with $A(B)$ laser beam, used in Chapters 7 and 11.

$P_{G(S)}$ 176
Pump power of excitation with the gate (source) laser beam, used in Chapters 9 and 10.

P_{NR} 63
Nonresonant pumping feeding the exciton reservoir, see equation (2.40).

P_{th} 70
Pump strength threshold for polariton condensation.

p 42
Momentum in the second quantization picture, see equation (2.8).

Q 4
High symmetry line on the surface of the Brillouin zone.

Q 16
Quality factor, see equation (1.28).

R 12
Reflectivity, see equation (1.17).

$\mathcal{R}$ 25
Real part of a complex function, see equation (1.41).

$\mathfrak{R}$ 65
Operator accounting for polariton energy-relaxation processes, see equation (2.42).

r 8
Electron-hole distance, see equation (1.3).

r 11
Fresnel amplitude reflection coefficient, see equation (1.16).

r 63
Rate at which polaritons scatter from the excitonic reservoir, see equation (2.39).

S 4
High symmetry line on the surface of the Brillouin zone.

S 170
Source.

s_0 34
Total degree of polarization, see equation (1.56).

$s_{x/y/z}$ 34
Degree of linear/diagonal/circular ($x/y/z$) polarization, see equation (1.57).

T 12
Transmittance, see equation (1.17).

T 35
Temperature, see equation (2.1).

$T_{\mathbf{on}}$ 196
Time delay between maxima of the source and collector intensities, see Chapter 9.

t 11
Fresnel amplitude transmission coefficient, see equation (1.16).

t_D 66
Linear coupling factor between the inactive and the dark exciton reservoir, see equation (2.45).

t_R/t'_R 66
Linear/nonlinear coupling factor between the inactive and the active reservoir, see equation (2.44).

$t_{down(up)}$ 196
Time spent by the polariton PL to drop (raise) from an intensity of 1 (0.5) up to the value of 0.5 (1), in a normalized scale, see Chapter 9.

U 4
High symmetry point on the surface of the Brillouin zone.

$\hat{U}/\hat{U}^\dagger$ 28
Upper polariton annihilation/creation operator, see equation (1.49).

$u_{\mathbf{p}}$ 43
Coefficient of the Bogoliubov transformation, see equation (2.19).

V 23
Matrix element describing the coupling strength between the exciton resonance and the cavity mode, see equation (1.36).

V_σ 161
Spin dependent effective potential experienced by polaritons, where $\sigma = \pm$ denotes the two circular polarizations of polaritons, see equation (8.4).

$V_{A(B)}$ 137
Local effective-barrier potential created by the A (B) excitation pulsed laser, used in Chapters 7 and 11.

$V_{e(h)}$ 7
Potential energy of electrons (holes) in band structure theory.

$\mathbf{v}_p$ 60
Flow velocity, see equation (2.37).

$v_{-\mathbf{p}}$ 43
Coefficient of the Bogoliubov transformation, see equation (2.19).

v^P 191
Speed of propagation of polaritons that propagate towards C.

v^S 190
Speed of propagation of polaritons at S.

W 4
High symmetry point on the surface of the Brillouin zone.

W_0 161
Peak condensation rate for the σ^+-polarized polaritons from the excitonic reservoir, see equation (8.3).

$W_{+/-}$ 161
Condensation rate for the $\sigma^{+/-}$-polarized polaritons from the excitonic reservoir, W_- is given by $W_- = \rho W_+$, see equation (8.3).

X 4
High symmetry point on the surface of the Brillouin zone.

$\hat{X}/\hat{X}^\dagger$ 28
Exciton annihilation/creation operator, see equation (1.45).

Z 4
High symmetry line on the surface of the Brillouin zone.

z 8
Axis in the confinement direction in a QW, see equation (1.3).

Part I

Background

Chapter 1

Semiconductor Microcavities

In this Chapter the main physical processes behind light-matter interaction in semiconductor microcavities (MCs) are described. Special attention is given to $AlGaAs$-based distributed Bragg reflector-microcavities (DBR-MCs), with embedded quantum wells (QWs), in the strong coupling regime (SCR), which is the physical system underlying all the results obtained in this thesis.

1.1 Semiconductor crystals

A first attempt to physically describe a semiconductor crystal is to write up the Hamiltonian describing all possible interactions between the crystal constituents. As this is clearly impossible to compute, a number of approximations has to be made, according to which phenomena are to be described. The first is to separate electrons into two groups: *core electrons*, the ones in the filled orbitals localized around the nuclei forming the ion cores; and the *valence electrons*, the ones in the unfilled orbitals that can move around the crystal.

The next approximation usually invoked is the *Born-Oppenheimer* or *adiabatic approximation*, that assumes that electrons respond almost instantaneously to the movement of the nuclei or, in other words, that to the electrons the ions are essentially stationary. On the other hand, ions cannot follow the motion of the electrons and they see only a time-averaged adiabatic electronic potential. The Hamiltonian of a semiconductor crystal can then be written as:

$$\mathcal{H} = \mathcal{H}_{ions} + \mathcal{H}_e + \mathcal{H}_{e-ions} \tag{1.1}$$

The first term, $\mathcal{H}_{ions}$, describes the interaction between atomic nuclei and cores electrons. Its ground state accounts for the crystalline structure. As an example, we describe Gallium Arsenide compounds, which are the materials used on the experiments performed in this work. $GaAs$ has a

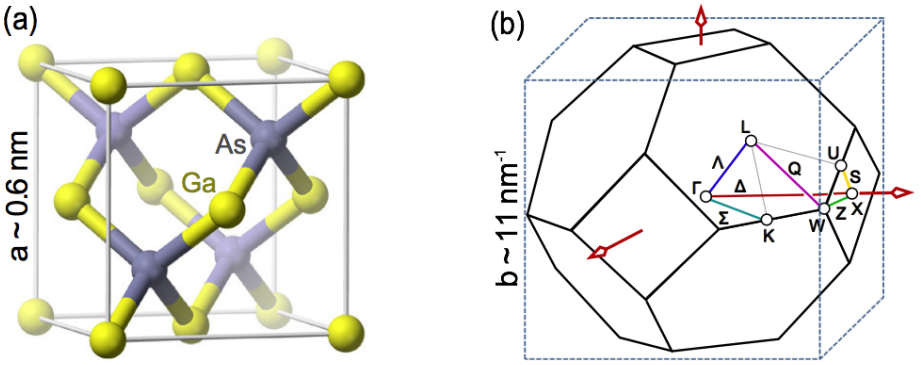

FIGURE 1.1: *GaAs* crystal structure in real and reciprocal spaces. (a) Zincblende unit cell, showing *Ga* and *As* atoms linked together in a tetrahedral structure. a is the lattice parameter. (b) 1^{st} Brillouin zone inside a cubic unit cell, with special high-symmetry points denoted by Γ, X, L, K, W and U, while high-symmetry lines joining some of these points are labeled as Λ, Σ, Δ, Q, Z and S. b indicates the typical lattice parameter in reciprocal space for GaAs. Figure adapted from Wikipedia site for Zincblende structure description.

zincblende cubic crystal structure, where each *Ga* (*As*) atom is surrounded by four *As* (*Ga*) atoms placed at the vertices of a tetrahedron [see Fig. 1.1(a)], where *Ga* atoms are represented by yellow spheres and *As* by grey ones. The square box in this figure defines the *unit cell* which, in a perfect crystal, is repeated side-by-side all over the crystal dimensions. In *GaAs*, the lattice parameter is $a = 0.565$ nm.

Before describing the other two terms in Eq. 1.1, let us first define a fundamental concept in condensed matter physics: the 1^{st} *Brillouin zone*. Eigenstates of the Hamiltonian described in Eq. 1.1 are usually written in momentum ($\mathbf{k}$) basis, defining a reciprocal space which is related to propagation directions inside the crystal. Periodical potentials implies Bloch-like solutions $\phi(\mathbf{k})$, whose values for any $\mathbf{k}$ are mapped into a small region in reciprocal space, the primitive unit cell, called 1^{st} *Brillouin zone*. Figure 1.1(b) shows the 1^{st} *Brillouin zone* of a *GaAs* crystal, whose typical size given by $b = 2\pi/a \sim 11$ nm^{-1}. Its high-symmetry points and directions are named by Greek and capital letters (see the Nomenclature list, where these symbols are alphabetically ordered and described).

The term $\mathcal{H}_{ions}$ also accounts for crystal collective excitations, such as *phonons* (quasi-particles representing vibrational excitations of the crystal, characterized by a definite energy and momentum). The phonon dispersion curves in a GaAs crystal are shown in Fig. 1.2 where, instead of showing the energy as a function of all possible three-dimension (3D) $\mathbf{k}$ values, high-symmetry directions defined in Fig. 1.1(b) are chosen. In the diamond- and zincblende-type lattices there are two atoms per primitive unit cell, and hence there are six phonon branches. These are divided into three acoustic-phonon (the three lower energy curves) and three optical-phonon branches

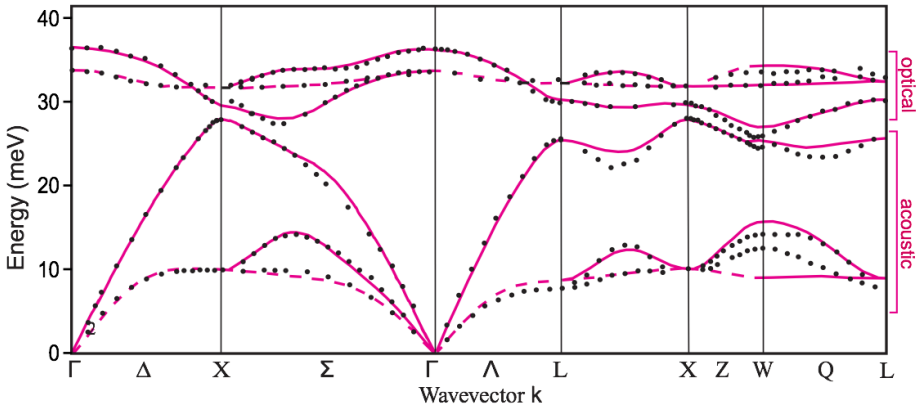

FIGURE 1.2: GaAs phonon dispersion curves along high-symmetry directions of the 1^{st} Brillouin zone, measured by inelastic neutron scattering (dots) and calculated using a rigid-ion model (lines). The horizontal axis and its dimensions are defined in Fig. 1.1(b). The three upper modes are known as optical-phonons and the three lower ones acoustic-phonons. Adapted from Ref. [67].

(Fig. 1.2). Along high-symmetry directions the phonons can be classified as transverse or longitudinal according to whether the displacements are perpendicular or parallel to the propagation direction.

The middle term in Eq. 1.1, $\mathcal{H}_e$, is the Hamiltonian for the *valence electrons* with the ions frozen in their equilibrium positions. Again, different approximations may be taken: in the *mean-field approximation*, every electron experiences the same averaged potential that includes the nuclei and core electrons. Also, the highly attractive nuclei potentials may be replaced by smoother *ion pseudopotentials* that include core electrons, yielding slowly oscillating valence electron wavefunctions. Such approximations yield to solutions that are determined by the specific chemical nature of each material. These solutions are again given in energy vs momentum basis as a *single electron dispersion*, also known as *band structure*. Figure 1.3 provides the $GaAs$ band structure, calculated by the pseudopotential technique [67], along the main symmetry directions of the 1^{st} Brillouin zone. According to the *Pauli's Exclusion Principle*, each eigenstate can only accommodate up to two electrons of opposite spin. At zero temperature, electron fill up all the *valence band* (VB), defined by the energy states below 0 eV. As temperature increases, or any other external excitation is given to electrons, they might acquire enough energy as to start filling also the *conduction band* (CB).

The energy difference between the maximum of the VB and the minimum of the CB is known as *bandgap*, E_{gap}. In $Al_xGa_{1-x}As$ compounds, the bandgap at room-temperature varies between 1.42 eV ($x = 0$, $GaAs$) and 2.16 eV ($x = 1$, $AlAs$). For $x < 0.35$, the bandgap is direct (the minimum of the CB and the maximum of the VB are at the same wave-vector $\mathbf{k} = 0$), which makes this material good for optical applications, since transitions of electrons from VB to CB and vice-versa happens without any change in momentum, and so no phonon contributions are needed.

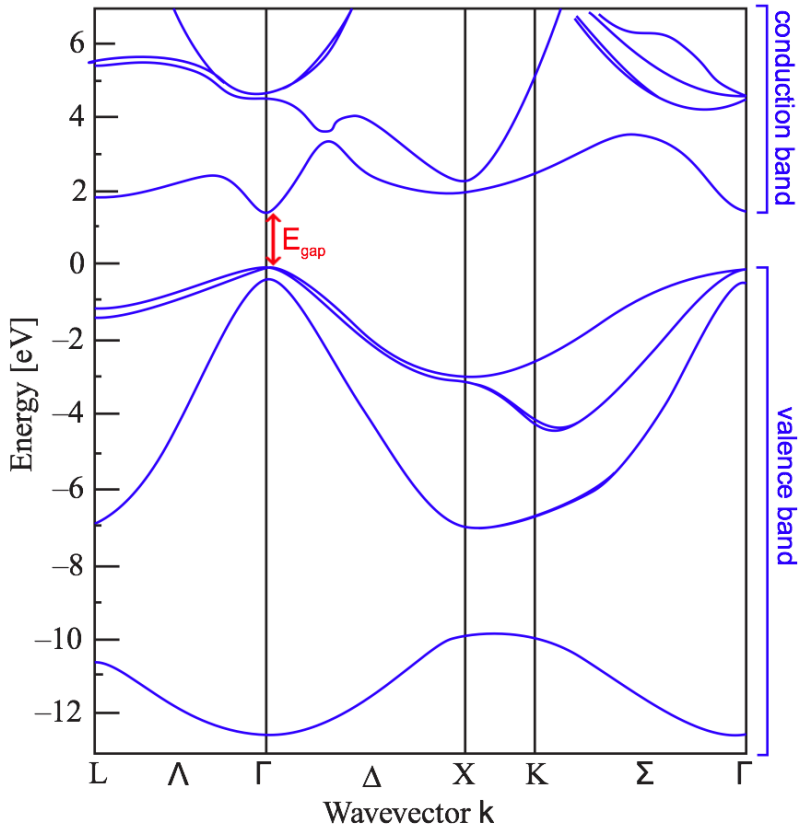

FIGURE 1.3: GaAs electron dispersion curves, calculated by the pseudopotential technique. The horizontal axis and its dimensions are defined in Fig. 1.1(b). Positive energy branches are named as *conduction band* whereas negative ones as *valence band*. Adapted from Ref. [67].

Finally, the last term in Eq. 1.1, $\mathcal{H}_{e-ions}$, describes changes in the electronic energy as a result of the displacements of the ions from their equilibrium positions. $\mathcal{H}_{e-ions}$ is also known as *electron-phonon interaction*, since under the second quantization picture it accounts for scattering between electron and phonon to final states through momentum and energy exchange. When electrons are excited from their equilibrium state to higher energy ones, $\mathcal{H}_{e-ions}$ accounts for electron thermalization by loosing energy to lattice phonons. When external radiation excites electron-hole pairs in the sample, close to the point $E = E_{gap}$, Γ, (see Fig. 1.2), electrons and holes relax to lower energy states by converting their excess energy to phonons. If the excess energy is higher (smaller) than the lattice optical-phonons energies, this relaxation is fast (slow) through interactions that exchange high (small) energy and momentum. Finally, the emission produced by the recombination of relaxed electron-hole pairs renders full information of the bandgap of the semiconductor.

1.2 Excitons

In a semiconductor at zero temperature, the fundamental optical excitation consists on the promotion of an electron from the top of the VB to the bottom of the CB. The state left empty in the VB can be pictured as a positive charge in an empty band, which is defined as a quasi-particle called hole. This enables us to consider the VB masses[1] as positive in all calculations, despite the fact that from the single electron picture they have negative curvature (see Fig. 1.3). The two highest energy branches in the VB dispersion are called heavy-hole and light-hole branches, according to their curvatures.

The properties of the electron and the hole are both described by the band structure within the one-electron approximation. Negatively charged electrons in the CB and positively charged holes in the VB are subject to Coulomb attraction. This electron-hole interaction gives rise to bound states called *excitons*. In most semiconductors, in particular in the $GaAs$ compounds used in this work, the Coulomb interaction is strongly screened by the valence electrons: the large dielectric constant causes that the electrons and holes are only weakly bound. Such excitons, known as Wannier-Mott excitons, have a typical size of the order of tens of lattices constants and a relatively small binding energy (typically, a few meV).

Confinement of matter excitations (electrons, holes and excitons) can be easily attained in heterostructures composed of layers of different semiconductor materials. 2D confinement is typically created in QWs by embedding a thin layer of a semiconductor crystal between two thick layers of a wider gap semiconductor. Matter excitations with low momentum that fall into the QW layer get trapped in a 2D structure in which movement in the z-direction is inhibited. In these heterostructures quantum confinement effects start to be important when the extension of the excitation wavefunctions are greater or of the same size than the confinement dimension. A characteristic dimension in the systems we are interested in is given by the excitonic size. In $GaAs$ based QWs, confinement sizes of the order of tens of nm or less are necessary to observe quantum confinement effects ($a_B = 11.4$ nm in $GaAs$). Several approaches have been traditionally considered when calculating the eigenfunctions and eigenenergies in a 2D heterostructure. The tight binding [68, 69], pseudopotential [70] and $\mathbf{k}\cdot\mathbf{p}$ [71] methods, which have been widely used in bulk semiconductors, have also proved successful in the determination of the band structure in QWs. Another intuitive method is the envelope wavefunction approach, explained below [72–74].

In 2D systems, the potential energy of electrons and holes, V_e and V_h, are described in the growth direction by QWs whose depth and size can be tuned by changing the layer composition and thickness (see insets in Fig. 1.4). The electron and hole ground state energies, E_e and E_h, and

[1] the effective mass is defined as $m^* = \hbar^2 / \left(\frac{\partial^2 E}{\partial k^2}\right)$, where $E(k)$ is the electron dispersion relation. Note that close to the Γ point in Fig. 1.3 the VB has a negative mass whereas the CB has a positive mass. Note also that the effective mass is inversely proportional to the dispersion curvature.

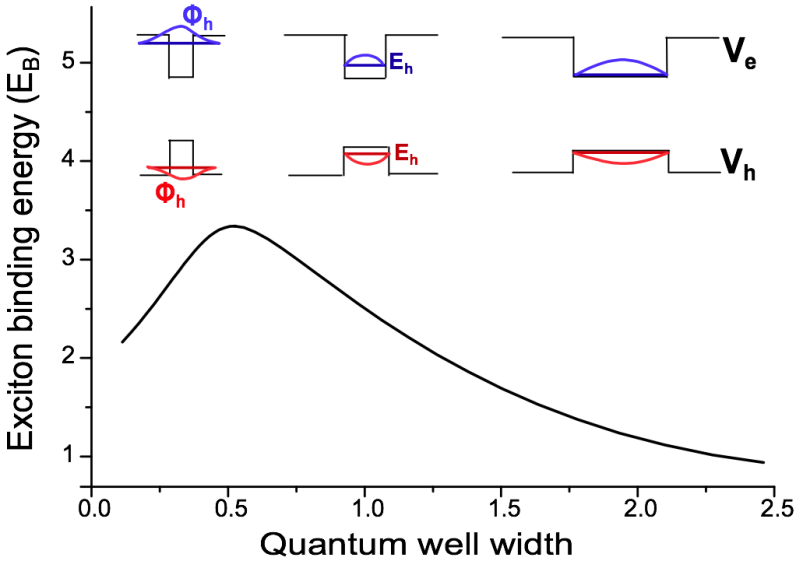

FIGURE 1.4: Exciton binding energy as a function of the QW width (scheme). The insets show the QW potentials, V_e and V_h, and ground state energies, E_e and E_h, and wave functions, Φ_e and Φ_h, of electron (blue) and hole (red), respectively, for different QW widths. Adapted from Ref. [75].

wave functions, Φ_e and Φ_h, are tuned accordingly. The large size of Wannier-Mott excitons makes them strongly sensitive to nanometre-scale variations in the QW size (see graph in Fig. 1.4). These QWs are placed inside the MCs used in this thesis in such a way that the exciton energy can be tuned to resonance with the photons[2] confined inside the MC, as will be discussed in § 1.3.1.

The relative electron-hole motion can be found from the Hamiltonian describing the exciton envelope wavefunction [67, 75]. We then add one extra term in the Hamiltonian 1.1 ($\mathcal{H}_{e-h}$) that describes the electron and hole states confined in a QW and accounts also for the coulomb interactions between them:

$$\mathcal{H} = \mathcal{H}_{ions} + \mathcal{H}_e + \mathcal{H}_{e-ions} + \mathcal{H}_{e-h} \tag{1.2}$$

$$\mathcal{H}_{e-h} = -\frac{\hbar^2}{2m_e}\nabla_e^2 - \frac{\hbar^2}{2m_h}\nabla_h^2 + V_e(z) + V_h(z) - \frac{e^2}{4\pi\epsilon r} \tag{1.3}$$

where $m_{e(h)}$ is the electron (hole) effective mass, z the axis in the confinement direction, e the elementary charge, ϵ the electric permittivity and r the electron-hole distance. Without the potentials $V_e(z)$ and $V_h(z)$, which describe the QW confinement, Eq. 1.3 is equivalent to one describing the electron state in a hydrogen atom (see also § 1.4.3 for a deeper explanation about the band structure and spin of confined excitons). The wavefunction of the $1s$ state of a bulk

[2]From now on we will use indistinctly the nomenclature: photon, photon mode, cavity mode, cavity resonance.

	GaAs **exciton**	**Hydrogen atom**
Reduced mass μ/m_e	0.058	∼1
Bohr radius a_B	15 nm	0.053 nm
Binding energy	4.1 eV	13.6 eV

TABLE 1.1: Comparison between GaAs exciton parameters in the reduced mass approximation and those of the hydrogen atom.

exciton reads:

$$f_{1s} = \frac{e^{-r/a_B}}{\sqrt{\pi a_B^3}} \tag{1.4}$$

with the Bohr radius a_B given as:

$$a_B = \frac{4\pi\hbar^2\epsilon}{\mu_{eh}e^2} \tag{1.5}$$

with $\mu_{eh} = \frac{m_e m_h}{m_e+m_h}$ the electron-hole reduced effective mass. The binding energy of the ground exciton state is

$$E_B = \frac{\hbar^2}{2\mu_{eh}a_B^2} \tag{1.6}$$

Table 1.1 presents the exciton parameters in the reduced mass approximation for $GaAs$, compared to those of the hydrogen atom. The description we have followed so far used the single electron picture. However, under high densities when both excitons and electron-hole plasma are present, the Coulomb carrier-carrier potential becomes important, changing the dielectric constant ϵ. Thus, the exciton binding energy gets progressively reduced. When dealing with materials with bandgap in the infrared region, *i.e.* $GaAs$, this corresponds to a blueshift in the electromagnetic spectra. If the carrier density is further increased, the excitons eventually dissociate [76].

1.3 Electromagnetic fields in matter

In this section we explain in detail how electromagnetic-waves propagate inside materials, giving special attention to DBR-MCs — engineered nanostructures that confine and guide light using index of refraction differences in different materials (see § 1.3.1) The *electric field*, **E**, and the *magnetic field*, **H**, inside a medium are related spatio-temporally to the *charge density* ρ_e, *current density* **J**, *electric polarization per unit volume* **P**, and *magnetic polarization per unit volume* **M**,

through the Maxwell equations (SI units) [77]:

$$\nabla\cdot\mathbf{D} = \rho_e \tag{1.7a}$$

$$\nabla\cdot\mathbf{B} = 0 \tag{1.7b}$$

$$\nabla\times\mathbf{E} = -\partial_t\mathbf{B} \tag{1.7c}$$

$$\nabla\times\mathbf{H} = \mathbf{J} + \partial_t\mathbf{D} \tag{1.7d}$$

The *electric displacement* $\mathbf{D}$, and *magnetic induction field* $\mathbf{B}$, are defined by:

$$\mathbf{D} = \epsilon_0\mathbf{E} + \mathbf{P} = \epsilon\mathbf{E} \tag{1.8a}$$

$$\mathbf{B} = \mu_0\mathbf{H} + \mathbf{M} = \mu\mathbf{H} \tag{1.8b}$$

$$\tag{1.8c}$$

Where ϵ is called *permittivity* and μ, *permeability*.

Considering a medium with neither free charge ($\rho_e = 0$) nor currents ($\mathbf{J} = 0$), taking the curl of Eq. 1.7(c) and using Eqs. 1.7(d) and 1.8, one gets to the following equation for the electric field [78]:[3]

$$\nabla^2\mathbf{E} = \mu\epsilon\frac{\partial^2\mathbf{E}}{\partial t^2} \tag{1.9}$$

which can be identified as a wave equation whose solutions propagate with velocity given by,

$$v = \frac{c}{n} = \frac{1}{\sqrt{\mu\epsilon}} \tag{1.10}$$

where the *refractive index*, n, accounts for the speed of an electromagnetic wave propagating inside a medium. In this thesis we consider n as a scalar with constant value for each material, however, in general it can be a tensor (accounting for birefringence in anisotropic materials), complex-valued (accounting for absorption) and dependent on the electric field (non–linear electric materials) and on the magnetic field (non–linear magnetic materials).

For a light wave propagating in a transverse plane along the z-direction in a medium with wave-vector $k = k_0 n$, where k_0 is the wave-vector in vacuum, solutions of Eq. 1.9 have the general form:

$$E(z) = A^+(z) + A^-(z) = |A^+|e^{ik_0nz} + |A^-|e^{-ik_0nz} \tag{1.11a}$$

$$B(z) = \frac{-i}{k_0c}\partial_z E(z) = \frac{n}{c}|A^+|e^{ik_0nz} - \frac{n}{c}|A^-|e^{-ik_0nz} \tag{1.11b}$$

[3] using the relation $\nabla\times\nabla\times\mathbf{E} = \nabla(\nabla\cdot\mathbf{E}) - \nabla^2\mathbf{E}$ and considering $\nabla\cdot\mathbf{E} = 0$.

which can also be represented using the positive, $A^+(z)$, and negative, $A^-(z)$, propagating electric fields:

$$A^+(z) = \frac{1}{2}\left(E(z) + \frac{c}{n}B(z)\right) \tag{1.12a}$$

$$A^-(z) = \frac{1}{2}\left(E(z) - \frac{c}{n}B(z)\right) \tag{1.12b}$$

The electromagnetic fields at two different positions along the propagation direction, z and $z+a$, are related through a transfer matrix [75]:

$$\mathbf{\Phi}_{z+a} = \mathbf{T}_a\mathbf{\Phi}_z \tag{1.13a}$$

$$\mathbf{\Phi}_z = \begin{pmatrix} E(z) \\ cB(z) \end{pmatrix} = \begin{pmatrix} E(z) \\ \frac{-i}{k_0}\partial_z E(z) \end{pmatrix} \tag{1.13b}$$

$$\mathbf{T}_a = \begin{pmatrix} \cos(k_0 na) & \frac{i}{n}\sin(k_0 na) \\ in\sin(k_0 na) & \cos(k_0 na) \end{pmatrix} \tag{1.13c}$$

Such an approach is very useful when solving Maxwell equations in multilayer dielectric structures, where the transfer matrix across m layers is found as:

$$\mathbf{T} = \prod_{i=1}^{m}\mathbf{T}_i \tag{1.14}$$

In condensed matter materials, light is guided modulating their refraction indices. When coming from the left side of a boundary between two media with refraction indices n_1 (left) and n_2 (right) — see Fig. 1.5(a), the matching of the tangential components of electric and magnetic fields yields:

$$A_1^+ + A_1^- = A_2^+ \tag{1.15a}$$

$$(A_1^+ - A_1^-)n_1 = A_2^+ n_2 \tag{1.15b}$$

The *Fresnel amplitude reflection*, r, and *amplitude transmission*, t, coefficients are defined as:

$$r = \frac{A_1^-}{A_1^+} = \frac{n_1 - n_2}{n_1 + n_2} \tag{1.16a}$$

$$t = \frac{A_2^+}{A_1^+} = \frac{2n_1}{n_1 + n_2} \tag{1.16b}$$

The *reflectivity* R (ratio of reflected to incident energy flux) and the *transmittance* T (ratio of transmitted to incident energy flux) are defined as

$$\mathrm{R} = |r|^2 \tag{1.17a}$$

$$\mathrm{T} = \frac{n_2}{n_1}|t|^2 \tag{1.17b}$$

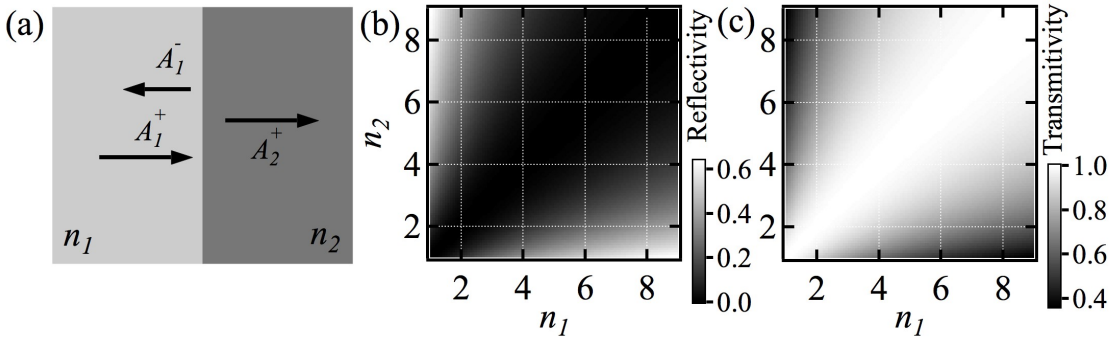

FIGURE 1.5: (a) Schematic representation of an electromagnetic wave incident perpendicularly on an interface between two media with refractive indices n_1 and n_2. Arrows represent the incoming, A_1^+ , the reflected, A_1^-, and the transmitted, A_2^+, amplitudes. (b) Reflectivity between the two media in (a) as a function of n_1 and n_2. (c) Transmitivity between the two media in (a) as a function of n_1 and n_2.

The factor n_2/n_1 comes from the ratio of light velocities in the two media. If losses are negligible, $\mathrm{T} = 1 - \mathrm{R}$.

Figure 1.5(b)/(c) shows the reflectivity R/transmitivity T between the two media with refraction indices n_1 and n_2 [Eqs. 1.16(a) and 1.17(a)]. Clearly the amount of reflected wave on an interface between two media is higher for higher index contrasts, but does not depend on which side of the interface has the higher index. On the other hand, it follows from Eq. 1.16(a) that, when incident on a higher n medium ($n_2 > n_1$), the reflected field has a π-phase shift (r is negative), whereas no shift appears when the field is reflected by a lower n medium ($n_2 < n_1$, r is positive). Moreover, from Eq. 1.16(b), t is always positive and so there is no phase-shift on the transmitted field.

The reflectivity can be improved with the use of multiple interfaces that reflect a wave multiple times. The amplitude reflection and transmission coefficients (r_s and t_s) of a structure containing m layers between two semi-infinite media with refractive indices n_{left} and n_{right} before and after the structure, respectively, can be found by solving the system [75]:

$$\mathbf{T} \begin{pmatrix} 1 + r_s \\ n_{left}(1 - r_s) \end{pmatrix} = \begin{pmatrix} t_s \\ n_{right} t_s \end{pmatrix} \tag{1.18}$$

Moreover, if such interfaces are engineered in such a way that multiple reflections interfere destructively for the transmitted wave, even higher reflectivity can be achieved. This is the main concept behind the high-reflectivity mirrors used in MC structures, described in the next Section.

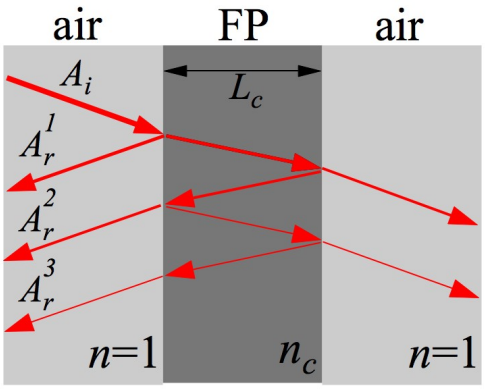

FIGURE 1.6: Schematic FP interferometer, showing a L_c-thick medium with refractive index n_c between air ($n = 1$). The incident, transmitted and reflected beams are represented by arrows, with amplitude on the left side labelled by A_i (incident) and A_r^n (reflected), with $n = 1, 2, 3$.

1.3.1 Microcavities

A microcavity is an optical resonator that confines light to small volumes by resonant recirculation. Its dimensions are related to the wavelength of the mode confined inside — micrometer scale for light modes, hence its name. Although geometrical and resonant properties of MCs are diverse [79], two basic different schemes are used to confine light. In the first, reflection off a single interface is used, for instance from a metallic surface, or from total internal reflection at the boundary between two dielectrics. The second scheme is to use the interference between multiple reflections on microstructures periodically patterned on the scale of the resonant optical wavelength, like *e.g.* in a photonic crystal. Below we describe two devices representative of the second scheme: the Fabry-Pérot interferometer and the DBR-MC. We illustrate all the devices with simulations using the Transfer Matrix Method (TMM), see Eq. 1.13, choosing for that the parameters of a sample investigated on this thesis — described in § 3.2.

1.3.1.1 Fabry-Pérot interferometer

A Fabry-Pérot (FP) interferometer consists ideally of a transparent plate with two reflecting surfaces. It can be found as a central part of most lasers, forming the cavity resonator, but also has its role on more fundamental physics, *e.g.* circuit quantum electrodynamics [80]. Figure 1.6 shows a simple version of a FP interferometer, made of a medium with thickness L_c and refractive index $n_c > 1$ surrounded by air. Let us consider only the waves reflected into the air on the left side of the FP. Light with amplitude A_i incident into the left interface is partially reflected with amplitude:

$$A_r^1 = -|r|A_i \tag{1.19}$$

where $r = (1 - n_c)/(1 + n_c)$ and the minus sign accounts for a π-phase jump from reflection by the higher refractive index FP medium. Another part is transmitted into the FP medium, being partially reflected on the right interface and partially transmitted into air at the left interface with amplitude:

$$A_r^2 = A_i t_- |r| t_+ e^{i\delta} \tag{1.20}$$

where $t_+ = 2/(1 + n_c)$ is the transmission coefficient *into* the FP medium, $t_- = 2n_c/(n_c + 1)$ the transmission coefficient *out from* the FP medium, and

$$\delta = \frac{2\pi}{\lambda_0} 2n_c L_c = \frac{\omega}{c} 2n_c L_c \tag{1.21}$$

is the phase acquired by the beam while propagating inside FP medium, with λ_0 the wavelength in air and ω the wave frequency multiplied by 2π.

The process described above happens many times with the field on the left side of the FP being then the sum of all the reflected beams:

$$A_r = \sum_{n=1}^{\infty} A_r^n = A_i \left(-|r| + t_- t_+ \sum_{n=2}^{\infty} |r|^{2n-3} e^{i\delta(n-1)} \right) = A_i \left[-|r| + \frac{t_+ t_-}{|r|} \left(\frac{1}{1 - r^2 e^{i\delta}} - 1 \right) \right] \tag{1.22}$$

Note that the relative phase between subsequent reflections is always δ. The amount of reflected light — and hence the reflective character of the FP interferometer — depends on interferences between multiple reflections, and so, from Eq. 1.21 on the wave frequency ω and on the FP parameters n_c and L_c.

Figure 1.7(a) shows the electric field profile (simulated using Eq. 1.13) with wavelength in air $\lambda_0 = 800$ nm incident on a FP interface with $n_c = 3.4$ and $L_c = 5\lambda_0/(2n_c) \sim 588$ nm. Putting these values into Eq. 1.21 we have $\delta = 10\pi$, meaning that all the $A_r^{n>1}$ come out of the mirror with the same phase, which have a π-phase difference with respect to the A_r^1 component. The result is that A_r^1 is destructively interfered by all the $A_r^{n>1}$ components, and the only component on the left side of the structure is A_i, making a flat electric field profile $|E| = |A_i|$. Since no light is reflected, the reflectivity of such a FP is zero at 800 nm — see the FP reflectivity dependence on wavelength in Fig. 1.7(c). Inside the FP medium, the difference in phase between right propagating components and left propagating ones is an integer multiple of 5π, generating a standing wave [Fig. 1.7(a)]. Following the same logic, if the incident field has a wavelength such that $\delta = 11\pi$ (or any other odd multiple of π), the second and third reflected components will sum up to:

$$A_r^2 + A_r^3 = A_i t_+ t_- (e^{i11\pi} + r^2 e^{i22\pi}) = A_i t_+ t_- (-1 + r^2) \tag{1.23}$$

which is a negative number since $r^2 < 1$. These two components then constructively interfere with the also negative A_r^1 component, the same holding for $A_r^4 + A_r^5$ and so on. The overall reflected field

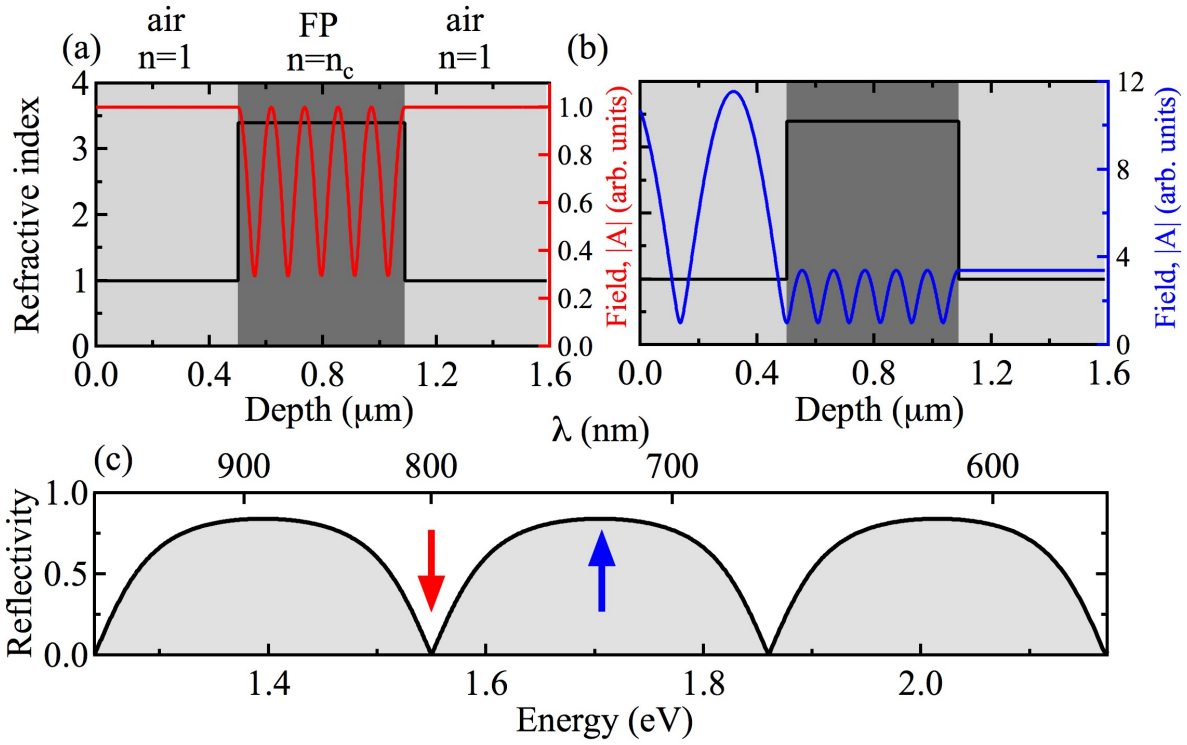

FIGURE 1.7: FP interferometer as simulated by the TMM — Eq. 1.13, using parameters $n_c = 3.4$, $L_c = 588$ nm. The squared-field spatial profile is plotted for (a) $\lambda_0 = 800$ nm (red line) and (b) $\lambda_0 = 727$ nm (blue line). In (a,b) the refractive index is represented by both the black line and the gray color scale. (c) Reflectivity curve for different incident light frequencies, calculated using Eq. 1.18. The red arrow marks the wavelength of the field plotted in (a) whereas the blue arrow marks the wavelength of the field plotted in (b). The choice for the red/blue colors of the arrows in panel (c) reflects the relative value of their higher/smaller wavelengths, whose values were used to simulate the two different light fields plotted in panels (a) and (b), respectively (same situation holds for the next Figs. 1.8 and 1.9).

is then greatly enhanced and the FP becomes reflective. This is indeed observed when calculating the electric field profile for $\lambda_0 = 2\pi/(11\pi)2n_cL_c \sim 727$ nm — see Fig. 1.7(b), where the reflected field generates an interference pattern on the left side of the FP. Accordingly, the reflectivity is maximum at 727 nm — blue arrow in Fig. 1.7(c).

Till now we have considered light impinging perpendicularly to the FP interface. For oblique incidence, the beam should be decomposed inside the cavity into its perpendicular and parallel components to the surface, and then apply a similar analysis to that already described for the perpendicular component. The perpendicular wave-vectors $k_\perp$ for which the FP reflectivity goes to zero are found when making $\delta = 2\pi q$, with q integer, and $k_\perp = 2\pi n_c/\lambda_0$ on Eq. 1.21:

$$k_\perp = \frac{\pi q}{L_c} \tag{1.24}$$

The modes defined by Eq. 1.24, known as *cavity modes*, have an integral number of half-wavelengths that fit into the MC. Their energy E_c is given by:

$$E_c = \hbar ck = \frac{\hbar c}{n_c}\sqrt{k_\parallel^2 + k_\perp^2} = \hbar c\sqrt{k_\parallel^2 + \left(\frac{\pi q}{L_c}\right)^2} \tag{1.25}$$

Equation 1.25 is the dispersion relation of a photon with energy E_c inside the FP cavity. Close to perpendicular incidence ($k_\parallel \ll k_\perp$) it can be approximated to:

$$E_c = E_c^0 + \frac{\hbar^2 k_\parallel^2}{2m_{ph}^*} \tag{1.26}$$

where $E_c^0 = (\hbar\pi qc)/(n_c L_c)$ is the mode energy for perpendicular incidence and $m_{ph}^* = (\hbar\pi q n_c)/(L_c c)$ is the so called *photon effective mass*.

Another important feature of a FP is its reflectivity. It is characterized by the finesse $\mathcal{F}$, which is the ratio between the mode separation (in energy) and the mode full width at half maximum (FWHM). It can be shown that it depends only on the reflectivity of the FP interfaces [75]:

$$\mathcal{F} = \frac{\pi r}{1 - r^2} \tag{1.27}$$

The higher the reflectivity between interfaces, the higher the photon lifetime inside the cavity. The cavity mode width depends on the reflectivity of each mirror and sets the photon lifetime inside the cavity. High quality samples are those with long photonic lifetimes, and so it is useful to define a *quality factor*, defined as the ratio of a resonant cavity frequency, ω_c, to the linewidth (FWHM) of the cavity mode, $\delta\omega_c$ [75].

$$Q = \frac{\omega_c}{\delta\omega_c} \tag{1.28}$$

The Q-factor is an indicator of the photonic losses in the MC in terms of absorption, scattering or leakage through the imperfect mirrors. Q^{-1} is the fraction of photonic energy that is lost in a single round-trip of a photon inside the cavity. The exponentially decaying cavity-photon number has a lifetime given by $\tau = Q/\omega_c$.

The best candidates to achieve high quality factors through the use of high reflectivity mirrors are described in next section.

1.3.1.2 DBR-mirror

The ideas based on multiple inferences described in previous sections to achieve high reflectivity mirrors can be further developed by adding more extra layers to the FP scheme in Fig. 1.6. In fact, if all the components reflected by each layer come out of the structure on the left side with

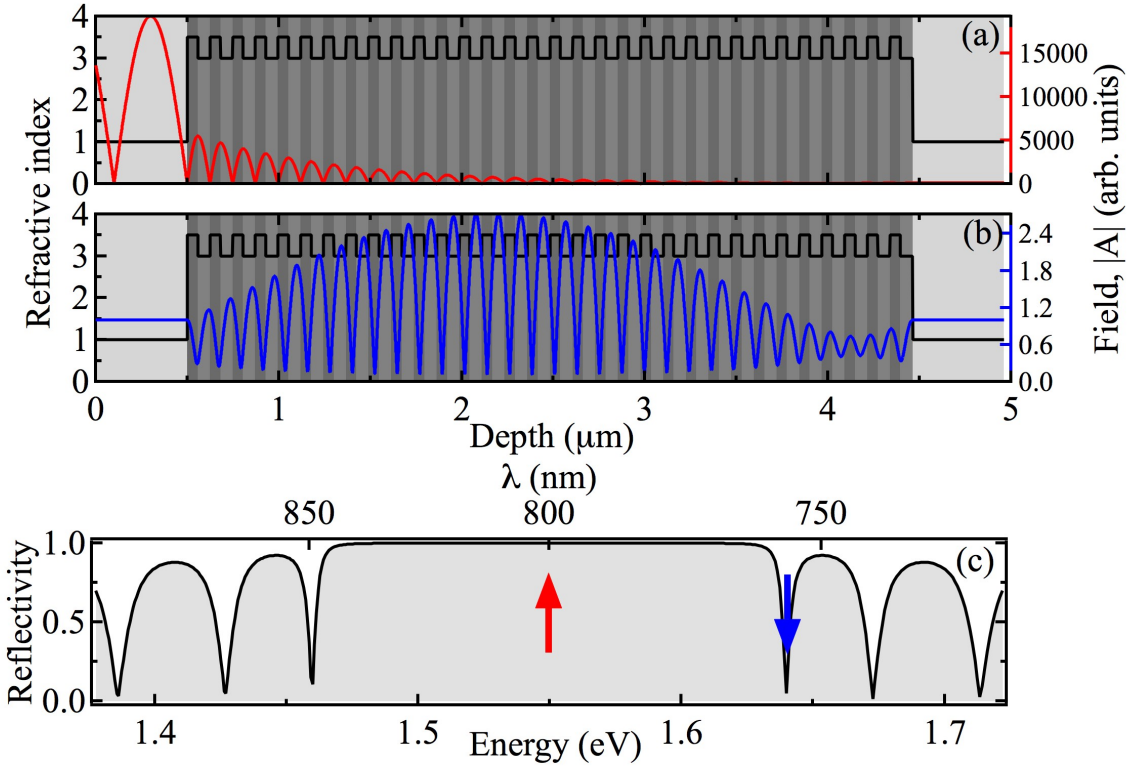

FIGURE 1.8: Bragg mirror as simulated by the TMM - Eq. 1.13, using 32 pairs of layers with $n_1 = 3.5$, $n_2 = 3$, $L_1 \sim 57$ nm and $L_2 \sim 67$ nm. The squared-field spatial profile is plotted for (a) $\lambda = 800$ nm (red line) and (b) $\lambda = 756$ nm (blue line). In (a,b) the refractive index is represented by both the black line and the gray color scale. (c) Reflectivity curve for different incident light frequency, calculated using Eq. 1.18. The red arrow marks the wavelength of the field plotted in (a) whereas the blue arrow marks the wavelength of the field plotted in (b).

the same phase, π-shifted with respect to the incident beam, they will all interfere constructively and the reflectivity will be maximum. This can be achieved, *e.g.*, for a given λ_0 for which we want the structure to be highly reflective, by using for the first layer $n_1 L_1 = \lambda_0/4$, and $n_2 L_2 = \lambda_0/4$ for the second, with $n_1 > n_2$, and then repeating this pair of layers a number of times. Such multilayer periodic structure is called *Bragg mirror*, also known as *distributed Bragg reflector* (DBR) mirror. The working principle relies on light interference: all the waves propagating on the reflection direction, after multiple reflections on all the interfaces present in the structure, are in phase. Conversely, all the waves propagating in the transmission direction interfere destructively.

Figure 1.8(a) shows the electric field profile (simulated using Eq. 1.13) with wavelength in air $\lambda_0 = 800$ nm incident on a DBR-mirror made of 32 pairs of layers with $n_1 = 3.5$, $n_2 = 3$, $L_1 \sim 57$ nm and $L_2 \sim 67$ nm. Under these conditions all the layer reflect the field with the same phase, creating a standing wave made of incident and reflected waves on the left side of the structure (air). Note that the standing wave nodes have zero intensity, meaning that the incident and reflected components have the same magnitude, and hence the mirror is $\sim$100% reflective. Differently from

a FP interferometer, a DBR-mirror possess a considerable field penetration on the cavity due to low index contrast.

Figure 1.8(c) shows the DBR reflectivity dependence on wavelength. Apart from the maximum expected at 800 nm (red arrow), the reflectivity is close to 1 for a wide range of wavelength values centered at 800 nm. Such a plateau region of high reflectivity, known as *stop-band*, becomes broader for higher index contrast between layers and higher number of pair layers. The stop-band is surrounded by transmissive energy modes called *Bragg modes*, whose name is due to the fact that the field distribution is mainly concentrated inside the DBR-mirror — see Fig. 1.8(b) for the field profile corresponding to a wavelength $\lambda_0 = 756$ nm, marked by a blue arrow in Fig. 1.8(c).

1.3.1.3 DBR-microcavity

A semiconductor MC is formed by two DBR mirrors separated by a dielectric layer (the cavity itself), whose thickness determines the cavity mode wavelength, in the same way as in a FP interferometer.

To illustrate how an electromagnetic field behaves inside a semiconductor MC, simulations are performed based on a semiconductor MC similar to the one described in § 3.2: the left DBR is made of 32 pairs of layers with $n_1 = 3.5$, $n_2 = 3$, $L_1 \sim 57$ nm and $L_2 \sim 67$ nm, whereas the right DBR is made of 35 pairs of layers with $n_1 = 3$, $n_2 = 3.5$, $L_1 \sim 67$ nm and $L_2 \sim 57$ nm. Between both mirrors there is a a $5\lambda_0/2$ cavity with $n_c = 3.4$ and $L_c = 5\lambda_0/(2n_c)$.

Figure 1.9(a) shows the electric field profile (simulated using Eq. 1.13) with wavelength in air $\lambda_0 = 800$ nm. Although the mirrors are ∼100% reflective under these conditions interferences with the components reflected by the cavity interfaces makes the whole structure transmissive at this specific wavelength — indicated by a blue arrow in Figs. 1.9(c,d). The effect of the cavity on the reflectivity spectra is to open a sharp minima on the DBR stop band. The field is mainly confined inside the cavity, and so photons entering the cavity remain inside for a long time, which is consistent with a extremely sharp energy linewidth [Figs. 1.9(d)] and high Q-factor. The standing-wave profile with 5 nodes is consistent with the condition $L_c = 5\lambda_0/(2n_c)$. Inside the cavity, the field has maximum amplitude at four antinodes that can be used to couple photons to exciton in QWs put at such positions, as it will be explained in § 1.4.

Figure 1.9(c) shows the DBR reflectivity spectrum. The mirror stop-band can be again observed, with the transmissive Bragg modes (red arrow) having again a field distribution mainly concentrated inside the DBR-mirrors — see Fig. 1.9(b) for the field profile corresponding to a wavelength marked by a red arrow in Fig. 1.9(c).

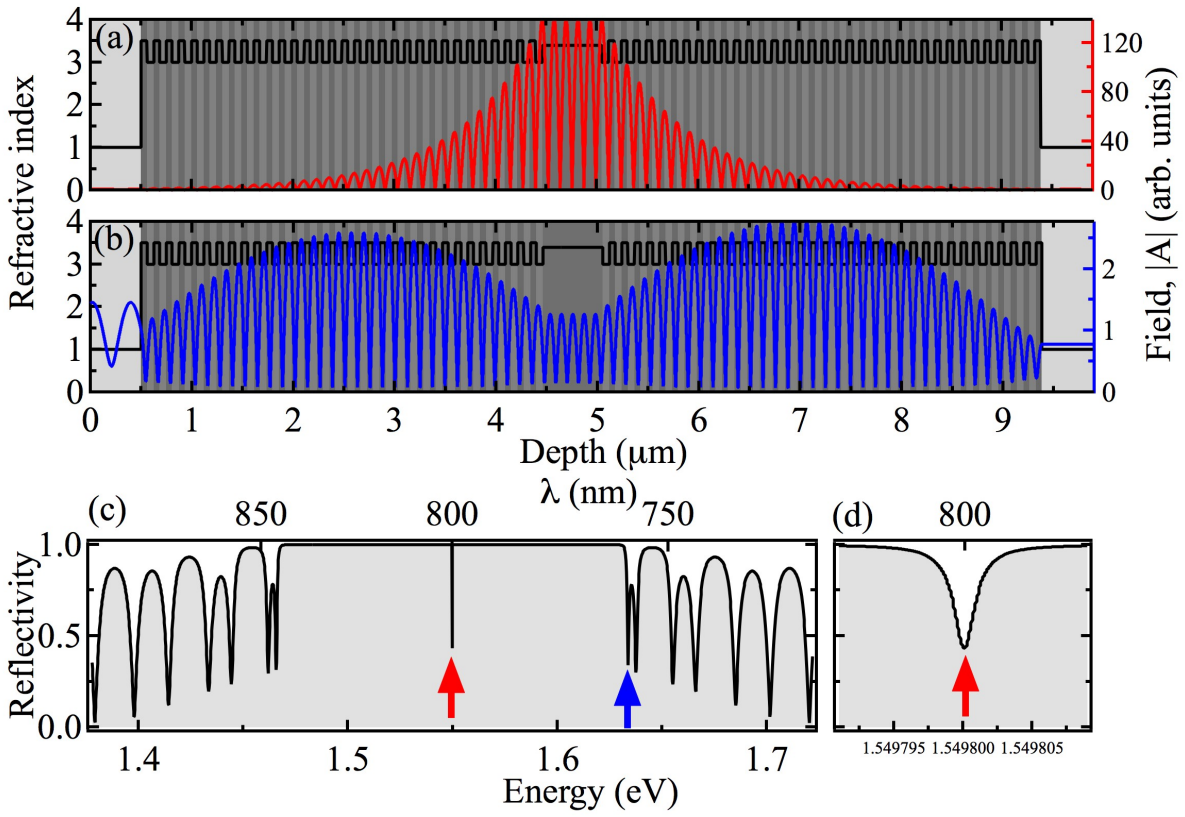

FIGURE 1.9: Semiconductor MC as simulated by the TMM — Eq. 1.13, using 32 pairs of layers with $n_1 = 3.5$, $n_2 = 3$, $L_1 \sim 57$ nm and $L_2 \sim 67$ nm for the left DBR, a $5\lambda_0/2$ cavity with $n_c = 3.4$ and $L_c \sim 588$ nm, and 35 pairs of layers with $n_1 = 3$, $n_2 = 3.5$, $L_1 \sim 67$ nm and $L_2 \sim 57$ nm for the right DBR. The field spatial profile is plotted for (a) $\lambda_0 = 800$ nm (red line) and (b) $\lambda_0 = 759$ nm (blue line). In (a,b) the refractive index is represented by both the black line and the gray color scale. (c) Reflectivity curve for different incident light frequency, calculated using Eq. 1.18. The red arrow marks the wavelength of the field plotted in (a) whereas the blue arrow marks the wavelength of the field plotted in (b). (d) is a zoom of (c) close to the cavity mode (800 nm).

Finally we consider oblique incidence. Reflectivity spectra as a function of incidence angle ϕ_{left} can be calculated by replacing on Eq. 1.18

$$n_{left} \rightarrow n_{left}\cos(\phi_{left}), n_{right} \rightarrow n_{right}\cos(\phi_{right}) \tag{1.29}$$

Figure 1.10 shows the transmittance (T = 1 − R) dispersion for the MC described in Fig. 1.9. As the in-plane momentum $k_{\|}$ increases, the energy of transmissive modes increase, including the weakly transmissive cavity mode.

The dispersion of the cavity mode is expected to be parabolic for a FP cavity (Eq. 1.26), but the wave vector k_z in the direction of the growth axis z is quantized: $k_z = (p+1)\pi/L_c$ [81], where p is an integer and positive number. We calculate the cavity mode energy for perpendicular incidence $E_c^0 = \hbar\pi 5c/(n_c L_c) = 1.5498$ eV and the photon effective mass $m_c^* = \hbar\pi 5 n_c/(L_c c) = 2.2276 \times 10^{-34}$

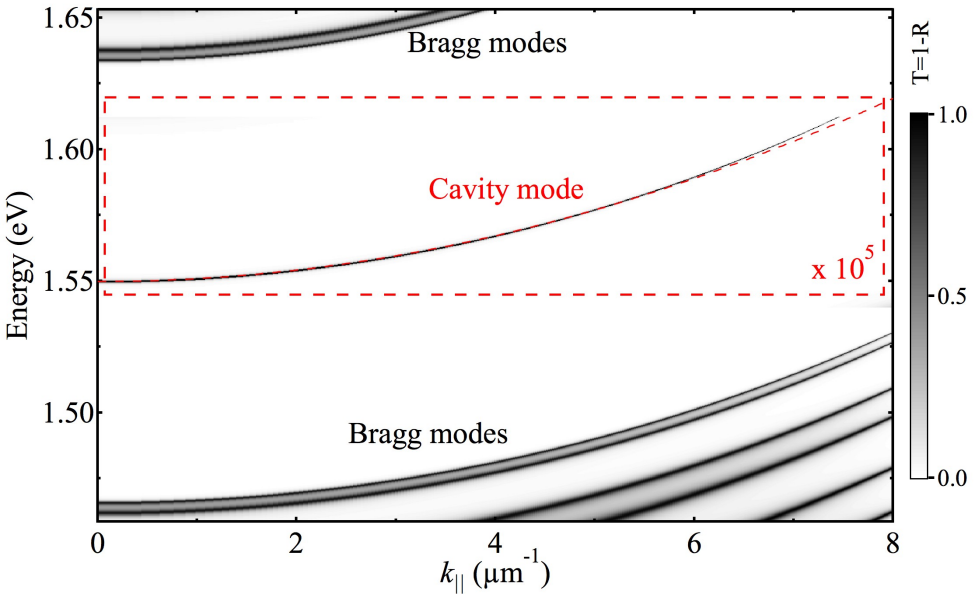

FIGURE 1.10: Transmittance spectra for the MC described in Fig. 1.9, as a function of incident wave energy and k-vector in air, simulated using Eqs. 1.18 and 1.29. High- and low-energy Bragg modes are indicated, as well as the weaker cavity mode. The transmittance of the region inside the dashed gray square has been multiplied by 105 to make the cavity mode to appear visible in the color scale. The cavity mode dispersion, estimated using Eq. 1.26, is plotted as a dashed red line.

kg $= 2.4454 \times 10^{-4} m_e$, where m_e is the electron mass. The resulting parabolic dispersion is plotted in Fig. 1.10 (dashed red line). It fits quite well the simulated cavity dispersion, seen as red.

Photons behave then as massive particles while propagating inside a cavity, with an effective mass extremely light if compared to that of an electron. The photon-exciton quasi-particles described in § 1.4 will also have a very light mass, what is crucial for observing the macroscopic quantum effects described in Chapter 2 at high temperatures.

1.4 Polaritons

When an intrinsic semiconductor crystal is held at cryogenic temperatures, like in all the results presented on this thesis, the thermal energy is not high enough as to promote electrons from the VB to the CB, and so the system remains electronically on its ground state. Excitation to higher modes can be done by laser beams, where the energy carried by photons are absorbed by electrons that acquire higher energy.

The photon dispersion relation was computed in § 1.3 when considering the electromagnetic field propagation inside materials. The cavity mode energy was considered to remain unaffected while propagating inside the media. This is equivalent to add a $\mathcal{H}_{ph}$ term to the Hamiltonian in Eq. 1.2 that accounts for *photonic dispersion*.

In this section we describe how photons drive excitonic-dipole oscillations that changes the energy modes of the system, introducing a last term in Hamiltonian described in Eq. 1.2 called *electron-photon interaction*, $\mathcal{H}_{e-ph}$:

$$\mathcal{H} = \mathcal{H}_{ions} + \mathcal{H}_e + \mathcal{H}_{e-ions} + \mathcal{H}_{e-h} + \mathcal{H}_{ph} + \mathcal{H}_{e-ph} \tag{1.30}$$

1.4.1 Semiclassical light-matter coupling

First we consider light coupling to elementary semiconductor crystal excitations — excitons — and discuss the optical properties of mixed light-matter quasi-particles named exciton-polaritons, which play a decisive role in optical spectra of MCs. Our considerations are based on the classical Maxwell equations coupled to quantum properties of excitons.

In the semiclassical approximation of light-exciton interaction, electron and hole are bounded together by an harmonic potential $\mu_{eh}\omega_x^2$, $\hbar\omega_x$ being the exciton energy and μ_{eh} its reduced mass, $1/\mu_{eh} = 1/m_e + 1/m_h$. The exciton oscillates when light irradiates the atom, $E(t)$, following [67, 75]:

$$\mu_{eh}\ddot{r_x} + \mu_{eh}2\gamma_x\dot{r_x} + \mu_{eh}\omega_x^2 r_x^2 = eE(t) \tag{1.31}$$

where r_x is the electron-hole distance and γ_x the damping caused by non-radiative processes such as scattering with phonons.

Solutions to Eq. 1.31 give a steady state where the exciton also oscillates harmonically with the frequency of the external field, ω [75]:

$$r_x(t) = \frac{e/\mu_{eh}}{\omega_x^2 - \omega^2 - 2i\omega\gamma_x}E(t) \tag{1.32}$$

Following the approach proposed by Hopfield [82], the excitonic influence on the dielectric constant can be calculated. The polarization density $\mathbf{P}$ created by excitons is taken to be proportional to the amplitude of the harmonic oscillator, which constitutes the so-called dipole approximation. Using Eq. 1.32,

$$\mathbf{P}(\omega) = \frac{\epsilon_B 2\omega_x\omega_{LT}}{\omega_x^2 - \omega^2 - 2i\omega\gamma_x}\mathbf{E}(\omega) \approx \frac{\epsilon_B\omega_{LT}}{\omega_x - \omega - i\gamma_x}\mathbf{E}(\omega) \tag{1.33}$$

where ω_{LT} is the so-called longitudinal-transverse splitting, which is proportional to the *exciton oscillator strength*, and ϵ_B is the normalized background dielectric constant that does not contain the excitonic contribution, and the approximation has been taken in the vicinity of the resonant frequency. It must be mentioned that the full derivation of Eq. 1.33 is detailed in the book of

Haug and Koch, see Ref. [83], and that, for the sake of simplicity, in this equation we assumed that excitons do not move, so that $k = 0$.

Equation 1.33 says that the polarization density of an excitonic media depends on the frequency of the electric field. From Eq. 1.8(a), the same holds for the permittivity ϵ, making the wave equation 1.9 a non-linear equation that changes the properties of the propagating field including its frequency.

1.4.1.1 Microcavities containing quantum wells

The frequency-dependent polarization, $\mathbf{P}(\omega)$, described by Eq. 1.33 is proportional to the exciton oscillator strength, but such expression is not valid in a system where the movement of excitons is restricted by the spatial confinement in QWs. In these conditions where the free exciton dynamics is prohibited, its wave vector is not defined in the confinement direction. In § 1.3.1.3 it was shown that the field inside a MC is concentrated at the antinodes of a standing wave profile [Figs. 1.9(a,b)]. It is then desirable that confined excitons are created at such antinode regions, what can be done by using QWs inside the MC. This also gives a second advantage, namely that the exciton energy, ω_x, can be tuned with the QW width — see § 1.2.

The theory of spatial dispersion in an optical media is applied to describe the dielectric response of quantum structures containing excitons, where the local presence of an exciton wavefunction affects the dielectric polarization. In this section we follow the semiclassical description of the exciton-photon coupling in QWs given in Ref. [75], it is based in the non-local dielectric response theory developed by the seminal works of Andreani, *et al.* [84], and Ivchenko [85]. The dielectric polarization changes in presence of an exciton according to the following expression:

$$\mathbf{P}(\omega, z) = \Phi(z) \int \Phi(z') \frac{\epsilon_B 2\omega_{LT} \pi a_B^3}{\omega_x - \omega - i\gamma_x} \mathbf{E}(\omega, z')\, dz' \tag{1.34}$$

where $\Phi(z)$ is the exciton wavefunction obtained when solving Eq. 1.3 using a potential well for $V_{e,h}(z_{e,h})$ and a_B is the Bohr radius of exciton in the bulk material (Eq. 1.5). Introducing Eq. 1.34 into Eqs. 1.8 and 1.9, the latter becomes an integro-differential equation and can be solved exactly using the Green's function method [75]. The reflection and transmission amplitudes can be then calculated using 1.16:

$$r_{QW}(\omega) = \frac{i\Gamma_x}{\omega_x - \omega - i(\Gamma_x + \gamma_x)} \tag{1.35a}$$

$$t_{QW}(\omega) = 1 + r_{QW}(\omega) \tag{1.35b}$$

where Γ_x is the so-called *exciton radiative broadening* which is connected to the exciton radiative lifetime.

A finite exciton radiative lifetime is a peculiarity of confined semiconductor systems. In an infinite bulk crystal, an exciton-polariton can freely propagate in any direction and its lifetime is limited only by non-radiative processes such as scattering with acoustic phonons. On the contrary, in a QW the exciton-polariton can disappear by giving its energy to a photon which escapes the QW plane. After calculating the transfer matrix of a DBR-MC containing a QW in the middle of the L_c-thick cavity layer, solving an eigenvalue equation yields [75]:

$$(\omega_x - \omega - i\gamma_x)(\omega_c - \omega - i\gamma_c) = V^2 \tag{1.36a}$$

$$\gamma_c = \frac{c(1-\sqrt{R})}{n_c\sqrt{R}(L_{DBR}+L_c)} \tag{1.36b}$$

$$V^2 = \frac{c(1+\sqrt{R})\Gamma_x}{n_c\sqrt{R}(L_{DBR}+L_c)} \tag{1.36c}$$

where R is the DBR reflectivity, γ_c the photon lifetime and $L_{DBR} = \frac{n_1 n_2 \pi c}{\omega_c(n_2-n_1)}$ is the so called DBR effective length, it accounts for the penetration depth of the electromagnetic field inside the mirror.

Equation 1.36(a) describes a system of two damped harmonic oscillators, namely the exciton and the cavity mode, coupled by a matrix element V. It has two complex solutions:

$$\omega_\pm = \frac{1}{2}\left[\omega_x + \omega_c - i(\gamma_x+\gamma_c) \pm \sqrt{4V^2 + (\omega_x - \omega_c - i(\gamma_x - \gamma_c))^2}\right] \tag{1.37}$$

If $\omega_x = \omega_c$, the splitting between the two values is given by the so-called Rabi splitting:

$$\Omega_R = \sqrt{4V^2 - (\gamma_x - \gamma_c)^2} \tag{1.38}$$

This coupling changes the modes of the electric field on the excitonic media. The splitting is analogous to the normal mode splitting observed in atoms inside cavities [86, 87].

The parameter V is the coupling strength between the cavity photon mode and the exciton. $2V$ reaches 15 meV in $GaAs$ MCs, 30 meV in $CdTe$ MCs, and 50 meV in GaN cavities [29, 88–90].

In order to discuss the influence of a finite linewidth of the uncoupled modes on the light-matter coupling in a MC, it is convenient to distinguish between homogeneous and inhomogeneous broadening mechanisms. Interpreting the homogeneous linewidths of exciton (γ_x) and cavity-photon (γ_c) as damping constants in analogy to the mechanically-coupled oscillators (see next § 1.4.2 and Fig. 1.13), the dephasing time can be approximated by Heisenberg's uncertainty principle: $\tau_{x,c} \simeq 2\pi/\gamma_{x,c}$. If now $\tau_{x,c}$ is shorter or close to the Rabi-oscillation period, given by $\tau_R = 2\pi/\Omega_R$, an efficient energy transfer between both oscillators is prevented and the system remains weakly coupled. This intuitive criterion for the occurrence of the so-called SCR can be

expressed as:

$$\tau_R \ll \min(\tau_x, \tau_c), \quad \text{or, equivalently} \quad \Omega_R \gg \max(\gamma_x, \gamma_c) \tag{1.39}$$

An alternative expression for the homogeneous linewidth limitation can be obtained via Eq. 1.38. As the Rabi-splitting is only defined as a real quantity, it holds:

$$\Omega_R \begin{cases} 0 & \text{when} \quad V \leq \frac{|\gamma_x - \gamma_c|}{2} \\ \sqrt{4V^2 - (\gamma_x - \gamma_c)^2} & \text{when} \quad V > \frac{|\gamma_x - \gamma_c|}{2} \end{cases} \tag{1.40}$$

When considering MCs with $\gamma_x \gg \gamma_c$, such as typical III-nitride based MCs featuring $Q \simeq 1000$ (in particular at room temperature), the SCR conditions should be stringent. In this case both above-mentioned approaches in Eqs. 1.39 and 1.40 would yield identical criteria for observing the SCR. Note that in low-quality cavities, where $\gamma_x \sim \gamma_c \gg 2V$, Eq. 1.40 would still yield finite values for the vacuum Rabi-splitting, even though the SCR could not be observed according to the criterion defined in Eq. 1.39 and the potential presence of any polariton mode would be blurred by the immense broadening. A more refined theory abolishing this artifact has been provided by Savona and co-workers in Ref. [91]. Therein, they examined the Rabi-splitting values that occur in the reflection (R), absorption (A), and transmission (T) spectra of the MC and evidenced that it should hold: $\Omega_R^A \leq \Omega_R^T \leq \Omega_R^R$. The most stringent condition is thus given by the absorption:

$$\Omega_R^A \begin{cases} 0 & \text{when} \quad V^2 \leq \frac{\gamma_x^2 + \gamma_c^2}{2} \\ 2\sqrt{V^2 - \frac{\gamma_x^2 + \gamma_c^2}{2}} & \text{when} \quad V^2 > \frac{\gamma_x^2 + \gamma_c^2}{2} \end{cases} \tag{1.41}$$

Note that for the case $\gamma_x \gg \gamma_c$ (or vice versa) all three criteria yield equivalent restrictions for the SCR.

Contrary to the homogeneous linewidth the impact of a statistical contribution, due to disorder, defects and layer-thickness fluctuations giving rise to an inhomogeneous broadening cannot be modeled within the mechanically-coupled oscillators. These non-idealities often play an only minor role in $GaAs$-based structures, but they are omnipresent in III-nitride ones. This is not necessarily due to the lower crystal quality, but rather caused by a much smaller exciton Bohr-radius and a therefore increased sensitivity to alloy composition fluctuations and crystal defects.

Lets consider the criteria for the SCR given by Eq. 1.40, suitable for $GaAs$-based MCs given the small values of γ_x and γ_c; when $2V > |\gamma_x - \gamma_c|$, in this case Ω_R is a real number and so $\omega_\pm$ are different frequencies from $\omega_{c,x}$, defining new eigenmodes of the MC spectra, called upper polariton, ω_+, and lower polariton, ω_-. On the other hand, in the *weak coupling regime*, $2V < |\gamma_x - \gamma_c|$

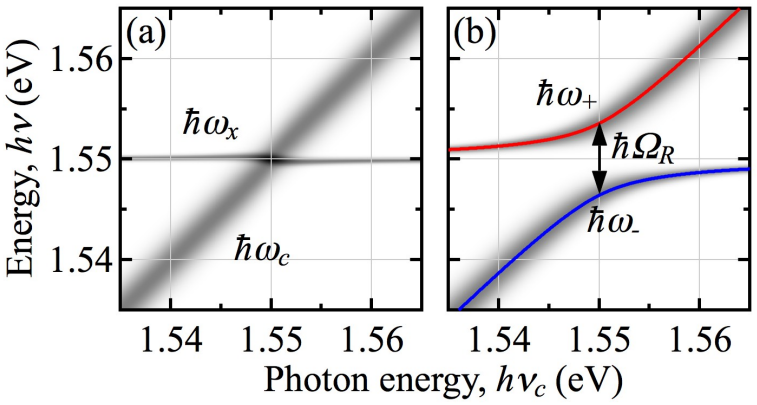

FIGURE 1.11: Comparison between WCR and SCR. Panels are solutions of Eqs. 1.37 and 1.42 using parameters $\hbar\gamma_x$ =0.4 meV ($\tau_x = 2\pi/\gamma_x$ =10 ps exciton lifetime [92]), $\hbar\gamma_c = 4$ meV ($\tau_c = 2\pi/\gamma_c$ =1 ps photon lifetime), $\hbar\omega_x$ =1550 meV and (a) $2V = 2.4$ meV $< |\gamma_x - \gamma_c| = 3.6$ meV (WCR) or (b) $2V = 8$ meV $> |\gamma_x - \gamma_c| = 3.6$ meV (SCR). In (a) the coupled modes are practically the same as bare ω_x and ω_c modes, with an decrease of the exciton decay rate at the crossing point. In (b) ω_+ and ω_- modes are separated by $\hbar\Omega_R$ at the anticrossing point.

making Ω_R a pure complex number, and so the eigenfrequencies $\omega_{c,x}$ remain unchanged except from their linewidth. VCSEL lasers operate under the WCR.

To illustrate better the difference between both regimes we simulate a cavity spectra as the sum of two Gaussians whose peaks and FWHMs are given by the real ($\mathcal{R}$) and imaginary ($\mathcal{I}$) parts, respectively, of $\omega_\pm$:

$$T(\omega) = e^{-\frac{(\omega-\mathcal{R}(\omega_+))^2}{2\left(\frac{\mathcal{I}(\omega_+)}{2\sqrt{2\ln 2}}\right)^2}} + e^{-\frac{(\omega-\mathcal{R}(\omega_-))^2}{2\left(\frac{\mathcal{I}(\omega_-)}{2\sqrt{2\ln 2}}\right)^2}} \tag{1.42}$$

Figure 1.11 shows the exciton and photon-cavity mode anti-crossing by comparing the transition from the WCR to the SCR; the cavity mode energy varies inside the MC (as shown in Fig. 1.10) and therefore the cavity mode crosses the exciton mode (with a constant energy). We use realistic parameters in order to reproduce the behavior of the cavities used in this thesis — see Chapter 3. In the WCR [Fig. 1.11(a)], the bare exciton and photon modes remain the eigenmodes of the system, with slight changes in lifetimes (observed in the width of the lines) at the crossing region. On the other hand, in the SCR [Fig. 1.11(b)], a clear distinction between upper and lower polariton branches (UPB and LPB, respectively) can be seen, with normal mode splitting given by Ω_R.

The conditions for SCR are thus high exciton-dipole oscillator strength, good field-exciton overlap and similar, and small, linewidths of the cavity photon (γ_c, controlled by the finesse)

and the exciton (γ_x, controlled by the inhomogeneous broadening of the excitons in the sample) compared to Ω_R [93].

1.4.2 Quantum description of light-matter interaction

In order to understand the consequences of the strong exciton-photon interaction inside the cavity, we are going to follow a second quantization approach, which provides very intuitive results. Nonetheless, the physics behind this phenomena do not require the use of a quantum mechanical treatment; similar results can be obtained following classical linear approaches [87, 94–96].

In the previous Section, a semiclassical approach to photon-exciton interaction inside a semiconductor MC has been shown to change the dielectric constant yielding a normal mode splitting that appears as two new modes. This is in close analogy to the classical two-coupled harmonic oscillator problem [97], where two masses m_A and m_B are attached to springs with constants κ_A and κ_B and linked together by a third spring with constant κ — see Fig. 1.12(a). The eigenfrequencies of the system are given by (damping is ignored):

$$\omega_{\pm}^2 = \frac{1}{2}\left[\omega_A^2 + \omega_B^2 \pm \sqrt{\left(\omega_A^2 - \omega_B^2\right)^2 + 4\Gamma^2\omega_A\omega_B}\right] \tag{1.43}$$

where $\omega_A = \sqrt{(k_A + \kappa)m_A}$, $\omega_B = \sqrt{(k_B + \kappa)m_B}$ and

$$\Gamma = \frac{\kappa}{\sqrt{m_A\omega_A m_B\omega_B}} \tag{1.44}$$

Each eigenmode correspond to both masses oscillating harmonically with a single frequency, for ω_- with the same phase and for ω_+ with a $\pi-$phase difference. Any other solution to the problem is a linear superposition of these two eigenmodes, and will be then characterized by a periodic beating of each mass oscillation. Figure 1.12(b) shows one of these possible solutions, with $k_A = k_B = 12.5\kappa$. Note the π-phase difference between the beating of each mass, which is responsible for a periodic transfer of energy from one oscillator to the other and vice-versa.

To illustrate the solutions given by Eq. 1.43 we set $k_A = k_0$, $k_B = k_0 + \Delta k$, and $m_A = m_B = m_0$. Figure 1.13(a) shows the frequencies of the two oscillators in the absence of coupling ($\kappa = 0$). As Δk is increased from $-k_0$ to $+k_0$, the frequency of oscillator increases from zero to $\sqrt{2}\omega_0$, while the frequency of oscillator A stays constant. The two curves intersect at $\Delta k = 0$. Once coupling is introduced, the two curves no longer intersect. Instead, as shown in Fig. 1.13(b), there is a characteristic anticrossing with a frequency splitting of Γ. It is remarkable that such coupling between the classical oscillators changes significantly the shape of the modes ω_B^0 and ω_- for negative values of Δk, away from $\Delta k = 0$ (where the maximum coupling occurs), compare their dependences as function of Δk in Figs. 1.13(a,b), respectively.

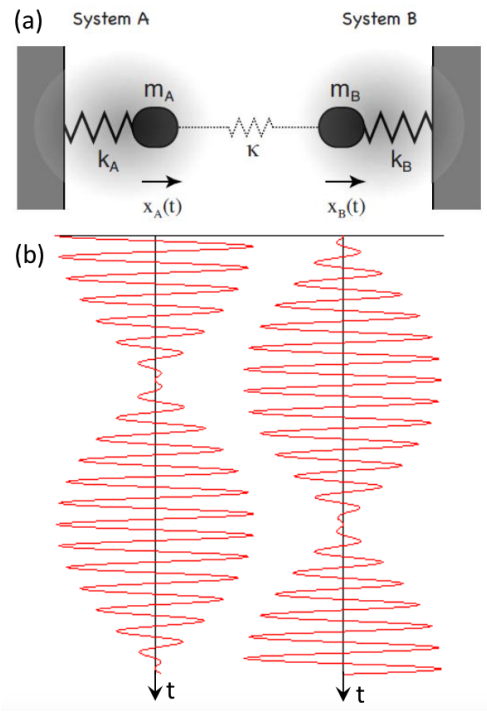

FIGURE 1.12: Coupled mechanical oscillators. (a) Schematic representation of two harmonic oscillators defined by masses m_A and m_B attached to springs (k_A and k_B) and coupled through a third spring of constant κ. Each mass position, $x_A(t)$ and $x_B(t)$, is displayed as a function of time in (b) for a superposition of the two eigenmodes taking $k_A = k_B = 12.5\kappa$. Adapted from Ref. [97].

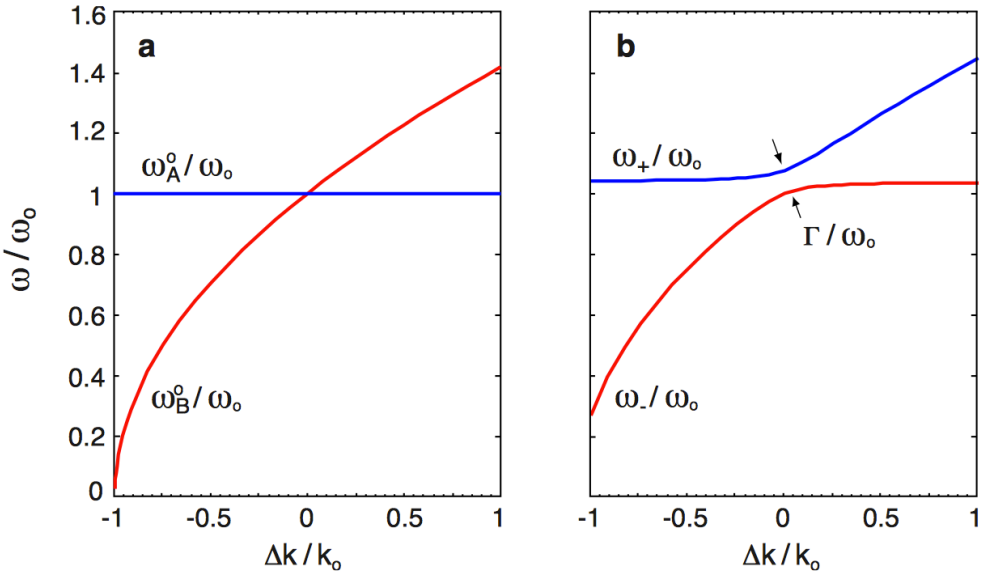

FIGURE 1.13: SCR illustrated by mechanical oscillators. (a) Eigenfrequencies of two uncoupled oscillators ($\kappa = 0$) with equal mass and spring constants k_0 and $k_0 + \Delta k$. (b) Frequency anticrossing due to coupling of strength $\kappa = 0.08k_0$. The coupling of the two oscillators leads to a shift of the eigenfrequencies and a characteristic frequency splitting Γ, which scales linearly with the coupling strength κ. From [97].

Equation 1.43 and Fig. 1.13 are in full analogy with polariton modes in a MC (Eq. 1.37 and Fig. 1.11), so one might look for a quantum description of photon-exciton interaction in a MC under the coupled oscillators picture. In fact, in the low excitonic density limit, the Hamiltonian describing photons, excitons and their mutual coupling through the dipole moment can be written, in the second quantization picture, as [75]:

$$\mathcal{H}_{e-ph} = \hbar\omega_C \hat{C}^\dagger \hat{C} + \hbar\omega_X \hat{X}^\dagger \hat{X} + \frac{\hbar\Omega_R}{2}\left(\hat{C}^\dagger \hat{X} + \hat{X}^\dagger \hat{C}\right) \tag{1.45}$$

where ω_C (ω_X) are the photon (exciton) frequencies and Ω_R the Rabi frequency in the exciton-photon basis $\left(\hat{X}, \hat{C}\right)$. The photon (exciton) creation and annihilation operators, $\hat{C}^\dagger$ and $\hat{C}$ ($\hat{X}^\dagger$ and $\hat{X}$), are to be understood, when applied in the uncoupled photon-exciton number basis, as:

$$\hat{C}^\dagger |n_C, n_X\rangle = \sqrt{n_C + 1}\, |n_C + 1, n_X\rangle \tag{1.46a}$$

$$\hat{C} |n_C, n_X\rangle = \sqrt{n_C}\, |n_C - 1, n_X\rangle \tag{1.46b}$$

$$\hat{X}^\dagger |n_C, n_X\rangle = \sqrt{n_X + 1}\, |n_C, n_X + 1\rangle \tag{1.46c}$$

$$\hat{X} |n_C, n_X\rangle = \sqrt{n_X}\, |n_C, n_X - 1\rangle \tag{1.46d}$$

Given an arbitrary state in the exciton-photon basis, $|\psi(t)\rangle = c(t)\,|1,0\rangle + x(t)\,|0,1\rangle$, its time-evolution can be found when solving the Schrödinger equation, $i\hbar\partial_t\,|\psi(t)\rangle = \mathcal{H}_{e-ph}\,|\psi(t)\rangle$

$$i\hbar\left[\dot{c}(t)\,|1,0\rangle + \dot{x}(t)\,|0,1\rangle\right] = \hbar\omega_C c(t)\,|1,0\rangle + \hbar\omega_X x(t)\,|0,1\rangle + \frac{\hbar\Omega_R}{2}\left(c(t)\,|1,0\rangle + x(t)\,|0,1\rangle\right) \tag{1.47}$$

Equation 1.47 can be written in its matrix from,

$$i\hbar\begin{pmatrix}\dot{c}(t)\\ \dot{x}(t)\end{pmatrix} = \mathcal{H}_{e-ph}\begin{pmatrix}c(t)\\ x(t)\end{pmatrix} = \begin{pmatrix}\hbar\omega_C & \frac{\hbar\Omega_R}{2}\\ \frac{\hbar\Omega_R}{2} & \hbar\omega_X\end{pmatrix}\begin{pmatrix}c(t)\\ x(t)\end{pmatrix} \tag{1.48}$$

which is a matrix differential equation that can be easily solved in a different basis where the $\mathcal{H}_{e-ph}$ matrix in Eq. 1.48 is diagonal. The diagonalization of $\mathcal{H}_{e-ph}$ is obtained under the transformation $\mathcal{H}_{pol} = P\mathcal{H}_{e-ph}P^{-1}$; P is known as the Hopfield matrix, this invertible matrix yields the diagonalization from the exciton-photon basis $\left(\hat{X}, \hat{C}\right)$ to the upper and lower polariton basis $\left(\hat{U}, \hat{L}\right)$.

$$\mathcal{H}_{pol} = \hbar\omega_+ \hat{U}^\dagger \hat{U} + \hbar\omega_- \hat{L}^\dagger \hat{L} \tag{1.49}$$

Equivalently to the case described in Eq. 1.45, the upper (lower) polariton creation and annihilation operators, $\hat{U}^\dagger$ and $\hat{U}$ ($\hat{L}^\dagger$ and $\hat{L}$), are to be understood, when applied in the coupled upper-lower polariton number basis.

In this way we obtain a pair of uncoupled differential equations:

$$i\hbar \begin{pmatrix} \dot{u}(t) \\ \dot{l}(t) \end{pmatrix} = \mathcal{H}_{pol} \begin{pmatrix} u(t) \\ l(t) \end{pmatrix} = \begin{pmatrix} \hbar\omega_+ & 0 \\ 0 & \hbar\omega_- \end{pmatrix} \begin{pmatrix} u(t) \\ l(t) \end{pmatrix} \tag{1.50}$$

where $\begin{pmatrix} u(t) \\ l(t) \end{pmatrix} = P \begin{pmatrix} c(t) \\ x(t) \end{pmatrix} = \begin{pmatrix} \chi & \varsigma \\ \varsigma & -\chi \end{pmatrix} \begin{pmatrix} c(t) \\ x(t) \end{pmatrix}$. The eigenfrequencies are given by:

$$\omega_\pm = \frac{1}{2}\left(\omega_X + \omega_C \pm \sqrt{\Delta^2 + \Omega_R^2}\right) \tag{1.51}$$

for detuning $\Delta = \omega_C - \omega_X$. Polaritons can then be seen in a simplified, but very accurate model, as the new eigenstates that arise from the coupling of two oscillators, *i.e.*, the photon and the exciton. On resonance, polaritons are half-light, half-matter quasi-particles, with wavefunctions that are superpositions between the excitonic and photonic ones, $\psi = \frac{1}{\sqrt{2}}(\psi_X \pm \psi_C)$.

The corresponding eigenvectors are $\begin{pmatrix} \chi \\ \varsigma \end{pmatrix}$ and $\begin{pmatrix} \varsigma \\ -\chi \end{pmatrix}$, where χ and ς are the Hopfield coefficients [82]:

$$\chi = \left(1 + 4\left(\frac{\omega_- - \omega_X}{\Omega_R}\right)^2\right)^{-1/2} \tag{1.52a}$$

$$\varsigma = -\left(1 + \frac{1}{4}\left(\frac{\Omega_R}{\omega_- - \omega_X}\right)^2\right)^{-1/2} \tag{1.52b}$$

This finally yields the time-evolution of $|\psi(t)\rangle$ in the uncoupled photon-exciton basis $\begin{pmatrix} c(t) \\ x(t) \end{pmatrix} = P^{-1} \begin{pmatrix} u(t) \\ l(t) \end{pmatrix}$. One possible solution is $u(t) = \frac{1}{\sqrt{2}} e^{-i\omega_+ t}$ and $l(t) = \frac{1}{\sqrt{2}} e^{-i\omega_- t}$, yielding:

$$c(t) \propto \chi e^{-i\omega_+ t} + \varsigma e^{-i\omega_- t} \tag{1.53a}$$

$$x(t) \propto \varsigma e^{-i\omega_+ t} - \chi e^{-i\omega_- t} \tag{1.53b}$$

The coefficients defined by Eq. 1.53 can be used to calculate the probability of having a photon or an exciton at a given time t. Taking the simple case $\omega_C = \omega_X = \omega$, we have, $\chi = -\varsigma = 1/\sqrt{2}$ and $\omega_\pm = \omega \pm \Omega_R/2$. Equation 1.53 yields:

$$|c(t)| \propto (1 + \cos \Omega_R t) \tag{1.54}$$

Equation 1.54 tells us that such a polariton state is seen as a chain process where the exciton annihilates, emitting a photon with the same energy E and momentum k, which is later reabsorbed

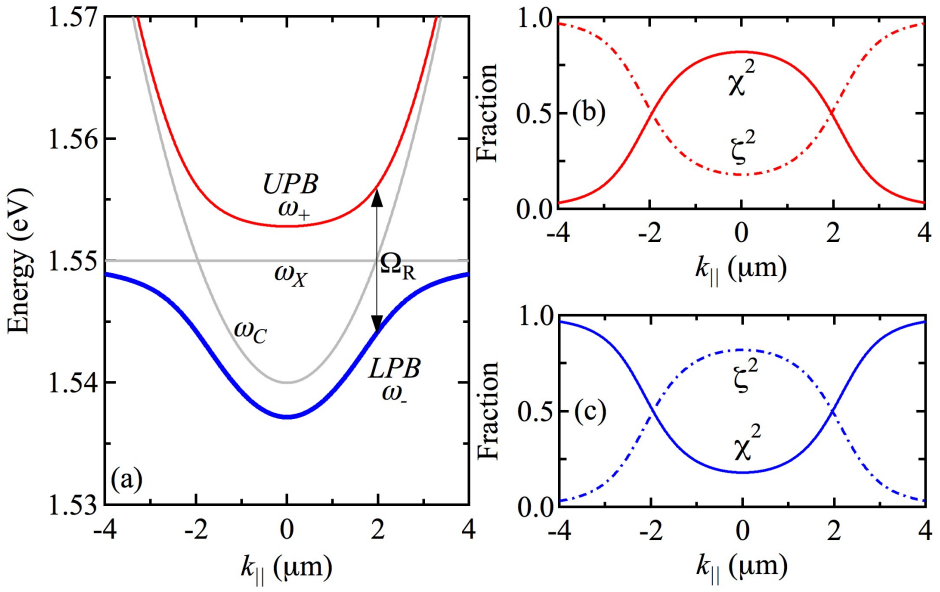

FIGURE 1.14: Computed dispersions of the upper ω_+ (thin, red line, UPB) and lower ω_- (thick, blue line, LPB) polariton branches as a function of in plane wave-vector ($k_{||}$) along with the uncoupled cavity ω_C and exciton ω_X modes (gray lines) for negative detuning, showing the Rabi splitting Ω_R where the two bare dispersions cross. (b)/(c) Corresponding exciton (χ) and photon (ς) fractions in full and dot dash lines, respectively, of the UPB/LPB.

by the medium, creating a new exciton with the same (E, k). This processes is repeated with a frequency $2\Omega_R$, very similarly to two classically coupled oscillators.

Other two possible solutions would be the polaritonic eigenmodes, taking $u(t) = 0$ or $l(t) = 0$. The first corresponds to an in-phase harmonic oscillation of the photonic and exciton fields, whereas with a π-relative phase in the second, again in close analogy with the classical coupled oscillators picture.

The dispersion of each polariton mode can be calculated from Eq. 1.51 or 1.37 by taking the momentum dependence of excitonic and photonic modes. Since the exciton mass is much heavier than the photonic one, we assume the excitonic dispersion to be flat and the photonic one to be parabolic. This yield the polariton dispersion for each Hamiltonian eigenvalue, known by the *upper polariton branch* (UPB) and the *lower polariton branch* (LPB) — see Fig. 1.14. The first measurement of a Rabi splitting of the normal modes of a semiconductor MC was done 20 years ago [11], where, using a five-QW MC, the exciton and photon dips in the reflectivity spectra anticrossed when they came into resonance [Fig. 1.15(a)]. Two years later, the PL dynamics of this semiconductor MC was studied [98] under femtosecond optical spectroscopy: vacuum Rabi oscillations between coupled exciton-photon modes were directly observed. When excited by a coherent optical pulse whose spectral bandwidth exceeds the normal-mode splitting, the initial state of the system is a linear superposition of normal modes corresponding to the photon mode.

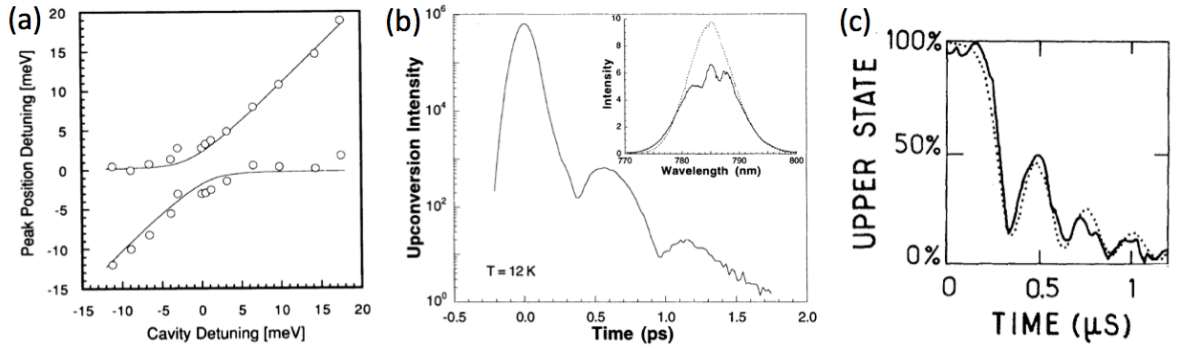

FIGURE 1.15: (a) Reflectivity peak positions as a function of photon-exciton detuning for a five-quantum-well MC sample at $T = 5$ K from Ref. [11]. (b) Time-resolved emission intensity from a MC with photonic and excitonic modes close to resonance, excited with a pulsed laser. In the inset, the dotted line shows the incident pump spectrum, and the solid line the reflected pump spectrum. The two dips in the selected pump spectrum correspond to the normal modes of the system resonance, from Ref. [98]. (c) Evolution of the normalized excited-state population of sodium Rydberg atoms inside a millimeter-wave cavity as a function of time (solid line: experiment; dotted line: theoretical calculation), from Ref. [99].

As the system evolves in time, the character of the excitation oscillates between the cavity and exciton modes at the vacuum Rabi frequency [Fig. 1.15(b)].

The interaction between a photon and an exciton in a semiconductor provides the solid-state analog of photon-atom interaction in cavity quantum-electrodynamics (CQED). In fact, when an ideal two-level absorber (atom or exciton) is resonantly coupled to a single mode of the electromagnetic field, the field induces a periodic excitation and deexcitation of the absorber excited state given by the Rabi frequency $\Omega_R = e\langle r\rangle E/\hbar$, where $\langle r\rangle$ is the transition dipole moment and E the electric field. Such Rabi dynamics has been measured 30 years ago with sodium Rydberg atoms prepared in a millimeter-wave FP resonator [99] — see Fig. 1.15(c). This Rabi flopping is manifested in the normal-mode spectrum as a splitting (or anticrossing) of the uncoupled atom and field modes [100, 101]. Analogous phenomena have been more recently observed between a single photon and a superconducting qubit using circuit quantum electrodynamics, where a superconducting two level system, playing the role of an artificial atom, is coupled to an on-chip cavity consisting of a superconducting transmission line resonator [102].

1.4.3 The spin of polaritons

The spin structure of exciton polaritons is determined by the underlying structure of excitons. As excitons are composite particles occurring from the Coulomb interaction of an electron with a hole, their spin depends on the spin of the two constituents. The spin of the CB electrons and the VB holes furthermore depends on the crystal structure (Zinc-blend crystal for $GaAs$ and $CdTe$) [103].

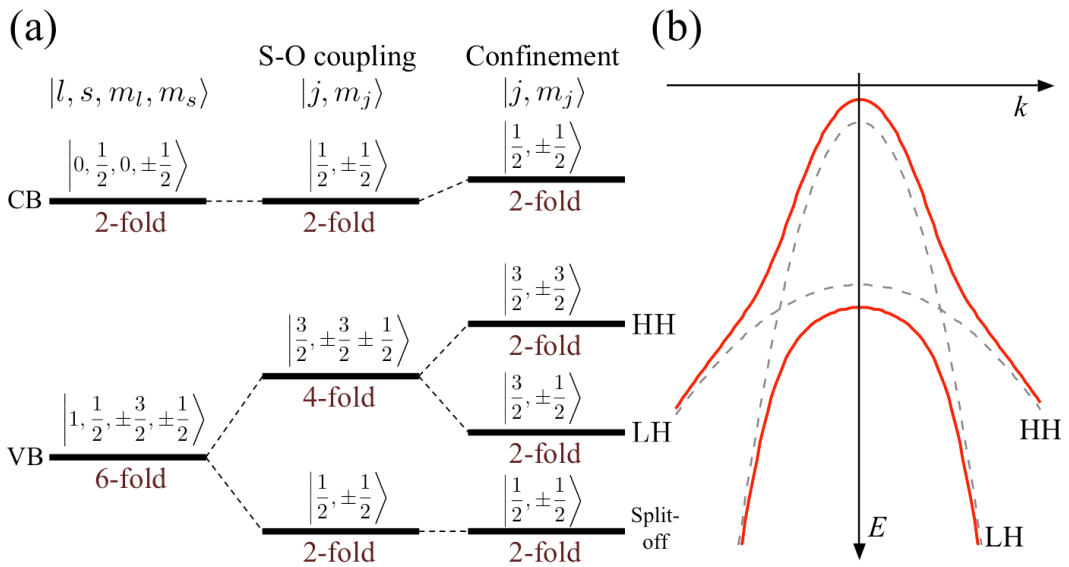

FIGURE 1.16: (a) The energy levels and their angular momentum states without S-O coupling (left), with S-O coupling middle and under confinement in a QW at $k = 0$. (b) Mass reversal: Strong mixing of heavy and light hole causes the heavy hole to have a lighter mass than the light hole close to the band edge. The uncoupled light and heavy hole excitons are represented in gray dashed lines and the mixed states in solid red lines. Adapted from Ref. [104].

The precise band structure of this type of crystals can be calculated using the $\mathbf{k} \cdot \mathbf{p}$ method [105]. The lowest CB is an s orbital ($l = 0$, $m_l = 0$, $s = 1/2$, $m_s = \pm 1/2$) which is two-fold degenerate, Fig. 1.16(a). The uppermost VB on the contrary is a p orbital which in the absence of spin orbit (S-O) coupling is a six-fold degenerate state ($l = 1$, $m_l = 0, \pm 1$, $s = 1/2$, $m_s = \pm 1/2$).

The initial and the new eigenstates after S-O coupling for $\mathbf{k} = \mathbf{0}$, are shown in Fig. 1.16(a). The $j = 3/2$ with $m_j = \pm 3/2$ eigenstate is the so called heavy hole band and is degenerate with the $j = 3/2, m_j = \pm 1/2$ which is the light hole band. The $j = 1/2$, $m_j = \pm 1/2$ is the so called S-O split off VB.

Up to here, the description does not include any confinement and hence it is applicable only for the bulk CBs and VBs. The effect of the QW confinement further modifies the band structure as was demonstrated by Luttinger [104, 105]. Confinement leads to a crossing of the light hole band by the heavy hole band, as shown in Fig. 1.16(b) with the dashed lines. In the framework of Luttinger, significant band mixing takes places and the two bands present anticrossing as seen in Fig. 1.16(b) (solid lines).

In the direction of confinement the otherwise heavy hole excitons are now lighter and the light hole excitons become heavier. This phenomenon is known as the "mass reversal" [104, 105]. Optical transitions can only take place if the total angular momentum of the created exciton coincides with the spin of the emitted/absorbed photon. More specifically, the spin of a photon m_p has to obey the equality $m_p = m_{je} + m_{jh}$. The excitons with total angular momentum ± 2 are optically inactive

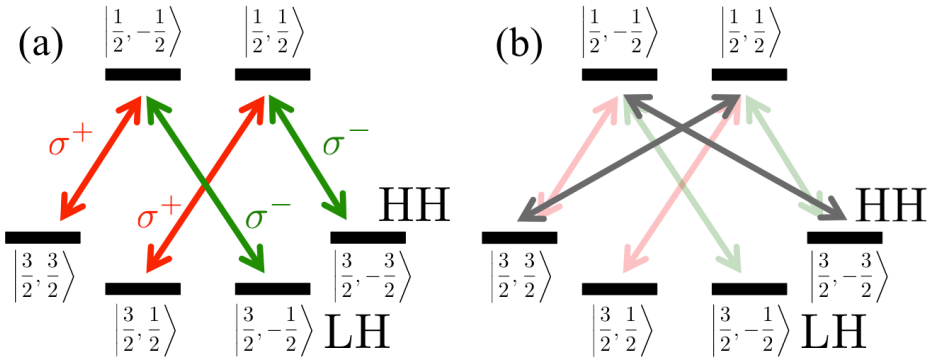

FIGURE 1.17: (a) The allowed optical transitions with the respective polarization of the emitted photon and (b) the dark transitions.

but can abundantly be created in non-resonant excitation experiments. A large amount of work has been done on the spin of excitons either for bulk semiconductors or for QWs and the reader can find more in [104–107] and references therein.

Excitons can decay via emission of a photon if $m_{je} + m_{jh} = \pm 1$, where ± 1 correspond to the two circular polarization [Fig. 1.17(a)]. The transition corresponding to $m_{je} + m_{jh} = \pm 2$ are optically inactive, this is why the quasi-particles involved in this process are called dark excitons [Fig. 1.17(b)]. These dark excitons, although they do not couple to light and do not form polaritons still play an important role. They interact with optically active polaritons, they are involved in relaxation mechanisms via the Coulomb interaction and they also contribute to the total exciton density that determines whether the system is below or above the Mott transition.

The final spin of the excitons and polaritons is always integer, which makes them bosons, according to the spin statistic theorem.

1.4.3.1 The Poincaré sphere

The polarization of emitted light is directly related to the spin of polaritons. The polarization of a plane monochromatic wave is fully characterized by the general Stokes parameters, defined by the following four quantities:

$$s_0 = \langle a_1^2 \rangle + \langle a_2^2 \rangle \tag{1.55a}$$

$$s_1 = \langle a_1^2 \rangle + \langle a_2^2 \rangle \tag{1.55b}$$

$$s_2 = 2 \langle a_1 a_2 \cos(\delta) \rangle \tag{1.55c}$$

$$s_3 = 2 \langle a_1 a_2 \sin(\delta) \rangle \tag{1.55d}$$

where, a_1 and a_2 are the instantaneous amplitudes of two orthogonal components E_x and E_y of the electric vector and $\delta = \phi_1 - \phi_2$ is their phase difference. Only three of them are independent

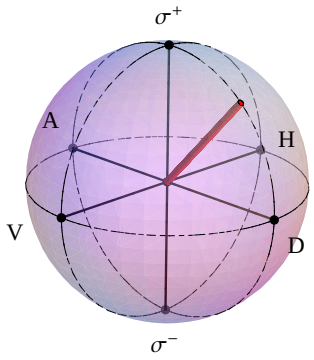

FIGURE 1.18: The Poincaré sphere representing the polarization state of light. The poles correspond to the circular polarization, the linear polarizations lie on the equator and all other latitudes represent elliptical polarizations. The red line indicates an arbitrary state of light.

since they are related by the identity:

$$s_0^2 = s_1^2 + s_2^2 + s_3^2 \tag{1.56}$$

which represents the equation of a sphere (Fig. 1.18).

The normalized quantities of $s_{1,2,3}$ are easily accessible by measuring the intensities of the light in the linear and circular polarization and calculates as

$$s_x = \frac{s_1}{s_0} = \frac{I_H - I_V}{I_H + I_V} \tag{1.57a}$$

$$s_y = \frac{s_2}{s_0} = \frac{I_D - I_A}{I_D + I_A} \tag{1.57b}$$

$$s_z = \frac{s_3}{s_0} = \frac{I_{\sigma^+} - I_{\sigma^-}}{I_{\sigma^+} + I_{\sigma^-}} \tag{1.57c}$$

where the intensity is analyzed in the different degrees of polarization: horizontal (H), vertical (V), diagonal (D), anti-diagonal (A), left-hand (σ^-) and right-hand circularly polarized (σ^+) detection. The poles of the sphere correspond to the circular polarization and the linear polarization lie on the equator (Fig. 1.18). All intermediate points represent elliptical polarization.

Chapter 2

Quantum liquids

QUANTUM liquids are many-particle systems in which not only the effects of quantum mechanics but also those of quantum statistics — specifically, indistinguishability of elementary particles — are important. Any elementary particle can be classified according to its intrinsic angular momentum: *bosons* have integer spin whereas *fermions* have a half-integer one. According to the *spin-statistics* theorem [108], the total wave function of any many-particle system must be even under an interchange of coordinates of any two bosons, and odd under interchange of any two fermions. This theorem implies that the distribution of particles in thermal equilibrium is given by:

$$n_i = \frac{1}{e^{\frac{\epsilon_i - \mu_c}{k_B T}} \pm 1} \tag{2.1}$$

where μ_c is the chemical potential, T the temperature, k_B the Boltzmann constant and the $\pm$ sign now refers to fermions or bosons, respectively. The distribution given by Eq. 2.1 with the plus sign is known as the Fermi-Dirac distribution, whereas with the minus it corresponds to the Bose-Einstein distribution.

Quantum effects start to be important when the thermal energy $k_B T$ falls below a typical single-particle excitation energy. A rough estimation for this energy [109] may be obtained by imagining each particle of mass m to move in a 3D cage of side $a \sim (N/V)^{-1/3}$ (N/V = particle density) formed by its neighbours; the typical single-particle excitation energy is then of order of the first energy state of a infinite potential well $\sim \hbar^2/(ma^2)$, so the criterion for quantum effects to be relevant is

$$T_c \sim \frac{\hbar^2 (N/V)^{2/3}}{m k_B} \tag{2.2}$$

Thus, a quantum liquid is a many-particle system in which (i) the temperature is less than or of the order of T_c, defined by Eq. 2.2, and (ii) the particles can change places relatively easily. The most

studied quantum liquids are the bosonic systems, such as liquid ^{4}He and Bose alkali gases, which undergo the phenomenon of BEC, and the fermionic systems, such as liquid ^{3}He and electrons in some metals, which display the related phenomenon of Cooper pairing. Another examples are neutrons in neutron stars and possibly more exotic forms of matter such as quark stars.

2.1 Bose-Einstein condensation

2.1.1 The ideal Bose gas

The chemical potential is the energy cost of adding a particle to a gas, and increases with the total number of particles. For a non-interacting gas of bosons described by the Bose-Einstein distribution, Eq. 2.1, the chemical potential μ_c has to be smaller then the lowest energy ϵ_0 in order that the occupation number n_i is always positive.

Let us write the total number of particles as

$$N = N_0 + N_T \tag{2.3}$$

where N_0 is the number of particles in the ground state (condensate) and

$$N_T = \sum_{i \neq 0} n_i \tag{2.4}$$

is the number of particles out of the condensate, also called the thermal component of the gas.

When the chemical potential μ_c approaches ϵ_0 from below, the ground-state occupation number

$$n_0 = \frac{1}{e^{\frac{\epsilon_0 - \mu_c}{k_B T}} - 1} \tag{2.5}$$

of the lowest energy state becomes increasingly large. This is actually the mechanism at the origin of BEC and it was used as a footprint for its first observation in 1995 [13], where a macroscopic occupation of a zero-momentum state was shown.

The value of n_i is proportional to the density of states, which for a 3D gas of free particles with a parabolic dispersion $\epsilon = \epsilon_0 + \frac{\hbar^2 k^2}{2m}$ is given by $g(\epsilon) = \frac{m^{2/3}}{\sqrt{2}\hbar^3 \pi^2}\sqrt{\epsilon - \epsilon_0}$. When $\mu_c \to \epsilon_0$, the density of particles out of the condensate is given by:

$$\frac{N_T^{\mu_c \to \epsilon_0}}{V} = \int_{\epsilon_0}^{\infty} \frac{m^{2/3}}{\sqrt{2}\hbar^3 \pi^2}\sqrt{\epsilon - \epsilon_0}\frac{1}{e^{\frac{\epsilon - \epsilon_0}{k_B T}} - 1} \mathrm{d}\epsilon = \frac{2.612}{\lambda_T^3} \tag{2.6}$$

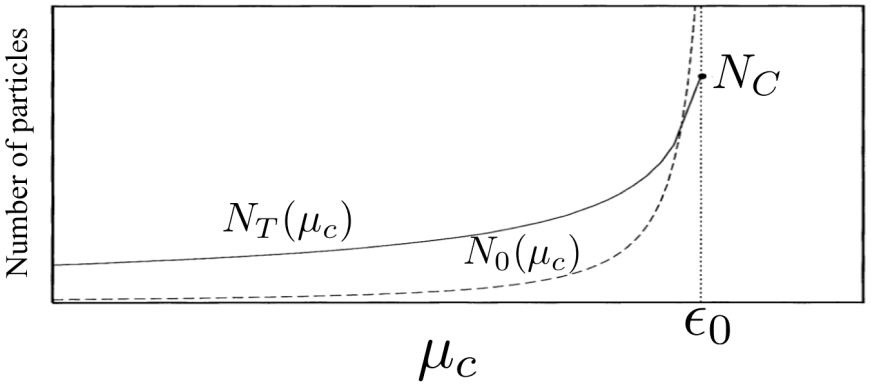

FIGURE 2.1: Ideal gas model. Number of particles out of the condensate (N_T, solid line) and in the condensate (N_0, dashed line) as a function of the chemical potential, for a fixed value of T. The system ground state energy is given by ϵ_0 and the maximum non-condensed number of particles is represented by N_c when $\mu_c = \epsilon_0$. Adapted from Ref. [111].

where

$$\lambda_T = \sqrt{\frac{2\pi\hbar^2}{mk_BT}} \tag{2.7}$$

is the *de Broglie wavelength*, which reflects the average quantum size of the particles conforming the gas at temperature T, and V is the volume of the gas. For a fixed value of T, the function N_T has a smooth behavior as a function of μ_c and reaches its maximum, critical value, $N_c = N_T^{\mu_c \to \epsilon_0}$ at $\mu_c = \epsilon_0$ (see Fig. 2.1). The behavior of No is very different: it diverges when μ_c is close to ϵ_0. If the total number of particles exceeds N_c then the additional particles, $N - N_c$, will populate the ground state. In other words, above N_c if we add a new particle in such a way that this particle does not change the temperature of the system, this particle will occupy the ground state. In this way, the ground state can achieve macroscopic occupations (in free space, this is the zero-momentum state), and BEC takes place [110]. Equivalently, at a finite T, when the number of particles increases and the chemical potential μ_c approaches the ground state ϵ_0 from lower values, the number of particles in all the excited states saturates asymptotically and the ground state occupation diverges (Fig. 2.2). In this way, the ground state can achieve macroscopic occupations, and BEC takes place.

2.1.2 Discussion about different systems for Bose-Einstein condensation

Equation 2.5 means that in order for a Bose gas to condensate in a BEC, the average distance between particles must be on the order of their quantum size (note that Eq. 2.5 defines a critical temperature T_c of the same order as the one defined by Eq. 2.2). Due to the heavy mass of the atomic bosons employed in BEC studies, Eq. 2.5 implies working at sub-μK temperatures. In the following lines we discuss three novel systems where BEC phenomena have been observed in the recent years.

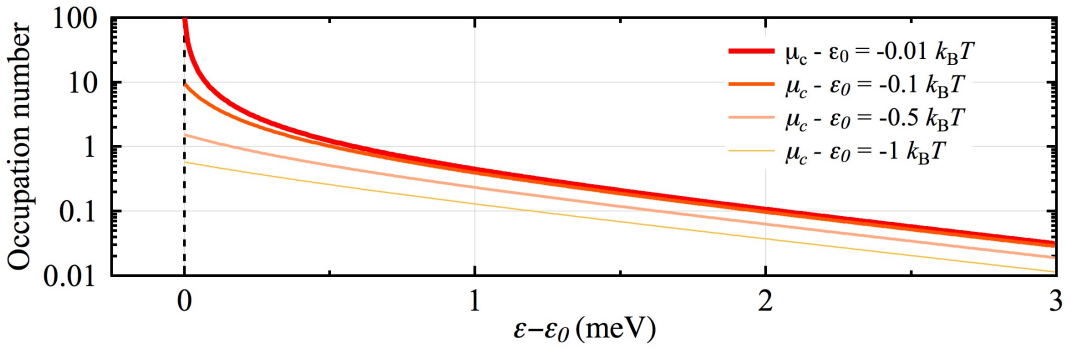

FIGURE 2.2: Bose-Einstein occupation distribution (Eq. 2.1) for increasing values of chemical potential (which is equivalent to higher particle densities).

Exciton-polaritons

Exciton-polaritons are bosonic quasi-particles composed by light and matter. Due to their photonic component, the polariton effective mass is 10^9 times smaller than that of atoms, yielding much higher temperatures for condensation — see Table 2.1 — even a room temperature in ZnO, GaN and organic MCs. The first theoretical proposal of this innovative system where BEC could be feasible was posed by A. Imamoğlu *et al.* [112]. They suggested to obtain coherent light emission from an out-of-equilibrium condensed state of exciton-polaritons for the realization of a "polariton laser" device. A few years later, the bosonic character of these quasi-particles was finally proven by the work of P. Savvidis *et al.* [52] and R. M. Stevenson *et al.* [113], who observed stimulated scattering of polariton particles in a pump-probe experiment. The full convincing evidence of polariton BEC was reported in 2006 by J. Kasprzak *et al.* [21] (subsequently followed by many others [23, 114]); in this work the most important characteristics of BEC were shown:

- Narrowing of the momentum-space distribution [Fig. 2.3(a)].
- Buildup of the first order temporal coherence measured by the line width emission [Fig. 2.3(b)].
- Change in the polariton distribution from Boltzmann-like to Bose-Einstein-like distribution with a degenerate ground state [Fig. 2.3(c)].
- Build-up of a collective spinor wavefunction by polarization measurements [Fig. 2.3(d)].
- Macroscopic phase coherence [Fig. 2.3(e)].

Excitons

For the sake of completeness, let us discuss also the quest for condensation with excitons. As already described in § 1.2, excitons are composite particles that form a hydrogen-like state out

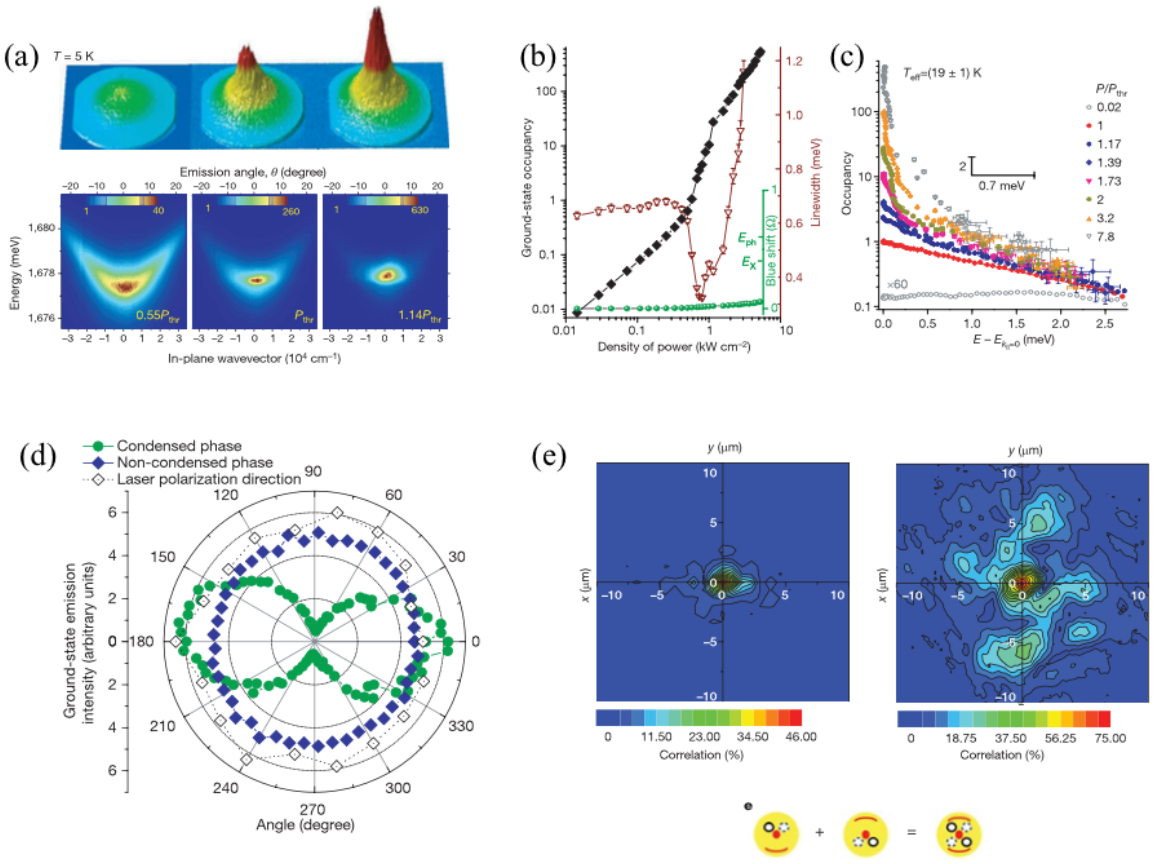

FIGURE 2.3: Summary of the most important characteristics of exciton-polariton BEC, shown by Kasprzak and co-workers, adapted from Ref. [21]. (a) Momentum space distribution narrowing as function of the pump power excitation and blueshift of the polariton emission. (b) Spectral narrowing and nonlinear increase of the ground state emission. (c) Polariton occupancy in ground- and excited-state levels for various excitation powers. (d) Polarization properties of the polariton emission. Below threshold (solid blue diamonds), the emission is completely depolarized for linear polarization, whereas above threshold (solid green circles) a linear polarization exceeding 80% is observed. (e) Real space distribution map of the coherence buildup, measured below and above threshold.

of an electron and a hole in a semiconductor. The spin adds up to a total integer spin, making the composite a boson. The suitability of excitons for BEC was theoretically investigated since the 1960s [115–117]. Excitons have smaller effective masses than that of the free electron and therefore should condense at temperatures of about ~ 1 K, attainable with helium refrigerators. Furthermore, in the case of bright excitons, BEC should be easily experimentally observed by emission of coherent light. Recent but inconclusive claims for experimental observation have been made for excitons in 1980 [118] and bi-excitons in 1979 [119]. Unfortunately, bright excitons have short lifetimes, preventing them to thermalize below quantum degeneracy. Therefore researchers focused on condensation of dark excitons [120] and excitons in coupled QWs where the electron and the hole are confined in separate QWs, typically dubbed indirect excitons. This increases their radiative lifetime and decreases their scattering time with acoustic phonons [121–123]. A few years ago, long-range spatial coherence has been confirmed in these systems [124].

Systems	**atomic gases**	**excitons**	**polaritons**
Effective mass (m^*/m_e)	10^3	10^{-1}	10^{-5}
Bohr radius a_B (Å)	10^{-1}	10^2	10^2
Particle spacing: $n^{-1/d}$	10^3 Å	10^2 Å	1 μm
Critical temperature T_c	1 nK − 1 μK	1 mK − 1 K	1 K − > 300 K
$\frac{\text{Thermalization time}}{\text{Lifetime}}$	$\frac{1\,\text{ms}}{1\,\text{s}} \approx 10^{-3}$	$\frac{10\,\text{ps}}{1\,\text{ns}} \approx 10^{-2}$	$\frac{1-10\text{ps}}{1-10\text{ps}} \approx 0.1 - 10$

TABLE 2.1: Summary of the critical values for condensation of atoms, excitons and polaritons [125]. The effective mass determines the condensation temperature. A lighter mass results in a higher condensations temperature. The Bohr radius determines the particle spacing at which the wave functions start overlapping and condensation occurs. d signifies the dimensionality of the system. The critical temperatures are given for typical experimental particle densities. The ratio of thermalization time and lifetime is given, as the particles need to thermalize within their lifetime for condensation to occur. Excitons and polaritons are superior candidates for condensation in all listed categories except for their short lifetime.

Photons

Finally, we comment some aspects about the condensation of photons. The fact is that photons cannot undergo BEC by lowering the temperature because it leads to photonic absorption, and therefore the total number of photons is not conserved. This phenomenon is commonly known as "*black body radiation*" [126], and it follows the Stefan-Boltzmann law, indicating that the total number of photons depends on the temperature of the system. The direct consequence of this is that photons are absorbed at low temperature instead of condensing in a macroscopic ground state. This idea was questioned by the group of M. Weitz, who observed a number of particles conserving thermalization [127] and subsequent BEC at higher excitation powers [128] in a high quality MC, filled with a dye [Fig. 2.4(a)]. This system operates in the WCR. In principle, the phenomenon can be interpreted as the weak coupling of photons with Frenkel-excitons of the dye molecules.

Photons are efficiently confined inside the cavity mirrors, which also provides a parabolic dispersion and therefore an effective photon mass. This makes the system formally equivalent to a 2D gas of trapped, massive bosons. Photons thermalize through multiple scattering events with the dye molecules in the cavity. At criticality the photons start to condense in the ground state at the centre of the trap [Fig. 2.4(a)]. The measured condensation threshold corresponds well to the density of photons where the de Broglie wave-packets start to overlap [$n\lambda_{db}^2$, Fig. 2.4(c)]. Finally thermal redistribution causes condensation in the trap centre even for a pump-spot, that is spatially displaced from the trap centre [Fig. 2.4 (d)]. This effect was previously observed in polariton BECs [22], but is unknown in lasers.

In lasers a macroscopic number of photons becomes coherent and occupies the same state, but both the light field and the gain medium are out of thermal equilibrium, which is in contrast to the observations described above.

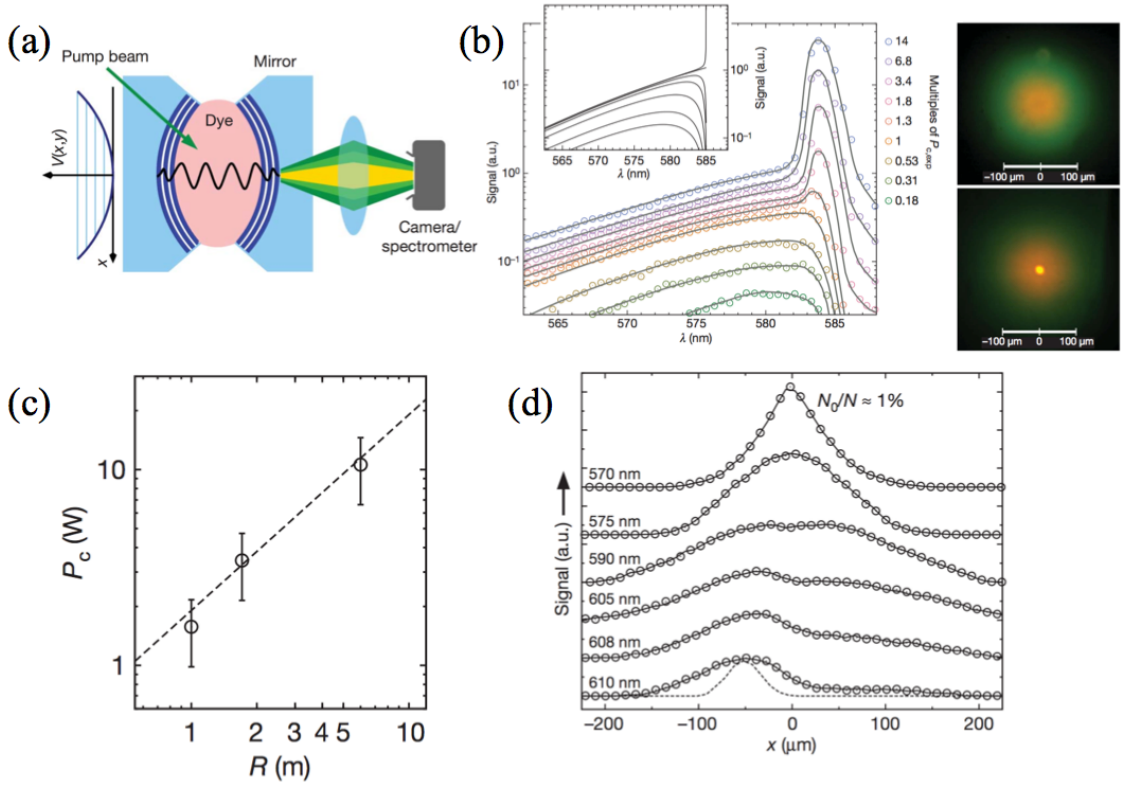

FIGURE 2.4: (a) Resonator geometry used for photon condensation. (b) Spectral and spatial distribution of the emission. Upper right panel below threshold, lower right panel above threshold. (c) Measured and calculated critical power as function of the curvature radius of the confining mirrors. (d) Spatial emission distribution for a spatially displaced pump spot [128].

2.1.3 Weakly-interacting Bose gas and the Bogoliubov approximation

The ideal Bose gas considered in the previous chapter does not take into account interactions between particles, which do affect the properties of the gas and are expected to play a role even for dilute species. Interactions are particularly important in this thesis since polaritons strongly scatter via the dipole moment of its excitonic part.

Let us deal with a weakly interacting 3D Bose gas, where the scattering length a is much smaller then the average distance between particles $d \ll (N/V)^{-1/3}$. This allows one to consider only configurations involving pairs of interacting particles, while configurations with three or more particles interacting simultaneously can be safely neglected. A similar phenomenon to BEC occurs, in thermal equilibrium, in a system of interacting bosons, provided that the interaction is overall positive (repulsive). We shall always consider gases at temperatures smaller than the critical temperature for BEC (Eq. 2.2). This implies that the relevant values of momenta always satisfy the inequality $pd \ll \hbar$.

Under such conditions, the Hamiltonian of a weakly-interacting Bose gas can be written in the second quantization picture as [111]:

$$\mathcal{H} = \sum_{\mathbf{p}} \frac{p^2}{2m} \hat{a}^\dagger_{\mathbf{p}} \hat{a}_{\mathbf{p}} + \frac{V_0}{2V} \sum_{\mathbf{p}_1, \mathbf{p}_2, \mathbf{q}} \hat{a}^\dagger_{\mathbf{p}_1+\mathbf{q}} \hat{a}^\dagger_{\mathbf{p}_2-\mathbf{q}} \hat{a}_{\mathbf{p}_1} \hat{a}_{\mathbf{p}_2}, \tag{2.8}$$

where $\hat{a}_{\mathbf{p}}$ ($\hat{a}^\dagger_{\mathbf{p}}$) is the operator annihilating (creating) a particle in the single-particle state with momentum $\mathbf{p}$ and V_0 is an macroscopic approximation to the microscopic two-body potential (V is the total volume).

In the so called Bogoliubov approximation [129], the single-particle annihilation operator is replaced by a number, $a \equiv \sqrt{N_0}$, which is valid for the effective smooth inter-particle potential V_0 [111]. For a Bose gas at $T = 0$, the occupation of states with $\mathbf{p} \neq 0$ is small, $N \sim N_0$, and V_0 depends only on the scattering length a in the Born approximation

$$V_0 = 4\pi\hbar^2 a/m = g \tag{2.9}$$

where g is called the interaction coupling constant. The ground state energy of the hamiltonian described in previous Eq. 2.8 takes the form

$$E_0 = \frac{N^2 g}{2V} \tag{2.10}$$

Contrary to the ideal case, the pressure of a weakly-interacting Bose gas does not vanish at zero temperature:

$$P = -\frac{\partial E_0}{\partial V} = \frac{g\,(N/V)^2}{2}, \tag{2.11}$$

Accordingly, the compressibility is also finite:

$$\frac{\partial(N/V)}{\partial P} = \frac{V}{gN}, \tag{2.12}$$

and tends to infinity when $g \to 0$. Using the hydrodynamic relation $\frac{1}{mc^2} = \frac{\partial(N/V)}{\partial P}$ for the compressibility one obtains the sound speed:

$$c_s = \sqrt{\frac{gN}{mV}} \tag{2.13}$$

The condition of thermodynamic stability implies that the value of the compressibility must be positive, *i.e.* $a > 0$ from Eqs. 2.9-2.12. Then a dilute uniform BEC gas can exist only if the scattering length is positive.

The chemical potential is given by:

$$\mu_c = \frac{\partial E_0}{\partial N} = \frac{gN}{V} = mc_s^2 \tag{2.14}$$

The momentum dependence on the energy (dispersion relation) of the weakly-interacting Bose gas can be calculated by considering the $\mathbf{p} \neq 0$ terms in the Hamiltonian 2.8. However now the lowest-order Born approximation for the two-body potential V_0 no longer holds. Using higher-order perturbation theory one finds the result [130]

$$V_0 = g\left(1 + \frac{g}{V}\sum_{\mathbf{p}\neq 0}\frac{m}{p^2}\right) \tag{2.15}$$

where g is related to the scattering length by Eq. 2.9. Equation 2.15 renormalizes the relationship between the effective potential and the physical coupling constant g. The Hamiltonian in Eq. 2.8 becomes quadratic in the operators $\hat{a}_{\mathbf{p}}$ and $\hat{a}^{\dagger}_{\mathbf{p}}$ and can be diagonalized to [111]

$$\mathcal{H} = E_0 + \sum_{\mathbf{p}} \epsilon(\mathbf{p})\hat{b}^{\dagger}_{\mathbf{p}}\hat{b}_{\mathbf{p}}, \tag{2.16}$$

where

$$E_0 = g\frac{N^2}{2V}\left[1 + \frac{128}{15\sqrt{\pi}}\sqrt{\frac{Na^3}{V}}\right] \tag{2.17}$$

is the ground state energy calculated to the higher-order of approximation [131, 132],

$$\epsilon(p) = \sqrt{\frac{gN}{mV}p^2 + \left(\frac{p^2}{2m}\right)^2} \tag{2.18}$$

is the so called *Bogoliubov dispersion law* for the elementary excitations of the system, and the new quasi-particle operators $\hat{b}_{\mathbf{p}}$ and $\hat{b}^{\dagger}_{\mathbf{p}}$ are related to the to the single-particle operator through the Bogoliubov transformation

$$\hat{a}_{\mathbf{p}} = u_{\mathbf{p}}\hat{b}_{\mathbf{p}} + v^{*}_{-\mathbf{p}}\hat{b}^{\dagger}_{-\mathbf{p}} \tag{2.19a}$$

$$\hat{a}_{\mathbf{p}}\dagger = u^{*}_{\mathbf{p}}\hat{b}^{\dagger}_{\mathbf{p}} + v_{-\mathbf{p}}\hat{b}_{-\mathbf{p}} \tag{2.19b}$$

where the coefficients $u_{\mathbf{p}}$ and $v_{-\mathbf{p}}$ are given by:

$$u_{\mathbf{p}}, v_{-\mathbf{p}} = \pm\sqrt{\frac{p^2/(2m) + gN/V}{2\epsilon(p)} \pm \frac{1}{2}} \tag{2.20}$$

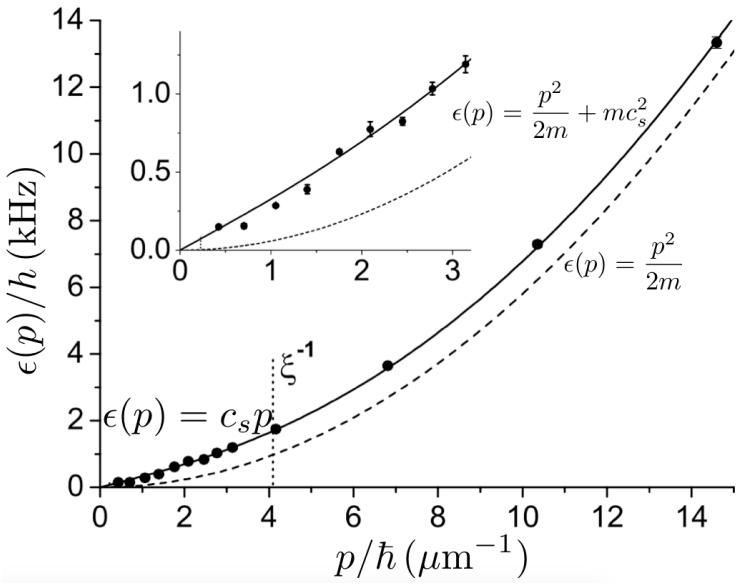

FIGURE 2.5: Excitation spectrum $\epsilon(p)$ of a ^{87}Rb trapped BEC measured with Bragg scattering (black circles). The solid line is the Bogoliubov spectrum, Eq. 2.18, and the dashed line is the parabolic free-particle spectrum. The inset shows the linear phonon regime. The transition between the phonon ($c_s p$) and the free-particle ($p^2/(2m)$) regimes takes place at $p \sim \hbar/\xi$. Adapted from Ref. [64].

Equations 2.16 and 2.18 mean that the original system of interacting particles can be described in terms of a Hamiltonian of non-interacting quasi-particles having energy $\epsilon(p)$ and whose annihilation and creation operators are given, respectively, by $\hat{b}_{\mathbf{p}}$ and $\hat{b}^{\dagger}_{\mathbf{p}}$. The ground state of the interacting system then corresponds to the vacuum of quasi-particles.

For small momenta $p \ll mc_s$ the dispersion law of quasi-particles takes the phonon-like form, $\epsilon(p) \approx c_s p$, where c_s is the sound velocity defined in Eq. 2.13 — see Fig. 2.5. The Bogoliubov theory then predicts that the long wavelength excitations of an interacting Bose gas are sound waves. These excitations can also be regarded as the Goldstone modes associated with breaking of a gauge symmetry caused by BEC. In the opposite limit $p \gg mc_s$ the dispersion law approaches the free particle law, $\epsilon(p) \approx \frac{p^2}{2m} + \frac{gN}{V}$ (see Fig. 2.5).

The transition between the phonon and particle regimes takes place when $p^2/(2m) \sim gN/V$, *i.e.* for $p \sim \sqrt{2}mc_s$. This allows to define the characteristic interaction length (also called the *healing length*) by making $p = \hbar/\xi$ (see Fig. 2.5):

$$\xi = \sqrt{\frac{\hbar^2 V}{2mgN}} = \frac{1}{\sqrt{2}} \frac{\hbar}{mc_s} \tag{2.21}$$

2.2 Superfluidity

The first observation of superfluidity was made simultaneously by Pyotr Kapitsa in Moscow [133] and John F. Allen in Cambridge [134] in 1938, using liquid ^4He. They measured the resistance to the flow of liquid helium clamped in narrow channels and subjected to a pressure drop. It was found that while the so-called He-I phase, *i.e.*, helium above 2.17 K, the "lambda" temperature, showed a behavior that could be described in terms of conventional viscosity, whereas below the lambda point (in the so-called He-II phase) the liquid flowed so easily that if the concept of viscosity was applicable at all, it would have to be at least a factor of 1500 smaller than in the He-I phase.

Superfluids can flow through narrow capillaries or slits without dissipating energy, their shear viscosity being equal to zero. The fact that superfluidity appear below a critical temperature and that the ^4He atom is composed of an even number of elementary particles (2 protons, 2 neutrons, and 2 electrons), and so the system should obey Bose statistics, have motivated the quest for an explanation to superfluidity phenomena based on BEC. Next section develops these ideas in a quantitative way.

2.2.1 Landau's criterion of superfluidity

To understand under which conditions a moving fluid can give rise to dissipation, let us follow the ideas of Landau [135, 136]. A moving fluid produces dissipation of energy, with consequent heating and decrease of the kinetic energy, through the creation of elementary excitations. If the excitation spectrum of given fluid is known on its reference frame, the same will be known under movement after Galilean transformations. Let us first consider a uniform fluid at zero temperature flowing along a capillary at constant velocity v. In the fluid reference system, if a single excitation with momentum p appears then the total energy is $E_0 + \epsilon(\mathbf{p})$, where E_0 and $\epsilon(\mathbf{p})$ are, respectively, the energy of the ground state and of the excitation. In the reference system where the capillary is at rest (this reference moves with velocity $-\mathbf{v}$ relative to the fluid) the energy E' and momentum $\mathbf{P'}$ are given, using Galilean transformations, by:

$$E' = E_0 + \epsilon(\mathbf{p}) + \mathbf{p}\cdot\mathbf{v} + \frac{1}{2}Mv^2 \tag{2.22a}$$

$$\mathbf{P'} = \mathbf{p} + M\mathbf{v} \tag{2.22b}$$

where M is the mass of the fluid.

Equations 2.22 show that the quantities $\epsilon(\mathbf{p}) + \mathbf{p}\cdot\mathbf{v}$ and $\mathbf{p}$ are, respectively, the change in energy and in momentum in the frame where the capillary due to the appearance of the excitation. The process of spontaneous creation of excitations can take place only if the excitation energy is

negative:

$$\epsilon(\mathbf{p}) + \mathbf{p}\cdot\mathbf{v} < 0 \Rightarrow v > \epsilon(\mathbf{p})/\mathbf{p} \tag{2.23}$$

In this case the flow of the fluid is unstable and its kinetic energy will be transformed into heat. If instead

$$v < v_c = \min_{\mathbf{p}} \epsilon(\mathbf{p})/\mathbf{p} \tag{2.24}$$

then the condition given by Eq. 2.23 is never satisfied and no excitation will spontaneously grow in the fluid. Condition 2.24 is the so called Landau's criterion for superfluidity. It ensures that if the relative velocity between the fluid and the capillary is smaller than the critical value v_c then there will be a persistent flow without friction.

By looking at the Bogoliubov excitation spectrum (Eq. 2.18 and Fig. 2.3), one easily concludes that the weakly-interacting Bose gas fulfills the Landau criterion for superfluidity and that the critical velocity is given by the velocity of sound c_s (Eq. 2.13). Superfluidity is then strongly related to the phenomenon of BEC. However according to the Landau criterion the ideal Bose gas is instead not superfluid since the value of v_c is equal to zero.

2.3 Long-range order

Given a field $\psi(r,t)$, the density matrix (also called correlation function), $\rho = |\psi\rangle\langle\psi|$, in space-time representation is given by:

$$\rho(\mathbf{r},\mathbf{r}',t,t') = \langle \mathbf{r},t|\rho|\mathbf{r}',t'\rangle = \langle \mathbf{r},t|\psi\rangle\langle\psi|\mathbf{r}',t'\rangle = \langle \psi(\mathbf{r},t)\psi^*(\mathbf{r}',t')\rangle \tag{2.25}$$

where the last $\langle\rangle$ denotes statistical average. It is clear that $\rho(\mathbf{r},\mathbf{r},t,t) = n(\mathbf{r},t)$ is a real number (since ρ is an Hermitean operator, $\rho^\dagger = \rho$) that represents the density of particles in position $\mathbf{r}$ at a time t.

The field can also be represented in energy-momentum space after Fourier transform, $\widetilde{\psi}(\mathbf{k},\omega) = \int \mathrm{d}\mathbf{r}\mathrm{d}t\, \psi(\mathbf{r},t)e^{i(\mathbf{k}\cdot\mathbf{r}-\omega t)}$. The Wiener-Khinchin identity [137–139] states that the energy and momentum distribution $|\widetilde{\psi}(\mathbf{k},\omega)|^2$ of such a field can be calculated from its density matrix through a simple Fourier transform:

$$|\widetilde{\psi}(\mathbf{k},\omega)|^2 = \int \mathrm{d}\mathbf{r}\mathrm{d}\mathbf{r}'\mathrm{d}t\mathrm{d}t'\, \rho(\mathbf{r},\mathbf{r}',t,t')e^{i[\mathbf{k}\cdot(\mathbf{r}-\mathbf{r}')-\omega(t-t')]} \tag{2.26}$$

As discussed in § 2.1, BEC appears when the main population occupies a single energy-momentum state. Using Fourier transform properties and the Wiener-Khinchin identity 2.26, a

narrow momentum distribution $|\widetilde{\psi}(\mathbf{k},\omega)|^2$ implies a broad correlation $\rho(\mathbf{r}-\mathbf{r}')$ and so the off-diagonal terms of the density matrix $\rho(\mathbf{r},\mathbf{r}')$ are different from zero. More specifically, if the $|\widetilde{\psi}(\mathbf{k},\omega)|^2$ distribution is concentrated on the $\mathbf{k}=0$ value, $\rho(\mathbf{r}-\mathbf{r}')$ tends to a plateau value different from zero as $|\mathbf{r}-\mathbf{r}'|\to\infty$. This corresponds to the existence of off-diagonal long-range order (ODLRO) and was proposed by Penrose and Onsager in 1956 [12] as a general definition of a BEC. This is equivalent to say that N_0, the largest eigenvalue of ρ, is of the order of the total number of particles in the quantum fluid.

The density matrix of a macroscopic quantum system can be then decomposed into its ground state part and the excited states part,

$$\rho(\mathbf{r},\mathbf{r}') = \langle\psi_0(\mathbf{r})\psi_0^*(\mathbf{r}')\rangle + \langle\psi_{exc}(\mathbf{r})\psi_{exc}^*(\mathbf{r}')\rangle \tag{2.27}$$

The second term in the right hand side of Eq. 2.27 goes to zero when $|\mathbf{r}-\mathbf{r}'|$ goes to ∞, while the first term has a finite and constant value due to the well defined phase of the macroscopically occupied ground state [140].

Figure 2.6 shows the measured spatial dependence of the normalized correlation function $\rho(\Delta r)/\rho(r)$ for ^{87}Rb atoms trapped and cooled by a magneto-optical trap, from Ref. [65]. The correlation values are extracted from the visibility of interferences between distant points of the gas. The thermal non-condensed fraction of the gas is responsible for a Gaussian decay of the correlation, with a a spatial scale given by the de Broglie wavelength, Eq. 2.5. Above the critical temperature for condensation, such a decay goes down to zero for large distances, differently for the non-zero plateau observed for temperatures bellow condensation threshold — see Fig. 2.6. Such a plateau has the value of the fraction of atoms occupying the zero-momentum state, N_0/N also called condensed fraction [111].

2.3.1 Condensation in low dimensions

Conventional long-range order, as in a ferromagnet or a crystal, is common in 3D systems at low temperature. However, in 2D systems with a continuous symmetry, true long-range order is destroyed by thermal fluctuations at any finite temperature [141]. Consequently, for the case of identical bosons, a uniform 2D fluid cannot undergo BEC, in contrast to the 3D case.

In fact, if one tries to calculate the critical density for condensation to take place, by performing an integral similar to Eq. 2.5 but using instead a 2D density of states, the result diverges at non-zero temperature. Thus, the non-interacting Bose gas cannot condense in an infinite 2D system. The same statement turns out to be also true when interactions are taken into account. A rigorous proof of the absence of BEC in two dimensions has been given by P. C. Hohenberg [142].

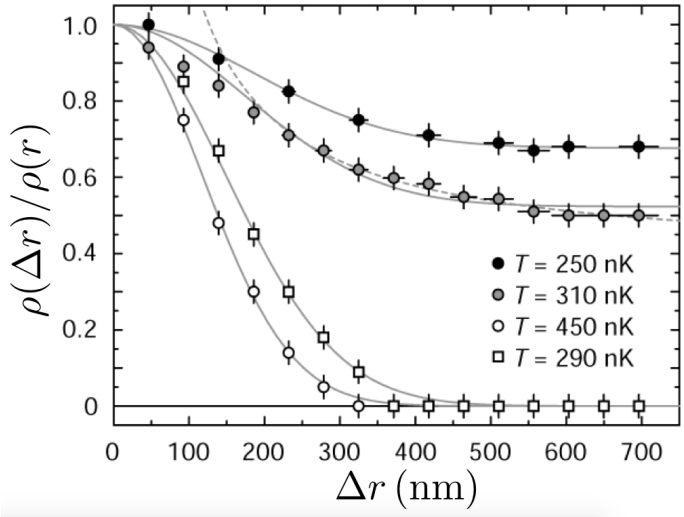

FIGURE 2.6: Normalized spatial correlation function $\rho(\Delta r)/\rho(r)$ of a ^{87}Rb trapped Bose gas, for temperatures above and below the critical temperature $T_c = 430$ nK. The white circles show the measurements for thermal gases at 450 nK. The grey data points (310 nK) and the black data points (250 nK) are the results obtained for temperatures below T_c, where the visibility decays to a nonzero value due to the long-range phase coherence of the condensate fraction. The data sets are plotted with a gaussian function and an offset. Adapted from Ref. [65].

However, the 2D system can form a quasi-condensate and become superfluid below a finite critical temperature. The Berezinskii-Kosterlitz-Thouless (BKT) theory [143, 144] associates this phase transition with the emergence of a topological order, resulting from the pairing of vortices with opposite circulation (see next § 2.4). At the transition temperature $T = T_{BKT}$, the spatial correlation function decays according to a power-law with a value of the decay exponent equal to 1/4 [111, 145]. Above the critical temperature, proliferation of unbound vortices is expected and the quasi-long-range order is lost.

2.4 Rotation of quantum fluids

To construct a quantitative theory of the flow properties of He-II, Landau postulated that it consisted of two components: the *superfluid* component, which he identified, in an intuitive way, with the part of the liquid that remained in its ground state, and a *normal* component, which corresponded to the thermal cloud. The superfluid component was conceived as carrying zero entropy and flowing irrotationally; by contrast, the normal component behaved like any other viscous liquid.

The presence of a large number of atoms in the ground state (forming a BEC) allows the introduction of a classical function $\psi_0(\mathbf{r}, t)$ to describe the order parameter. In the mean field approximation, assuming that ψ_0 varies slowly on distances of the order of the range of the interatomic forces, one can introduce interactions to the Schrödinger Hamiltonian by means of the

density-dependent chemical potential defined in Eq. 2.14:

$$i\hbar\partial_t\psi_0(\mathbf{r},t) = \left(-\frac{\hbar^2\nabla^2}{2m} + V + g|\psi_0(\mathbf{r},t)|^2\right)\psi_0(\mathbf{r},t) \tag{2.28}$$

where g is the interaction coupling constant defined by Eq. 2.9.

Equation 2.28 was derived independently by Gross and Pitaevskii in 1961 [146, 147] and is the main theoretical tool for investigating non-uniform dilute Bose gases at low temperatures. An important peculiarity is the nonlinearity arising from the interaction among particles, which introduces an important analogy between BEC and nonlinear optics.

Equation 2.28 holds the continuity equation[1],

$$\partial_t|\psi_0|^2 + \nabla\cdot\mathbf{j} = 0 \tag{2.29}$$

where the current density $\mathbf{j}$ is given by

$$\mathbf{j}(\mathbf{r},t) = -i\frac{\hbar}{2m}(\psi_0^*\nabla\psi_0 - \psi_0\nabla\psi_0^*) = \frac{\hbar}{m}\nabla|\psi_0|^2\phi \tag{2.30}$$

Here ϕ is the phase of the order parameter, $\psi_0(\mathbf{r},t) = |\psi_0|e^{i\phi(\mathbf{r},t)}$. Equation 2.30 shows that the vector

$$\mathbf{v}_s(\mathbf{r},t) = \frac{\hbar}{m}\nabla\phi(\mathbf{r},t) \tag{2.31}$$

is the velocity of the condensate flow, which turns out to be irrotational ($\nabla\times\mathbf{v}_s = 0$), a typical characteristic of superfluids. For a simply connected region of space in which $|\psi_0(\mathbf{r},t)|$ is everywhere nonzero, the application of Stokes' theorem to the curl of Eq. 2.31 leads to the conclusion that the integral of $\mathbf{v}_s$ around any closed curve is zero.

2.4.1 Quantized vortices

The GP equation 2.28 also admits non-trivial solutions with a core region where the density goes to zero. Such a solution is no longer imposed by the Stokes' theorem to have a vanishing integral of the velocity around a circuit that encloses the core. The fact that the phase $\phi(\mathbf{r})$ must be single-valued, modulo 2π, leads to the Onsager-Feynman quantization condition

$$\oint \mathbf{v}_s \mathrm{d}l = \frac{Mh}{m} \tag{2.32}$$

The parameter M is an integer in order to ensure that the wave function is single valued.

[1] This is not the case of the GP equation for the polaritons simulation (see next § 2.5.2), where pumping and decay terms are included in the Hamiltonian.

Such vortex solutions are written in cylindrical coordinates as

$$\psi_0(\mathrm{r}) = e^{iM\varphi}|\psi_0(r)|, \tag{2.33}$$

with φ the azimuthal angle and r the radius. The size of the zero-density core in $|\psi_0(r)|$ is of the order of the healing length, Eq. 2.21 [111]. Equation 2.33 is an eigenstate of the third component of the angular momentum[2] with $l_z = M\hbar$, so that the vortex carries a total angular momentum equal to $L_z = N_0 M\hbar$. This wave function represents a gas rotating around the z-axis with tangential velocity $v_s = \frac{M\hbar}{mr}$, completely different from the rigid rotational field, which is also tangential, but whose modulus increases with r.

The result obtained in Eq. 2.32 is independent of the radius of the contour. This is a consequence of the fact that the vorticity ϖ of the velocity field is concentrated on the z-axis according to the law

$$\varpi = \nabla \times \mathrm{r}_s = \frac{Mh}{m}\delta^{(2)}(\mathrm{r})\hat{z} \tag{2.34}$$

where $\delta^{(2)}(\mathrm{r})$ is the 2D Dirac delta function and r is the radial position vector perpendicular to $\hat{z}$. Results compiled in Eqs. 2.33 and 2.34 show that the irrotationality criterion, associated with the occurrence of BEC, is satisfied everywhere except on the line of the vortex. This equations establishes the irrotationality of the superfluid motion, the phase of the order parameter playing the role of a velocity potential.

The existence of vortices was first predicted in superfluids [148, 149], and later in coherent waves [150]. Nowadays, quantum vortices have been the subject of extensive research across several areas of physics and have been observed in type-II superconductors, ^4He, ultracold atomic gases and nonlinear optics media (for a review see, *e.g.*, [151, 152]). The direct visualization of vortices was achieved in the experiments by Packard and Sanders [153]. In this experiment one injects a beam of electrons inside a rotating cylinder of liquid ^4He. Vortex lines trap the electrons, which are then accelerated along the vertical line by an electric field and are eventually detected after escaping from the liquid. Figure 2.7 (upper graph) show the electrometer voltage output as a function of the rotating cylinder angular velocity. Clearly a rotation threshold is needed for the superfluid to start rotating and the electron signal to be detected. As the rotation is further increased, the detected signal increases by quantized jumps, which are related to the creation of extra vortices.

A similar apparatus with spatial resolution have been used to image arrays of quantized vortex lines distributed in a regular geometry, through electrons that create spots on a fluorescent screen [154] — Fig. 2.7 (lower panels).

[2]For the sake of simplicity, and making an abuse of language, we shall call in the rest of the manuscript angular momentum to its third component.

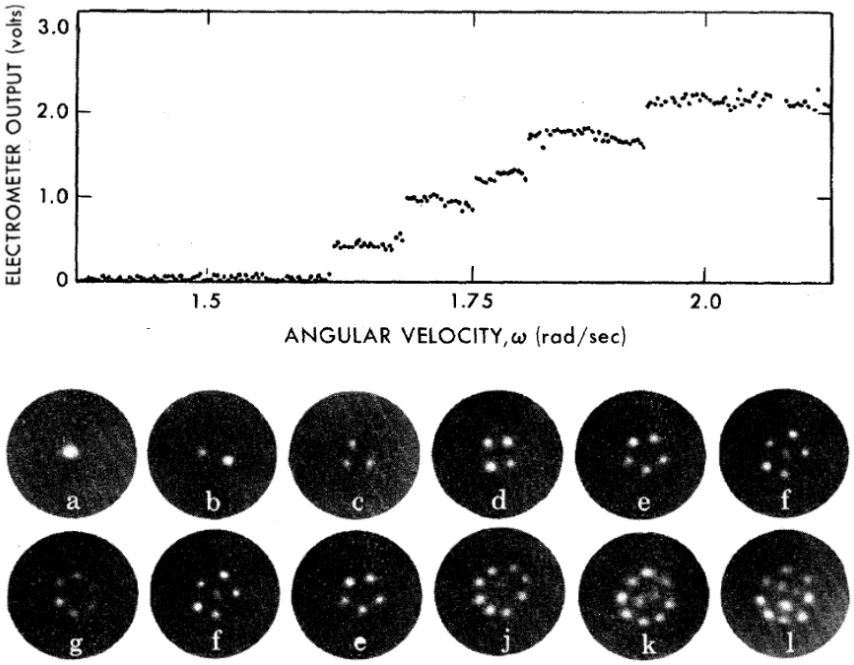

FIGURE 2.7: Quantized rotation of superfluid helium. (upper graph) Measured voltage of an electrometer that detects electrons transmitted by rotating superfluid helium through its vortex lines, as a function of the container angular velocity. The signal is proportional to the number of vortices in the system. (lower panels) Photographs of stable vortex arrays in superfluid helium for different angular velocities. Upper graph from Ref. [153]. Lower panels from Ref. [154].

Quantized vortices in trapped Bose gases have become experimentally available by making use of a suitable rotating modulation of the trap to stir the condensate [155], in close resemblance with the rotating bucket experiment of superfluid helium. However in situ measurements cannot provide any evidence of the vortex core, whose size (typically less than one micron) is too small, which introduces the need to expand the condensate cloud in order to enlarge the vortex to become visible. Above a critical angular velocity one observes the formation of the vortex. A typical picture is shown in Fig. 2.8, where one can see that, at sufficiently high angular velocities, arrays with more vortices are also formed. It is possible to create arrays containing a very large number of vortical lines — see Ref. [66] and last panels of Fig. 2.8. These arrays form a typical triangular lattice, which is similar to what happens in superconductors [156].

2.5 Exciton-polariton quantum fluids

As previously discussed in § 2.1.2, the phenomenon of condensation has not only resided in the atomic or superfluid helium community but it has rather stimulated the semiconductor community from the early years. As early as 1962, excitons were proposed by Blatt and Moskalenko as promising candidates for the realization of BEC [157]. The bosonic nature of these quasi-particles and their light mass, were the main reasons for the long efforts to demonstrate condensation, with

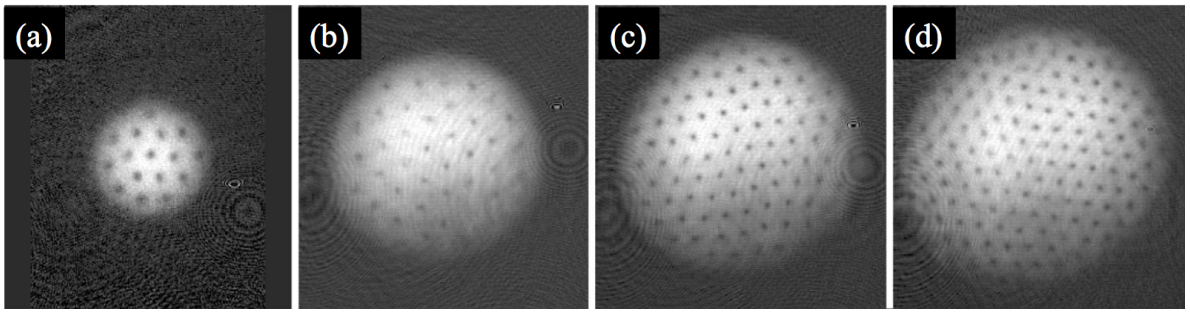

FIGURE 2.8: Observation of vortex lattices in an atomic BEC. The examples shown contain approximately (a) 16, (b) 32, (c) 80, and (d) 130 vortices. The vortices have "crystallized" in a triangular pattern. Extracted from [66]

good progresses made in bilayer systems [158]. More recently excitons have been shown to display spontaneous spatial coherence at cryogenic temperatures [124].

The observation of SCR in semiconductor MCs [11] showed that polaritons — composite bosons with a half exciton- half photon-nature — could be a new system to study condensation in semiconductor materials. The polariton dispersion can act as a trap in momentum space and the mass of polaritons is four orders of magnitude lighter than that of excitons, theoretically allowing condensation even at room temperatures, according to Eq. 2.2.

The first theoretical discussion on the strong potential of exciton-polaritons for the realization of novel quantum degenerate Bose gases was done by A. Imamoğlu and co-workers in 1996 [112]. It was suggested that, provided that the thermal de Broglie wavelength λ_T exceeds the exciton Bohr radius a_B, an exciton laser would operate without electronic population inversion — the light emitted by a polariton condensate after decay is coherent, hence the analogy with a laser.

The properties of a polariton condensate differ from those of other known condensates, such as ultracold atomic BECs and superfluid ^{4}He. In particular, polaritons have a short lifetime of the order of picoseconds, which allows to study their phase and coherence in a direct way through the photons leaking out of the cavity, a feature not accessible to other bosonic quasi-particles. Therefore a continuous pumping is necessary to balance the polariton decay and reach a steady-state regime. Rather than a drawback, the intrinsic non-equilibrium nature enriches the features of polariton condensation.

Condensation-related phenomena has been experimentally observed in polaritons in different samples, excitation setups and temperatures [20–23, 26, 27, 36, 41, 42, 49, 50, 54, 113, 114, 159, 159–176]. However, there are still many open questions about the best way to qualify a polaritonic macroscopically occupied quantum state [177, 178]. Polaritons are 2D quasi-particles which cannot exhibit a strict BEC phase transition, but possibly a local condensation or a BKT phase transition (§ 2.3.1). However such a description is also inaccurate since, being an out-of-thermodynamical

equilibrium system, neither a temperature nor even a phase transition can be defined in planar semiconductor MCs.

2.5.1 Excitation schemes

Polaritons can exist in semiconductor MCs with long photon lifetimes (high-Q optical cavities) and large light-matter Rabi coupling exceeding thermal energies ($\hbar\Omega_R > k_B T$). The physical processes underlying the creation of a polariton condensate are strongly dependent on the way the driving field is injected into the cavity. We classify the many available excitation geometries into three different groups in the following sections, starting with the one most related with cold atom BECs.

2.5.1.1 Non-resonant pumping

In the non-resonant scheme, no coherence is introduced in the system via the excitation laser. It allows for thermodynamics to play an important role in the mechanism of polariton condensation. The laser beam excites free hot electron-hole pairs, whose main excess energy is relaxed by several very fast emissions of LO-phonons in the lattice — see Fig. 2.9. A hot exciton gas is thus formed [179]. For this population to relax into the polariton states of lowest energy, a few tens of meV below, acoustic phonon emission is the main possible channel. As the energy dispersion of polaritons is very steep as compared to acoustic phonons, this relaxation mechanism happens through very small momentum-energy exchanges, so it is very inefficient. This problem, known as the relaxation bottleneck was well identified both experimentally [180, 181] and theoretically [182], using a Boltzmann description of the dynamics in the latter case. At high excitation intensity, *i.e.* at high exciton density, the relaxation bottleneck can be overcame by polariton-polariton inelastic scattering in such a way that the polariton ground state occupancy can be high enough to trigger bosonic stimulation of the relaxation [183]. However, there is a limit in the polariton density above which the photo-induced electron-hole plasma bleaches the electron-hole coupling and so the exciton oscillator strength decreases.

There are three main solutions to achieve high enough polariton populations, without breaking the SCR, as to surpass the relaxation bottleneck: the first is to use MCs with higher number of QWs inside, reducing then the carrier density per QW while the overall polariton density is unaffected; the second is to use DBRs mirrors with high reflectivity as to increase the polariton lifetime allowing enough time for the slow bottleneck relaxation towards low energies to take place; the third is to use materials where the exciton oscillator strength is high enough.

The choice of the material is also important when evaluating the critical temperature for condensation T_c. Equation 2.2 says that in principle such a temperature can be made arbitrary low by increasing the boson density n. However, in excitonic systems, if the thermal energy $k_B T$ is

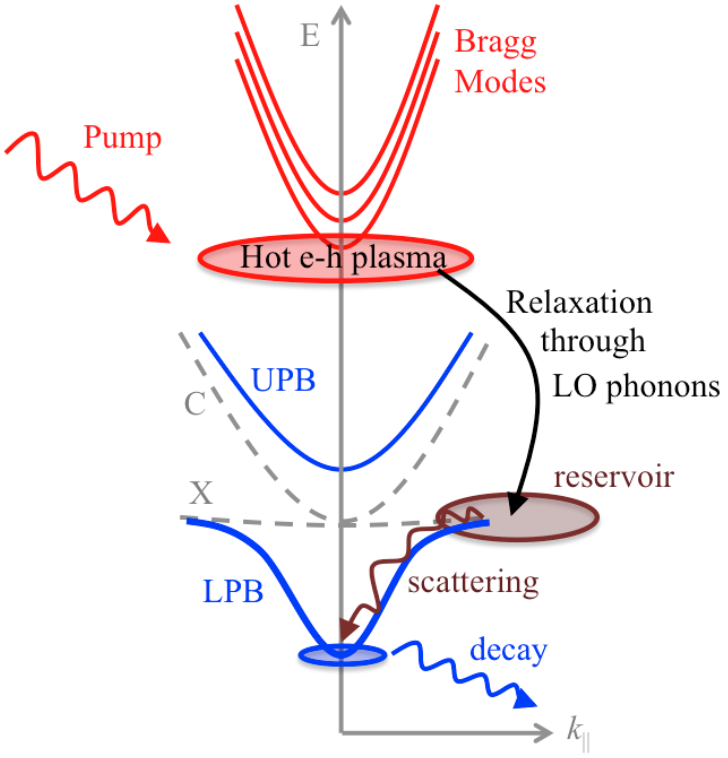

FIGURE 2.9: Non-resonant excitation scheme. A pump laser enter the cavity through the reflectivity minima of the Bragg modes, creating a hot electron-hole plasma that loses energy after many collisions with lattice LO-phonons. Electron-hole pairs then bind together to create an exciton reservoir at high-k values, that continues losing energy (through the acoustic phonon emission channel) until the bottom of the polariton dispersion relation. A macroscopically occupied state is formed at the bottom of the LPB, eventually emitting a photon. This photon carries full information about the condensed polaritons.

higher than the biding energy the exciton dissociates and the fermionic nature of its constituents is recovered. The critical temperature for exciton unbinding in $GaAs$ compounds is ∼70 K [184], reaching ∼120 K in $CdTe$ materials where the exciton binding energy is higher.

In fact, a first clear observation of bosonic stimulation within a polariton gas was obtained by L.S. Dang and co-workers in 1998, in a $CdTe$-based MC with 16 embedded QWs, in which a non-linear increase of polariton PL has been observed when increasing the pump power, followed by VCSEL lasing from an electron-hole plasma at much higher powers [161]. Some years later the pioneering work of Richard *et al.* [162] showed that such a non-linear increase of the polariton emission originates from a spectrally narrow ring in **k**-space, exhibiting enhanced spatial and angular coherence. Soon after, by increasing the excitation spot size, emission from a single quantum state lying at the bottom of the LPB was reported [185], giving a direct evidence for spontaneous formation of a non-equilibrium BEC. Although this ground state emission had an spatial origin in many small islands where polaritons where trapped by sample disorder, such a state has been show to have macroscopic long-range order in the work of J. Kasprzak *et al.* [21], where the condensate has been shown to spontaneous develop out of a thermalized Boltzmann-like incoherent reservoir.

The reason for such a spatially extended coherence lies in phase-locking mechanisms between many condensates localized by the sample disorder potential [186]. The final energy-momentum state chosen by the condensate is strongly dependent on the excitation spot size: whereas big pumps create a ground state stopped ($k = 0$) condensate [21], tighter pump spots favors the appearance of a expanding condensate at a finite k-ring [36, 160, 162]. The continuously adjustable proportion of exciton to photon in a polariton allows exploring a wide range of non-equilibrium situations. At higher excitonic fractions of the LPB (positive photon-exciton detuning), higher collision rates and therefore faster thermalization allows for condensation at quasi-equilibrium with a defined temperature, whereas higher photonic fractions (negative detunings) yield out of equilibrium condensation without thermalization [163].

Although many achievements have been done in $CdTe$-based samples, their strong disorder and consequently short lifetimes limit polariton free propagation. Because $GaAs$ and $AlAs$ are practically lattice-matched, the MC-layers have very little induced strain, which allows many DBR layers (yielding long photon lifetimes) to be grown and with very weak disorder.

The first $AlGaAs$-based MC, with 12 QW, showing evidences for condensation [20] were excited in a pumping scheme closely related but, strictly speaking, different from the one previously described: instead of creating a hot excitonic reservoir after relaxation from the electron-hole plasma, the reservoir was resonantly excited by a pump laser at very high angles, where the LPB is purely excitonic. Under fully non-resonant excitation, BEC has been observe in $GaAs$ MCs under stress [22]. Better quality samples with low disorder and long lifetimes showed recently spontaneous condensation of polaritons in both the LPB ground state [165] or in a **k**-space ring, with a large spatial extension in the latter case [36].

Condensation of polaritons under non-resonant excitation has been demonstrated through the observation of a macroscopic occupation of a narrow ground energy-momentum state, which corresponds, according to the Wiener-Khinchin identity, Eq. 2.26, to extended spatial- [21] and long time- [22] correlations. The spatial correlation function of a polariton condensate has a power-law decay [172] as expected in a 2D condensate (see § 2.3.1), a signature of a BKT transition which is related to spontaneous creation of vortex-antivortex (V-AV) pairs [171]. However this decay is much shaper, with a decay exponent around four times bigger than the one in an equilibrium BKT transition. Reduced energy linewidths provide high correlation times, which have been studied as a footprint of polariton condensation. However the correlation time-decay is influenced by a number of factors related to the non-equilibrium nature, including pump noise, interactions and reservoir fluctuations [164].

In large bandgap materials the critical temperature for exciton unbinding is as high as 400 K (GaN), where the first room-temperature polariton laser has been demonstrated [23, 114], and 560 K (ZnO), where many recent works report on high temperature polariton non-linearities and condensation [187–191].

2.5.1.2 Coherent drive in the pump-only configuration

Thanks to their photonic component, polaritons can be coherently excited by an incident laser field resonant with the LPB at a small k vector, creating a moving polariton fluid with the same energy and momentum as the pumping laser. Its coherence clearly do not appear spontaneously due to bosonic condensation, but is inherited from the pumping field. Under continuous-wave (*cw*) excitation, the phase is imprinted by the laser beam, however it can evolve freely out from the excitation spot if the polariton lifetime is long enough [175, 176]. An extra pulsed beam resonant with the *cw* one can also be used to trigger a moving extra population [38]. Under pulsed-only excitation, the fluid phase, initially imprinted by the pulsed laser, freely evolves according to the quantum hydrodynamics of the system [159, 173].

The advantage of using the pump-only excitation scheme is that an accurate control of the polariton dynamics can be achieved by properly tuning the external laser. However care should be taken when detecting the polariton emission pumped resonantly by a *cw*-laser. Since both laser and polariton fields have the same energy and momentum, the latter cannot be detected in the direction of the reflected laser beam, because the laser bleaches the much less intense polariton luminescence. In this case, the detection has to be made in transmission geometry [27], all the light that passes through the cavity acquires a polaritonic character before being transmitted, and so fully carries information about the polaritonic field inside. When propagating out from the excitation area [175, 176], the polariton PL is not superimposed with the excitation field and therefore it can be detected in both the transmitted or reflected directions. Under pulsed excitation [38, 159, 173], separation between polariton and laser fields are done in time since the pulse beam lasts much less than the polariton population lifetime.

2.5.1.3 Excitation in the optical-parametric-oscillator (OPO) regime

Thanks to their excitonic component, polaritons have strong non-linear behavior inherited from the exciton-exciton interactions. In the parametric scattering process, two polaritons from a pump mode, with wave-vector and frequency $[\mathbf{k}_p, \omega_p]$, scatter into a lower energy signal mode $[\mathbf{k}_s, \omega_s]$ and a higher energy idler mode $[\mathbf{k}_i, \omega_i]$. This scattering process has to conserve energy and momentum, therefore requiring the phase matching conditions:

$$2\mathbf{k}_p = \mathbf{k}_s + \mathbf{k}_i \tag{2.35a}$$

$$2\omega_p = \omega_s + \omega_i \tag{2.35b}$$

This condition cannot be satisfied by any particle dispersion. For example, parametric scattering is forbidden for particles with a quadratic dispersion. On the other hand, the "S"-shape of

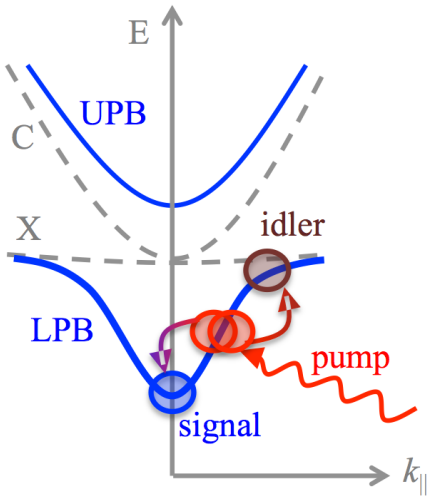

FIGURE 2.10: Illustration of parametric scattering excitation scheme, where polaritons injected by a laser beam resonant with the inflection point of the LPB scatter from the pump state $[k_p, \omega_p]$ towards the signal $[k_s, \omega_s]$ (here at zero momentum) and the idler state $[\mathbf{k}_i = 2\mathbf{k}_p - \mathbf{k}_s, \omega_i = 2\omega_p - \omega_s]$ (at higher momentum), conserving momentum and energy.

the LPB makes it a good candidate to have the conditions described in Eq. 2.35 satisfied, since the LPB is approximately symmetric in energy and momentum around its inflection point — see Fig. 2.10. In fact, if $\mathbf{k}_s = 0$ then the momenta of pump and idler are uniquely selected, for a given the value of the pumping angle — also referred to as the "magic angle" — located close to the inflection point of the LPB.

The simplest way of reach experimentally parametric scattering in a MC is to pump it resonantly close to the inflection point of the LPB. Parametric instabilities populate signal and idler modes which, at a certain threshold, have a state occupancy of order one, and so bosonic final-state stimulation causes polariton pairs to coherently scatter from the pump state to the signal and idler states [113], in the so-called OPO excitation regime of a polariton condensate [54].

A second laser beam can be used to trigger parametric processes if there are more available states (called conjugate states) in the LPB in such a way that the phase matching conditions 2.35 are satisfied by probe, pump and conjugate states (whose may be in principle different from the signal and idler states). This holds even if the pump beam is below OPO threshold (but close to it), in which case the probe state will still be amplified. This optical parametric amplification (OPA) regime — also called triggered optical parametric oscillator (TOPO) regime [26] when the process is ignited by a pulsed probe that fulfills the phase matching conditions described in Eq. 2.35 — was first observed in an $InAlGaAs$ MC [52]. Ultrafast parametric amplification of polaritons with extraordinary gains up to 1500 and temperatures up to 220 K has been reached, in this regime, in $CdTe$-based MCs [29].

On the other hand, when a *cw* pump laser drives the system above OPO threshold, the probe and conjugate states are extra population states, on top of the steady state OPO signal and idler states. When triggered by a pulsed laser, both probe and conjugate states are traveling decaying states that can evolve freely from the laser probe constraints once the pulse switches off. If the pulse lies at a region of the LPB with a large exciton content, the small-**k** conjugate extra population lasts for up to the nanosecond timescale [192], and its energy and momentum can be tuned by the pulsed probe as long as phase-matching conditions are satisfied [26]. When the trigger is resonant with the OPO signal, the extra-population lifetime is shorter, but still bigger than the polariton lifetime [28, 49].

The OPO state, characterized by the macroscopic occupation of three polariton states only, looks at first sight very different from an equilibrium weakly interacting BEC, where the macroscopic occupation of the ground state occurs from a thermal distribution of bosons. The OPO state does, however, share with a BEC the fundamental property of spontaneous symmetry breaking of the phase symmetry [193]. In fact, the external laser fixes the phase of the pump state ϕ_p and parametric scattering processes constrain the sum of the signal and the idler phase only, $2\phi_p = \phi_s + \phi_i$ [194], but leaves the system to arbitrarily choose the phase difference $\phi_s - \phi_i$. In fact, above OPO threshold, the signal and idler spontaneously select their phase, though not independently. This spontaneous symmetry breaking when choosing a phase above OPO threshold implies that the long-wavelength excitations (Bogoliubov) of the OPO signal state have similarities to the ones of an equilibrium BEC.

The excitation spectrum of the OPO signal state is expected to have a vanishing energy linewidth [193], which would give extremely long correlation times, another footprint of condensation, according to the Wiener-Khinchin identity Eq. 2.26. In fact, using an extremely low noise pump laser, correlation times in the nanosecond time scale has been reported [167] one order of magnitude longer if compared to non-resonant excitation geometries [164], where the reservoir noise play an important role.

In addition, the appearance of spontaneous spatial coherence in the OPO signal has been shown via quantum Monte Carlo simulations [195], and recently confirmed by experiments [167, 168] through the divergence of the coherence length when the pump energy approaches that of the LPB from below.

2.5.2 Modelling polariton phenomena

Unlike BECs of weakly interacting Bose gases for which the GP equation has been shown to accurately represent the states of the condensates, the polariton condensates are nonequilibrium systems, which are best understood as a steady-state balance between pumping and decay, rather than true thermal equilibrium.

Using a mean-field description of the condensate [196, 197] one can recover a complex GP equation (cGPE), including terms representing gain, loss and an external trapping potential, describing the dynamics of the lower polariton wavefunction, ψ,

$$i\hbar\partial_t\psi = \left(\hat{E}_{LP} + \alpha|\psi|^2 + V\right)\psi + \frac{i\hbar}{2}(P - \Gamma)\psi \tag{2.36}$$

where the operator $\hat{E}_{LP} = -\frac{\hbar^2\nabla^2}{2m_P}$ represents the parabolic dispersion of the LPB, with m_P being the polariton effective mass, Γ is the polariton decay rate, P the pumping rate, α the polariton repulsive interaction coupling constant[3], V the external potential.

This modification of the GP equation to account for such nonequilibrium properties of the condensates is a complex Ginzburg-Landau equation (cGLE), a universal equation of mathematical physics describing the behavior of systems in the vicinity of an instability and symmetry breaking [198], *e.g.* nonlinear waves, superconductivity, superfluidity, liquid crystals and strings in field theory, and capable of spontaneous pattern formation. Formally, it is a nonlinear Schrödinger equation with complex coefficients.

The superfluid properties of nonequilibrium condensates in a dissipative environment still need to be completely understood [199]. For polariton fluids, one has to singularly assess the system properties in the three different pumping schemes available.

2.5.2.1 Pump-only configuration

Let us consider the propagation of a resonantly created polariton fluid in the presence of a static small defect $V(\mathbf{r})$. The driving field is assumed to be a coherent and monochromatic laser field of frequency ω_p, $P(\mathbf{r}, t) = e^{i(\mathbf{k}_p\cdot\mathbf{r}-\omega_p t)}$, which generates a polariton fluid with a nonzero flow velocity and a spatial plane-wave profile of wave vector $\mathbf{k}_p$ along the cavity plane.

Under resonant excitation, the polariton field oscillation frequency is not fixed by an equation of state relating the chemical potential to the particle density, but it can be tuned by the frequency of the exciting laser. This opens the possibility of having a collective excitation spectrum which has no analog in usual systems close to thermal equilibrium.

The response of the system to a weak perturbation is obtained using a linearized theory analogous to the well-known Bogoliubov theory of the weakly interacting Bose gas. Close to the bottom of the LPB, $\omega_{LPB}(\mathbf{k} = 0)$, the spectrum of the Bogoliubov excitations can be approximated

[3]The inter-particle repulsive interaction coupling constant in the GP equation, typically defined as g, will be dubbed as α for polaritons, keeping this same nomenclature from now on.

by the simple expression [196]

$$\omega_{Bog}^{\pm} \simeq \omega_p + (\mathbf{k}-\mathbf{k}_p)\cdot\mathbf{v}_p - i\Gamma \pm \sqrt{\left[2\alpha|\psi|^2 + \frac{(\mathbf{k}-\mathbf{k}_p)^2}{2m_P} - \Delta_p\right]\left[\frac{(\mathbf{k}-\mathbf{k}_p)^2}{2m_P} - \Delta_p\right]} \tag{2.37}$$

where $\mathbf{v}_p = \hbar\mathbf{k}_p/m_P$ is the flow velocity and $\Delta_p = \omega_p - \omega_{LPB}(\mathbf{k}_p) - \alpha|\psi|^2$ the effective pump detuning. The $\pm$ branches correspond to, respectively, the particle- and the hole-like branches of the Bogoliubov dispersion, and are images of each other under the transformation $\mathbf{k} \to 2\mathbf{k}_p - \mathbf{k}$, $\omega \to -\omega$.

The solutions of Eq. 2.37 for different pump conditions are plotted on the left column of Fig. 2.11. The effect of the finite flow velocity $\mathbf{v}_p$ is to tilt the standard Bogoliubov dispersion via the term $(\mathbf{k}-\mathbf{k}_p)\cdot\mathbf{v}_p$. When colliding against the static defect, polaritons can scatter elastically, exciting modes given by the intersections of the Bogoliubov dispersion with the horizontal dotted lines. The spectrum of the Bogoliubov-like excitations reflects onto the shape and intensity of the resonant Rayleigh scattering (RRS) emission pattern in both momentum and real space. The central and right panels of Fig. 2.11 show the polariton intensity in the momentum and the real space for the different regimes on the left column, respectively.

In the resonant case ($\Delta_p = 0$), the $\pm$ branches (full/dashed lines, respectively) touch at $\mathbf{k} = \mathbf{k}_p$ [Figs. 2.11(a,d,g)]. In the noninteracting case [Fig. 2.11(a)] the dispersion remains parabolic, with the $\mathbf{k}$-space emission pattern [Fig. 2.11(b)] containing a peak at the incident wave vector $\mathbf{k}_p$, plus the RRS ring. In the real space pattern [Fig. 2.11(c)], as the polariton fluid is moving to the right, the defect at $\mathbf{r} = (0,0)$ induces a propagating perturbation with parabolic wave fronts oriented in the left direction.

In the presence of interactions [Fig. 2.11(d,g)] the dispersion slope has a discontinuity at $\mathbf{k} = \mathbf{k}_p$: on each side of the corner, the + branch starts linearly with group velocities, respectively, given by $v_g = c_s \pm \mathbf{v}_p$, c_s being the usual sound velocity of the interacting Bose gas $c_s = \sqrt{\hbar\alpha|\psi|^2/m_P}$. In this resonant case, when $\alpha|\psi|^2$ is large enough for the sound velocity c_s in the polaritonic fluid to be larger than the flow velocity $\mathbf{v}_p$, there is no intersection of the Bogoliubov branches [Fig. 2.11(d)] with the horizontal dotted line any longer. In this regime, RRS is no longer possible [Fig. 2.11(e)], and the polaritonic fluid behaves as a superfluid in the sense of Landau criterion. As no propagating mode is resonantly excited, the perturbation in real space remains localized around the defect, as shown in Fig. 2.11(f).

Still in the resonant case, but now with $v_p > c$, the stronger Bogoliubov tilt of the dispersion is responsible for an intersection with the horizontal dotted line [Fig. 2.11(g)] that forms a RRS curve in a ∞-like shape, with the low-k lobe more intense than the high-k one [Fig. 2.11(h)], a sign of the disappearance of superfluidity. The aperture angle 2ϕ of the singularity at $\mathbf{k}_p$ satisfies the simple condition $\cos\phi = c_s/v_p$. In this Čherenkov regime where the polariton fluid is moving

at a supersonic speed, the defect produces a peculiar real-space pattern [Fig. 2.11(i)] showing linear Čherenkov-like wavefronts. The aperture 2θ of the Čherenkov angle has the usual value $\sin\theta = c_s/v_p$.

Coming back to excitation below the sound velocity, $v_p < c_s$, but now decreasing the mean-field shift $\alpha|\psi|^2$ in such a way that the effective pump detuning Δ_p is positive, the argument of the square root in Eq. 2.37 is negative for the wave vectors $\mathbf{k}$ such that $\Delta_p > (\mathbf{k}-\mathbf{k}_p)^2/(2m_P) > \Delta_p - 2\alpha|\psi|^2$. In this region, the $\pm$ branches stick together and have an exactly linear dispersion of slope v_p [Fig. 2.11(j)]. The resonant Rayleigh scattering intensity in this non-superfluid regime is a deformed RRS ring strongly amplified on a segment parallel to y including the point $\mathbf{k}_p$ because of the reduced linewidth of the Bogoliubov modes in the regions where the $\pm$ branches stick together [Fig. 2.11(k)]. The main consequence of this in the real-space pattern of Fig. 2.11(l) is an overall amplification of the density modulation induced by the defect, in stark contrast with the superfluid regime. In particular, the derivative of the dispersion at the rightest point of the ring gives a group velocity point towards the right, which is responsible for the long "shadow" in the downstream direction with respect to the central defect, which extends to relatively far distances thanks to the linewidth narrowing effect.

By increasing the pumping strength $|P|$, the mean-field shift $\alpha|\psi|^2$ increases and the effective pump detuning Δ_p becomes negative. In this case, as it is shown in Fig. 2.11(m), the branches no longer touch each other at $\mathbf{k} = \mathbf{k}_p$. The two lobes in the RRS circle are separated by a gap [Fig. 2.11(n)]. The real-space wavefronts shown in Fig. 2.11(o) are still Čherenkov-like, if the separation between the two branches is relatively small. A full gap between them opens up for sufficiently negative values of Δ_p or for smaller $\mathbf{k}_p$ values (not shown). In this case, there are no available states for scattering and the system becomes superfluid in the sense of Landau.

In conclusion, superfluidity of resonantly-excited polaritons depends on the pump-polariton mode detuning Δ_p. Three qualitatively different types of spectra appear for the interacting case: linear for $\Delta_p = 0$, diffusive-like for $\Delta_p > 0$ and gapped for $\Delta_p < 0$. A moving polariton fluid is superfluid if its velocity is smaller than a critical value and $\Delta_p = 0$ or $\Delta_p < 0$. In this case, analogously to liquid Helium and atomic condensates, the resonantly-driven polariton fluid has a superfluid behavior in the sense of Landau criterion with respect to both elastic and inelastic processes.

The $\Delta_p = 0$ detuning is the only one that can be achieved experimentally, since if the laser is not resonant with the (blueshifted) polariton mode no field enters the cavity and so no polaritons are excited. Indeed, recent experiments agree with the theoretical predictions [27]: below the sound velocity, a quenching of the RRS intensity due to polariton-polariton interactions can be observed in both momentum and real space; above the sound velocity, linear Čherenkov waves were also observed.

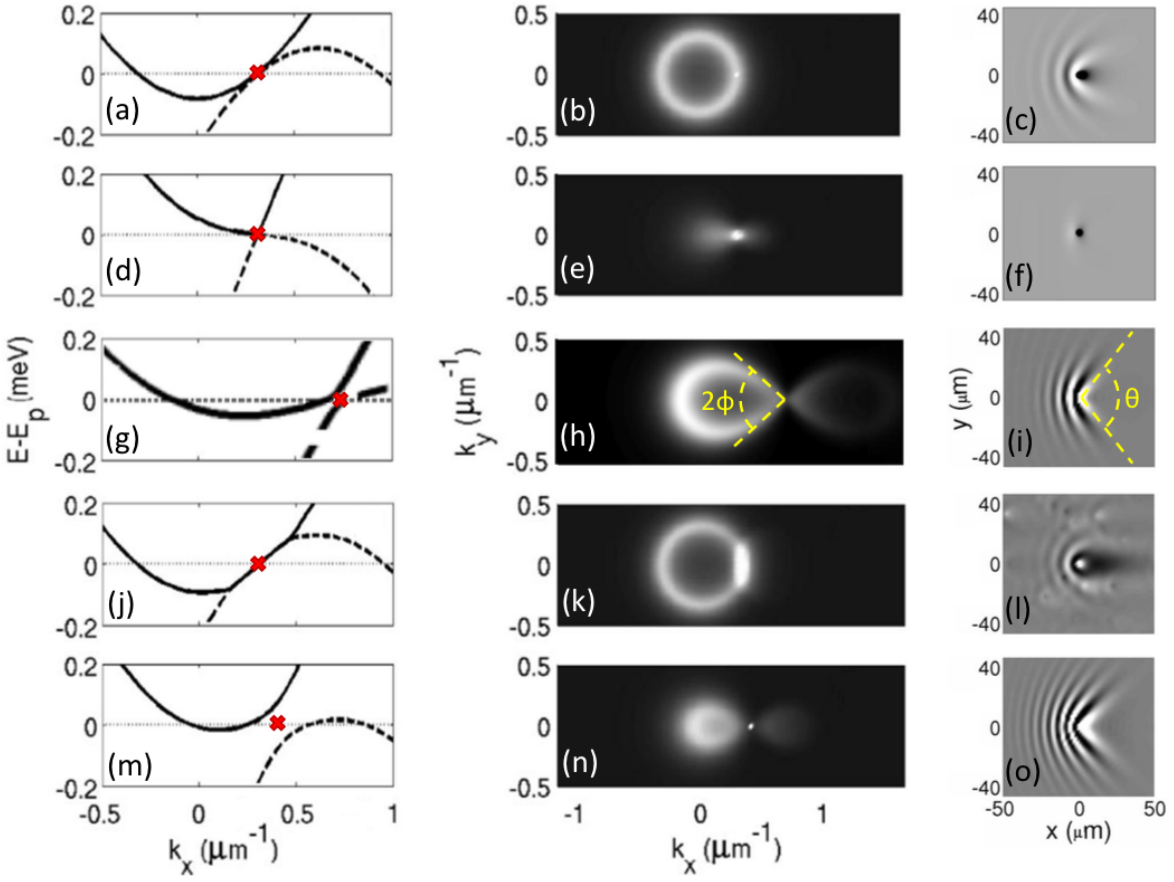

FIGURE 2.11: (left column) Bogoliubov dispersions $\hbar(\omega^{\pm}_{Bog} - \omega_p)$ (full/dashed lines, respectively) of the elementary excitations in MC polaritons under resonant excitation, calculated from Eq. 2.37, and their effect on the intensity and shape of the resonant Rayleigh scattering by defects in (central column) momentum space and (right column) real space. Red crosses represent the resonant pump energy and momentum for each row. The dispersion in (a) is parabolic ($\alpha|\psi|^2 = 0$, $\Delta_p = 0$). For $\alpha|\psi|^2 > 0$, close to Δ_p the dispersions are (d,g) linear ($\Delta_p = 0$), (j) diffusive ($\Delta_p > 0$) and (m) gapped ($\Delta_p < 0$). Adapted from Refs. [196, 201].

Under a monochromatic and spatially homogenous plane-wave pump, neither vortices can be observed in the polariton fluid, nor solitons. The local phase of the polariton field is in fact fixed by the pump phase, which inhibits the appearance of topological defects. By using a properly spatially-shaped pump profile, polaritons can be resonantly created immediately before a defect and made to freely propagate past it with no phase imposed by the pumping field [200]. If the defect size is big enough, rich phenomena appear: for low enough fluid speeds and high densities, the flow is superfluid and no excitation appear; as the density is decreased, turbulence occurs in the form of vortex pairs ejection [159, 173, 175], vortex streets [174] and dark solitons [175].

The superfluid behavior of a system can also be characterized as a function of the drag force exerted by the defect on the flowing fluid [202–205]:

$$\mathbf{F}_d = \int \mathrm{d}\mathbf{r}|\psi(\mathbf{r},t)|^2 \nabla V(\mathbf{r}) \tag{2.38}$$

For a flowing polariton condensate satisfying the Landau criterium, like in Fig. 2.11(d), the broadening of the polariton modes due to its finite lifetime allow for a weak amount of scattering, which is asymmetric in the propagation direction [Fig. 2.11(e)]. This yields an also asymmetric small density perturbation close to the defect [Fig. 2.11(f)], and so the fluid always experiences a residual drag force, Eq. 2.38. When flowing through defects, non-equilibrium superfluids do not have zero viscosity even in the superfluid regime.

However, the drag force and the onset of fringes in the density profile have a sharp threshold as a function of the velocity [204, 205] and so a generalized Landau criterion, with a critical velocity v_c, can still be defined. This is true for all the cases in Fig. 2.11 [linear, (d), diffusive, (g), and gapped, (m)], the critical velocity for pronounced drag being the same as the sound velocity in the linear and diffusive cases [Figs. 2.11(d,g)] but higher in the gapped case [Fig. 2.11(m)]. The crossover becomes sharper for increasing polariton lifetimes [204, 205]: in the supercritical regime, $v_p > v_c$, the lifetime tends to suppress the propagation of the Čherenkov waves away from the defect and therefore to suppress the drag, whereas in the subcritical regime, $v_p < v_c$, the residual drag increases linearly from zero when the polariton lifetime decreases.

2.5.2.2 Nonresonant pumping with a single reservoir

When creating a polariton condensate by means of non-resonant excitation (§ 2.5.1.1), the macroscopically coherent field ψ in Eq. 2.36 is fed by an incoherent reservoir of excitons $N(\mathbf{r},t)$ instead of directly by the laser beam [206]:

$$P(\mathbf{r},t) = rN(\mathbf{r},t) \tag{2.39}$$

where r is the rate at which polaritons scatter from the reservoir. Equation 2.39 means that, in this case, the amplification rate of the condensate due to stimulated scattering of polaritons from the excitonic reservoir increases linearly with N.

The full system is described by two populations: polaritons around the lower energy minimum of the dispersion, $\psi(\mathbf{r},t)$, and polaritons with larger momenta at the reservoir (excitons in practical terms), $N(\mathbf{r},t)$. These two populations are weakly coupled, which allows us to define a quasi-thermal equilibrium for each one. The exciton density dynamics is fully determined by N [41, 206]:

$$\partial_t N(\mathbf{r},t) = -\left(\Gamma_R + \beta r|\psi|^2\right) N(\mathbf{r},t) + P_{NR}(\mathbf{r}) + D\nabla^2 N(\mathbf{r},t) \tag{2.40}$$

The reservoir is fed by the laser beam at a rate $P_{NR}(\mathbf{r})$ and relaxes at a rate Γ_R. D is the reservoir spatial diffusion coefficient, but it must be mentioned that sometimes D is neglected due to the huge effective exciton mass compared to that of polaritons, having a negligible contribution in Eq.

2.40. β is a phenomenological coefficient whose value is chosen to describe particular experimental situations [41].

It is very important to account for energy shifts originated from Coulomb repulsion between condensed and reservoir polaritons. The potential V is assumed to be:

$$V(\mathbf{r},t) = \hbar g_R N(\mathbf{r},t) + V_0(\mathbf{r}) \tag{2.41}$$

The polariton repulsive interactions are produced by the terms (i) polariton-polariton $\alpha|\psi|^2$, (ii) polariton-exciton $\hbar g_R N(\mathbf{r},t)$ and (iii) a static potential $V_0(\mathbf{r})$ (conditioned by the geometry of the MC, see § 3.2.1.1).

The Bogoliubov spectrum of a non-equilibrium condensate described by Eqs. 2.36, 2.39, 2.40 and 2.41 has a diffusive Goldstone mode around $k = 0$ [206], and so a naïve application of the Landau criterion predicts a vanishing critical velocity, $v_c = 0$. Even though strictly speaking there cannot be superfluid behavior, there are regimes close to equilibrium, where the drag force exerted on a small moving defect shows a sharp threshold at velocities close to the speed of sound [203]. For velocities below the sound velocity, the drag force increases as the decay, Γ, increases [203].

There has been experimental indications of a diffusive Bogoliubov mode in non-resonantly excited polariton condensates [166], where the diffusive region of the spectra could be tuned with power from zero diffusion at threshold up to a $\Delta k \sim 0.8\ \mu\text{m}^{-1}$ diffusive region at high powers an negative photon-exciton detunings. However the condensate excitation spectrum and the LPB luminescence are superimposed and so it is not immediately clear whether the equilibrium Bogoliubov dispersion or the diffusive Goldstone mode dispersion corresponds better to the experimental results. The existence of an equilibrium Bogoliubov mode has been reported in a previous work [207].

As a result of the non-equilibrium nature of the polariton condensate in an inhomogeneous system, there are spontaneous supercurrents that may carry polaritons from gain- to loss-dominated regions. This give rise to spontaneous formation of vortices pinned by sample defects [169, 170] in analogy to classical water sinks, which do not necessarily imply superfluidity [197, 199].

In conclusion, apart from having a diffusive excitation spectra, the superfluid behavior of a non-equilibrium polariton condensate can also be characterized by a dramatic increase in the lifetime of a quantized vortex, analogously to BECs that persist rotating after stirring [208], showing one more connection between the two intriguing phenomena of superfluidity and long-range spatial coherence.

2.5.2.3 Polariton energy relaxation under nonresonant pumping with a three exciton-types reservoir

The theoretical model of the experimental results described in Part IV (except those included in § 9.2) make use of a phenomenological treatment of polariton energy-relaxation processes taking place in the system. Such processes are not only responsible for the relaxation of hot excitons (injected by the pump) into polaritons in the form of a condensate, but also for the further relaxation in energy of the polariton condensate as it propagates. This latter energy relaxation process can be strongly influenced by a spatially dependent potential coming from repulsion from the hot excitons. Let us first introduce the description of the polariton condensate.

A fundamental feature of BECs is their spatial coherence that allows them to be well described with a mean-field approach [140]. The GP equation, previously presented in Eq. 2.36, includes a new term $i\hbar\Re\left[\psi(x,t)\right]$, accounting for polariton energy-relaxation processes:

$$i\hbar\partial_t\psi(x,t) = \left[\hat{E}_{LP} + \alpha|\psi(x,t)|^2 + V(x,t) + i\hbar\left(rN_A(x,t) - \frac{\Gamma}{2}\right)\right]\psi(x,t) + i\hbar\Re\left[\psi(x,t)\right] \quad (2.42)$$

Here, $\hat{E}_{LP}$ is the kinetic energy dispersion of polaritons, which at small wave vectors can be approximated as $\hat{E}_{LP} = -\hat{\nabla}^2/(2m)$ with m the polariton effective mass. The polariton-polariton interactions, being repulsive ($\alpha > 0$), allow both a spatially dependent blueshift of the polariton condensate energy and energy-conserving scattering processes. Our analysis shows, however, that neither of these effects will play a dominant role in our experiments. The effective potential acting on polaritons caused by repulsive interactions between polaritons and higher energy excitons is more significant, and is responsible for the blocking of polariton propagation in the presence of a gate pump (see the introduction to Part IV for a further description on the gating of polaritons). The effective potential $V(x,t)$ can be divided into a contribution from three different types of hot exciton states, which will be described shortly, as well as a static contribution due to the structural potential, $V_0(x)$ (see § 3.2.1.1 for a further description and experimental characterization of such static potential in our ridge structure):

$$V(x,t) = \hbar\left[g_R N_A(x,t) + g_I N_I(x,t) + g_D N_D(x,t)\right] + V_0(x) \quad (2.43)$$

N_A, N_I and N_D correspond to density distributions of "active", "inactive" and dark excitons, respectively, as described below. g_R, g_I and g_D define the strengths of interaction with the various hot exciton states.

N_A represents the density distribution of an "active" hot exciton reservoir [139, 209]. These excitons have the correct energy and momentum for direct stimulated scattering into the condensate and so appear as an incoherent pumping term in Eq. 2.42 with r the condensation rate.

To describe the dynamics of the system, it is important to note that not all excitons in the system are in this active form. In fact, the non-resonant pumping creates excitons with very high energy and they must first relax in energy before becoming active. Therefore, it can be identified an "inactive" reservoir of hot excitons that is excited by the non-resonant pump but not directly coupled to the condensate. The three exciton densities (N_A , N_I , and N_D) are in general spatially and time dependent. Therefore, the dynamics of the exciton densities are described by the following rate equations:

$$\frac{dN_A(x,t)}{dt} = -\left(\Gamma_A + r|\psi(x,t)|^2\right) N_A(x,t) + \left(t_R + t'_R N_I(x,t)\right) N_I(x,t) \tag{2.44}$$

$$\frac{dN_I(x,t)}{dt} = -\left(\Gamma_I + t_R + t'_R N_I(x,t) + t_D\right) N_I(x,t) \tag{2.45}$$

$$\frac{dN_D(x,t)}{dt} = t_D N_I(x,t) - \Gamma_D N_D(x,t) \tag{2.46}$$

When solving the equations the following conditions are imposed: the initial condition $N_A(x,0) = 0$, $N_D(x,0) = 0$ and a density proportional to the Gaussian intensity profile of the pump in the inactive reservoir, $N_I(x,0)$. In case of having an excitation pulsed beam, the temporal profile of the pump is Gaussian. This represents an instantaneous injection by the non-resonant ultra-short pulse used in the experiment. The inactive reservoir is coupled by both linear and non-linear terms to the active reservoir, described by t_R and t'_R, respectively.

As previously mentioned, in Part IV the theoretical models that reproduce the experimental findings (aside those included in § 9.2) are based on the one described in the present section. There are small differences between these versions and we note here that the described exciton rate Eqs. 2.44 and 2.45 are the same as those used in § 9.3.2 (see Eqs. 9.7 and 9.8). However, in Chapters 10 and 11 the rate equations for the active and inactive reservoirs do not contain the coupling term $t'_R N_I(x,t)$; we noticed that it was not relevant for the simulation of the experiments contained in the cited Chapters.

The model also accounts for a linear coupling from the inactive to the dark exciton reservoir, $N_D(x,t)$, described by coupling rate t_D. Dark excitons are long-lived states that are optically inactive yet can nevertheless be populated as high energy excitations from the non-resonant pump relax in energy. The dark excitons introduce a long-lived repulsive contribution to the effective polariton potential, $V(x,t)$, and are thus efficient at gating propagating polaritons at long-times. Γ_A, Γ_I and Γ_D describe the decay rates of each of the reservoirs.

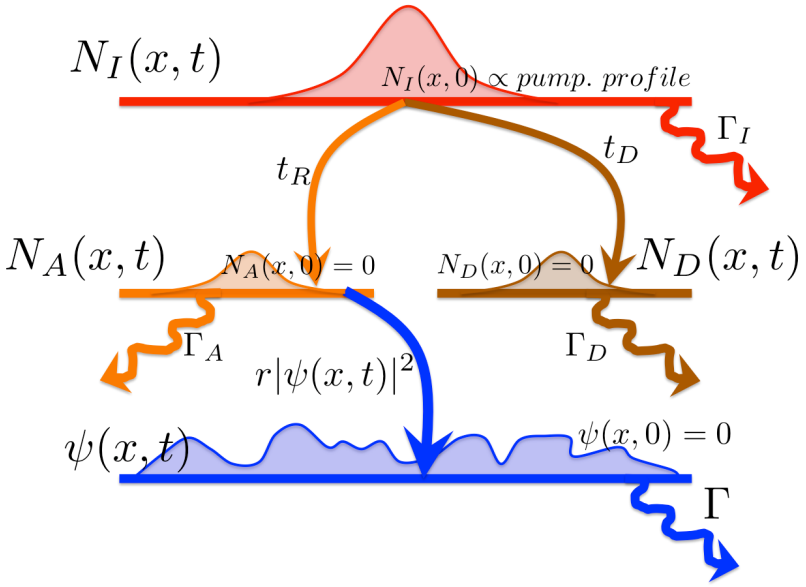

FIGURE 2.12: Schematic representation of the rate Eqs. 2.44-2.46, describing the dynamics of the density distributions of "active", "inactive" and dark excitons. "Active" excitons are coupled to polaritons according to Eq. 2.42.

The model neglects any further conversion between bright and dark excitons. Nonlinear conversion has been shown to generate oscillations between bright and dark excitons [210, 211]. However, these processes require coherent excitation of exciton-polaritons near the dark exciton resonance. In this case, it is not expected accumulation of exciton-polaritons at such an energy. Furthermore, the fact that no oscillations in the polariton condensate density were observed, suggests that any coupling between bright and dark states is slower than the condensation rate.

It is worthwhile mentioning that the very first version of the model included a term accounting for the hot-exciton diffusion in the system (using typical exciton diffusion rates) when solving Eqs. 2.44-2.46. Let us note that this term, $D\nabla^2 N(\mathbf{r},t)$, was considered in Eq. 2.40 for the model describing the nonresonant pumping with a single reservoir (§ 2.5.2.2). However, in the present model, the inclusion of the exciton diffusion term produced no noticeable effects on the polariton dynamics. Consequently, we decided to remove it for the sake of simplicity.

Returning to Eq. 2.42, the decay of polaritons is accounted for by the decay rate Γ. The final term in Eq. 2.42 accounts for energy relaxation processes of condensed polaritons. Polaritons are expected to condense at the pump position into the lowest energy state, where they have zero kinetic energy and potential energy given by $V(x,t)$ (and an additional blueshift due to polariton-polariton interactions). While this is the lowest energy state available at the pump position, one notes that the potential energy can be reduced if polaritons propagate away from this position ($V(x,t)$ decreases away from the source, where the reservoir densities are weaker). If polaritons were to conserve their energy, then they would convert this potential energy into kinetic energy as they move away from the reservoir, accelerating down the potential gradient. However,

the polariton kinetic energy can be lost as polaritons scatter with acoustic phonons [182] or hot excitons [183]. Surface scattering could be also responsible for this loss; however since the model considers a phenomenological energy relaxation, the actual mechanism that causes that relaxation does not play a direct role in the calculations.

Previous methods to introduce energy relaxation into a description of polariton condensates have been based on the introduction of an additional decay of particles depending on their energy [40, 203, 212, 213] (occasionally known as the Landau-Khalatnikov approach). The polariton number can be conserved in such a process via the introduction of an effective chemical potential [203, 213]. The energy relaxation term is:

$$\Re[\psi(x,t)] = -\left(\nu + \nu'|\psi(x,t)|^2\right)\left(\hat{E}_{\rm LP} - \mu(x,t)\right)\psi(x,t), \tag{2.47}$$

where ν and ν' are phenomenological parameters determining the strength of energy relaxation [40, 203, 212, 213] with justification arising from consideration of Boltzmann scattering rates [214]. Equivalently, the relaxation is due to the scattering of particles into and out of the condensate, which introduces an imaginary component to the kinetic energy operator as recently demonstrated within a Keldysh functional integral approach [215]. The local effective chemical potential, $\mu(x,t)$, is chosen to enforce particle number conservation [213, 216]. We must mention that Eq. 2.47 differs from that used in § 9.2.2, Eq. 9.3, when modeling the dynamics of a polariton transistor switch. The inclusion of the phenomenological parameter $\nu'|\psi(x,t)|^2$ in Eq. 2.47 yields an optimum matching in the polariton energy relaxation dynamics between experiments and theory, addressed in § 9.3. The term $\nu'|\psi(x,t)|^2$ is also included in the model of the following Chapters 10 and 11.

The model does not attempt a microscopic derivation of the energy relaxation terms, it only accounts energy relaxation at low polariton densities (described by the parameter ν) as well as a stimulated component of the relaxation proportional to the polariton density, $|\psi(x,t)|^2$ (described by the parameter ν'). The energy relaxation rate is assumed proportional to the kinetic energy of polaritons; polaritons will relax in energy until they decay from the system or until their kinetic energy is zero (such that they have zero in-plane wave-vector).

The local effective chemical potential, $\mu(x,t)$, can be obtained from the condition:

$$\left.\frac{\partial\sqrt{n(x,t)}}{\partial t}\right|_{\Re} = 0, \tag{2.48}$$

where, $\psi(x,t) = \sqrt{n(x,t)}e^{i\theta(x,t)}$ for $n(x,t)$ real, and:

$$\left.\frac{d\psi(x,t)}{dt}\right|_{\Re} \equiv \Re[\psi(x,t)] = \left.\frac{\partial\sqrt{n(x,t)}}{\partial t}\right|_{\Re} e^{i\theta(x,t)} + i\sqrt{n(x,t)}e^{i\theta(x,t)}\left.\frac{\partial\theta(x,t)}{\partial t}\right|_{\Re}. \tag{2.49}$$

$|_{\mathfrak{R}}$ denotes the components of the derivatives due to the term $\mathfrak{R}[\psi(x,t)]$ in Eq. 2.42. Other terms in Eq. 2.42, namely the pumping and loss terms, do not conserve the number of condensed polaritons.

A clarification must be done concerning other sources of polariton energy-relaxation processes. Given the fact that in this thesis we study edged MCs, another energy loss contribution might be related to surface scattering at the surface of the etched ridge. In this respect, studies with different widths of the ridges might be interesting. Nevertheless, we have not performed such studies since our wires have a fixed dimension ($20\times300\ \mu m^2$, see Fig. 3.5). Furthermore, since we have considered a phenomenological energy relaxation, the actual mechanism that causes that relaxation does not play a direct role in our calculations.

It would be also interesting to define an energy-dependent "mean free path" between scattering events in order to assess how far the polaritons can be transferred along the ridges. Nevertheless, it is not intuitive and trivial to define such "mean free path" because the energy-relaxation rate is both energy and density dependent. Consequently, it is non-uniform in space and it is time dependent.

2.5.2.4 OPO regime

When excited under the OPO geometry (see § 2.5.1.3 for details), the full LPB dispersion, calculated in § 1.4.2, has to be taken into account. The quantum fluid dynamics of a non-equilibrium polariton condensate excited under the OPO geometry can be then simulated by adding excitonic interactions, pump and decay to the Hamiltonian defined by Eq. 1.48

$$i\partial_t \begin{pmatrix} \psi_X \\ \psi_C \end{pmatrix} = \left[\mathcal{H}_{e-ph} + \begin{pmatrix} g_X|\psi_X|^2 & 0 \\ 0 & V_C(\mathbf{r}) \end{pmatrix} \begin{pmatrix} \psi_X \\ \psi_C \end{pmatrix} \right] + \begin{pmatrix} \psi_X \\ \psi_C \end{pmatrix} + \begin{pmatrix} 0 \\ P \end{pmatrix} \tag{2.50}$$

Here the polariton field is described by a spinor containing its excitonic, ψ_X, and photonic, ψ_C, parts. g_X is the excitonic repulsive interaction coupling constant, $V_C(\mathbf{r})$ is the potential seen by photons due to fluctuations and disorder in the cavity width and P is the pumping field acting on the cavity mode. The non-interacting Hamiltonian $\mathcal{H}_{e-ph}$ accounts for the polariton modes dispersion including decay broadening:

$$\mathcal{H}_{e-ph} = \begin{pmatrix} \omega_X - i\Gamma_X & \frac{\Omega_R}{2} \\ \frac{\Omega_R}{2} & \omega_C - i\Gamma_C - \frac{\nabla^2}{2m_C} \end{pmatrix} \tag{2.51}$$

Here the excitonic dispersion is assumed to be flat, $\omega_X(\mathbf{k}) = \omega_X$, due to its heavy mass, whereas the photonic dispersion is parabolic, $\omega_C(\mathbf{k}) = \omega_C + \mathbf{k}/(2m_C)$. Γ_X and Γ_C are the excitonic and photonic decay rate, respectively and Ω_R the exciton-photon Rabi splitting.

Above a pump strength threshold $P = P_{th}$, the system is driven into the OPO regime where the solutions to Eq. 2.50 are three-mode (pump, signal and idler) states [196]. Such solutions are in principle invariant under a simultaneous phase rotation of both signal and idler states, however the signal and idler spontaneously select their phase in the OPO regime, spontaneously breaking the phase rotation symmetry. The Goldstone theorem [217] states that this symmetry breaking implies that the excitation spectrum goes to zero (both in the real and imaginary parts) in the long wavelength limit $\mathbf{k} \to 0$. This can be better understood as follows: as any global phase rotation maps into the same eigenvector of the Bogoliubov Hamiltonian, no restoring force opposes a global rotation of the signal-idler phases.

The dispersion for the Goldstone mode in the OPO regime has been derived in Ref. [196] by analytically solving Eq. 2.50 in momentum representation, with the calculated gap-less excitation spectrum being diffusive ($\partial_k E = \text{constant}$) at $k = 0$, in analogy with positively-detuned-resonant and non-resonant excitation schemes — see § 2.5.2.1 and 2.5.2.2, and Fig. 2.11(j). This implies that a polariton condensate created under the OPO excitation regime is not a superfluid when the Landau criterion is applied.

Moreover recent calculations [218] show that coupling between two coherently-injected, at different momenta and energies, polariton condensates requires that either both components flow without friction or both scatter against the defect. This suggests that when investigation superfluidity of a multimode OPO state, all of its modes have to be taken into account.

However, when triggered by a short-duration pulse, the traveling parametrically-scattered polariton wave-packet has been shown to display superfluid-like behavior in the form of frictionless flow and suppression of Rayleigh scattering [26].

Part II

Samples and Experimental Techniques

Introduction: Samples and Experimental Techniques

Since polaritons have both electronic and photonic character, their creation, manipulation and detection can be achieved by both electrical and optical means. Looking back in time, the current inorganic MCs, in which we have performed our experiments, are the result of a vast research during the last 40 years on FP interferometers (used for the study of optical bistabilities), non-linear etalons and VCSELs. After the pioneering work of C. Weisbuch and coworkers in 1992 [11], where the light-matter coupling in a semiconductor MC was demonstrated for the first time, some other key experimental steps were performed in the 90s. These works, pursuing the enhancement of the light-matter coupling, were responsible for further improvements in the engineering of semiconductor MCs, such as (i) the modification of the exciton dipole moment, (ii) the spatial overlap between the cavity mode and the QWs and (iii) the control of the exciton-cavity detuning on the samples. Following the review of G. Khitrova and coworkers [219], here we cite below some of those experiments.

In the first place, Y. Yamamoto and coworkers [220] studied the light-matter coupling in III-V semiconductor MCs with a single 20-nm $GaAs$ QW embedded in a λ cavity. They spectrally investigated the spontaneous emission from confined excitons under different excitation schemes. Abram and coworkers [221], used an alternative design of the MC with two QWs in a $\lambda/2$ $AlAs$ spacer, showing an exciton-photon splitting of 4 meV. Larger normal-mode coupling was achieved in II-VI MCs ($ZnCdSe$) in 1995 by Kelkar *et al.* [222], reporting an oscillator strenght of $\sim$ 20 meV.

In the second place, the control on the spatial overlap between the exciton and cavity mode function was optimized by tuning the relative location of the QW with respect to the position of the antinodes of the cavity mode. Zhang *et al.* [223] performed such experiments by selectively comparing the exciton-photon coupling in a sample containing two different types of QWs: one of them was centered in the antinode of a λ spacer, showing a remarkable mode-splitting in the reflectivity spectra, and the other type of QWs were sitting at each of the optical-field node positions, without signatures of coupling between the modes. These results demonstrated the controllability on the exciton-photon coupling as function of the optimal engineering of the cavity-QW distribution.

In the third place, the modification of the exciton-cavity detuning was studied with different approaches. When the MC quality is uniform enough, the scanning of the cavity mode across the sample can be done by moving the spot excitation throughout the sample surface. Initially, this scan was not linear, difficulting the conversion between spot-scanning position and relative mode-detuning. The works reported in Refs. [221, 224] could clearly map the evolution of the

spectral position of the exciton and the cavity modes, from the region of resonance to those with uncoupled modes. Other works [225] also reported the possibility to control the exciton-photon detuning through electric-field and temperature tuning.

Semiconductor MCs based in inorganic compounds such as II-VI $CdTe$ and III-V $GaAs$ require cryogenic temperatures ($\sim$ 10 K) for the observation of SCR, with the exception of GaN [23] and ZnO [191] semiconductors MCs, where SCR has been reported at room temperature. The $\sim$ 10 K limit in the SCR temperature for the former compounds arises from the weak interaction strength binding together electrons and holes in Wannier–Mott (inorganic) excitons [226]. At higher temperatures, the thermal energy is responsible for the dissociation of the exciton, hindering the SCR. We recall here that a typical value of the vacuum Rabi splitting in III–V ($GaAs$) based MCs structures is $\sim$9 meV [227] and $\sim$26 meV in II–IV ($CdTe$) MCs [228].

The scenario in inorganic semiconductor crystals, conditioned by Wannier excitons, totally changes in organic semiconductor compounds. In the latter case the binding energy of the organic exciton species (Frenkel-type excitons) largely exceeds the thermal energy at room temperature and therefore SCR is accessible. Frenkel excitons were found in ionic crystals, where electrons and holes are strongly bind together, having their wavefunctions localized in the same or nearest unit cell of the crystal. Analogously, organic Frenkel-type excitons in semiconductors possess a strong molecular localization whose binding energy is larger than $k_BT \simeq 26$ meV (thermal energy at $T = 300$ K).

Lidzey *et al.* [229] were the first to prove SCR at room temperature on a planar MC where the active medium of the system was made by a thin film of organic dye (they measured a Rabi splitting as large as 160 meV). Similarly as done by Weisbuch *et al.* [11], Lidzey and coworkers performed reflectivity measurements detecting the PL emission at different angles, obtaining the polariton anti-crossing as proof and clear signature of SCR. This work has triggered the research in obtaining higher quality MCs and fabricating organic polariton devices. It must be mentioned that the physics of organic semiconductors is not explored in this thesis, despite of the fact that nowadays these systems are attracting the interest of a broad audience in the polariton community [229–231].

Great progresses have been made also in inorganic MCs towards electrical injection [232–234] and manipulation [30, 235, 236] of polaritons. In these cases, the injection of free carries to the system screened the Coulomb interaction in such a way that excitons dissociate at densities below the condensation threshold. A recent work [237], has reported an electrically pumped polariton laser, based on a MC containing multiple QWs. Additionally, Bhattacharya and coworkers have claimed the demonstration of polariton condensation through electrical injection of carriers [24, 25] (additional discussion about this work is addressed in the conclusions contained in Chapter 12).

In this thesis, we restrict the creation and manipulation of polariton condensates to optical excitation. Moreover, polaritons, being neutral particles, are detected by optical means, through the photons emitted after recombination processes. A crucial advantage with respect to superconductors, superfluids and atomic BECs is the possibility of fully reconstructing both the density and the phase pattern of the polariton condensate from the properties of the emitted light. This provides a direct measurement of the condensate properties.

In this Part we describe the experimental setups to create, manipulate and detect the polariton condensates that were used to acquire the data presented in Parts III and IV. Two samples are described, as well as the data analysis methods used to recover and reconstruct the time dynamics, the condensate density, the phase and the coherence in both real and momentum spaces.

Chapter 3

Samples

The semiconductor structures used in this thesis to create cold polariton 2D fluids are planar DBR-MCs with embedded QWs, already described in Chapter 1. These are basically constituted of tens of parallel layers, with widths in the nanoscale, of $Al_xGa_{1-x}As$ alloys, where the ratio between Aluminium and Gallium concentration determines the layer refractive index and electronic band structure. They are grown by a MBE process [238], where Aluminium and/or Gallium solid sources are heated releasing a high-velocity beam traveling in a ultra-high vacuum chamber, directed towards a $GaAs$ substrate where the layers grow epitaxially. Usually, the substrate wafer, typically circular of ∼10 cm-diameter, is mounted on a rotating platter to provide equal grow rates all over the substrate. By controlling the flow of each component over the wafer, different concentrations of Al and Ga are achieved for each layer. The surface geometry, morphology and constitution can be further controlled by electron diffraction techniques, allowing precise control of the thickness of each layer down to a single layer of atoms.

When growing cavity layers, the wafer rotation is stopped and a growth rate gradient appears, yielding a cavity whose thickness varies along the radial direction of the sample. This wedge allows for the cavity mode energy to be chosen by moving the excitation spot around the sample, selecting the cavity-exciton detuning. However, the wedge is small enough so that it can be neglected within the extension of the excitation spot.

3.1 Single-QW sample

The sample used in the experiments described in Chapter 5 has been grown under the supervision of Dr. Aristide Lemaître in the group of Prof. Jacqueline Bloch at the Laboratoire de Photonique et de Nanostructures (LPN-CNRS, Marcoussis, France), see a scheme of the sample structure in Fig. 3.1. It consists of a $\lambda/2$ $AlAs$ MC (nominal width of ∼120 nm) with a 20 nm $GaAs$ QW

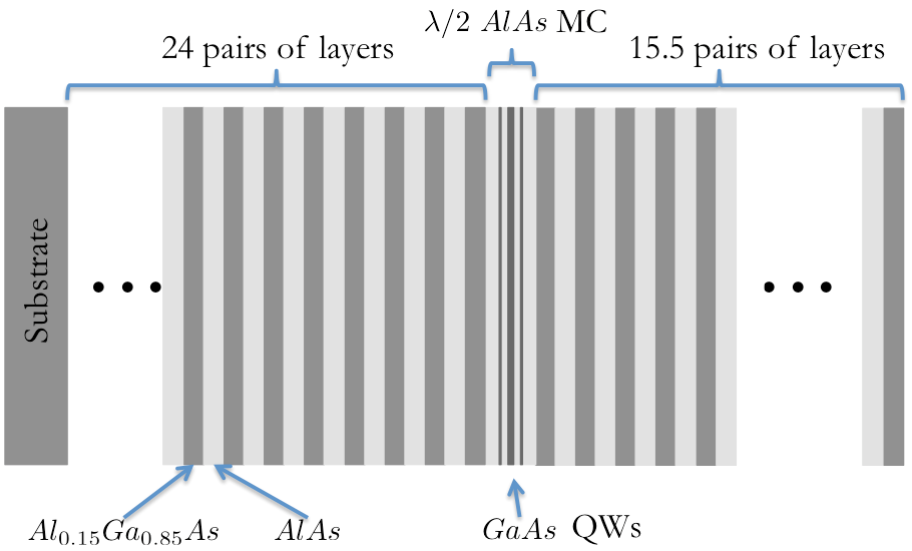

FIGURE 3.1: Scheme of the DBR and MC distribution of the single-QW sample; the thickness of the DBR pairs, *AlAs* MC and *GaAs* QW are not at their corresponding scale.

placed at the antinode of the cavity electromagnetic field. The cavity is surrounded by two Bragg mirrors made of alternating $\lambda/4$ layers of $Al_{0.15}Ga_{0.85}As$ (57.2 nm thick) and $AlAs$ (67.5 nm thick), with 24 pairs of layers at the bottom (left DBR in Fig. 3.1) and 15.5 on the top of the structure (right DBR in Fig. 3.1). One additional narrow $GaAs$ QW (2.6 nm thick) is present at each side of the wide QW, separated by an $AlAs$ layer of 10 nm. The exciton resonances of these QWs are much higher in energy than any of the polariton resonances of interest here (in fact these QWs can be excited by a $HeNe$ laser to study polariton relaxation dynamics in the presence of an electron gas [239–241]), and do not affect the polariton physics.

Figure 3.2 shows the sample luminescence at 10 K when excited with a low power *cw* laser tuned to the first Bragg mode of the cavity (∼1.65 eV), for three different positions of the excitation spot on the sample corresponding to decreasing photon-exciton detuning. The emission comes mainly from three branches that we fit to three polariton modes whose energies are given by the eigenvalues of the coupling frequency matrix — analogously to Eq. 1.48 but with three modes:

$$\begin{pmatrix} \omega_C(k_\parallel) & \frac{\Omega_{HH}}{2} & \frac{\Omega_{LH}}{2} \\ \frac{\Omega_{HH}}{2} & \omega_{HH} & 0 \\ \frac{\Omega_{LH}}{2} & 0 & \omega_{LH} \end{pmatrix} \tag{3.1}$$

where $\omega_{C,HH,LH}$ are the photon, heavy- and light-hole excitons frequencies, $k_\parallel$ the in-plane wavevector and $\Omega_{HH,LH}$ are the photon-heavy-hole and photon-light-hole Rabi splittings. The three fits are done using the same photon mass and Rabi splittings $\hbar\Omega_{LH} = 3.0$ meV and $\hbar\Omega_{HH} = 4.4$ meV.

The use of a single QW results in very narrow exciton linewidths, as the effect of interface

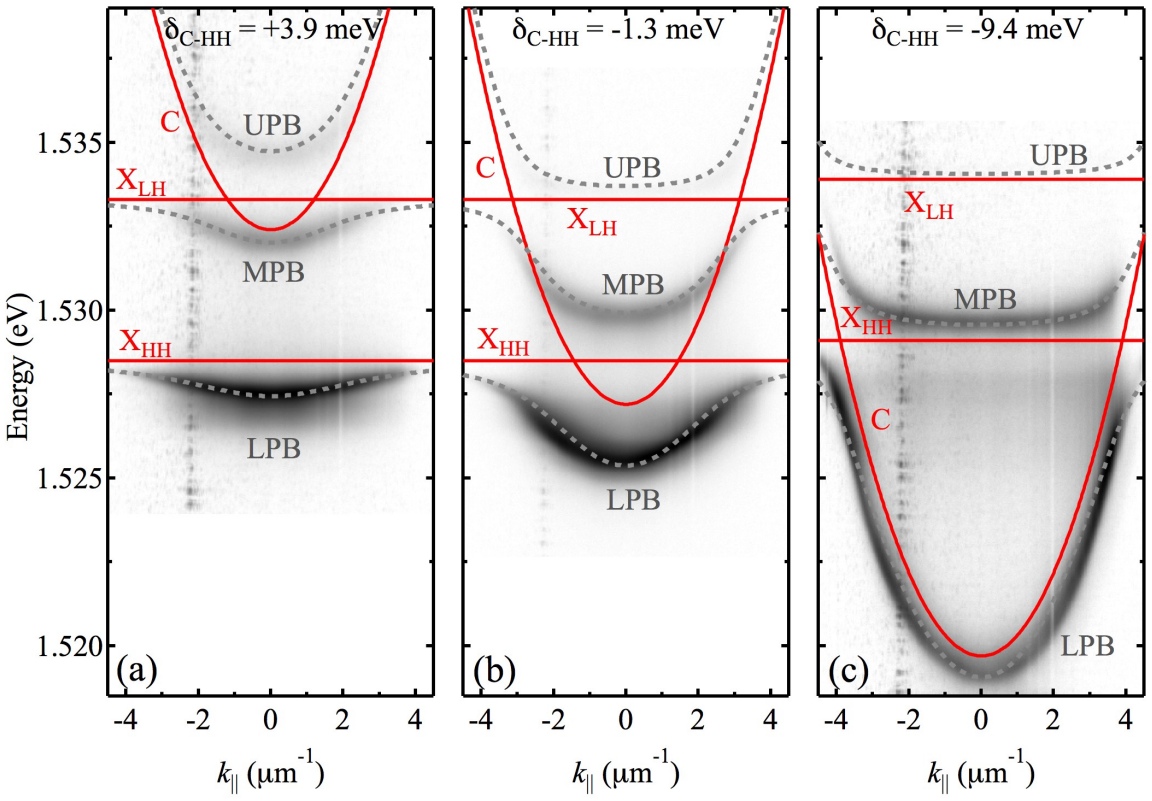

FIGURE 3.2: Single-QW MC PL dispersion images for different photon-heavy-hole-exciton detunings δ_{C-HH} (indicated on top of each panel): (a) +3.9, (b) −1.3 and (c) −9.4 meV, respectively, taken at 10 K, showing fitted (red, full line) bare light- and heavy-hole excitons (X_{LH} and X_{HH}) and cavity mode (C) and (gray dashed line) lower, middle and upper polariton branches (LPB, MPB and UPB). The photon-light hole splitting is $\hbar\Omega_{LH} = 3.0$ meV and the photon-heavy hole splitting is $\hbar\Omega_{HH} = 4.4$ meV. In panel (c), for the sake of a better parameter fitting we assume that the energy of X_{HH} and X_{LH} is blueshifted by ~ 0.6 meV with respect to panels (a,b) due to a local modification of the QW width in the growth process. The PL is coded in a false, logarithmic color scale (not shown).

fluctuations and width distributions are greatly suppressed. In this case the heavy-hole QW exciton presents a low-temperature linewidth of about 0.3 meV, while the cavity-mode lifetime is sf the order of 4 ps, which yields a Q-factor of ~ 9000.

3.2 Multiple-QW sample

The sample used in the experiments described in Parts III (except Chapter 5) and IV has been grown under the supervision of Prof. Zacharias Hatzopoulos in the group of Prof. Pavlos Savvidis at the Institute of Electronic Structure and Laser (FORTH, Heraklion, Greece). It consists of a $5\lambda/2$ $Al_{0.3}Ga_{0.7}As$ cavity (nominal width of 583.1 nm) containing four sets of three 10 nm-thick $GaAs$ QWs placed at the antinodes of the cavity electric field — see Fig. 3.3(a). The cavity is surrounded by two Bragg mirrors made of alternating $\lambda/4$ layers of $Al_{0.15}Ga_{0.85}As$ (57.2 nm thick)

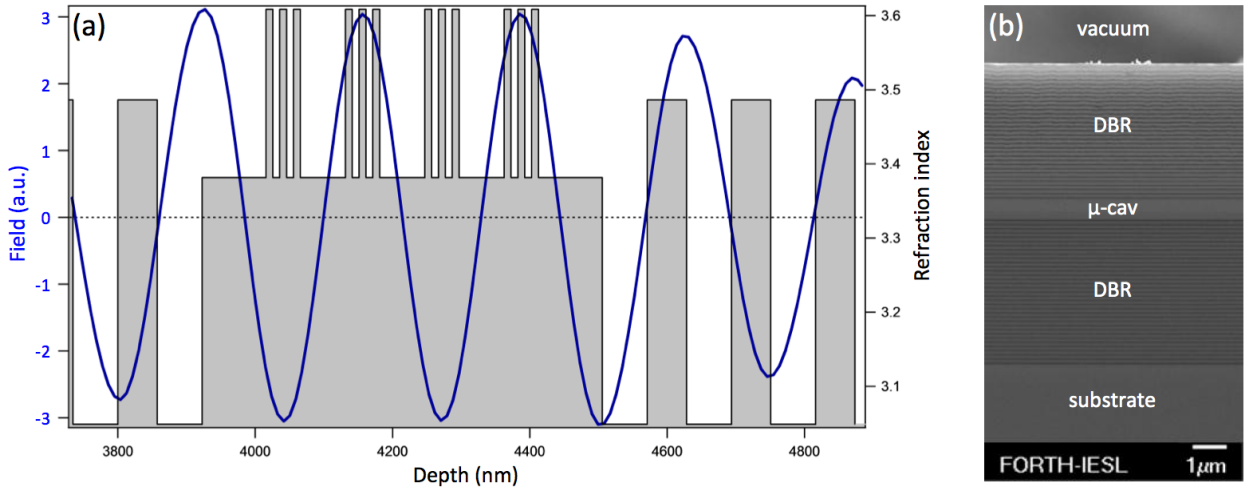

FIGURE 3.3: (a) Refractive index profile of the cavity with 12 QWs and first Bragg layers surrounding it, together with the electric field profile simulated with a transfer matrix code. (b) SEM image of the full MC structure showing the cavity (μ-cav) and DBR layers on the top of the GaAs substrate. Courtesy from Prof. P. G. Savvidis group, FORTH-IESL, Crete.

and $AlAs$ (65.4 nm thick), with 35 pairs of layers at the bottom and 32 on the top of the structure, respectively. Fig. 3.3(b) shows a Scanning Electron Microscopy (SEM) image of the cavity, where it is possible to appreciate the MC between the two Bragg mirrors, the substrate at the bottom and vacuum on the top.

Figure 3.4 shows the sample luminescence at 50 K when excited with a low power cw laser tuned to the first Bragg mode of the cavity. We fit the emission to the three polariton modes whose energies are given by the eigenvalues of the coupling frequency matrix, Eq. 3.1. The fit yield Rabi splittings $\hbar\Omega_{LH} = 6.0$ meV and $\hbar\Omega_{HH} = 11.2$ meV

The linewidth of the LPB at very negative detuning ($\delta_{C-HH} = -9.4$ meV) is measured to be 90 μeV, corresponding to an experimental Q-factor of at least 16000 (cavity photon lifetime $\tau_C = 9$ ps) [242] in close agreement with the simulations of the TMM, where $Q \sim 20000$. The sample is capable of polariton lasing in the SCR for temperatures of up to ∼50 K [242], in accordance to theory [184].

The sample (with dimensions 4 × 13 mm) has been patterned through reactive ion etching; the pattern, shown in Fig. 3.5(a), has been repeatedly printed over all the surface of the sample. A total number of 15 pillars with different diameters (ranging from 1 up to 40 μm) have been printed in the pattern, including the numbers that indicate their corresponding diameter (in μm units). The sculpted structures used in the experiments are: the thickest pillar [with 40 μm-diameter, see detail in Fig. 3.5(b)] and a ridge [with dimensions 20 × 300 μm^2, see detail in Fig. 3.5(c)].

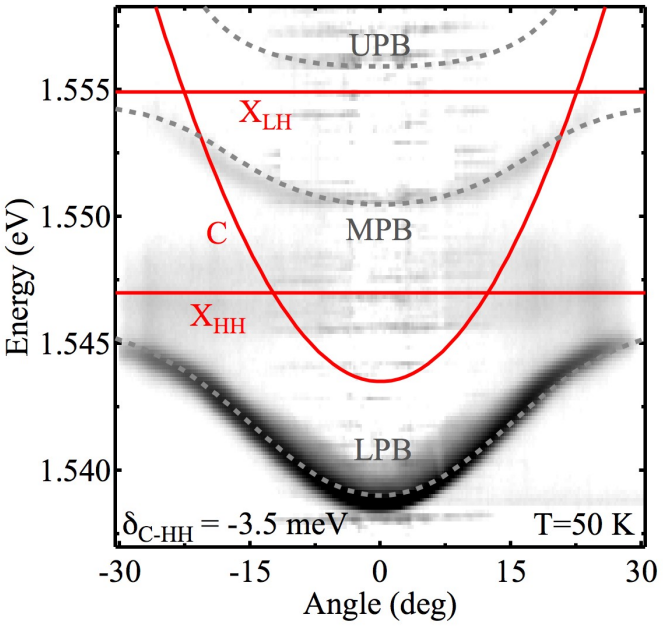

FIGURE 3.4: Multiple-QW MC PL dispersion relation image taken at 50 K, showing fitted (red lines) bare light- and heavy-hole excitons (X_{LH} and X_{HH}) and cavity mode (C), and (gray dashed lines) LPB, MPB and UPB. The detuning is found to be $\delta_{C-HH} = -3.5$ meV, the photon-light hole splitting is $\hbar\Omega_{LH} = 6.0$ meV and the photon-heavy hole splitting is $\hbar\Omega_{HH} = 11.2$ meV. The PL is coded in false, logarithmic color scale. Experimental data is a courtesy from P. G. Savvidis group, FORTH-IESL, Crete.

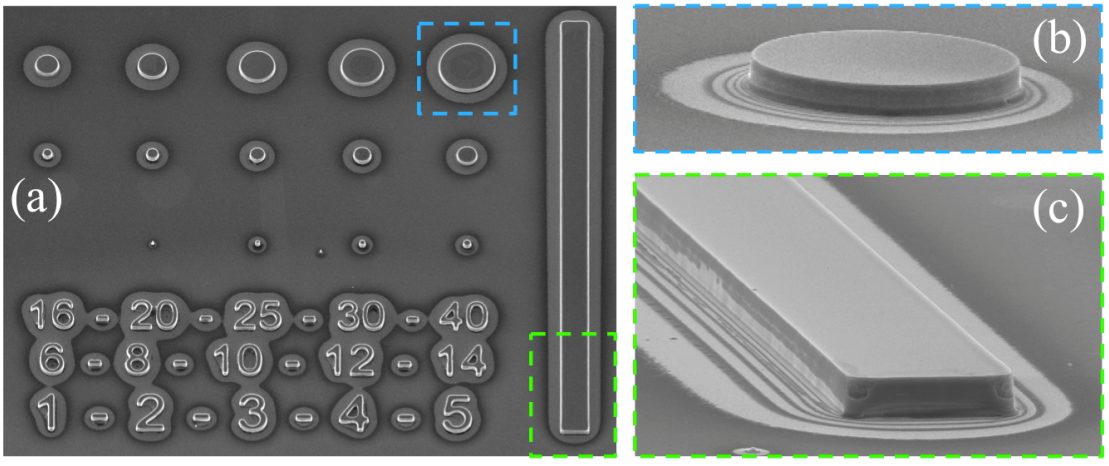

FIGURE 3.5: (a) Top-view SEM image of the unitary pattern printed on the sample through reactive ion etching on the sample. (b) and (c) detail of the two structures, a 40 μm-diameter pillar and a 20 $\times$ 300 μm^2 ridge, respectively. SEM images are a courtesy from P. G. Savvidis group, FORTH-IESL, Crete.

3.2.1 Dispersion relation of quasi-1D structures

Hitherto we have discussed the dispersion relation of our samples in planar MCs, where we observe the typical LPB, explained with Eq. 1.51. Now we turn our attention to the dispersion relation in the quasi-1D structure shown in Fig. 3.5(c). The lateral confinement in a MC (added to the confinement in the growth axis z) yields a lateral discontinuity in the refractive index. The additional real-space confinement, with dimension L_y, along the in-plane, confinement axis (y) introduces a quantization of the momentum k_y: $k_{y,j} = (j+1)\pi/L_y$, where j is a quantization number, integer and positive, identifying each LPB sub-band composing the fan of the photonic modes. The relationship between energy and wave vector in 1D-MCs reflects this additional quantization and is only continuous along k_x (propagation direction along the long axis of the 1D structure, x). We must note that in our ridges the lateral confinement is smaller compared to, much thinner (~ 2 μm), 1D-MC wires [36, 40]. Nevertheless, as we show below, the quantification of k_y is present in the dispersion relation and it must be considered as a fundamental effect in the experiments that we performed in our ridges (for example, the polariton energy relaxation).

The ridges have been aligned along the cavity wedge so that the exciton-photon detuning varies ~ 2 meV/mm on the sample. All the experiments on the ridges have been performed in a region of the sample corresponding to a detuning between the bare exciton and bare cavity mode $\delta \backsim 0$. We start by describing the dispersion relations of polaritons along two orthogonal directions in the ridge, k_x at $k_y = 0$ and k_y at $k_x = 0$. The confinement in the y axis of the ridge results in the discretization of the k_y in-plane momentum, splitting the LPB in many subbands, Fig. 3.6(b), whose antinodes along k_y are visible in Fig. 3.6(d). It is important to emphasize that only even subbands are visible in Fig. 3.6(b), since along k_x we spectrally resolve the PL at $k_y = 0$. Odd modes (with a node at $\mathbf{k} = 0$) are visible in Fig. 3.6(d), see for example the subband at 1.5405 eV. The scenery seen in these dispersion relations is very interesting because it reveals the possibility of parametric scattering processes among many different sub-branches. Recent works on 1D semiconductor MCs exploit these extra-confinement effects to study new parametric phenomena (see, for example, Refs. [189, 243] and references therein).

In planar MCs, the energies of the linear polarizations TM and TE are split due to the long-range exciton interaction [244] and the transverse electric and magnetic mode splitting of the cavity [245]. This splitting vanishes for the normal incidence ($\mathbf{k} = 0$) and acts as a directionally dependent effective magnetic field in the plane of the MC, which causes the precession of the pseudospin for polaritons with a finite $\mathbf{k}$ vector [246].

Confinement in a quasi-1D cavity enhances the splitting between the two light polarizations TM and TE, parallel and perpendicular to the x axis of the ridge, respectively. We identify TM (TE) as the H (V) direction used to define the linear degree of polarization $s_x = \frac{I_{\mathrm{TM}} - I_{\mathrm{TE}}}{I_{\mathrm{TM}} + I_{\mathrm{TE}}}$, where I_{TM} (I_{TE}) is the PL intensity under TM (TE) detection (see § 1.4.3 for further information about s_x

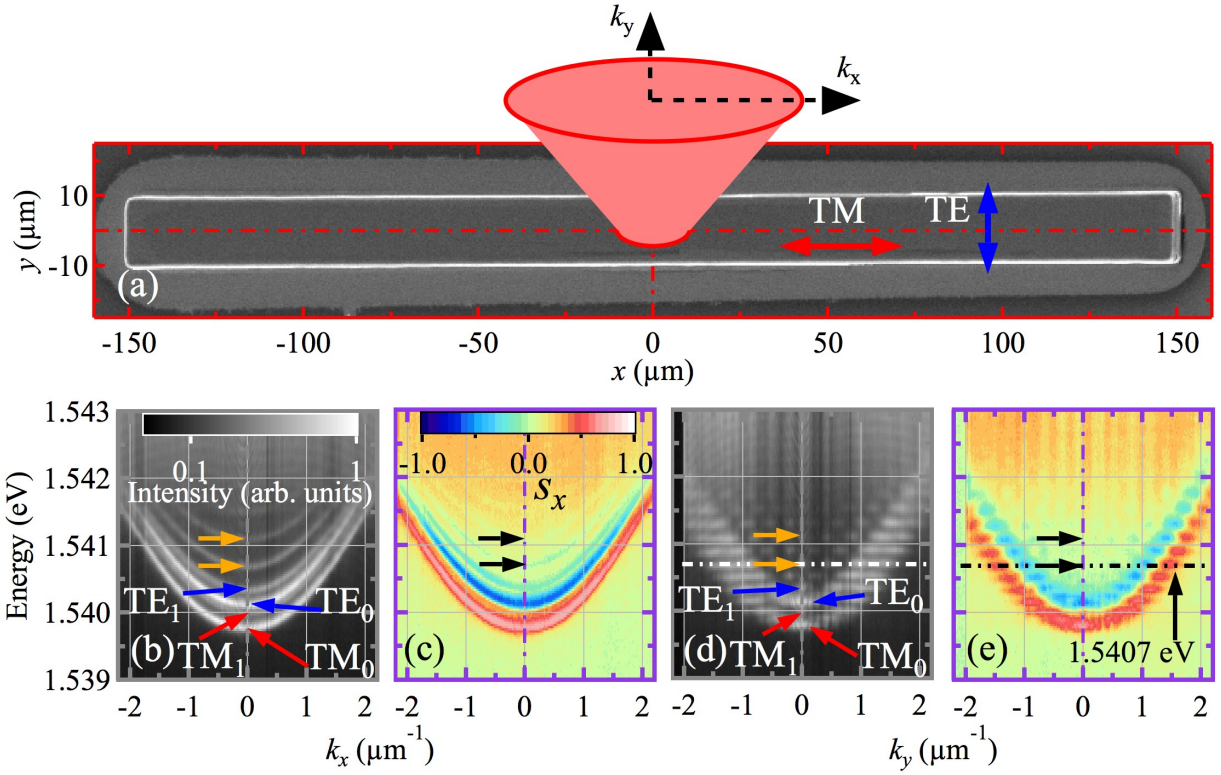

FIGURE 3.6: (a) SEM image of a 20-μm wide ridge, including an angular scheme of the PL emitted from the center of the ridge (see cone of light as a guide to the eye), z direction is perpendicular to the plane of the paper. The bottom panels display, under non-resonant (1.612 eV), weak, circularly polarized-light excitation: (b) and (d) energy dispersions of the PL along k_x and k_y, respectively; (c) and (e) linear degree of polarization (s_x) versus energy and k_x and k_y, respectively. Dot-dot-dashed white and black lines in panels (d,e) mark the energy value (1.5407 eV) used for Fig. 3.7(b). Red and blue arrows in panels (a,b,d) mark the TM and TE character of the even subbands in the dispersion relations, respectively. Orange and black arrows in panels (b-e) mark the energy positions of weakly-polarized, consecutive higher subbands. The PL and s_x are coded in linear, normalized, false color scales.

and the different degrees of polarization). Considering the k_x direction, the lowest energy subband is TM_0 polarized, see label in Fig. 3.6(b), and its corresponding s_x is shown in Fig. 3.6(c), where an intense, red subband appears, whose minimum is at $E = 1.5397$ eV and $k_x = 0$. The next TM_1 mode is 0.2 meV blueshifted, lying very close to the TE_0 mode [intense blue subband in Fig. 3.6(c)]. The splitting between TM_0 and TE_0 is 0.36 meV. Higher energy modes, with a weaker degree of polarization, are visible at 1.5407 and 1.5411 eV, marked by orange and black arrows in Figs. 3.6(b,d) and Figs. 3.6(c,e), respectively. Analyzing the dispersion relation k_y, Figs. 3.6(d,e), a further, horizontal discretization of the energy levels is clearly observed. The separation in k_y between consecutive antinodes of a single state is $\sim$0.4 μm^{-1}.

Detailed spectra at $k_x = 0$, both for intensity (thick, gray line) and s_x (thin, purple line), are given in Fig. 3.7(a), with different, labelled modes indicated by arrows. The aforementioned higher energy modes are marked by orange arrows. Figure 3.7(b) details a profile of the PL and s_x versus

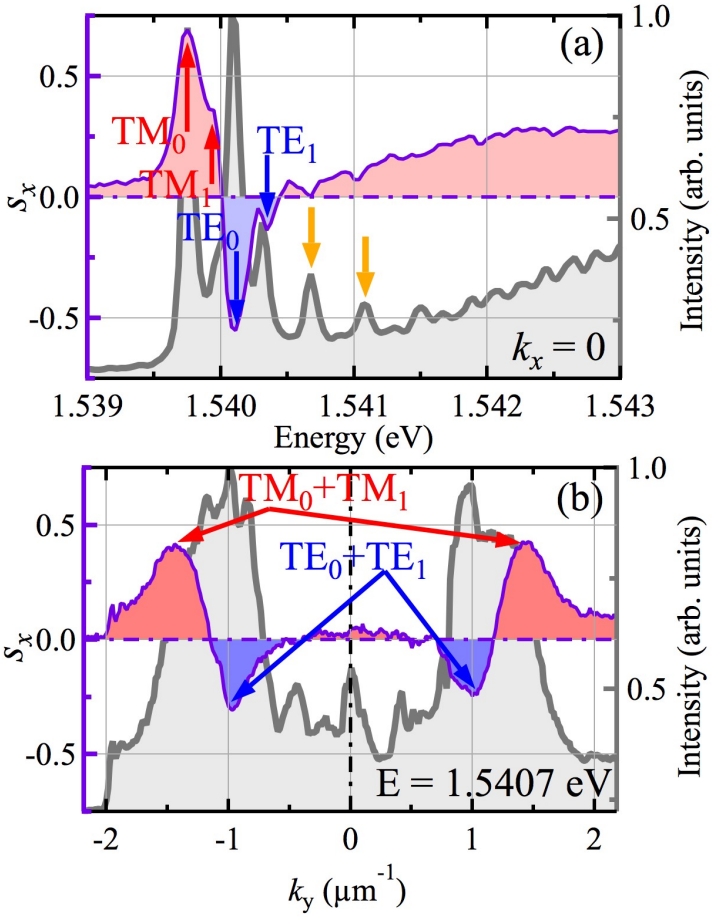

FIGURE 3.7: (a) PL (s_x) as a function of energy at $k_x = 0$ in a gray, thick (purple, thin) line. (b) PL (s_x) as a function of k_y at $E = 1.5407$ eV in a gray, thick (purple, thin) line. Red and blue arrows in panels (a,b) mark the TM and TE character of the even subbands in the dispersion relations, respectively. Orange arrows in panel (a) mark the energy positions of weakly-polarized, higher subbands.

k_y, at $E = 1.5407$ eV: the predominant structures at $|0.7| < k_y < |1.8|$ μm^{-1} in thick gray line are constituted by the modes (TM$_0$+TM$_1$) and (TE$_0$+TE$_1$) modes at high k_y values, while the three central antinodes correspond to other confined modes at lower k_y values. Only when a polarization analysis is performed, TE and TM distributions are resolved (thin purple line), as marked in the figure.

Assuming a square well type potential in the y direction, the energies of the TM- and TE-polarized photonic modes can be approximated by:

$$E_{\mathrm{C;TM,TE}}(n, k_x) = \frac{(n+1)^2\hbar^2\pi^2}{2m_C L_y^2} + \frac{\hbar^2 k_x^2}{2m_C} \pm \Delta_{\mathrm{TM,TE}} \tag{3.2}$$

where $n = 0, 1, 2...$ is the subband index, m_C is the photon effective mass, L_y is the ridge width and $\Delta_{\mathrm{TM,TE}}$ characterizes the splitting between the H and V polarizations. The dispersion of the upper (+) and lower (−) polariton modes is given by the standard two oscillator formula (up to a

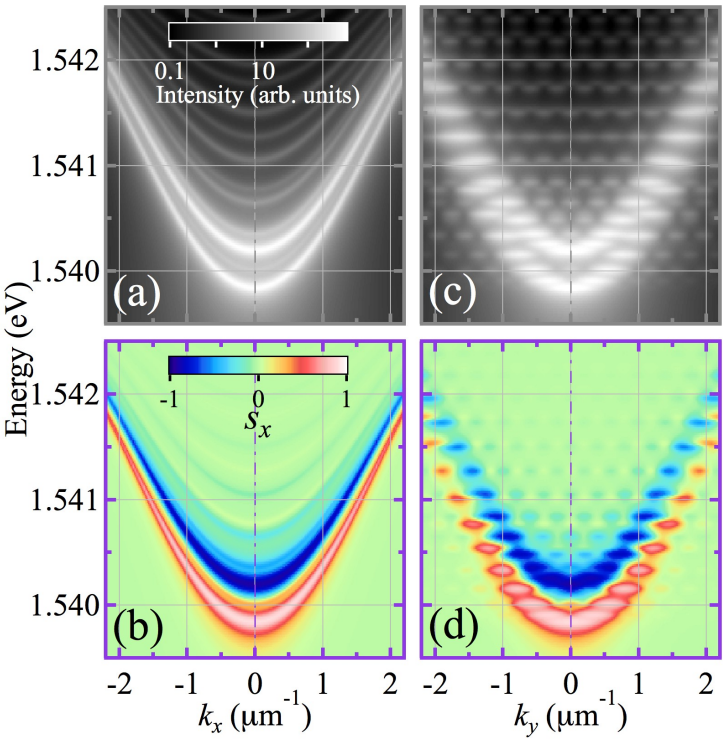

FIGURE 3.8: (a) and (c) Calculated energy dispersion relations of lower polariton modes along k_x (at $k_y = 0$) and k_y (at $k_x = 0$), respectively; (b) and (d) corresponding linear degree of polarization (s_x). The intensity and s_x are coded in linear, normalized, false color scales.

constant energy shift):

$$E^{\pm}_{\mathrm{TM,TE}}(n,k_x) = \frac{1}{2}E_{\mathrm{C;TM,TE}}(n,k_x) \pm \sqrt{E^2_{\mathrm{C;TM,TE}}(n,k_x) + 4\Omega^2} \tag{3.3}$$

where $\Omega = \Omega_R/2$ is the exciton-photon coupling constant. Assuming a Lorentzian line-shape (with a FWHM corresponding to a 18 ps lifetime) and an independent Boltzmann population of the TM and TE polarized energy levels ($T = 10$ K), we calculate the dispersions corresponding to lower polariton modes (E^-) shown in Fig. 3.8. As in the experiments, we show the $k_y = 0$ ($k_x = 0$) PL when resolving the dispersion along k_x (k_y). The results show that the TM bands are hidden by the stronger populated TE bands at slightly higher energies.

3.2.1.1 Trapping potentials in the lateral edges of the quasi-1D structures

Stunning energy relaxation effects have appeared in recent experiments on polariton microwires [36]. In particular, the striking appearance of harmonic modes, roughly equally spaced in energy, due to a potential trap formed between the wire edge and the pump-induced potential (constituting a semi-harmonic potential), $V(x)$, has been reported both experimentally and theoretically [36, 216]. The positioning of the optical pump near the wire edge introduces a strong asymmetry between

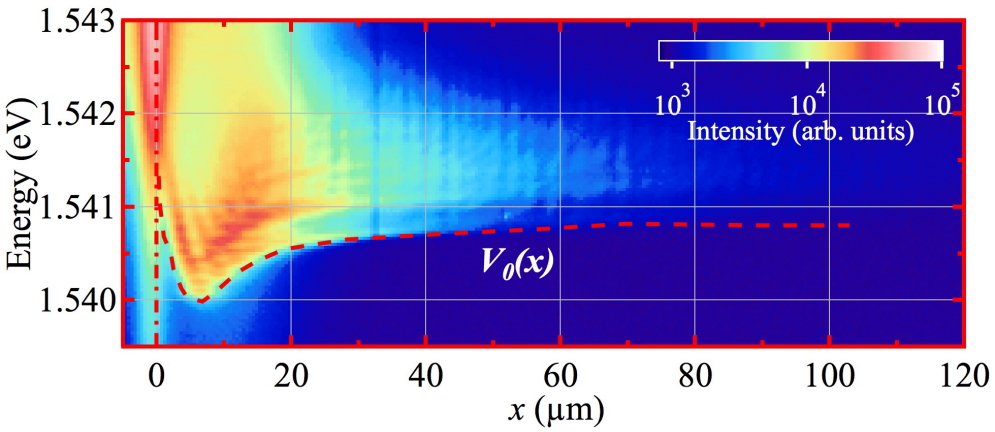

FIGURE 3.9: Polariton PL map as function of the emission energy and spatial position (x) under a pulsed, non-resonant (1.612 eV) and very weak (7 μW) excitation pump, placed at $x = 10$ μm. The dashed red line shows, as a guide to the eye, the sample-geometry induced potential, $V_0(x)$. The intensity is encoded in a logarithmic, false-color scale.

relaxation on the two sides of the pump. It is observed that relaxation is more effective when polaritons interact with the wire edge. These effects have been described theoretically accounting for both the energy relaxation of excitons into condensed polaritons and relaxation of polaritons *within* the condensed fraction of the polariton gas (polaritons can relax their energy by scattering with phonons or hot excitons). While the first-order process is included in most kinetic theories of polariton condensation, the second was theoretically addressed by M. Wouters and coworkers [216].

Similar effects on harmonic potential traps have been reported by G. Tosi and coworkers [41], where two close, non resonant pump spots create a potential yielding the polaritons relaxation in energy. In this work, the authors claim that the resulting new polariton density profile modifies the polariton potential itself, leading to more parabolic and equally spaced energies, thus speeding up scattering and feeding back positively.

In the following, we discuss the intrinsic structural potential $V_0(x)$ of our quasi-1D structures (see Eq. 2.41), which has been created by the etching process on the planar MC. We do not consider the potencial suffered by condensed polaritons, sculpted by the presence of an excitonic, repulsive reservoir (the described case up to now).

The existence of this structural trapping potential in the two borders of our ridges has constituted a fundamental part in our polariton devices for the obtention of confined condensates at low energy, regarded as output signals of our polaritonic switches and gates. Therefore it is important to obtain a quantitative description of $V_0(x)$. To do so, we create a dilute polariton gas at the border of the ridge by a pulsed, non-resonant (1.612 eV) and very weak (7 μW) excitation pump, placed at $x = 10$ μm far from the left edge of the ridge, see Fig. 3.9: the polariton PL map is plotted as function of the emission energy and spatial position (x). The potential trap, induced by

the sample geometry, is visualized by the emission of the non-condensed polariton gas. The trap is located at a distance of ~ 7 μm from the end of the ridge and it is ~ 1 meV deep.

For the sake of completeness in the description of polariton energy relaxation processes and intrinsic, structural, confined potentials, we must mention that, in this sense, a different approach was accomplished by Savenko and coworkers in Ref. [247]. They addressed a theoretical description of the polariton energy relaxation based on the polariton coupling to only a thermal bath of phonons. In this work they assumed that the structural potential $V_0(x)$ can be considered as a linear potential gradient function $V_0(x) = V_0 - \beta x$ composed of the potential defining the walls of the polariton wire V_0 and a potential gradient $\beta = 9$ meV/mm, what actually it was almost 5 times overestimated with respect to our samples ($\beta \sim 2$ meV/mm) and those reported in Ref. [43]. They based the polariton relaxation, mediated by phonos, on a structural potential $V_0(x)$ that is not experimentally realistic.

We present now the dispersion relations of polaritons in relevant, different ridge's regions used in the experiments, obtained under non-resonant (1.612 eV), weak, pulsed excitation conditions ($\sim$20 μW). Figure 3.10 (a) shows a SEM image of the 20-μm wide ridge. Two rectangles centered at $x = 0$ and 90 μm mark the spatial regions from where the real-space emission was collected in order to obtain the corresponding dispersion relations. The different sub-branches, originating from the quasi-1D confinement in the y direction of the ridge, are clearly resolved at $x = 0$ in Fig. 3.10(b). The two bands centered at 1.545 and 1.547 eV correspond to the emission from bare exciton levels (we discuss them in detail below). The experiments described in Chapters 7 and 11 were carried out by exciting at the energy indicated by the dashed arrow. The dispersion obtained close to the ridge's border, Fig. 3.10 (c), reveals the lack of translational invariance of polaritons at this position, evidenced by the formation of additional, non-dispersive low energy states at $\sim$1.5388, 1.5391, 1.5393 and 1.5394 eV. Since the dispersion relation is obtained at the right ridge's border, only states in the dispersive branches with negative k_x are occupied by left propagating polaritons (we recall here that in this case the pump spot is placed on the right edge of the ridge, therefore the propagation is possible only leftwards).

Figure 3.11 shows the PL spectra at the center and border of the ridge, integrated in momentum space from Fig. 3.10(b,c), in a green green and orange traces, respectively. There are two remarkable bare exciton levels X_{1c} and X_{2c} [X_{1b} and X_{2b}] that have been obtained with a double gaussian fit, see dot-dashed green [orange] lines. Their energy peaks, located at $\sim$1.5447 and $\sim$1.5467 [$\sim$1.5438 and $\sim$1.5460] eV, respectively, differ $\delta E \simeq 2$ meV (same value at the center and the edge of the ridge). It is very interesting that the bare exciton energy levels at the border are redshifted by $\Delta E = 0.95$ meV with respect to those at the center of the ridge. This redshift affects to the distribution of the polariton subbands, where the lowest-energy, confined polariton state (at $\sim$1.5388 eV) is ΔE redshifted at the border of the ridge with respect to the minimum value of the lowest-energy polariton subband at the center of the ridge ($\sim$1.5398 eV). The FWHMs

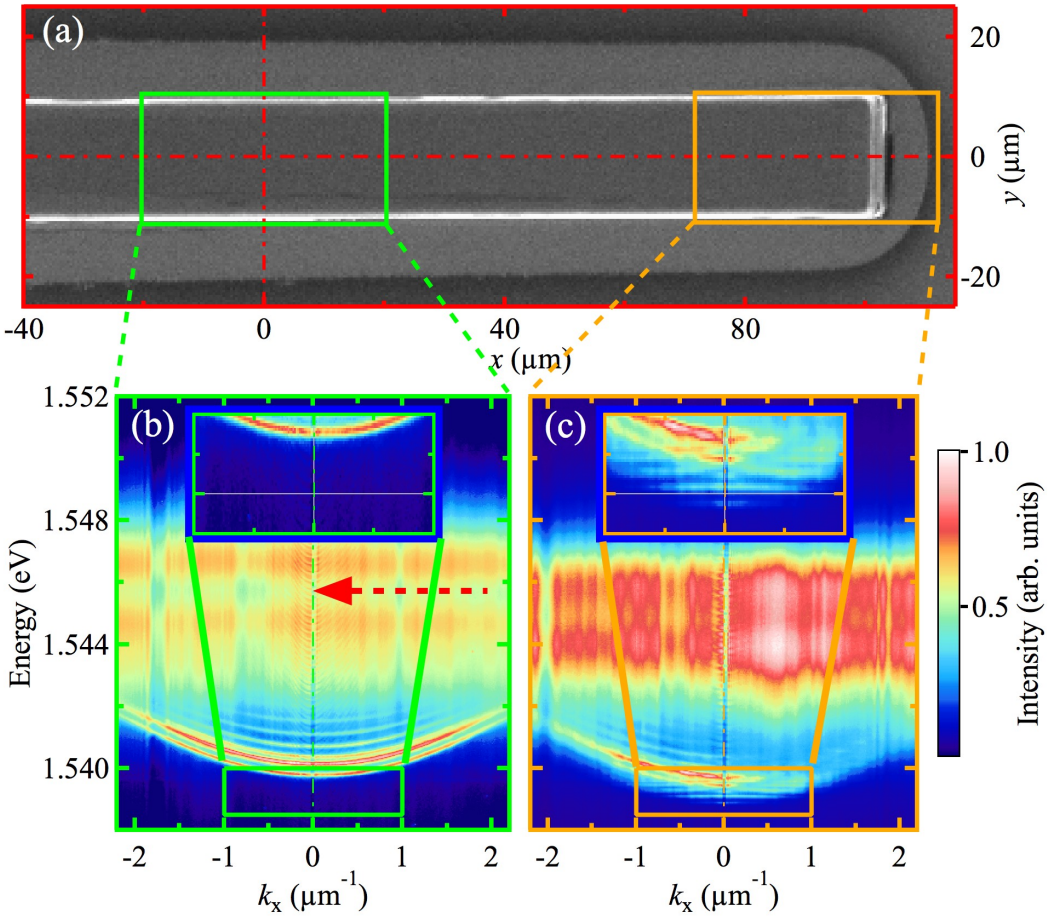

FIGURE 3.10: (a) SEM image of a 20-μm wide ridge, including the filtered areas where time-integrated dispersion relations were measured under weak, non-resonant (1.612 eV), pulsed excitation: (b) far from its borders; (c) at the right ridge's border. The insets in panels (b) and (c) compare the dispersion relation quantization of polaritons at low energies. The dashed arrow indicates the energy of the excitation laser used for the experiments described in Chapters 7 and 11. The intensity is coded in a linear, normalized, false color scale.

of X_{1c} and X_{2c} [X_{1b} and X_{2b}] gaussian fits are $\sim$1.44 and 1.11 [$\sim$2.34 and 1.44] meV. Therefore we observe that the bare exciton levels at the border are broaden by a factor of ~ 1.5 with respect to the those at center of the ridge. This effect, added to the energy-redshift already discussed, highlights the presence of exciton complexes at the lateral edges of the ridge due to (probably) the particular chemical etching used for the patterning of our samples and the presence of impurities at the lateral, edged interfaces of the MC. These results explain the presence of the intrinsic, structural potential trap $V_0(x)$, which is a fundamental characteristic of our polariton devices in order to obtain trapped polariton states.

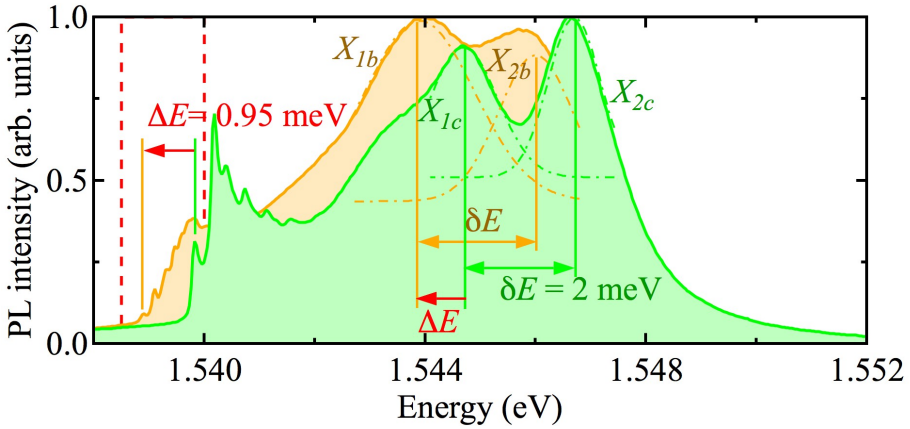

FIGURE 3.11: PL spectrum at the center [border] of the ridge integrated in momentum space, from Fig. 3.10(b) [(c)], in a green [orange] trace. The dashed, vertical lines depict the energy range shown in the insets of Figs. Fig. 3.10(b,c), with the lowest energy polariton state at the center [border] of the ridge highlighted with a green [orange], vertical line. The two bare exciton levels X_{1c} and X_{2c} [X_{1b} and X_{2b}] are obtained with a double gaussian fit, see dot-dashed, green [orange] lines, whose maxima are marked with two vertical, green [orange] lines. The energy difference between the bare exciton peaks, $\delta E \simeq 2$ meV, has the same value in both center and border regions of the ridge. The bare exciton levels in the border of the ridge are $\Delta E = 0.95$ meV redshifted and broaden by a factor ~ 1.5 with respect to the bare excitons at center of the ridge. The exciton energy-redshift equals the one of that of polaritons, explaining the existence of the structural trapping potential at the edges of the ridge.

3.2.2 Dispersion relation of a 40 μm-$\varnothing$ pillar

In the last section we described the effects on the discretization of k_y by reducing the lateral size of the MC, we now discuss the dispersion relation of the pillar shown in Fig. 3.5(b). Figure 3.12(a) displays the dispersion relation of the 40 μm-$\varnothing$ pillar, obtained under weak ($\sim$20 μW), non-resonant (1.612 eV), pulsed excitation. The comparison between the pillar dispersion relation and the one of the planar multiple-QW MC, shown in Fig. 3.4, yields no significant differences [apart from the fact that the former (latter) one was obtained in a region of the sample at 0 (-3.5 meV) detuning]. No apparent discretization in many sub-bands of the LPB is observed for the pillar structure given the macroscopic surface of the edged area, k_y is a continue variable. Nevertheless, we include in Fig. 3.12(b) a zoomed area of an enclosed region highlighted in Fig. 3.12(a), it details the shape of the LPB between ± 1 μm^{-1}; the dashed red line hints the presence of a weak additional polariton subband.

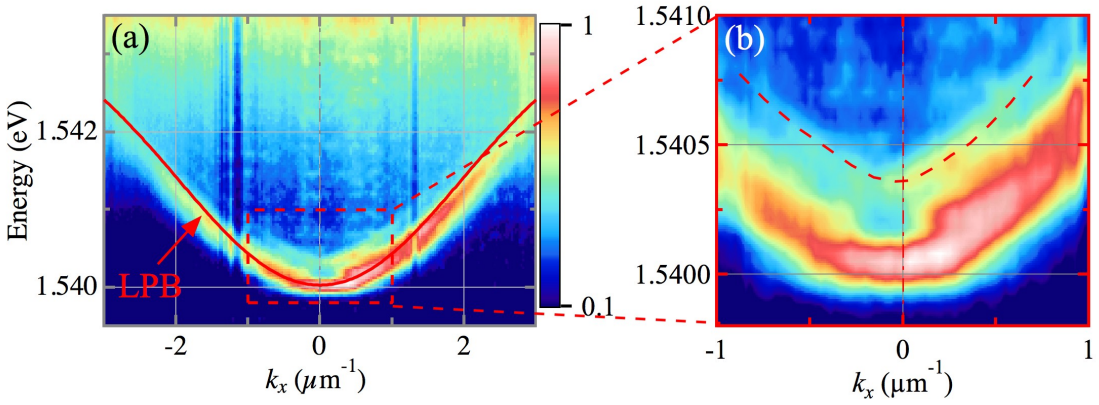

FIGURE 3.12: (a) Experimental LPB dispersion obtained under non-resonant (1.612 eV), weak ($\sim$20 μW) excitation conditions; the overlapping thin, full curve is a guide to the eye. The area enclosed with a red, full-line rectangle indicates the zoomed dispersion relation displayed in panel (b). (b) Detail on the dispersion relation around $k = 0$, the quantization of the in-plane momentum in the pillar barely shows a second subband, highlighted with a dashed red line. The PL is coded in a false, normalized, logarithmic color scale.

Chapter 4

Experimental setups

The samples are kept in cold finger-cryostats, which are connected to high-vacuum pumps yielding pressures on the order of 10^{-7} mbar inside. The cryostats are also connected to a liquid helium dewar and to another weaker pump. This last pump is responsible for a flow of helium gas through the cryostat, making possible to decrease the sample temperature down to ~ 4 K. A temperature sensor is placed very close to the sample holder, where the sample is attached with silver paint to ensure a good thermal contact. All the data presented in this thesis were taken with the samples at 10 K.

Excitation lasers are focused onto the sample by an objective lens (see Fig. 4.1) which is chosen accordingly to better suit the specific experiment to be performed — see § 4.1. The same objective lens is used to collect the polariton PL, in the retro-reflection direction. The sample emission comes from a region on the micrometer-scale, which can be considered as a point-like source since the objective diameters are in the centimeter scale. It follows that the beam of the condensate light emission acquires a plane wavefront after the objective, and propagates parallel to the objective optical axis over a long distance before being focused, by an imaging lens, into the detection apparatus, where images are taken — see § 4.2.

In the region between the objective lens and the detection, different combinations of optical elements are used depending on what is to be measured. If only mirrors are used, the image created by the two lenses is simply a magnified image of the sample emission, and in this case the setup is equivalent to an optical emission microscope. If one is interested in resolving the angular emission of the sample, which is equivalent to image the momentum space (also dubbed far-field or **k**-space) [162], a third lens is placed between the imaging real space lens and the detection, in such a way that the momentum space lens' focus coincides with the objective lens' Fourier

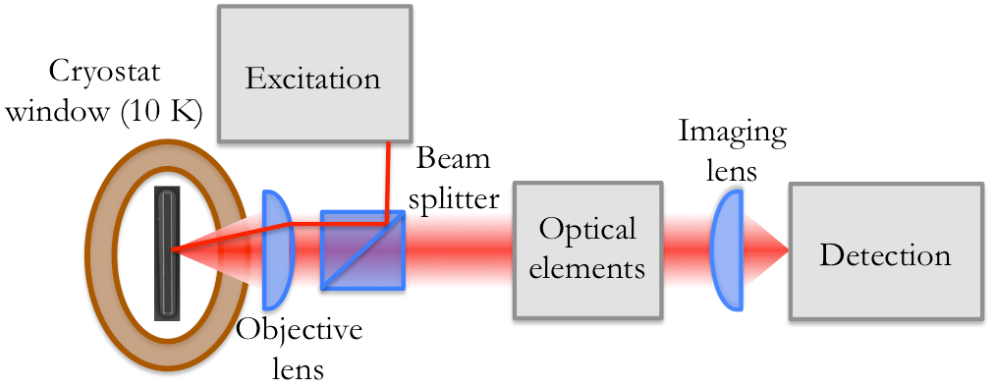

FIGURE 4.1: Excitation and detection setup scheme. The "Excitation" labelled rectangle represents *cw* and pulsed lasers used to pump polariton condensates. They propagate through a beam splitter and are focused by a objective lens onto the sample, held at 10 K inside a cold finger cryostat, whose window is shown in the figure. The objective lens also collects the emitted PL, which passes through the beam-splitter and enters a region between the objective lens and the detection ("Optical elements") that might contain either mirrors, if the light path has to be redirected, pinholes and/or slits, if filtering measurements are performed, a lens, if momentum-space intensity images are recorded, or interferometers, if interferometric or coherence experiments are required. The field is finally focused by another lens into the "Detection" apparatus, which contains a spectrometer coupled to a CCD and/or to a streak-camera.

plane[1], and in this case the image formed by the momentum space imaging lens is the Fourier (momentum) space of the sample emission. The specific position and focal distance of the third lens determines the momentum space magnification. Note that switching from the real to the momentum space configuration, and vice-versa, is straightforward taking just a few seconds, and the excitation conditions are not altered.

When taking position- (momentum-) space images, a pinhole can be placed at the emission in far- (near-) field to select a specific momentum (position-space) area and take the profile of such a local region. This filtering is done, *e.g.*, in Chapters 5 and 6, where only the spatial profile of the signal state is measured by filtering-out in far-field the pump and idler states under OPO excitation configuration. Further details on filtering analysis are discussed in § 4.2.2.

When performing non-resonant excitation and imaging the full, not resolved in energy, emission of the sample, a filter is used (typically placed just before the CCD camera) to filter out the laser reflection without blocking the polariton emission which is at a different wavelength[2].

[1]The objective Fourier plane is defined as the plane perpendicular to the optical axis and located at the objective focus opposed to the focus where the sample is located. All rays coming out from the sample at a given angle (which correspond to a well defined in-plane momentum) form a point in the Fourier plane, which is therefore a map of the angular emission from the sample. In other words, the third lens is a Fourier transform performer.

[2]The PL energy in our experiments is ~ 805 nm, therefore, the filter used in our non-resonant excitation experiments was a *Iridian* 752 nm low pass filter (1 inch-$\varnothing$).

Finally, combinations of beam-splitters and mirrors can be used to build interferometers in the region between the objective lens and the detectors. Interferometry provides information about the polariton PL coherence and phase as it will be described in § 4.3.

4.1 Excitation

The samples have been excited with *cw* and pulsed laser beams. The *cw* laser is a *3900S Titanium:Sapphire CW Laser–Spectra Physics®* model based on a $Ti:Al_2O_3$ crystal. The wavelength can be continuously tuned between 720 nm and 860 nm. This *cw* laser is pumped by a *Millennia Prime Spectra Physics®* laser, whose wavelength is 532 nm. This pumping laser contains a $Nd:YVO_4$ laser crystal and a LBO frequency-doubling crystal), which is pumped by a diode laser. The output power of the *cw* laser varies from 200 mW to 1 W (maximum at $\sim$ 800 nm) under a 5 W-pumping from the *Millennia Prime* laser (the maximum output power for this laser is 10 W).

The pulsed laser is a *Tsunami Spectra Physics®* model, the laser wavelength can be tuned from 700 nm to 1μm (in this case using adapted optics in the laser). The $Ti:Al_2O_3$ crystal of the pulsed laser is pumped by a *cw* laser (*Millennia Pro Spectra Physics®*, similar to that used for the *Millennia Prime* model, the only difference is the maximum output power, 15 W in this case). The time-integrated output pump power of the pulsed laser ranges between 1 and 2 W (maximum at $\sim$ 825 nm), under a 7 W-pumping from the *Millennia Pro* laser. The pulsed laser is mode-locked with the help of an acousto-optical modulator, and it was operated in the picosecond configuration, yielding pulses with a temporal width of $\sim$2 ps and a repetition rate of 82 MHz.

Under OPO excitation configuration, used in Chapters 5 and 6,[3] a good angular resolution is needed. In this case, the first lens after the sample is an achromatic, $\sim$6.4 cm-$\varnothing$ lens, its focal length is 4 cm and the numerical aperture is $NA = 0.6$. The excitation beam is directed towards the sample by an independent mirror. By positioning them at different distances from the optical axis (Δx) of the objective lens, the angle of incidence θ_{inc} of each beam can be selected ($\theta_{inc} = \arctan(\Delta x/f)$, where f is the focal distance of the objective lens), see an schematic description of this setup in Fig. 4.2.

Under non-resonant excitation configuration, we have used two different schemes: (i) excitation at the first high-energy Bragg mode of the MC (1.612 eV) (Chapters 8-10) and (ii) excitation at the bare exciton level ($\sim$1.545 eV) (Chapters 6, 7 and 11). Under non-resonant excitation configuration different lenses and objectives have been used in the experimental setups, depending on the purpose of each experiment. For the sake of clarity, details about the optical specifications of these lenses and objectives are detailed on each Chapter.

[3] In Chapter 6 a *pump+probe* excitation is used, the *pump* excites under OPO configuration, while the *probe* is tuned to the bare exciton level (non-resonant excitation configuration), see § 6.1 for further details.

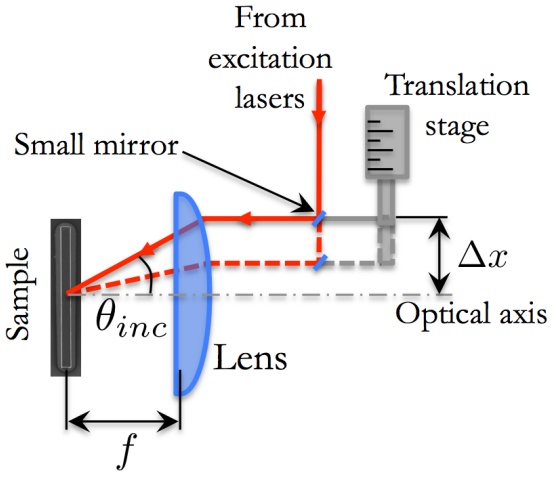

FIGURE 4.2: Scheme of the selective angular excitation in the OPO excitation regime. The OPO pump excitation beam is directed towards the sample by an independent (small) mirror, mounted in a translation stage that moves perpendicularly to the optical axis (dot dashed line). By positioning the mirror at different distances from the optical axis (Δx) of the lens, the angle of incidence θ_{inc} of the beam can be selected, $\theta_{inc} = \arctan(\Delta x/f)$, where f is the focal distance of the objective lens.

The lens collecting the light emitted by the sample provides a spatial resolution given by $R = \lambda/(2NA)$, depending on the NA of the lens: ~ 0.5 μm in the case of the collecting lens ($\sim$6.4 cm-$\varnothing$ and 4 cm-focal length) used in Chapters 5-7 and ~ 1 μm in the rest of the thesis (Objective Lens Nikon 10$\times$ $f = 20$ mm, $NA = 0.30$).

4.2 Detection

The simplest way of detecting the polariton PL is to place a Charge-coupled device (CCD) camera at the focus of the imaging lens. We used a *Hitachi® KP-M2RN* CCD. In this case, the emission intensity is time-averaged (acquisition time-scales are usually on the millisecond or second range) and all the wavelengths are superimposed.

Alternatively, the PL intensity can be resolved into its energy components by using a spectrometer, whose working principle goes as follows: a 1D slice of the image on the focus of the imaging lens passes through the spectrometer's entrance slit and reaches a diffraction grating. Here each energy component is reflected at a different angle in the perpendicular direction to the entrance slit. After propagating over tens of centimeters, the PL is collected by a CCD, recording an image that contains the energy-dependent map intensity for each point of the image that passes through the slit. We use a 0.50 m imaging triple-grating spectrometer (*Acton SpectraPro 2500i* with a 1200 lines/mm diffraction grating) with a high resolution CCD (*Acton Pixis 1024* with 1024×1024 pixels).

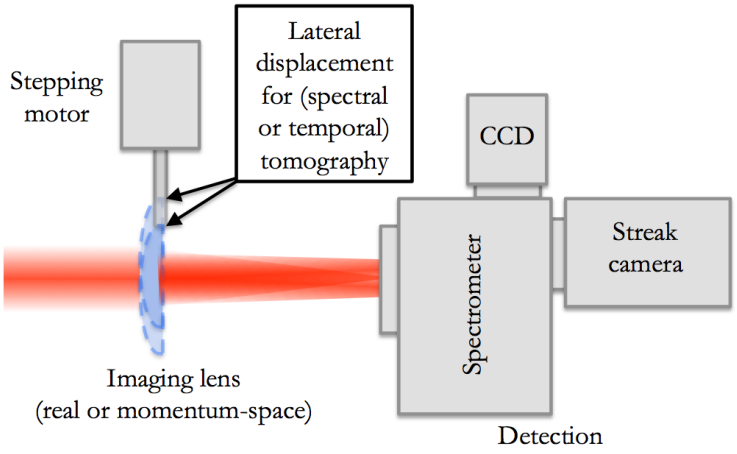

FIGURE 4.3: Apparatus used in the spectral and temporal tomography detection. A stepping motor moves laterally the imaging lens (forming the real or momentum-space PL distribution), sweeping the total PL distribution over the slit entrance and focusing the PL onto the entrance slit of the spectrometer. The PL is dispersed by the grating of the spectrometer and its spectrum is recorded by either a CCD camera (time-integrated measurement) or a streak-camera (time-resolved measurement).

More complete information about the sample emission and its energy dependence is provided by tomographically reconstructing its 2D image onto the spectrometer slit (§ 4.3.1 describes this method for spectral analysis). This is done by sequentially translating the imaging lens perpendicularly to the optical axis, which moves the image across the entrance slit of the spectrometer, thus recording spectra for each line scan of the image — see a scheme of the apparatus in Fig. 4.3. By acquiring a number of these 1D spatial slices vs energy, the energy dependence of each point of the 2D image is composed. The step-motors, as well as the image acquisition sequence, are controlled by a home-made software programmed with *LabView®*.

4.2.1 Streak-camera

The streak camera is a device used to measure ultra-fast time-dynamics of the light emitted by the samples. We use a *Hamamatsu® C5680* streak camera with a *M5675 synchroscan sweep* unit and a *C5680 blanking* unit, coupled to a *Hamamatsu® C4742-95 digital camera*. In order to measure the polariton dynamics presented in this thesis, the streak-camera is coupled to one of the exit windows of the spectrometer — see Fig. 4.3. In Fig. 4.4(a) we depict an scheme of the temporal PL signal detection and its spectral analysis through the spectrometer and the streak-camera. The emitted polariton PL is composed by a "droplet" of photons, whose physical information about polaritons is: their real space distribution (x, y) (or equivalently, momentum space distribution (k_x, k_y), if the angular distribution is imaged onto the spectrometer's slit), the time dynamics and the energy of this distribution.

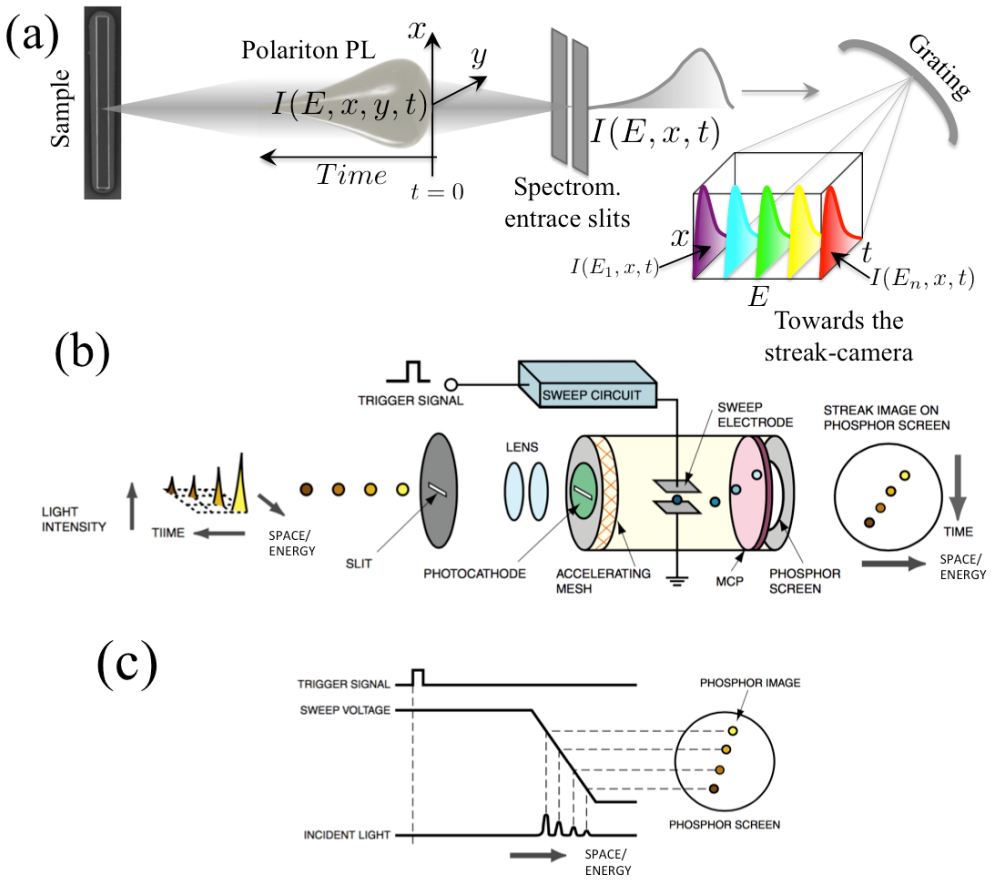

FIGURE 4.4: (a) Schematic representation of the temporal PL signal detection and spectral analysis through the spectrometer and the streak-camera. (b) Operating principle of a Streak Tube and (c) operation timing of the streak-camera where a trigger signal (synchronized to the pulsed laser frequency) indicates the start of the sweeping voltage which deflects electrons on the phosphor screen, yielding the pico-second time-resolution.[4]

We have to analyze this (initially) mixed information in order to provide a comprehensive interpretation of the polariton spectrum and dynamics. Firstly, the "droplet's" perpendicular direction to the spectrometer's slit is filtered out (y axis, or k_y axis) leaving a single cross-section of the droplet at a given position of y_0, whose information becomes $I(E,x,t)$ (x is the parallel axis to the slits orientation). This PL cross-section is spectrally analyzed by the spectrometer's grating yielding a continuum of cross-sections with individual energy values, this constitutes an analyzable set of information where one can retrieve the intensity of polaritons as function of x, energy and time (see in Fig. 4.4(a) the 4D matrix represented as a box with x, E and t axis).

If the streak-camera is oriented in such a way that its entrance slit is oriented in the same direction as the spectrometer one, we will measure $I(x,t)$ at a given value of energy (that we can adjust by changing the grating rotation). This configuration has been used in Chapters 6, 7, 9-11, providing a temporal and spectral resolution of $\sim$ 15 ps and 0.4 meV, respectively. The

[4]Adapted from Interactive Java Tutorials–Streak Lifetime Imaging (FLIM) Camera.

tomography technique described before (see Fig. 4.3) would provide the additional reconstruction of the y (k_y) axis and therefore the total real (momentum) space distribution. If the grating is oriented in such a way that we image the 0^{th} diffraction order in the streak camera (Chapter 5) we achieve a better time-resolution ($\sim$ 2 ps). If the streak-camera is oriented perpendicularly to entrance slit of the spectrometer (by carefully rotating 90° the streak camera), we will measure $I(E,t)$ at a given position of the x axis (that we can adjust by changing the grating rotation).

The principles of the streak camera operation are depicted in Fig. 4.4(b). The PL, whose dynamics is to be measured, passes through a slit and is focused by a lens into a photocathode of the streak tube, where photons are converted into electrons. The latter are accelerated by an accelerating mesh passing then between a pair of sweep electrodes, where a high-speed sweeping voltage is applied, making electrons swept in the direction from top to bottom). The electrons are deflected at different times, and at slightly different angles in the perpendicular direction [Fig. 4.4(c)], and are then conducted to a micro-channel plate (MCP). As the electrons pass the MCP, they are multiplied several thousands of times, after which they impact against a phosphor screen, where they are converted back into photons.

On the phosphor screen, the earliest electron to arrive is placed in the uppermost position, with the other electrons being arranged in sequential order from top to bottom. In other words, the vertical direction on the phosphor screen serves as the time axis. Also, the brightness of the various phosphor images is proportional to the intensity of the respective incident light. The position in the horizontal direction of the phosphor image corresponds to the horizontal location of the incident light. Finally, the light emitted by the phosphor screen is recorded by a CCD (not shown). In the CCD the vertical direction means time while the horizontal direction has the same meaning as the horizontal dimension of the light arriving at the photocathode, which can be wavelength or spatial dimension (real space or momentum space).

The emission intensity of a polariton condensate is very weak to be time-resolved with picosecond resolution in a single-shot measurement, even a high excitation powers. This yields a very low signal/noise ratio, which can be improved by making multiple-shot measurements. In this case, each laser pulse excites the polariton condensate under the same conditions, with the follow-up dynamics being recorded multiples times, one per pulse, by the streak camera, and averaged over the many realizations. To perform such a measurement, the sweeping voltage that deviates the photoelectrons is synchronized with the same repetition rate as that of the excitation laser via a fast photodiode. The acquisitions times employed in this thesis are on the order of 1 second, meaning that a single image is a average over 82 million experiments (82 MHz being the laser repetition rate). The sweeping voltage has a sinusoidal shape, but only the linear part of the sinusoidal is employed. The largest time window of the streak camera has a size of 2100 ps with a resolution of about 30 ps. However the resolution can be improved below 10 ps by operating the camera in regimes with smaller time windows.

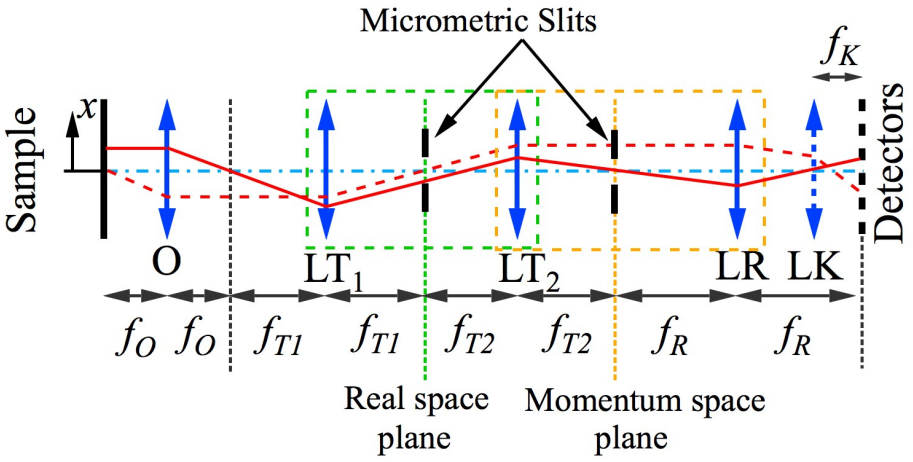

FIGURE 4.5: Scheme of the real and momentum-space filtering setup: The lenses "LR" and "LK" image the Fourier plane of the microscope objective "O", which collects the PL emitted from the sample (x is a perpendicular axis to the optical axis of the setup, dot-dashed blue line). If lens "LK" is removed, lens "LR" images the real space distribution. f_O, f_R, and f_K are the focal lengths of the objective, "LR," and "LK" lenses, respectively. A slit is placed in the common focal plane of two lenses "LT_1" and "LT_2" (focal lengths $f_{T1}$and f_{T2}, respectively), providing the filtering in the real space plane (all the different lenses' Fourier planes are marked with a dashed vertical line). A second slit is placed in the common optical plane between "LT_2" and "LR" in order to perform filtering in the momentum space place. A schematic full (dashed) red trace depicts the path of a light beam emitted at $x > 0$ and $\mathbf{k} = 0$ ($x = 0$ and $\mathbf{k} < 0$) when collecting the real- (momentum-) space PL distribution. [5]

4.2.2 Real and momentum-space filtering analysis

In this section we describe the standard optical setup used for detection in the experiments compiled in Chapters 7 and 10. Real and/or momentum space filtering has been used to selectively analyze the local polariton distribution, this detection technique renders rich information about the local dynamics of polaritons and also the local properties of certain regions of the sample selected at will (see, for example, § 7.2.0.1 and Appendices C and D).

Figure 4.5 depicts the disposition of five lenses in order to image the polariton distribution in real (momentum) space in a plane, green (orange) dashed line, where we introduce a slit that placed between "LT_1" and "LT_2" ("LT_2" and "LR") lenses, see green (orange), dashed box. The magnification factor in the mentioned, real (momentum) space plane is $-\frac{f_{T1}}{f_O}$ ($-\frac{f_{T2}f_O}{f_{T1}}$). This set of lenses produces a final real (momentum) space image of the PL in the detectors with a magnification factor given by $\frac{f_R f_{T1}}{f_O f_{T2}}$ ($\frac{f_O f_K f_{T2}}{f_R f_{T1}}$). The dashed line depicting lens "LK" means that this lens should be used only in the case that momentum distribution is imaged in the detector plane.

[5] Follow the link Ray Diagrams for Microscope and Telescope, by V. Holovatsky at Wolfram Demonstration Project, in order to gain insight in the ray diagrams of optical system described in Fig. 4.5.

4.3 Methods

4.3.1 Spectral tomography techniques

One common technique used during this thesis was the spectral tomography. This is done by decomposing a real (momentum) space image into several slices by the entrance slit of the monochromator oriented along x. Laterally shifting along y the imaging lens with respect to its optical axis, induces a displacement of the luminescence real (momentum) space image with respect to the entrance slit of the monochromator.

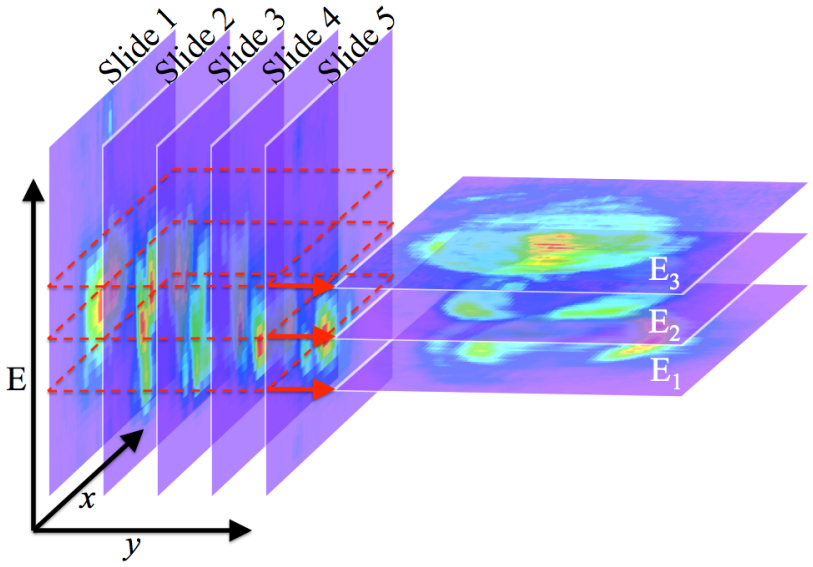

FIGURE 4.6: Illustration of spectral tomographic technique here done in real space. Each of the slices on the left side corresponds to a specific y and have energy versus x information. After the decomposition, access to the real space image for any energy is possible as shown with the three reconstructed layers at E_1-E_3.

Figure 4.6 presents an example to obtain slices at different energies of the PL in real space of a polariton condensate. If for each displacement an acquisition is made, the real (or momentum) space is effectively "cut" in slices. At the output of the monochromator, each slice is a 2D image with real space (momentum space) information on one axis and energy on the other axis. The number of slices used in a given experiment varied depending on the size of real (or momentum) space PL distribution at the plane of the spectrometer slit entrance. This method can also be used to spectrally resolve an interference pattern.

4.3.2 Temporal tomography techniques

The same technique can be used redirecting the PL from the spectrometer to the streak camera. A streak-camera image contains the time-dynamics of a 1D slice of the image created at the focus of

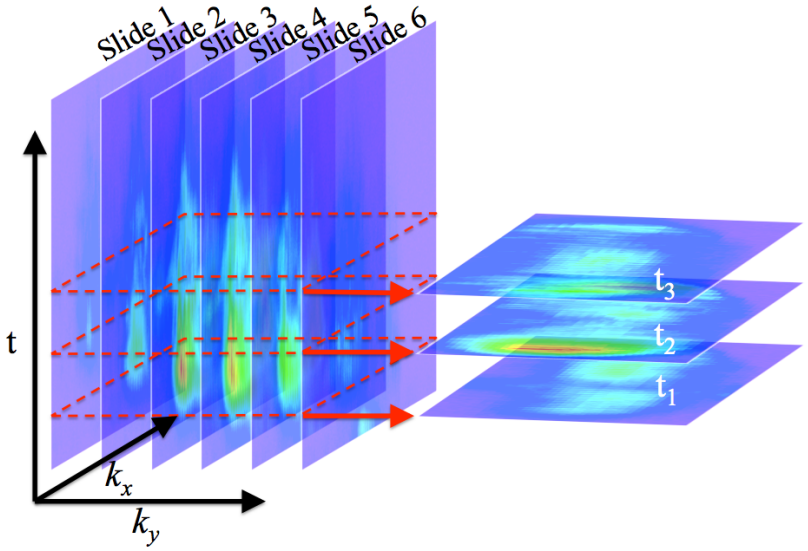

FIGURE 4.7: Temporal tomographic technique. On the left side an illustration of the slicing of a momentum space image is shown where each of the slices is an image taken at the output of the streak camera (k_x momentum space vs. time). Different slices correspond to subsequent k_y momentum space positions. After the decomposition in slices, access to the full momentum space image at any time t, is accessible by looking at the layer that corresponds to the desired time. Here (on the right side) three layers at three different times t_1-t_3 are shown.

the imaging lens. The dynamics of the full image can be measured using a tomographic procedure similar to the one described to measure the energy dependence of the PL: by progressively moving the imaging lens, the time-dynamics is measured for each 1D slice of the 2D image.

To perform such a measurement, we take the time dynamics sequence of about 100 slices of the condensate, each image being integrated for about a second. Figure 4.7 presents an example to obtain snapshots at different times of the emission in momentum space of a polariton condensate. The full measurement lasts some minutes, during which care should be taken that the lasers and the sample are extremely stable in such a way that all the steps correspond to the same excitation conditions. The full experiment is stored in a 3D matrix whose time-slices correspond to the condensate image at a specific time. This allows for tomographic reconstructions of real space, momentum space and interferometric images with full temporal resolution.

4.3.3 Interferometry

The milestone for the demonstration of condensation is the appearance of long range spatial coherence (§ 2.3). This section describes the interferometry methods that were used in this thesis for the demonstration of the coherence of polariton condensates.

In general, the interference between two fields, $\psi_1(\mathbf{r}) = A_1 e^{i\phi_1}(\mathbf{r})$ and $\psi_2(\mathbf{r}) = A_2 e^{i\phi_2}(\mathbf{r})$, is given by:

$$I_{12} = \langle|\psi_1 + \psi_2|\rangle = \left\langle|\psi_1|^2 + |\psi_2|^2 + \psi_1^* \cdot \psi_2 + \psi_2^* \cdot \psi_1\right\rangle \tag{4.1}$$

$$I_{12}(\mathbf{r}) = \left\langle A_1(\mathbf{r})^2\right\rangle + \left\langle A_2(\mathbf{r})^2\right\rangle + \left(g^{(1)} + g^{(1)*}\right) \cdot \sqrt{\langle A_1(\mathbf{r})^2\rangle + \langle A_2(\mathbf{r})^2\rangle} \tag{4.2}$$

Where $\langle\rangle$ denotes statistical average in Eqs. 4.1 and 4.2. For non-stationary states, such as a decaying polariton condensate created by a pulsed laser, the ensemble is made up by many pulses. When one deals with stationary states, where the statistical properties do not change with time, such as those created in *cw* experiments, one can replace the ensemble average with a time average.

$g^{(1)}$ is the degree of coherence between ψ_1 and ψ_2, given by [248]:

$$g^{(1)}(\psi_1, \psi_2) = \frac{\langle\psi_1^* \cdot \psi_2\rangle}{\sqrt{\langle|\psi_1|^2\rangle + \langle|\psi_2|^2\rangle}} \tag{4.3}$$

$$g^{(1)}(\psi_1, \psi_2)(\mathbf{r}) = \frac{\left\langle A_1(\mathbf{r}) \cdot A_2(\mathbf{r}) \cdot e^{i(\phi_2(\mathbf{r}) - \phi_1(\mathbf{r}))}\right\rangle}{\sqrt{\langle A_1(\mathbf{r})^2\rangle + \langle A_2(\mathbf{r})^2\rangle}} \tag{4.4}$$

The argument of $g^{(1)}$ gives the averaged phase difference between the two fields and its modulus the predictability of such a phase difference, known as coherence. $g^{(1)}$ is a complex number in general satisfying the following properties:

- $g^{(1)}(\psi_1, \psi_1) = 1$ (autocorrelation)
- $g^{(1)}(\psi_1, \psi_2)^* = g^{(1)}(\psi_2, \psi_1)$

The first order correlation function is very important when fully describing a quantum state as it is related to the density matrix, $\rho = |\psi\rangle\langle\psi|$, since:

$$\rho(\mathbf{r}, \mathbf{r}') = \langle\mathbf{r}|\rho|\mathbf{r}'\rangle = \langle\mathbf{r}|\psi\rangle\langle\psi|\mathbf{r}'\rangle = \psi(\mathbf{r})\psi^*(\mathbf{r}') = g^{(1)}(\mathbf{r}, \mathbf{r}')|\psi(\mathbf{r})||\psi(\mathbf{r}')| \tag{4.5}$$

4.3.3.1 Interferometers

Let $\psi_1 = A_1 e^{i\phi_1}$ be the wavefunction of a polariton condensate. Its intensity, $|A_1|^2$, is directly recorded by a CCD camera. Its phase, ϕ_1, and coherence properties are recorded by placing an interferometer on the region between the objective lens and the detectors (Fig. 4.1) and recording interference maps. The way interferences are obtained, given by the interferometer geometry, depends on the physical magnitudes to be determined.

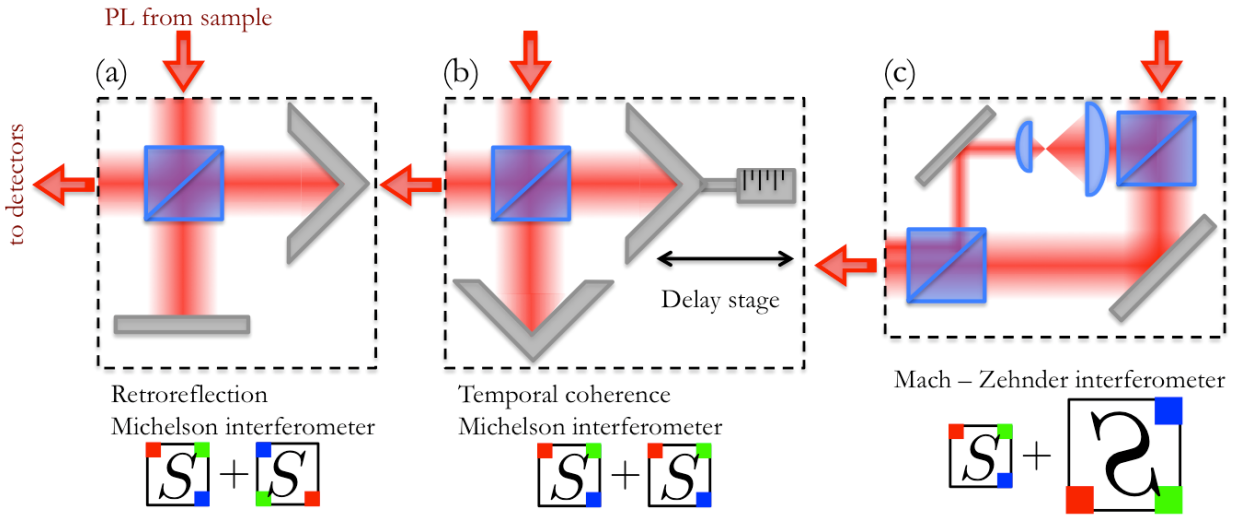

FIGURE 4.8: Interferometer geometries used to split the sample PL into two separate beams that are made to interfere again on the spectrometer slit entrance, providing fringes for interferometry. The bottom boxed-S images schematically represent, in each panel, the two images originating from each interferometer arm that are made to interfere. In (a) each spatial point is interfered with another one on the opposite side of the condensate, whereas in (b) each spatial point is interfered with itself at a different time delay. In the Mach-Zehnder interferometer (c), one of the arms contains two lenses that decreases the far-field propagation diameter and so magnifies the emission image, making the condensate emission to be interfered with an small expanded part of itself.

When measuring spatial coherence it is convenient to use a Michelson interferometer in the so-called retroreflected configuration, in which one of the interferometer arms contains a normal mirror whereas the other arm contains a retroreflector [Fig. 4.8(a)]. In this way, at the image plane on the entrance slit of the spectrometer, each point of the condensate is interfered with another one at the opposite side with respect to the condensate centre. The visibility of the interference fringes is related to $g^{(1)}\left(\psi_1(\mathbf{r}), \psi_1^*(-\mathbf{r})\right)$ [21]. Such a measurement also provides a phase-map [169], given by the difference between two phases in opposite sides of the condensate, so it clearly does not represent the wave-function phase.

When measuring time coherence, the most appropriate configuration is a Michelson interferometer with one retroreflector in each arm, with one of them mounted on a delay stage [Fig. 4.8(b)]. Under this geometry, each condensate point is interfered with itself at a time delay that can be controlled by the path difference between both arms. Again, the fringe visibility is related to the coherence $g^{(1)}(\mathbf{r}, \mathbf{r}, \Delta t)$, which can be extracted after performing Fourier transform analysis — see § 4.3.3.2.

In order to correctly extract the condensate phase, $\phi_1(\mathbf{r})$, a constant-phase field $\psi_2(\mathbf{r}) = A_2 e^{i\phi_2}$ is needed as a reference. When the condensate is created resonantly by a pump laser, the laser itself can be used as a reference [159, 173–175] — note that the polariton emission and the reference wave should have the same energy in order to see interferences in a time-averaged measurement. An alternative is to use an expanded small part of the condensate which can be considered as a constant

phase reference. In this technique, introduced in Refs. [28, 50], the condensate emission is split into two arms of a Mach-Zehnder interferometer, one of them containing two lenses that magnify the emission [Fig. 4.8(c)]. A small portion of the expanded image, considered as a constant phase reference, is interfered with the sample emission. After Fourier transform analysis (§ 4.3.3.2), a phase map is extracted which contains the relative phase between both interfering fields. Since the expanded image is assumed to have a constant phase, the extracted phase map actually contains the condensate phase spatial profile.

4.3.3.2 Off-axis digital holography

Interferometric measurements have proved an extremely powerful tool for the evaluation of the degree of coherence in the emitted luminescence and consequently the evaluation of the condensate fraction. It is actually more powerful than that. The mere interference pattern also contains information on the phase of the interfering beams and can consequently provide access to the condensate wavefunction phase.

A widely used method for the extraction of the phase of an interference pattern is the so called (off axis) digital holography, widely used for optical metrology purposes [249]. The evaluation of the condensate phase is described in this section using the Fourier transform phase evaluation method [250].

Here a well known wavefunction, a single-charged vortex [Eq. 4.6(a)], will be used and it will be interfered with an oblique plane wave [Eq. 4.6(b)] for reasons of simplicity.

$$\psi_1(x,y) = A_1(x,y)\, e^{i\phi_1(x,y)} \tag{4.6a}$$

$$\psi_2(x,y) = A_2(x,y)\, e^{i(k_x x + k_y y)} \tag{4.6b}$$

The amplitude $A_1(x,y)$ of the vortex field [with a FWHM$\sim$ 8 μm, see 4.9(a)] is defined by the Laguerre-Gauss (LG) profile when the charge of the vortex is +1 [the phase increases in the clockwise direction, increasing by 2π in a complete turn, see Fig. 4.9(b)]. The amplitude $A_2(x,y)$ of the plain wave is represented with a gaussian profile, with a FWHM$\sim$ 20 μm [Fig. 4.9(c)], twice bigger than the vortex size [depicting a similar situation of that represented in the Mach-Zenhder interferometer in Fig. 4.8(c)]. We note that the momentum of the plain wave is $(k_x, k_y) = (-4, +4)$ $\mu\mathrm{m}^{-1}$, this angle determines the phase field of the plain wave, Fig. 4.9(d), where moving a distance of 2π μm either along the x or y axis implies a total phase change of $4 \times 2\pi$.

The resulting interference pattern [Fig. 4.9(e)], formed by the interference of the fields described in Eqs. 4.6(a) and 4.6(b), is described in a similar way to that shown in Eq. 4.2:

$$I(x,y) = a(x,y) + c(x,y) + c^{\star}(x,y) \tag{4.7}$$

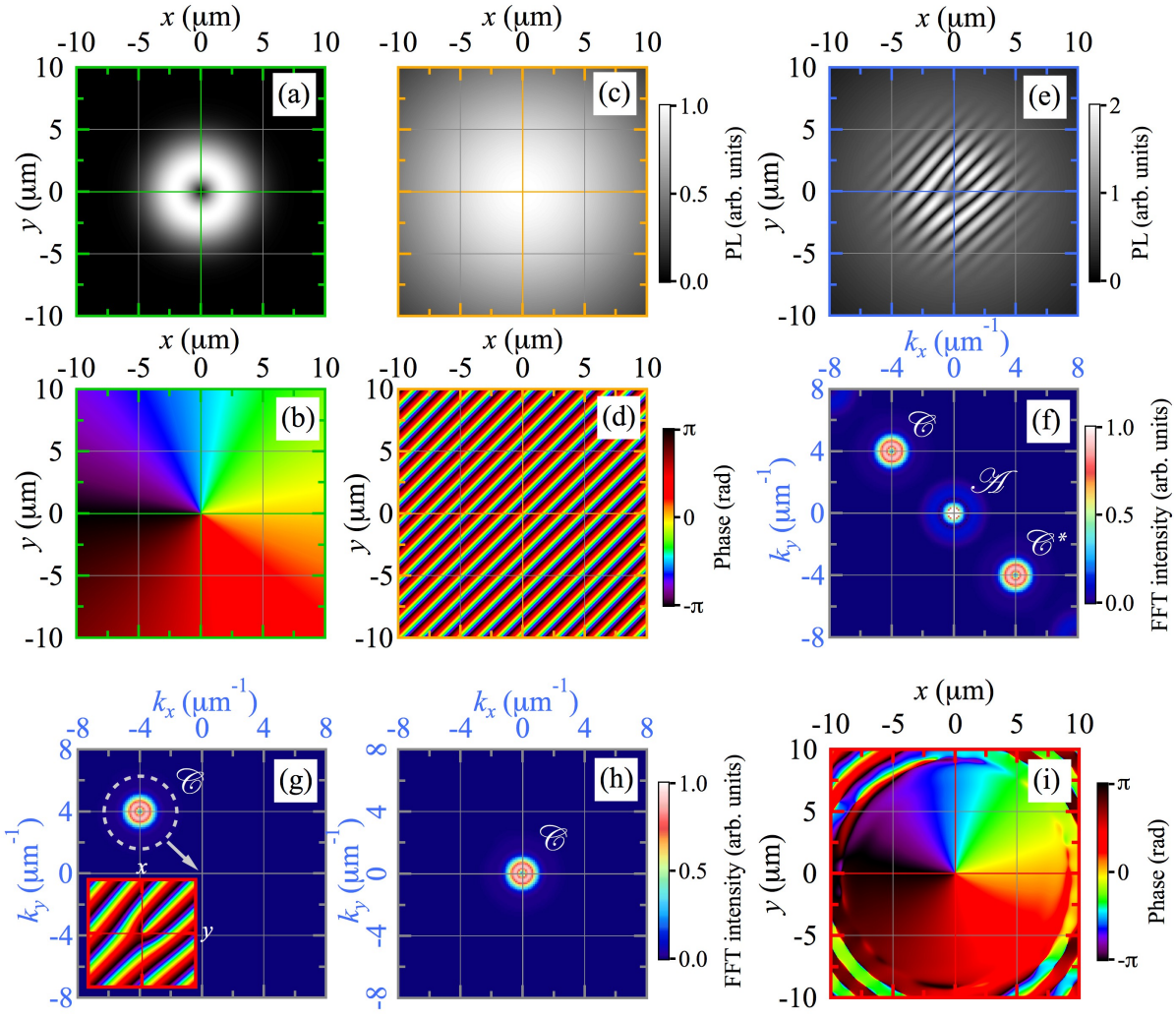

FIGURE 4.9: Phase retrieval of light using the off-axis digital holography technique. (a)/(b) [(c)/(d)] Distribution in real space of the amplitude/phase of a vortex field [plain wave]. (e) Resulting interference pattern of the vortex and the plain wave, (f) corresponding absolute value of the FFT of previous panel (e). (g) Filtering out the terms $\mathscr{C}^*$ and $\mathscr{A}$ of the FFT shown in panel (f). The left-bottom inset depicts the corresponding iFFT retrieved phase-map of panel (g) in a zoomed real space region of $5{\times}5$ μm^2 around the origin $(x, y) = (0, 0)$. (h) Shifting of $\mathscr{C}$ term to Fourier origin. (i) Distribution of the retrieved vortex-phase in real space after calculating the iFFT of the complex field, $\mathscr{C}$, shown in panel (h). Note the similarity between panels (b) and (i), apart from those far regions from the origin where the intensity of the interferogram is very low and the phase retrieval is hindered by the noise introduced by the filtering process in Fourier space.

The right hand side terms are:

$$a(x,y) = A_1(x,y)^2 + A_2(x,y)^2 \tag{4.8a}$$

$$c(x,y) = A_1(x,y)\,A_2(x,y)\,e^{i[k_x x + k_y y - \phi_1(x,y)]} \tag{4.8b}$$

$$c^\star(x,y) = A_1(x,y)\,A_2(x,y)\,e^{-i[k_x x + k_y y - \phi_1(x,y)]} \tag{4.8c}$$

The discreet 2D Fourier transform (FFT) of the interference pattern (using the FFT algorithm) will give in momentum space an intensity pattern, $\mathscr{I}(k_x, k_y)$, of the form [Fig. 4.9(f)]:

$$\mathscr{I}(k_x,k_y) = \mathscr{A}(k_x,k_y) + \mathscr{C}(k_x,k_y) + \mathscr{C}^\star(k_x,k_y) \tag{4.9}$$

Since the intensity profile in real space is real-valued, in the frequency space it will be Hermitian obeying $\mathscr{C}(k_x,k_y) = \mathscr{C}^\star(-k_x,-k_y)$.

The term $\mathscr{A}$ is centered around the frequency $(0,0)$ and its form is related to the terms A_1 and A_2. $\mathscr{C}$ and $\mathscr{C}^\star$ are centered around the frequencies $(-4,+4)$ and $(+4,-4)$ $\mu\mathrm{m}^{-1}$, respectively. By filtering the components $\mathscr{A}$ and $\mathscr{C}^\star$ in the momentum space domain, we obtain a pattern in frequency space that is not Hermitian, Fig. 4.9(g). The inverse FFT (iFFT) of field $\mathscr{C}$ at $(-4,+4)$ $\mu\mathrm{m}^{-1}$ renders a phase field that adds the vortex singularity and constant oscillation (given by the position of $\mathscr{C}$ in momentum space).

In order to obtain the corrected, vortex phase-field, one has to shift the complete Fourier space, so that the term $\mathscr{C}$ is located in the origin $(k_x,k_y) = (0,0)$ [Fig. 4.9(h)]. We perform its iFFT, retrieving a complex field in real space, whose phase contains the original vortex phase-field, see Fig. 4.9(i). This figure has to be compared with the initial phase field previously shown in Fig. 4.9(b). Divergence with respect to the initial phase can be found only for intensities that are more that 3 orders of magnitude lower that the maximum intensity of the interferograms. The amplitude of the vortex (absolute value of the retrieved complex field, not shown) contains the real space distribution previously depicted in Fig. 4.9(a).

If the aforementioned shift of the term $\mathscr{C}$ would have not been performed, the iFFT would have yielded a non-corrected phase map where a constant phase ramp would have been added to the phase dislocation, impeding the correct retrieval of the initial phase map. To visualize this artifact, such effect is observed in the red-framed inset of Fig. 4.9(g), which shows a zoomed real space region of 5×5 $\mu\mathrm{m}^2$ around the origin $(x,y) = (0,0)$, when the shift of $\mathscr{C}$ has not been done.

Part III

Some fundamental phenomena of polaritons physics

Introduction: Some fundamental phenomena of polaritons physics

Bose-Einstein condensation of quasi-particles in solid-state systems has been observed in excitons in quantum Hall bilayers [158], exciton-polaritons in semiconductor MCs [21], gases of magnons [251, 252], cavity photons [128], indirect excitons [124] and dark excitons [120, 253]. Exciton-polaritons, mixed light-matter quasi-particles behaving as bosons, can form condensates which exhibit fundamental properties of quantum gases and also new fascinating phenomena related to their out-of-equilibrium character [254]. The photonic component of polaritons is responsible for their light mass, which makes condensation possible up to room temperature [23], and for their easy creation, manipulation and detection by using "simple" optical-microscopy setups. On the other hand, their excitonic component yields strong Coulomb repulsive interactions that make them promising candidates for future non-linear optical technologies.

The peculiar quantum fluid properties of polariton condensates are under intense research nowadays. Recent findings include: robust propagation of coherent polariton bullets [26] and elucidation of the validity of the Landau criterion for frictionless flow in the presence of weak structural defects [27], persistent quantized superfluid rotation [28, 255], and solitary waves resulting from compensation between dispersion and particle interaction [38, 174, 175, 256]. Moreover, the intrinsic out-of-equilibrium character of polariton condensates has motivated recent theoretical studies on how to describe properly the energy flow from an optically-injected hot exciton reservoir to the coherent polariton modes [125, 213].

In this Part, we discuss some of the many different fundamental phenomena that can be investigated with polaritons (superfluidity, quantized rotation, soliton physics, spin-phenomena, etc.). We illustrate their potential as an experimental platform to realize, in a relatively "easy" way as compared to atomic gases, complex experiments of BEC phenomena. The topic that we address in this Part are the followings:

Topological defects in a OPO polariton condensate

Quantum vortices (Vs) are topological defects occurring in macroscopically coherent systems. Their existence was first predicted in superfluids [148, 149], and later in coherent waves [150]. Nowadays, quantum Vs have been the subject of extensive research across several areas of physics and have been observed in type-II superconductors, ^{4}He, ultracold atomic gases, nonlinear optics media (for a review see, *e.g.*, [151, 152, 257–260]) and very recently MC polaritons [28, 159, 169–171, 173, 194, 209]. The phase of a quantized V winds around its core from 0 to $2\pi m$ (with m integer), implying that the V carries a quantized angular momentum, $\hbar m$. In contrast with the classical counterpart, quantum Vs with the same m are all identical, with a size (or healing length) determined by the system nonlinear properties.

Recently, the study of quantized Vs imprinted in polariton condensates using pulsed laser fields has attracted noticeable interest both experimentally [28] and theoretically [255, 261–263], providing a diagnostics for superfluid properties of such a non-equilibrium system. In particular, resonantly pumped polaritons in the OPO regime [54, 113] have been recently shown to exhibit a new form of nonequilibrium superfluidity [26, 28]. In Chapter 5, polaritons are continuously injected into the pump state, undergoing coherent stimulated scattering into the signal and idler states. An additional pulsed probe can initiate a traveling decaying gain, which evolves freely from the probe constraints. By using a pulsed LG beam, vorticity has been shown to persist not only in absence of the rotating drive, but also longer than the gain induced by the probe, and therefore to be transferred to the OPO signal, demonstrating metastability of quantum Vs and persistence of currents [28, 255]. However, if the extension of the probe carrying a V/AV with charge $m = \pm 1$ is smaller than the size of the V-free OPO signal, continuity of the polariton wave function requires that necessarily an AV/V with charge $m = \mp 1$ has to form at the edge of the probe. In Chapter 5, we demonstrate that "unintended" AVs do appear in the signal at the edge of the imprinting V probe and explain, both theoretically and via experiments, the origin of the deterministic behavior of the AV onset and dynamics.

Ignition and formation dynamics of a polariton condensate on a semiconductor microcavity pillar

Exciton-polaritons in semiconductor MCs, when injected with a *pump* laser close to the inflection point of the LPB dispersion, undergo a nonlinear process above a pump power threshold. Carrier-carrier interactions self-stimulate a coherent scattering from the *pump* state into *signal* and *idler* polariton states, whose frequency and in-plane momentum fulfill phase-matching conditions. The *signal* state population, generated by this OPO process [29, 52–54, 113], reaches occupation values above one, exhibiting a new form of non-equilibrium superfluid behavior [26], metastability of quantum vortices [194, 264] and persistence of currents [28, 49, 51].

Lateral etching of planar MCs has been successfully exploited for the creation of a new, large variety of geometries: the resulting discretization of the energy spectrum opens an interesting scenario of different OPO phase-matching conditions in one- (1D) and zero-dimensional (0D) MCs. In the former case, the 1D discretization of the LPB in several energy sub-bands yields the opportunity to obtain exotic intra- and inter-branch OPO processes [243, 265–267]. Furthermore, interesting studies of the second order coherence of both signal and idler states have been performed recently [268]. In the latter case (0D OPO polaritons), although the most common excitation scheme for micro pillars is non-resonant excitation [269–273], different groups have reported the possibility to induce a parametric oscillation between discrete energy states: from the initial injected energy mode to two neighboring, signal and idler states [274–276].

In Chapter 6, we study a 40 μm-$\varnothing$ pillar MC, which is sufficiently large to neglect 0D confinement effects, but still with a bounded spatial extension where polaritons cannot propagate large

distances. We excite the sample using a new *pump+probe* excitation scheme, that differs from common resonant excitation [29, 52–54]. We ignite a long lived OPO polariton signal and observe a transient behavior, characterized by a collective oscillation of the condensed OPO polaritons in the pillar. Thereafter, they reach a quasi-steady state displaying a ring-like emission pattern, due to repulsive interaction with the exciton population in the center of the pillar [277]. The OPO signal is switched on with the pulsed *probe* at the exciton energy level, which blueshifts the LPB making the *cw pump* enter in resonance conditions in a OPO-process that lives for ∼1 ns. We study the full dynamics of the creation and decay of this confined OPO condensate in real and momentum-space (**k**-space). The interpretation of the experimental measurements of the spatial emission dynamics is supported by theoretical simulations using the 2D coupled GP equations for excitons and photons.

Quantum coherence in momentum space of light-matter condensates

Cold atoms and exciton-polaritons in semiconductor MCs are systems where their capability to constitute BECs has been demonstrated in recent years [14, 21, 278]. These BECs, due to their dual wave-particle nature, share many properties with classical waves as, for instance, interference phenomena [15, 279–281], which are crucial to gain insight into their undulatory character [248, 282]. One of the main differences between atomic and polariton condensates resides in the particles lifetime: the finite lifetime of polaritons, in contrast with the infinite one of atoms, can be regarded as a complication. But making virtue of necessity, a short lifetime also implies a significant advantage: polaritons have a mixed exciton-photon character [283], their lifetime being determined by the escape of their photonic component out of the cavity. These photons are easily measured either in real- (near field spectroscopy) or momentum-space (far field spectroscopy) [284], rendering full information about the polariton BECs wave-function and, in particular, about its coherence [21]. Our goal is to profit from these measurements in momentum space to experimentally investigate something far from accessible in atomic condensates: the interference in momentum space produced by the correlation between two components of a condensate, which are, and have always been, spatially separated. Understanding coherence is important for a large number of disciplines spanning from classic optics to quantum information science and optical signal processing [285, 286].

Pitaevskii and Stringari made a theoretical proposal to investigate experimentally these interference effects in momentum space via the measurement of their dynamic structure factor [287]. In related experiments, coherence between two spatially separated atomic BECs has been indirectly obtained using stimulated light scattering [288, 289]. In Chapter 7 we perform a direct measurement of this phenomenon in polariton BECs, which moving in a symmetrical potential landscape, acquire a common relative phase, obtaining a positive answer to Anderson's question: "*Do two components of a condensate, which have never seen each other, possess a definitive phase?*" [56, 111, 290, 291], which opens new perspectives in the field of multi-component condensates.

On the route of spin-based devices: spin textures within the macroscopic propagation of polaritons

Semiconductor MCs in the strong coupling regime are excellent candidates for designing novel "spinoptronic" devices due to their strong optical nonlinearities [292], polarization properties [246, 293, 294], and fast spin dynamics [295]. The control of polariton condensates propagation and their polarization[246] provide the necessary ingredients for future optical circuits. The first steps towards the fabrication of spin-based polariton condensate switches [33, 256, 296, 297], gates [298] and memories [34, 299] have been recently achieved. They fulfill the fundamental technological requirements for the operation with polarization-encoded signals: micrometric size, non-local action triggering and high-speeds (of the order of ~ 1 μm/ps due to the ballistic polariton propagation). New schemes for the realization of spinoptronics devices [300, 301] and "polariton neurons" in circuits, the building blocks of all-optical integrated logic circuits [31, 32, 302], have been recently proposed. 1D and quasi-1D patterned high-finesse MCs provide an ideal platform for all-optical manipulation [36], ballistic propagation and amplification [40] and gating of polariton condensates [43–47]. The waveguide nature of these structures induces the channeling of polariton propagation, while the discretization of energy levels results in a rich relaxation dynamics [62, 213].

In Chapter 8, we investigate optically the collective spin dynamics of polariton condensates moving along macroscopic distances in a quasi-1D MC ridge. We adopt the pseudospin formalism, described in Section 1.4.3, in order to describe the polarization state of exciton-polaritons [303].

All the results, obtained in the Laboratorio de Espectroscopia Ultrarrápida at the Universidad Autónoma de Madrid, under the supervision and leadership of Prof. Luis Viña, are collaborative achievements by the SemicUAM group. The experiments compiled in this Part have been performed by: Chapter 5 Dr. Guilherme Tosi and the author of this thesis (the holograms used to generate a V profile in the pulsed-laser beam have been produced by the group of Prof. Lorenzo Marrucci at the Università di Napoli), Chapter 6 by the author of this thesis and partially by Dr. Guilherme Tosi, Chapter 7 by the author of this thesis and, finally, Chapter 8 by Dr. Peter Eldridge, Dr. Tingge Gao and the author of this thesis.

The simulations and theory presented in this Part have been performed by: Chapter 5 by the theoretical members of the group, leaded by Prof. Carlos Tejedor, in special by Dr. Francesca M. Marchetti and Dr. Marzena H. Szymańska (from the University of Warwick), with help from Andrei Berceanu, Chapter 6 Dr. Dmitry Solnyshkov (Université Blaise Pascal), member of the group "*Theory of light-matter coupling in semiconductor nanostructures*", leaded by Prof. Guillaume Malpuech (CNRS Senior Researcher), in Chapter 7 the theoretical description of the experiments has been proposed by Prof. Carlos Tejedor, and finally, in Chapter 8 the simulations and theoretical model have been performed by Skender Morina and Dr. Tim Liew (Nanyang Technological University), members of the group "*Mesoscopic Optics and Transport*", leaded by Prof. Ivan A. Shelykh (University of Iceland).

Chapter 5

Onset and dynamics of vortex-antivortex pairs in polariton OPO superfluids

The vortex (V) state of an $m = 1$ Laguerre-Gauss (LG) probe beam can be transferred into a polariton condensate created under OPO excitation [28, 49, 50, 194]. In those cases, the extension of the probe is smaller than the size of the vortex-free OPO signal, an hence the single-valued condensate phase has to be continuously linked between the doughnut-shaped region where the V is imprinted and the vortex-free condensate region. Imposing a topological defect requires the branch-cut ($-\pi \rightarrow \pi$ phase jump), present in the new vortical state, to terminate where the phase is not imposed by the probe, *i.e.*, at the border between the probe and the OPO signal state. This is only possible if a V, with a charge opposite to the injected one, is created at the probe edge.

The Chapter is organized as follows. In § 5.1 we describe the simulations of the GP equation that predict the experiments on the V-AV onset and dynamics. In § 5.2 we present the experiments that demonstrate the creation of "unintended" polariton AVs/Vs after the resonant injection of a pulsed V/AV beam in a continuously pumped OPO signal. In § 5.2.1 we excite V-AV pairs with a resonant, gaussian probe that impinges on the sample at a certain angle. Finally, in § 5.3 we draw the conclusions of this study.

5.1 Numerical simulations

We start with numerical solutions to the two-component GP equation defined by Eqs. 2.50 and 2.51, that we include here again, respectively:

$$i\partial_t \begin{pmatrix} \psi_X \\ \psi_C \end{pmatrix} = \left[\mathcal{H}_{e-ph} + \begin{pmatrix} g_X|\psi_X|^2 & 0 \\ 0 & V_C(\mathbf{r}) \end{pmatrix} \begin{pmatrix} \psi_X \\ \psi_C \end{pmatrix} \right] + \begin{pmatrix} \psi_X \\ \psi_C \end{pmatrix} + \begin{pmatrix} 0 \\ P \end{pmatrix} \tag{5.1}$$

and

$$\mathcal{H}_{e-ph} = \begin{pmatrix} \omega_X - i\Gamma_X & \frac{\Omega_R}{2} \\ \frac{\Omega_R}{2} & \omega_C - i\Gamma_C - \frac{\nabla^2}{2m_C} \end{pmatrix} \tag{5.2}$$

The polariton field is described by a spinor containing its excitonic, ψ_X, and photonic, ψ_C, parts. g_X is the excitonic repulsive interaction coupling constant. P is the pumping field acting on the cavity mode. We consider a static photonic disorder potential $V_C(\mathbf{r})$ that varies spatially in a ~ 20 μm scale with 0.1 meV standard deviation. Note that the presence of the photonic disorder does not influences qualitatively our results. Its role is to break the $y \to -y$ symmetry left by the pump with $\mathbf{k}_p = (k_p, 0)$ and to change the supercurrents accordingly.

In order to reproduce properly multiple-shot experiments, simulations of the time-dynamics are averaged over a thousand times with random relative phase between pump and probe, what is done by considering the external pumping term as

$$P = F_p + F_{pb} e^{i\Phi_{\text{rdm}}} \tag{5.3}$$

where F_p represents the *cw* laser defined as,

$$F_p(\mathbf{r}, t) = f_p\left(|\mathbf{r} - \mathbf{r}_p|\right) e^{i(\mathbf{k}_p \cdot \mathbf{r} - \omega_p t)} \tag{5.4}$$

with frequency ω_p and incidence parallel momentum $\mathbf{k}_p$, and with the strength f_p having a top-hat profile with FWHM σ_p, centered at $\mathbf{r}_p$; and F_{pb} is the pulsed probe, defined as

$$F_{pb}(\mathbf{r}, t) = f_{pb}\left(|\mathbf{r} - \mathbf{r}_{pb}|\right) e^{-\frac{|\mathbf{r}-\mathbf{r}_{pb}|^2}{2\sigma_{pb}^2}} e^{im\varphi(\mathbf{r})} e^{-\frac{(t-t_{pb})^2}{2\sigma_t^2}} e^{i(\mathbf{k}_{pb} \cdot \mathbf{r} - \omega_{pb} t)} \tag{5.5}$$

centered at $\mathbf{r}_{pb}$ with a density increasing linearly at its centre and decaying gaussianly with width σ_{pb}. The probe, with frequency ω_{pb} and in-plane momentum $\mathbf{k}_{pb}$ (resonant with the OPO signal frequency and momentum), lasts σ_t and contains a V with charge $m = 1$. Finally, in Eq. 5.3 Φ_{rdm} is a random relative phase between pump and probe.

Figure 5.1(a) shows the density profile of the steady state signal before the arrival of the probe, together with the currents streamlines, obtained by taking the spatial gradient of the signal phase.

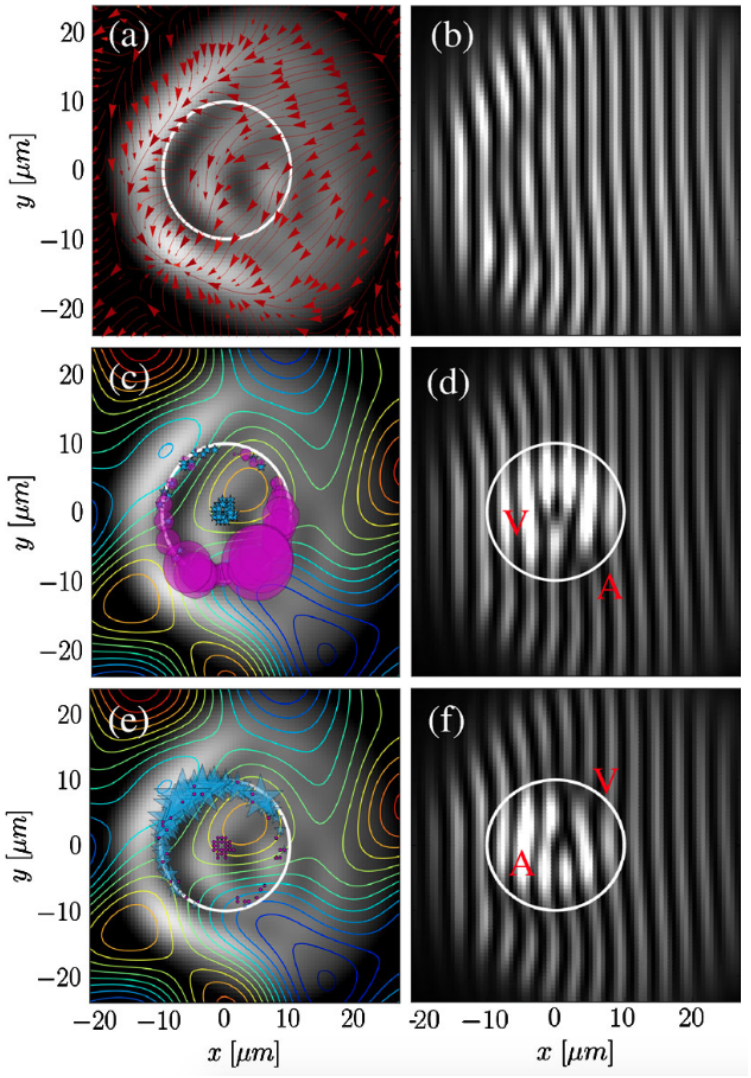

FIGURE 5.1: Simulated profile and supercurrents of the steady state OPO signal, before the arrival of the probe (a) and associated interference fringes (b). Location of (c) antivortices (AVs) (dots) and (e) Vs (stars) at the arrival ($t = 0$) of (c) a V (stars) or (e) an AV (dots) probe, for 1000 realizations of the random relative phase between pump and probe. The size of the dots in (c) [stars in (e)] is proportional to the number of times the AVs [Vs] appear in that location. Panel (d) [(f)] shows single shot interference fringes when the probe carries a V [AV]. Contour-level lines in (c) and (e) represent the photonic disorder $V(\mathbf{r})$. The white circle represents the edge of the probe.

The photonic disorder is represented by the contour-level lines in Figs. 5.1(c,e). In order to identify Vs by fork-like dislocations in interference images, analogously to what is done in experiments, we plot the intensity of the signal state interfered with the pump state — which has a flat phase imposed by the pumping field — in the right panels of Fig. 5.1. The OPO conditions are chosen to give a vortex-free signal [see Figs. 5.1(a,b)]. The signal currents have a dominant component pointing leftwards and an equilibrium position where all currents point inwards at around $(-8, -14)$ μm.

In single shot simulations (one realization of the random phase $\Phi_{\rm rdm}$), it is found that if the probe is positioned well inside the OPO signal, then the imprinting of an $m = +1$ V at $t = 0$ imposes the system to spontaneously generate, at the same time, an $m = -1$ AV at the edge of the probe [Fig. 5.1(d)]. Equivalently an injected $m = -1$ AV forces the appearance of an $m = +1$ V — see Fig. 5.1(f). This is a consequence of the continuity of the photonic and exciton wave functions already discussed. However this argument alone does not predict the specific position around the probe where the AV appear.

When simulating the dynamics following the arrival of a V probe for 1000 different random realizations of the relative phase $\Phi_{\rm rdm}$, uniformly distributed between 0 and 2π, it is found that the AV appear in different locations around the V probe. The pink circles in Fig. 5.1(c) mark the positions where the AV appear, with its size being proportional to the number of random phase realizations in which it appears at that specific position. It is found out that the AVs are more likely to appear on positions where the current of the steady state OPO signal, before the probe arrival, and the probe current are opposite. For example, for a V probe $m = +1$ [Fig. 5.1(c)], the current constantly winds anti-clockwise, therefore, comparing with the OPO signal steady currents [Fig. 5.1(a)], ones realizes that both currents are mostly anti-parallel in the bottom right region on the probe edge, where is found that very likely an AV is formed. Similarly, both currents are parallel in the top left region on the probe edge, where is very unlikely that an AV is formed.

In the same way, if the probe carries an AV $m = -1$, it is expected that the spontaneous V is more likely to appear in the top left border of the probe, *i.e.* in a location given by changing (x, y) to $(-x, -y)$ with respect to the previous case. The blue stars in Fig. 5.1(e) mark the positions where the V appear, with its size being proportional to the number of random phase realizations in which it appears at that specific position. The upper left border of the probe containing the highest concentration of big stars confirms our expectations. Finally, let us note that phase continuity arguments allows the formation of additional V-AV pairs on the probe edge, which are in fact observed in simulations, but are however rare events.

If we now take the signal wave function, triggered by a V probe, averaged over the 1000 realizations, $\langle|\psi_C^s(\mathbf{r},t)|e^{i\phi_C^s(\mathbf{r},t)}\rangle_{\Phi_{\rm rdm}}$, similarly to what is done in multiple-shot experiments, neither the imprinted V nor the AV can be seen at the probe arrival time $t = 0$ ps (see the first column of Fig. 5.2), because on average the differently positioned branch-cuts wash away both phase

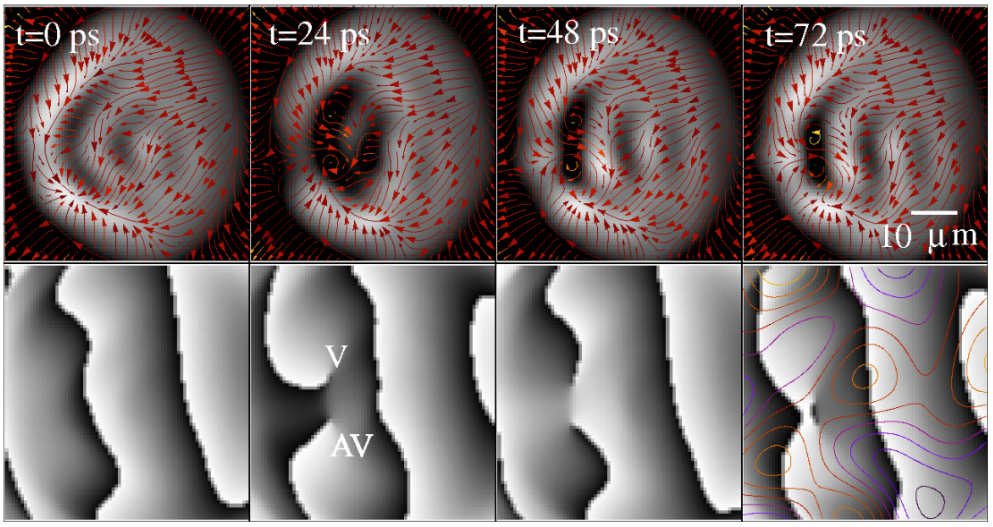

FIGURE 5.2: Simulated time evolution of signal after the arrival of the V probe, averaged over 1000 realizations of the random phase $\Phi_{\rm rdm}$, $\langle|\psi^s_C(\mathbf{r},t)|e^{i\phi^s_C(\mathbf{r},t)}\rangle_{\Phi_{\rm rdm}}$. Spatial profiles of density and currents (top) and phase (bottom). Contour-level lines in the last panel represent the photonic disorder.

singularities. However, remarkably, the steady state condensate currents push the V and AV, initially positioned in different locations, towards the same equilibrium position where all currents point inwards. As a consequence, as shown in the other panels on Fig. 5.2, while at $t = 0$ ps, on average, we do not see the V-AV pair, after ~ 10 ps both V and AV appear and last ~ 75 ps, till they eventually annihilate.

5.2 Experimental results

In order to check whether the theoretical predictions indeed describe properly the onset and dynamics of V-AV pairs, we perform experiments where the single-QW sample is resonantly pumped, in a region where the photon-exciton detuning is $\delta_{C-HH} = -0.7$ meV, by a *cw*-laser at 1.528 eV and $\mathbf{k}_p = 1.4\ \mu\text{m}^{-1}$. Since we are interested in the regime where the V is transferred into the OPO signal, which is preferably achieved when the polariton condensate is highly dense, the *cw*-pump power is set to 450 mW ($4 \times P_{th}$). The OPO signal is created at 1.5268 eV, ~ 1 meV blueshifted from the LP bare dispersion.

In order to confirm the role played by the relative currents of probe and OPO signal on the appearance of the unintended AV, we inject the V probe with a power of 3 μW, far above threshold for the V to be transferred into the condensate [49], and with a finite in-plane momentum with respect to that of the signal. In Fig. 5.3(a) we plot the momentum distribution of the probe as a function of $\mathbf{k} - \mathbf{k}_{pb}$, indicating with a straight arrow the value of $\mathbf{k}_s - \mathbf{k}_{pb}$. Figure 5.3(b) shows the real space profile of the probe carrying an $m = 1$ vortex. The relative in-plane momentum

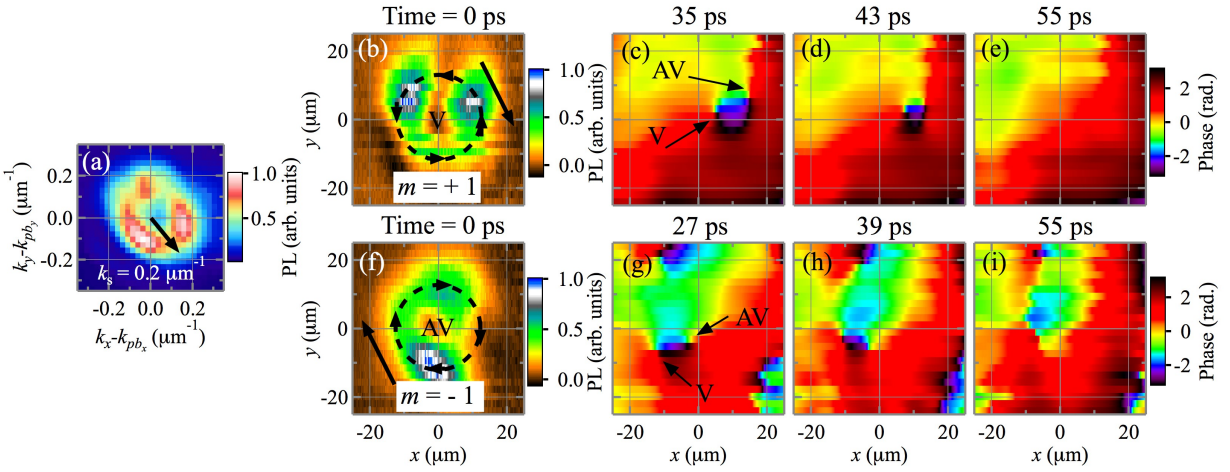

FIGURE 5.3: (a) Measured momentum distribution of the V probe vs $\mathbf{k} - \mathbf{k}_{pb}$. The arrow indicates the signal momentum $\mathbf{k}_s - \mathbf{k}_{pb}$. Panel (b) [(f)] shows the real space intensity profile of the $m = 1$ ($m = -1$) LG probe. The straight arrow in (b),(f) represents the signal current direction in the probe reference frame, while the probe current winds anticlockwise for $m = 1$ (clockwise for $m = -1$). Panels (c-e) [panels (g-i)] compile, through phase images, the time evolution of an imprinted $m = 1$ V ($m = -1$ AV) and its associated $m = -1$ AV ($m = 1$ V). The unintended AV (V) appears in (c) [(g)] at the edge of the probe where the signal and probe currents are antiparallel. V-AV pair dynamics can be followed in both cases for about 30 ps, after which they annihilate.

between signal and probe means that, sitting in the reference frame of the probe, the OPO signal has a definite homogeneous current [straight arrow in Fig. 5.3(b)], while the V probe has anti-clockwise winding currents. According to the previous theoretical analysis (see Fig. 5.1), we can therefore predict the location of the unintended AV, namely where the signal and probe currents are anti-parallel, which is in the upper-right corner of Fig. 5.3(b).

In order to measure the time-dynamics of the condensate phase after the arrival of the probe, therefore being available to track the appearance and dynamics of Vs and AVs, we interfere the region where the V is injected with an expanded, flat-phase, part of the condensate by using a Mach-Zehnder interferometer. The interferograms are later analyzed using Fourier transform techniques in order the extract the condensate phase.

Figs. 5.3(c-e) show the time-evolution of the condensate phase (now in its own reference frame), after the V have been imprinted into it. In accordance to our predictions, the unintended AV in Fig. 5.3(c) appears on the upper-right side of the injected V. Despite the many-shot average, the dynamics of the V-AV pair can be experimentally followed after its onset for tens of picoseconds [Figs. 5.3(c-e)], thereafter the pair eventually annihilates.

If we now invert the topological charge of the probe LG beam (which is done by taking the opposite diffraction order of the pulsed laser beam after the hologram) and inject an $m = -1$ AV at the same position and with the same in-plane momentum as in the just described $m = 1$ case, the unintended V should now appear at the inverse side of the probe, namely the lower-left corner of

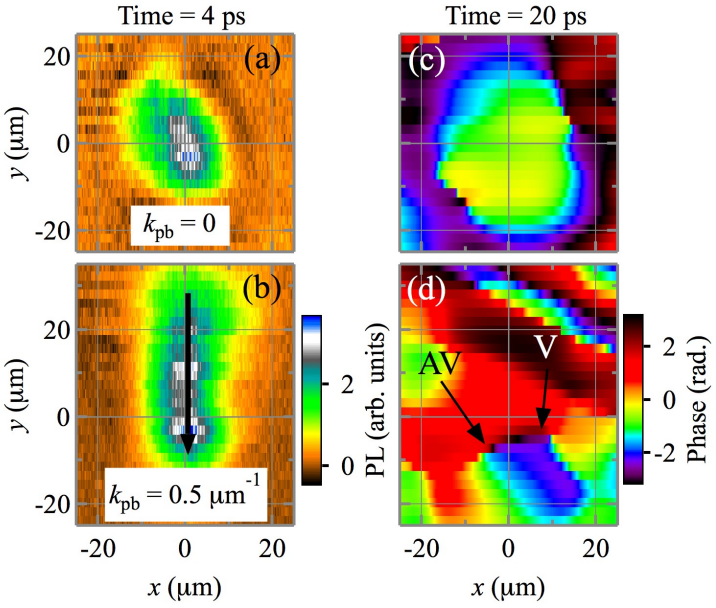

FIGURE 5.4: Spatial profile of the Gaussian probe at rest $\mathbf{k}_{pb} = 0$ (a) and moving $\mathbf{k}_{pb} \neq 0$ (b) shone on the vortex-free OPO signal. The condensate phase, measured 20 ps after the probe arrival, shows that no V-AV pair is created if the probe is at rest (c), while a V-AV pair appears for a moving probe (d).

Fig. 5.3(f), which is where the clockwise currents of the probe are antiparallel to the strait current of the OPO signal. In fact, this is observed in the phase spatial dynamics shown Fig. 5.3(g-i), where here the V-AV pair also annihilates at long times.

5.2.1 Gaussian probe

For the sake of compactness, this section contains a shortened version of the experimental results reported in Ref. [51]. This work reports a detailed time-resolved, interferometric analysis of the polariton emission, where it is observed the creation and annihilation of polariton V-AV pairs in the signal state of a polariton OPO by means of short optical gaussian probe-pulses at a certain finite pump wave-vector. We extract the phase of the perturbed condensate, revealing the dynamics of the supercurrents created by the pulsed probe. This flow is responsible for the appearance of the topological defects when counter-propagating to the underlying currents of the OPO signal.

We have already shown that Vs are likely to appear where the currents of an injected probe and the ones of the OPO signal counter-propagate. To check that this idea is valid in the more general case when the probe carries no angular momentum, we shine a flat-phase Gaussian probe, with a tunable in-plane momentum, onto a vortex-free condensate, pumped under similar conditions to those described at the beginning of this section.

Figure 5.4(a) shows the spatial profile of a Gaussian pulsed beam shone at rest with respect to the OPO signal, $\mathbf{k}_{pb} \simeq \mathbf{k}_s$. Since in this case no appreciable counter-propagating currents are generated in the condensate, we do not expect any topological defect to be created. Indeed, by inspecting the condensate phase 20 ps after the probe injection, no branch-cut is observed [Fig. 5.4(c)].

Figure 5.4(b) shows the spatial profile of a Gaussian probe beam injected with a finite momentum with respect to the OPO signal one, $\mathbf{k}_{pb} = 0.5\ \mu\text{m}^{-1} \neq \mathbf{k}_s = 0$. Note that tilting the beam implies that its shape is elongated in the direction of incidence (vertical in the figure). We have chosen the momentum of the probe to be $\mathbf{k}_s - \mathbf{k}_{pb} = 0.5\ \mu\text{m}^{-1}$ based on the experimental findings, shown in Fig. 5.3, that counter-propagating currents with a magnitude of $|\mathbf{k}_{pb} - \mathbf{k}_s| \simeq 0.2\ \mu\text{m}^{-1}$ were enough to create a topological defect. Since there is a difference in the signal and probe currents in the upper and lower edges of the probe, according to the experiments and simulations described above we expect that Vs appear at such places. More precisely, an anti-clockwise $m = 1$ V should appear at the upper border whereas a clockwise $m = -1$ AV should appear at the lower border. The dynamics of the condensate indeed agree with the predictions, with its phase, 20 ps after the probe injection, showing a V in the right part and an AV in the left part [Fig 5.4(d)].

5.3 Conclusions

We have demonstrated that unintended AVs appear in the signal at the edge of an imprinting V probe and explained, both theoretically and experimentally, the origin of the deterministic behavior of the AV onset and dynamics. In particular, we showed where AVs are more likely to appear in terms of the supercurrents of the imprinting probe and the currents of the underlying OPO. The theoretical predictions are borne out by the experimental observations. In addition, our study reveals that the onset of Vs in polariton superfluids does not require a LG imprinting beam, but instead V-AV pairs can also be generated when counter-propagating currents are imposed, similarly to what happens in normal (classical) fluids.

Crucially, via numerical simulations, we elucidate the reason why an experimental average over many shots allows detecting a V by direct visualizing the density and phase profiles. Recently, it has been suggested by stochastic simulations [261] that Vs in non-resonantly pumped polariton condensates undergo a random motion which will hinder their direct detection, unless they are close to being pinned by the stationary disorder potential and thus follow a deterministic trajectory [209]. In the case considered here of a superfluid generated by the OPO, we can instead explain a deterministic dynamics of the V-AV pair in terms of the OPO steady state supercurrents, which determine a unique trajectory for the pair, allowing their observation in multishot measurements.

The mechanism for V-AV pair formation reported here differs from the V-AV binding-unbinding associated to the BKT phase transition — see § 2.3.1 —, recently adopted to interpret the V-AV observation in non-resonantly pumped polaritons [171]. In our case, the pair onset can be explained in terms of the OPO and probe relative currents, a simple mechanism which does not require resorting to phase fluctuations induced by the pump.

Chapter 6

Ignition and formation dynamics of a polariton condensate on a semiconductor microcavity pillar

In this Chapter we study the time-resolved ignition and decay of a polariton OPO in a semiconductor MC pillar. The combination of a *cw* laser *pump*, under quasi phase-matching conditions, and a non-resonant, pulse *probe*, together with the use of spectral tomography techniques, allows us to obtain the full dynamics of the system.

This Chapter is organized as follows. In § 6.1 we describe the details of the pillar MC sample and the specific excitation conditions used for the experiments. § 6.2, which compiles the experimental results and discussion, it is divided in four parts: § 6.2.1, where we perform a *cw* spectroscopy characterization of the OPO signal emission, § 6.2.2, which compiles the experiments where we ignite a long-living OPO-process with a *probe*-induced blueshift, § 6.2.3, where the pillar is excited with a non-resonant pulsed *probe* only and finally, § 6.2.4, where we compare the polariton dynamics under the two excitation schemes involving a *probe*. § 6.3 compiles the theoretical description of the 2D coupled GP equations for photons and excitons that reproduce and interprete the results of § 6.2.2. Finally, in § 6.4 we discuss the conclusions of this work.

6.1 Experimental setup

We investigate the high-quality $5\lambda/2$ *AlGaAs*-based MC described in § 3.2, we have chosen a 40 μm-$\varnothing$ pillar. Figure 6.1 shows a SEM image of such a pillar, including the excitation scheme.

The sample is excited with *pump* and *probe* laser beams under the following conditions: (a) for the *cw* experiments, § 6.2.1, we use only a *pump* beam obtained from a *cw* Ti:Al_2O_3 laser. It is

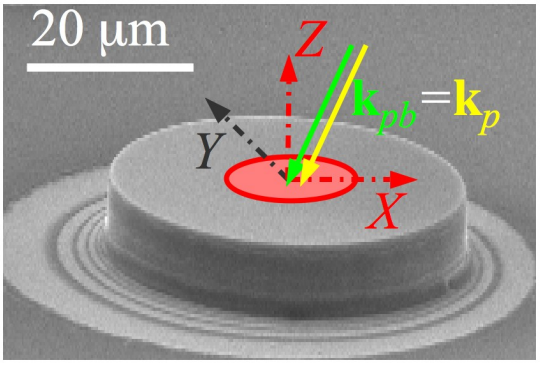

FIGURE 6.1: SEM image of a 40 μm-$\varnothing$ pillar with the *pump+probe* excitation scheme: the full arrows, contained in the XZ plane, sketch the beams directions, $\mathbf{k}_{pb}$ and $\mathbf{k}_p$, impinging at the center of the pillar. Three dot-dashed arrows define the coordinates origin chosen for the experiments.

tuned at $E_p = 1.5416$ eV, impinging on the sample with an in-plane momentum $(\mathbf{k}_p)_x = -1.9\ \mu\text{m}^{-1}$, fulfilling the phase-matching conditions $2E_p = E_s + E_i$ and $2\mathbf{k}_p = \mathbf{k}_s + \mathbf{k}_i$ (where the subindex s/i means *signal*/*idler*). Its power is set to $P_p = 160$ mW. (b) For the time-resolved experiments, § 6.2.2 and 6.2.3, the excitation scheme is represented in Fig. 6.2. In this case the *cw pump* beam is out of OPO phase-matching conditions, since now its energy is tuned slightly above the LPB ($E_p = 1.5419$ eV). The second excitation source, *probe*, is a pulsed Ti:Al_2O_3 laser (2 ps-long pulses); it is tuned into resonance with the exciton mode ($E_{pb} = 1.5445$ eV), and its power, $P_{pb} = 230$ mW, is strong enough to trigger the OPO-process together with the *pump*. The origin of time $t = 0$ is set to the instant when the *probe* impinges on the pillar. The two excitonic lines labelled X_1 and X_2 originate from excitons uncoupled to the cavity modes, due to slight QW thickness variations, of the order of a monolayer, between different QWs. Further information about the origin of the exciton emission is given in Ref. [277].

For the experimental results described in § 6.2, the laser beams are focused on the sample through a high numerical-aperture (0.6) lens, forming two overlapping elliptically shaped spots (10/20 μm-$\varnothing$ minor/major axis along the Y/X axis) impinging on the pillar with an in-plane momentum $\mathbf{k}_{p/pb} = \{(\mathbf{k}_{p/pb})_x, (\mathbf{k}_{p/pb})_y\} = \{-1.9, 0\}\ \mu\text{m}^{-1}$, see full arrows in Fig. 6.1. The same lens is used to collect and direct the emission towards a 0.5 m spectrometer coupled to a CCD (§ 6.2.1) and a streak camera (§ 6.2.2 and 6.2.3). The PL can be resolved in the near- (real-space) as well as in the far-field (**k**-space). The distribution of polaritons in **k**-space is accessed by imaging the Fourier plane of the lens used to collect the PL, taking advantage of the direct relation between the angle of emission and the in-plane momentum of polaritons [162]. To avoid the direct reflection of the *pump* and *probe* beams, we block the emission in **k**-space for $|\mathbf{k}| > 1.5\ \mu\text{m}^{-1}$ and we spectrally filter the polariton PL with an energy detection range of 1 meV around 1.54 eV. The lens that focuses the real or **k**-space PL distribution into the spectrometer entrance slit is displaced laterally by discrete steps, yielding a tomographic reconstruction of energy- and time-resolved images.

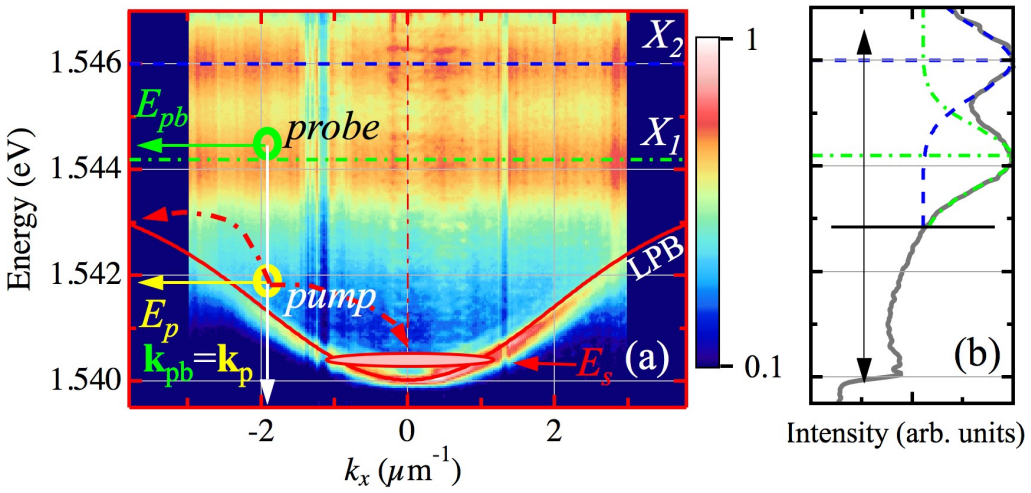

FIGURE 6.2: (a) Experimental LPB dispersion obtained under non-resonant (1.612 eV), weak excitation conditions; the overlapping thin, full curve is a guide to the eye. The horizontal dot-dashed and dashed lines mark the energies 1.544 eV and 1.546 eV of the excitons $\mathbf{X_1}$ and $\mathbf{X_2}$, respectively. The energy, E_p (E_{pb}), and momentum, $\mathbf{k}_p$ ($\mathbf{k}_{pb}$), of the *pump* (*probe*) is marked with a circle and pointing arrows to the energy and k_x axis. Dot-dashed arrows depict the OPO process that yields the OPO signal at E_s and $\mathbf{k}_s \approx 0$, marked with an elongated circle. The PL is coded in a false, normalized, logarithmic color scale. (b) Spectrum emission integrated in **k**-space depicted in a full line. The two bare exciton levels are obtained with a double gaussian fit: the dot-dashed (dashed) horizontal line marks the energy of the maximum PL emitted by the X_1 (X_2) exciton. A horizontal full line schematically separates, at 1.543 eV, the spectrum that correspond to excitons (above, upward pointing arrow) and polaritons (below, downward pointing arrow) in the pillar.

6.2 Experimental results and discussion

This section compiles the results of *cw* and time-resolved experiments in the pillar, which are organized as follows. In § 6.2.1 we address the tomographic spectral distribution of polaritons in the pillar under *cw*-OPO excitation, in both real- and **k**-space. In § 6.2.2 we study the dynamics of the polariton emission under *pump*+*probe* excitation. In this case, the *cw pump* laser beam is out of OPO-conditions (slightly blue-detuned from the LPB); only after the arrival of the *probe*, the induced blue-shift of the LPB is large enough to start the OPO-process. In § 6.2.3, for the sake of completeness, we present the polariton dynamics with the *probe* excitation only, where the decay of the polariton PL is faster and limited by the relaxation dynamics from photo-generated excitons towards the polariton ground state.

6.2.1 CW spectroscopy characterization of OPO signal emission

Figure 6.3 summarizes the spectral tomography of the polariton emission in both real- and **k**-space under a *cw pump* excitation. The OPO signal energy is $E_s \approx 1.54$ eV, with a full width $\Delta E_s \approx 0.8$ meV. Figure 6.3(a)/(e) shows the polariton emission in real-/**k**-space (Y/k_y) at the

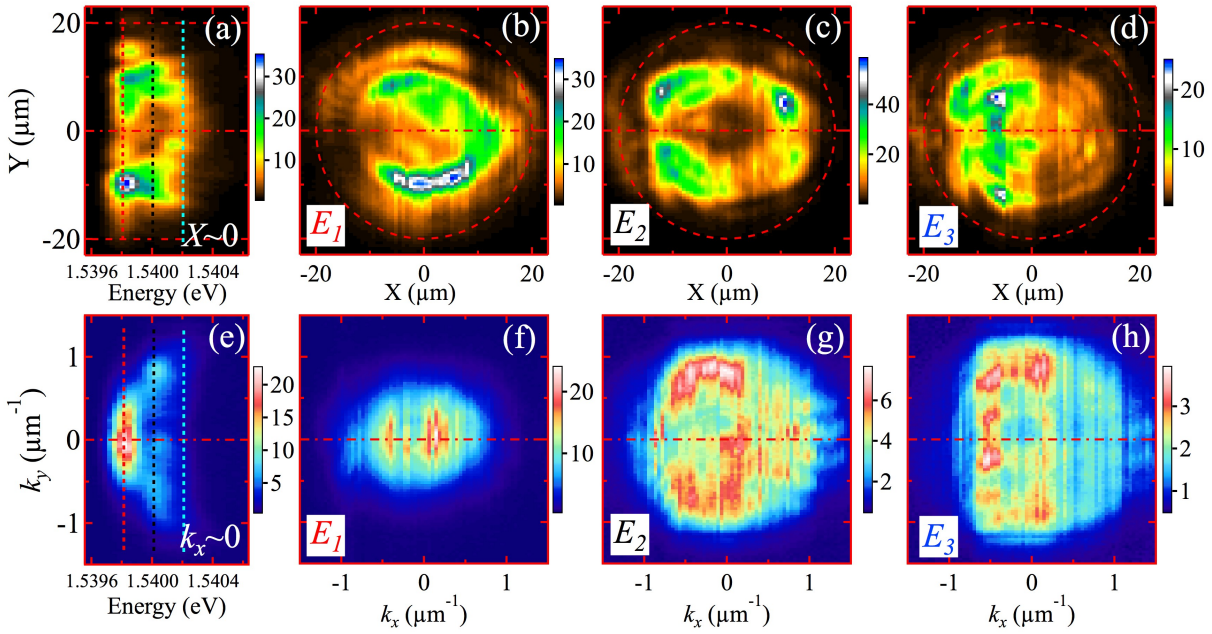

FIGURE 6.3: (a)/(e) Real-/Momentum-space polariton spectrum emission at $X = 0/k_x = 0$ cross-section in the pillar. The three, dashed, vertical lines mark the position where the full $X - Y/k_x - k_y$ PL map has been reconstructed in panels (b-d)/(f-h). The three selected energies are: $E_1 = 1.5398$ eV, $E_2 = 1.5400$ eV and $E_3 = 1.5402$ eV. In panels (b-d) dashed, red circles mark the limits of the pillar. Vertical, dashed lines in panels (a)/(e) mark the resolved cross-section of the spectrum shown in panels (b-d)/(f-h) for real-/**k**-space. The PL maps are coded in linear, false color scales.

central $X = 0/k_x = 0$ cross-section. Since the *pump* is impinging at the center of the pillar, the polariton emission displays a ring-like distribution, as can be seen in the cross-section in Fig. 6.3(a), where the emission is spatially enclosed in the area $5 < |\mathbf{r}| < 15$ μm. Figure 6.3(e) shows that polaritons are static at low energies (∼1.5398 eV), since their emission is confined at $\mathbf{k} \sim 0$, and they spread in a disk of radius $|\mathbf{k}| < 1.2$ μm^{-1} at slightly higher energies (∼1.540 eV).

We perform a 2D reconstruction of the spectrum emission, showing the full $X - Y/k_x - k_y$ PL distribution of polaritons at three, selected energies: $E_1 = 1.5398$ eV, $E_2 = 1.5400$ eV and $E_3 = 1.5402$ eV, Figs. 6.3(b-d)/(f-h). Figure 6.3(b) reveals the ring-like distribution of polaritons at E_1. The angle of incidence of the *pump* creates an asymmetrical blueshift in the left side of the pillar due to polariton propagation, so the polariton ring-shaped emission is broken in the region $\{x, y\} = \{-10, 0\}$ μm. At a higher energy E_2, Fig. 6.3(c), polaritons emit from a ring of radius 10 μm with a smaller side gap. Figure 6.3(d) shows an almost flat disk of emission, whose radius is ∼15 μm.

In **k**-space, Fig. 6.3(f) shows a small disk (radius 0.7 μm^{-1}) in the polariton distribution. This demonstrates that polaritons lying at low energy (E_1), which are distributed along the ring in Fig. 6.3(b), are confined in real space, with a small amount of kinetic energy. The confinement of polaritons at E_1 is also hinted in the momentum cross-section in Fig. 6.3(e). Figures 6.3(g) and

6.3(h) evidence a flat distribution in momentum space, where polaritons have all possible values of momenta inside a disk of radius $|\mathbf{k}| < 1$ and 1.5 μm^{-1}, respectively. For energies higher than E_3, polariton emission is distributed in a ring (not shown) corresponding to a cloud of uncondensed, hot polaritons in the LPB.

6.2.2 Igniting a long-living OPO-process with a *probe*-induced blueshift

In this section we show how the OPO process is triggered by the arrival of a *probe* beam. Moreover, through real-space measurements, we reveal the ring-shape distribution of *signal* polaritons and, analyzing **k**-space images, we characterize their movement around the pillar.

The *pump* (*cw*) + *probe* (pulsed) excitation configuration activates a long-lived stimulated OPO scattering process. The time during which the OPO is active is much longer than the photon lifetime, estimated from the Q-factor to be $\sim$ 10 ps. The real- and **k**-space dynamics or the signal emission are presented in Figs. 6.4 and 6.5, respectively. In these time-resolved experiments, the energy resolution is similar to that of the energy width of the OPO signal ΔE_s.

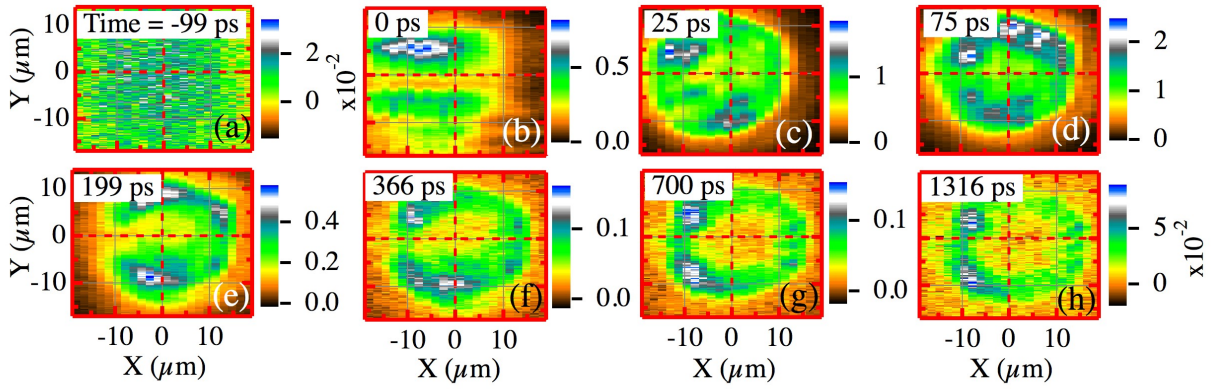

FIGURE 6.4: Real-space polariton emission dynamics in the pillar under *pump* and *probe* beam excitation. The time is shown by the labels in each panel. The time $t = 0$ coincides with the arrival of the *probe*. The PL is coded in a linear, false color scale shown on the right of each panel. The complete $X - Y$ polariton emission dynamics is available as a supplemental movie in http://link.aps.org/supplemental/10.1103/PhysRevB.90.155311.

Figure 6.4 compiles 2D images of the polariton signal emission at different times in real-space. For each panel, the time is displayed at the left upper corner, being the temporal origin set at the instant when the *probe* impinges on the sample. Fig. 6.4(a) shows that, before the arrival of the *probe* pulse ($t = -99$ ps), there is no signal emission since the *pump* is off of phase-matching conditions. At $t = 0$, Fig. 6.4(b), the *probe* impinges on the pillar; the spot shape is distorted due to the fact that $\mathbf{k}_{pb} \neq 0$. The polariton emission rapidly arises from the whole pillar surface, seen as a flat homogeneous disk, Fig. 6.4(c). The PL increases during $\sim$100 ps, as shown in Fig. 6.4(d); thereafter, the extra-population of polaritons induced by the *probe* decreases. When the OPO

process has switched-on, the polariton dispersion becomes ring-shaped, Fig. 6.4(e): the real-space polariton distribution resembles that shown in Fig. 6.3(c). Polaritons emit close to the border of the pillar, due to the blueshift induced by the *cw pump*. This polariton emission persists for more than ∼1 ns, see Figs. 6.4(f-h).

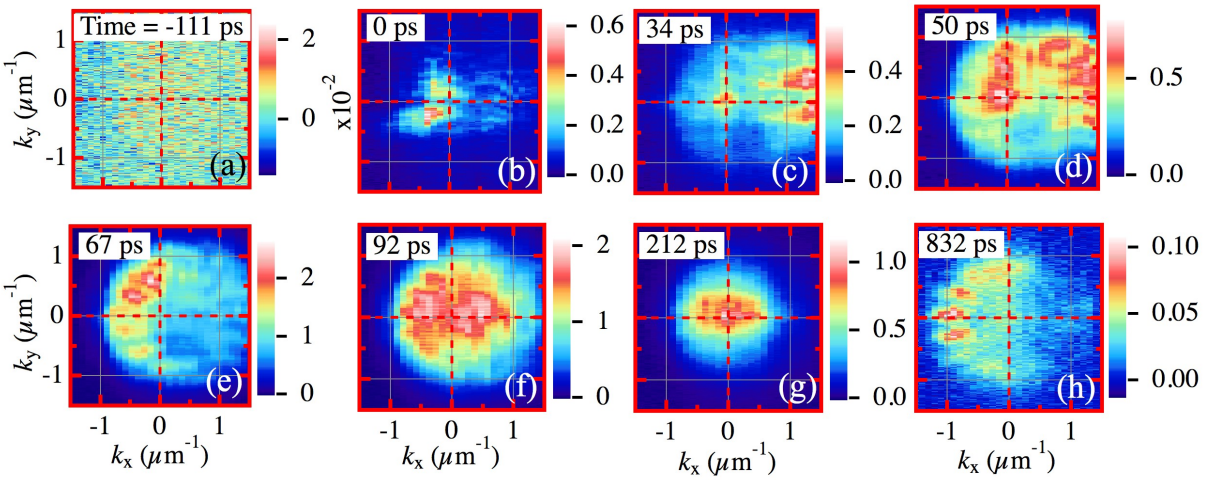

FIGURE 6.5: Momentum-space polariton emission dynamics in the pillar. Same excitation conditions as in Fig. 6.4. The time is shown by the labels in each panel. The PL is coded in a linear, false color scale shown on the right of each panel. The complete $k_x - k_y$ polariton emission dynamics is available as a supplemental movie in http://link.aps.org/supplemental/10.1103/PhysRevB.90.155311.

Figure 6.5 shows the dynamics in **k**-space of the polariton population. As observed in real-space, there is no OPO signal emission before the arrival of the *probe*, Fig. 6.5(a). The pulsed *probe* arrives to the pillar at $t = 0$, Fig. 6.5(b), the spurious emission from $\mathbf{k} \sim 0$ is unfiltered scattered laser light. The *probe* creates an extra polariton population around $\mathbf{k} = \{-1.5, 0\}$ μm^{-1} that rapidly moves in the $+k_x$ direction. At $t = 34$ ps, Fig. 6.5(c), the population has moved towards $\mathbf{k} = \{1.5, 0\}$ μm^{-1}. Fig. 6.5(d) shows that, at $t = 50$ ps, the polariton emission is homogeneously distributed in a disk of radius $|\mathbf{k}| \approx 1$ μm^{-1}. At $t = 67$ ps, Fig. 6.5(e), the population reverts its angle of emission towards $-k_x$. As it was mentioned for Fig. 6.4, ∼ 100 ps after the arrival of the *probe*, its induced extra-population weakens and the OPO signal is redistributed at the center of **k**-space, Fig. 6.5(f).

The oscillations arise from the *probe*-injected excitons, which are excited with a certain angle. The relaxation of excitons yields polaritons that possess a non-zero momentum. As clearly inferred from the dynamics of the **k**-space distribution, polaritons change their initial momentum due to several bounces against the MC wall. The gain follows the injected *probe* distribution as it moves within the pillar, until the excitonic population dies off and a more stable, switched-on OPO process takes place, which resembles the polariton distribution in real and **k**-space shown in Fig. 6.3. For longer times, $t = 212$ ps [Fig. 6.5(g)], the emission is mainly perpendicular to the sample surface, *i.e.* at $\mathbf{k} \approx 0$. At later times, Fig. 6.5(h), two effects are observed: firstly, there is a lobe-like

structure at $\mathbf{k} = \{1.0, 0\}$ μm^{-1} and, secondly, there is a progressive decay of the central ($\mathbf{k} = 0$) population.

There are several possible explanation to address the former effect on the lobe-like structure. One possible reason is that a real-space separation between polaritons generate a **k**-space modulation (analogous phenomenology is also reported in next Chapter 7). In Fig. 6.4(e) polaritons are occupying upper and lower sides of the ring, separated by $\sim$ 16 μm. These two populations interfere in **k**-space, giving a $2\pi/(16\mu m) = 0.4$ μm^{-1} fringe separation, which is the one we see in Fig. 6.5(e,h). This agrees with the message of Chapter 7, and, in this case, it proves that the OPO polariton condensate maintains the coherence over its spatial extension. An alternative explanation for the lobe-like structure in **k**-space could be the discretization of the dispersion relation due to the spatial dimensions of the pillar. But this effect is not observed in the dispersion relation of Fig. 6.2(a), obtained under non-resonant excitation in the center of the pillar (as mentioned in the figure caption). Maybe, the excitation close to the border of the pillar could reveal some discretized structure in the dispersion relation, as thoughtfully discussed in § 3.2.1.1.

The latter effect, the progressive decay of the $\mathbf{k} = 0$ population, is due to the fact that the emission energy is red-shifting with time and we have not been following this red-shift with the streak camera since its energy detection is fixed for these experiments.

6.2.3 Non-resonant excitation solely with a pulsed *probe*

In this section, for completeness, we address the polariton dynamics obtained when only the pulsed *probe* beam excites the pillar. The polariton emission dynamics in real- and **k**-space is summarized in Figs. 6.6(a-d) and Figs. 6.6(e-h), respectively. Fig. 6.6(a) shows the absence of emission before the arrival of the *probe*. Figs. 6.6(b,c) show the switch-on of the polariton emission, following a similar dynamics to that shown in Fig. 6.4, during the first $\sim$100 ps. Fig. 6.6(d) demonstrates the shorter lifetime of the polariton population created under these excitation conditions; after $\sim$250 ps, the polariton PL has disappeared.

In a similar fashion, Figs. 6.6(e-h) show the dynamics of the emission in **k**-space. An oscillation of the polariton momentum similar to that described in Fig. 6.5(c-e) is obtained here during the first $\sim$100 ps. The polariton emission moves in the k_x direction, going from -1.5 μm^{-1} to $+1.5$ μm^{-1} in $\sim$70 ps. At later times, Fig. 6.6(g), the emission originates from $k \approx 0$, and for $t = 355$ ps, the lack of emission is confirmed, Fig. 6.6(h).

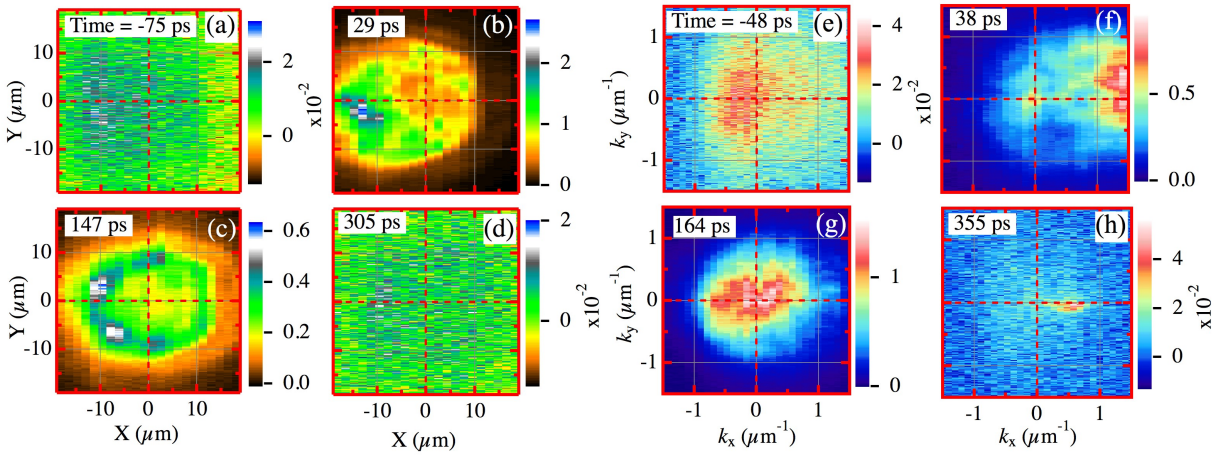

FIGURE 6.6: (a)-(d) Real/(e)-(h) **k**-space polariton emission distribution in the pillar, the time is shown by the labels in each panel. Only the *probe* beam excites at the center of the pillar. The time $t = 0$ coincides with the arrival of the *probe*. The PL is coded in a linear, false color scale shown on the right of each panel. The complete $X - Y$ and $k_x - k_y$ polariton emission dynamics is available as a supplemental movie in http://link.aps.org/supplemental/10.1103/PhysRevB.90.155311.

6.2.4 Comparison of the dynamics of the two excitation schemes involving a *probe*

The dynamics of the spatially integrated emission build-up and decay is depicted in Fig. 6.7. A similar behavior is obtained for the build-up in both cases: *pump*+*probe* (blue line) and *probe*-only (orange line) excitation conditions. The PL reaches its maximum emission ∼50 ps after the *probe* is gone. It is on the decay dynamics that differences between the two excitation conditions appear. Under *probe*-only excitation we observe a mono-exponential decay of the PL, with a characteristic decay time of 63 ps. The decay is markedly different in the presence of the out-of-resonance *pump*. In this case, the PL decay is bi-exponential, with a fast decay time of 76 ps, and a long-lived polariton population lasting more than 1 ns, evidenced by the slow, ∼ 500 ps, decay time.

6.3 Theoretical description

To model our experimental results under the OPO configuration, described in § 6.2.2, we make use of the 2D coupled GP equations for photons $\psi(x, y)$, Eq. 6.1, and excitons $\varphi(x, y)$, Eq. 6.2:

$$i\hbar\frac{\partial\psi}{\partial t} = -\frac{\hbar^2}{2m_{ph}}\Delta\psi + \frac{\hbar\Omega_R}{2}\varphi + U\psi - \frac{i\hbar}{2\tau_{ph}}\psi + P + P_X + f \tag{6.1}$$

$$i\hbar\frac{\partial\varphi}{\partial t} = -\frac{\hbar^2}{2m_X}\Delta\varphi + \frac{\hbar\Omega_R}{2}\psi + \alpha_1|\varphi|^2\varphi + U\varphi \tag{6.2}$$

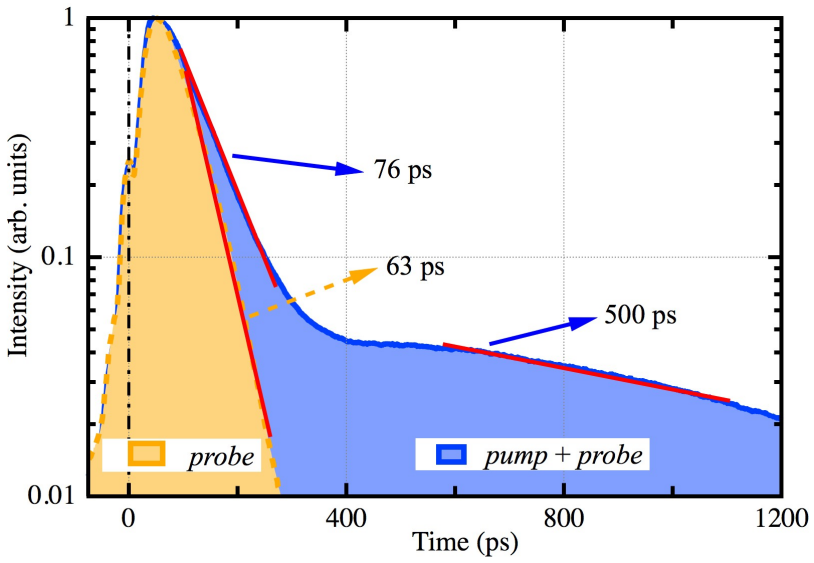

FIGURE 6.7: Dynamics of the integrated polariton PL under the two excitation conditions: *pump+probe* (full line) and *probe*-only (dashed line). Full, straight lines are included in the different exponential decays as guides to the eye. PL is plotted in a logarithmic axis.

Here, $m_{ph} = 4 \times 10^{-5} m_0$ is the photon mass, $m_X = 0.6 m_0$ is the exciton mass (m_0 is the free electron mass), $\hbar\Omega_R = 9$ meV is the Rabi splitting, $\alpha_1 = 6 E_b a_B^2$ is the triplet interaction constant [304] ($E_b = 10$ meV is the exciton binding energy and $a_B = 10$ nm is the exciton Bohr radius).

The confinement potential of the pillar, acting on the photonic and excitonic parts, is described by U. $\tau_{ph} = 1$ ps is the photon lifetime (the exciton decay is neglected), P is the quasi-resonant pumping term, exciting the system at a given frequency and in-plane momentum (same values as in the experiments), blue-detuned with respect to the polariton branch, and f is the noise, which serves to account for the effects of spontaneous scattering. The *cw* pumping provides an average of 10 particles in a unit cell of length 0.25 μm in the steady state, while the spontaneous scattering creates 0.01 particles. To describe the non-resonant *probe*, we use a pulsed pumping term P_X, tuned at the exciton resonance, with the same duration and wave-vector as in the experiments. No disorder potential was taken into account, because its effects were not observed in the experiments.

The results of the theoretical simulations are presented in Fig. 6.8. We plot the spatial distribution of the PL from the MC for the *signal* state, by applying a filter in **k**-space, blocking the emission for $\mathbf{k} > 1.5$ μm^{-1} as in the experiments. This spatial distribution is plotted at two different instants, in order to demonstrate the agreement between experiment and theory. Figure 6.8(a)/(b) (25/400 ps delay) is to be compared with Fig. 6.4(c)/(g).

First of all, the main conclusion is that both in experiment and theory the creation of excitons by the *probe* laser leads to a blue-shift of the polariton dispersion, which moves it into resonance

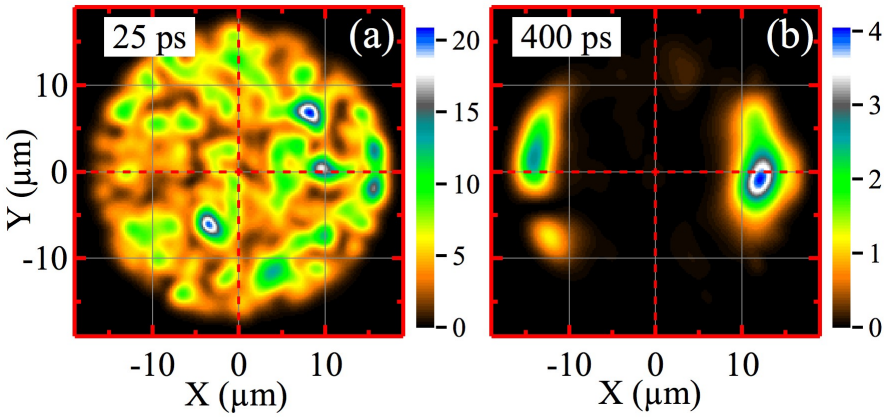

FIGURE 6.8: Real-space polariton emission dynamics in the pillar under *pump* and *probe* beam excitation. Panel (a)/(b) correspond to 25/400 ps after the *probe* excitation. The PL is coded in a linear, false color scale.

with the *pump* laser. The density of the *pump* state becomes then sufficient to start OPO scattering into the *signal* and *idler* states.

Because of the hysteresis of the polariton system in the bistable regime, the *pump* density remains high even when the probe excitons have decayed through relaxation and emission from strongly photonic states. The OPO regime persists for more than 1 nanosecond, much longer than the characteristic decay times in the system. The presence of the confinement potential of the pillar prevents the escape of the *signal* polaritons under the influence of the potential of the *pump*, contributing to the persistence of the OPO. The decay of the OPO is due to the overall imbalance between pumping and losses. The small difference between pumping and losses becomes more and more important because the decrease of the total polariton density leads to a redshift of the pumped mode, bringing it out of OPO resonance, decreasing the efficiency of pumping even further. This is evidenced in the experiments by the fact that the time evolution of the intensity becomes a concave function of time (the effective lifetime becomes progressively shorter at longer times). In the simulations, increasing the pumping allows to overcome this decay and to maintain a permanently stable OPO regime. However, one should note that in the bistable configurations, the presence of noise (spontaneous scattering) leads to spontaneous transitions between the two stable solutions at long time scales. This noise also contributes to drive the system towards the low-intensity state and to switch-off the OPO.

More conclusions can be drawn from the spatial shape of the signal at different moments of time, which results from the interplay of several effects. At initial moments of time, the density becomes sufficient to surpass the OPO threshold everywhere in the pillar, with a large spreading in the reciprocal space caused by different phase matching conditions (different signal wave vectors and energies) in different points because of the non-homogeneous pump profile. However, the *signal* exhibits a homogeneous emission over the whole surface of the pillar, the rapid spreading of

polaritons being caused by the strong interactions between all particles: those created by the *pump* (once the bistability is passed) and those injected with the *probe*. This is well reproduced by the theoretical simulations [Fig. 6.8(a)]. At later times [Fig. 6.8(b)], as the total density drops down and the spatial redistribution stabilizes, the signal concentrates around opposite sides of the pillar along the X axis. This is due to the spatial shape of the *pump* laser, which creates the conditions favorable for the OPO only in these points, located at the minima between the *pump* spot and the pillar boundary: the *pump* density at the center of the pillar is too high to maintain resonant OPO, because the signal polaritons are pushed away from the center and there their density becomes insufficient to maintain stable OPO. The overall good agreement between theory and experiment supports our interpretation of the experimental observations.

6.4 Conclusions

We have presented new experimental conditions to obtain a long-lived polariton condensate in a pillar MC and allowing to study the dynamics of its formation and decay. It involves two excitation beams impinging at the center of the pillar with the same wave-vector: a *cw pump*, slightly blue-detuned from the inflection point of the LPB, and a pulsed *probe*, resonantly creating excitons. The polariton population created with the arrival of the *probe* induces a blue-shift of the LPB, which enters into resonance with the *pump* beam, triggering the OPO-process. The *cw pump* keeps on feeding the OPO after the pulsed *probe* has disappeared, because of the hysteresis of the polariton bistability. As a result of the combined effect of both beams, the OPO signal emission lasts for more than 1 ns, much longer than any of the characteristic times of the MC. The polariton condensate dynamics observed when using just the *probe* beam is remarkably similar, but much shorter lived, to that obtained for the two beam excitation. The exciton population created by the *probe* beam efficiently relaxes to the LPB and from there follows the OPO dynamics. The characteristic decay time is one order of magnitude shorter than that obtained under the two beam excitation conditions.

Chapter 7

Quantum coherence in momentum space of light-matter condensates

Exciton-polariton BECs, due to their dual wave-particle nature, share many properties with classical waves as, for instance, interference phenomena, which are crucial to gain insight into their ondulatory character. In this Chapter, we show that the use of momentum-space optical interferometry, which avoids any spatial overlap between two parts of a macroscopic quantum state, presents a unique way to study coherence phenomena in polariton condensates.

We address a longstanding question in quantum mechanics: "*Do two components of a condensate, which have never seen each other, possess a definitive phase?*" [56]. A positive answer to this question is experimentally obtained here for light-matter condensates, created under precise symmetry conditions, in semiconductor MCs, taking advantage of the direct relation between the angle of emission and the in-plane momentum of polaritons.

This Chapter is organized as follows. In § 7.1 we explain the experimental setup used for the experiments. § 7.2 compiles the experimental results and discussion of the observation of coherence in momentum space between spatially separated polariton bullets. The following additional sections compile supplemental results on this phenomena, such as: § 7.2.2, Young interference experiment with polariton bullets, § 7.2.3, invariance morphology of the bullets after their real space overlap, § 7.2.4, scaling behavior of the relation $\Delta k_x = 2\pi/d$, § 7.2.1, study on the visibility dynamics of the interference patterns observed in local regions of momentum and real space, and, finally, in § 7.2.5 we include the experiments that show coherence in momentum space using a single spot excitation. Conclusions are drawn in § 7.3.

7.1 Experimental setup

The sample is the high-quality $5\lambda/2$ *AlGaAs*-based MC described in § 3.2. We perform our experiments in the ridge structure shown in Fig. 3.5, whose dimensions are 20×300 μm^2.

The sample is excited with 2 ps-long light pulses from a Ti:Al_2O_3 laser. We split the laser beam to produce two twin photon beams, named as A and B, whose intensities, spatial positions and relative time delay can be independently adjusted. For the results presented here, the time delay between A and B is zero. In Fig. 7.1(b) we sketch the spatial position of A and B beams. We focus both beams on the ridge to form 10-μm ⌀ spots spatially separated by $d = 70$ μm.

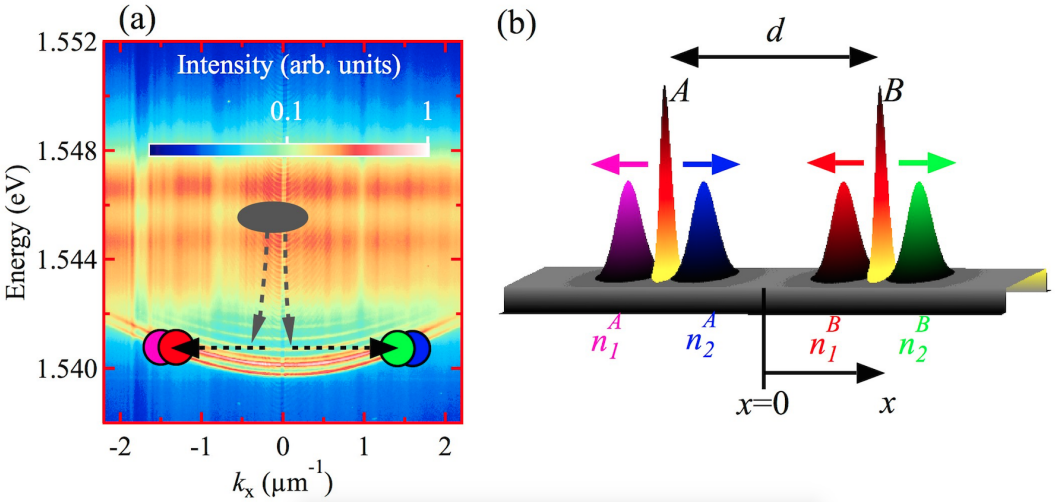

FIGURE 7.1: (a) Sketch of the excitation and relaxation processes to form propagating polariton WPs on a background showing the energy vs. k_x emission obtained under non-resonant, low power excitation conditions. The grey ellipse depicts the excitation laser at 1.545 eV and $k_x \sim 0$. The dashed lines indicate the energy relaxation of excitons into polariton WPs. Polariton WPs, propagating with $k_x \approx \pm 1.6$ μm^{-1} (slightly displaced for the sake of clarity), are depicted with circles, coded in colors explained in (b). The emission intensity is coded in a logarithmic, false color scale. (b) Sketch in real space of the experimental configuration. A laser beam is split into two arms, A and B, distanced by d. They create four propagating polariton WPs, coded in different colors, $n^A_{1,2}$ (magenta, blue) and $n^B_{1,2}$ (red, green) moving along the x axis of a MC ridge in the direction depicted by the arrows.

In all the experiments described in this Chapter the emission has been filtered at the energy of the polariton condensates. Every picture is the result of an average over millions of shots[1], as single-shot measurements would give a too low signal-to-noise ratio. For the excitation conditions used in our experiments, the density power required for polariton condensation, P_{th}, is relatively large, since the reflectivity at the excitation energy, 1.545 eV, is high; we use a power $P_A = P_B = 5 \times P_{th} = 22$ mW. The choice of the power used in the experiments determines the final value of k_x [see Figs. A.1(d,f) in Appendix A]. We must stress that our setup is able to measure either interferences of polariton wave packets (WPs) in real space, by means of near-field detection, or

[1] Laser repetition rate 82 MHz and integration time 1.1 s, see § 4.1 for further information.

interferences of WPs in reciprocal space by means of far-field detection. Therefore, it is unable of directly measuring Wigner functions that would be a good alternative for describing WPs dynamics in phase space. Our experimental approach, as any amplitude interference experiments, can never present negative intensities, while Wigner functions of quantum states do.

7.2 Experimental results and discussion

A crucial issue when optically creating polaritons is the excess energy of the excitation laser. There are two well explored alternatives: non-resonant excitation at very high energies [21] and strictly resonant excitation [27]. The latter situation generally produces macroscopic polariton states with a phase inherited from that of the laser, unless special care is taken in the experiments [175]. The former case is appropriate to avoid phase heritage, but it does not provide the momentum distribution, shown below, required for our experiments. In order to avoid these difficulties, we opt for a different alternative, depicted in Fig. 7.1(a): the laser beams excite the sample at the energy of bare excitons and $k_x \sim 0$, where our sample shows a non-negligible absorption. The broad bands between 1.542 and 1.548 eV corresponds to excitonic emission bands; the sub-bands below 1.542 eV are the confined LPBs. After energy relaxation, polariton condensates are created in a process that involves a non-reversible dressing of the excitons and therefore an erasure of the laser phase. For the sake of completeness, in Appendix B we detail the polariton energy relaxation process that takes place under pulsed excitation at the bare exciton level with one beam only.

Above a given pump intensity threshold, polaritons with $k_x \sim 0$ evolve towards two states with momenta $\pm k_x$ [Fig. 7.1(a)]. As sketched in Fig 7.1(b), this procedure results in the formation of four propagating polariton WPs. We label the macroscopic state of the WPs as ψ_1^A, ψ_2^A, ψ_1^B, ψ_2^B, where the superscript refers to the excitation beam, the subscript 1(2) is for WPs initially moving to the left (right), *i.e.* with $k_x < 0$ ($k_x > 0$). The direction of propagation is determined by the presence of local effective-barrier potentials (V_A and V_B), associated to a blue-shifted dispersion relation, coming from carrier-carrier repulsive interactions [36]. The densities of the polariton WPs are given by $n_j^{A,B} = \left|\psi_j^{A,B}\right|^2$, $j = 1, 2$.

WPs created by A have never been together with those generated by B, as sketched in Fig. 7.1(b). However, WPs with the same subscript j are in the same quantum state. Since all WP have the same spreading, we employ the usual terminology simply labeling each WP by its central value k_x. Using the capability of measuring directly in momentum space, a unique condition only achievable in light-matter condensates, we can assess whether or not WPs ψ_1^A and ψ_1^B (or ψ_2^A and ψ_2^B) are correlated to each other, being components of the same condensate. The two WPs propagating to the left are described by a common macroscopic order parameter

$$\Psi_1^{coh}(x) = \psi_1^A(x) + e^{i\phi}\psi_1^B(x), \tag{7.1}$$

while those propagating to the right are described by

$$\Psi_2^{coh}(x) = e^{i\phi}\psi_2^A(x) + \psi_2^B(x). \tag{7.2}$$

The phases are chosen to have inversion symmetry with respect to $x = 0$, because in our experiments we tune the intensities of the two lasers in order to get a symmetrical potential $V(x) = V(-x)$. In that respect, our condensates are related to each other through the symmetry of the excitation process.

Furthermore, our potential landscape renders an equal motion for ψ_j^A and ψ_j^B, *i.e.* equal momenta $|(k_x)_j^A| = |(k_x)_j^B| = k_x$. These are precisely the suitable conditions to observe coherence between two components spatially separated by d, *i.e.* $\psi_j^A(x - d/2) = \psi_j^B(x + d/2) = \psi_0(x)$, of a given condensate Ψ_j^{coh}. This coherence can be observed in **k**-space as we discuss now.

For the sake of clarity, we focus in the following discussion only on the left-propagating WPs. The corresponding order parameter in **k**-space can be written as:

$$\Psi_1^{coh}(k_x) = \psi_1^A(k_x) + e^{i\phi}\psi_1^B(k_x) = e^{-ik_x d/2}\psi_0(k_x) + e^{i(\phi + k_x d/2)}\psi_0(k_x) \tag{7.3}$$

with $\psi_0(k_x)$ being the Fourier transform of $\psi_0(x)$ [287]. This yields a momentum distribution

$$n_1^{coh}(k_x) = \left|\Psi_1^{coh}(k_x)\right|^2 = 2\left[1 + cos\left(k_x d + \phi\right)\right]\left|\psi_0(k_x)\right|^2. \tag{7.4}$$

The coherence between the two components produces interference fringes with a period

$$\Delta k_x = 2\pi/d. \tag{7.5}$$

Our aim is to observe the existence of interferences in **k**-space coming from this macroscopic two-component condensate. Far-field detection allows the direct measurement of momentum distributions, *i.e.* it gives a direct determination of the existence, and the period, of these interference fringes. It must be taken also into account that the measured total polariton density is formed by a condensed population, n^{coh}, coexisting with a thermal one [305], therefore the interference patterns visibility, ν, is expected to be lower than 1 (see § 7.2.1 where we study the visibility of the interference fringes in both real and momentum space versus time).

Our most important result is shown in Fig. 7.2(b): we indeed observe the interference fringes in **k**-space, described by Eq. 7.4, directly in the polariton emission. This certifies the correctness of our hypothesis that each couple of WPs (ψ_j^A, ψ_j^B) constitutes a two component condensate. Figure 7.2(a) shows the actual evolution in time of the four WPs schematically depicted in Fig. 7.1(a):

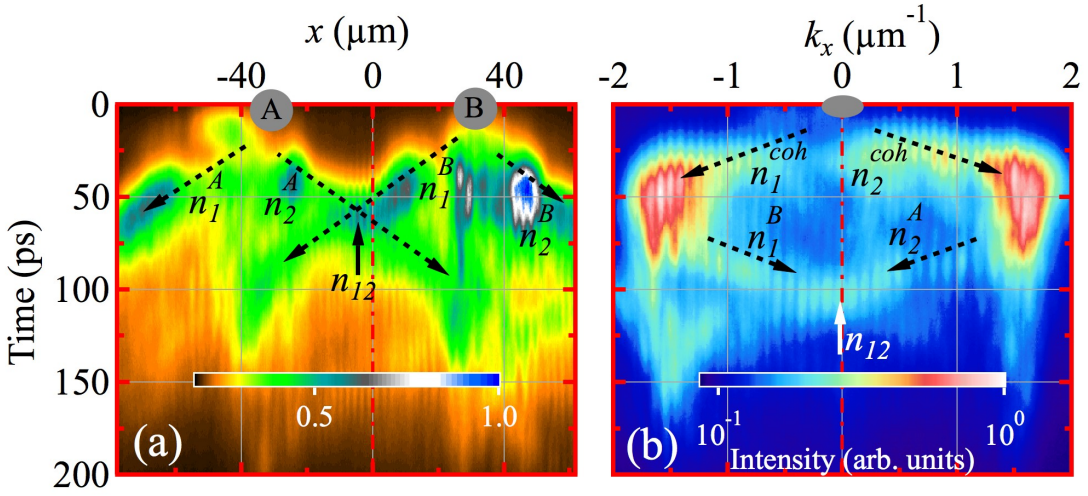

FIGURE 7.2: (a) Emission in real space, along the x axis of the ridge, versus time. Gray circles at $x = \pm 35$ μm indicate the spatial location of the A and B laser beams; the trajectories of the four WPs, n_1^A, n_2^A, n_1^B and n_2^B, are indicated by the dashed arrows. (b) Momentum space emission, along k_x, versus time. The grey circle indicates that the laser beams, A and B, excite the ridge at $k_x \sim 0$. The dashed, black arrows indicate the acceleration of the condensates n_1^{coh} and n_2^{coh}, as well as the deceleration of the WPs n_1^B and n_2^A. Intensity is coded in a normalized, logarithmic false color scale.

our results clearly demonstrate that the distance d between the two components of each condensate (n_j^A, n_j^B where $j = 1, 2$) remains constant with time during the first $\sim$ 70 ps ($d = d_{AB}$), as evidenced by the dashed parallel arrows. Figure 7.2(a) contains also interesting real-space interferences when WPs ψ_2^A and ψ_1^B overlap in real space at 66 ps that we shall discuss in more detail below. A peculiarity of our experiments is that we observe the dynamics of the coherence; this allows us to determine that the two components of the condensate are phase locked since there is not any drift in the interference patterns.

As readily seen in Fig. 7.2(b), an initial acceleration of the four WPs, from rest, $k_x = 0$, to $k_x = \pm 1.6$ μm^{-1} during the first 40 ps, is followed by a uniform motion taking place from 40 ps to 70 ps. The interference pattern of each condensate is observed until $\sim$ 75 ps, instant at which ψ_1^A and ψ_2^B disappear from the sample region imaged in the experiments. Then WPs ψ_1^B and ψ_2^A are progressively slowed by the presence of the barriers at the excitation spots (V_A/V_B halts ψ_1^B/ψ_2^A). When these two WPs, which are the components of two different condensates Ψ_1^{coh} and Ψ_2^{coh}, are stopped (at $\sim$ 100 ps) another interference appears in **k**-space, but now at $k_x = 0$ as it corresponds to WPs at rest. This means that these two condensates also interfere with each other, being remarkable that Ψ_1^{coh} and Ψ_2^{coh} still preserve some kind of mutual coherence, supporting the functional form of Eqs. 7.1 and 7.2. For longer times, the two WPs move again, as can be observed in Figs. 7.2(a,b), becoming more difficult to track their trajectories.

Note that our measurements are performed averaging over millions of shots of the pulsed laser, therefore if ϕ were a phase determined by the projection involved in the measurement process [290,

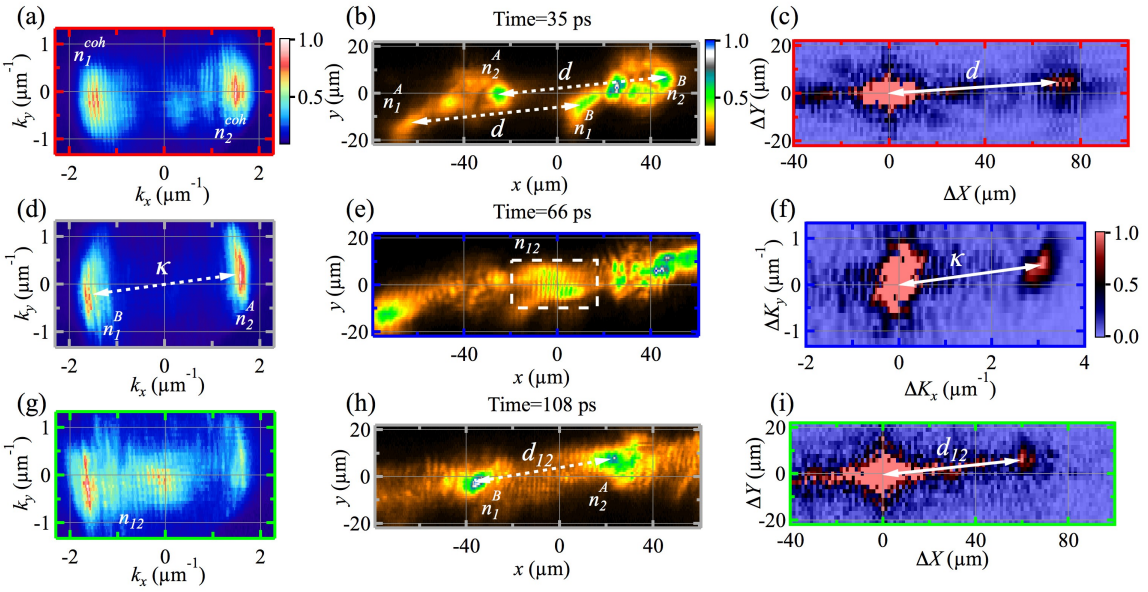

FIGURE 7.3: (a) Momentum distribution $n(\mathbf{k})$, at 35 ps after the excitation, showing the condensates n_1^{coh}/n_2^{coh} at $k_x = \mp 1.6\ \mu\text{m}^{-1}$, respectively. (b) Corresponding $n(\mathbf{r})$ distribution showing WPs n_1^A, n_2^A, n_1^B and n_2^B. (c) Fourier transform of $n(\mathbf{k})$, obtaining a frequency at $\Delta X = d = 70\ \mu$m. (d) Momentum distribution $n(\mathbf{k})$ at 66 ps showing n_1^B and n_2^A at $k_x = \mp 1.6\ \mu\text{m}^{-1}$, respectively. (e) Real space distribution $n(\mathbf{r})$ showing the interferences of n_{12} at $x = 0$, created by the overlapping in real space of ψ_1^B and ψ_2^A. White dashed rectangle marks the region of interest where the interference occurs. (f) Fourier transform restricted to the region of interest in $n(\mathbf{r})$, showing a frequency at $\Delta K_x = \kappa = 3.2\ \mu\text{m}^{-1}$. (g) Momentum distribution $n(\mathbf{k})$ at 108 ps, showing the interferences n_{12} at $k_x \sim 0$. (h) Corresponding $n(\mathbf{r})$ distribution showing n_1^B and n_2^A. (i) Fourier transform of $n(\mathbf{k})$, obtaining a frequency at $\Delta X = d_{12} = 60\ \mu$m. Intensities in the false color scales for momentum, real and Fourier spaces are normalized to unity. The tilt in all panels originates from the orientation of the ridge with respect to the entrance slit of the spectrometer. The white dashed arrows mark the distances in real- and momentum-space between WPs. The full arrows show these distances in the corresponding Fourier transform. See supplemental videos of the polariton dynamics in real and momentum space at http://link.aps.org/supplemental/10.1103/PhysRevB.90.081407 for further details.

291], it would take a random value in each realization. Then, averaging over all the possible results, the interference pattern would not be observed. In first place we must emphasize that the WPs $n_1^{A(B)}$ and $n_2^{A(B)}$, created by the A (B) beam, possess the same phase since they initially split from the same condensate with a given phase. In second place, as a consequence of the symmetry $V(x) = V(-x)$ of the potential, the whole state of the four WPs, Ψ, is symmetric, both in real- and momentum-space. In other words, the spatial symmetry involved in the buildup of the condensates determines the relative phase $\phi = 0$. In this sense, they are not independent from each other although they have never before coincided in real space.

Further insight into the quantum coherence is obtained by analyzing in detail the interferences occurring in momentum- and real-space. Accordingly, we present in Fig. 7.3 2D maps of the polariton emission at three consecutive, relevant times. Given the lateral width of 20 μm of our

MC ridges, we provide full images of the PL emission in 2D spaces. We focus on the correspondence between the period of the interference patterns in each space (real and momentum) and the separation between the WPs in the complementary space. Figure 7.3(a) shows the momentum distribution $n\left(k_x, k_y\right)$, 35 ps after the impinging of the laser beams on the sample. The coherence of each Ψ_j^{coh} is observed by the conspicuous interference patterns, n_j^{coh}, centered at $k_x = \pm 1.6\ \mu\text{m}^{-1}$. In both cases, the fringes period amounts to $\Delta k_x = 0.088(5)\ \mu\text{m}^{-1}$ that, according to Eq. 7.5, should correspond to a distance between WPs of $d = 71(4)\ \mu$m. This is in very good agreement with the experimental distance seen in Fig. 7.3(b): the two components of each condensate, n_j^A and n_j^B, are separated by $d \simeq 70\ \mu$m (see dashed arrows). Our findings are further supported by the Fourier transform map of $n\left(k_x, k_y\right)$ shown in Fig. 7.3(c): a well-defined Fourier component at $\Delta X = d = 70\ \mu$m is obtained, in accordance with the separation directly observed in real space.

Coherence in real space have been profusely studied in cold atoms [15, 280, 306], excitons [124, 307] and polariton condensates [21, 22, 139, 168, 172, 308]. In the recent years, new time-resolved studies on the phase-locking mechanisms of polariton condensates have been performed [309–311]. G. Christmann and coworkers demonstrated in Ref. [310] the phase locking dynamics of two independent, spatially separated and expanding condensates by means of time-resolved and interferometric measurements, under pulsed, non-resonant excitation. H. Ohadi and coworkers have claimed to observe the dissipative coupling between two spatially separated condensates leading to a relative in-phase or out-of-phase locking between them [311]. In this work, the authors recall Ref. [312], which studies theoretical mechanisms of radiative coupling between individual condensates via polaritons that are emitted outside the MC through the DBR mirrors. This coupling mechanism might be also interesting for the results reported here.

Our experiments also show interferences in real space between two condensates, similar to those reported in atomic BECs [15, 280]. This is shown in Fig. 7.3(e) at 66 ps when WPs ψ_2^A and ψ_1^B meet each other at $x \sim 0$. The appearance of interference fringes in real space, n_{12}, signals unambiguously to coherence between these two WPs. Since real and momentum spaces are reciprocal to each other, equivalent results for the interference patterns are expected. The complementary expression in real space to Eq. 7.5 reads now $\Delta x = 2\pi/\kappa$, where Δx is the period of the fringes and κ the difference in momentum of the propagating WPs. The experimental period of the fringes, seen in the dashed-rectangle area in Fig. 7.3(e), $\Delta x = 1.99(17)\ \mu$m, should correspond to $\kappa = (k_x)_2^A - (k_x)_1^B = 3.2(2)\ \mu\text{m}^{-1}$. This is again borne out by our results, as shown in Fig. 7.3(d), where the emission in $\mathbf{k}$-space shows clearly that WPs ψ_2^A and ψ_1^B are counter-propagating with $k_x = \pm 1.6\ \mu\text{m}^{-1}$, respectively. Figure 7.3(f) shows the Fourier transform of n_{12} in the region enclosed by the rectangle in Fig. 7.3(e). It reveals a strong ΔK_x Fourier component at $3.1\ \mu\text{m}^{-1}$, in full agreement with the value of κ displayed in Fig. 7.3(d). Let us also emphasize that WPs first meet in real space at 66 ps, while interferences in momentum space are seen as early as ~ 10 ps demonstrating that the phase locking occurs before the WPs spatially overlap.

The third result that we present corresponds to the arrival at 108 ps of ψ_2^A and ψ_1^B to the excitation regions B and A, respectively. Here, they run into the hills of the photogenerated potentials V_B and V_A that elastically convert their kinetic energy into potential energy [62]. They slow down, halting, providing a new separation between WPs n_2^A and n_1^B, $d_{12} \sim 60$ μm [see Fig. 7.3(h)]. Their emission in momentum space, arising from $k_x \sim 0$, evidences an interference pattern with $\Delta k_x = 0.108(5)$ μm^{-1} [n_{12}, see Fig. 7.3(g)]. Once again, Eq. 7.5 predicts a separation $d_{12} = 60(4)$ μm between n_2^A and n_1^B, as observed in the experiments. For completeness, we also show in Fig. 7.3(i) the Fourier transform map of the density that exhibits an emerging component at $\Delta X = d_{12} = 60$ μm.

7.2.0.1 Filtering the emission of polariton droplets in real space

The filtering process presented in § 4.2.2 is also very useful in this experiment to determine the distance in momentum space, with high accuracy, between the counter propagating bullets that overlap at $x = 0$, giving rise to the buildup of coherence in real space, we recall here that instant at $t = 66$ ps compiled in Figs. 7.3(d-e).

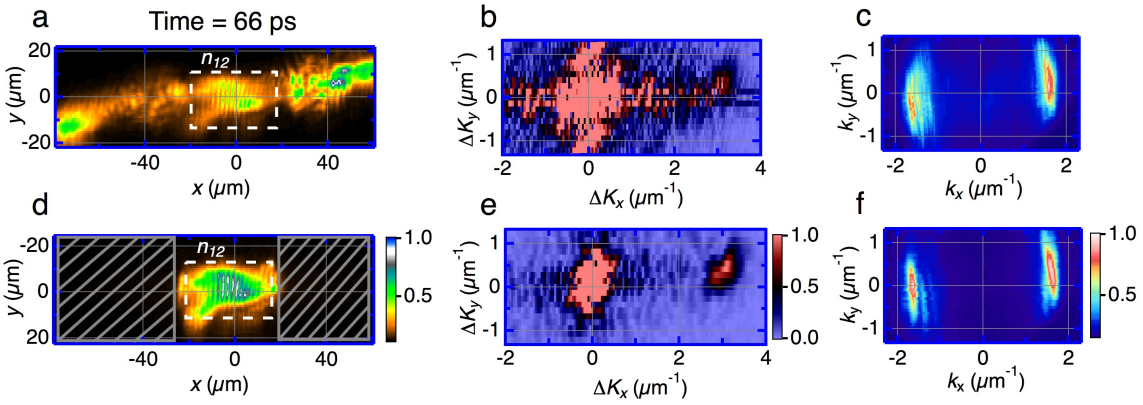

FIGURE 7.4: Improving the determination of frequencies in the Fourier analysis. (a) Real space map at $t = 66$ ps showing the polariton emission: the bullets ψ_1^B and ψ_2^A meet at $x \simeq 0$ giving rise to the interference pattern, n_{12}, enclosed by a white dashed rectangle. n_1^A/n_2^B is escaping from the imaged area at the left/right part of the figure and additional residual emission is seen at the excitation regions ± 35 μm. (b) and (c) corresponding *noisy* Fourier transform map of (a) and emission in momentum space, respectively. In the latter figure, some weak interferences at $k_x = \mp 1.6$ μm^{-1} emerge from the intensity emission of the escaping n_1^A and n_2^B bullets, respectively. (d) A much better defined interference pattern between ψ_1^B and ψ_2^A is obtained when razor blades are used to cover the spurious contributions away from $x \sim 0$. (e) Corresponding Fourier transform exhibiting a well-defined frequency at $\Delta K_x = 3.2$ μm^{-1}. (f) The filtering in real space gives rise also to a neat emission in momentum space, where the interference fringes at $k_x = \mp 1.6$ μm^{-1} are absent.

Figure 7.4(a,c,e) are the same real-space PL map, momentum-space PL map and FFT intensity map as those already described in Figs. 7.3(e,d,f), respectively.

Now, in Fig. 7.4(b) we plot the FFT intensity map of the total real-space distribution of polariton shown in Fig. 7.4(a). The direct FFT from this PL map renders a noisy distribution of frequencies, mainly from $\Delta K_x = \Delta K_y = 0$ [compare with Fig. 7.4(e)], hindering the possible identification of κ[2]. This FFT map noise arises from those regions far from $x = 0$ whose intensity is relatively higher (for example, the PL emitted from B area at $x = 40$ μm). These intensities, without any oscillation in real space and therefore contributing to the zero frequencies in the FFT map, blind other relevant frequencies (such as κ) in the FFT intensity map.

However, if real space filtering is applied in the overlapping region between n_2^A and n_1^B, Fig. 7.4(d), in first place the momentum space distribution, Fig. 7.4(f), is cleaned in the sense that only the velocities of these internal bullets are recorded. The obtention of their relative distance is done in a more proper way, as compared to Fig. 7.4(c). In second place, when the FFT is applied over this filtered real space PL map, we obtain a FFT map, Fig. 7.4(e), where now it is very clear to extract the value of κ and therefore, to obtain the total matching between this value and the relative distance in momentum space between n_2^A and n_1^B.

7.2.1 Visibility of the interference patterns

We address now the visibility of the interference fringes as an indication of the amount of polaritons participating in condensed states at a given time. We define the experimental visibility, either in real (ν_R) or momentum (ν_K) space, as $\nu = (I_{max} - I_{min})/(I_{max} + I_{min})$, where $I_{max(min)}$ is the maximum (minimum) intensity of the interference patterns. The time evolution of the maximum visibility of the coherent states at selected regions in each space is compiled in Fig. 7.5.

For the coherent states constituted by the left/right propagating WPs (n_1^{coh}/n_2^{coh}), for $t < 75$ ps, ν_K, grows from 4% at t=0 up to 24% in 25 ps with a later decay indicating a progressive loss of coherence. The visibility can be tracked up to 75 ps when ψ_1^A and ψ_2^B escape from the imaged area. From this instant on, we follow the visibility at $k_x = 0$ (n_{12}), when WPs ψ_2^A and ψ_1^B interfere as they are gradually stopped by V_B and V_A. Again an initial buildup of ν_K, *i.e.* of the coherence between the two WPs, is obtained followed by a rapid decay. The time-evolution of the coherence in real space, ν_R, in the region enclosed by the dashed rectangle in Fig. 7.3(e), is depicted in Fig. 7.5(b). As the WPs ψ_2^A and ψ_1^B counter-propagate towards B and A, respectively, ν_R slowly increases, reaching a maximum value of 32% at 66 ps, when they meet for the first time at midpoint, $x = 0$. Further crossings, originating from the oscillatory movement of ψ_2^A and ψ_1^B in the potential landscape created by V_A and V_B, give rise to a stair-like decay of ν_R extending more than 200 ps.

[2] As we already mentioned before, κ is the difference between the k_x values of the counter-propagating bullets n_2^A and n_1^B at $t = 66$ ps.

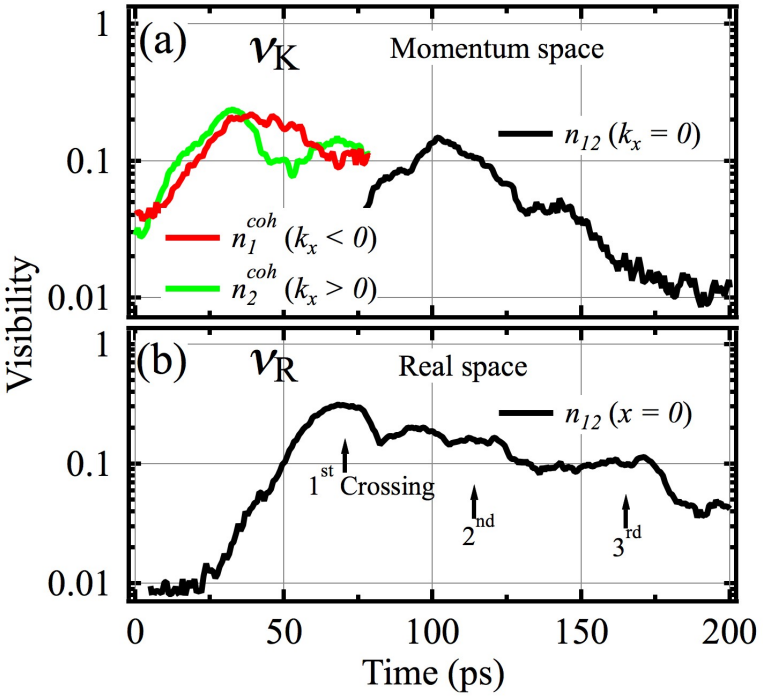

FIGURE 7.5: (a) Time evolution of the maximum visibility, ν_K, of the coherent states at selected regions (given in parenthesis) in momentum space: $n_1^{coh}\,(k_x < 0)/n_2^{coh}\,(k_x > 0)/n_{12}\,(k_x = 0)$ depicted with red/green/black lines. (b) Time evolution of the maximum visibility in real space, ν_R, of n_{12} at $x = 0$: black arrows mark the consecutive crossings between WPs ψ_2^A and ψ_1^B at this position. The ordinate axis is in logarithmic scale.

7.2.2 Young interference experiment with condensed polariton bullets

Experimentally, a priori, it is not trivial to identify which pair of propagating bullets in real space is forming the condensate manifested by the interference patterns in momentum space. This identification can be performed by a series of experiments in which we excite either with only one beam or with two beams (blocking the emission at certain regions in real space, using razor blades) as described in § 4.2.2. This procedure is presented in Fig. 7.6 compiling six related experiments, representing the same instant $t = 53$ ps after the laser excitation, to fully identify the components of the condensates. It is worthwhile to mention that bullets n_1^A and n_2^A (or n_1^B and n_2^B) do not show any interference pattern since they never overlap either in real- or momentum-space, even though they are mutually coherent.

Figure 7.6(a) shows the real space distribution of polaritons at $t = 53$ ps under A and B excitation. At this instant, the leftward [rightward] propagating bullets n_1^A and n_1^B [n_2^A and n_2^B] flow away from the exciton reservoir with a in-plane wave vector $k_x = -1.3$ [+1.3] μm^{-1}, Fig. 7.6(b), yielding interference fringes in momentum space given the spatial separation between them (see n_1^{coh} [n_2^{coh}]). We note that the tails of n_2^A and n_1^B wave packets start overlapping at $x = 0$ since an interference pattern between them is visible in real space, Fig. 7.6(a).

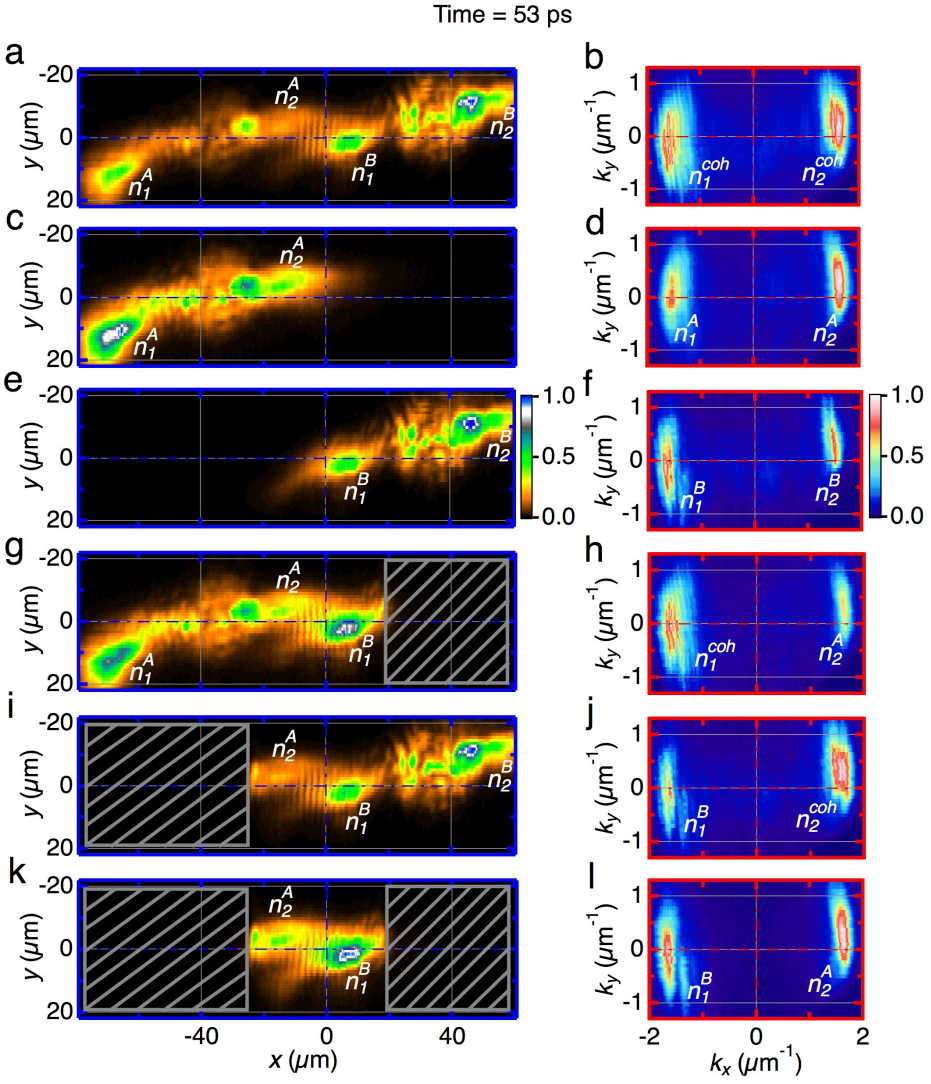

FIGURE 7.6: Filtering images in real space to identify the bullets forming the condensates in momentum space. Real- (left column) and momentum-space (right column) emission at 53 ps for different experimental conditions. (a) shows the four propagating bullets n_1^A, n_2^A, n_1^B and n_2^B at positions $x \sim -65, -15, +5, +55$ μm, respectively, created by two, A and B, laser beams. The equal separation between $n_1^A \leftrightarrow n_1^B$ and $n_2^A \leftrightarrow n_2^B$ gives rise to interference patterns in momentum space, (b) with the same fringe period, Δk_x, at both, positive/negative, values of k_x. When only the A beam excites the sample, (c) bullets n_1^A and n_2^A do not give rise to any interference pattern in momentum space, (d) due to the absence of the corresponding n_1^B and n_2^B counterparts. An analogous situation is shown in (e,f) when exciting only with the B beam. A more subtle case is show in (g)/(i), where both beams, A and B, excite the sample but the emission from $x > 20$ μm/$x < -20$ μm is blocked by the right/left razor blade: This measurement process filters out the emission from the bullet n_2^B/n_1^A and destroys the n_2^{coh}/n_1^{coh} state, (h)/(j), where only an interference pattern is detected at $k_x = \mp 1.6$ μm^{-1}, respectively. Finally, when both bullets n_1^A and n_2^B are blocked by the razor blades, (k), the interference patterns are completely absent in momentum space, (l).

Now we consider the simple case in which we only excite the ridge with the A [B] pulse, Fig. 7.6(c) [(e)]. Only two bullets are created, n_1^A and n_2^A [n_1^B and n_2^B] and therefore interference patterns are not visible in real nor momentum space, see Fig. 7.6(d) [(f)] where bullets n_1^A and n_2^A [n_1^B and n_2^B] propagate with $k_x = \mp 1.3$ μm^{-1}, respectively.

For the following panels in Fig. 7.6 we discuss the situation in which A and B impinge on the ridge and real space filtering is performed in the polariton PL in order to systematically analyze the origin of the interference fringes in momentum space. In Fig. 7.6(g) [(i)] the bullet n_2^B [n_1^A] is filtered out in the left [right] region of the real space distribution (see gray, filled rectangle) in order to remove the interference pattern in momentum space, Fig. 7.6(h) [(j)], produced by the mutual overlap with the bullet n_2^A [n_1^B], propagating with the same k_x value ($+1.3$ [-1.3] μm^{-1}). We only observe interferences in momentum space, n_1^{coh} [n_2^{coh}], arising from the leftward [rightward] propagating polariton bullets.

Finally, in Fig. 7.6(k) we filter out the bullets n_1^A and n_2^B, propagating in the external sides of the A and B potentials. In this situation, only the real space interference at $x = 0$ between n_2^A and n_1^B survives. We are totally erasing the overlap between bullets moving at the same k_x in momentum space, see Fig. 7.6(l) where no interference patterns are visible in comparison with the initial situation shown in Fig. 7.6(b).

7.2.3 Labeling bullets after a real space encounter

An interesting question that can be discussed in the encounter of bullets ψ_2^A and ψ_1^B at $x = 0$ and $t = 66$ ps, is whether the propagating bullets after the mutual overlap are a mixture of the initial crossing bullets and therefore whether they conserve their identity. The answer to this question can be elucidated by inspecting the morphology of the bullets at times slightly larger than 66 ps, as shown in Fig. 7.7, which indicates that they do maintain their identity, as we discuss in the following.

Figure 7.7(a,b,c) shows the real space distribution of polaritons at 74 ps after the laser excitation with A, B and $A + B$ beam(s), respectively. Figure 7.7(a) [(b)] shows the rightward [leftward] propagating bullet n_2^A [n_1^B] located at $x \sim 0$, a full white [red] line depicts the PL profile distribution of the bullet. Figure 7.7(c) displays an interference pattern n_{12} at $x = 0$, formed by the mutual overlap between n_2^A and n_1^B, as a guide to the eye, we depict again the profile lines, shown before, under the excitation configuration $A + B$. As we can see, the morphology of the bullets is preserved after the real space encounter, and therefore we conclude that the bullets conserve their identity in the whole crossing process.

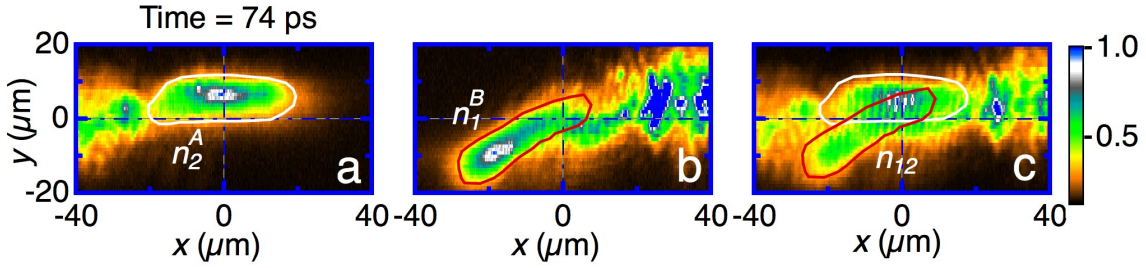

FIGURE 7.7: Labeling bullets after a real space encounter. Emission in real space at 74 ps: (a) exciting the ridge with laser beam A only, where the bullet n_2^A is identified and its shape is highlighted by the white line; (b) exciting the ridge with laser beam B only, where the bullet n_1^B is identified and its shape is highlighted by the red line; (c) exciting the ridge with both laser beams A and B, where bullets ψ_2^A and ψ_1^B give rise to the interference pattern labeled n_{12}. The highlighting contours are copied from panel a and b to identify the individual bullets involved in the crossing, demonstrating that both retain their identity after the encounter.

7.2.4 Scaling behavior of $\Delta k_x = 2\pi/d$ and temporal matching between pulses

In this section we discuss how the relative spatial-temporal coordinates of the A and B excitation beams modify the interference patterns in momentum space. In the first case, Eq. 7.5 predicts the spatial separation between the two components of a condensate, d, when they display interference patterns in momentum space with a certain modulation of the fringes given by Δk_x. In the second case, the temporal variation between the pulses impinging on the sample creates two delayed pairs of ballistic bullets which do not overlap in the acceleration process.

Let us first consider the spatial variation between pulses. Figure 7.3 describes two instants, $t = 35$ and 108 ps, where different Δk_x are obtained under different spatial separations between WPs (d and d_{12}), determined by the movement of polariton bullets in the potential profile. In this subsection, we compile in Fig. 7.8 three cases where the A and B lasers impinge, on a similar ridge to that used in the previous sections, at three chosen separations, 120, 100 and 60 μm. Now the new experimental conditions yield that the main $|k_x|$ value of propagating polaritons is ~ 1.1 μm^{-1}. An analysis of the data of Fig. 7.8(a) yields a value of $\Delta k_x = 0.053(4)$ μm^{-1}, corresponding to a distance $d = 119(9)$ μm. Similarly, Fig. 7.8(b)/(c) displays a period of $\Delta k_x = 0.065(3)/0.105(3)$ μm^{-1}, corresponding to a distance $d = 97(4)/60(2)$ μm, respectively, reinforcing the aforementioned prediction.

For the sake of clarity, Fig. 7.8(d) compiles the PL versus k_x of the time integrated area (from 0 to 20 ps) corresponding to the acceleration process (the bullet pairs are spatially separated in the whole process) for the three distances explained before. This representation of the momentum space oscillation clearly shows that the periodicity in k_x, for the distance $d = 60$ μm, is doubled for the case of $d = 120$ μm.

We now turn our attention to the case where we introduce a relative temporal delay between A and B pulses, keeping constant their spatial separation, $d \simeq 80$ μm. Figure 7.9 compiles the real-

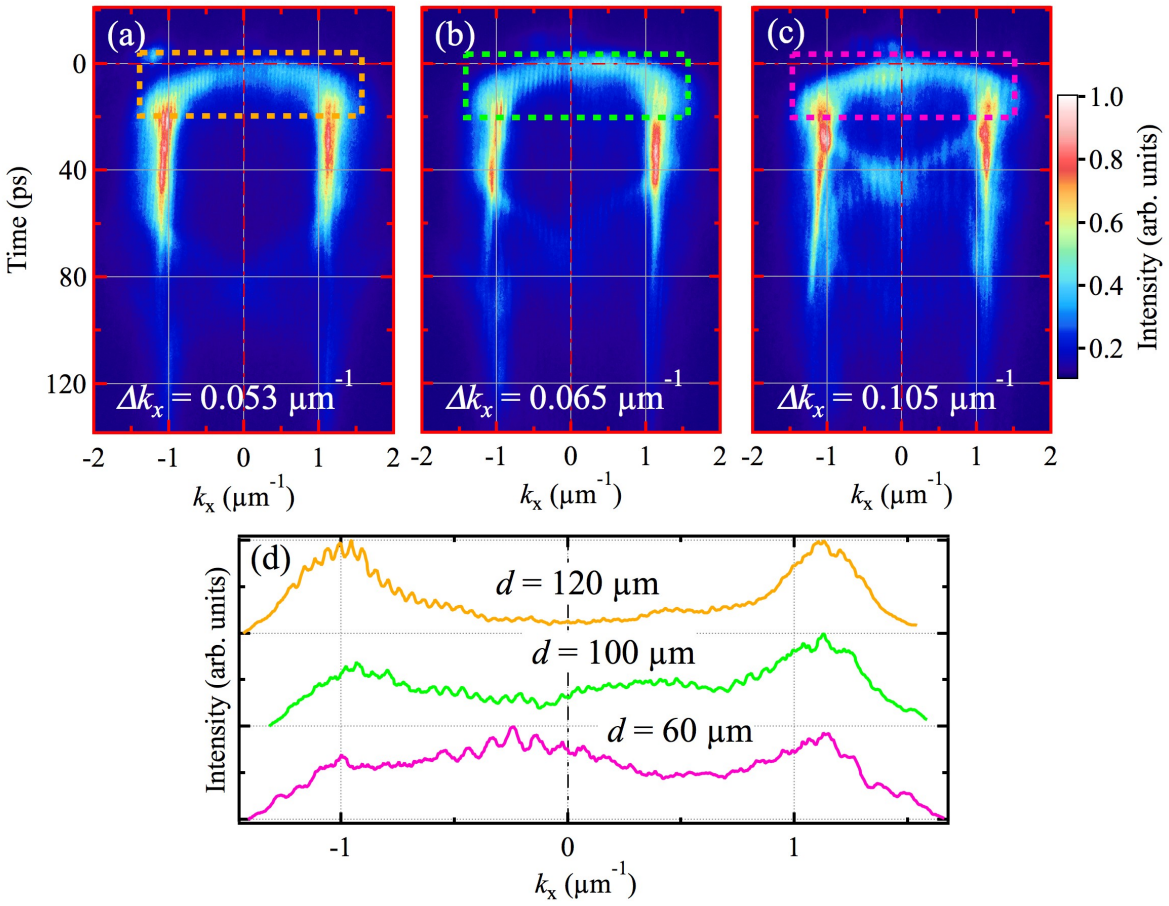

FIGURE 7.8: Momentum space emission along k_x versus time, showing interference patterns (see dashed rectangles), for different distances d between two pulsed excitation laser beams: (a), 120 μm; (b), 100 μm; and (c), 60 μm. (d), Time-integrated momentum distribution in the regions enclosed by the rectangles.

(upper row) and momentum-space (lower row) dynamics of polaritons for three different temporal delays $\Delta t = t_A - t_B$: $\Delta t_1 = 0$ delay (first column), $\Delta t_2 = 15$ ps (second column) and $\Delta t_3 = 45$ ps (third column).

In the first case the simultaneous arrival of the beams yields an equivalent situation to the one discussed previously in this section, an interference pattern in the acceleration process spans from 0 to $|1.2|$ μm $^{-1}$, Fig. 7.9(b), given the identical speeds between leftward and rightward propagating bullets in real space, Fig. 7.9(a). Further instants in the real space dynamics correspond to situations that we have deeply discussed in this Chapter, such as: the mutual overlap at $x = 0$ ($t \simeq 20$ ps), re-amplification of the internal bullets intensity when halting in the tails of the A and B repulsive potentials, etc. Figures 7.9(c,d) shows the case of a $\Delta t_2 = 15$ ps temporal delay, which totally changes the experimental configuration of the experiment. In such a configuration, the polariton WPs are created at a different time and the subsequents instants of equal acceleration and mutual overlap at $x = 0$ do not happen anymore, see Figs. 7.9(c) and 7.9(d), respectively. It is remarkable to note that in Fig. 7.9(d) a weak interference pattern is observed at the coordinates

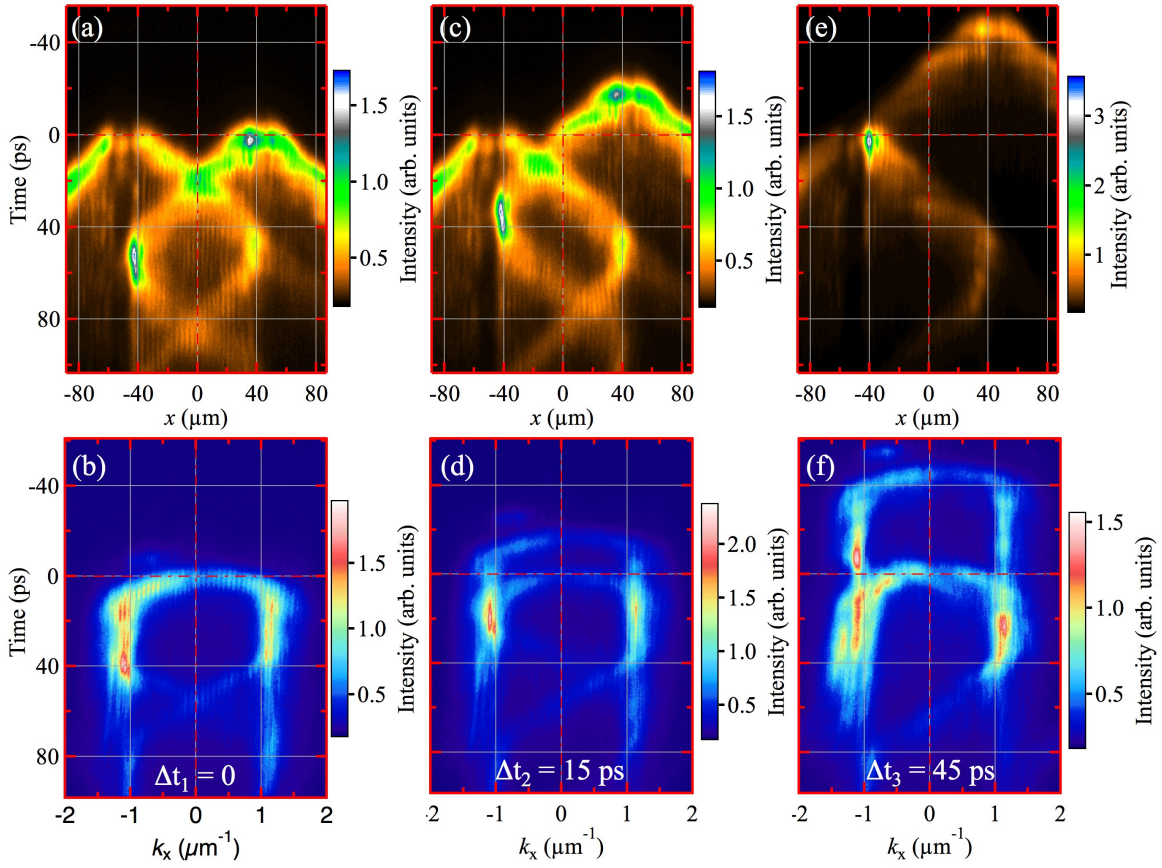

FIGURE 7.9: Temporal variation between pulses and eventual disappearance of interferences in momentum space, three different delays are used: $\Delta t_1 = 0$ delay (first column), $\Delta t_2 = 15$ ps (second column) and $\Delta t_3 = 45$ ps (third column). The dynamics of the polariton PL is resolved in real space (upper row) and momentum space (lower row). The PL is coded in a linear, false color scale.

$(k_x, t) = (+0.5\ \mu\text{m}^{-1}, 50\ \text{ps}\ )$ arising from the overlap in momentum space between two spatially separated WPs, distanced by $\sim 75\ \mu$m. At this instant, they are accelerating rightwards, moving away the repulsive barriers at the pump spots and the WPs are located at the spatial coordinates ~ -25 and $\sim 50\ \mu$m, respectively. A longer delay $\Delta t_3 = 45$ ps, Figs. 7.9(e,f), further increases the asymmetry of the experimental situation, where now the bullet n_1^B impacts against the A barrier and n_2^A, which was starting his propagation at that moment. As expected, no interferences in momentum space are observed again in this last case.

7.2.5 Coherence in momentum space using a single spot excitation

The observation of coherence in momentum space between two spatially separated condensates can be achieved in a simple way under single spot excitation. In this case, the pump spot excites an excitonic reservoir that, in turn, creates a polariton condensate that is ejected rightwards and leftwards ($\pm k_x$, respectively), away from the repulsive potential, similarly to what happened with

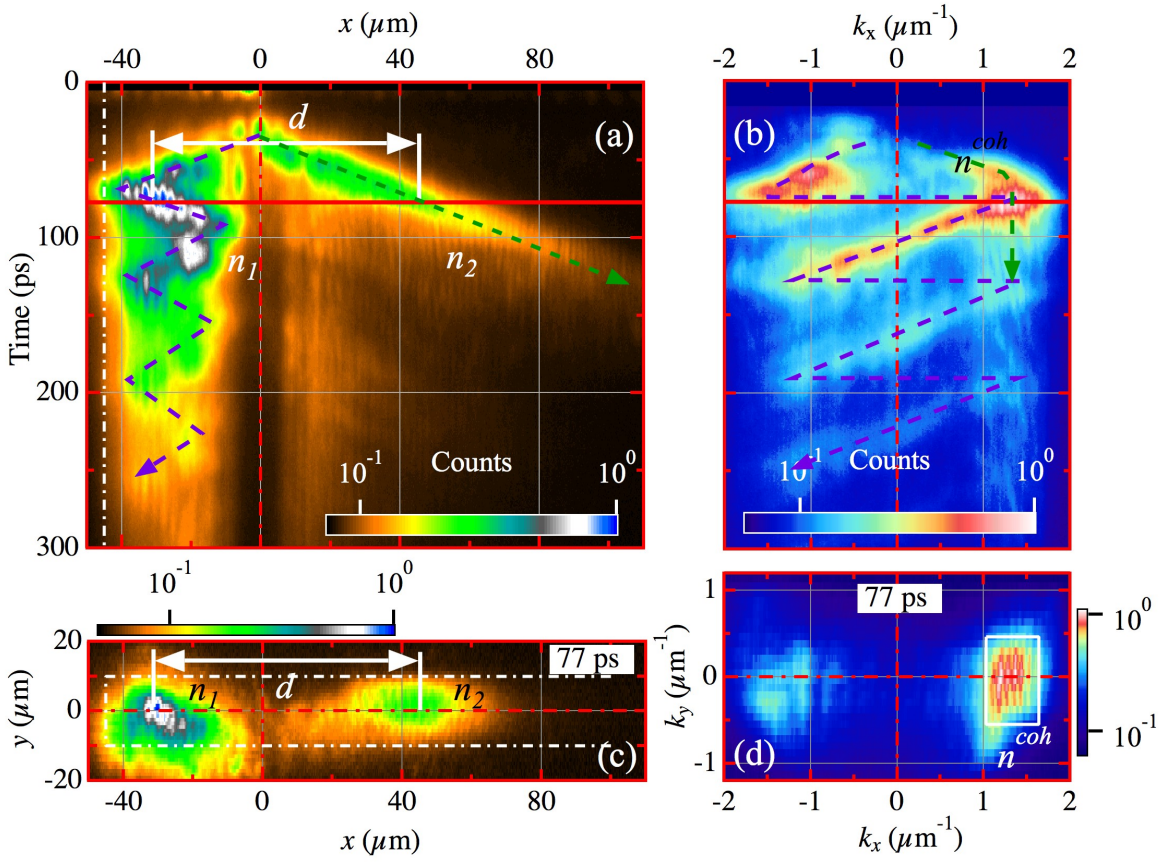

FIGURE 7.10: (a)/(b) Dynamics of the polariton PL versus x/k_x at $y = 0/k_y = 0$, same excitation conditions as those described for the A and B pulses are used in this experiment, the laser spot is placed at the real space origin, 45 μm far from the left edge of the rige. The trajectory in real and momentum space of the leftward/rightward propagating bullet $n_{1/2}$ is highlighted with a purple/-green, dashed arrow. The full, horizontal, red line at $t = 77$ ps points out the instant when n_1 and n_2, distanced in real space by $d \simeq 75$ μm overlap in momentum space, n^{coh}, at $k_x \simeq +1.3$ μm^{-1}. (c)/(d) Real/momentum space PL distribution at 77 ps after the pulsed excitation, panel (c) shows the n_1 and n_2 polariton droplets, spatially separated by d, propagating rightwards, whilst panel (d) shows the mutual overlap of these bullets in momentum space, forming the interference pattern n^{coh}, boxed in a full-line, while rectangle. A white, dot-dashed line marks the limits of the ridge. The PL is coded in all panels in a normalized, logarithmic, false color scale.

each of the excitation spot in the experiments described in § 7.2. In order to produce interferences in momentum space, we have to force the direction of propagation reversal in one of the polariton bullets. The way to do so is to force the elastic reflection of one of the bullets at the edge of the ridge, which constitutes an infinite potential wall (more details about these elastic reflections are discussed in § 11.2.1 and 11.2.3), whilst the other one propagates freely at a constant speed. In this manner, both polariton droplets propagate with the same speed (same k_x) and yield interferences in the momentum space distribution while being spatially separated.

Figure 7.10(a,b) compiles the polariton PL dynamics map in both real and momentum spaces at $y = 0$ and $k_y = 0$, respectively. The photo-generated excitons within the excitation area of the pump spot [$x = 0$, see vertical, dot-dashed, red line in Fig. 7.10(a)] create a repulsive potential

barrier whose spatial width is ~ 17 μm. The two leftward and rightward propagating bullets (n_1 and n_2) originate from $x = 0$ and rapidly accelerate in presence of the excitonic potential. The bullet n_2 propagates freely along the positive direction of x, at a constant speed of $v_x = +0.82$ μm/ps, where its dynamics is time-resolved in the spatial region of visualization up to $t = 120$ ps. The vertical interference fringes observed along the propagation of n_2, and also at subsequent instants and $x > 0$ positions arise from backscattered polaritons within the disordered photonic potential of the MC ridge (similar effects have been previously reported in Ref. [61]). We further discuss on this backscattering phenomenon in Appendix D. The polariton condensate n_1 remains trapped between the left edge of the ridge and the excitonic barrier (dot-dashed white and red lines, respectively). n_1 performs a zig-zag movement in real space [see dashed, purple arrow in 7.10(a)] having elastic collisions agains the ridge's border and soft decelerations and accelerations in the surroundings of the exciton barrier (due to the exchange between kinetic and potential energy). The dynamics of this bullet is lost after ~ 250 ps, the PL of n_1 is longer (more than 300 ps) than the one of n_2 since the former one is continuously amplified by the excitons at $x = 0$ (further details on the re-amplification of polariton bullets in presence of an excitonic reservoir are addressed in § 11.2.4).

Reciprocally, Fig. 7.10(b) shows the momentum space (k_x and $k_y = 0$) dynamics of n_1 and n_2. In the latter case, an initial acceleration from $k_x \approx 0$ is observed, n_2 acquires a constant momentum value of $\sim +1.3$ μm^{-1} when its position is sufficiently far away from the repulsive interactions of the reservoir at $x = 0$. In the former case, n_1 is initially accelerated leftwards, reaching a minimum value of -1.3 μm^{-1} at $\sim$70 ps. Then, the elastic reflection agains the border of the ridge instantaneously changes its speed from -1.3 to $+1.3$ μm^{-1}, yielding the overlap of n_1 and n_2 at $\{k_x[\mu\text{m}^{-1}], t[\text{ps}]\} = \{+1.3, 77\}$, and therefore forming the coherent state in momentum space, dubbed n^{coh}, that shows a conspicuous interference pattern [a full, red, horizontal line marks this relevant instant in both Figs. 7.10(a,b)]. After this remarkable instant, the trajectory of n_1 in momentum space draws a sawtooth function, due to its confinement between the wall and exciton potentials.

Figure 7.10(c) shows the PL map of the polariton real space distribution at 77 ps. We mark again the relative distance $d \simeq 75$ μm between the rightward propagation bullets n_1 and n_2. Figure 7.10(d) displays the momentum space distribution of polariton at the same instant, 77 ps, where n_1 and n_2 mutually overlap at $k_x \approx + \pm 1.3$ μm^{-1}. The fringes periodicity is $\Delta k_x = 2\pi/d = 0.083$ μm^{-1}, given by the bullets separation in real space. Polaritons propagating with negative values of k_x (visible in the PL map at $k_x \simeq -1.3$ μm^{-1}) corresponds to polaritons re-amplified by the exciton reservoir that move leftwards in the $x < 0$ region and also to backscattered polaritons in the region $x > 0$.

7.3 Conclusions

In summary, the convenience of monitoring the evolution of exciton-polaritons in semiconductor MCs, through the detection of emitted light, makes this system an ideal platform to study quantum coherence properties in real- as well as in momentum-space. Profiting from this fact, we have demonstrated the existence of quantum remote coherence between spatially separated polariton condensates whose phase is determined by the symmetry of the excitation conditions and therefore is constant in each realization of our multi-shot experiments. This issue is related to the superposition principle in quantum mechanics and it is crucial to understand how mutual coherence is acquired.

Chapter 8

Spin textures in quasi-one-dimensional polariton condensates

This Chapter is devoted to the investigation, through polarization-resolved spectroscopy, of the spin transport by propagating polariton condensates in a quasi-1D MC ridge along macroscopic distances. In planar semiconductor MCs, the splitting of the transverse electric (TE) and magnetic (TM) modes of the cavity [245] induces an effective magnetic field, which on its own produces a precession of the polaritons spin, when they propagate over macroscopic distances. This effect is well-known as the optical spin Hall effect [246, 313] and it was first predicted by Kavokin and co-workers [314] as an analogue of the electronic spin Hall effect [315, 316]. Initial experiments were conducted with resonant excitation [313] making use of Rayleigh scattering [317] or tightly focused laser spots [318] to excite multiple states in reciprocal space. These experiments represented purely linear effects, not relying on the excitonic component of polaritons [319]. The presence of quantum well excitons is required for non-resonant excitation, leading to the spontaneous formation of a propagating polariton condensate [246]. The effective magnetic field representing the optical spin Hall effect can be utilized, for example, to generate polarization textures [246, 320], where the polaritons propagate in rings spreading in real space, showing oscillations of the polarization degree in azimuthal angle and time; to convert the spin to orbital angular momentum [321]; to create spin-polarized vortices [321–324] and to form half dark solitons [176, 325] and very similar structures [326] in the wake of an obstacle. Recent theoretical work has also studied the role of the optical spin Hall effect in driving polarized bright solitons [327] and other spin patterns [328, 329].

In this Chapter, we investigate optically the collective spin dynamics of polariton condensates moving along macroscopic distances in a quasi-1D MC ridge. The discretization in energy of the

LPB in our quasi-confined structure has notable consequences in the coherent transport of the spin vector. In the first place, the confinement renders a TE-TM mode splitting, which remains for zero in-plane wavevector, and acquires larger values than the TE-TM splitting in 2D MCs. Furthermore, a spectral analysis of the spin transport reveals different polariton spin textures to those observed in 2D systems [246]. The richness of these textures is related to the energy dependent speed of propagation of polaritons in our system with lowered dimensionality. The ballistic propagation of spin polarized polaritons along the ridge is observed over distances of ~ 100 μm.

This Chapter is organized as follows. In § 8.1 we discuss the sample and the experimental setup. In § 8.2 we present and discuss our results; we first show, under *cw* excitation, the optical spin Hall effect [246, 314] in a quasi-1D structure, discussing the s_z oscillations in real space, for a σ^+-polarized pump. In § 8.2.1 we systematically investigate the distribution of the Stokes components as function of the PL energy and position along the ridge. In § 8.2.2 we demonstrate that the s_z precession is lost under linear excitation and/or high power excitation conditions. In § 8.3 the experiments are compared with simulations of the spinor-polariton condensate dynamics based on a generalized GP equation, modified to account for incoherent pumping, decay and energy relaxation within the condensate. Finally, in § 8.4 we provide the conclusions of this work.

8.1 Experimental setup

The sample used for the experiments is the high-quality $5\lambda/2$ *AlGaAs*-based MC described in § 3.2. We perform our experiments in the ridge structure shown in Fig. 3.5, whose dimensions are 20×300 μm^2.

The sample is excited with a *cw* laser, tuned to the first high-energy Bragg mode of the MC (1.612 eV). The *cw* laser is chopped at 300 Hz with an on/off ratio of 1:2 in order to prevent unwanted sample heating. We focus the laser beam on the sample through a microscope objective to form a 10 μm-$\varnothing$ spot. The same objective is used to collect (angular range $\pm 18°$) the PL, which is directed towards a 0.5 m imaging spectrometer. Calibrated wave plates and polarizers were positioned in the excitation line, to control the polarization state of the excitation beams, and also in the detection path, to analyze the polarization state of the emitted polariton PL.

In our experiments, polaritons propagate predominantly along the x axis of the ridge [see Fig. 3.6(a)]. Therefore in all the images presented in the Chapter, where the y direction is not shown, the spectral PL distribution is analyzed along the x axis from a $\Delta y = 2$ μm-wide, central region of the ridge. However, for the sake of completeness, the full 2D polariton intensity and degree of circular polarization distributions are presented when appropriate.

8.2 Experimental results and discussion

Recently, E. Kammann and coworkers reported an analogue of the optical spin Hall effect of an exciton-polariton condensate in a planar MC, under *cw*, non-resonant, circularly-polarized excitation [246]. Circularly polarized condensates propagate over macroscopic distances, while the collective condensate spins coherently precess around an effective magnetic field. This effective magnetic field can be expressed as $\overrightarrow{H}_{\text{eff}} = \frac{\hbar}{\mu_B g}\overrightarrow{\Omega}_k$, where μ_B is the Bohr magneton, g is the electron g-factor, and $\overrightarrow{\Omega}_k$ is the in-plane vector with the following components:

$$\Omega_x = \frac{\Delta_{\text{TM,TE}}}{\hbar k^2}(k_x^2 - k_y^2), \quad \Omega_y = \frac{\Delta_{\text{TM,TE}}}{\hbar k^2}k_x k_y, \tag{8.1}$$

where $\overrightarrow{k} = (k_x, k_y)$ is the in-plane wave vector of the polariton.

Here we study a similar phenomenon in our quasi-1D structure: we start focusing on the polariton distribution in real space and its degree of circular polarization, under *cw*, circular excitation, without resolving the PL energy.

Figure 8.1(a) shows the energy-integrated distribution of the polariton PL in real space, under σ^+-polarized, non-resonant excitation at $(x, y) = (0, 0)$ with a pump power of $3.75 \times P_{th}$. The power threshold for polariton condensation is $P_{th} = 2$ mW. The pump creates outflowing polariton condensates due to the repulsive interactions with the excitonic reservoir [36, 62]. The propagation inside the ridge is not purely 1D since slanted traces of the polariton flow are visible (see white dashed arrows as a guide to the eyes), as a result of the reflection of the fluid against the lateral borders at $y = \pm 10$ μm. Interference patterns in the PL, due to polariton-polariton scattering, are also observed (see, for example, the region enclosed by a dashed box). This effect has been also reported in the 2D case [160]. A FFT of this enclosed region, shown in Fig. 8.1(c), obtains the frequencies corresponding to counter-propagating polariton wave packets, with a difference in momentum propagation of $\Delta K_x \approx 3.4$ μm^{-1} (see the area enclosed by a dot-dashed box). The corresponding value of k_x matches the typical speed of polariton wave packets in 1D systems (~ 1 μm/ps) [40, 62].

Outside the pump spot, the potential energy is converted into kinetic energy. Polaritons also relax and lose energy through scattering with the excitonic reservoir and through intra-branch scattering [47, 62, 213]; the energy of condensed polaritons spans ~ 1.5 meV across the subbands (see below). Therefore, the description of the spin distribution in our quasi-1D structure, in the presence of polariton energy relaxation, becomes more complex than in 2D (where the ballistic spin precession occurs in a simpler dispersion relation). However, for the sake of simplicity, we show in Fig. 8.1(b) the energy-integrated distribution of the circularly-polarized component of the PL (s_z). The large red area in the central region corresponds to the predominantly spin-up aligned polaritons at the excitation area. The spin of leftwards and rightwards propagating polaritons

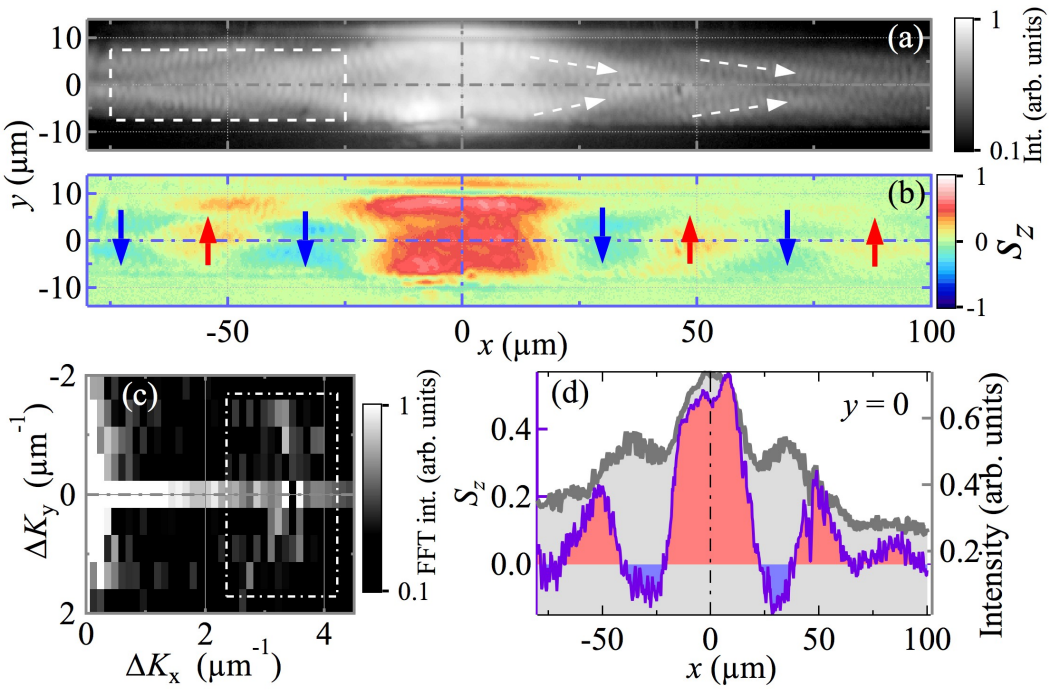

FIGURE 8.1: Collective polariton condensate spin precession in a quasi-1D ridge. (a) Polariton PL distribution in real space under non-resonant (1.612 eV), circular-polarized (σ^+) excitation at the center of the ridge. The pump power is $3.75 \times P_{th}$. Dashed white arrows sketch the direction of the polariton flow along its propagation. (b) Corresponding circular degree of polarization distribution (s_z). Vertical blue and red arrows highlight the spin precession, oscillating from negative (σ^-) to positive (σ^+) values, respectively. (c) FFT intensity of the region enclosed by a dashed, white rectangle in panel (a). The dot-dashed, white rectangle marks the region of relevant frequencies arising from interferences between propagating and backscattered polaritons in real space. The PL and the FFT map are coded in a logarithmic, false color scale, while a linear one is used for s_z. (d) PL (s_z) versus x in the central region of the ridge $y = 0$, plotted with a thick-gray (thin-purple) line.

precesses with a periodicity of ≈ 40 μm (see up- and down-arrows). The energy integration is responsible for the relatively low values of s_z. In Fig. 8.1(d) we quantify both the total PL (thick gray line) and s_z (thin purple line) as function of x at the central cross-section of the ridge ($y = 0$). The oscillations in the PL are caused by the fluid reflections against the borders of the ridge, obtaining large intensities when polaritons merge at the center [see arrows in Fig. 8.1(a)]. The spin oscillation and its damping along its propagation are clearly visible (thin purple line). Note that the periodicities of the PL and the spin oscillations do not match since they arise from different phenomena.

8.2.1 PL spectroscopy on the spin Hall effect

Figure 8.2 shows the energy- and space-resolved Stokes components of the polarized PL under the same excitation conditions as those described in Fig. 8.1. The polariton condensates span an energy of 1.5 meV around ~1.540 eV. We present here a spatial analysis of s_x, s_y and s_z at two

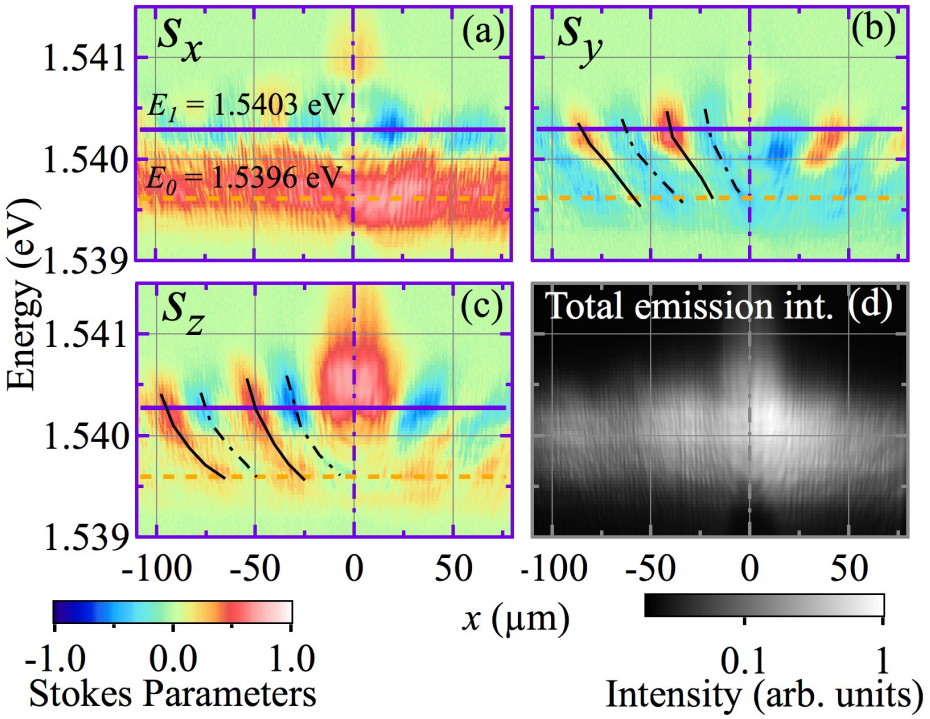

FIGURE 8.2: Stokes parameters of the polariton PL as function of energy and spatial position (x): (a) s_x, (b) s_y, and (c) s_z, respectively, under non-resonant (1.612 eV), circular-polarized (σ^+) excitation. (d) Corresponding PL. The pump power is $3.75 \times P_{th}$. Slanted, dot-dashed (solid) lines in panels (b,c) sketch the continuos shift with energy of the minima (maxima) values of s_y and s_z. The horizontal purple, solid (orange, dashed) line at $E_1 = 1.5403$ eV ($E_0 = 1.5396$ eV) marks the energy of interest used for the data depicted in Fig. 8.3. The PL (degree of polarization) is coded in a logarithmic (linear), false color scale.

different energies $E_0 = 1.5396$ eV and $E_1 = 1.5403$ eV, which correspond to those of polaritons condensing into the TM's and the TE's subbands (see in Figs. 8.2(a-c) dashed and solid horizontal lines), respectively. Figure 8.2(a) shows a weak spatial oscillation of s_x at E_1. Additionally, a small positive s_x from higher-energy excitons (from 1.5405 to 1.5415 eV) is present at $x = 0$; this was already present in Fig. 3.6(c), under below-threshold excitation. At E_0, s_x is large and positive, as expected from the TM-character of the lowest polariton subband [see Figs. 3.6(c) and 3.7(a)]. The diagonal component s_y displays a significant spatial oscillation with a period of ~ 40 μm at E_1 [see Fig. 8.2(b)]. In contrast, s_y barely oscillates around a value of ~ -0.2 at E_0. Figure 8.2(c) shows a highly σ^+-polarized population at $x = 0$ at E_1 and above, set by the excitation laser. At E_1 the condensed, spreading polaritons exhibit a precessing s_z, again with the same period of ~ 40 μm. This precession, although weaker, is also seen at E_0.

These oscillations in the Stokes parameters are similar to those previously reported in planar MCs, considering that in our case the propagation takes place along the ridge channel (equivalent to a given radial direction of the 2D rings, see Fig. 3 of Ref. [246]). The effective magnetic field, induced by the splitting of the TE-TM modes, is responsible for this precession of the polaritons

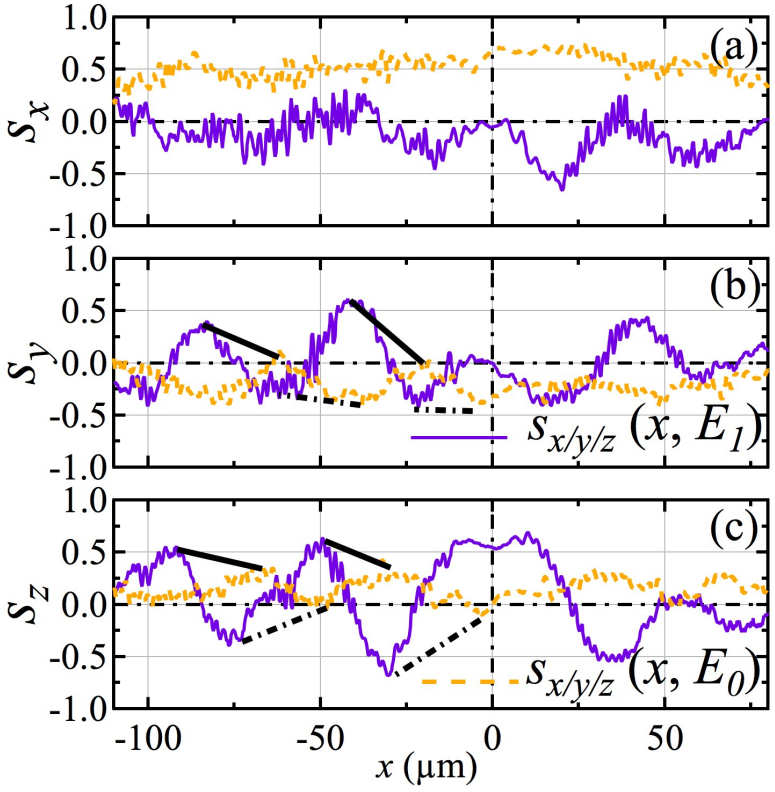

FIGURE 8.3: Stokes parameters of the polariton PL as function of x at energies $E_0 = 1.5396$ eV (dashed line) and $E_1 = 1.5403$ eV (solid line), extracted from Fig. 8.2. Dot-dashed (solid) lines in panels (b,c) are guides to the eye linking the minimum (maximum) value of s_y and s_z at the two energies, respectively, highlighting the spatial shift with energy of their oscillations.

spin, while they propagate over the ridge, due to the optical spin Hall effect [314]. The main difference in our case lies in the energy-dependence of the precession pattern, giving rise to distinct spin textures. The phase of the spatial s_z oscillations shifts continuously with increasing energies, so that at E_0 and E_1 they are shifted with respect to each other by a π phase approximately. In Figs. 8.2(b) and 8.2(c) the slanted, dot-dashed (solid) lines highlight the minimal (maximal) points of the s_y and s_z oscillation across the PL energy, respectively. This phase shift arises from the different propagation speeds of polaritons at different energies: polaritons at higher energies move at higher speeds and therefore travel longer distances for each precession of the spin. Nevertheless, the spin spatial-periodicity does not change significantly with energy. Finally, Fig. 8.2(d) displays, for completeness, the PL along the x axis, from 1.5395 to 1.5405 eV. In figure 8.3 we detail the different $s_{x,y,z}$ profiles at the two selected energies E_0 and E_1. The dashed line at E_0 shows a constant $s_x \approx 0.5$ profile as function of x; at E_1 (solid line) s_x varies weakly [see Fig. 8.3(a)]. Figures 8.3(b) and 8.3(c) detail the s_y and s_z oscillations, respectively, at E_0 and E_1. The displacement in real space of the minimal (maximal) points of the s_y and s_z oscillation from the lower energy E_0 to the higher one E_1 are evidenced by straight, dot-dashed (solid) lines.

8.2.2 Spin precession collapse

A recent study shows that a transfer of the polarization of a non-resonant excitation laser to polariton condensates occurs for excitation powers slightly above the condensation threshold and that the transfer efficiency decays with increasing pump power [330]. We also profit from the former fact to non-resonantly create polariton condensates with a predominant circular polarization. In this section, we investigate not only the latter fact, *i.e.* the influence of the pump power, but also that of its spin polarization (circular or linear) on the collective polariton spin state and on its propagation.

Two different pump powers are used for the experiments compiled in Fig. 8.4: 3.75 (4.75)$\times P_{th}$ for the left (right) column. s_z maps as a function of energy and x under σ^+ (linear excitation) are shown in Figs. 8.4 (a-1) and 8.4(a-2) [Figs. 8.4(b-1) and 8.4(b-2)]. Finally, for the sake of completeness, Figs. 8.4(c-1) and 8.4(c-2) show the polariton PL. In Fig. 8.4(a-1) s_z oscillations are clearly observed from 1.5395 to 1.5408 eV. The σ^+-polarized, non-resonant excitation induces a highly σ^+-polarized, blueshifted population at $x = 0$, whose PL spans from 1.5400 to 1.5415 eV. A 25% increase of the pump power strongly reduces the amplitude of the spin precession, which becomes barely visible in Fig. 8.4(a-2). These oscillations are also suppressed for linear excitation, as shown in Figs. 8.4(b-1) and 8.4(b-2). The PL map at high excitation power, 4.75$\times P_{th}$, reveals a non-emitting region around $x = 0$ with an energy-width of 0.7 meV and a spatial extent FWHM of $\sim$ 20 μm, highlighted with a dashed line in Fig. 8.4(c-2). This dark region is caused by the excitonic reservoir, which ejects polariton outwards from $x = 0$.

8.3 Model

To model the spatial structure of polariton condensates we use a mean-field description including incoherent pumping and decay [206] as well as energy relaxation [213]. The version of the model followed in this Chapter is slightly different from that previously described in § 2.5.2.3, which will be used in Part IV to describe the dynamics of condensate transistors in our microwire ridges. In the current experiment it is important to use a 2D model that accounts for the subband structure reported in Fig. 3.6 as well as a two-component spinor wavefunction to account for the spin degree of freedom. The spinor polariton wavefunction $\psi_\sigma(\vec{r},t)$ obeys the dynamical equation

$$i\hbar\frac{d\psi_\sigma(\vec{r},t)}{dt} = \Big[\hat{E}_{LP} + (\alpha_1 - i\Gamma_{NL})\,|\psi_\sigma(\vec{r},t)|^2 + \alpha_2|\psi_{-\sigma}(\vec{r},t)|^2 + V_0(\vec{r}) + V_\sigma(\vec{r}) + i\left(W_\sigma(\vec{r}) - \frac{\Gamma}{2}\right)\Big]\psi_\sigma(\vec{r},t) + \Delta_{\mathrm{TM,TE}}\psi_{-\sigma} + i\hbar\Re\left[\psi(\vec{r},t)\right]. \tag{8.2}$$

where $\sigma = \pm$ denotes the two circular polarizations of polaritons. α_1 and α_2 represent the strengths of interactions between polaritons with parallel and antiparallel spins, respectively. Here, $\vec{r}$ is a

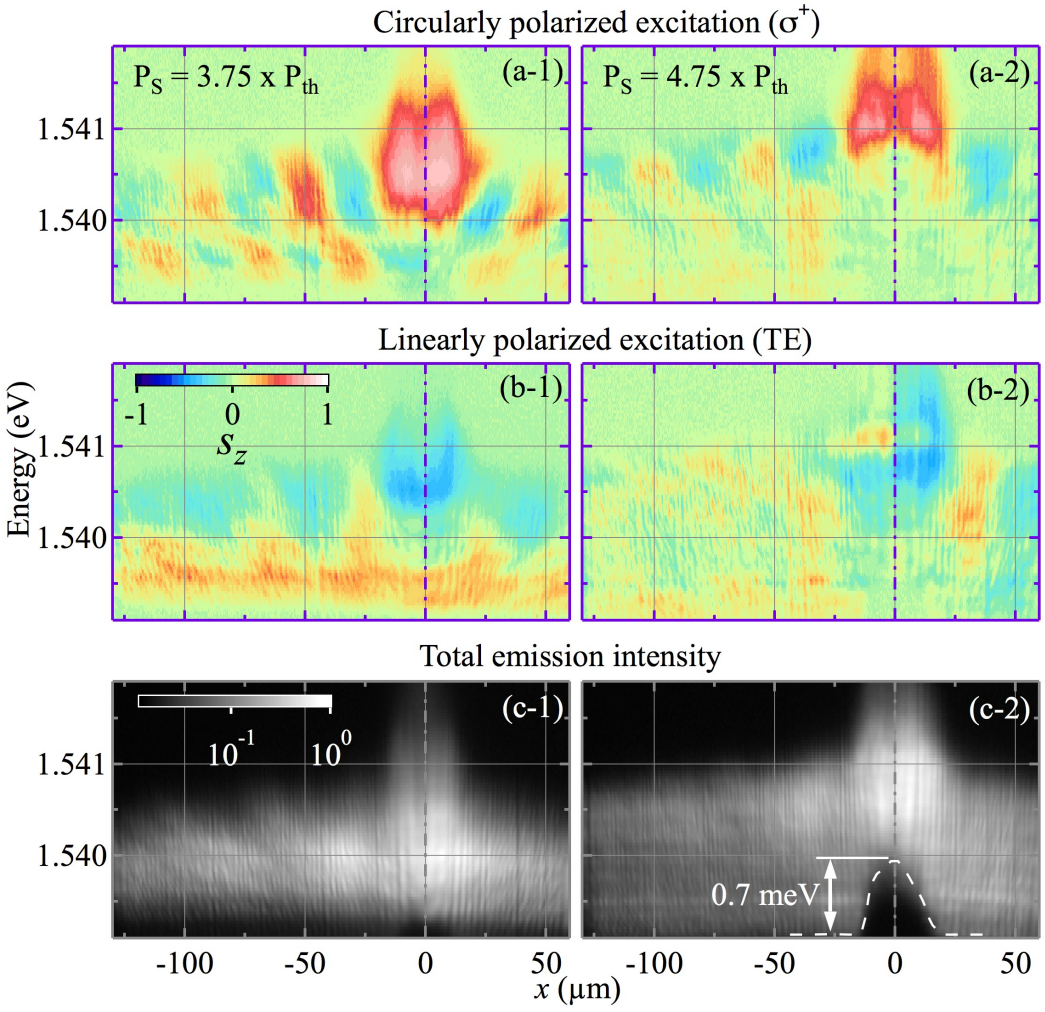

FIGURE 8.4: Polariton spin precession and PL as a function of pump power at $3.75 \times P_{th}$ (left column), and $4.75 \times P_{th}$ (right column). The non-resonant excitation (1.612 eV) at $x = 0$ is circularly- (linearly-) polarized in the first (second) row. Panels (a,b) depict the circular degree of polarization (s_z); panels (c) show the polariton PL. In panel (c-2) the local repulsive potential induced by photo-generated excitons at $x = 0$ is sketched by a dashed line. The PL (s_z) is coded in a logarithmic (linear), false color scale.

two-component vector consisting of the real space coordinates lying on the ridge, the origin of this coordinate system being in the center of the ridge.

Polaritons enter the condensate at a rate determined by $W_\sigma(\vec{r})$, which is both polarization and space dependent. While the non-resonant laser used in the experiment is polarized, due to the presence of spin relaxation, one does not expect a full polarization of the photocreated hot excitons. Consequently we expect a partially polarized reservoir of excitons to drive the polariton condensates, eventually yielding both possible circular polarizations. The condensation rate for the σ^+-polarized polaritons from the excitonic reservoir is given by:

$$W_+(\vec{r}) = W_0 e^{-r^2/L^2} \tag{8.3}$$

where W_0 is the peak condensation rate and L is the width. In principle, the spatial profile of the condensation rate includes the effects of exciton dispersion, diffraction and nonlinear repulsion after excitons are excited by the non-resonant laser pump. In practice, the effective mass of excitons is four orders of magnitude larger than that of polaritons and there is very little spreading of the excitons over length scales relevant for polaritons, such that L can be taken to be the same as the pump-spot diameter. The condensation rate for the σ^--polarized polaritons is smaller and given by $W_- = \rho W_+$, where ρ is a parameter that is fitted to the experimental results. In this form, the condensation rate is explicitly spin anisotropic.

The spin dependent effective potential experienced by polaritons can be described by:

$$V_\sigma(\vec{r}) = G_\sigma W_\sigma(\vec{r}) \tag{8.4}$$

where G_σ is a constant representing the strength of forward scattering processes between excitons in the reservoir and in the condensate.

We also consider a spin-independent component in the effective potential, V_0, which is the profile potential of the ridge. We assume it to be that of a 2D infinite square well, where the confinement in the y direction gives rise to the subband structure observed experimentally (Fig. 3.6) and theoretically (Fig. 3.8).

The polaritons decay with a decay rate Γ. They also experience a nonlinear loss corresponding to scattering out of the condensate. According to estimates in Ref. [197], $\Gamma_{\rm NL} \approx 0.3\alpha_1$. Once injected, different circular polarizations are also coupled by the linear polarization splitting $\Delta_{\rm XY}$ in the system, which can give rise to oscillations between spin components. While in 2D MC the dominant polarization splitting is wave-vector dependent, the dominant splitting in polariton channels is due to strain giving an anisotropic lattice constant [331]. A splitting occurs between polarizations aligned parallel and perpendicular to the channel axis, which remains for zero in-plane wave-vector [as can be seen in Figs.3.6(c,e)], and takes larger values than the TE-TM splitting in 2D MCs.

The final term in Eq. 8.2 accounts for energy relaxation processes of condensed polaritons:

$$\Re[\psi(\vec{r},t)] = -\nu\left(\hat{E}_{\rm LP} - \mu(\vec{r},t)\right)\psi(\vec{r},t), \tag{8.5}$$

where ν is a phenomenological parameter determining the strength of energy relaxation [40, 213] and $\mu(\vec{r},t)$ is a local effective chemical potential that conserves the polariton population. These terms cause the relaxation of any kinetic energy of polaritons and allow the population of lower-energy states trapped between the pump-induced potentials. For the simulation that produce the results in Figs. 8.5 and 8.6, the following parameters are used: $\alpha_1 = 2.4\times10^{-3}$ meVμm^2, $\hbar\nu = 0.14$, $\Gamma = 0.0366$ meV (Ref. [62]), $\alpha_2 = -0.2\alpha_1$ (Ref. [34]). The LP dispersion is characterized by an

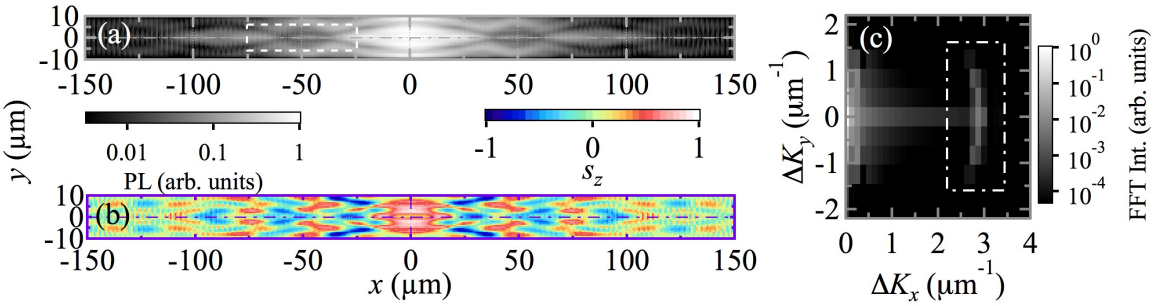

FIGURE 8.5: Simulations of the collective polariton condensate spin precession in a quasi-1D ridge. (a) PL rendering polariton distribution in real space under non-resonant, circularly polarized excitation at the center of the ridge, with a pump power $P = 3.75 \times P_{th}$. The dashed, white box marks the spatial region that is Fourier transformed. (b) Corresponding simulation on the circular degree of polarization distribution (s_z). (c) FFT intensity of the simulated polariton PL distribution in the framed area in panel (a); remarkable FFT frequencies arise at ~ 3 μm^{-1} from the counter propagating polariton populations, see the delimited region by a dot-dashed, white box. The PL and the FFT map are coded in a logarithmic, false color scale, while a linear one is used for s_z.

effective mass $m = 7.3 \times 10^{-5} m_e$, fitted to Fig. 3.6, where m_e is the free electron mass. $G_+ = 1.0$ and $G_- = 0.7$ are fitted to the measured space- and polarization-resolved energy distributions. $W_0 = 0.185$ meV, $\rho = 0.5$ and $\Delta_{\mathrm{TM,TE}} = -0.15$ meV. The width of the condensation rate profile is taken to be $L = 10$ μm. The calculations were performed using an adaptive step Adams-Bashforth-Moulton error-corrector procedure in a grid with 384×32 points. The polariton wavefunctions were initialized with a weak intensity noise, the distribution of which was found to have no effect on the end result. After a period of initial dynamics, energy distributions are obtained from Fourier transformation over a time window of 250 ps.

The simulated images shown in Figs. 8.5 and 8.6, can be compared to the experimental results in Figs. 8.1(a,b) and 8.2(a-c), respectively. The calculated dependence of s_z on pump power can be observed in Figs. 8.6(c,d): a blueshift of the maximum polariton energy as well as a slight reduction of the spin precession with increasing power is obtained, in agreement with the experiments reported in Figs. 8.4(a-1,a-2). The localized, polarized, incoherent pumping generates two distributions of polaritons separated both in polarization and in energy at $x = 0$: while the majority of polaritons are σ^+-polarized, a significant number of polaritons also condense into a σ^--polarized state, which has lower energy due to the spin-dependent blueshifts in the system $V_\sigma(\vec{r}, t)$. A very good agreement between the experimental and theoretical (x, y) maps is obtained.

The potential $V_\sigma(\vec{r})$, which is mostly induced by hot excitons with the same spatial distribution as the pump, represents a strongly repulsive potential in the system that accelerates polaritons outwards. The simulated energy- and space-resolved map of the s_x Stokes parameter, shown in Fig. 8.6(a) is also in reasonable agreement with the experimental results depicted in Fig. 8.2(a). As the accelerated polaritons move outward, their spins precess, due to the polarization splitting, giving rise to oscillations in s_y and s_z [see Fig. 8.6(b,c)] as in the experiments [Fig. 8.2(b,c)]. Note

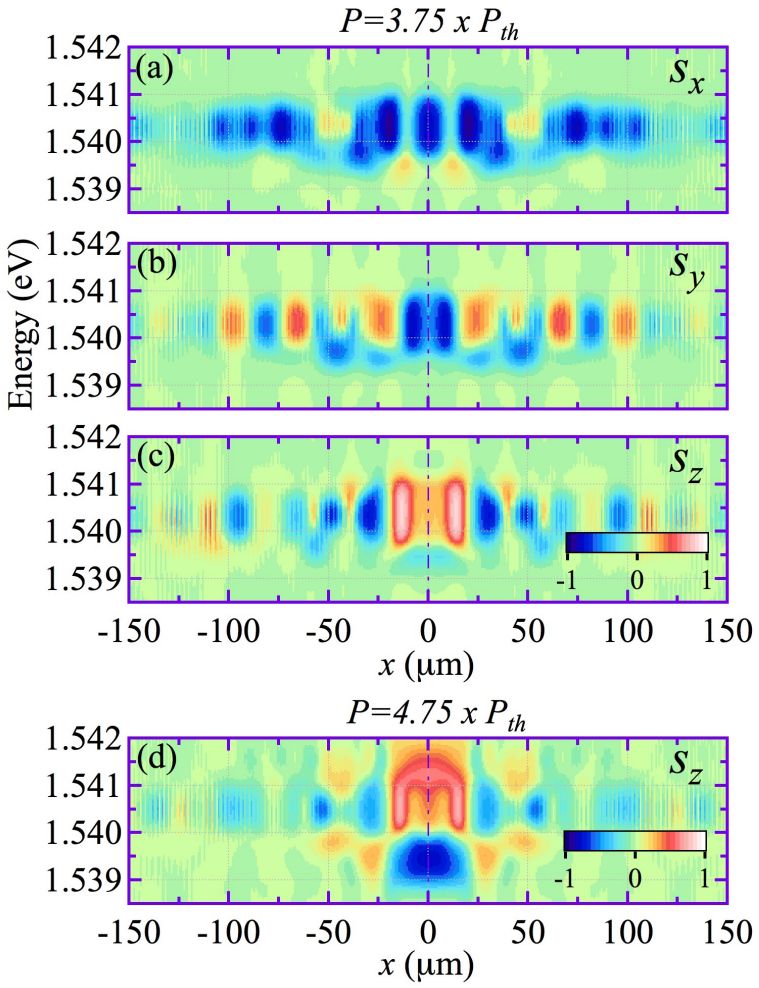

FIGURE 8.6: Simulation on the Stokes parameters of the polariton PL as function of energy and spatial position (x): (a) s_x, (b) s_y, and (c) s_z, respectively, under non-resonant, circular-polarized excitation. The degree of polarization is coded in a linear, false color scale.

that the theoretical model does not reproduce directly oscillations in the spatial distribution of s_x. Theoretically, any polarization splitting in the system can always be represented by an effective magnetic field about which the Stokes' vector rotates. It is impossible to find a effective magnetic field that causes oscillations between both negative and positive values in all three components of the Stokes' vector simultaneously (even if multiple forms of splitting are present, the total effective magnetic field cannot make an angle greater than 45° with the s_x, s_y and s_z axes simultaneously). We thus conclude that the experimentally observed oscillation in s_x is not directly due to spin precession caused by the polarization splitting. Instead, we speculate that the oscillations in s_x are linked to the oscillations in the total PL intensity, which competes with a background of incoherent polaritons that are linearly polarized due to the TE-TM splitting. Where the condensate intensity is high, s_x is given by the mean-field theoretical value, while when the condensate intensity is low there may well be incoherent polaritons, not accounted for in the mean-field theory, that give a different polarization. Consequently, oscillations in intensity give the impression of oscillations in

the linear polarization degree represented by s_x. The oscillations in intensity are due to the 2D nature of the propagation, where both theory and experiment show that polaritons tend to travel at an angle to the x axis, being guided by reflections from the ridge edges. The intensity viewed along the x axis is then greatest when polaritons propagating off-axis cross the x axis.

8.4 Conclusions

In summary, we have studied the optical spin Hall effect in a quasi-1D MC, where the lateral confinement yields a suitable scenario for the intra-branch polariton energy relaxation, enriching the phenomenology of the polariton spin patterns. Thanks to a spectroscopic analysis of the optical spin Hall effect, we have shown that a phase-shift in the oscillations of the s_y and s_z Stokes parameters results from the different speeds of propagation of polaritons. These oscillations collapse either when linear-polarized excitation is used or when the pump power of the circular-polarized excitation exceeds a certain level. Our results are interpreted within the framework of a mean-field model for polariton dynamics, which includes incoherent gain from a polarized exciton reservoir, the energy shift due to the reservoir, TE-TM splitting and energy relaxation. The demonstration of the inversion of the polariton spin as it propagates or relaxes in energy is an important ingredient for realizing polaritonic circuits based on the spin degree of freedom.

Part IV

All-optical devices based on polariton condensates

Introduction: All-optical devices based on polariton condensates

In this introduction we discuss the state-of-the-art on the development of all-optical based devices in several platforms: atoms, quantum dots (QDs) and exciton-polaritons. Particularly, we also discuss the contribution of this thesis to the advance in polariton-circuits and polariton-based transistor switches and gates.

During the last two decades, the fundamental research on the development of ultrafast communication and signal processing systems has been devoted to conceive new all-optical devices (as potential candidates to substitute to electronic ones) profiting from their reduced noise, power dissipation and higher data transfer rates. However, typically photons do not interact with each other, what implies a fundamental drawback to devise photonic building blocks for all-optical computers. Photon-photon coupling can be only achieved in special materials with the help of coherent, intense light, whilst electrons, benefiting from their strong interactions, permit much easier ways to perform logical operations based on Coulomb interactions.

In the following text, we discuss three different systems where light interaction is mediated by matter at three different (low to high) scales: (i) at the atomic level, (ii) within accumulations of atoms at the nanoscale (QDs) and (iii) macroscopic, multilayer semiconductor nanostructures (MCs).

Rydberg atoms

Rydberg states are optically excited atoms in high-excitation states and they have shown their potential to intervene the photon-photon coupling [332–334]. In the recent years, single-photon sources [332], photon phase-shifters [333, 335] and a single-photon transistors [336, 337] have been demonstrated. The latter achievement, a single-photon transistors with high gain, constitutes an important breakthrough in the route of "*future Data-Highways*" to conceive worldwide optical networks for quantum information.

The modus operandi of these Rydberg atom-based transistors is similar to the electronic ones: a few photons are able to gate the amplification of an output light signal. These optical transistors are constituted by three basic elements: (i) an optical medium sensible to light at the single-photon level, (ii) a photon acting as "gate" that determines the properties of the medium and (iii) the amplified optical signal, constituted by a certain number of incoming, delayed photons encountering the medium after the photon gate acts on it. Depending on the single-photon gate, the output signal can be switched ON (transmitted photons) or OFF (blocked photons). The efficiency (gain) of the optical transistor is given in this case by the ratio of the number of incoming photons and the number of gate photons.

S. Baur and coworkers have demonstrated the optical switching in an atomic system using a single-photon gate [338]. However, in these experiments the efficiency of the transistor is 0.24, quite below unity. This reduced gain compromise the cascadability and fan-out of the device (the cascadability problem is also discussed in our polaritonic devices, see below). This is why atom-based optical transistors with gains above unity are required: the solution to this problem is the obtention of strong photon-photon interactions in the Rydberg blockade that occurs in clouds of identical atoms [339, 340].

The Rydberg blockade mediates the photon-photon interactions in the following manner. A highly-excited atomic state possesses a large electric dipole. Within an area called the "blockade radius", this dipole provokes a shift in the energy levels of the surrounding atoms. In such conditions, the energy detuning of an excitation beam on the energy state of a Rydberg atom conditions the optical properties of the neighboring atoms, which become transparent or nontransparent within the "blockade radius" region (outside this area the effect does not happen) [341]. The Rydberg blockade can have "nonlocal" effects when the interaction between several Rydberg atoms is probed, forming a quantum nonlinear medium. This way, when photons travel inside a cloud of strongly interacting atoms, it provides a huge photon-photon interaction providing strongly correlated states of light [333].

The research groups of G. Rempe [337] and that of S. Hofferberth [336] have reported recently the realization of a single-photon transistor, whose net gain amounted to a value of 20 and ~ 10, respectively. In the first case, the experiments were performed on a *Rb*-atom cloud of Rydberg states confined in an optical trap and kept at 0.33 μK. One single atom of the cloud was excited into a Rydberg state by a gate photon tuned at 795 nm. The lifetime of the excited state was on the order of 0.1 ms, before the gate photon was re-emitted again. During that time, the energy state of the neighboring atoms in the aforementioned "blockade radius" area were shifted and thus the atomic gas became nontransparent for the following, incoming 20 signal photons. In other words, the efficiency of the device was 20, since the gate was operated by a single-photon, and it is a remarkable achievement as compared to previous mentioned attempts. In the second case, done by the S. Hofferberth's team, the experiments were carried in similar conditions were the *Rb*-atomic cloud was at 0.40 μK. The efficiency of this single-photon transistor demonstrated a final optical gain of ~ 10.

In conclusion, the state-of-the-art on Rydberg atoms phenomena probes their potential to control high-sensitive photonic transistors working on the single-photon level. The potential of such systems applied to quantum information purposes seems to be very promising. Finally, we want to add to the previously discussed systems that recent studies in CQED with only **two** isolated neutral cesium atoms confined in a magneto-optical-trap [342] have proven the control in the atomic scattering emission (enhanced or suppressed) from the two atoms as function of the relative spatial separation. Parallel to these studies, Ref. [343] has reported the control in the

super- and sub-radiant emission of a CQED system depending on the entanglement configuration between **two** $^{40}Ca^{+}$ ions embedded in a cavity.

Quantum dots

On the side of solid-state physics, semiconductor materials are a very suitable choice for the realization of such devices (see Ref. [6]). Impressive progress in the perspective of building a quantum network based on semiconductor QDs have occurred in recent years. To a large extend, QDs have been shown to behave as artificial atoms that can emit single-photons [344], entangled photon pairs [345, 346] and even indistinguishable photons [347–352].

Like atoms, QDs offer the possibilities to perform optical nonlinearities at the few photon scale, where the absorption of a photon would enable or prohibit the transmission of a second one [353–356]. Nevertheless further research is necessary for the realization of QD-based devices operating at the single-photon level. Very recent works have demonstrated the implementation of optical switches or optical gates based on QDs [357]. Taking advantage from all the semiconductor technology, one can also dope the system so as to have a single spin (electron or hole) in a QD [358]. Recently, many works have shown optical, coherent manipulation of a single spin [359–365]. Lately, spin photon entanglement was also demonstrated [366, 367].

While all these results are exciting, most of them lack the level of efficiency required to build a solid-state quantum network. Indeed, only few percent of the photons emitted by a QD, embedded in a bulk host, can be collected out of such a structure. Reciprocally, dozens of photons must be sent on a QD in bulk for only one to interact with it. In the last few years, an important research effort has been devoted to building an efficient interface between a QD and a propagating mode of the electromagnetic field [351, 368–371]. Two approaches have shown to be most successful: inserting the QD in a monomode nanowire [369] or coupling the QD to a pillar MC [351]. In both cases, ultra-bright single-photon sources have been demonstrated, with brightness as large as 70-80%.

For the cavity-based approach, the photons have been shown to be highly indistinguishable, opening the way to optical quantum computing, with first demonstration of an entangling CNOT gate operating on single photons [372]. This QD-photon interface has also allowed the implementation of optical nonlinearity with a threshold of eight incident photons [353]. Such highly nonlinear device could be brought to the single-photon level with the current state-of-the-art technology. With a spin in a cavity, such devices could also open a new paradigm in quantum computing with the possibility for instance to entangle delayed-photons [373].

Exciton-polaritons

Exciton-polaritons, due to their mixed light-matter nature and their optical nonlinearities, are suitable to create optical amplifiers [54, 113, 374], optical gates [30, 39, 47, 375], transistors

[43, 46, 48], spin-switches [33, 293, 295, 296, 376], diodes [44, 377] and circuits [31, 45, 302]. For the sake of completeness, it is worth to mention that excitonic-based circuits have been proposed [378] and demonstrated [379–382] in the recent years.

Further functionalities can be achieved creating polariton condensates and reducing the dimensionality by patterning the MCs. Propagation of such condensates over macroscopic distances has been achieved in wire MCs with very long polariton lifetimes [36]. The addition of a periodic modulation along the 1D MC has been demonstrated to show a mini-band structure that dramatically influences the condensation process [383, 384]. These systems are foreseen as building blocks for polaritonic circuits, where propagation and localization are optically controlled and reconfigurable. Further studies on 2D lattices of coupled micropillars etched in a planar semiconductor MC have been performed in the group of J. Bloch and G. Malpuech. These systems offer a workbench to engineer the band structure of polaritons [385, 386].

The condensates can be conveniently manipulated using repulsive local potentials created by photogeneration of excitons [387]. Large band-width amplification of polariton condensates under non-resonant excitation has been proven by a proper location of the laser excitation spot to create a condensate close to the edge of a 1D microwire [40]. In these systems, thanks to their superfluid character, one can benefit from high lateral speed of propagation and ballistic transport without energy loss [61].

Using wider microwire ridges, a polariton condensate transistor switch has been realized through optical excitation with two beams [43]. Figures IV-1(a,b) show an schematic description of the device performance on its two ON and OFF states, respectively. One of the beams creates a polariton condensate which serves as a source (S) of polaritons. The ON state of the transistor corresponds to forming a trapped condensate ($\mathscr{C}_C$) at the edge of the ridge (collector, C), Fig. 3.2.1.1(a). The polariton propagation is gated using a second weaker gate beam (G) that controls the polariton flow by creating a local blueshifted barrier, Fig. 3.2.1.1(b). The presence of G hinders the propagation of polaritons towards C, remaining blocked between S and G (OFF state), this condensate is dubbed as $\mathscr{C}_{S-G}$.

In this Part, we discuss in detail the dynamics of such polariton transistor switch, where we time-resolve the logic ON/OFF operation of $\mathscr{C}_C$, shown in Fig. IV-1, Chapter 9. The energy relaxation processes within the polariton condensate are also addressed in this Chapter, where a systematic study of energy relaxation and trapping dynamics of polariton condensates propagating in the quasi-1D MC structure, under one and two beam excitation is reported. We also determine the optimum conditions of the ON state in terms of fast formation (for a given relative distance between laser pulses and C) and the longest lifetime of the state. In Chapter 10 we address the operation speed of the device by means of excitonic gating. Finally, in Chapter 11 the approach for the implementation of a logic AND gate is performed under two pulsed, spatially separated

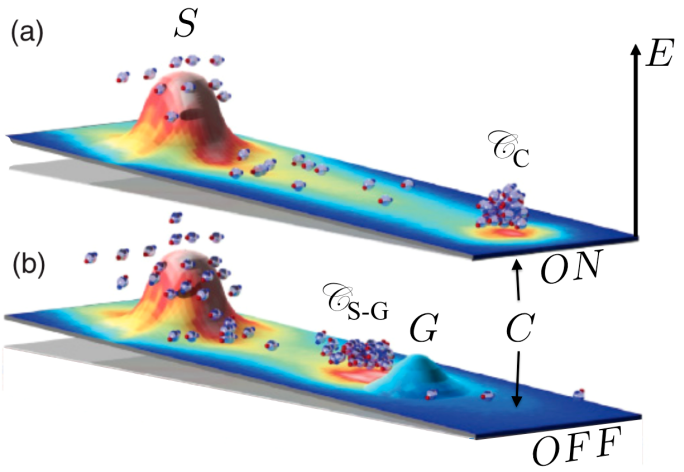

FIGURE IV-1. Schematic of the polariton condensate transistor based on a MC ridge: (a) ON state of the device without G, forming a trapped condensate $\mathscr{C}_C$ at C and (b) OFF state of the device with the G barrier that blocks the $\mathscr{C}_C$ formation and, on the contrary, forms $\mathscr{C}_{S-G}$, trapped between S and G. The vertical axis is energy, representing the repulsive potentials created by excitons. The polariton PL is coded in a false, color scale (not shown). Adapted from Ref. [43].

and delayed excitation-beams. Energy-relaxation processes allow the delayed relaxation into a long-living coherent ground state.

All the results, obtained in the Laboratorio de Espectroscopia Ultrarrápida at the Universidad Autónoma de Madrid, under the supervision and leadership of Prof. Luis VIÑA, are collaborative achievements by the SemicUAM group. The experiments compiled in this Part have been performed by the author of this thesis. The simulations and theory presented in this Part have been implemented by Dr. Tim Liew (Nanyang Technological University).

Chapter 9

Dynamics of a polariton condensate transistor switch and polariton energy relaxation processes in quasi-one-dimensional microcavities

The functionalities of MCs in the SCR, as integrated optical elements, promote polaritons as an emergent platform to create new logical devices [37]. Thanks to their interactions with non-condensed excitons, polaritons can be easily accelerated, propagating over macroscopic distances in high finesse MCs [36, 160]. In this case, new devices can be built by properly shaping the excitation profile [42, 388–391] as well as the MC etching [44–46, 383–385]. Optical devices incorporating such condensates are promising candidates for new ultrafast, low-power consuming information processing components [299, 392, 393]. Different structures, including 1D ones, have been proposed recently for the realization of transistors [301, 394], diodes [377], optical routers [60], spin current controllers [395], logic gates [31] and for building a universal set of logic AND- and NOT-type gates [302].

In this Chapter we present and discuss, in first place, a time-resolved study of a polariton transistor switch, which is optically controlled through laser excitation with two beams (source, S, and gate, G) in quasi-1D microwire ridges. We provide a complete insight of the ON/OFF states of such a transistor and we compare them with a theoretical description of the device, based on the generalized GP equation, which was modified to account for incoherent pumping, decay and energy relaxation within the condensate. In second place, we make a systematic study of the influence of the density of polaritons created in S and G on the propagation and the gating of polariton bullets, of their energy and density relaxation and of the optimal conditions for realizing an all-optical polariton condensate transistor switch. Our experiments are compared again with

simulations of the polariton condensate dynamics based on a generalized GP equation, slightly modified and improved to that used in the first part of this Chapter, where the addition of certain phenomenological parameters render a better description of the polariton energy relaxation.

This Chapter is organized as follows. In § 9.1 we describe the experimental setup used to perform the experiments and we include a general scheme of the polariton transistor switch for the sake of clarity. In first place in § 9.2 we present de time-resolved working principle of the polariton transistor switch. § 9.2.1 describes the experimental results on the ON and OFF dynamics of the transistor and in § 9.2.2 we theoretically reproduce the ON/OFF states through the simulations of the GP equation, coupled to an exciton reservoir and accounting for polariton energy relaxation. In second place, in § 9.3 we further discuss the energy relaxation phenomena occurring in our quasi-1D MC; in § 9.3.1 we compile the polariton PL dynamics under one- and two-beam excitation conditions for different pump powers of S and G. We analyze the pump power dependance of the polariton energy and intensity emission decays and we also probe the optimal excitation conditions of the switching time of the ON state. In § 9.3.2 we compile the simulations for the one- and two-beam excitation conditions and we compare the theoretical results with our experiments. The simulations on the power dependance of the energy and intensity decays are analyzed.

9.1 Experimental setup

The sample is the high-quality $5\lambda/2$ $AlGaAs$-based MC described in § 3.2. We perform our experiments in the ridge structure shown in Fig. 3.5, whose dimensions are 20×300 μm^2. Figure 9.1(a) shows a SEM image of such a ridge, including the excitation scheme; a temporal scheme of the excitation and emission processes is given in Fig. 9.1(b).

The sample is excited with 2 ps-long light pulses from a Ti:Al_2O_3 laser, tuned to the first high-energy Bragg mode of the MC (1.612 eV). We split the laser beam into two independent beams, S and G, whose intensities, spatial positions and relative time delay (zero for these experiments) can be independently adjusted. We focus both beams on the sample through a microscope objective to form 5 μm-$\varnothing$ spots spatially separated by $\backsim$40 μm along the ridge. The same objective is used to collect (angular range $\pm 18°$) and direct the emission towards a spectrometer coupled to a streak camera obtaining energy-, time- and spatial-resolved images. In our experiments polaritons propagate along the X axis of the ridge. There is also some diffusion of polaritons in the Y direction, but it is not relevant for the operation of our device (further discussion about this lateral propagation of polaritons is explained in § 10.2.3). All the images in this Chapter show the PL emission collected along the X axis from a 10-μm wide, central region of the ridge. The power threshold for condensation of polaritons is $P_{th} = 1.5$ mW.

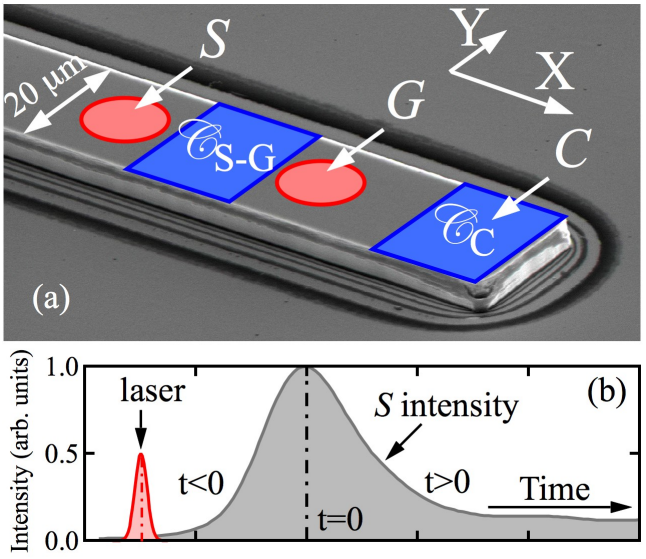

FIGURE 9.1: (a) SEM image of a 20-μm wide ridge, including the excitation scheme with the S and G beams, and the position of the trapped condensates: $\mathscr{C}_{S-G}$, between S and G, and $\mathscr{C}_C$, at C. (b) Temporal scheme to clarify the choice of the time origin: the instant $t = 0$ is set at the maximum S-intensity, the arrival of a given laser beam takes place at an instant $t < 0$.

Figure 9.2 shows, as an example, under *cw* conditions, the intensity distribution of the polariton emission as a function of energy and of the position in the ridge: when we only use the S beam, Fig. 9.2(a), we place it $\backsim$75 μm away from the right ridge border; in the $S+G$ beam excitation, G is placed $\backsim$35 μm away from the border, Fig. 9.2(b). In Fig. 9.2(a), exciting with a power $P_S = P_{th}$, a blue-shifted ($\backsim$ 3 meV) emission at S, together with a weak condensate emission $\mathscr{C}_C$, are clearly observed. $\mathscr{C}_C$ emits from an energy lower than that of the propagating polaritons as a result of an unintentional modification of the MC structure created by the etching process at the edge of the ridge (see § 3.2.1.1 for details). Polaritons propagate at a constant energy towards the left and right sides of the ridge. Exciting with both laser beams, under different excitation conditions for a typical OFF state, $P_S = 7.2 \times P_{th}$ and $P_G = 0.4 \times P_{th}$, the gating state of the switch is readily seen with the stopped, condensed polaritons just before the G position.

9.2 Dynamics of a polariton condensate transistor switch

From the different configurations presented in Fig. 3 of Ref. [43], where the S power is kept constant and the G one is varied, we present in this section the dynamics of the two most relevant cases, corresponding to the ON and OFF states of the transistor switch, corresponding to the presence and absence of the $\mathscr{C}_C$ condensate at C, respectively.

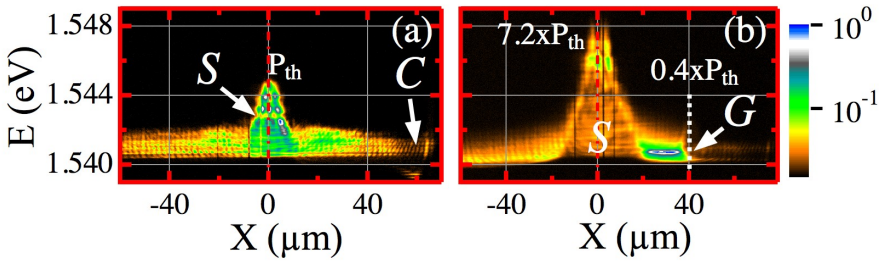

FIGURE 9.2: Polariton PL emission as function of energy and real space (X) image of a cross-section along the ridge under non-resonant *cw*-excitation. (a) Only one beam (S) at $\backsim$75 μm from the right ridge border. (b) Two beam (S+G) placed at $\backsim$75 μm and $\backsim$35 μm from the border, respectively; the dashed vertical line indicates the gate position. The intensity is coded in a false, logarithmic color scale shown on the right.

9.2.1 Experimental results

In our experiments, the ON (OFF) state has been obtained under the following pump power conditions at S and G: P_S = 10.8 mW and P_G = 0(0.6) mW, respectively. The S spot is placed 80 μm away from the right ridge border (location of C), the G beam is placed in between S and G, spatially separated by 40 μm away of S. P_S correspond to $\sim$ 7 times the power threshold for condensation of polaritons, while P_G is well below threshold.

Figures 9.3(a-e) show the dynamics for the ON state. X = 0 and time 0 ps, in the panels, are chosen at the S position and when the PL reaches its maximum intensity. In Fig. 9.3(a), the initial S signal, at an energy of $\sim$1.546 eV, arises from the PL of large momentum excitons, extending $\sim$10 μm. At longer times, these excitons relax rapidly their energy and concomitantly polaritons that are formed at S expand in space. These two processes give rise to an emission at S relaxing rapidly its energy in a doubly exponential fashion with a fast decay time τ_1 and a slow one τ_2, the latter corresponding to the polariton energy relaxation. Further discussion about the polariton energy relaxation processes at S are addressed in momentum- and real-space in § 9.3.1.2 and § 9.3.1.5, respectively.

Simultaneously with these decay processes at S, two polariton populations emerge at lower energy than that of S; they travel left (not shown in these time-resolved figures, see Fig. 9.2 to appreciate the free leftward propagation of polaritons in the ridge under *cw* detection) and right away from the excitation spot due to the local energy potential landscape (see § 3.2.1.1) [36]. Initially the right traveling polaritons decrease their energy as they move away from S, Fig. 9.3(b), until a condensate propagates ballistically and reaches C, see Fig. 9.3(c), the interferences appearing around 65 μm corroborate that the flowing polaritons are in a condensed state. At later times, Fig. 9.3(d), a large fragment of this population becomes trapped just before the end of the ridge forming the $\mathscr{C}_C$ condensate, at 1.539 eV, while a smaller part bounces back from the edge and travels back towards S at a constant energy $\sim$1.540 eV. At very long times, $\sim$600 ps, Fig.

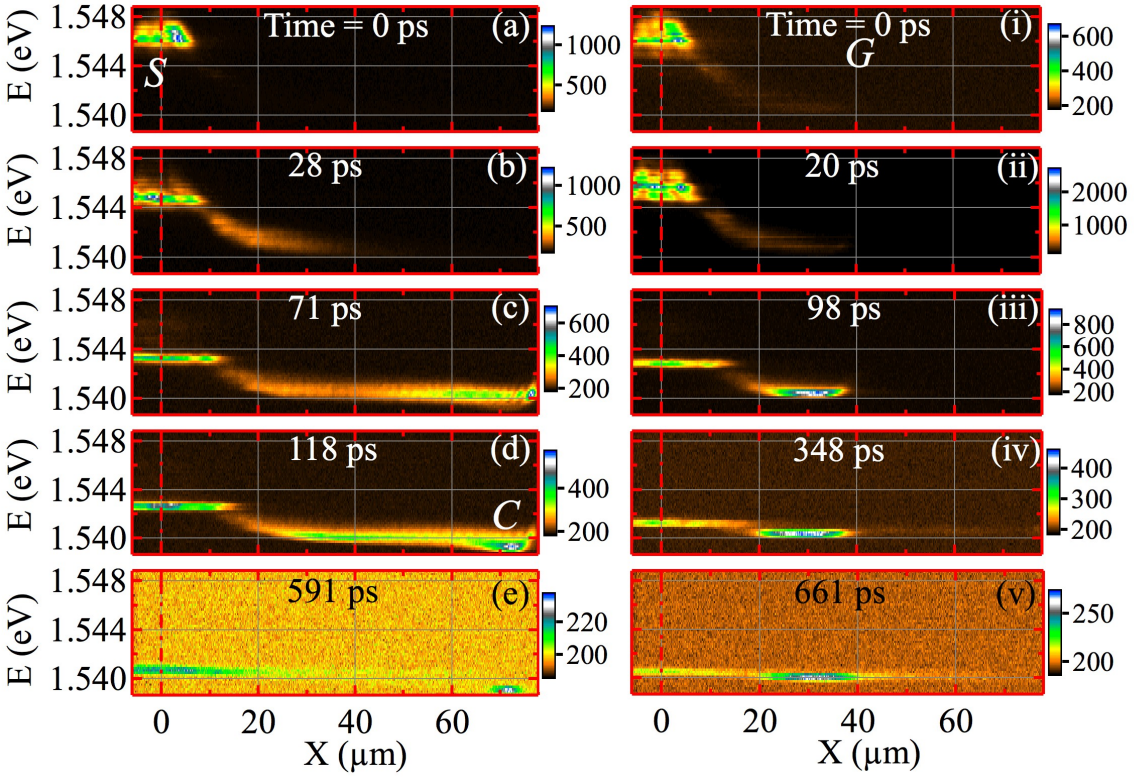

FIGURE 9.3: (a-e)/(i-v) Experimental results on the polariton PL dynamics as function of energy and position for the ON/OFF transistor state. The snapshots are taken at the times shown in the labels. The PL is coded in a false, linear color scale shown on the right of each panel. The complete dynamics of the ON [OFF] transistor state is available in the video following http://dx.doi.org/10.1063/1.4773376.2 [http://dx.doi.org/10.1063/1.4773376.1].

9.3(e), only the $\mathscr{C}_C$ condensate and the polaritons at S remain. The gradual decrease of the PL is due to recombination processes.

It is also important to note that the duration over which the condensate is present greatly exceeds the polariton lifetime. This is because the condensate is continuously fed by high energy excitons (not visible in the spectrum and distinct from the excitonic states initially emitting at S) excited by the non-resonant pulse. The emission at S is determined by repulsive interactions with hot excitons which contribute a blueshift to the potential energy. As hot excitons decay from the system, either through recombination or condensation, this potential energy decreases over time [see the energy relaxation dynamics of the PL emitted at S, $X = 0$, in the different instants represented in Figs. 9.3(a-e)]. Once the polariton condensate has formed, due to the low density of polaritons, there are minimal energy relaxation processes, such that the propagating polaritons tend to conserve their energy as they spread out from S [see, for example, Fig. 9.3(d)].

The corresponding dynamics of the OFF state is compiled in Figs. 9.3(i-v). In this case, the G-laser beam, which arrives simultaneously with the S-beam, is placed at 40 μm and constitutes an invisible barrier as its power is only $0.4 \times P_{th}$, but the G becomes visible at higher powers

(see § 9.3.1.4). The right propagating polaritons display a similar initial behavior to that shown before, compare Fig. 9.3(b) with Fig. 9.3(ii). However, a very large population, which dominates the PL emission, Fig. 9.3(iii), gets trapped between S and G, which has been previously dubbed $\mathscr{C}_{S-G}$. It emits at a slightly larger energy, 1.541 eV, than that of C, due to the addition of the S and G potential profiles and to its own blueshift. When the G barrier becomes lower, Fig. 9.3(iv), a tiny part of the trapped population tunnels through and reaches the border of the ridge without becoming confined at C. At long times, Fig. 9.3(v), the emission arises only from $\mathscr{C}_{S-G}$. The dynamics of the distant filling of the condensate at C by the population at S is presented in § 9.3.1.6.

9.2.2 Theory

A theoretical description of the polariton condensate transistor can be based on the generalized GP equation, described in Eq. 2.42 and repeated here for the sake of clarity (Eq. 9.1), for the condensed polariton wavefunction $\psi(x,t)$ [206]:

$$i\hbar\partial_t\psi(x,t) = \left[\hat{E}_{LP} + \alpha|\psi(x,t)|^2 + V(x,t) + i\hbar\left(rN(x,t) - \frac{\Gamma}{2}\right)\right]\psi(x,t) + i\hbar\Re\left[\psi(x,t)\right], \quad (9.1)$$

$\hat{E}_{LP}$ is the kinetic energy dispersion of polaritons, which at small wave vectors can be approximated as $\hat{E}_{LP} = -\hat{\nabla}^2/(2m)$ with m the polariton effective mass. α represents the strength of polariton-polariton interactions. $V(x,t)$ represents the effective potential acting on polaritons, and we will refer to it again a few paragraphs below. There are a few differences between the model used in this section and that described in § 2.5.2.3 (used in the following section § 9.3 in Chapters 10 and 11). The reason of these differences is that the model was developed alongside the experiments, and thus many modifications and improvements to mach experiments and theory were required and accomplished. For the sake of clarity, we explain these differences in the following lines. In this section, the description of the hot exciton reservoir feeding the polariton condensate (see § 2.5.2.3) is simplified to a single reservoir $N(x,t)$ (whose initial conditions are $N(x,0) \propto P(x)$, being $P(x)$ the shape of the pulsed pump laser), whilst, as we will discuss below in § 9.3.2, the active exciton reservoir that feeds the polariton condensate is determined by the rate equations 2.44-2.46 (these equations are also included in § 9.3.2, see Eqs. 9.7-9.9).

The incoming rate of polaritons into the condensate is determined by the exciton reservoir density, which was calculated from the evolution equation given in Ref. [206] and included here for the sake of clarity:

$$\frac{dN(x,t)}{dt} = P(x,t) - \left(\Gamma_R + r|\psi(x,t)|^2\right)N(x,t) + D\nabla^2 N(x,t), \quad (9.2)$$

where $P(x,t)$ is the pulsed pump beam, Γ_R is the decay of the exciton reservoir, whose lifetime was taken as 200 ps, r is the coupling term between the polariton wavefunction $\psi(x,t)$ and the reservoir and D is the spatial diffusion rate of the excitons.

This theory, or similar versions, has been used to describe a variety of recent experiments under incoherent pumping, including the dynamics of vortices [209] as well as various spatial patterns [160, 396] and spin textures [246] (and also § 8.3).

Here, we recall that $V(x,t) = V_0(x) + gN(x,t)$ is the polariton potential, given by the static potential defining the wire edge, $V_0(x)$, and a potential shift, proportional to the constant g, due to the presence of a hot exciton reservoir, $N(x,t)$.

Experimentally, the energy relaxation of polariton condensates is most clearly observed as they propagate down static [22, 43] or pump induced [36] potentials. Previous descriptions of energy relaxation have been based on the introduction of an additional decay of particles depending on their energy [36, 212, 213, 216] (occasionally known as the Landau-Khalatnikov approach).

In this section, the energy relaxation processes are given in Eq. 9.1 by the term described in Eq. 9.3:

$$\Re\left[\psi(x,t)\right] = -\nu\left(\hat{E}_{LP} - \mu(x,t)\right)\psi(x,t) \tag{9.3}$$

where ν is a phenomenological parameter determining the strength of energy relaxation [36, 212, 213, 216], we neglected any spatial dependence of ν. The $\Re\left[\psi(x,t)\right]$ term present in Eq. 2.47 (Eq. 9.4 in § 9.3.2), is redefined this time to a simpler version without the term $\nu'|\psi(x,t)|^2$, see Eq. 9.3. The inclusion of the phenomenological parameter $\nu'|\psi(x,t)|^2$ in Eq. 2.47 yields an optimum matching in the polariton energy relaxation dynamics between experiments and theory. We will come back to this modification in the model section of energy relaxation processes § 9.3.2.

The mechanism of polariton energy relaxation remains a debatable topic. In some experiments [36, 397], polariton scattering with hot-excitons is dominant; however, it is insufficient to describe our case where significant energy relaxation occurs far from the pump spot (where hot excitons are not present). Phonon scattering is expected across the whole sample [247], although alone may not give the complete picture due to limited scattering matrix elements. In § 9.3.1.3 we discuss a experiment that could address the phonon scattering as a channel of relaxation for polaritons. In this experiment, we study the pump power dependence of the polariton energy relaxation at C, where excitons (a hundred microns away) are not present and therefore phonon scattering might drive the polariton relaxation in energy.

The parameters used in these calculations are: $m = 7.3 \times 10^{-5} m_e$ (obtained from fits to the dispersions measured in § 3.2.1; m_e is the free electron mass), $\hbar r$ =0.01 meV μm; $\nu = 0.425$

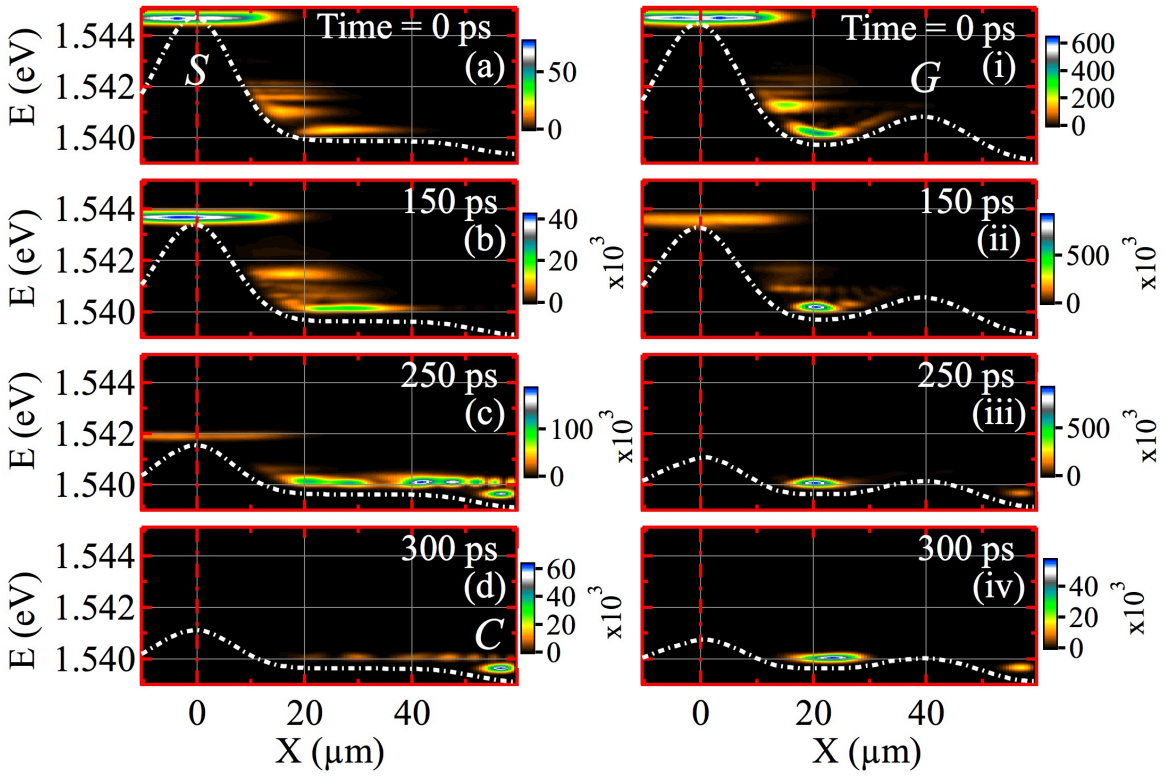

FIGURE 9.4: Theoretical dynamics of the polariton PL dynamics as function of energy and position in the ON (a-d)/OFF (i-iv) transistor state, evaluated from Fourier transforms of $\psi(x,t)$. The white dashed lines show the effective potential experienced by polaritons, $V(x,t)$. On the right of each panel, the false, linear false-color scale of the PL is depicted in arbitrary units.

meV^{-1} ps^{-1}; the reservoir lifetime was taken as 200 ps. The calculated evolution of the energy-position distribution is shown in Fig. 9.4 and reproduces satisfactorily the experimental findings. As polaritons move away from S, their potential energy decreases and is converted into kinetic energy. Due to the term in Eq. 9.3, this kinetic energy is relaxed and the polariton energy follows the effective potential, $V(x,t)$. In the absence of G (ON state), the polaritons can be reflected from the ridge edge giving rise to the interference fringes seen at $t = 250$ ps [Fig. 9.4(c)]. At longer times, further energy relaxation results in trapping in a potential minimum near the ridge edge (C), whose depth was inferred from the experimental results. In addition, the fraction of polaritons that remain at the S position also relax their energy, as the effective potential lowers due to decay of the exciton reservoir. The blocking of polaritons in the presence of G (OFF state) is also observed, in agreement with the experiments, where polaritons are trapped between S and G constituting the $\mathscr{C}_{S-G}$ condensate. Some quantum tunneling across G occurs, particularly at later times when the barrier height has decreased.

While the theoretical model captures the main qualitative features of the experiment, there are differences in the timescales involved. This is partly due to an oversimplification of the hot

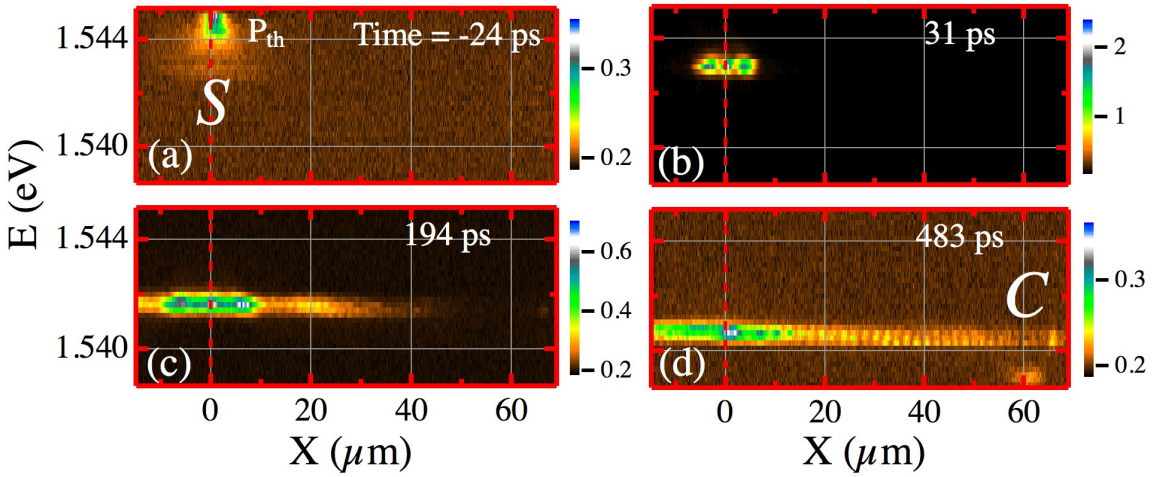

FIGURE 9.5: Polariton PL emission as function of energy and real space (X) for $P_S = P_{th}$ at different times shown by the labels. S and C mark the source and collector positions, respectively. The intensity is coded in a false, linear color scale shown on the right of each panel. See the complete dynamics of this figure at http://journals.aps.org/prb/supplemental/10.1103/PhysRevB.88.035313/Video1.mov.

exciton dynamics, which is treated as a single reservoir [206]. In reality, a cascade between many different states can contribute to a richer and slower dynamics.

9.3 Energy relaxation processes of polariton condensates in quasi-one-dimensional microcavities

In this section, a systematical study of the energy relaxation processes occurring along the propagation of polariton condensates in the MC ridges is performed, and their trapping dynamics in presence of one and two pulsed beams. In our experiments, we time-resolve the different excitation configurations presented in Ref. [43]: Fig. 2 (where the P_S is varied whilst $P_G = 0$, § 9.3.1.1) and Fig. 3 ($P_S = const.$ and P_G is varied, § 9.3.1.4). Our study obtains intensity- and energy-dynamics of exciton and polariton emission in the ridge. In the former case varying P_S, we fully characterize the ON state response of a polariton transistor switch; in the latter one, we modulate the polariton condensate trapping potential [36].

9.3.1 Experimental results and discussion

9.3.1.1 One-beam excitation

In this section we present three time-resolved cases for different P_S pump powers, Figs. 9.5-9.7. Figure 9.5 shows the dynamics of the emission when $P_S = P_{th}$. For each panel the time

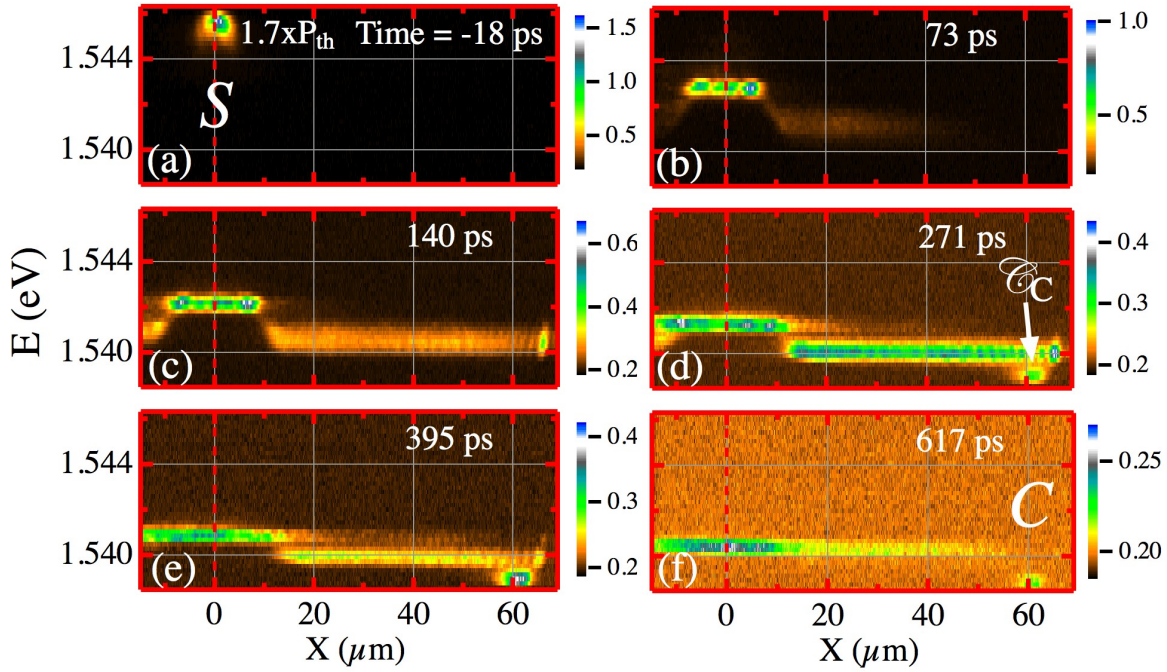

FIGURE 9.6: Polariton PL emission as function of energy and real space (X) for $P_S = 1.7 \times P_{th}$ at different times shown by the labels. S, C and $\mathscr{C}_C$ mark the source, the collector and the trapped condensate positions, respectively. The intensity is coded in a false, linear color scale shown on the right of each panel. See the complete dynamics of this figure at http://journals.aps.org/prb/supplemental/10.1103/PhysRevB.88.035313/Video2.mov.

is displayed at the right upper corner, being the temporal origin set at the instant when the S intensity is maximum. Fig. 9.5(a) shows that the emission from S at -24 ps occurs at 1.545 eV; at 31 ps, Fig. 9.5(b), the emission redshifts and a small spatial expansion around 0 μm is observed; propagating polaritons, expanding more rapidly towards the border, at an energy of 1.542 eV, are detected at 194 ps Fig. 9.5(c), eventually reflecting backwards, interfering coherently and creating the $\mathscr{C}_C$ condensate, weakly emitting at 1.539 eV at later times, 483 ps Fig. 9.5(d). Since the pump power is at threshold, the emission intensity of polaritons is weak and slightly higher than the noise level in all panels of Fig. 9.5.

Let us note that at early times, the emission observed in Fig. 9.5 appears blueshifted from the lower polariton minimum by an amount comparable to one-half of the Rabi splitting. This suggests that the emission at the source comes from polaritons with a strong excitonic character (see next § 9.3.1.2 for a clear characterization of the carriers at S). For this reason we will refer to the emission from S as arising from excitons, although the decrease in the blueshift over time corresponds to a continuous transition from excitonic polariton states to those with roughly equal excitonic and photonic fractions. The emission from the propagating states and collector region, at lower energy, is clearly a polaritonic emission.

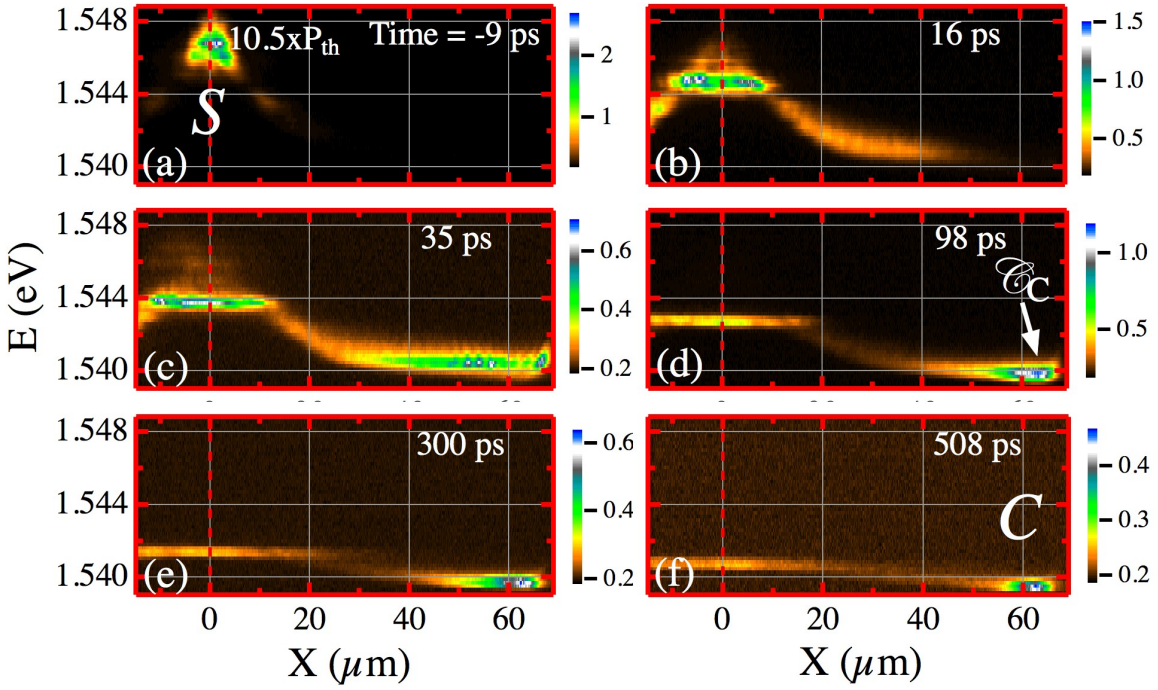

FIGURE 9.7: Polariton PL emission as function of energy and real space (X) for $P_S = 10.5 \times P_{th}$ at different times shown by the labels. S, C and $\mathscr{C}_C$ mark the source, the collector and the trapped condensate positions, respectively. The intensity is coded in a false, linear color scale shown on the right of each panel. See the complete dynamics of this figure at http://journals.aps.org/prb/supplemental/10.1103/PhysRevB.88.035313/Video3.mov.

The dynamics of the emission increasing P_S to $1.7 \times P_{th}$ is shown in Fig. 9.6: the initial excitonic emission at S takes place at 1.546 eV Fig. 9.6(a), slightly higher than before, due to increased blueshift due to a larger hot-exciton repulsion. At $t = 73$ ps, Fig. 9.6(b), an essential difference with respect to the case of Fig. 9.5(b) is revealed: polaritons emit from a lower energy than that of S, which is $\backsim$2 meV blueshifted; this situation holds during the first $\backsim$200 ps of the decay process. Figure 9.6(c) shows the arrival of polaritons at the ridge border at 140 ps, and the eventual condensation of $\mathscr{C}_C$, Fig. 9.6(d). This final relaxation phase in the dynamics takes place into a state defined in a minimum of the wire structural potential located at the wire edge. A clear indication of the polariton coherence is evidenced by the interference at 1.540 eV between counter-propagating wave-packets. The source population at S, still 1 meV blueshifted with respect to propagating polaritons, expands around $X = 0$ as it decays in energy, and continuously feeds the propagating polariton condensate, increasing its effective lifetime, Fig. 9.6(e). Finally, as shown in Fig. 9.6(f) at 617 ps, polaritons at S merge with those propagating along the ridge. The emission is still observed for times as large as $\backsim$ 1 ns (not shown).

The case of the highest source power used in our experiments is shown in Fig. 9.7: at -9 ps the excitonic source population emits at 1.547 eV, Fig. 9.7(a). The progressive spatial expansion of the excitonic population and the fast relaxation of the polariton condensate, as it propagates

towards the right side, at 1.541 eV, reaching the ridge edge at 35 ps, is shown in Figs. 9.7(b) and 9.7(c). $\mathscr{C}_C$ is now slightly blueshifted, with respect to its energy at lower P_S conditions, to 1.540 eV, due to the higher density condensate population at this place of the ridge, Fig. Fig. 9.7(d). At later times, as those shown in Figs. 9.7(e,f) for 300 and 508 ps, the population at S decreases and expands in space whilst $\mathscr{C}_C$ redshifts its energy emission due to its reduced occupancy.

9.3.1.2 Analysis of the carriers relaxation phenomena at S in momentum space

Hitherto, we have discussed the polariton relaxation phenomena in the frame energy-real space. In this section we complementarily analyze the polariton PL decay in energy and intensity in momentum space. The energy-momentum space distribution of polaritons yields a rich insight for time-resolved experiments since, in this case, we are able to distinguish at a glance different types of carriers according to the dynamics of their dispersion relations.

Figure 9.8(a) shows a single snapshot at $t = 10$ ps of the polariton PL dynamics in momentum space under single spot excitation $P_S = 2 \times P_{th}$. In this panel there are two species of emitting carriers and they are very well differenced by their spectroscopic characteristics: see full, horizontal, red line at 1.544 eV, dividing Fig.9.8(a) in two upper and lower regions with an up- and down-pointing arrows, respectively. In first place we consider the region below the red line; we observe left- and rightward propagating polaritons moving away from the exciton reservoir with in-plane wave vectors $k_x = \mp 1\ \mu\text{m}^{-1}$, respectively, their energy emission is $\sim$ 1.542 eV. In second place we turn our attention to the upper region, where we observe a flat distribution of carriers at high energy, 1.545 eV, corresponding to PL emitted from $X = 0$, they are very well localized at the pump spot in real space, without spreading away (not shown). The dispersion relations of the ridge, previously studied in § 3.2.1, permit us to clearly identify this second type of carriers as excitons, according to the energy of their PL emission and their momentum space distribution.

Now we restrict the analysis of the momentum space dynamics of carriers to those that we have been identified initially as excitons. We track closely their spectral characteristics (spectral peak position, FWHM and PL intensity) as function of time. This way we are able to identify in the relaxation process the gradual change when the PL emission properties evolve from excitonic-like to polariton-like. Figure 9.8(b) compiles the dynamics of two of those features: spectral position of the PL peak and its FWHM (left and right, linear axis, respectively). A double exponential decay fit (dot-dashed green line) to the peak spectral position dynamics (full, red line) highlights two different regimes in the energy relaxation process. The decay times of the resulting fitting are a fast decay time $\tau_X = 30$ ps, corresponding to excitons and a second, slower decay time $\tau_{pol} = 10 \times \tau_X$, corresponding to polaritons at S. The linewidth (FWHM), blue line, also suffers a remarkable transition from the exciton-like behavior, whose value is around $\sim$0.8 to $\sim$ 0.4 meV when $t < 45$ ps, to the situation from 45 ps and so on, where the linewidth of the emission remains

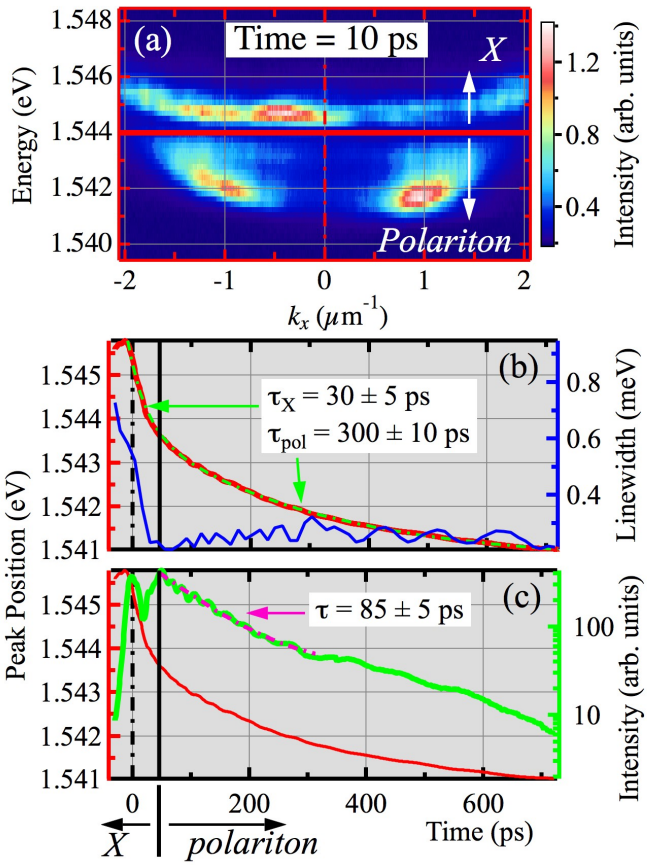

FIGURE 9.8: Analysis of the relaxation phenomena of the PL at S in momentum space. (a) Snapshot of the PL dynamics at $t = 10$ ps under single spot excitation $P_S = 2 \times P_{th}$. A red, horizontal line at 1.544 eV divides the panel in an upper and lower region, differencing between excitons and polaritons, respectively. Panels (b,c) analyze the relaxation dynamics of carries that are initially identified as excitons at high energies: (b) Dynamics of the peak spectral position (PL linewidth FWHM) in red (blue) line in the left (right) axis. The dot-dashed, green line is a double exponential decay fit to the energy decay of carriers. (c) Again, for the sake of comparison the red line shows the dynamics of the peak spectral position in the left axis and the green line shows the PL dynamics in the right axis of the panel. The dot-dashed magenta line is a single exponential decay fit to the PL decay dynamics. Panels (b,c) have a vertical, full, black line at $t = 45$ ps indicating the transition from exciton- to polariton-like of carriers at S.

more or less constant at ~ 0.3 meV (oscillations of this value in the order of $\sim$0.1 meV correspond to the accuracy limit of the gaussian fittings to the PL peak profiles at each time). For the sake of comparison, Fig. 9.8(c) reproduces the same plot for the peak spectral position (red line, left axis) and we also plot the PL intensity dynamics in a green, full line (right, logarithmic axis). In this case there is a noteworthy feature and it is the fact that the PL emission from excitons is very bright at $t = 0$, then it decreases as it redshifts in energy, having a PL intensity minimum at $t = 20$ ps, and then the PL reaches its maximum value at 45 ps in the transition from excitonic to polaritonic carriers, see black vertical, full line evidencing the distinction between the two regimes. Inside the polariton-like regime, *i.e.* $t > 45$ ps, a single exponential decay fit is done to the polariton PL [see dot-dashed, magenta line in Fig. 9.8(c)] yielding a PL intensity decay time of 85 ps.

9.3.1.3 Pump power dependence of the polariton energy relaxation at C

After studying the carrier relaxation at S, where we have observed a transition from excitons to polaritons, we now turn our attention to those polariton phenomena taking place at C. This case is particularly interesting because the processes of energy relaxation at the border of the ridge, under single pulse excitation (S-beam), occur in absence of an excitonic environment (the most determining factor for polariton energy relaxation), since these carriers are very well localized at the pump spot, tents of microns away (in this case).

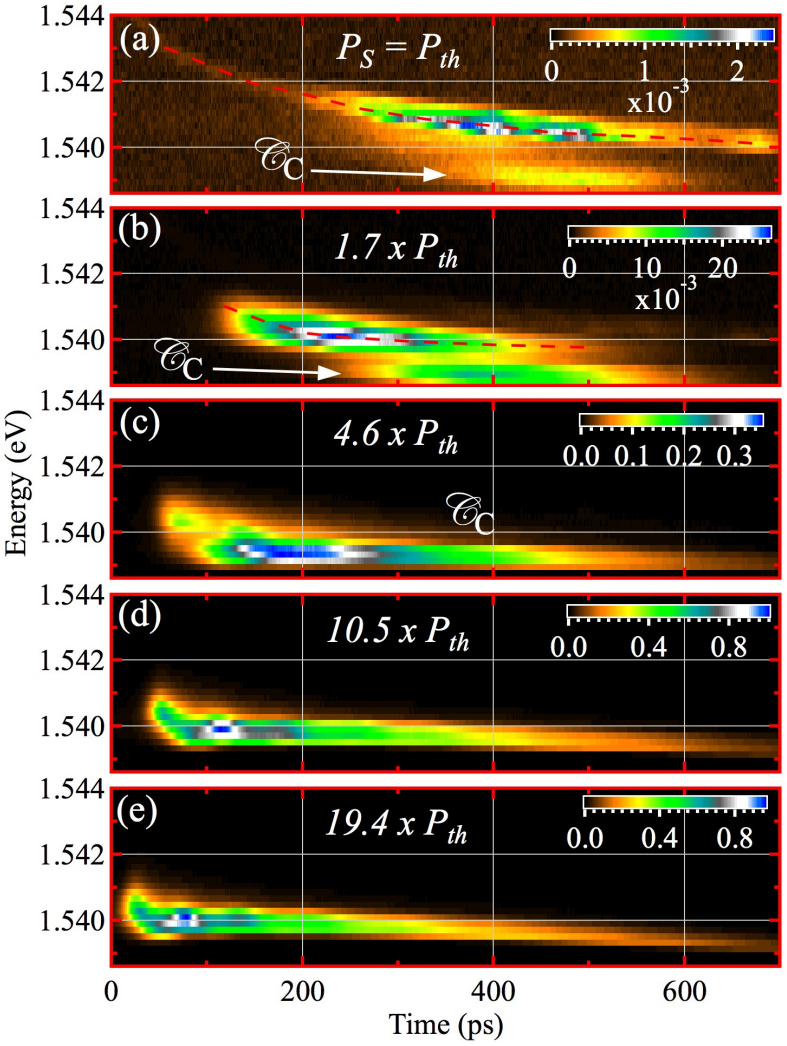

FIGURE 9.9: Polariton PL emission as function of energy and time at C for different pump powers of P_S: P_{th} (a), $1.7 \times P_{th}$ (b), $4.6 \times P_{th}$ (c), $10.5 \times P_{th}$ (d) and $19.4 \times P_{th}$ (e). The PL maps have been integrated in a spatial region 5 μm wide centered at C, the S spot has been placed 60 μm away from the right edge of the ridge. The intensity is coded in a false, linear color scale shown on the right of each panel.

Figure 9.9 shows the formation and decay dynamics of $\mathscr{C}_C$ for five different P_S pump powers. In this set of experiments, S is placed 60 μm away from C, and the PL maps have been integrated in an area of 5 μm-wide at C in order to fully observe the dynamics of the trapped condensate

$\mathscr{C}_C$. In Figs. 9.9(a,b), where P_S equals P_{th} and $1.7 \times P_{th}$, respectively, there is a clear difference between propagating polaritons, lying in at $\sim$ 1.541 eV, highlighted by a dashed, red trace, at higher energy than that of $\mathscr{C}_C$ ($\sim$ 1.539 eV). We observe that $\mathscr{C}_C$ is formed at the minimum of the structural potential, $V_0(x)$, and its energy remains constant along the whole dynamics (total duration of $\sim$200 and 400 ps in Fig. 9.9(a) and 9.9(b), respectively). An alternative analysis of the $\mathscr{C}_C$ formation and energy decay dynamics is described in Fig. 9.13 of § 9.3.1.5, where energy and intensity maps of the polariton PL are shown and discussed.

In the polariton dynamics presented in previous Fig. 9.5 [lowest excitation power corresponding to Fig. 9.9(a)] is observed that $\mathscr{C}_C$ appears only when the propagating polaritons bounce for the first time at the ridge border, and then eventually relax and get trapped in this condensate. The same process applies in Fig. 9.9(b). In Figs. 9.9(c-e) a different $\mathscr{C}_C$ formation is observed. Now, there is not any energy gap between the incoming flow of polaritons (previously depicted with the dashed, red line) and $\mathscr{C}_C$, but there is a continuous PL trace in energy, placed below 1.541 eV where the propagating polariton and $\mathscr{C}_C$ overlap in energy. This over populated $\mathscr{C}_C$ condensate experiments an increasing blueshift, due to polariton-polariton interactions, and a faster formation, due to a faster propagation of the incoming polariton flow, for increasing P_S values. The $\mathscr{C}_C$ energy remains almost constant for $\sim$ 700 ps and placed at 1.5395, 1.5399 and 1.540 eV in Figs. 9.9(c,d,e), respectively.

9.3.1.4 Two-beam excitation

The introduction of a new secondary pulse, dubbed before as gate (G), between S and C, adds new interaction phenomena. The existence of two condensates becomes very clear in this case: one of them located initially between S-G, $\mathscr{C}_{S-G}$, which eventually becomes propagating, and a second one, already labelled as $\mathscr{C}_C$. The polariton propagation towards C along the ridge can be hindered with a below-threshold intensity gate beam, see Fig. 9.2(b) and Fig. 9.10, rendering the $\mathscr{C}_C$ switch-off and creating the trapped condensate $\mathscr{C}_{S-G}$. As the G-repulsive potential gradually decreases in time, a tiny fraction of $\mathscr{C}_{S-G}$ is able to tunnel through the barrier and it spreads between 40 and 80 μm, see Fig. 9.10(d). This configuration has been already discussed in detail in previous § 9.3.

Figure 9.11 shows the dynamics for $P_S = 7.2 \times P_{th}$ and $P_G = 1.8 \times P_{th}$. The visibility of the emission at G is delayed by $\backsim$20 ps with respect to that at S, despite of the fact that both beams reach the sample simultaneously, Figs. 9.11(a,b). This delay is due to the power dependence of the emission rise time, which increases with decreasing power. The $\mathscr{C}_{S-G}$ condensate lies at a constant energy, 1.541 eV, remaining trapped, Fig. 9.11(c). On their own account, the emission energy of S and G decay, at a rate determined by the carrier density and the carrier-carrier interactions, until they reach 1.542 eV for both. The population between G and C, mainly created by the G

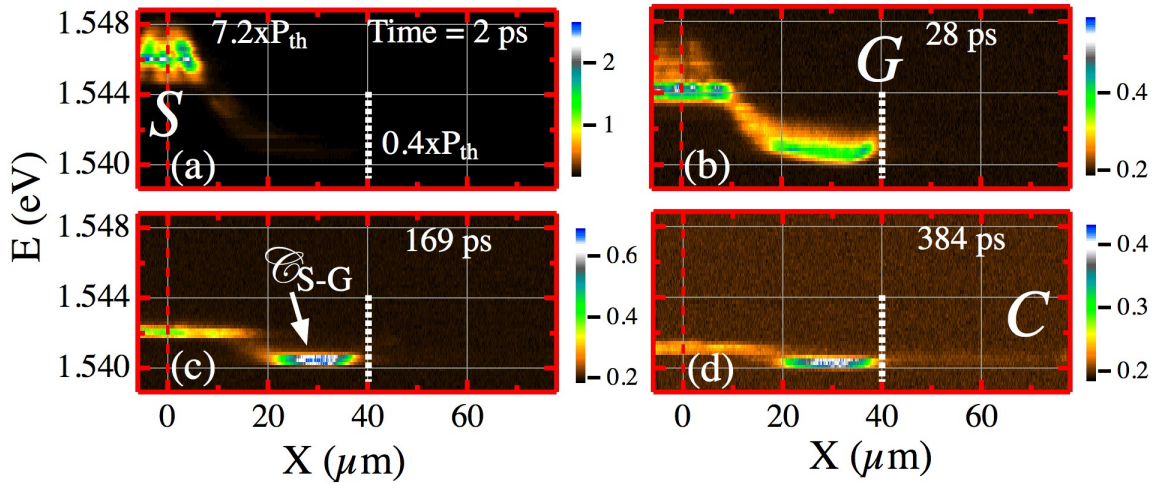

FIGURE 9.10: Polariton PL emission as function of energy and real space (X) for $P_S = 7.2 \times P_{th}$ and $P_G = 0.4 \times P_{th}$ at different times shown by the labels. S, G, C and $\mathscr{C}_{S-G}$ mark the source, the gate, the collector and the, between S-G, trapped condensate positions, respectively. The intensity is coded in a false, linear color scale shown on the right of each panel. See the complete dynamics of this figure at http://journals.aps.org/prb/supplemental/10.1103/PhysRevB.88.035313/Video4.mov.

pulse, propagates towards the border, Fig. 9.11(c), being reflected, Fig. 9.11(d), and forming the $\mathscr{C}_C$ condensate, Fig. 9.11(e). When the G barrier further decays the $\mathscr{C}_{S-G}$ condensate becomes propagating and coherent interference patterns are generated from counter-propagation, see Fig. 9.11(f).

For completeness, Fig. 9.12 depicts the case corresponding to large values of P_G. Figure 9.12(a) depicts the excitonic emission at 1.547 eV when the laser beams arrive at S and G. $\mathscr{C}_{S-G}$ is trapped around X=20 μm, blueshifted up to 1.542 eV, due to repulsive interactions, Fig. 9.12(b), whilst polaritons between G and C propagate towards the border. At 76 ps, a new condensate, $\mathscr{C}_C$, becomes trapped at 1.540 eV, and the emission energy of S and G reaches that of $\mathscr{C}_{S-G}$, see Fig. 9.12(c). Due to the barrier reduction at G, $\mathscr{C}_{S-G}$ propagates along the ridge from 0 to 60 μm, Fig. 9.12(d). $\mathscr{C}_C$ remains confined for later times at a constant energy, whereas $\mathscr{C}_{S-G}$ decays and interferes with itself, Figs. 9.12(e,f).

9.3.1.5 Power dependance of the energy/intensity decays

In our sample, the emission above 1.544 eV is coming from excitonic states. The polariton emission lies at lower energies, down to 1.538 eV at the C region. In this section, we analyze the dynamics of the energy and population relaxation along the full region of propagation of the condensates between S and C both in the presence or absence of G, obtaining quantitative values for the energy time-decays and the optimal working conditions for the ON-state.

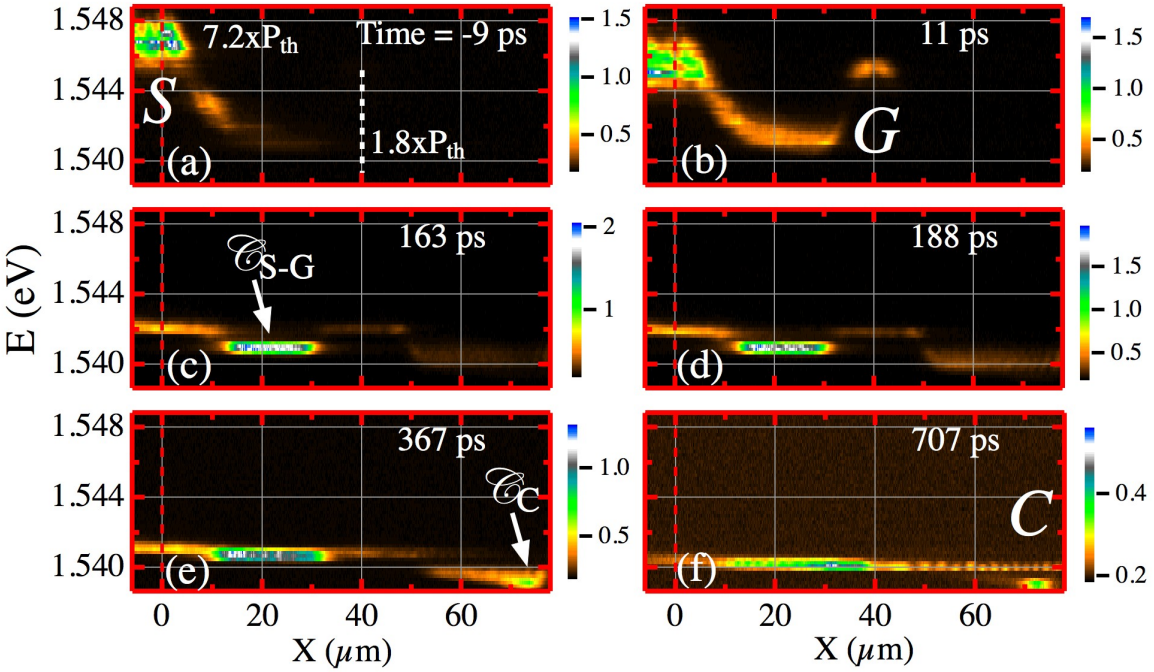

FIGURE 9.11: Polariton PL emission as function of energy and real space (X) for $P_S = 7.2 \times P_{th}$ and $P_G = 1.8 \times P_{th}$ at different times shown by the labels. S, G, C, $\mathscr{C}_{S-G}$ and $\mathscr{C}_C$ mark the source, the gate, the collector, the trapped condensate between S-G and the trapped one at C positions, respectively. The intensity is coded in a false, linear color scale shown on the right of each panel. See the complete dynamics of this figure at http://journals.aps.org/prb/supplemental/10.1103/PhysRevB.88.035313/Video5.mov.

Figures 9.13 and 9.14 show spatial-temporal maps of the energy (a-c)/intensity (d-f) evolution of the emission for the same power values as those used in Figs. 9.5-9.7 and 9.10-9.12, respectively. Figures 9.13(a-c) and 9.14(a-c) have been obtained identifying the time at which the maximum PL emission takes place, at a given X position on the ridge, for every energy: this gives a point in the map whose energy is coded with the false-color scale shown on the right-hand side of the upper row. Note that all the information concerning the strength of the emission, and therefore the polariton population, is lost in this representation. The energy maps consider a cutoff based on the experimental background noise, leaving white points when the intensity is below that noise level. The complementary information is encoded in the second row in Figs. 9.13 and 9.14, giving in this case the polariton population from integrating all emission energies. These plots provide a straight and precise insight on the energy/intensity decay of the population at every position along the ridge.

Let us start by considering the one-beam excitation compiled in Fig. 9.13. In Figs. 9.13(a,b) the energy trap created at $\backsim 60$ μm due to the potential discontinuity close to the border of the ridge is clearly observed: $\mathscr{C}_C$, emitting at 1.539 eV, is separated by a small energy gap from the polaritons propagating above at 1.540 eV. The horizon, $\mathscr{D}^P$, on the right upper corners, between white and

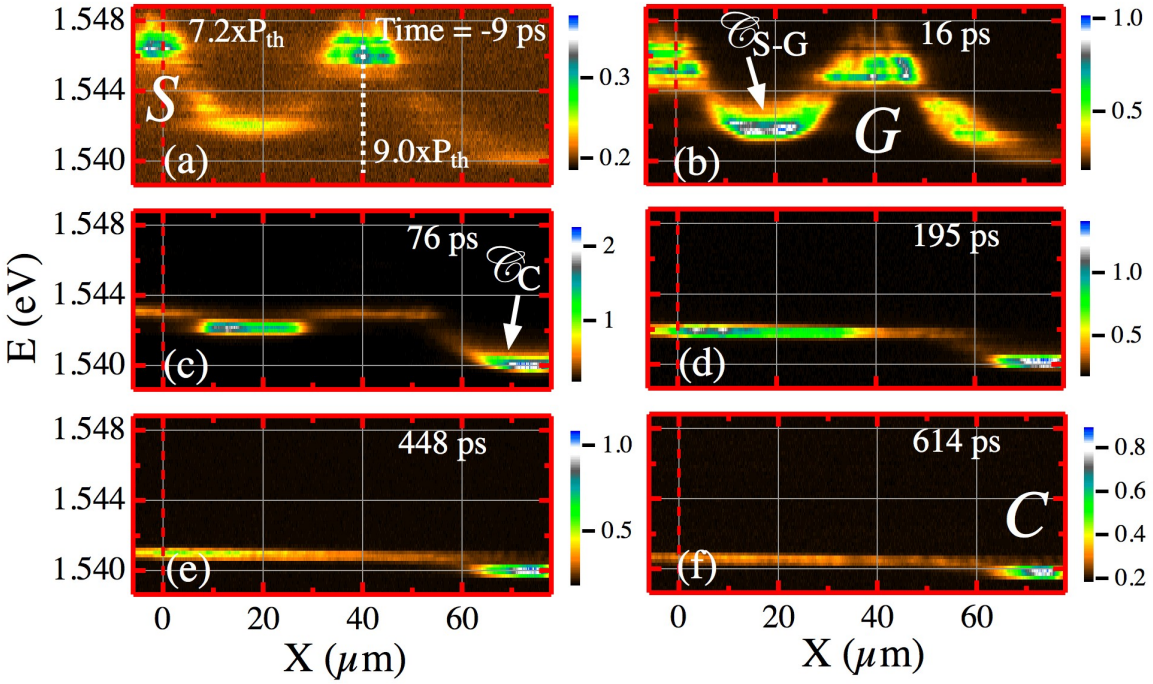

FIGURE 9.12: Polariton PL emission as function of energy and real space (X) for $P_S = 7.2 \times P_{th}$ and $P_G = 9.0 \times P_{th}$ at different times shown by the labels. S, G, C, $\mathscr{C}_{S-G}$ and $\mathscr{C}_C$ mark the source, the gate, the collector, the trapped condensate between S-G and the trapped one at C positions, respectively. The intensity is coded in a false, linear color scale shown on the right of each panel. See the complete dynamics of this figure at http://journals.aps.org/prb/supplemental/10.1103/PhysRevB.88.035313/Video6.mov.

colored points is given by the arrival of polaritons at different positions along the ridge. Another discontinuity is observed between the decay of carriers at S and the propagating polaritons, $\mathscr{D}^{S-P}$. The power dependence of both discontinuities is evident in these panels and gives information about the speed of propagation of different emitting species. At P_{th}, the border, $\mathscr{D}^{S-P}$, between carriers at S and polaritons, whose propagation is seen for $X \gtrapprox 15$ μm, is absent [Fig. 9.13(a)], because the energy of excitons and polaritons decay at the same rate, but it becomes very clear in Figs. 9.13(b,c). The speed of propagation of the carriers can be obtained from the slope of $\mathscr{D}^{S-P}$ and $\mathscr{D}^{P}$ lines. For the carriers at S in Fig. 9.13(b), $\mathscr{D}^{S-P}$ is almost straight, therefore a mean speed value, $v^{S}{}_{(@1.7\times P_{th})}$, can be obtained amounting to $\backsim 0.02$ μm/ps. At the highest power Fig. 9.13(c), $v^{S}{}_{(@10.5\times P_{th})}$ initially has increased by a factor of $\backsim 3$ as compared to $v^{S}{}_{(@1.7\times P_{th})}$, but the strong non-linearities associated with the high carrier densities lead to the appearance of deceleration rendering a gradual decrease of v^S. The spatial extension of the carriers around S also widens with increasing power, almost doubling its value from $\backsim 30$ to $\backsim 60$ μm at 400 ps as seen in Figs. 9.13(b) and 9.13(c). It is also noticeable that the energy decay of the carriers is spatially flat in the region enclosed by $\mathscr{D}^{S-P}$.

The acceleration/deceleration of the propagating polaritons is distinct in the slope changes of

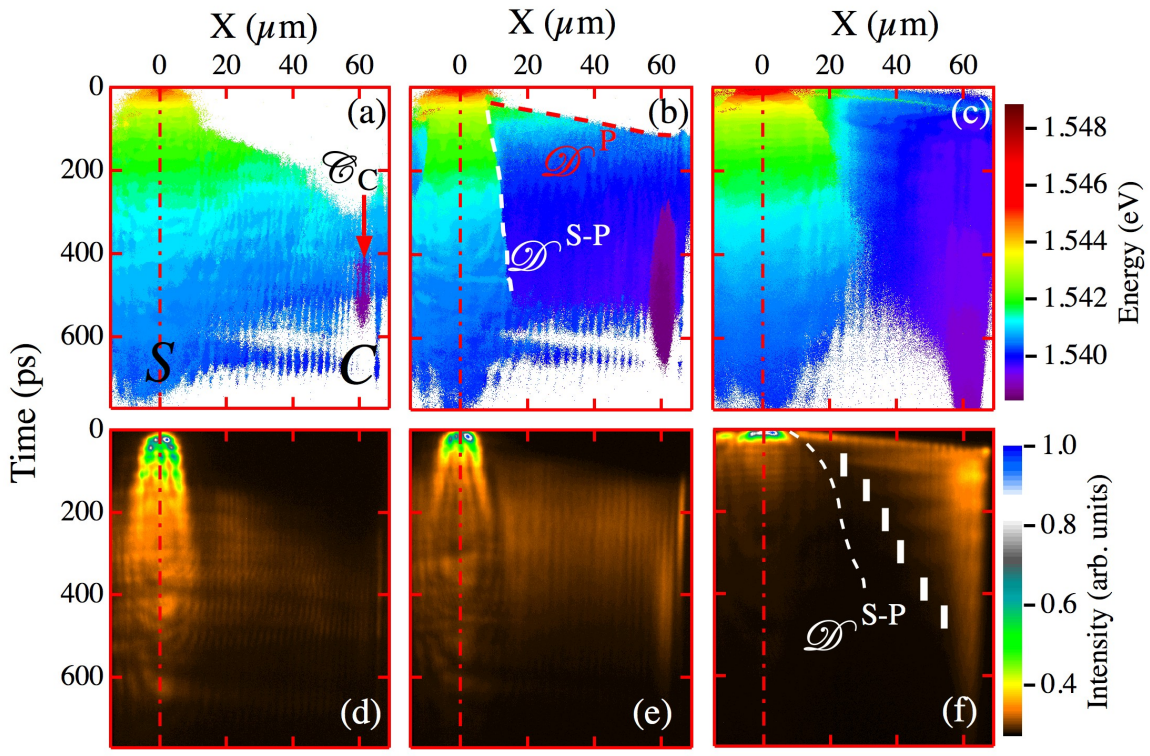

FIGURE 9.13: (a-c) Energy/(d-f) Intensity of the emission vs. real space (X) and time for different source excitation powers: (a/d) $1.0\times P_{th}$ (b/e) $1.7\times P_{th}$ and (c/f) $10.5\times P_{th}$. S, C and $\mathscr{C}_C$ mark the source, the collector and the trapped condensate at C positions, respectively. The $\mathscr{D}^P$ ($\mathscr{D}^{S-P}$) line marks the horizon between propagating polaritons and noise (carriers at S and propagating polaritons), see text for further details. The information is coded in a linear/logarithmic false color scale shown on the right side of the upper/lower row.

$\mathscr{D}^P$, Figs. 9.13(a-c). For $P_S = P_{th}$, a rough estimation of the speed obtains $v^{P(@P_{th})}$= 0.4 μm/ps; v^P increases to 0.6(1) and 1.1(1) μm/ps for $P_S = 1.7 \times P_{th}$ and $10.5 \times P_{th}$, respectively. In the later case v^P amounts to 0.3 % of the speed of light in vacuum. The formation of $\mathscr{C}_C$ at threshold, Fig. 9.13(a), is seen by the purple (1.539 eV) oval shape at ($\backsim$ 60 μm, 400-600 ps). The enhancement of v^P together with that of stimulated scattering processes with power give rise to an earlier appearance of $\mathscr{C}_C$ at $\backsim$280 ps lasting for 400 ps, almost doubling its spatial extent, at $P_S = 1.7 \times P_{th}$, Fig. 9.13(b). The values for v^P are in agreement with others reported in the literature (see, for example, Ref. [26]). The much smaller values for v^S are due to the larger exciton mass compared to that of polaritons. The energy gap between $\mathscr{C}_C$ and the propagating polaritons dissolves at $P_S = 10.5 \times P_{th}$ due to the very large number of polaritons and the very fast formation of this condensate. Finally, let us remark that the ballistic propagation of polaritons is evidenced in Fig. 9.13(b) by the constant energy (same color), for a given time, seen in the region enclosed by the $\mathscr{D}^{S-P}$-border and C. However, in case shown in Fig. 9.13(c) a gradual change in energy (color) is observed, indicating the energy loss during the polariton propagation towards C.

We briefly discuss now the density maps for different power excitation shown in the lower

row of Fig. 9.13, in a normalized, logarithmic false-color scale shown on their right-hand side. Figures 9.13(d-f) show that the main emission intensity arises from the population at S, with a gradual expansion towards C with a much lower polariton population. The emission-intensity decay becomes faster with increasing P_S power. For $P_S = 1.7 \times P_{th}$, Fig. 9.13(e), an enhanced emission following the $\mathscr{D}^{S-P}$ is apparent; interferences of polaritons in the region between $\backsim$20 and $\backsim$60 μm are visible; the formation of $\mathscr{C}_C$ appears at 280 ps. Figure 9.13(f) shows several reflections of condensed polaritons between the ridge edge and the left-bouncing positions marked with white bars, which are determined by the potential delimited by $\mathscr{D}^{S-P}$ and the energy of the bouncing condensates: the longer the time, the larger the energy loss of the polaritons, which become less able to climb the barrier side, as borne out by the progressively increasing distance between the bars and the $\mathscr{D}^{S-P}$ line, obtained from Fig. 9.13(c) and depicted with a white dotted line. At $\backsim$60 μm and 100 ps a considerable amount of population forms the $\mathscr{C}_C$ condensate.

We turn now to the two-beam excitation compiled in Fig. 9.14. Figure 9.14(a) displays the energy decay of the polaritons in the OFF-state for $P_S = 7.2 \times P_{th}$ and $P_G = 0.4 \times P_{th}$. The $\mathscr{C}_{S-G}$ condensate, extending 20 μm, reveals an almost constant energy emission in time. The contrast of the OFF-state is high as assessed by the negligible amount of polaritons that goes through the G potential, Fig. 9.14(d); only a hint of the polaritons that were able to tunnel through is seen at (80 μm, 400 ps) in Fig. 9.14(a), that codifies the energy but not the intensity of the signal. The ratio $I(\mathscr{C}_{S-G})/I(S)$ is much larger than $I(\mathscr{C}_C)/I(S)$, obtained in the one beam case since $\mathscr{C}_{S-G}$ is trapped closer to S and its feeding process is more efficient. Increasing P_G to $1.8 \times P_{th}$ both S and G beams contribute to the formation and trapping of polariton condensates, Fig. 9.14(b), $\mathscr{C}_{S-G}$ and $\mathscr{C}_C$. Figure 9.14(c), for $P_G = 9.0 \times P_{th}$, shows that, for the first $\backsim$ 100 ps, the energy decays at S and G are much faster than those of the polariton condensates. For longer times, $t \geq 100$ ps, the energy decay of the populations at S, $\mathscr{C}_{S-G}$ and G is almost identical; however, $\mathscr{C}_C$ is always at a lower energy due to the trapping at C.

A further inspection of the energy-integrated intensity maps shows that in Fig. 9.14(e), at 300 ps, when the G-barrier has considerably decayed, so that its energy coincides with that of $\mathscr{C}_{S-G}$, the $\mathscr{C}_{S-G}$ condensate starts expanding along the ridge; concomitantly a slanted interference pattern is obtained, revealing the dynamics of merging counter-propagating polaritons.

The $\mathscr{C}_{S-G}$ formation time, $\backsim$70 ps, is much shorter than that of $\mathscr{C}_C$, $\backsim$350 ps, due to the fact that P_S is much larger than P_G and that both beams contribute to feed $\mathscr{C}_{S-G}$ while only the population at G refills the $\mathscr{C}_C$ condensate, which reaches its maximum intensity emission at 400 ps. In Fig. 9.14(f), the high S- and G-pump powers make the $\mathscr{C}_{S-G}$ condensate very intense at 40 ps. The confluence of the S- and G-population with $\mathscr{C}_{S-G}$ takes place at 100 ps and 1.542 eV. Then $\mathscr{C}_{S-G}$ doubles its spatial width, as observed by the spreading cone of polaritons extending 20 μm at 40 ps to 40 μm at 250 ps. A clear back and forth bouncing of the $\mathscr{C}_C$ condensate between the G-barrier and the ridge edge is observed during the first 100 ps. After losing its kinetic energy

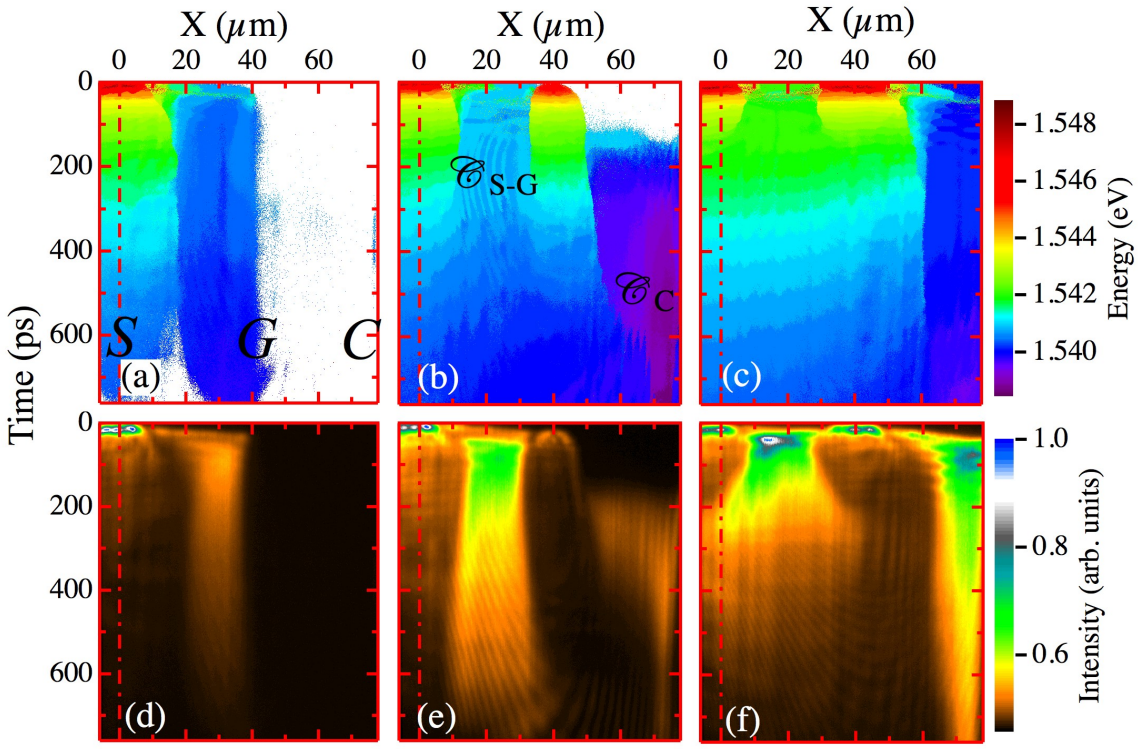

FIGURE 9.14: (a-c) Energy/(d-f) Intensity of the emission vs. real space (X) and time for a constant source excitation power $P_S = 7.2 \times P_{th}$ and different gate powers P_G: (a/d) $0.4{\times}P_{th}$ (b/e) $1.8{\times}P_{th}$ and (c/f) $9.0{\times}P_{th}$. S, G, C, $\mathscr{C}_{S-G}$ and $\mathscr{C}_C$ mark the source, the gate, the collector, the trapped condensate between S-G and the trapped condensate at C positions, respectively, see text for further details. The information is coded in a linear/logarithmic false color scale shown on the right side of the upper/lower row.

at $t \backsim 150$ ps, $\mathscr{C}_C$ stops and emits for more than 600 ps, as its population is continuously fed by propagating polaritons at $\backsim 1.541$ eV.

The energy maps shown in Figs. 9.13-9.14(a-c) allow to quantitatively analyze the energy decay at every X-position; in particular we present in Fig. 9.15 this decay at the S position for $P_S = 10.5 \times P_{th}$. The solid white line in Fig. 9.15(a) corresponds to its best fit to the sum of two exponentially decaying functions, shown separately by the dashed and dot-dashed lines. The double fashion decay is attributed to two different physical processes: a fast decay due to relaxation driven by exciton-exciton interactions and a slow one, attributed to the decreasing blueshift caused by the diminishing exciton and polariton populations. The rate of condensation can be expected to be faster at early times due to larger densities of carriers resulting in stronger stimulated scattering processes. A fast condensation rate results in an initial fast drop in the exciton density since excitons condense rapidly into polaritons that quickly decay. This drop in the exciton population gives a corresponding drop in the polariton population and so both blueshifts, due to polariton-exciton and polariton-polariton repulsion, drop sharply at early times. At longer times polariton condensation proceeds slower, due to weaker stimulated scattering and the exciton populations

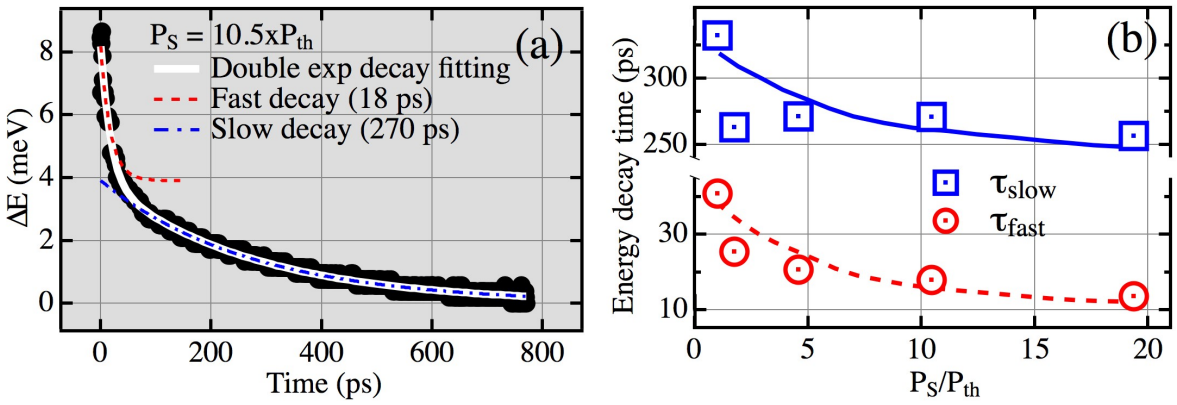

FIGURE 9.15: (a) Energy shift at S vs. time for $P_S = 10 \times P_{th}$ (black circles). Double exponential decay fit(solid white line): fast component (τ_{fast} = 18 ps, red dashed line), slow component (τ_{slow} = 270 ps, dot-dashed blue line). (b) τ_{slow}/τ_{fast} decay times (blue square/red circle markers, blue full/ dashed red line is a guide to the eye) vs. normalized P_S power.

decay with a slow exponential dependence due to exciton recombination. Figure 9.15(b) compiles the power dependence of the decay times: both decrease with increasing power, more markedly for τ_{fast} (circles), which decreases by $\backsim$ 65% for a 20 fold increase of power, whilst τ_{slow} (squares) only diminishes by $\backsim$ 20%, revealing the larger influence of density in exciton-exciton scattering processes than in exciton-polariton ones.

The spatial integration of the data shown in Figs. 9.5-9.12 reveals the total energy and intensity decay dynamics for the different configurations under study as shown in Fig. 9.16: Figs. 9.16(a-c)/(i-iii), correspond to one/two beam excitation under different P_S/P_G powers. The addition of contributions from different population species gives rise to a very rich dynamics. Figures 9.16(a-c) exhibit a critical difference in the power dependence of the total decay: Fig. 9.16(a) shows a collective energy decay for **all** spatial positions along the ridge. Figures 9.16(b,c) show a low energy streak corresponding to a polariton condensate drop that propagates along the ridge with an almost constant energy, unveiling the ballistic propagation of the condensate. The two streaks presented in Fig. 9.16(i) correspond to the decay of population at S (high energy one) and the emission of $\mathscr{C}_{S-G}$ for a typical switch OFF state (low energy one): the dynamics of both streaks is similar to those shown in Fig. 9.16(c), with the difference, not appreciated in the figure, that polaritons now are stopped just before the G barrier.

The three traces appearing in Fig. 9.16(ii), ordered by decreasing energy, compile the emission from: the population at S and G (S+G), the $\mathscr{C}_{S-G}$ condensate and the $\mathscr{C}_C$ condensate, respectively. It is worthwhile noting the identical decay dynamics of the S and G populations, observed by the existence of only one streak for both populations. The $\mathscr{C}_C$ condensate shows an emission at $\backsim$1.539 eV, with a dynamics similar to that shown in Fig. 9.16(b). As the S power is kept constant in this subset of experiments, the G power permits manipulating on demand the amount of condensed

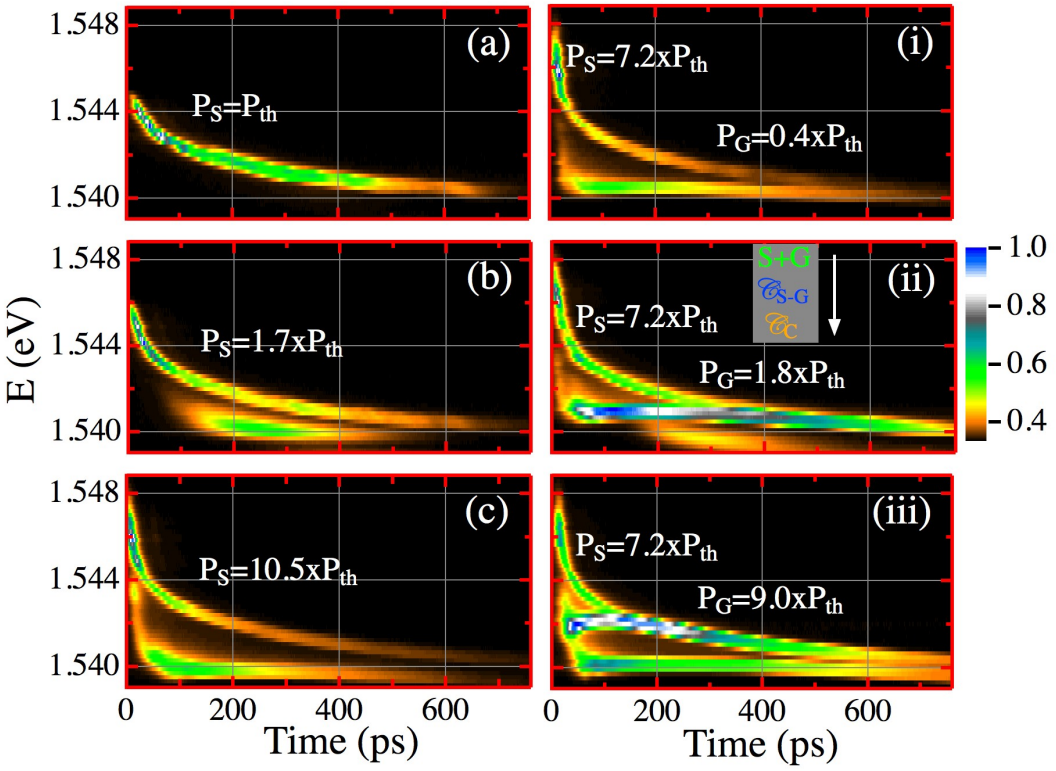

FIGURE 9.16: Energy decay, spatially-integrated, vs. time for one (a-c) and two beams (i-iii) excitation conditions. (a) $P_S = 1.0 \times P_{th}$, (b) $1.7{\times}P_{th}$ and (c) $10.5{\times}P_{th}$. For $P_S = 7.2 \times P_{th}$: (i) $P_G = 0.4 \times P_{th}$, (ii) $1.8{\times}P_{th}$ and (iii) $9.0{\times}P_{th}$, see text for further details. The intensity is coded in a logarithmic false color scale shown on the right.

polaritons at $\mathscr{C}_{S-G}$: if it would have been formed only by the S pulse, its energy should decay slightly; however, the extra population injected by the G pulse contributes with an additional blueshift giving rise to an increase of the $\mathscr{C}_{S-G}$ emission energy, hinted at $\backsim$ 300 ps in Fig. 9.16(ii), which becomes clearly visible in Fig. 9.16(iii). In this latter panel, the $S{+}G$ decays are also superimposed and $\mathscr{C}_C$ emits at a constant energy of 1.540 eV for $t > 50$ ps. It is important to note that in Figs. 9.16(ii,iii), the additional polaritons provided by the G pulse make the $\mathscr{C}_{S-G}$ condensate the highest populated state in the device with an emission intensity even larger than that of $S + G$ together.

9.3.1.6 Optimization of the switching time

We are going to discuss now the optimal power conditions for the ON state for a S-C spatial separation of $\backsim$ 60 μm. We present in Fig. 9.17 the main effects of the P_S power on the transistor switch ON state, which was illustrated before in Figs. 9.5-9.7. Figure 9.17(a) plots the normalized intensity dynamics of the source, at $X = 0$, (shadowed traces) and that of $\mathscr{C}_C$, at $X = 60$ μm, (full lines), for different P_S/P_{th} values.

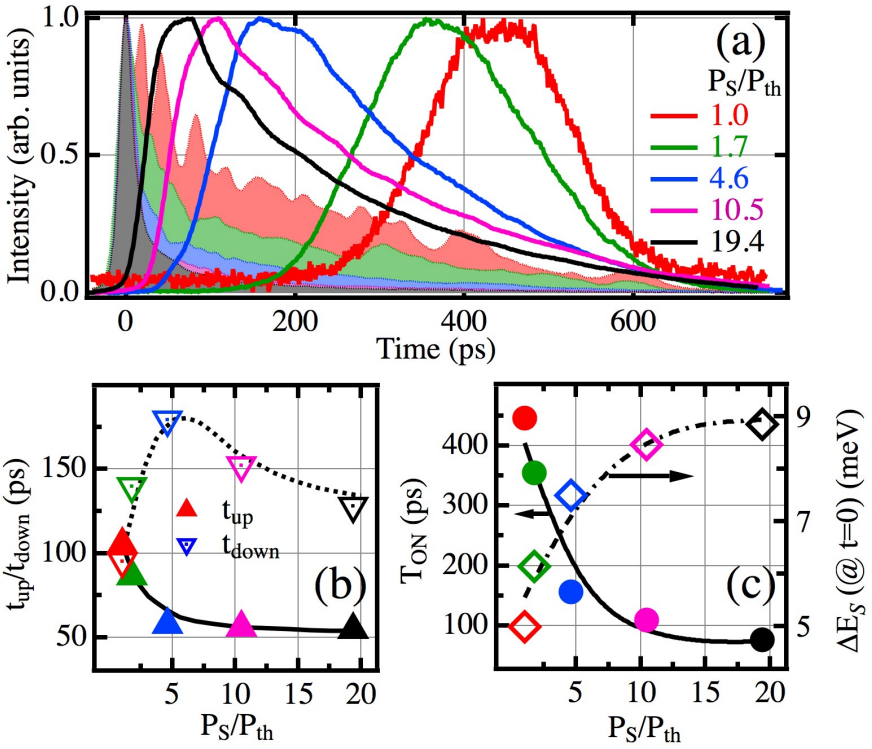

FIGURE 9.17: (a) Integrated PL at S position in filled lines and integrated intensity at C in full line for $P_S = 1.0, 1.7, 4.6, 10.5, 19.4 \times P_{th}$. (b) Up/ Down triangles show the raising/decreasing time t_{up}/t_{down} from 0.5 to 1/1 to 0.5. (c) Full circles show the temporal separation between S and C intensity peaks; open diamonds depict the initial energy shift of the emission at S. Same color legend for the values of P_S are used in (a), (b) and (c).

We define the switch ON time, T_{ON}, as the temporal delay between the S maximum intensity and that of the $\mathscr{C}_C$. It is clearly observed that T_{ON} decreases, and the shape of the $\mathscr{C}_C$ time-evolutions becomes more asymmetric with increasing P_S. The asymmetry of the $\mathscr{C}_C$ temporal evolution [see Fig. 9.17(a)], which strongly depend on P_S, is characterized in Fig. 9.17(b), where we define a raise time, t_{up} (up triangles), given by the time spent to raise from an intensity of 0.5 up to the maximum value of 1. Similarly, t_{down} (down triangles) is given by the time interval in which the intensity falls from a value of 1 to 0.5. A non monotonic dependence of t_{down} on power is observed with a sharp raise at low P_S values and a gradual fall for high ones: if the aim is to create a long lived ON state, the optimal power corresponds to $P_S/P_{th} \approx 7$, where $t_{down} \backsim 175$ ps. On its own hand, the raise time, t_{up}, decreases monotonically with increasing P_S, reaching a minimum value of $\backsim 50$ ps: a marked dependence at small powers, followed by an almost negligible decay at high ones, results in an optimum power to create a fast response transistor at similar powers than those required for a long lived ON state.

Figure 9.17(c) shows the power dependence of T_{ON} (full circles) together with the initial energy shift of the emission at S (ΔE_S, open diamonds). The monotonous decrease of T_{ON} with power (increase of switching rate) is linked to the increase of ΔE_S, due to the enhanced polariton

acceleration from S to C produced by the augmented photo-generated repulsive excitonic potential, but other contributions as, for example, increase of stimulated scattering processes in the creation of $\mathscr{C}_C$ are also responsible for the quickening of T_{ON}. The minimum value of T_{ON}, $\backsim$ 80 ps, corresponds to a polariton propagation speed of $\backsim$ 1.1 μm/ps in agreement with the values of v^P obtained from the horizon established by $\mathscr{D}^P$ in the energy maps of Fig 9.13(a-c). Finally, we should mention that our results indicate that the optimal conditions for gating are obtained for $P_G = 0.6 \times P_{th}$, in agreement with the previous results of Ref. [43]. At this power, the maximum attenuation of the $\mathscr{C}_C$ condensate is obtained yielding the highest contrast for the OFF state; at lower values of P_G the traveling polaritons are not gated efficiently and at higher values G starts feeding $\mathscr{C}_C$.

9.3.1.7 Drifting interference fringes in the *X-t* maps

In this section we investigate in detail the interference fringes in the polariton $X-t$ maps observed, for example, in Figs. 9.5(d), 9.6(d) and 9.11(f). In Chapter 7 we have discussed the polariton interferences in the momentum space distribution, as result of two polariton condensates propagating in the same direction at the same speed. The polariton interferences have been also observed in the real space distribution when two counter-propagating polariton condensates overlap in the same spatial position. Recalling this latter case, in this section we extract the value of Δk_X between two counter propagating polariton flows (from the interferences in real space) through an FFT analysis of the $X-t$ maps.

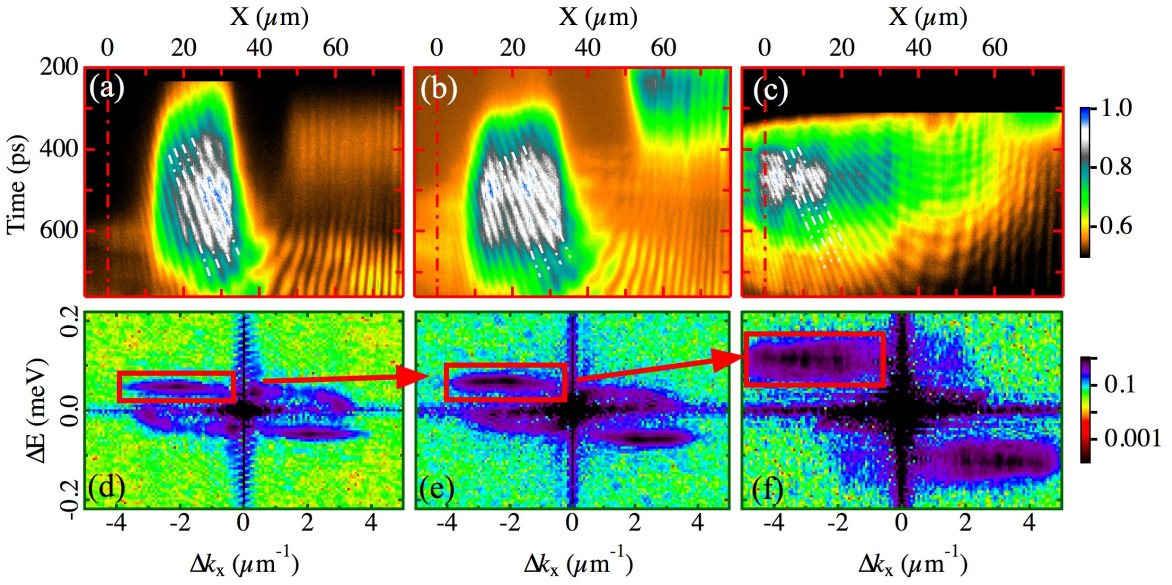

FIGURE 9.18: (a-c) Integrated intensity of the emission vs. real space (X) and time for a constant source excitation power $P_S = 7.2 \times P_{th}$ and three different gate powers P_G: (a) $0.4 \times P_{th}$ (b) $1.8 \times P_{th}$ and (c) $9.0 \times P_{th}$. White dashed lines mark as guide to the eyes the fringes drift in a region of the X-t map. (d-f) Corresponding Fourier transform of the X-t map. Red boxes mark the relevant information in the reciprocal space as guide to the eyes. The X-t origins in (a-c) panels are the same as those used in Fig. 9.13.

In these maps we also observe a temporal drift in the interferences, see for example Fig. 9.14(e-f), producing curved fringes in the $X-t$ maps and therefore producing interferences in the time domain. This effect is produced at instants with spatial overlap between polariton flows emitting at slightly different energies. From the interferences in the temporal axis we infer the difference in energy ΔE, extracted in the FFT analysis, which renders a complete characterization of the interferences in both real and time domains.

We analyze in the maps of Fig. 9.18 a spatial-temporal region with conspicuous interference patterns that was previously energy-integrated within a selected range of the total spectrum of the polariton PL presented in Figs. 9.14(d-f). Figures 9.14(d-f) display barely visible interferences because the main emission arises from S, $\mathscr{C}_{S-G}$ and $\mathscr{C}_C$, hindering the visualization of the oscillatory patterns. Since the polariton oscillations take place at a relatively small range of energy (< 1 meV) as compared to the spectral extension of the PL in such experiments (~ 8 meV), we display in Fig. 9.18 the corresponding, integrated ranges of energy of those $X-t$-maps shown in Figs. 9.14(d-f) in order to enhance the interferences visualization. The limits of integration of the polariton PL shown in Figs. 9.14(d-f) are the following: (a) $1.5396-1.5402$ eV, (b) $1.5396-1.5404$ eV and (c) $1.5404-1.5411$ eV, respectively.

We discuss the drifting patterns in the spatial-temporal region $\Delta X = \{10, 30\}$ μm and $\Delta t = \{400, 700\}$ ps. White dashed lines sketch the interference fringes as a guide to the eye in Figs. 9.18(a-c). Their periodicity along the X-axis is given by $\Delta X = 2\pi/\kappa$, where κ is the difference in the in-plane momentum of the polariton flows overlapping and counter-propagating in real space (for further details, see the complementary expression in real space to Eq. 7.5 discussed in § 7.2). In the FFT map we identify the value of κ in the horizontal axis, Δk_X. The angle of the polariton oscillations with respect to the temporal axis is determined by the energy difference $\Delta E = |E_S - E_G|$, between the polariton populations created at S and G. An increase in P_G induces a higher $\{E_G, k_G\}$ resulting in an increase of the slope in the fringes and in the spatial periodicity, respectively.

Figures 9.18(d-f) depict the FFT of the interferences shown in Figs. 9.18(a-c), respectively. The FFT maps display two conjugated off-axis contributions spanning a difference of momentum of the counter-propagating polaritons, $|\Delta k_X|$, from $\backsim 0.5$ to $\backsim 4$ μm^{-1} [Figs. 9.18(d,e)], which increases slightly with P_G, see how the FFT values spans in a broader range in Fig. 9.18(f) from $|\Delta k_X| \backsim 0.5$ to $\backsim 5$ μm^{-1}. The distribution of ΔE is blue-shifted and broadens with increasing P_G: it is centered at $\{0.05, 0.07, 0.11\}$ meV with a width $\sigma_E = \{0.01, 0.03, 0.08\}$ meV when the value of P_G is $P_G = \{0, 4, 1.8, 9.0\} \times P_{th}$, respectively (see red boxes). When the pump power of G increases, in first place, the polariton density of the ejected flow increases, enhancing the polariton-polariton interactions and blue-shifting the emission, the polariton propagation also takes place at higher energy subbands of the ridge's dispersion relation, this explains the broadening in ΔE and its blueshift. In second place, a denser exciton reservoir at G enhances the repulsive interactions with

the ejected polaritons, imprinting on them a bigger value of k_x. This effect accounts for a broader range of Δk_x values in the FFT maps for increasing P_G values.

9.3.2 Model

To model our experimental results theoretically, we make use of the phenomenological treatment described in § 2.5.2.3, accounting for the polariton energy-relaxation processes taking place in the system. The GP Eq. 2.42 is also included here for the sake of clarity (see new Eq. 9.4), it has been developed to describe the non-equilibrium dynamics of condensed polaritons, where losses due to the short polariton lifetime [196] and gain due to non-resonant pumping [193, 197] were included phenomenologically.

$$i\hbar\partial_t\psi(x,t) = \left[\hat{E}_{LP} + \alpha|\psi(x,t)|^2 + V(x,t) + i\hbar\left(rN_A(x,t) - \frac{\Gamma}{2}\right)\right]\psi(x,t) + i\hbar\Re\left[\psi(x,t)\right] \quad (9.4)$$

The term accounting for the polariton energy relaxation, $\Re\left[\psi(x,t)\right]$, in Eq. 9.4 is called back from § 3.2.1.1, it is differently defined as it was previously introduced in Eq. 9.3 for experiments described in § 9.2, see Eq. 9.5:

$$\Re[\psi(x,t)] = -\left(\nu + \nu'|\psi(x,t)|^2\right)\left(\hat{E}_{\mathrm{LP}} - \mu(x,t)\right)\psi(x,t), \quad (9.5)$$

In the present case, $\Re[\psi(x,t)]$ accounts for the energy relaxation at low polariton densities (described by the parameter ν) as well as a stimulated component of the relaxation proportional to the polariton density, $|\psi(x,t)|^2$ (described by the parameter ν'). The energy relaxation rate is assumed proportional to the kinetic energy of polaritons; polaritons will relax in energy until they decay from the system or until their kinetic energy is zero (such that they have zero in-plane wave-vector).

The two terms accounting for repulsive interactions in Eq. 9.4 are the polariton-polariton interactions, $\alpha|\psi(x,t)|^2$ ($\alpha > 0$), and the effective potential $V(x,t)$ acting on polaritons caused by repulsive interactions between polaritons and higher-energy excitons. The latter term is more significant than the former one and it is responsible for the blocking of polariton propagation in the presence of a G pump. $V(x,t)$ can be divided into a contribution from three different types of hot-exciton states (described below) as well as a static contribution due to the wire structural potential $V_0(x)$ (it is experimentally characterized in § 3.2.1.1):

$$V(x,t) = \hbar\left[g_R N_A(x,t) + g_I N_I(x,t) + g_D N_D(x,t)\right] + V_0(x) \quad (9.6)$$

It is worth to remember that N_A, N_I and N_D correspond to density distributions of "active", "inactive" and dark excitons, respectively. g_R, g_I and g_D define the strengths of interaction with the various hot exciton states. The description of the GP Eq. 9.4 that includes the interaction with

a three-exciton level reservoir is addressed in § 2.5.2.3, nevertheless we recall again the dynamics of the exciton densities described by the following rate equations:

$$\frac{dN_A(x,t)}{dt} = -\left(\Gamma_A + r|\psi(x,t)|^2\right) N_A(x,t) + \left(t_R + t'_R N_I(x,t)\right) N_I(x,t) \tag{9.7}$$

$$\frac{dN_I(x,t)}{dt} = -\left(\Gamma_I + t_R + t'_R N_I(x,t) + t_D\right) N_I(x,t) \tag{9.8}$$

$$\frac{dN_D(x,t)}{dt} = t_D N_I(x,t) - \Gamma_D N_D(x,t) \tag{9.9}$$

The dark excitons (Eq. 9.9) introduce a long-lived repulsive contribution to the effective polariton potential, $V(x,t)$ (Eq. 9.6), and are thus efficient at gating propagating polaritons at long-times. Polaritons are expected to condense at S into the lowest energy state, where they have zero kinetic energy and potential energy given by $V(x,t)$ (and an additional blueshift due to polariton-polariton interactions). While this is the lowest energy state available at S, one notes that the potential energy can be reduced if polaritons propagate away from S ($V(x,t)$ decreases away from S, where the reservoir densities are weaker). If polaritons were to conserve their energy, then they would convert this potential energy into kinetic energy as they move away from S, accelerating down the potential gradient.

Equations 9.4-9.9 were solved numerically for different initial density profiles $N_I(x,0)$, corresponding to the different source and gate configurations studied experimentally. We used the following parameters in the theory: $m = 7.3 \times 10^{-5} m_e$ (obtained from fits to the dispersion relations measured in § 3.2.1; m_e is the free electron mass), $\alpha = 2.4 \times 10^{-3}\text{meV}\mu m^2$ (Ref. [246]), $\Gamma = 1/18$ ps^{-1}, $\Gamma_A = 0.01$ ps^{-1}, $\Gamma_I = \Gamma_D = 10^{-3}$ ps^{-1}, $t_R = 10^{-4}$ ps^{-1}, $t_D = 2 \times 10^{-4}$ ps^{-1}, $t'_R = 10^{-4}$ ps$^{-1}\mu$m^2, $g_R = g_I = 0.04$ ps$^{-1}\mu$m^2, $g_D = 0.5$ ps$^{-1}\mu$m^2, $\hbar\nu = 0.014$, $\hbar\nu' = 0.075\mu$m^2.

9.3.2.1 Simulations for the one-beam excitation

Figure 9.19 shows the evolution of the spectrum in real space for $P_S = P_{th}$. As in the experimental case (Fig. 9.5), condensation initially takes place into a state blueshifted due to the repulsive interactions from the hot exciton reservoirs contributing to the effective potential $V(x,t)$. Over time, this blueshift decays resulting in progressively lower energy of S state. In addition, a propagating polariton state can be observed, which forms interference fringes due to reflection from the end of the ridge. Energy relaxation is slow, appearing only at very long times due to the lack of stimulation by the low polariton density.

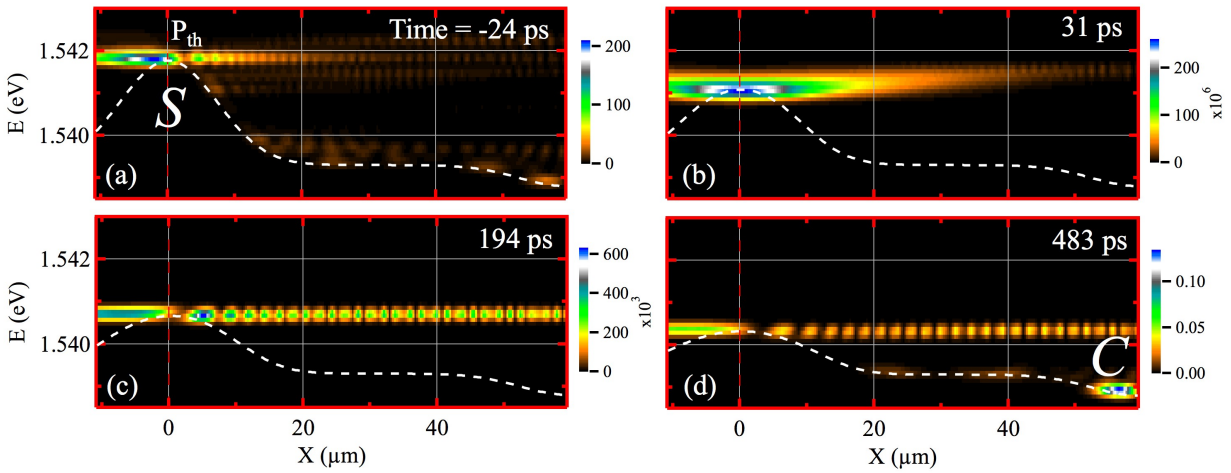

FIGURE 9.19: Polariton PL emission as function of energy and real space (X) for $P_S = P_{th}$ at different times shown by the labels. The white dashed curves show the evolution of the effective potential $V(x,t)$ due to hot exciton repulsion as well as the ridge structural potential (same for Figs. 9.20-9.22). S and C mark the source and the collector positions, respectively. The intensity is coded in a false, linear color scale shown on the right of each panel.

For higher power ($P_S = 1.7 \times P_{th}$), Fig. 9.20 shows the onset of stimulated energy relaxation processes. As in the experimental case (Fig. 9.6) the relaxation takes place in two subsequent stages: first there is relaxation from the S state into the extended state with energy set by the ridge potential, followed by relaxation into the $\mathscr{C}_C$ condensate at low energy.

At $10.5 \times P_{th}$, Fig. 9.21 shows that the energy relaxation occurs rapidly. As in the experimental case (Fig. 9.7) $\mathscr{C}_C$ is rapidly populated. It is interesting to note that, as shown for the experiments in Fig. 9.17(c), the blueshift of the condensate at the S position does not increase linearly with the pump power. This is because even though the injected hot exciton population can be expected to increase linearly, the increased carrier density results in a faster condensation rate due to the stimulation of scattering processes (hot exciton relaxation processes as well as processes that cause excitons to relax into condensed polaritons). Polaritons decay much faster than uncondensed hot excitons, such that a high intensity pumping of hot excitons is quickly depleted giving rise to a limited blueshift of polaritons at S.

9.3.2.2 Simulations for the two-beam excitation

In the presence of the gating pulse, the propagation of the $\mathscr{C}_{S-G}$ condensate is blocked, as shown in Fig. 9.22. This is due to the injected hot exciton density at G position that adds to the polariton effective potential profile, $V(x,t)$. At long times, the theory predicts a small transmission across G pulse, due to the decay of the potential barrier, as previously reported in the discussion of the OFF transistor state experiments presented Fig. 9.3.

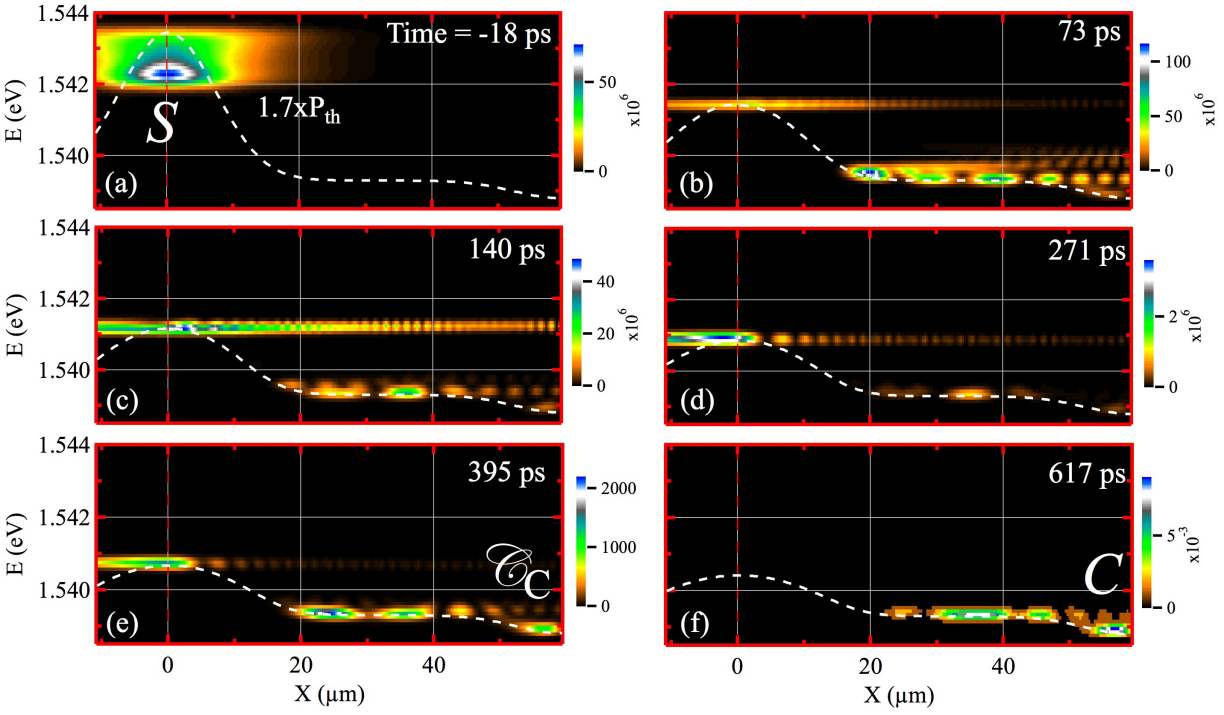

FIGURE 9.20: Polariton PL emission as function of energy and real space (X) for $P_S = 1.7 \times P_{th}$ at different times shown by the labels. S, C and $\mathscr{C}_C$ mark the source, the collector and the trapped condensate at C positions, respectively. The intensity is coded in a false, linear color scale shown on the right of each panel.

9.3.2.3 Simulations on the power dependance of the energy/intensity decays

Spatial-temporal maps of the peak emission energy with one-beam excitation are shown in Fig. 9.23. In Fig. 9.23(a) there is a fast propagation of a high energy mode from S followed by a decrease in energy of the emission over the whole space. At longer times, one identifies relaxation into $\mathscr{C}_C$, near the wire edge. This behavior is in qualitative agreement with the experimental result, however, it can be noted that the speed of propagation appears overestimated in the theory. This is because the theory neglects changes in the shape of the polariton dispersion caused by the hot-exciton induced blueshift, which can be particularly important at early times when the particles are strongly excitonic with a larger effective mass and slower group velocity. Figures 9.23(b) and 9.23(c) show the peak emission energy maps for increasing source intensity, where the relaxation into an extended state with lower energy than S can be identified. The relaxation is stronger at the highest pump power, due to increased stimulated energy relaxation processes. This is also evidenced by the shorter time required for $\mathscr{C}_C$ to appear with increasing pump power.

We discuss now the simulated energy- and intensity maps under two-beam excitation conditions compiled in Fig. 9.24. Figure 9.24(a) shows the case when a gate pulse, $P_G = 0.4 \times P_{th}$, is present. At short times the energy of $\mathscr{C}_C$ is low, although it should be noted that it is populated with a small density, Fig. 9.24(d). The weak tunneling of particles across G is better evidenced

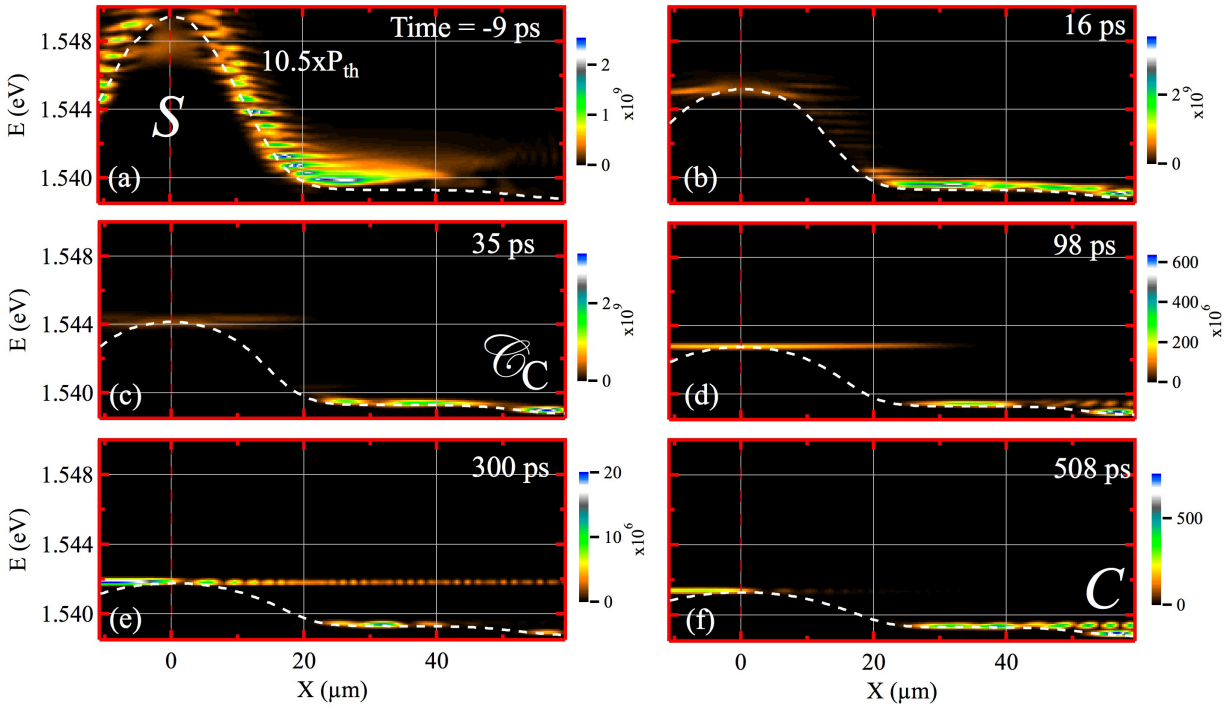

FIGURE 9.21: Polariton PL emission as function of energy and real space (X) for $P_S = 10.5 \times P_{th}$ at different times shown by the labels. S, C and $\mathscr{C}_C$ mark the source, the collector and the trapped condensate at C positions, respectively. The intensity is coded in a false, linear color scale shown on the right of each panel.

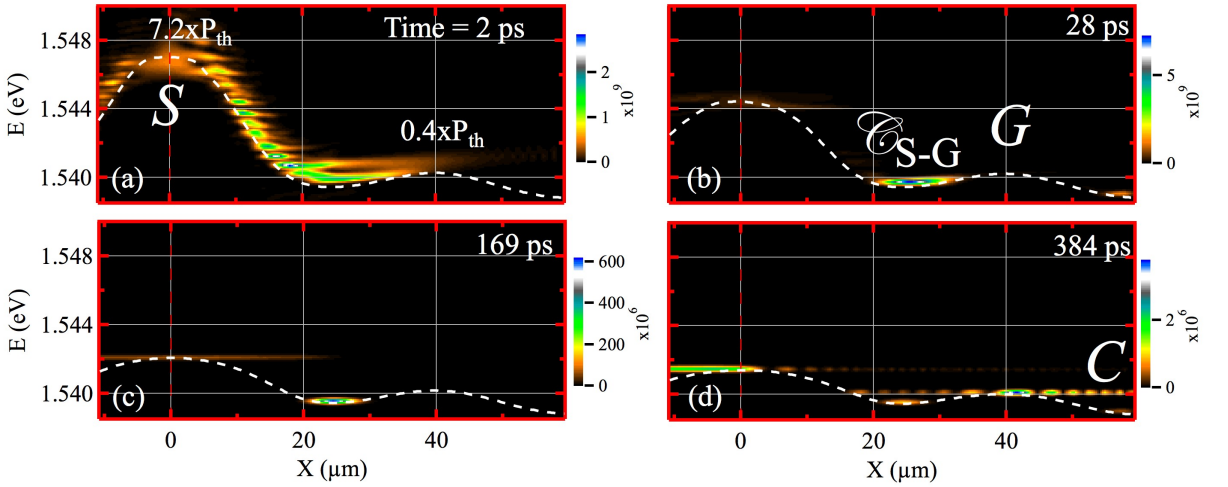

FIGURE 9.22: Polariton PL emission as function of energy and real space (X) for $P_S = 7.2 \times P_{th}$ and $P_G = 0.4 \times P_{th}$ at different times shown by the labels. S, G, C and $\mathscr{C}_{S-G}$ mark the source, the gate, the collector and the, between S-G, trapped condensate positions, respectively. The intensity is coded in a false, linear color scale shown on the right of each panel.

by the increase of the $\mathscr{C}_C$ energy, since the tunneling particles have higher energy than the $\mathscr{C}_C$ ground state. At these low gate powers, the theory appears to predict a high number of polaritons passing G. These polaritons have relatively high momentum and are expected to be less

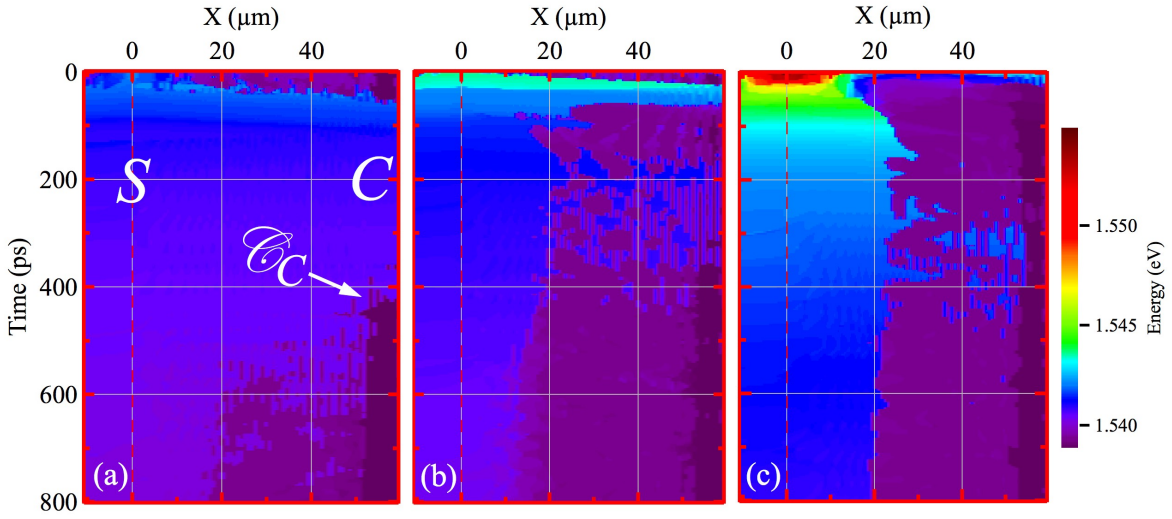

FIGURE 9.23: Energy of the emission vs. real space (X) and time. (a)$P_S = P_{th}$, (b) $P_S = 1.7 \times P_{th}$, (c) $P_S = 10.5 \times P_{th}$ and (d) $P_S = 7.2 \times P_{th}$ and $P_G = 0.4 \times P_{th}$. S, C and $\mathscr{C}_C$ mark the source, the collector and the trapped condensate at C positions, respectively. The intensity is coded in a false, linear color scale shown on the right.

visible experimentally due to their reduced photonic fractions. An increase of the G power above threshold, Figs. 9.24(b,c,e,f), leads to an enhanced collector signal, as in the experimental case, see Figs. 9.14(b,c,e,f), and the device leaves the OFF state. This is expected as additional excited polaritons move directly from G to C.

Figure 9.25 shows the time evolution of the spatially integrated spectra. In agreement with the experimental results (Fig. 9.16) there is a decay with two different time scales of the emission energy. At early times, the fast drop is due to the fast condensation rate in the presence of strong stimulated scattering. As mentioned earlier, this fast condensation rapidly depletes the hot exciton reservoir and the total particle density quickly drops as polaritons quickly decay. At longer times, reduced relaxation between the active and inactive reservoirs limits the effective condensation rate. The condensate is continuously fed while the reservoir intensities slowly decay.

The short lifetime of the condensate for pumping at threshold [Fig. 9.25(a)] is expected from the theoretical definition of threshold where the incoming rate $rN_A(x,t)$ is slightly larger than the polariton decay rate Γ in Eq. 9.4. As soon as condensation starts, the reservoir density N_A drops below threshold such that continued condensation cannot take place. For higher pump powers, Figs. 9.25(b,c) show that both emission into a high energy mode, corresponding to the source, and a lower energy emission coexist. This fact is in close agreement with the experimental data shown in Figs. 9.16(b,c) and 9.16(i), with the relaxation into the lower energy state occurring earlier for increased pumping power.

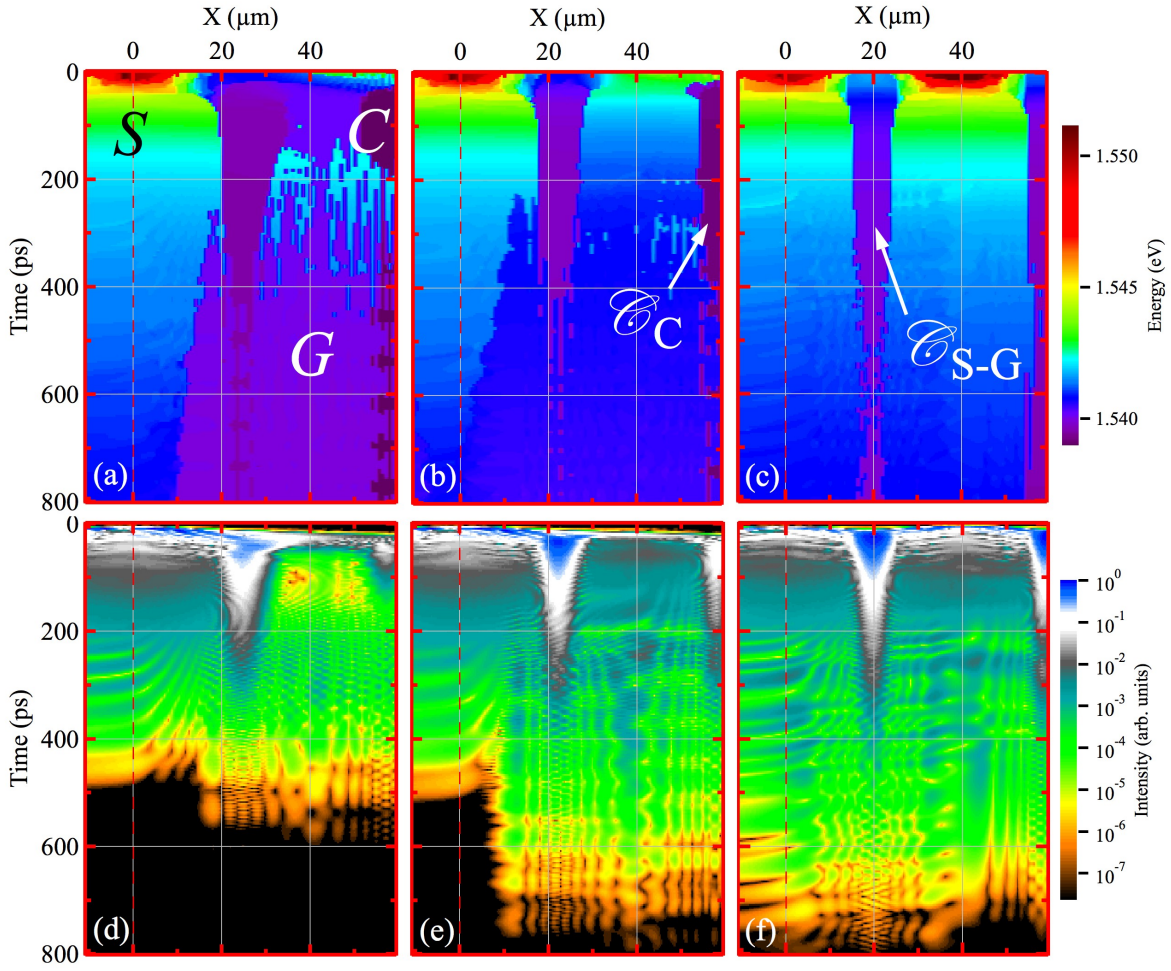

FIGURE 9.24: (a-c) Energy/(d-f) Intensity of the emission vs. real space (X) and time for a constant source excitation power $P_S = 7.2 \times P_{th}$ and different gate powers P_G: (a/d) $0.4{\times}P_{th}$ (b/e) $1.8{\times}P_{th}$ and (c/f) $9.0{\times}P_{th}$. S, G, C, $\mathscr{C}_{S-G}$ and $\mathscr{C}_C$ mark the source, the gate, the collector, the trapped condensate between S-G and the trapped condensate at C positions, respectively, see text for further details. The information is coded in a linear/logarithmic false color scale shown on the right side of the upper/lower row.

9.4 Conclusions

In the first part of this Chapter, § 9.2, we have presented the full dynamics of an all-optical transistor switch, which is promising for high-speed inter-chip and intra-chip communication for core-based integrated circuits. The results are interpreted as a result of polariton propagation and energy relaxation in a dynamic potential due to the exciton reservoir, which can be optically controlled.

In the second part of this Chapter, § 9.3, we have time-resolved the energy and intensity relaxation processes of excitons and polaritons in a MC ridge. Two different excitation configurations have been studied with one and two non-resonant, pulsed laser beams, permitting polariton condensate trapping on demand. A detailed analysis of the decay processes has been accomplished

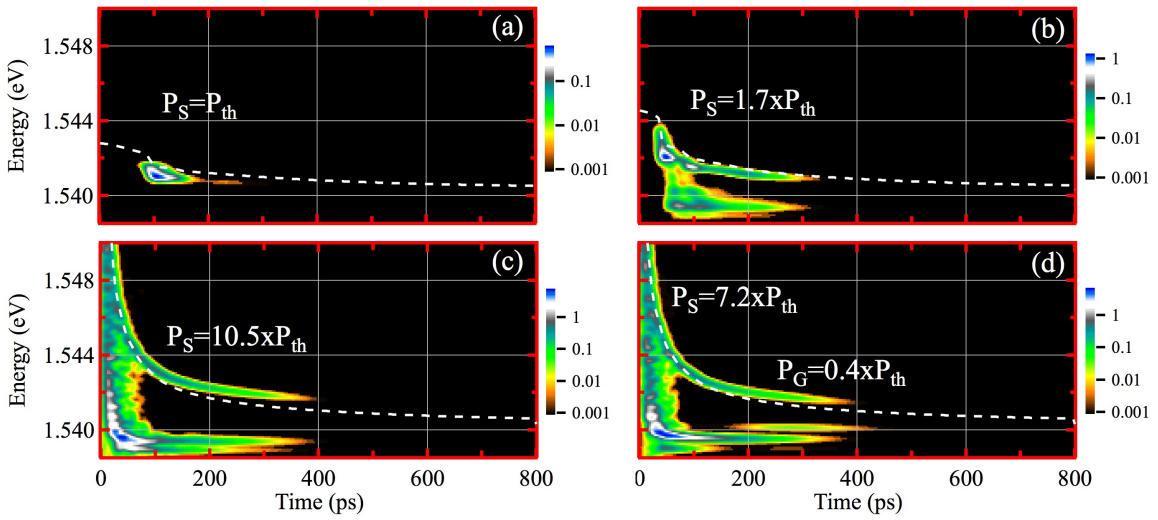

FIGURE 9.25: Energy decay, spatially-integrated, vs. time. (a)$P_S = P_{th}$, (b) $P_S = 1.7 \times P_{th}$, (c) $P_S = 10.5 \times P_{th}$ and (d) $P_S = 7.2 \times P_{th}$ and $P_G = 0.4 \times P_{th}$. The intensity is coded in a logarithmic, false color scale shown on the right. The dashed curve shows the evolution of the polariton effective potential at S, $V(x = 0, t)$.

by mapping the energy and intensity emission along the ridge. Decay times of the S emission are reported under one-beam excitation, where we show the acceleration of the decaying processes as a function of increasing P_S. The time response of the polariton transistor switch is characterized and optimized.

In both parts we used a generalized GP model to describe the spatial dynamics of our propagating polariton condensates, which includes a phenomenological treatment of energy-relaxation processes that cause condensates to further thermalize as they travel in a non-uniform effective potential. In the theoretical description of the first part, § 9.2.2, a single exciton reservoir was used to describe the repulsive interactions that mediate the gating in the polariton transistor. A more depurated model including a three-exciton level reservoir was developed in § 9.3.2 to describe the pump power dependence under one and two beam excitation in the polariton energy relaxation processes.

The nonlinearity of energy-relaxation processes throughout the system, those causing relaxation between polariton states as well as relaxation between higher energy exciton states, is necessary to explain features of the experimental results. Approximating the system as a 1D system, we are able to describe the main qualitative features of the experiment. While the system is essentially 1D, lateral expansion could result in a lower propagation speed than that predicted theoretically. We investigate lateral propagation effects in next Chapter 10, see § 10.2.3 concerning the leakage effects in the operation of the polariton device.

The optimization of individual condensate transistor elements, as we have reported here, is an essential step towards developing information processing devices with the present scheme. In

the future, an important goal is the achievement of cascadability and fan-out of multiple elements for the construction of extended circuits. Such a feat was very recently achieved in polariton based systems with coherent near-resonant excitation [39]. Achieving the same with the gating of incoherently generated polariton condensates, as we study here, would be particularly promising as it would open up routes toward electrically injected devices and consequently hybrid electro-optical processing systems.

Chapter 10

Operation speed of polariton condensate switches gated by excitons

In the previous Chapter 9 we have shown that the use of two non-resonant laser beams on 20-μm wide ridges are capable to block the polariton flow by optical means [43, 46, 62]. In this Chapter we investigate the dynamics of the device focussing on the operating conditions in terms of speed and ON/OFF-signal contrast. In particular, we show that the speed is mainly limited by the OFF-ON switching processes, which is conditioned by the lifetime of excitons at G.

This Chapter is organized as follows. We discuss in § 10.1 the sample and the experimental setup. In § 10.2, we present and discuss our results. We first show (§ 10.2.1) the principle of operation, *i.e.* we discuss the switching dynamics for a selected G power P_G. In § 10.2.2, we systematically investigate the dynamics of the device for varying P_G in order to find an optimized operation point with an acceptable ON/OFF-signal ratio. Finally, in § 10.2.3, we show that the actual 2D character of the device does not affect adversely the operation for high and wide enough barriers at G, *i.e.*, basically no significant amount of polaritons circumvents G. In § 10.3, our experiments are compared with numerical simulations of the polariton condensate dynamics based on a generalized GP equation, which is accordingly modified to account for incoherent pumping, decay and energy relaxation within the condensate.

10.1 Experimental setup

The sample is the high-quality $5\lambda/2$ $AlGaAs$-based MC described in § 3.2. We perform our experiments in the ridge structure shown in Fig. 3.5, whose dimensions are 20×300 μm^2.

Figure 10.1(a) shows a SEM image of the 20-μm wide ridge and illustrates the nomenclature we use, in close analogy to the terminology used in the previous Chapter 9 and in conventional

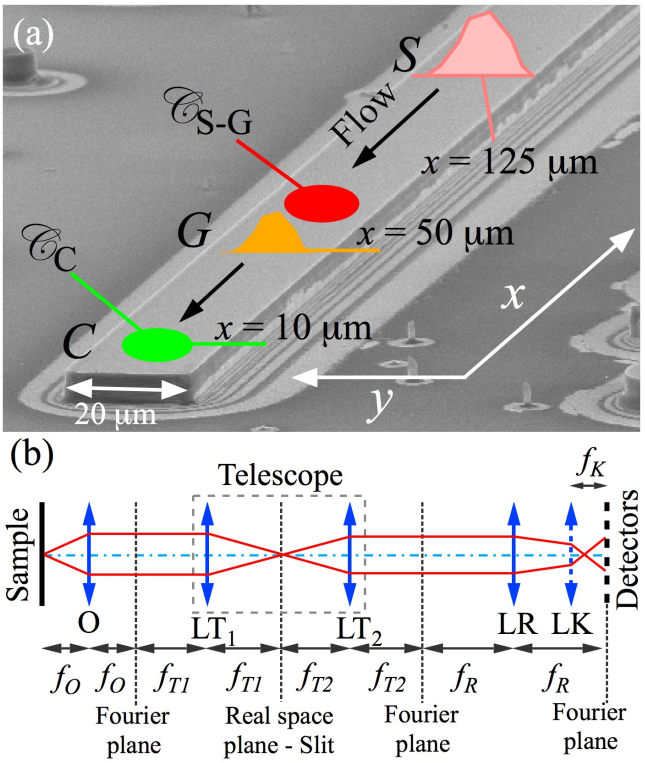

FIGURE 10.1: (a) SEM image of a 20-μm wide ridge, including the excitation scheme with the continuous wave S and pulsed G beams, and the position of the trapped condensates: $\mathscr{C}_{S-G}$, between S and G, and $\mathscr{C}_C$, at C. (b) Scheme of the imaging setup: The lenses LR and LK image the Fourier plane of the microscope objective O. If lens LK is removed, lens LR images the real space. A slit is placed in the common focal plane of two lenses LT_1 and LT_2 with focal length $f_{T1} = 80$ mm and $f_{T1} = 150$ mm, respectively. f_O mm (numerical aperture = 0.3) , f_R mm and f_K mm are the focal lengths of the objective, LR and LK lenses, respectively.

electronic devices. We refer to different locations on the device as S, G, and C in accordance with the functionality of conventional transistor terminals. We assign correspondingly the symbols $\mathscr{C}_C$ and $\mathscr{C}_{S-G}$ to polariton condensates at and in-between these locations, respectively. In this Chapter we choose the origin $x = 0$ of the x-axis at the left border of the ridge [see schematic $x - y$ axis in Figure 10.1(a)]. The threshold power for condensation of polaritons under cw/pulsed excitation is $P_{th}^{cw} = 7.5$ mW / $P_{th} = 1.5$ mW.

Figure 10.1(b) shows a scheme of the experimental imaging setup. The sample is mounted in a cold-finger cryostat and kept at 10 K. It is excited with cw and pulsed Ti:Al_2O_3 lasers, both tuned to the first high-energy Bragg mode of the MC at 1.612 eV. The cw-laser acts as a source, and creates a continuous flow of polaritons towards both ends of the ridge. It is chopped at 300 Hz with an ON/OFF ratio of 1:2 in order to prevent unwanted sample heating. The pulsed laser actuates as a gate at G by means of 2 ps-long light pulses. The intensities and spatial positions of the S and G laser beams can be independently adjusted. We focus both beams on the sample through a microscope objective (O) to form two spots at S and G of 20 μm and 5 μm diameter,

respectively. The distance between S and G (C) is $\backsim$ 75 μm ($\backsim$ 115 μm). Although a more compact device could be realized (S-C distance $\backsim$ 50 μm), we have chosen larger separations between the terminals to clearly monitor the polariton dynamics, including the macroscopic propagation of the polariton flow, the trapping of polaritons between S and G ($\mathscr{C}_{S-G}$ formation) and the dynamics of the OFF/ON transition at C. The same objective is used to collect the photoluminescence (PL) within an angular range of $\pm 18°$. For momentum-space imaging [162], an additional lens (LK) is placed in the optical path in order to image the Fourier plane of the microscope objective (O). We filter out the signal from $x > 125$ μm, in order to facilitate the analysis of the momentum space images, placing a slit at the real-space image plane [Fig. 10.1(b)]. The PL is analyzed with a spectrometer coupled to a streak camera obtaining energy-, time- and spatial-resolved images. Time $t = 0$ corresponds to the pulse arrival at G.

In our experiments polaritons propagate predominantly along the x-axis of the ridge, as demonstrated in § 10.2.3. The propagation in the y-direction, if any, is not crucial for the operation of our device. Therefore, all the images in the manuscript, where the y-direction is not shown, collect the PL along the x-axis from a $\Delta y = 2$ μm-wide, central region of the ridge.

10.2 Experimental results and discussion

10.2.1 Characterization of the device: polariton flow dynamics in real and momentum space

We present a description of the polariton-flow switching dynamics in real- and momentum-space for a given power $P_G = 0.55 \times P_{th}$. We show that the $\mathscr{C}_C$ PL intensity can be manipulated modulating temporarily the polariton flow by a potential barrier at G, which is induced by photo-generated excitons. The use of P_G as a tuning parameter is of central interest in this work, and will be discussed in detail later in § 10.2.2.

Figure 10.2 shows the energy relaxation dynamics of the switching process versus real-space (x). The PL intensity is presented in false-color maps using a linear scale for different times. In Fig. 10.2(a), at $t = -100$ ps, the PL of the polariton condensates $\mathscr{C}_C$ at ~ 10 μm (C) and of the excitons located at ~ 125 μm (S) are observed, respectively. The excitons at S, created by the *cw*-laser, act as source and emit at 1.544 eV. This energy is considerably blue-shifted with respect to the rest of the polaritons shown in the figure due to the high carrier density and repulsive interactions at this position.

Dashed white lines in Fig. 10.2 outline the potential landscapes. They are the sum of potentials due to sample geometry and optically induced blue-shifts. It is experimentally impossible to separate both contributions quantitatively, however, an idea of the former potential is obtained in

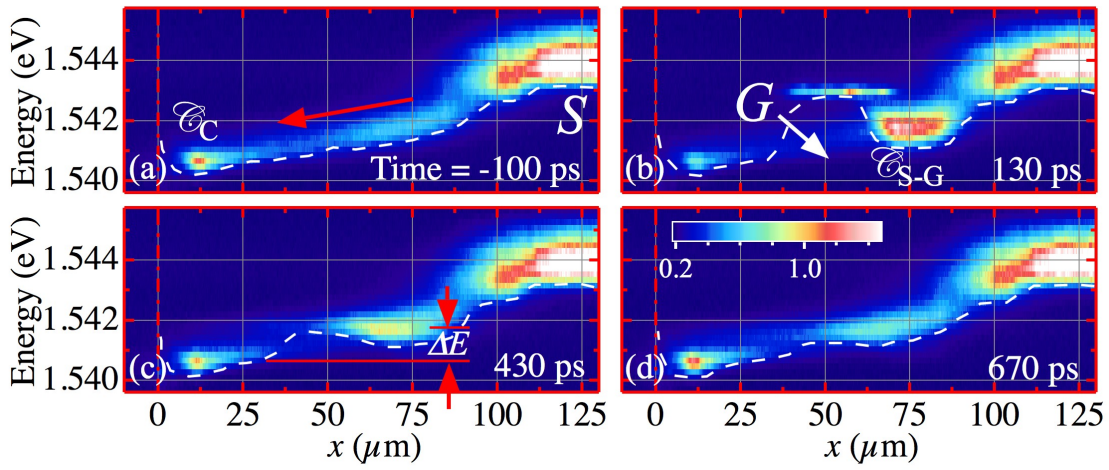

FIGURE 10.2: Energy vs. real space (x) at different times shown by the labels. S, G, $\mathscr{C}_{S-G}$ and $\mathscr{C}_C$ mark the source, the gate, the trapped condensate between S-G and the trapped one at C positions, respectively. The white dashed lines show, as a guide to the eye, the effective potential experienced by polaritons, $V(x,t)$. The continuous flow of polaritons from S to C (in absence of G) is indicated with a red arrow in panel (a). The relative blueshift ΔE between $\mathscr{C}_{S-G}$ and $\mathscr{C}_C$ is indicated with red arrows in panel (c). The intensity is coded in a linear false-color scale. The movie corresponding to this figure is provided following http://link.aps.org/supplemental/10.1103/PhysRevB.89.235312.

Fig. 3.9 of § 3.2.1.1. By comparison with the results shown in Fig. 10.2, we observe that the trap is shallower in the present experiments. This is due to the strong blue-shift induced by the high density of the condensate at C. Furthermore, we can conclude that the slope of potential along the ridge is almost entirely governed by the density of the polariton population and not by the sample geometry.

The potential slope causes polaritons to flow towards lower energies away from S to the left and right (not shown) along the x-direction of the ridge. This flow is observed as a weak PL between S and C. At C the flow is stopped and polaritons accumulate at $\mathscr{C}_C$, emitting at 1.5407 eV. This energy is lower than that of the propagating polaritons as a result of a static potential, which has a minimum near the edge of the ridge (for further information about this static potential see § 3.2.1.1). $\mathscr{C}_C$ corresponds to the ON-state of our polariton transistor device, as reported in Ref. [43] and previous Chapter 9. At $t = 130$ ps, the barrier induced by the high carrier density created by the pulse at G hinders the polariton flow towards C [Fig. 10.2(b)]. At G, carriers emit at 1.543 eV. The polaritons accumulate before G and form the condensate $\mathscr{C}_{S-G}$ emitting at an energy of 1.5408 eV, lying ΔE=1.1 meV above $\mathscr{C}_C$. This configuration corresponds to the OFF-state of the device, since the polariton density at C has decreased by ~ 40 %, compared to the situation shown in Fig. 10.2(a). At t = 430 ps [Fig. 10.2(c)] the barrier height at G lowers, since the carrier density has decreased, allowing polaritons again to move towards C, where the PL intensity increases again. Finally, at $t = 670$ ps [Fig. 10.2(d)], the device is basically back in the ON-state.

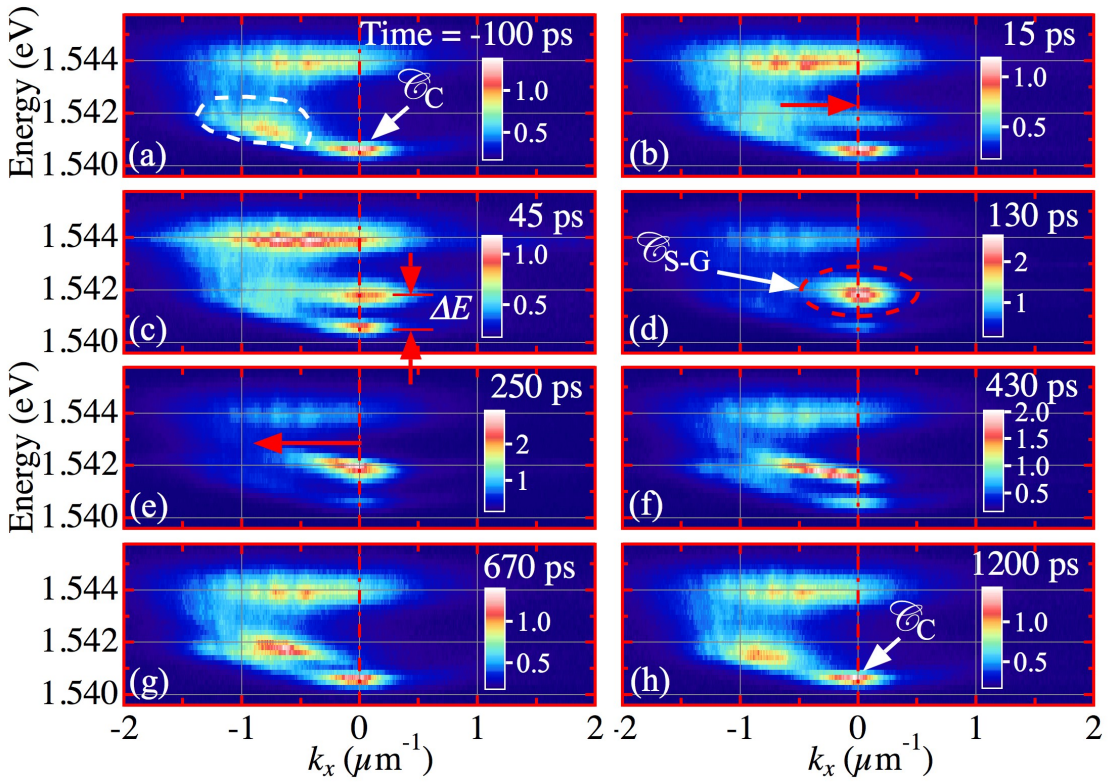

FIGURE 10.3: Energy vs. momentum space (k_x) at different times as shown by the labels. $\mathscr{C}_{S-G}$ and $\mathscr{C}_C$ mark the trapped condensates between S-G and the trapped one at C positions in real space, respectively. The acceleration of flowing polaritons is indicated by horizontal red arrows in panels (b) and (e). The relative blueshift ΔE between $\mathscr{C}_{S-G}$ and $\mathscr{C}_C$ is indicated by vertical red arrows in panel (c). The intensity is coded in a linear, false-color scale. The movie corresponding to this figure is provided following http://link.aps.org/supplemental/10.1103/PhysRevB.89.235312.

One can obtain a wealth of useful information on the polariton dynamics of the system from the real-space dynamics. However, an analysis of the momentum space images complements and deepens the insight into the dynamics of the device operation. Figure 10.3 shows PL intensity maps versus PL energy and momentum along the k_x-direction. The PL intensity is coded in a linear false-color scale. Figure 10.3(a) shows the PL at $t = -100$ ps. The flat and broad PL in momentum space, up to $k \approx -1.5\ \mu\text{m}^{-1}$, at $E = 1.544$ eV stems from excitons at S, as demonstrated in the analysis made previously in real-space. Below that energy, all polaritons appear to move mainly leftwards ($k_x < 0$) towards C (region enclosed by the white dashed line). Note that the right propagating flow from S has been blocked, for the sake of clarity, as mentioned in § 10.1. The peak energy and momentum of polaritons flowing towards C is 1.541 eV and $k_x = 0.8\ \mu\text{m}^{-1}$, respectively. The polaritons slow down while approaching C, coming to a rest ($k_x = 0$) at an energy $E = 1.5405$ eV, where they form the trapped condensate $\mathscr{C}_C$. After the laser pulse has arrived at G, shown in Fig. 10.3(b) and Fig. 10.3(c) at $t = 15$ ps and $t = 45$ ps, respectively, the polaritons decelerate (decrease of $|k_x|$). Concomitantly, an increasing PL is observed at $k_x = 0$ and $E = 1.542$ eV. At $t = 130$ ps [Fig. 10.3(d)] all the polaritons have been stopped and accumulate

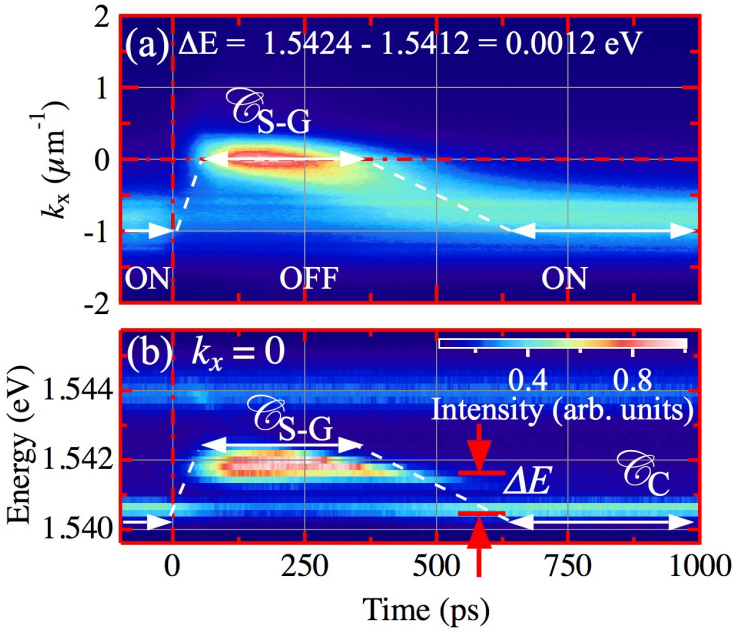

FIGURE 10.4: (a) Map of the polariton PL intensity, energy-integrated between 1.5412 and 1.5424 eV, versus k_x and time. (b) Polariton PL intensity map for $k_x = 0$ versus energy and time. $\mathscr{C}_{S-G}$ and $\mathscr{C}_C$ mark the trapped condensates between S and G as well as the trapped one at C, respectively. Red arrows indicate the energy difference ΔE between $\mathscr{C}_{S-G}$ and $\mathscr{C}_C$. Both intensity maps are encoded in a normalized false-color scale shown in panel (b). The white arrows sketch the duration of the ON- and OFF-states. The white dashed lines sketch the duration of the switching process.

in the highly populated $\mathscr{C}_{S-G}$ (region enclosed by the red dashed line): this condition corresponds to the OFF-state of the switch. At longer times, the $\mathscr{C}_{S-G}$ polaritons start to accelerate towards C again, as can be inferred from the shift of the PL peak from $k_x = 0$ to more negative values [Figs. 10.3(e) and 10.3(f)]. The polaritons reach a maximum value of $k_x \approx -1.3\ \mu\text{m}^{-1}$ with a peak at $k_x = -0.8\ \mu\text{m}^{-1}$ [Fig. 10.3(g)]. Finally, Fig. 10.3(h) shows that at $t = 1200$ ps, the same situation as shown in Fig. 10.3(a) is encountered. The initial ON-state is completely recovered, *i.e.* polaritons are able to flow again from S to C; $\mathscr{C}_{S-G}$ disappears, and only the trapped $\mathscr{C}_C$ is present at $k_x = 0$.

Figure 10.4 completes the analysis of the switching dynamics in momentum space by paying attention to the flow in the $S-G$ region and $\mathscr{C}_{S-G}$. PL intensity maps are shown in a normalized, linear false-color scale. Figure 10.4(a) shows a PL map, integrated between 1.5412 and 1.5424 eV, versus k_x and time. The chosen range corresponds to the energy of the flow and $\mathscr{C}_{S-G}$. This figure clearly illustrates differences between the speed of the two switching processes. The OFF-state, which is characterized by PL from $\mathscr{C}_{S-G}$ at $k_x = 0$, is reached within one hundred picoseconds after the G pulse has arrived at $t = 0$. In contrast, the ON-state, which is distinguished by the flow with a peak momentum of $k_x \sim -0.8\ \mu\text{m}^{-1}$, is recovered only after several hundreds of picoseconds. This asymmetry is a clear signature of the fast formation and slow decay dynamics of excitons.

Figure 10.4(b) provides a complementary perspective on the dynamics by showing the PL at $k_x = 0$, *i.e.* that of both $\mathscr{C}_C$ and $\mathscr{C}_{S-G}$. The energy of the latter condensate is blue-shifted by $\Delta E \approx 1$ meV with respect to that of $\mathscr{C}_C$ at ~ 1.5405 eV. There are two remarkable effects on the dynamics of $\mathscr{C}_{S-G}$ and $\mathscr{C}_C$. First, there is a marked PL intensity drop of $\mathscr{C}_C$ during the OFF-state from ~ 50 to ~ 400 ps. Secondly, the temporal variation of the blueshift, which is induced by carrier density dependent polariton-polariton interactions, gives rise to an 'airfoil'-like shape of the $\mathscr{C}_{S-G}$ PL.

10.2.2 Dependence of the off-state on P_G

The lateral width of the ridge is in principle a relevant parameter that should be taken into account optimizing these 1D devices. Narrower ridges than the typical extension of the excitonic reservoir (whose spatial dimensions are determined by the pump spot) would ease the efficient blocking of the polariton flow and therefore improve the signal contrast between the ON/OFF-states at C, but surface losses could be detrimental. Therefore, instead of varying the width of the ridge, we change the G pump power P_G, which modifies the height and width of the G barrier. This is in some degree equivalent to changing the width, while keeping the G power constant. Also, in practical terms, it is more convenient to change the laser power than using different devices, where different potential landscapes would influence the results in an uncontrollable manner.

After having demonstrated the working principle of the device in the previous subsection, we discuss now how to establish its optimal point of operation in the sense of a compromise between speed and an acceptable ON/OFF-signal ratio. The speed of our device is mainly determined by the exciton dynamics at G. As shown in the previous § 10.2.1, this dynamics is of the order of hundreds of picoseconds, implying that the device cannot reach the THz range. As we will show here, weaker barriers allow a faster switching. However, the signal-ratio between both states diminishes, so that a trade-off between ON/OFF-signal ratio and device speed has to be made.

In order to characterize the device operation, we present in Fig. 10.5 a systematic study based on the PL intensity dynamics. This is analyzed at different regions as a function of the normalized G power P_G/P_{th}. Figure 10.5(a) shows a top-view scanning electron microscope image of the part of the ridge relevant for the experiment. The dynamics in three centrally located rectangular regions, indicated by dot-dashed boxes, are investigated in detail. These regions correspond to the polariton flow against the gate $(S-G)$, G and C. Figures 10.5(b) - 10.5(d) compile the PL dynamics versus P_G (logarithmic ordinate) and time (linear abscissa) in each of the aforementioned regions. The up-pointing arrows on the linear false-color bars indicate the PL intensity at $t \leq 0$; the left/right down-pointing arrows mark the minimum/maximum PL intensities. Figure 10.5(b) shows that for $P_G/P_{th} > 0.01$ the PL increases after the G pulse arrives, since the G barrier blocks the polariton flow, resulting in the formation of $\mathscr{C}_{S-G}$. $\mathscr{C}_{S-G}$ persists longer for increasing P_G: for $P_G \sim P_{th}$, it lasts longer than 400 ps. The white line in Fig. 10.5(b) identifies the time when the maximum PL

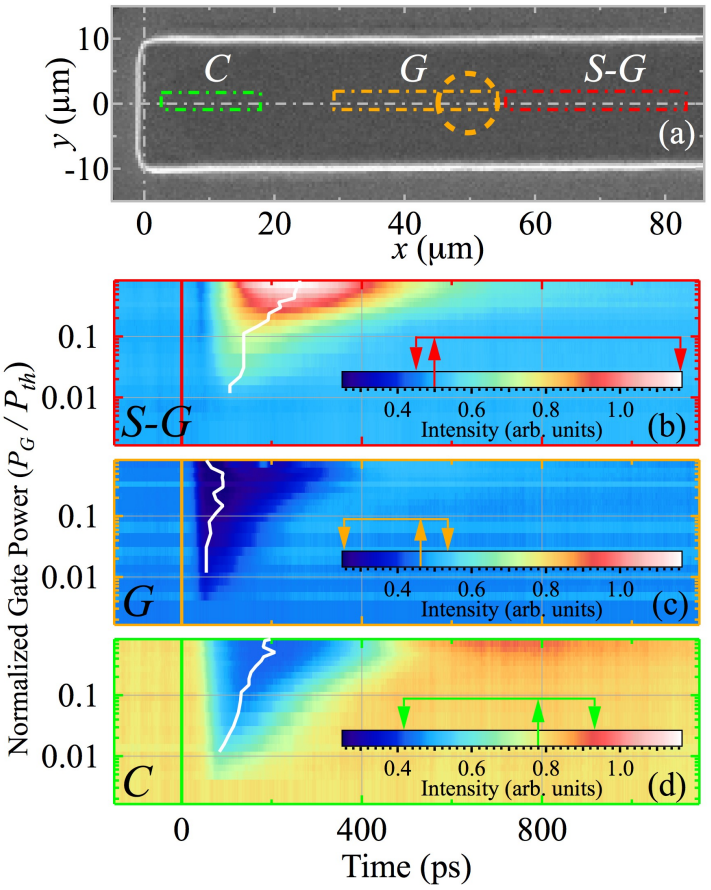

FIGURE 10.5: (a) SEM image of a 20-μm wide ridge, marking in dot-dashed lines three selected spatial areas under study: flowing polaritons [red, (S-G)], the gate [orange, (G)] and the collector [green, (C)]. The position of G is indicated with a dashed orange circle as a guide to the eye. (b) Polariton PL dynamics (spatially integrated in region S-G) as a function of P_G; for large values of P_G polaritons are trapped forming the $\mathscr{C}_{S-G}$ condensate. (c) Polariton PL dynamics (spatially integrated in region G) as a function of P_G. (d) Polariton PL dynamics (spatially integrated in region C) as a function of P_G; in this case the polariton PL corresponds to the $\mathscr{C}_C$ condensate. The intensity is coded in a linear false-color scale. The initial value of the intensity at each region is indicated with an up-pointing arrow at the color scale. The left/right down-pointing arrows mark the minimum/maximum PL intensities. The white lines give the times when the extreme PL intensity values are obtained as a function of P_G.

intensity of $\mathscr{C}_{S-G}$ is reached as a function of P_G. Note, that for powers $P_G > 0.1 \times P_{th}$ there is a small decrease of the PL at $t = 45$ ps, which is due to thermal effects caused by the G pulse [398].

Together with the formation of $\mathscr{C}_{S-G}$, the blockade of the polariton flow is observed as a sudden decrease of the polariton population at G and C, as shown in Figs. 10.5(c) and 10.5(d), respectively. The conspicuous PL drop observed in Fig. 10.5(c) is caused by the repulsive interactions between the photo-generated excitons and the passing polaritons at G. The time when the PL minimum intensity occurs is nearly independent of P_G, as shown by the white line in Fig. 10.5(c). In Fig. 10.5(d), the decrease of the PL intensity at C is exclusively caused by the ceasing of the polariton flow. The best ON/OFF ratio obtained at C is of the order of 50 %. The temporal width

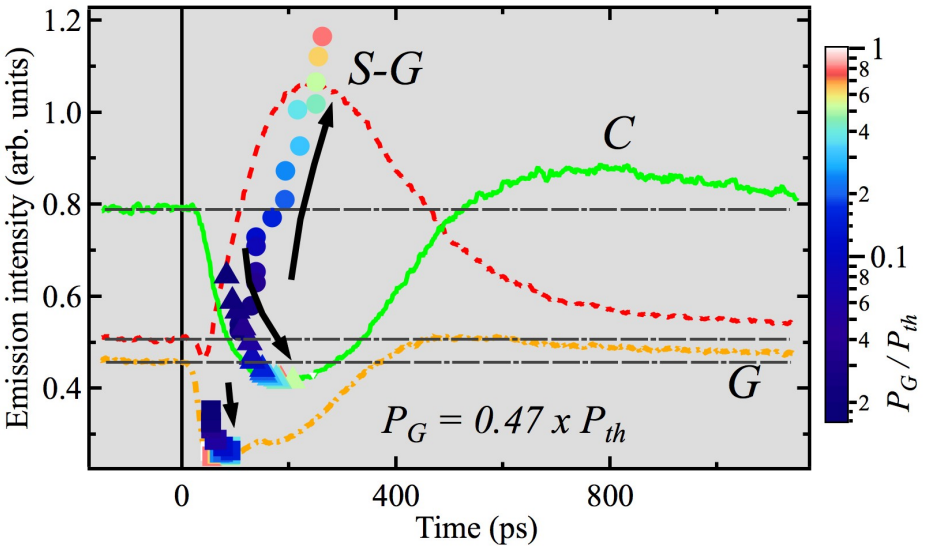

FIGURE 10.6: Polariton PL dynamics at S, G, C regions in full red, orange and green colors, respectively, for $P_G = 0.47 \times P_{th}$. The initial value of the intensity is indicated with a dot-dashed horizontal line. The scattered circles/(squares, triangles), extracted from the white curves in Fig. 10.5, represent the maximum/minimum PL values and their time of occurrence for the S-G/(G, C) regions. Their colors correspond to the P_G value, encoded in a logarithmic, false-color scale shown at the right side of the figure.

of the drop at C increases significantly with P_G, as evidenced by the blue region in Fig. 10.5(d), reaching a value of ~ 380 ps at $P_G = 0.8\, P_{th}$. It is worthwhile mentioning that the leading edge of the PL drop at C appears at later times than that at G, due to the time of flow from remaining polaritons from G to C.

The optimal power P_G for the best ON/OFF-signal ratio is discussed in detail in Fig. 10.6. The three curves correspond to horizontal cuts at $P_G/P_{th} = 0.47$ in Figs. 10.5(b)-10.5(d) and show the PL intensity at the regions $S - G$, G and C. In region S-G (dashed line), there is a small dip in intensity at $t = 45$ ps as discussed previously. Thereafter, the PL intensity strongly increases and reaches its maximum at $t = 250$ ps, where it doubles the initial value. The intensity at G (dot-dashed line) quickly decreases by ~ 50 % and recovers after a few hundred picoseconds. After recovering, it surpasses the initial value, due to the large polariton population released from the condensate $\mathscr{C}_{S-G}$. The higher value of the initial intensity at C (full line) reflects the larger population in C as compared with the other regions of interest of the device. It drops down to ~ 50 % of its initial value at ~ 150 ps. Again, as observed for G, there is an intensity overshoot due to the release of a large polariton flow from $\mathscr{C}_{S-G}$. Since the PL at C does not drop down to zero, the ON/OFF signal contrast, $(I_{\mathrm{ON}} - I_{\mathrm{OFF}})/(I_{\mathrm{ON}} + I_{\mathrm{OFF}})$, is merely ~ 30 %. This contrast is slightly better at G than at C due to the fact that in the former case we have a potential hill, forcing polaritons away from G, while in the latter one there is a potential trap for the polaritons.

The data presented as white curves in Fig. 10.5 are shown now in Fig. 10.6 as scattered data points. The symbol color encodes P_G/P_{th} in a logarithmic, false-color scale, as shown by the bar

at the right of the figure. For the region $S-G$, the full circles indicate the maximum PL intensity (ordinate) and the time when it is reached (abscissa) for different P_G/P_{th}. Similarly, the squares and triangles show, for G and C, respectively, the minimum PL intensity and the time when this is obtained. As aforementioned, in region $S-G$, the maximum PL intensity is increased and delayed with increasing P_G. The minimum intensity at G drops down rapidly by ~ 50 % and then remains almost constant for $P_G/P_{th} \gtrsim 0.2$. An inspection of the points corresponding to C reveals that the lowest PL intensities are reached also for the same P_G. Therefore, the optimum operation point, which gives the best compromise regarding contrast and speed is $P_G \sim 0.2\, P_{th}$.

Recently, different approaches have been investigated experimentally and theoretically to realize polariton switching systems in MCs, in the following lines we compare the capabilities of our device with others reported in the literature focusing on the pump power requirements for their operation. These approaches involve various methods and features of polariton systems including parametric scattering [298] [power per gate/switch $9-40$ mW, operation time 1 ns (theoretical)], hysteresis control [392] ($\sim$ 30 mW, 5 ps switching + 1 ns recovery), resonant blueshift [39] ($\sim$ 5 mW, 1 ns), spin domain walls [33, 296] [140 mW (pump)+ 4.5 mW (probe), $\sim$ 70 ps] and polariton condensate bullets [47] (44 mW, 150 ps switching + 250 ps recovery). Compared with these studies, our procedure lies within the lower range of gate pump powers of a few mW.

Regarding the speed of the device, the switching into the OFF-state is faster than the reversing from OFF- to ON-state. The speed of this reversal is certainly the main drawback of this device. It is determined by the long-lived exciton reservoir created at G in the OFF-state. Solutions would imply to find a way to make the excitons decay faster, or not making use of long-lived excitons at all. An ON/OFF-transition time of a few picoseconds, but the reversal OFF/ON-transition time still being in the hundreds of picoseconds, has been reported for resonant injection of polaritons in the LPB, avoiding the generation of excitons [392]. Ultrafast shifts of the LPBs and UPBs exploiting the Stark effect in MCs [399] have been proposed to implement optical switches with high repetition rates [393]. Furthermore, one can envision more complex geometries where, instead of excitons, polaritons flowing in a crosswise direction are employed to create the G barrier. The present work is a conceptual study of a polariton switch and this particular design may not provide an easy way for cascadability so far. However, there are other schemes, where the connectivity of propagating polariton signals has been recently demonstrated by a complex set of resonantly tuned lasers [39].

10.2.3 Leakage effects

So far, for the sake of simplicity, we have considered 1D dynamics of polaritons, analyzing the PL along the x-axis of a 2-μm wide, central stripe only. We have discussed the effect of the G barrier height only, disregarding its lateral extension. In the following, we take into account that our system is not strictly 1D, *i.e.* we also discuss the lateral effects depending on the size of G. For

a given laser spot size at G, both the resulting extent and height of the excitonic barrier depend strongly on the power of the gaussian laser beam. We show that the choice of working parameters is essential for a proper operation of the device, minimizing leakage currents around G. In order to observe the dynamics of these currents, it is convenient to avoid the steady state flow that is obtained under *cw*-pumping at S. Therefore, we use now a pulsed laser with a power $P_S = 4\,P_{th}$.

Figure 10.7 compiles the 2D real space dynamics of polariton propagation for two different G powers P_G, keeping the laser spot size constant. The left and right columns show energy-integrated PL intensities, encoded in a logarithmic false-color scale, for $P_G = 0.07 \times P_{th}$ and $P_G = 0.5 \times P_{th}$, respectively. The former case creates a low and small barrier V_L, sketched by a dashed circle, which still permits polaritons to flow towards C. The latter case, which corresponds to the typical OFF-state discussed so far, induces a higher and larger barrier V_H, outlined by the bigger dashed circle.

We discuss both situations in parallel. Initially, the front of the polariton flow approaches the barriers V_L and V_H at $x = 50$, as shown in Figs. 10.7(a) and 10.7(e), respectively. Polaritons occupy the full width of the ridge, indicated by the dot-dashed lines, and propagate uniformly with a well-defined velocity of $v_x = -1.8$ μm/ps, with negligible k_y components. Figures 10.7(b) and 10.7(f) show instants when polaritons have collided against the V_L and V_H barriers, respectively. Since V_L is significantly smaller than V_H, polaritons are able to overcome the V_L barrier, basically bypassing it laterally, close to the edge of the ridge.

In contrast, this is not possible in the case of V_H, where all polaritons remain blocked by the higher and wider barrier V_H. At times 75 and 60 ps, shown in Figs. 10.7(c) and 10.7(g), respectively, polaritons continue to propagate. In Fig. 10.7(c), a complex structure is observed in the real-space density distribution of polaritons in the region from $x = 40$ to 20 μm. Here, polaritons, which bypass the barrier, propagate in negative x-direction but with a small k_y component, sketched by the slanted arrows. Further apart from G, there are two lobes of polaritons with $k_y \sim 0$, indicated by horizontal arrows. Figures 10.7(d) shows that at longer times polaritons do not bypass the V_L barrier anymore: the fast energy relaxation of polaritons as compared with the decay rate of V_L results in the trapping of $\mathscr{C}_{S-G}$. Furthermore, the weak PL at $x \sim 10$ μm arises from $\mathscr{C}_C$, formed by polaritons which have formerly overcome V_L. The trapping of $\mathscr{C}_{S-G}$ at very long times is also clearly observed in Fig. 10.7(h).

Figures 10.7(i) and 10.7(j) show the real-space dynamics in x-direction as PL intensity maps encoded in a logarithmic false-color scale for the two P_G values, respectively. In the y-direction the full lateral width of the ridge is integrated. The widths of the potential barriers V_L and V_H are sketched by vertical, dashed lines. The trajectories of the polariton flow are indicated by white arrows. Figure 10.7(i) illustrates that polaritons, having bypassed the barrier, experience a zig-zag movement on the left side of V_L in the time range from $\sim$ 50 to $\sim$ 200 ps. They are reflected between the barrier and the potential wall at the end of the ridge [40, 47], where, finally

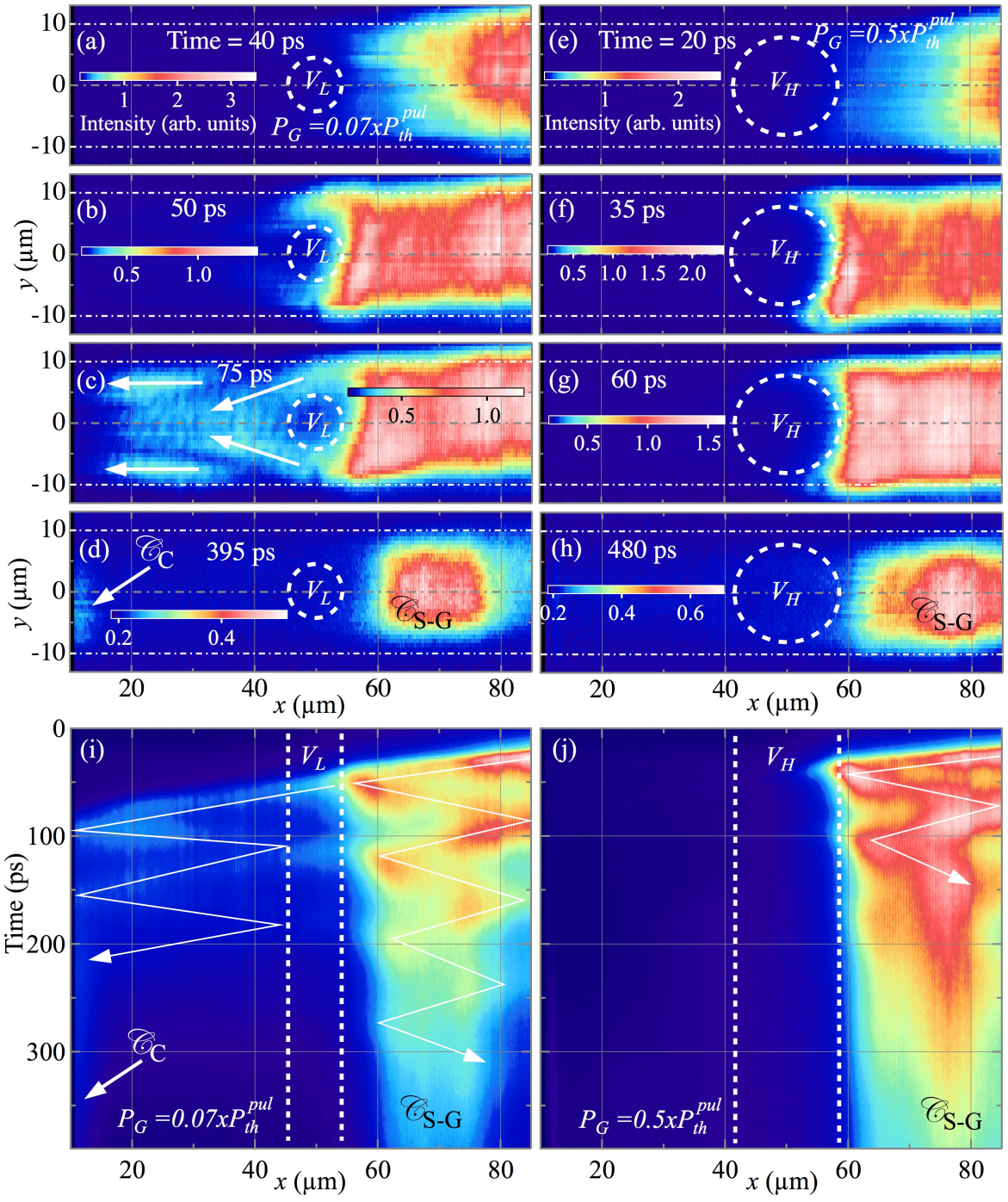

FIGURE 10.7: (a)-(h) Real-space PL intensity maps for different times as indicated by the labels. The intensity is encoded in a logarithmic false-color scale. $P_S = 4 \times P_{th}$ and $P_G = 0.07 \times P_{th}$ and $0.5 \times P_{th}$ for the left and right column, respectively. A sketch of the extension of the barriers V_L and V_H is show by dashed white circles. White arrows in panel (c) visualize the direction of the flow behind the barrier. (i)-(j) PL intensity maps versus time and the real space x-direction. Real space in the y-direction is integrated from $y = -10$ to 10 μm. The widths of the potential barriers V_L and V_H are sketched by vertical, dashed lines. The trajectories of the polariton flow are indicated by white arrows. Movies corresponding to this figure are provided in http://link.aps.org/supplemental/10.1103/PhysRevB.89.235312.

at $\sim$ 250 ps, a part of these polaritons is trapped and form $\mathscr{C}_C$. The main part of the initial polariton flow remains trapped between S and G, also moving in a zig-zag path. The polaritons gradually lose their kinetic energy, which is evidenced in the figure by the changing slope of the white lines. This is caused by a decrease of the potential gradient due to a reduced blue-shift originating from a falling carrier population. In principle, this could affect the device operation speed. However, this effect can be neglected in our device since the limiting factor is the existence of long-lived excitons at G. Eventually at $\sim$ 250 ps, the stationary $\mathscr{C}_{S-G}$ forms at $\sim$ 70 μm. Figure 10.7(j) shows the case of the higher and wider barrier V_H. The high exciton density at G forms a $\sim$ 20 μm-wide barrier potential. It completely blocks and reflects the polariton flow, which rapidly loses its kinetic energy. Finally at $\sim$ 100 ps, $\mathscr{C}_{S-G}$ is formed at $\sim$ 80 μm. In the movies provided by http://link.aps.org/supplemental/10.1103/PhysRevB.89.235312, for times around 60 ps, the just discussed zig-zag oscillations in the propagation of polaritons between S and G are clearly observed.

We have shown here the influence of P_G on the existence of leakage currents around the G barrier, which implies the worsening of the ON/OFF-ratio of the device. An alternative approach to avoid leakage could be either a geometrical constriction at G and/or the use of an elongated profile, along y, for the laser spot at G.

10.3 Model

10.3.1 Simulations of the experimental results

In this section we recall the theoretical model used in previous Chapter 9 (and described in § 2.5.2.3), and we simulate our experimental results, based on a phenomenological treatment of polariton energy-relaxation processes. It is important to recall that energy relaxation occurs in multiple stages in our experiment. First, the non-resonant pump creates a reservoir of hot excitons, which can relax in energy to form polaritons. Given that excitons diffuse very slowly and that energy relaxation is local, these polaritons form initially at the same position as the pump S. The polaritons then travel down a potential gradient, which is caused by repulsion between polaritons and hot excitons. It is the ability of polaritons to further relax their energy as they travel that allows them to be so sensitive to a changing potential landscape, as seen in a variety of different experiments in planar MCs [22, 388], 1D microwires [36, 383] and in condensate transistors, see Ref. [43] and previous Chapter 9.

The polaritons, having condensed from excitons, are known to be coherent [21], which allows their description in terms of a GP type Eq. 2.42 for the polariton wave-function, $\psi(x,t)$. For the

sake of clarity, this equation is written here again:

$$i\hbar\partial_t\psi(x,t) = \left[\hat{E}_{LP} + \alpha|\psi(x,t)|^2 + V(x,t) + i\hbar\left(rN_A(x,t) - \frac{\Gamma}{2}\right)\right]\psi(x,t) + i\hbar\Re\left[\psi(x,t)\right] \quad (10.1)$$

Here, $\hat{E}_{LP}$ represents the kinetic energy dispersion of polaritons, which at small wavevectors can be approximated as $\hat{E}_{LP} = -\hat{\nabla}^2/(2m)$ with m the polariton effective mass. α represents the strength of polariton-polariton interactions. $V(x,t)$ represents the effective potential acting on polaritons [193] and can allow or block the polariton propagation depending on its shape. $V(x,t)$ can be divided into a contribution from three different types of hot exciton states (see Eq. 2.43 in § 2.5.2.3), which will be described shortly, as well as a static contribution due to the wire structural potential, $V_0(x)$:

$$V(x,t) = \hbar\left[g_R N_A(x,t) + g_I N_I(x,t) + g_D N_D(x,t)\right] + V_0(x) \quad (10.2)$$

where subindices A, I, D refer to active, inactive, and dark excitons, respectively. In this Chapter we assume that the three different exciton-polariton interactions $g_{A/I/D}$ have the same value g. As discussed in Chapter 9 and in § 2.5.2.3, previous studies of polariton dynamics have revealed that not all excitons are available for direct scattering into the polariton states [400]. Rather, one can distinguish between "active" excitons and "inactive" excitons [209, 401]. The active excitons have the correct energy and momentum for direct stimulated scattering into the condensate (and so appear as the incoherent gain term in Eq. 10.1 with r the condensation rate). However, nonresonant pumping creates initially excitons with very high energy that must first relax before becoming active. We thus identify the "inactive" reservoir that feeds the active reservoir. In principle, inactive excitons can also relax into dark exciton states that are uncoupled to polaritons. The three exciton densities (N_A , N_I , and N_D) are in general spatially and time dependent. They each give a repulsive contribution to the effective polariton potential (see Eq. 10.2) with strength described by the parameter g, previously mentioned. In the simulations reported in this Chapter, the dynamics of the exciton densities is slightly different from that previously used in Chapter 9, in the present case the term $t'_R N_I(x,t)$ is not considered in the coupled exciton equations of N_I and N_A:

$$\frac{dN_A(x,t)}{dt} = -\left(\Gamma_A + r|\psi(x,t)|^2\right)N_A(x,t) + t_R N_I(x,t) \quad (10.3)$$

$$\frac{dN_I(x,t)}{dt} = P(x,t) - \left(\Gamma_I + t_R + t_D\right)N_I(x,t) \quad (10.4)$$

$$\frac{dN_D(x,t)}{dt} = t_D N_I(x,t) - \Gamma_D N_D(x,t) \quad (10.5)$$

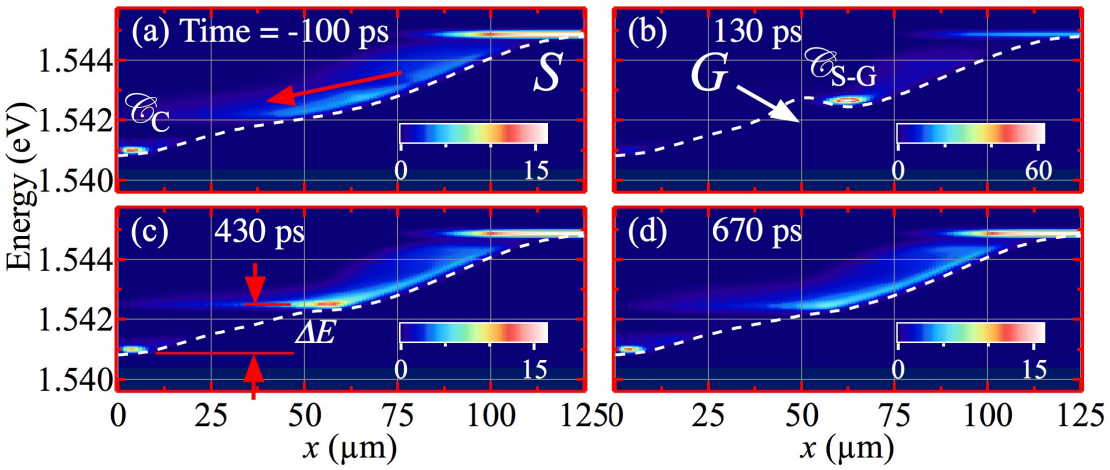

FIGURE 10.8: (a)-(h)Calculated PL intensity false-color scale maps vs. energy and real space (x) for different times shown by the labels. $\mathscr{C}_{S-G}$ and $\mathscr{C}_C$ mark the trapped condensates between S-G and the trapped one at C positions in real space, respectively.The relative blueshift ΔE between $\mathscr{C}_{S-G}$ and $\mathscr{C}_C$ is indicated by vertical red arrows in panel (c).

The constants t_R and t_D describe the transfer of inactive excitons into lower-energy active and dark exciton states, respectively. $P(x,t)$ represents the incident pumping intensity distribution. This includes Gaussian spots for the continuous wave S and pulsed G, which also has a Gaussian time dependence. We neglect any nonlinear conversion between bright and dark excitons [210, 211], which we only expect to be significant under coherent excitation resonant with the dark exciton energy. Finally, the term accounting for the phenomenological energy relaxation of condensed polaritons in Eq. 10.1 is recalled here:

$$\Re[\psi(x,t)] = -\left(\nu + \nu'|\psi(x,t)|^2\right)\left(\hat{E}_{\mathrm{LP}} - \mu(x,t)\right)\psi(x,t), \tag{10.6}$$

where ν and ν' are parameters determining the strength of spontaneous and stimulated energy relaxation, respectively.

For the calculations we used the following parameters: $m_P = 7.3 \times 10^{-5}\, m_0$, with m_0 the free electron mass, $\alpha = 2.4 \times 10^{-3}$ meV μm^2, $\Gamma = 1/18$ ps^{-1}, Γ_A=1/100 ps^{-1}, $\Gamma_I = \Gamma_D = 1/250$ ps^{-1}, $t_R = t_D = 0.02$ ps^{-1}, $g = 0.018$ ps^{-1} μm^2, $\hbar r = 0.02$ meV μm^2, $\hbar\nu = 0.014$, $\hbar\nu' = 0.075$ μm^2.

Figure 10.8 shows the variation with time of the energy spectrum in space. Before the arrival of the G pulse, polaritons are free to relax down to the C state. As in the experiment, the application of G introduces a potential barrier that blocks polariton propagation. This is temporary, as at later times the excitons in the reservoir at the G position decay and polaritons are able to once again flow to the C region.

For simplicity, the theoretical model assumes perfect Gaussian shaped laser spots and neglects the influence of disorder. Differences in the exact pump profiles and a complicated disorder potential

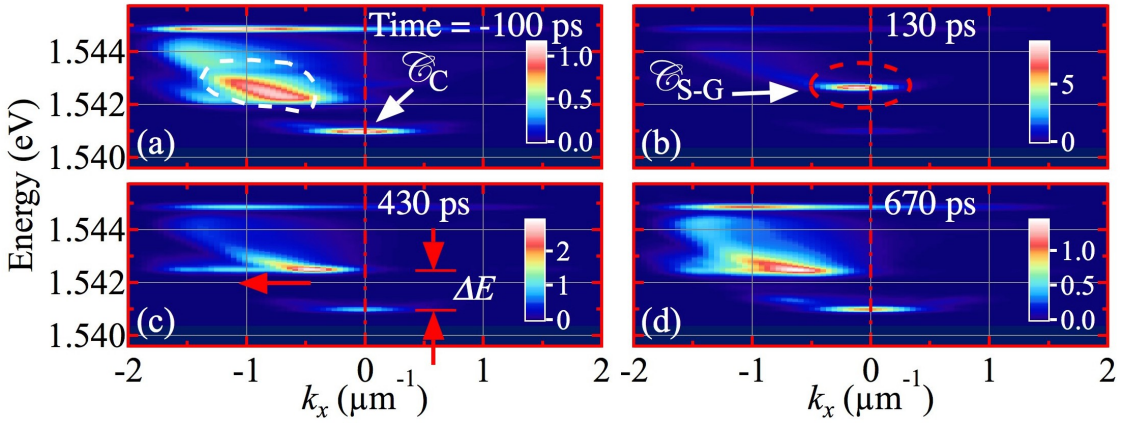

FIGURE 10.9: Calculated PL false-color scale maps vs. energy and momentum space (k_x) for different times shown by the labels. $\mathscr{C}_{S-G}$ and $\mathscr{C}_C$ mark the trapped condensates between S-G and the trapped one at C positions in real space, respectively. The acceleration of flowing polaritons is indicated by horizontal red arrows in panel (c). The relative blueshift ΔE between $\mathscr{C}_{S-G}$ and $\mathscr{C}_C$ is indicated by vertical red arrows in panel (c).

give rise to a slightly different shape of the effective polariton potential in the experiments. However, the overall form of the potential is similar, allowing the theory and experiment to demonstrate the same phenomenology. The presence of disorder in the experiments also gives rise to inhomogeneous broadening, not accounted for in the theory. Fluctuations in the laser intensities may also contribute to broader experimental frequency distributions than in the theory.

Figure 10.9 shows the corresponding energy spectrum in reciprocal space for the same selected times as those used in Fig. 10.8. The results of the simulations are very similar to the experimental ones shown in Fig. 10.3. Before the arrival of G one can identify polaritons propagating to the left, with negative in-plane wave-vector, which have relaxed from S. At C, these polaritons have lost their kinetic energy. The application of G blocks the polaritons, such that they remain trapped in a higher energy state without kinetic energy [see Fig. 10.9(b)]. Polaritons become accelerated towards C again as the G barrier disappears, recovering the initial situation [see Fig. 10.9(d)], in a similar fashion to that observed in the experiments.

10.3.2 Predictions for multiple switches

While we have focused on the behavior of an individual condensate transistor switch, future studies will likely be devoted to the linking of multiple elements in analogy to transistors based on coherent excitation [39]. Here the flexibility in controlling the strength of the individual gate powers may be particularly useful in going beyond the optical replication of CMOS-type logic and considering a neural-type logic inspired by biological networks. For artificial neural networks [402], one typically aims to combine the signals of different transistors but with arbitrary controllable weights, which can be engineered to give different functionalities. The sum of the weighted signals is then compared

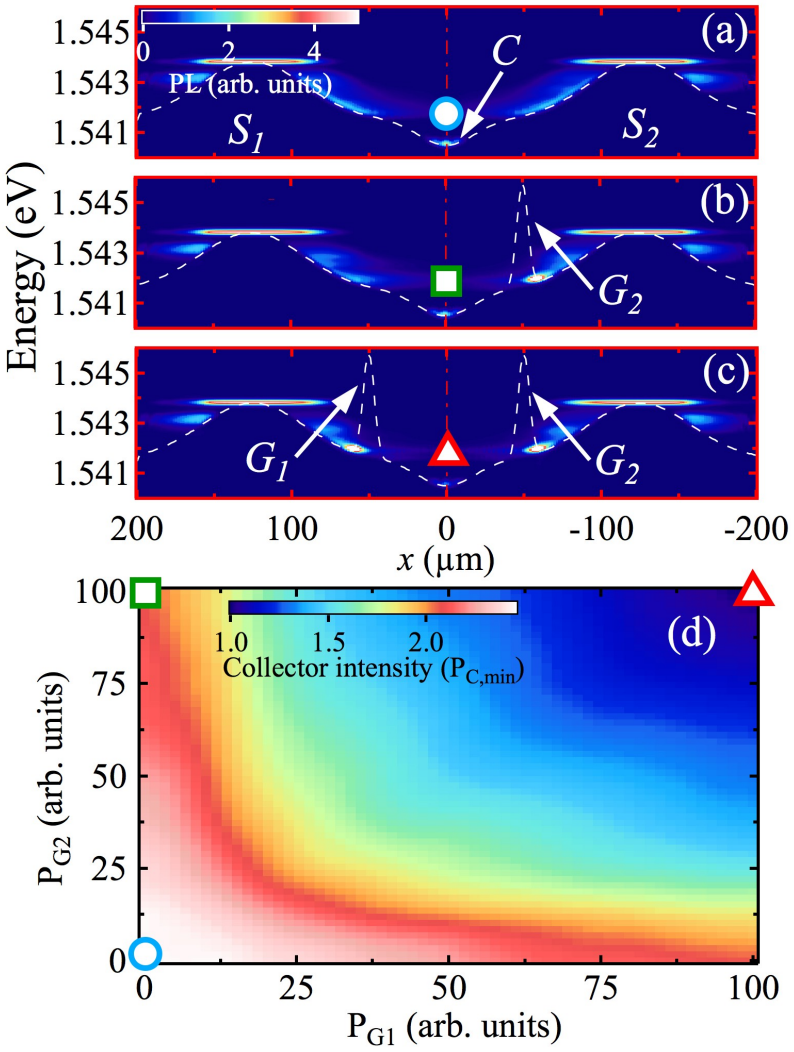

FIGURE 10.10: (a)-(c) Calculated PL false-color scale maps vs. energy and real space (x), for a neural-type logic gate with two inputs, for different gate power combinations: $P_{G1} = P_{G2} > 0$, $P_{G1} = P_{G2} = 0$ and $P_{G1} > P_{G2} = 0$, respectively. (d) Calculated PL at C in a false-color scale versus gate powers P_{G1} and P_{G2}. The powers used in panels (a)-(c) are marked by a circle, square, and triangle, respectively.

to some threshold to determine the result. This ability is known to allow the implementation of certain tasks with significantly fewer elements than with using chains of typical Boolean logic gates, which is why neural networks can be particularly efficient even if their individual elements may be slow.

As a theoretical example, we consider here the combination of the signals from two condensate transistors in a single polariton channel. Polaritons are excited at two source positions and travel toward the C region, which is at the mid-point between the two sources. The weighting of the number of polaritons arriving from each source can be independently controlled by two gates. The weighted input from each source is then summed at C. In Fig. 10.10(d) we present the dependence of the C intensity on the two gate intensities. It is well-known that neural-type logic [402] can

reproduce many Boolean-type logic gates. Among the conceivable regimes of operation it is, for example, possible that the device acts as an AND- or OR-type logic gate, depending on the choice of collector threshold (if the collector intensity exceeds some value the result is considered 1 while if not it is considered 0). Situations where the C signal is weak and strong are shown in Figs. 10.10(a)-10.10(c), which correspond to the different points marked in Fig. 10.10(d) by a circle, square, and triangle, respectively. We stress that the combination of two weighted inputs at the collector is only a first step. In principle the combination of larger numbers of inputs could also be imagined, by designing patterned MCs where multiple ridges join together.

10.4 Conclusions

In summary, we have presented a time-resolved PL study in real and momentum space of a polariton transistor switch consisting of a 20 micron-wide ridge where the optimal conditions for the switching were demonstrated through pump power dependence studies. A polariton flow in real space from S to C is gated by a potential barrier induced by optically generated excitons at G. By choosing comparatively low gate powers interruption of the flow can be achieved within tens of picoseconds, while maintaining a reasonably high ON/OFF-signal contrast. However, the inverse process, *i.e.* switching from the OFF- to the ON-state, takes hundreds of picoseconds due to the long-lived excitons at G. Numerical simulations based on the modified GP equation reproduce well the dynamics of our device.

Chapter 11

Quantum reflections and shunting of polariton condensate wave trains: Implementation of a logic AND gate

As discussed in the previous introduction to Part IV and Chapters 9 and 10, research on exciton-polariton condensates in semiconductor MCs has initiated a quest for novel technological applications. This research effort is motivated by the fusion of photon and exciton properties that appear in exciton-polariton systems, giving rise to a fast (picosecond scale) response time, a long (nanosecond scale) dephasing time [403] and strong nonlinearities.

In the preliminary comments to Part II we have discussed briefly the importance of the injection and manipulation of polaritons by electrical means for the development and integrability of polariton optical information processing. This objective may well require designs using incoherent or non-resonant carrier injection methods. For this reason we focus again in this Chapter on non-resonantly excited polariton condensates, in contrast to previous studies aimed at developing functional logical switches based on polaritons [33, 296, 392]. In Chapters 9 and 10 we have found that repulsive interactions between polaritons and hot excitons in the system, which are inevitably excited with a non-resonant scheme, allow the acceleration of polariton condensates [43, 46, 48]. This is consistent with earlier experiments by Wertz, *et al.* [40], and measurements under *cw* excitation [36, 43]. In this Chapter, we introduce a time-dependent control of propagating polariton condensates using optically-induced tunable repulsive potential barriers. These barriers block propagation, causing reflection of an incident polariton condensate WP. The presence of multiple barriers allows multiple reflections and the re-routing of the WP into a confinement region. Differently to the situation presented in the previous Chapters 9 and 10 on the gating of polariton condensates, in the results reported here the confined polaritons are still propagating and in excited states.

Following the work of R. W. Keyes [404], the five mainstays that must characterize a fully operational device are:

1. *Universal Logic*: AND- and NOT-type logic gates (or equivalent ones) should operate the device
2. *Cascadability*: the output signal, ruled by a gate in a device, must be able to control the gate of a second device and so on.
3. *Fan Out*: it has to be possible to split or duplicate an output signal, facilitating the cascadability of many devices.
4. *Amplification*: related to the previous point on the manipulability of the output signal, its losses should be compensated somehow; the re-amplification of the output signal must be feasible to conserve its logical value.
5. *Input-Output Isolation*: the device operation must be unidirectional, the output signal should not interfere with the inputs of the device.

In the experiments presented in this Chapter, we were able to fulfill points 1 (half of it), 3 (partially), 4 and 5. Concerning the first point, we demonstrate the ability of our system to function as an AND-type logic gate, considering the signal represented by propagating polariton condensates, and the output by a trapped condensate at the border of the ridge (as similarly reported in previous Chapters of Part IV). When the propagating condensate is strongly confined, the energy-relaxation present in the system causes the formation of a long-living coherent ground-state. Taking this as the output state, its formation requires both the initial injection beam and the presence of the optically-induced barrier. Our approach using only non-resonant excitation anticipates the implementation of new ultrafast, non-linear switches based on the electrical injection of polariton condensates. Despite of the many efforts put on it, no alternatives were found to reproduce the NOT-type logic operation in our device. The negation operation is certainly difficult to be realized under the present conceptual premises of excitation and the available sample.

The cascadability problems in our present ridge structure, corresponding to point 2 in the "Keyes-list", was previously discussed in § 10.2.2 of Chapter 10. We stress again that it was not possible to conceive a cascade-process from an static polariton condensate output. Interesting alternatives have been proposed by T. Espinosa-Ortega and T. C. H. Liew [302], where a special patterning of a 1D MC grid could lead to a feasible signal-cascade. To the best of our knowledge, a few research groups are pursuing the experimental demonstration of this theoretical proposal.

As previously said in point 2, the impossibility to generate a propagating polariton signal from an static, trapped polariton condensate at the border of the ridge obstructs the cascadability fulfillment and biases the way of fanning-out the signal to subsequent devices in our proposed

scheme. However, we say that point 3 is partially verified because, in principle, a propagating polariton WP can be split (see for example § 10.2.3 or also the polariton circuiting reported in Ref. [45]) and duplicated. Point 4 is clearly demonstrated in 11.2.4, the intensity of a propagating polariton WP is amplified when it comes into contact with a repulsive exciton barrier; we observe the continuous repetition of such process when the WP bounces back and forth in a region delimited by the repulsive potential and the border of the ridge. We note also that the first demonstration of the amplification process of propagating polariton WPs in a similar structure was reported in by E. Wertz and coworkers [40]. Finally, point 5 is positively checked in the list because, first, the gate of our device is constituted by excitons, whose effective mass is ~ 4 orders of magnitude more massive than that of polaritons, their dynamics is typically ~ 3 orders of magnitude slower as compared to the picosecond-lifetime of polaritons. In second place, while it is true that there are mechanisms in with propagating polariton WPs can interfere with themselves when overlapping in real space (see, for example, § 11.2.3 in this Chapter, § 7.2), it must be mentioned that in our device no negative feedback effects can happen between input and output signals. Furthermore, making virtue of necessity, the interference effects between overlapping WPs can drive the working principle of polariton-based devices in elegant ways [45].

It is important to remark that in computing science, the crucial, entangling gate that constitutes the key building block to conceive a "quantum" computer is the CNOT-type logic gate (controlled-NOT gate) [405].[1] The modus operandi of such gate, with two inputs and two outputs, consist on flipping the second output if and only if the logic value of the first input (typically dubbed control input) is 1. In the recent scientific literature there several experimental realizations of the NOT-operation using parametric down-conversion as photonic sources [406–409], and also using highly efficient QD emitters embedded in a MC [372]. We emphasize that, despite of the fact that the implementation of this logic operation would be a key step in polaritonics, it was not considered in our experiments.

This Chapter is organized as follows. In § 11.1 we briefly present the sample used for the experiments and we explain the excitation scheme chosen in this case for obtaining ballistic propagation of condensed polariton WPs. In § 11.2 we describe the main experimental results divided in two parts: the optimal conditions for AND gating (§ 11.2.1) and the corresponding unsuitable conditions (shown in a particular case, § 11.2.2). Some other interesting aspects are analyzed in this section such as the observation of real space interferences from counter propagating polariton WPs and the amplification of polariton WPs in presence of excitonic reservoirs, § 11.2.3 and 11.2.4, respectively. In § 11.3 we discuss the polariton dynamics, which has been modeled again using a generalized GP description. Finally in § 11.4 we draw the conclusions of this Chapter.

[1] The classical analog to the CNOT-gate is a reversible XOR-gate.

11.1 Experimental setup

The sample is the high-quality $5\lambda/2$ *AlGaAs*-based MC described in § 3.2. We perform our experiments in the ridge structure shown in Fig. 3.5, whose dimensions are 20×300 μm^2.

We excite the sample with 2 ps-long light pulses from a Ti:Al_2O_3 laser, tuned to the bare exciton energy level (1.545 eV). Two independent, twin beams, dubbed A and B, are split from the laser: their intensities, spatial positions and relative time delay ($\Delta t = t_B - t_A$) can be independently adjusted. We have determined that the power threshold to produce polariton condensates by each of the beams is $P_{th} = 4.4$ mW. The two laser beams are focused on the sample through a high numerical-aperture (0.6) lens, to form 10-$\varnothing$ μm spots. The laser beams impinge on the sample at a certain angle so that their direct reflection is filtered out in far-field to prevent it from blinding the polariton emission. The excitation at normal incidence would hinder the observation of the polariton emission since the laser is only 5 meV blue-detuned with respect to the polariton emission energy.

11.1.1 Excitation scheme for ballistic propagation of condensed polariton WPs

Before presenting the device operation, let us discuss first briefly the choice of the excitation conditions used for these new set of experiments. In this case the sample is excited with a laser tuned to the bare exciton level, as similarly done in the experiments presented in Chapters 6 and 7. This excitation choice allows to obtain polariton WPs propagating almost ballistically, reducing as much as possible the effects of the polariton energy relaxation in presence of a dense excitonic reservoir at the pump spot (obtained under excitation at the first minimum of the stop band). We illustrate this effect in the following Fig. 11.1. It shows the energy of the emission in the ridge, in both real- and momentum-space under excitation at the first minimum of the stop band, 1.612 eV, [Figs. 11.1(a,b)] and under excitation at the excitonic resonance, 1.544 eV, [Figs. 11.1(c,d)].

While in the former case polaritons have to relax their energy by almost 2 meV (from 1.5419 eV to 1.5406 eV) and ballistic propagation is never achieved for any pump power, in the latter one polaritons propagate ballistically at 1.541 eV.

11.2 Experimental results and discussion

In this section we describe our main results which demonstrate the AND gating operation. In first place, § 11.2.1 discusses the optimal conditions for the gating. In second place, in § 11.2.2 we report a particular case where the choice of certain unsuitable conditions for the operation breaks the logic AND operation. Further interesting phenomenology in polariton physics observed in this device,

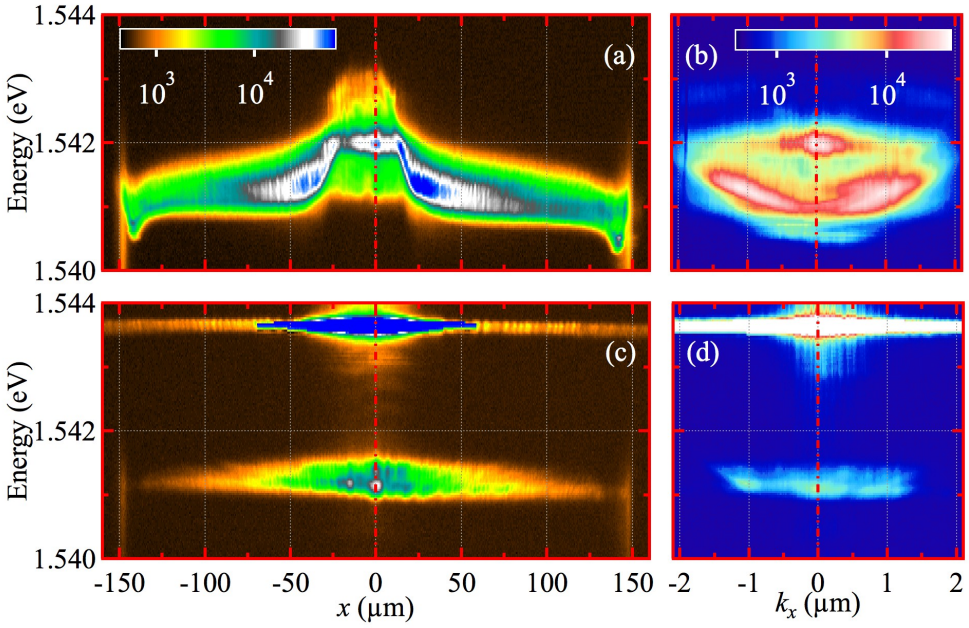

FIGURE 11.1: (a)/(b) [(c)/(d)] Energy vs real-space (x)/momentum-space (k_x) image of a cross-section along the ridge under excitation at the first minimum of the stop band (1.612 eV) [at the excitonic resonance (1.544 eV)], with a *cw* beam of $\varnothing{-}30$ μm in the center of the ridge. The pump power is set to 16.7 mW in both excitation regimes, corresponding to: (a,b) $11.1{\times}P_{th}^{1}$ and (c,d) $6.7{\times}P_{th}^{2}$, the two different pump power thresholds, $P_{th}^{1,2}$, correspond to the two different absorptions of the MC at 1.612 eV and 1.544, respectively.

such as real space interferences and polariton amplification in presence of the exciton reservoir is analyzed in § 11.2.3 and § 11.2.4, respectively.

11.2.1 Optimal conditions for and gating

To achieve the AND gating operation of the device a proper choice of (i) the A and B beam locations, (ii) their power and (iii) the delay, Δt, between them must be made. Concerning the power, for the experiments described in this subsection we have used $P_A = 7{\times}P_{th}$ and $P_B = 3{\times}P_{th}$ (P_{th} = 4.4 mW), which are appropriate to obtain the AND response of the device. Although we have used a non-resonant excitation, the power requirements remain comparable to previous MC switch designs based on hysteresis control (> 30 mW) [392] or resonant blueshift (∼ 5 mW) [39]. As for the positioning and Δt, the A beam is located ∽100 μm away from the right ridge's border, Fig. 11.2 (a), the A and B beams are spatially separated by ∼50 μm and $\Delta t \approx 80$ ps, Fig. 11.2 (b).

As described in Ref. [36], the photo-generated excitons within the excitation area of a given beam, A (B), create a repulsive potential barrier; in our case at $\{x,t\} = \{0,0\}$ ($\{x,t\} = \{50\ \mu\text{m}, 80$ ps$\}$), labeled as V_A (V_B). As discussed below, V_A and V_B determine the dynamics of the propagating polaritons in the ridge. Under the experimental conditions $(B,A) = (1,1)$ (indicating that both

beams excite the sample) we obtain at long times a quasi-static, trapped polariton condensate, dubbed as $\mathscr{C}_{B\wedge A}$, Fig. 11.2 (c), which constitutes the [ON] state ($B \wedge A = 1$) of the device. The other states, given by $(B, A) = (0, 1)$ and $(1, 0)$, correspond to the [OFF] states ($B \wedge A = 0$). Figure 11.2(d) shows the evolution of the emission, spatially-integrated in the enclosed areas by the squares in Figs. 11.2(a-c). The emission from $\mathscr{C}_{B\wedge A}$ (filled area) displays a fast rise time after the arrival of the B pulse, with its maximum obtained at ~ 200 ps; this is followed by a decay, with a weakly oscillating behavior. The corresponding emission, from the same enclosed region, in the A-only (B-only) configuration is negligible in this scale, see dotted (dot-dashed) trace, verifying the AND operation of the device.

The truth table of the device in real- and momentum-space is summarized in Figs. 11.3 and 11.4, respectively. The emission along the perpendicular coordinate, y/k_y, has been integrated.

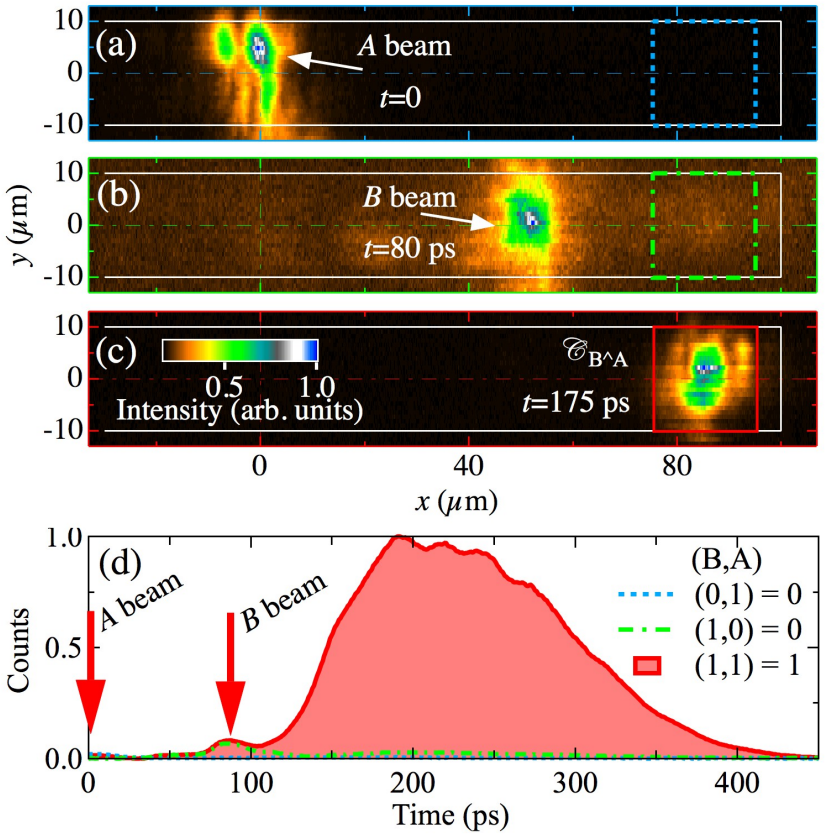

FIGURE 11.2: Real space intensity emission of the ridge at 1.539 eV: (a) scattered reflection of A pulse impinging on the sample at $t = 0$ and at $x = 0$; (b) scattered reflection of a second B pulse, with a temporal delay of $\Delta t = 80$ ps, at $x = 50$ μm; (c) output polariton emission, $\mathscr{C}_{B\wedge A}$, (at 175 ps after the arrival of the A pulse) close to the ridge's border, $x = 85$ μm. The dotted, dot-dashed and full line boxes enclose the region of the output signal 0, 0 and 1, respectively. The intensity is coded in a normalized, linear, false color scale. (d) Corresponding time evolution of the spatially integrated intensity from the boxes described before, the three traces are background-noise subtracted and normalized to the maximum of the $(B, A) = (1, 1)$ trace. The vertical arrows mark the arrival of the A and B beams at 0 and 80 ps, respectively.

The polariton dynamics is shown at three-selected different energies, in the rows (a) 1.5415, (b) 1.5400 and (c) 1.5392 eV, since a full understanding of the device operation is only obtained when a spectroscopic analysis of its emission is performed. For the sake of clarity, we have included an additional row in both Figs. 11.3 and 11.4, labeled (b[t]), where the trajectories in real- and momentum-space, respectively, are sketched with colored arrows. The A (B) beam creates two, initially left/right propagating condensates along the x-axis, named A_L/A_R (B_L/B_R).

We start describing the dynamics of the system under only one beam excitation. The first column in Figs. 11.3(1) and 11.4(i) show, for the different detection energies, the configuration $(B, A) = (0, 1)$, where the output address level reads zero, [OFF]. Figure 11.3 (a-1) displays hot polaritons propagating rapidly away from the A excitation area (the large intensities at very short times arise partially from scattered laser light), and subsequently decaying into lower energy states, Fig. 11.3(b-1), where an elastic reflection of the A_R polariton condensate at the ridge's border is clearly observed at ∼125 ps. A_R reaches the hill of V_A at $\{x[\mu\text{m}],t[\text{ps}]\} \approx \{0, 225\}$, as depicted in Fig. 11.3(b[t]-1) (at this instant the emission is very weak). It is remarkable that interference fringes exist in the polariton emission after the elastic reflection of A_R at the border of the ridge, see the zoomed inset in Fig. 11.3(b-1). They evidence the system coherence, even after the energy loss processes experienced by the original condensate created close to A. Figure 11.3(c-1) shows only scattered light arising from the A pulse at $\{x, t\}$ ={0,0}; the absence of any emission establishes the [OFF] state.

The corresponding momentum space dynamics is compiled in the first column, (i), of Fig. 11.4. Hot polaritons at 1.5415 eV show a quasi-homogeneous distribution of momenta in a **k**-space ring; these polaritons rapidly decay in energy, Fig. 11.4(b-i) (1.540 eV): in the time interval 50 to 100 ps, A_L and A_R propagate at $k_x = \pm 1.1\ \mu\text{m}^{-1}$, as sketched in Fig. 11.4(b[t]-i). The elastic reflection of A_R at ∼125 ps is evidenced by the jump observed in **k**-space from +1.1 to −1.1 μm^{-1} [horizontal segment of the dashed yellow arrow in (b[t]-i)]. Figure 11.4(c-i) (1.5392 eV) demonstrates the [OFF] state, where only scattered light by A is present.

We discuss now the second configuration where the output address level reads zero under B-only excitation, $(B, A) = (1, 0)$, shown in columns (2) and (ii) of Figs. 11.3 and 11.4, respectively, for the three detection energies. Figure 11.3(a-2) displays hot polaritons created at t =80 ps, propagating rapidly away from the B area and subsequently decaying to lower energy states, Fig. 11.3(b-2), in a similar fashion to what has been described before in the $(B, A) = (0, 1)$ configuration, but with a more conspicuous B_R trajectory due to the vicinity of V_B and the ridge's border. B_L moves at a constant speed of $v_x = -0.74\ \mu$m/ps and the several reflections of B_R take place at the positions sketched by the trajectory line, shown in Fig. 11.3(b[t]-2). At each reflection against V_B, where a reservoir of excitons exist, an amplification of B_R is observed, as previously reported in Ref. [40]. Figure 11.3(c-2) shows information concerning only the scattered light by the B pulse at $\{x[\mu\text{m}],t[\text{ps}]\} = \{50, 80\}$.

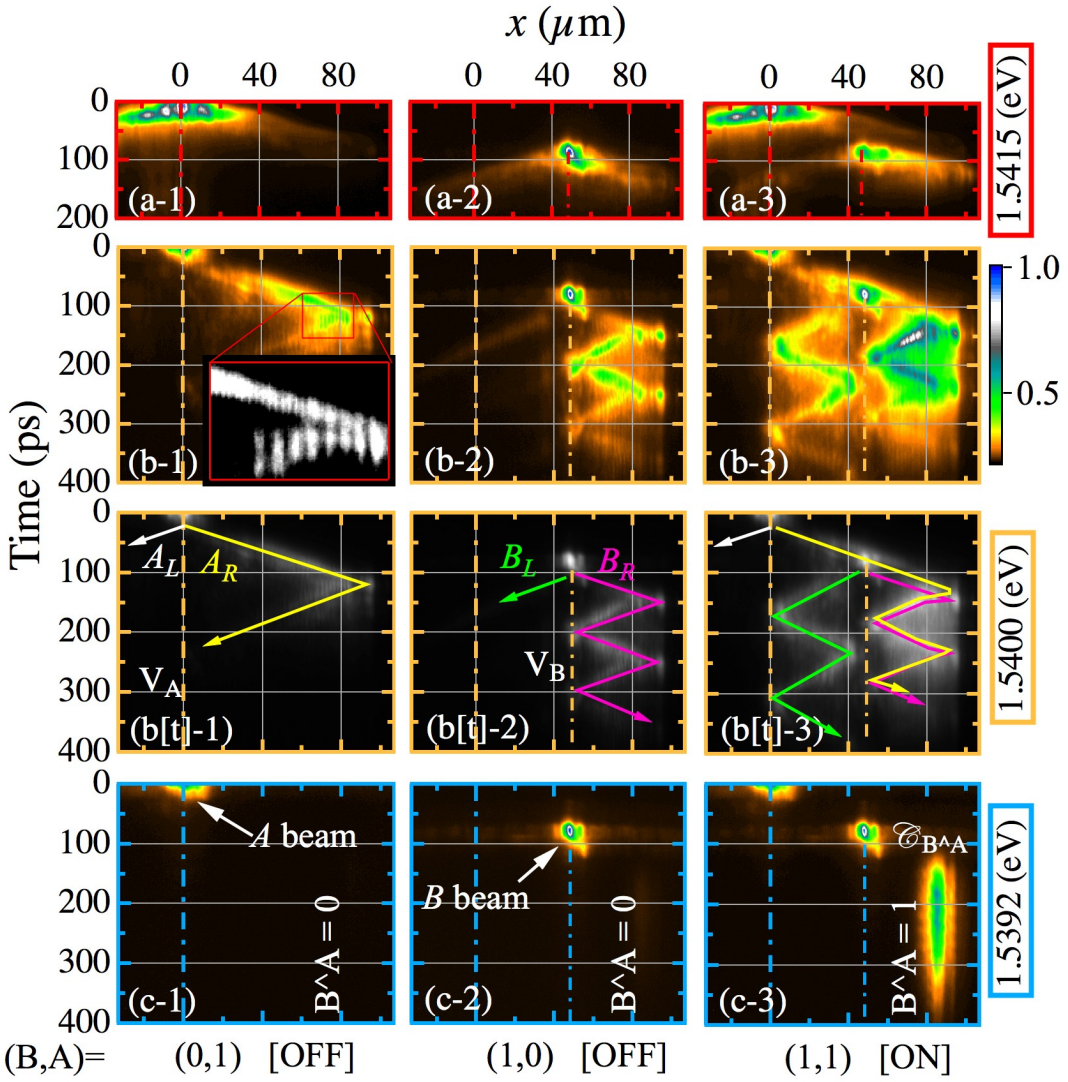

FIGURE 11.3: Real-space dynamics of the polariton emission, exciting with three logic address inputs, (B, A) (see lower labels): $(0, 1)$ A-only [column (1)]; $(1, 0)$ B-only [column (2)] and $(1, 1)$ $A + B$ beams [column (3)], at different detection energies: 1.5415 eV (a), 1.5400 eV (b,b[t]) and 1.5392 eV (c). The inset in (b-1) shows the detail of the elastic reflection of A_R against the ridge's border in the framed area. The trajectories of the polariton condensates at 1.540 eV are sketched by colored arrows in row b[t], on a background, false, grey color scale for the corresponding intensities in row (b). The intensities are coded in logarithmic, normalized, false color scales, shown at the left side of row (b). See supplemental videos of this figure at http://link.aps.org/supplemental/10.1103/PhysRevB.88.245307 for further details on the polariton dynamics in real space.

The corresponding momentum-space dynamics for the configuration $(B, A) = (1, 0)$ is compiled in the second column, (ii), of Fig. 11.4. The momenta of hot polaritons at 1.5415 eV show a similar behavior to that discussed previously for the $(B, A) = (0, 1)$ case, see Fig. 11.4(a-i). The evolution of the emission in **k**-space, appearing in Fig. 11.4(b-ii), evidences the four reflections of B_R in the same instants as those in Fig. 11.3(b-2). The 1^{st} and 3^{rd} reflections show a sudden

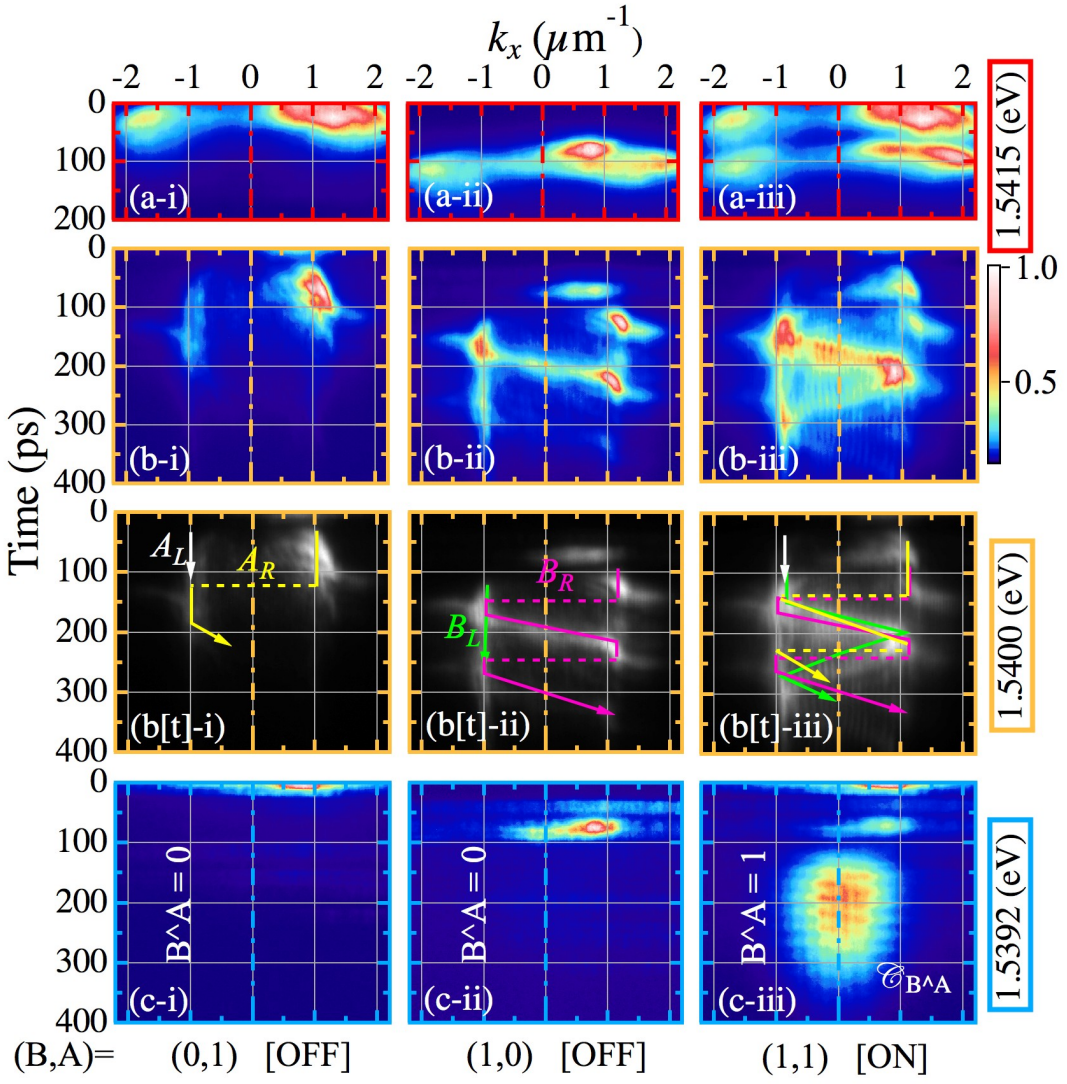

FIGURE 11.4: Momentum-space dynamics of the polariton emission, exciting with three logic address inputs, (B, A) (see lower labels): $(0, 1)$ A-only [column (i)]; $(1, 0)$ B-only [column (ii)] and $(1, 1)$ $A + B$ beams [column (iii)], at different detection energies: 1.5415 eV (a), 1.5400 eV (b,b[t]) and 1.5392 eV (c). The trajectories of the polariton condensates at 1.540 eV are sketched by colored arrows in row b[t], on a background, false, grey color scale for the corresponding intensities in row (b). The intensities are coded in logarithmic, normalized, false color scales, shown at the left side of row (b). See supplemental videos of this figure at http://link.aps.org/supplemental/10.1103/PhysRevB.88.245307 for further details on the polariton dynamics in momentum space.

reversal in the propagation direction during an elastic scattering process [horizontal dashed segments of the arrow in Fig. 11.4(b[t]-ii)]. However, the 2^{nd} and 4^{th} ones correspond to a continuous trade off between potential and kinetic energy [slanted segments of the arrow in Fig. 11.4(b[t]-ii)]: B_R propagates towards V_B decelerating until it comes to a halt, and then it flows back towards the edge of the ridge; the continuous conversion of kinetic into potential energy are observed as continuous lines in the k_x vs. time diagram from -1.1 to $+1.1$ μm^{-1}. Figure 11.4(c-ii), shown for completeness, displays only the scattered light by B.

The [ON] state of the device is demonstrated in columns (3) and (iii) of Figs. 11.3 and 11.4, respectively; the input address level reads now $(B, A) = (1, 1)$. Figure 11.3(a-3) displays the real-space dynamics of hot polaritons at 1.5415 eV, propagating rapidly and decaying to lower energy states: it is clearly seen that A_R surpasses the position of the B pulse, before the latter impinges on the sample, in its way towards the edge of the ridge. Now, this edge and the double excitonic barrier, composed by V_A and V_B, determine the trajectories of the polariton condensates, as shown in Fig. 11.3(b[t]-3). The creation of V_B is delayed by Δt, which is precisely set to 80 ps in order to allow the passage of the A_R condensate and its subsequent trapping together with B_R, Fig. 11.3(b-3). The combination of V_A and V_B constitutes a potential trap, in which B_L oscillates periodically. Its amplification by the excitons at A and B is proven by a significantly stronger emission intensity than that shown in Fig. 11.3(b-2) for B_L, where V_A was absent.

The confinement of polaritons in a potential trap increases their density and when polaritons exceed an occupation threshold (at a certain high energy level), they scatter, relaxing into lower energy states [36, 41]. This stimulated scattering process mediates the creation of $\mathscr{C}_{B\wedge A}$: it occurs only when A_R and B_R are simultaneously confined between V_B and the ridge's border, resulting in an over-populated energy state at 1.540 eV compared to that shown in Fig. 11.3(b-2), where only B_R was present. The former situation, shown in Fig. 11.3(b-3), evolves so that part of the population of the A_R and B_R condensates relaxes and gives rise to the $\mathscr{C}_{B\wedge A}$ condensate, Fig. 11.3(c-3), which lasts for ∼200 ps displaying weak oscillations. A detailed study of the formation of such a trapped condensate, using different (but equivalent for the trapping process) beam-configuration conditions, has been performed in § 9.3.1. The $\mathscr{C}_{B\wedge A}$ lifetime, as already shown in Fig. 11.2(d), is notably larger than that of those condensates expelled far away from the laser position, since the presence of the excitonic reservoir continually feeds $\mathscr{C}_{B\wedge A}$.

The dynamics of the [ON] state in **k**-space is summarized in the third column, (iii), of Fig. 11.4. In Fig. 11.4(a-iii), the two populations of hot polaritons, delayed with respect to each other, manifest the same behavior as that obtained for the individual emissions, reported separately in Figs. 11.4 (a-i,ii). Figure 11.4(b-iii) displays a complex distribution of polariton momentum from $t \approx 100$ ps to $t \approx 400$ ps, since A_R, B_L, and B_R momenta are superimposed in a range of $|k_x| \lesssim 1.5\ \mu\text{m}^{-1}$. A_R and B_R suffer elastic collisions almost simultaneously against the ridge's border at ∼150 and ∼250 ps [dashed segments in Fig. 11.4(b[t]-iii)]; their dynamics is similar to the one of B_R reported in Fig. 11.4(b[t]-ii). On its own account, B_L shows a zig-zag movement in **k**-space, since it suffers continuous accelerations/decelerations in the $V_A + V_B$ potential sculpted by the A and B beams. In this case, the absence of collisions against a hard-well potential (as described for A_R and B_R) yields only slanted trajectories from ± 1.0 to $\mp 1.0\ \mu\text{m}^{-1}$ for the B_L movement. The conspicuous interference patterns around $|k_x| \lesssim 0.9\ \mu\text{m}^{-1}$ arise from the mutual coherence between different condensates. Finally, Fig. 11.4(c-iii) shows the quasi-steady dynamics of the $\mathscr{C}_{B\wedge A}$ condensate ([ON] state): the confined population sustains an oscillatory movement with a period of 25 ps and an amplitude of $\sim 0.75\ \mu\text{m}^{-1}$. The $\mathscr{C}_{B\wedge A}$ effective lifetime is determined by

the excitons at B, which feed the scattering process towards this final state, lasting for more than 200 ps, as reported in Fig. 11.2 (d).

11.2.2 Unsuitable conditions for and gating: a particular case

The choice of the spatial-temporal coordinates of the A and B beams is crucial to obtain the AND-type logic gate. We illustrate this fact in this subsection presenting a particular case, among the plethora of possible choices for these coordinates, where a trapped condensate is also formed at the ridge's edge but the AND operation is not obtained. The spatial distance and the temporal delay between A and B are ∼20 μm and ∼25 ps, respectively. The position of the A beam is 45 μm away from the right border. Due to the fact that the beams are closer together to each other and also to the edge of the ridge, the used power beam are slightly lower, $P_A = 6 \times P_{th}$ and $P_B = 1.5 \times P_{th}$, than those used in § 11.2.1.

Here we present only the polariton dynamics in real space, as summarized in Fig. 11.5, where again the emission along y has been integrated. We follow the same nomenclature for the polariton WPs as the one used before in Fig. 11.3. Due to the rich dynamics obtained under these new excitation conditions, and its strong dependence on the detection energy, four selected energies (a) 1.5411 eV, (b) 1.5405 eV, (c) 1.5400 eV and (d) 1.5396 eV are now shown.

The first row (a) in Fig. 11.5 shows similar dynamics to those already shown in § 11.2.1, Fig. 11.3(a), with hot polaritons rapidly decaying into lower energies. Figure 11.5 (b-1) reveals several reflections of A_R at the ridge's border (x =100 μm) and at V_A (x =55 μm). At 1.5400 eV, Fig. 11.5(c-1), the zig-zag movement of A_R overlaps with the incipient formation of a trapped condensate, dubbed $\mathscr{C}_A$, which is clearly observed at x = 90 μm and 1.5396 eV, Fig. 11.5(d-1). Therefore, under this single-beam excitation, a trapped condensate is already created, lasting for more than 300 ps, evidencing that these excitation conditions are unsuitable to achieve an AND operation.

Column (2) in Fig. 11.5 compiles the polariton emission under B-only excitation. Figure 11.5(b-2) shows that the lower intensity used in this case for the B beam creates a B_R WP with a shorter propagation and weaker emission than A_R. Figure 11.5(c-2) depicts the B_R re-amplification and its tunneling trough the V_B barrier [40] (see the magenta arrows as a guide to the eye for the tunneling processes). At 1.5396 eV, Fig. 11.5(d-2), there is not any trace of a trapped condensate and only the scattered light by the B pulse is observed.

Finally, we show in column (3) of Fig. 11.5 the polariton emission under A+B excitation. The propagation at high energy, 1.5411 eV, of polaritons rapidly decaying into lower energy states is shown in Fig. 11.5(a-3): in this case, the proximity of the A and B beams results in an apparent overlap of the A_R and B_R emission, but the choice of $\Delta t \approx 25$ ps still allows that A_R surpasses the

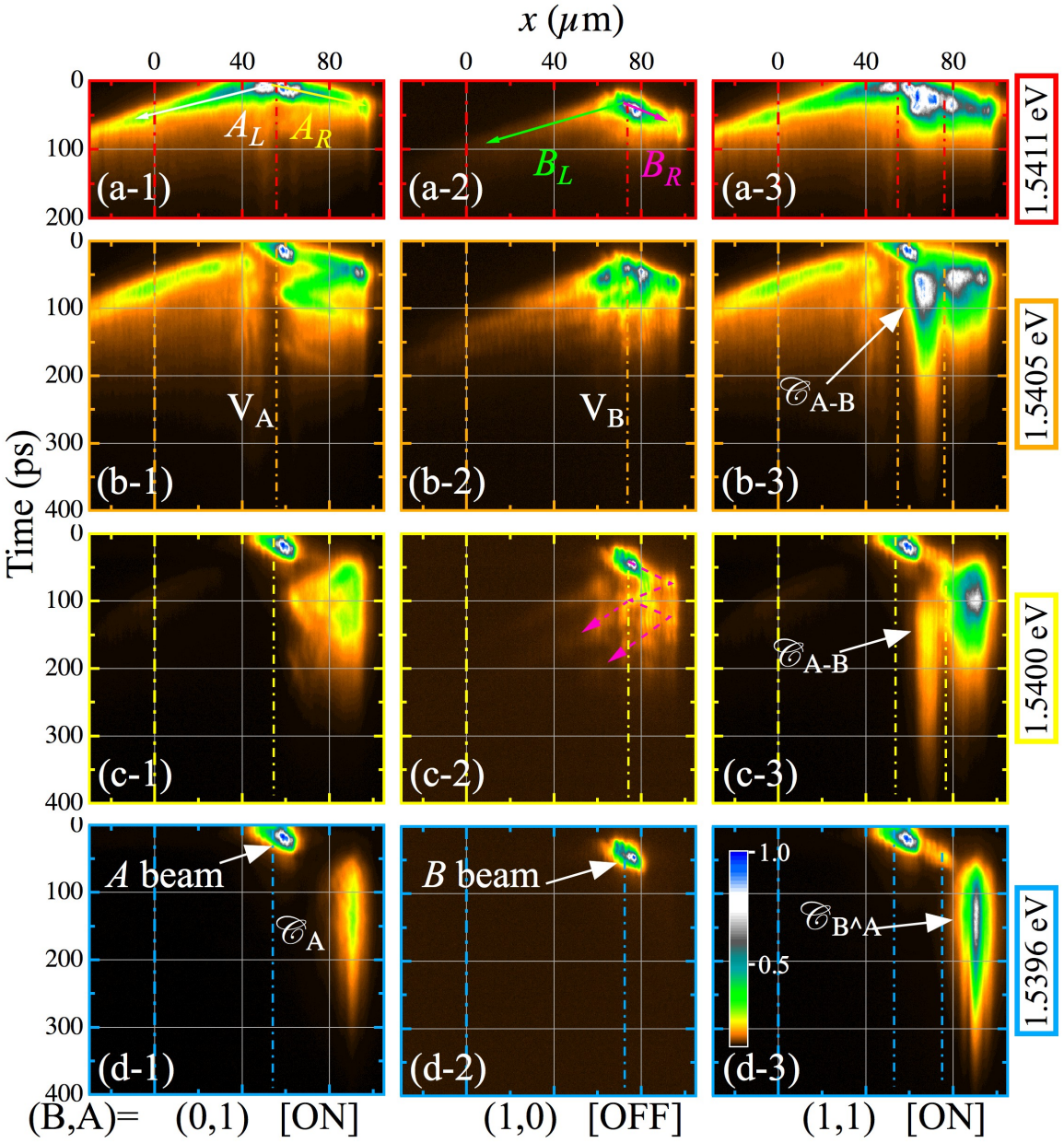

FIGURE 11.5: Real-space dynamics of the polariton emission, exciting with three logic address inputs, (B, A) (see lower labels): $(0, 1)$ A-only [column (1)]; $(1, 0)$ B-only [column (2)] and $(1, 1)$ $A + B$ beams [column (3)], at different detection energies: 1.5411 eV (a), 1.5405 eV (b), 1.5400 eV (c) and 1.5396 eV (d). The trajectories of the polariton WPs $A_{L/R}$ and $B_{L/R}$ at 1.5411 eV are sketched by colored arrows in panels (a-1) and (a-2), respectively. The re-amplification and tunneling of B_R is marked with dashed arrows in panel (c-2) (see text for further details). The intensities are coded in a logarithmic, normalized, false color scale, shown in the panel (d-3). The same spatial-temporal origin is used as that shown in Fig. 11.3.

barrier V_B created by the B beam. The short $A-B$ distance used in this configuration creates a trapped condensate between them, dubbed as $\mathscr{C}_{A-B}$, lasting for more than 200 ps, Fig. 11.5(b-3). The polariton emission at the ridge's edge (region between 80 and 100 μm) lasts $\lesssim$150 ps at this energy, polaritons rapidly decay in energy forming a trapped condensate, $\mathscr{C}_{B\wedge A}$. Figure 11.5(c-3) shows the coexistence of both $\mathscr{C}_{A-B}$ and $\mathscr{C}_{B\wedge A}$ condensates at 1.5400 eV, the latter being three times more intense than the former one. At 1.5396 eV, Fig. 11.5(d-3) shows the output signal $\mathscr{C}_{B\wedge A}$. This was the [ON] state under suitable excitation conditions (§ 11.2.1), which appeared only for the $(B, A) = (1, 1)$ input address, however in the present excitation conditions such a signal appears also in the $(B, A) = (0, 1)$ case, violating the AND truth table.

It is remarkable that the $\mathscr{C}_{A-B}$ emission, Fig. 11.5(b-3), is 1 meV blue shifted with respect to the $\mathscr{C}_{B\wedge A}$, Fig. 11.5(d-3). This difference is due to the combination of the V_A and V_B barriers and the short distance between them: the potential created by the barriers increases the $\mathscr{C}_{A-B}$ energy, while $\mathscr{C}_{B\wedge A}$ emits from the available lower energy states close to the ridge's border [shown in the inset of Fig. 3.10(c)]. Focusing now at the lowest energy, 1.5396 eV, a comparison between the trapped condensates $\mathscr{C}_A$ and $\mathscr{C}_{B\wedge A}$, Figs. 11.5(d-1,3), shows that the $\mathscr{C}_{B\wedge A}$ emission is 4 times stronger and lasts $\sim$ 50 ps longer than the $\mathscr{C}_A$ emission. The addition of A_R and B_R populations and the re-feeding of $\mathscr{C}_{B\wedge A}$ in presence of the V_B exciton barrier yield this intense and long-living condensate.

From these experiments we conclude that (i) a single WP (A_R) is able to create a trapped condensate ($\mathscr{C}_A$) close to the border (**unsuitable** condition for the AND operation), (ii) inadequate parameters of beam power and distance to the border hinder the formation of this trapped condensate (case of the B beam excitation), and (iii) the photo-generated excitonic potentials permit to create blue shifted, trapped condensates on demand (as it has been demonstrated by the creation of $\mathscr{C}_{A-B}$).

11.2.3 Real space interferences from counter propagating polariton WPs

Figure 11.6 compiles a deeper analysis of the inset of Fig. 11.3(b-1), demonstrating that the interference comes from backscattered polaritons. The integrated profiles at different times (100, 117 and 129 ps), Fig. 11.6(i-iii), demonstrate the appearance of the interference fringes, in the region from 70 to 85 μm, arising from counter-propagating polariton WPs. The additional oscillations, between 50 and 60 μm, seen in Fig. 11.6(a) are due to backscattering of polaritons at the lower horizontal edge of the ridge.

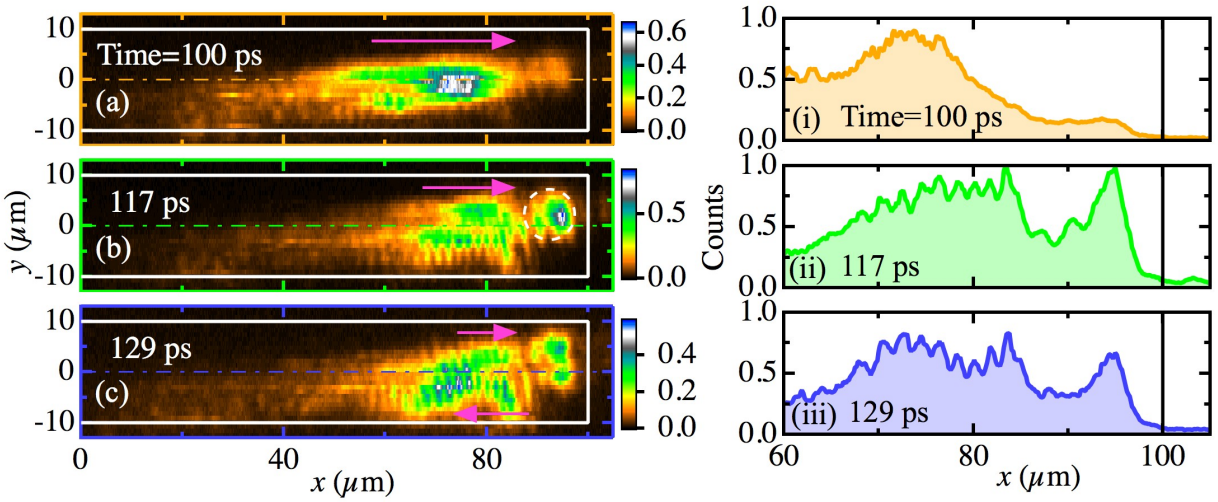

FIGURE 11.6: Detailed snapshots of the emission maps in real space, corresponding to the y-integrated emission shown in Fig. 11.3(b-1). (a) A_R WP, extending from ∼50 to ∼90 μm at 100 ps. (b) A_R impact against the right border at 117 ps and creation of a counter-propagating WP. (c) The two counter-propagating WPs at a later time, 129 ps. A full white line depicts the borders of the ridge; magenta arrows indicate the direction of propagation of A_R. Intensity is coded in a linear, false color scale. (i-iii) Corresponding PL intensity versus x, integrated along the y direction of the ridge, for the instants compiled in panels (a-c), a PL profile free from fringes is seen in panel (i), while in panels (ii,iii) interference fringes, with a periodicity of ∼2 μm, are clearly observed from 70 to 85 μm.

11.2.4 Amplification of polariton WPs in presence of excitonic reservoirs

The polariton amplification phenomena, in presence of photo-generated excitonic reservoirs [40], has been also observed in our experiments since potentials V_A and V_B act as excitonic re-amplifiers of polariton WPs when approaching them. Figure 11.3 shows two amplifying mechanisms. In the former case, Fig. 11.3(b-2), B_R is trapped between V_B and the ridge border, B_R is amplified when it approaches the excitonic area of B. In the latter case, Fig. 11.3(b-3), B_L becomes trapped in a repulsive potential sculpted by $V_A + V_B$; B_L experiments a strong amplification in every reflection against the barriers.

Figure 11.7 describes the former case where B_R bounces back and forth between the V_B potential and the right border of the ridge. We track the integrated B_R PL emission, Fig. 11.7(a), showing its amplification at the instants where B_R touches the tails of the excitonic potentials, Fig. 11.7(i-viii).

The first peak at 80 ps in panel (a) mark the arrival of the B pulse, then Figs. 11.7(i-viii) capture the following instants where the amplification is evidenced. At 130 ps, B_R propagates towards the border of the ridge, Fig. 11.7(i): the bounce against this hard-well potential is evidenced at 150 ps, Fig. 11.7(ii), where a very strong emitting peak emerges from this border [see dark blue point in Fig. 11.7(a)]. After the elastic reflection of B_R, it propagates leftwards, 167 ps,

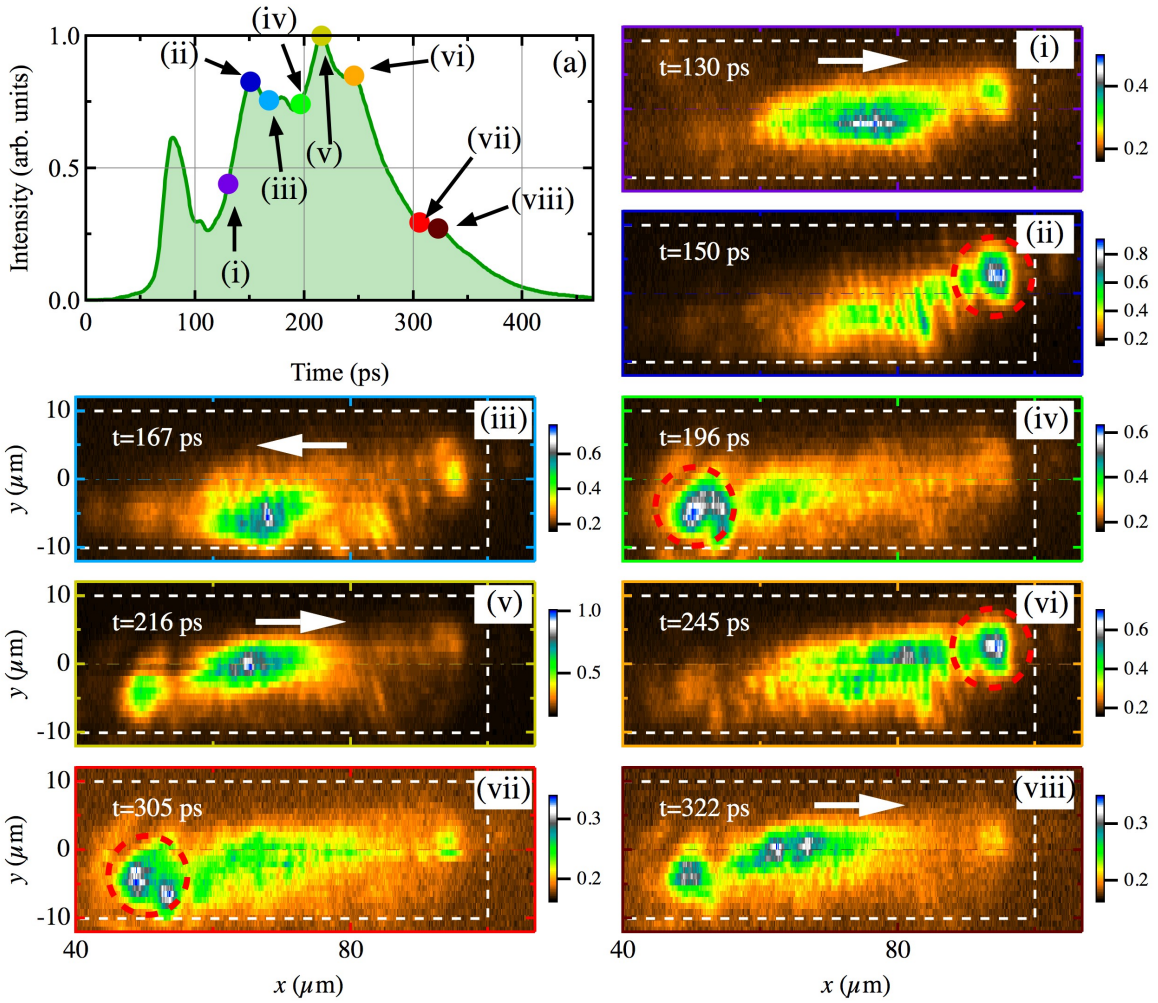

FIGURE 11.7: (a) Integrated emission dynamics in the region between V_B and the right border of the ridge, under the $(B, A) = (1, 0)$ configuration excitation [Fig. 11.3(b-2)]. The colored points on the filled trace indicate consecutive instants in the 2D dynamics shown in panels (i-viii) (the time is indicated by the upper left labels): (i)/(v)/(viii) free right WP propagation, (ii)/(vi) impact and reflection of the WP against the ridge border, (iii) free left WP propagation, (iv)/(vii) impact and reflection of the WP against V_B. White arrows indicate the direction of propagation of B_R, dashed circles mark the impact of the WP against V_B or the ridge border. The intensity is coded in a false color scale shown on the right of each panel.

Fig. 11.7(iii), and its impact against V_B is clearly seen at 196 ps, Fig. 11.7(iv). The polariton amplification occurs at 216 ps, Fig. 11.7(v), where the intensity emission of B_R increases by a factor of 2 compared to the same situation reported in Fig. 11.7(i). Figure 11.7(vi), corresponding to a time $t = 245$ ps, shows the impact of B_R against the border of the ridge (see dashed red circle), then B_R is elastically reflected leftwards (not shown). A second re-amplification process of B_R is observed in Figs. 11.7(vii,viii). In first place, at 305 ps [Fig. 11.7(vii)], B_R halts at $x = 50$ μm in presence of the excitonic reservoir, this spatial overlap enhances amplification of the WP for the second time. In second place, at 322 ps [Fig. 11.7(viii)], B_R propagates rightwards, the analysis of its integrated intensity in Fig. 11.7(a) (see brown circle at 322 ps over the integrated PL dynamics

trace) reveals that, even 200 ps after the WP injection, the B_R intensity is slightly enhanced after the excitonic amplification.

11.3 Model

The simulations on the polariton dynamics are modeled following the generalized GP description, Eq. 11.1, that has been used in the previous Chapters 9 and 10.

$$i\hbar\partial_t\psi(x,t) = \left[\hat{E}_{LP} + \alpha|\psi(x,t)|^2 + V(x,t) + i\hbar\left(rN_A(x,t) - \frac{\Gamma}{2}\right)\right]\psi(x,t) + i\hbar\Re\left[\psi(x,t)\right] \quad (11.1)$$

$\hat{E}_{LP}$ represents the kinetic energy dispersion of polaritons, which at small wavevectors can be approximated as $\hat{E}_{LP} = -\hat{\nabla}^2/(2m)$ with m the polariton effective mass. α represents the strength of polariton-polariton interactions. The effective potential, given by the Eq. 11.2

$$V(x,t) = \hbar\left[g_R N_A(x,t) + g_I N_I(x,t) + g_D N_D(x,t)\right] + V_0(x), \quad (11.2)$$

describes both the static structural potential of the microwire, $V_0(x)$ (see § 3.2.1.1 for a further description of this static potential), and a dynamic contribution from a repulsive potential caused by hot excitons in the system (responsible for the pulse induced barriers). In this way, the evolution equation for the polariton mean-field wavefunction, $\psi(x,t)$, is coupled to a system of semiclassical rate equations for higher energy excitations, Eqs. 11.3-11.5 [206], they are identical as those described in the previous Chapter.

$$\frac{dN_A(x,t)}{dt} = -\left(\Gamma_A + r|\psi(x,t)|^2\right)N_A(x,t) + t_R N_I(x,t) \quad (11.3)$$

$$\frac{dN_I(x,t)}{dt} = P(x,t) - \left(\Gamma_I + t_R + t_D\right)N_I(x,t) \quad (11.4)$$

$$\frac{dN_D(x,t)}{dt} = t_D N_I(x,t) - \Gamma_D N_D(x,t) \quad (11.5)$$

A, I , and D describe the decay rates of each of the exciton types. t_R and t_D are inter-reservoir coupling constants, while r gives the rate of condensation, which enters into Eq. 11.1. Γ is the decay rate of polaritons. The non-resonant pumping $P(x,t)$, excites different states in an "inactive" reservoir, which is coupled to the "active" reservoir. As it has been indicated in § 10.3.1 and also in Chapter 10, the model considers equal, repulsive-interaction constants for the "active", "inactive" and dark exciton reservoirs, so that $g_{A/I/D} = g$ in Eq. 11.2. The final term in Eq. 11.1 accounts

for energy relaxation processes of condensed polaritons:

$$\Re[\psi(x,t)] = -\left(\nu + \nu'|\psi(x,t)|^2\right)\left(\hat{E}_{\rm LP} - \mu(x,t)\right)\psi(x,t), \tag{11.6}$$

where ν and ν' are phenomenological parameters determining the strength of energy relaxation [40, 213] and $\mu(x,t)$ is a local effective chemical potential that conserves the polariton population.

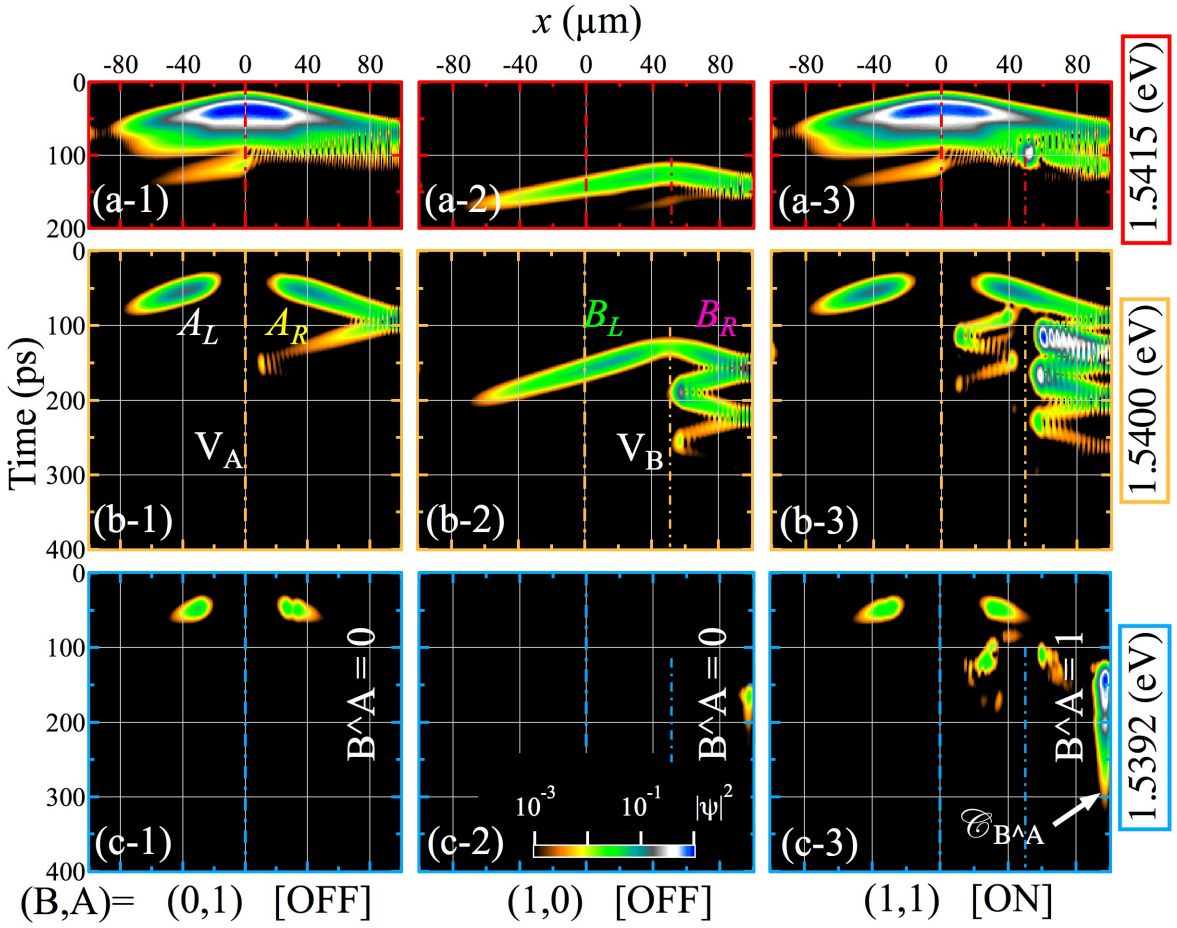

FIGURE 11.8: Calculated real-space dynamics of the polariton emission, filtered at high (a), intermediate (b) and low (c) energies. The columns (1), (2) and (3), correspond to the cases $(B,A) = (0,1)$, $(1,0)$ and $(1,1)$, respectively, as in the experimental Fig. 11.3. The intensity is coded in a logarithmic, normalized, false color scale, shown in (c-2).

Equations 11.3-11.5 were solved numerically with Gaussian pulses corresponding to the experimental configurations, with the results shown in Fig. 11.8. We used the following parameters (compare with those used in § 9.3.1): $\alpha = 2.4 \times 10^{-3}$ meVμm^2, $\Gamma = 1/18$ ps^{-1}, $\Gamma_A = 0.01$ ps^{-1}, $\Gamma_I = \Gamma_D = 10^{-3}$ ps^{-1}, $\hbar\nu = 0.014$ μm^2, $\hbar\nu' = 0.075$ μm^2, $t_R = t_D = 0.02$ ps^{-1} μm^2, $g = 0.018$ ps$^{-1}\mu$m^2. The dispersion was characterized by an effective mass $m = 7.3 \times 10^{-5} m_e$, obtained from fits to the dispersion relations measured in § 3.2.1; m_e is the free electron mass. The simulated excitation pulses A and B, described by $P(x,t)$, had the same shape, size and duration but were

separated by 80 ps and 50 μm. The B pulse was taken with 60% the intensity of the A pulse, similar to the experimental situation discussed in § 11.2.1.

At high energies, the pulses create polariton condensates at their impinging positions, which spread out over time. After a time delay, the polaritons relax their energy entering trapped states, which undergo multiple reflections depending on the excitation configuration, as in the experimental case. In the case when both pulses are present, $(B, A) = (1, 1)$, an enhanced polariton density in a trapped state near the wire edge allows further stimulated energy relaxation, populating the low energy condensate, $\mathscr{C}_{B\wedge A}$, seen in Fig. 11.8(c-3). The localization of this condensate is partly due to a static potential $V_0(x)$, which is known to have a minimum near the wire edge. Note that the theory only reproduces the emission from condensed polaritons; it does not show the scattered light responsible for the peaks at the pulse positions and arrival times seen in Fig. 11.3.

11.4 Conclusions

Using time- and energy-resolved measurements, we studied the dynamics of polariton condensate WPs propagating in a 1D semiconductor MC ridge. The WPs were created by two pulsed excitation laser whose energy was tuned to the bare exciton level, yielding a ballistic propagation of polaritons, in contrast to the previous cases studied in Chapters 9 and 10, where strong polariton energy relaxation was present. The introduction of dynamic, fully controllable potential barriers allows the reflecting and re-routing of the WPs. Multiple reflections occurring between pairs of barriers (optical induced or formed by the wire edge) allow the confinement and storage of propagating polariton states. This localization also gives rise to an enhancement of energy relaxation into a coherent ground-state, which forms a convenient output of a logical AND gate. The total dynamics in real- and momentum-space has been tracked yielding the modus operandi of the device. Theoretical simulations based on a generalized GP description reproduce the experimental dynamics and confirm our understanding of the system. These results pave the way for the realization of ultrafast, compact switches based on the manipulation of Bose-Einstein-like condensates. Due to the use of incoherent/non-resonant excitation, this framework provides a path toward hybrid electro-optical information processing devices and offers additional functionalities for different applications ranging from coherent matter transport to interferometry.

Chapter 12

Conclusions and future perspectives

In the introduction of this thesis it was mentioned that this year 2015 has been proclaimed the "*International Year of Light and Light-based Technologies*". Such honorific celebration has almost coincided with the Nobel Prize of Physics in 2014 rewarding to the researchers I. Akasaki, H. Amano and S. Nakamura, for their relentless pursuit of new **blue light-emitting LEDs**. The implications of such success, yielding the obtention of white LED-light, will have notable and positive consequences in our society during the 21st century. This stately achievement in semiconductor physics is part of the huge efforts done by the scientific community during the last $\sim$ 60 years to investigate and develop photonic devices based on semiconductor technology, starting from the engineering and devising of practical semiconductor light emitters in the early 1960s (see an interesting paper about the origins of the LED discovery in Ref. [410]) and optical fibers in the 1970s. Following the timeline of these great inventions, VCSEL structures were realized in the late 1970s by A. Scherer and J. Jewell, accounting nowadays for a broad number of applications among which include gesture recognition, "touchless" sensing and chip-interconnection.

The research addressed in this thesis has been carried on a new generation of semiconductor samples that belong to the "close" family of VCSEL structures. The development of the MBE techniques (invented in the *Bell Telephone Laboratories* in the late 1960s [238]), as we know them today, permitted the realization of MCs with high enough quality to yield SCR in an exciton-cavity system [11]. The attainment of this milestone motivated the start of the era of CQED in nanostructured semiconductors, as an alternative to atom-based CQED systems. The recent results obtained in this new frontier of solid-state physics are helping to deepen in the understanding of fundamental quantum physics phenomena and also in the realization of new quantum protocols for future information processing and communication [411].

The work described in this PhD thesis is framed in the context of solid-state physics in semiconductor MCs. The inorganic semiconductor MCs studied in this thesis, working in the SCR under laser light excitation, allow for the carriers density (formed by a macroscopic number of

particles in a micrometrical region of space) to be increased up to values of occupation where the quantum nature of the bosonic quasi-particles drives the system into an out-of-equilibrium exciton-polariton BEC, occupying a single "quantum" state. Polaritons form an experimental system in which the frontiers of BEC physics can be investigated in a relatively easy way. Their properties are inherited by the photons emitted by the MCs and therefore can be readily measured by means of optics and spectroscopic setups including ultrafast detection systems.

In this polariton BEC regime, analogous to an atomic-BEC, polaritons can propagate over macroscopic distances without loosing their coherence [36, 246, 412] and be electrically [236]) and optically manipulated in planar [41, 42, 387–391, 396] and etched MCs [40, 383–385, 397]. Polariton-based logic operational routines have been theoretically proposed and implemented [39, 47, 302] as well as polariton circuits [31, 35, 37, 45], diodes [30, 44, 232, 234, 377, 413] and ultrafast switches and transistors [33, 43, 46, 48, 267, 300, 301, 392], some of the theoretical proposals and experimental results in the interesting time-response range of terahertzs [59, 414–416].

Apart from a new platform for promising technological applications, coherent polariton fluids have been shown to present a number of non-linear phenomena as quantized rotation [28, 169, 170, 401, 417] (cited only a few of them, for the sake of extension) and solitons, dark- [174–176, 200, 325, 418, 419] and bright-type ones [38, 256, 420]. An interesting debate about the role of polariton nonlinearities in dark-soliton phenomena has recently discussed in the work of P. Cilibrizzi and coworkers [326], reporting the observation of polaritonic dark-solitons having a negligible excitonic character and therefore excluding nonlinear polariton contributions to the effect.

Although polaritons present many analogies with atomic BEC and superfluidity phenomena, their out-of-equilibrium character poses fundamental questions about the proper way of describing their behavior. Our research group SemicUAM in Universidad Autónoma de Madrid has observed the suppression of Rayleigh scattering when creating polariton bullets, excited in the OPO regime, and the flow against defects [26]. A year later, in 2010, the group demonstrated the persisten flow of polariton quantum fluids, injected by a resonant LG probe and also created in the OPO regime [28, 421].

12.1 Conclusions of this thesis

In the next lines we summarize the main achievements of this thesis, following the ordering of the Chapters and highlighting the main findings of each one.

Polariton OPO phenomena: quantized rotation and OPO ignition in micropillars

Following the research line of our group SemicUAM in polariton quantized rotation phenomena, in Chapter 5 we have demonstrated that unintended AVs appear in the signal at the edge of an imprinting V probe and explained, both theoretically and experimentally, the origin of the deterministic behavior of the AV onset and dynamics [50]. In particular, we showed where AVs are more likely to appear in terms of the supercurrents of the imprinting probe and the currents of the underlying OPO. The theoretical predictions are borne out by the experimental observations. In addition, our study reveals that the onset of Vs in polariton superfluids does not require a LG imprinting beam, but instead V-AV pairs can also be simply generated when counter-propagating currents are imposed, similarly to what happens in normal (classical) fluids [51].

Again under OPO excitation, in Chapter 6 we have presented the experimental conditions to obtain a long-lived polariton condensate in a pillar MC [55]. The process involves two excitation beams impinging at the center of a 40 μm-$\varnothing$ pillar: a *cw* pump, slightly blue-detuned from the inflection point of the LPB, and a pulsed probe, which resonantly creates excitons. The polariton population excited by the arrival of the probe induces a blueshift of the LPB, which enters into resonance with the pump beam, triggering the OPO process. As a result of the combined effect of both beams, the OPO signal emission lasts for more than 1 ns, much longer than any of the characteristic times of the MC.

Interfering in momentum space two spatially separated polariton condensates

In Chapter 7 we have conceived innovative measurement schemes in momentum space in order to probe the remote coherence between spatially separated polariton condensates [57]. The convenience of monitoring the evolution of exciton-polaritons in semiconductor MCs, through the detection of emitted light, makes this system an ideal platform to study quantum coherence properties in real space as well as in momentum space. We have profited from the finite lifetime of polaritons inside the MC to demonstrate the existence of quantum interferences between spatially separated polariton condensate WPs, propagating with the same k_x value.

The optical spin Hall effect and the spin textures in a polariton circuit

In Chapter 8 we have studied the optical spin Hall effect in a quasi-1D MC. In such system the lateral confinement yields a suitable scenario for the intra-branch polariton energy relaxation, enriching the phenomenology of the polariton spin patterns. Thanks to a spectroscopic analysis of the optical spin Hall effect, we have shown that a phase-shift in the oscillations of the s_y and s_z

Stokes parameters results from the different speeds of propagation of polaritons. These oscillations collapse either when linear-polarized excitation is used or when the pump power of the circular-polarized excitation exceeds a certain level of pump power excitation. Our results are interpreted within the framework of a mean-field model for polariton dynamics, which includes incoherent gain from a polarized exciton reservoir, the energy shift due to the reservoir, TE-TM splitting and energy relaxation [58].

On the route of polariton-based, all-optical, ultrafast devices (I): a polariton transistor switch

Great efforts of the research carried out in this thesis have been dedicated to optimize and control the dynamics of the polariton condensate transistor switch, initially reported by T. Gao and coworkers [43]. The first step in this research line was described in the first part of Chapter 9, where we presented the full dynamics of this all-optical transistor switch. It constitutes a promising first step for future high-speed inter-chip and intra-chip communication in core-based integrated polariton circuits [46].

In order to fully address the underlying physics of such device, in the second part of Chapter 9 we have time resolved the energy and intensity relaxation processes of excitons and polaritons in a MC ridge [62]. A detailed analysis of the decay processes has been accomplished by mapping the energy and intensity emission along the ridge structure. Decay times of the source emission are reported, where we also show the acceleration of the decay processes as a function of the S pump power. The ON time-response of the polariton transistor switch was characterized and optimized. We used a generalized GP model to describe the spatial dynamics of our propagating polariton condensates.

Finally, in Chapter 10 we presented an alternative time-resolved study of the polariton transistor switch, in both real and momentum spaces, giving full insight on the speed of operation of our proposed transistor [48]. By choosing comparatively low G powers, the interruption of the flow can be achieved within tens of picoseconds, while maintaining a reasonably high ON-OFF signal contrast. However, the inverse process, *i.e.*, switching from the OFF to the ON state, takes hundreds of picoseconds due to the long-lived excitons at G. The results compiled in this Chapter have dispelled the doubts about the operation speed of the transistor switch under excitonic gating, which is ~ 3 GHz, similar to the values that, nowadays, silicon-based devices have.

On the route of polariton-based, all-optical, ultrafast devices (II): conceiving logical gates

Following this innovative research line of implementing new functionalities in polariton condensates, in Chapter 11 we implemented a logic AND gate by means of polariton condensate wave trains propagating in a 1D semiconductor MC ridge [47]. The introduction of dynamic, fully controllable potential barriers allows the reflecting and re-routing of the wave trains. Multiple

reflections occurring between pairs of barriers (optical induced or formed by the wire edge) allow the confinement and storage of propagating polariton states. This localization also gives rise to an enhancement of energy relaxation into a coherent ground state, which forms a convenient output of a logical AND gate. The total dynamics in real and momentum space was tracked yielding the modus operandi of the device.

12.2 Conclusiones de esta tesis

En las siguientes líneas resumimos las conclusiones principales de esta tesis, en dicha descripción seguiremos el orden de los capítulos y destacaremos los puntos principales de cada uno.

Fenómenos de polaritones en régimen de excitación de oscilador paramétrico óptico (OPO): rotación cuantizada e ignición de procesos OPO en micropilares

Siguiendo la línea de investigación previa del grupo SemicUAM, en el Capítulo 5 hemos estudiado algunos aspectos relacionados con fenómenos de rotación cuantizada en polaritones. En estos experimentos hemos demostrado la creación no intencionada de antivórtices (AVs) en el condensado de polaritones OPO. Estos AVs surgen en el borde del vórtice (V) contenido en el haz de prueba como consecuencia de su impresión resonante en el condensado. Hemos explicado tanto teóricamente como experimentalmente el origen del comportamiento determinista de la aparición de dichos AVs y su dinámica [50]. En particular, hemos mostrado que la probabilidad de aparición de los AVs en una determinada región del espacio depende de las supercorrientes locales inducidas por la prueba y las corrientes subyacentes del condensado de polaritones OPO. Las predicciones teóricas respaldan las observaciones experimentales. Además, nuestro estudio revela que la formación de los Vs en condensados de polaritones superfluidos no requiere la impresión de un haz de tipo Laguerre-Gauss, ya que los pares de V-AV también pueden formarse simplemente en presencia de corrientes polaritónicas contrapropagantes, de manera similar a lo que ocurre en los fluidos normales (clásicos) [51].

Siguiendo en la configuración de excitación OPO, en el Capítulo 6 hemos estudiado las condiciones experimentales óptimas para obtener un condensado de polaritones con un tiempo de vida muy largo en una microcavidad (MC) con forma de pilar cilíndrico, cuyo diámetro es de 40 μm-$\varnothing$ [55]. Este experimento se ha llevado a cabo con dos haces de excitación incidentes en el centro del pilar, los describimos a continuación: en primer lugar, hemos usado un haz de bombeo ("bomba") con excitación de onda continua, cuya energía estaba sintonizada ligeramente fuera de las condiciones de resonancia de excitación OPO; en segundo lugar hemos empleado un haz de prueba ("prueba"), con su energía sintonizada resonantemente a la misma que la de los excitones de la MC. Tras la excitación con la prueba, la rama polaritónica inferior entra en resonancia con el haz de bombeo produciendo la ignición del proceso OPO de los polaritones. Como resultado del efecto combinado de ambos haces, hemos observado que la emisión de la señal de polaritones OPO perdura durante más de 1 ns, suponiendo mucho más tiempo que cualquiera de los tiempos característicos de la MC.

Interferencia en el espacio de momentos de dos condensados de polaritones separados espacialmente

En el Capítulo 7 hemos investigado esquemas experimentales innovadores para estudiar en el espacio de momentos la coherencia de condensados de polaritones separados espacialmente [57].

Los polaritones se recombinan y emiten luz fuera de la MC. La detección de dicha luz permite seguir la evolución de los condensados de polaritones excitónicos, haciendo de este sistema una plataforma ideal para estudiar las propiedades de coherencia cuántica tanto en el espacio real como en el espacio de momentos. En particular, dicha propiedad nos ha permitido demostrar la existencia de interferencias cuánticas remotas en el espacio de momentos entre paquetes de onda de polaritones condensados separados espacialmente, propagándose con el mismo valor de k_x.

El efecto spin-Hall óptico y las texturas de spin en un circuito polaritónico

En el Capítulo 8 hemos estudiado el efecto spin-Hall óptico en una MC cuasi-1D. En este sistema el confinamiento lateral de la estructura cuasi-1D ofrece un escenario adecuado para la relajación de energía de los polaritones entre las distintas sub-bandas de la relación de dispersión. Esto enriquece la fenomenología de los patrones del spin de los polaritones. Gracias al análisis espectroscópico del efecto spin-Hall óptico, hemos demostrado la existencia de un desplazamiento de la fase en las oscilaciones a distintas energías de los parámetros de Stokes s_y y s_z, ya que para distintas energías los polaritones se propagan a distinta velocidad. Las oscilaciones de spin desaparecen bajo excitación linealmente polarizada o también cuando la potencia de bombeo, bajo excitación circularmente polarizada, supera un cierto nivel. Hemos interpretado nuestros resultados empleando un modelo de campo medio para la dinámica de los polaritones, el cual incluye la descripción de la ganancia polaritónica incoherente desde un reservorio de excitones polarizados, el incremento en energía de los polaritones debido al reservorio, el desdoblamiento TE-TM y la relajación de energía [58].

En la búsqueda de dispositivos totalmente ópticos y ultra-rápidos basados en polaritones (I): un transistor-interruptor de polaritones

Gran parte del esfuerzo en la investigación de esta tesis se ha dedicado a optimizar y controlar la dinámica del transistor-interruptor de condensados de polaritones, el cual fue inicialmente demostrado por T. Gao y sus colaboradores [43]. El primer paso en esta nueva línea de investigación se recogió en la primera parte del Capítulo 9, donde se presentó la dinámica completa del transistor-interruptor totalmente óptico. Este dispositivo constituye un primer paso prometedor en comunicaciones futuras "inter-" e "intra-chip", basadas en circuitos polaritónicos integrados [46].

Para describir completamente la física involucrada en el funcionamiento de este dispositivo, en la segunda parte del Capítulo 9 hemos resuelto en tiempo los procesos de relajación de energía y decaimiento de los polaritones en la MC cuasi-1D [62]. Del análisis detallado de los procesos

dinámicos de decaimiento, haciendo mapas espacio-temporales de la energía y la intensidad de la emisión de los polaritones en la MC cuasi-1D, hemos obtenido los tiempos de decaimiento de la emisión localizada en la fuente. También hemos mostrado la aceleración de los procesos de decaimiento como función de la potencia de bombeo de la fuente. Hemos caracterizado y optimizado el tiempo de respuesta del estado ON del transistor-interruptor de polaritones. Hemos empleado un modelo basado en la ecuación de Gross-Pitaevskii generalizada para describir la dinámica espacial de los condensados de polaritones.

Finalmente, en el Capítulo 10 hemos presentado un estudio alternativo del transistor-interruptor de polaritones, tanto en espacio real como en el espacio de momentos, que nos ha permitido determinar la velocidad de operación del dispositivo [48]. Hemos conseguido bloquear el flujo de los polaritones en decenas de picosegundos empleando potencias excitación en la puerta G comparativamente bajas. Hemos obtenido un contraste de intensidad de las señales ON-OFF razonablemente alto. Hemos identificado una de las debilidades de nuestro dispositivo, la lentitud en la transición del estado de OFF al estado de ON, debida al largo tiempo de vida de los excitones en la puerta. Los resultados recogidos en este Capítulo han demostrado que la velocidad de operación del transistor bajo control excitónico es de ~ 3 GHz. Dicha frecuencia de repetición es comparable a los valores actuales de los dispositivos electrónicos basados en silicio.

En la búsqueda de dispositivos totalmente ópticos y ultra-rápidos basados en polaritones (I): diseñando puertas lógicas

Siguiendo la línea de investigación para implementar nuevas funcionalidades de los condensados de polaritones, en el Capítulo 11 hemos realizado una puerta lógica tipo AND por medio de trenes de ondas de polaritones en una MC semiconductora cuasi-1D [47]. El empleo de barreras de potencial dinámicas ópticamente controlables permite la reflexión y la re-dirección de los trenes de onda. La reflexión multiple que tiene lugar en las barreras de potencial (excitadas ópticamente o constituidas por el borde de la estructura cuasi-1D) ha permitido el confinamiento y almacenamiento de los trenes de onda de polaritones. Esta localización también estimula la relajación en energía a un estado polaritónico coherente fundamental, el cual constituye la señal de salida de la puerta lógica tipo AND. El estudio de la dinámica completa tanto en el espacio real como en el de momentos nos ha permitido explicar detalladamente el modus operandi del dispositivo.

12.3 A few general remarks on the future perspectives of polaritonics

Following the same subdivision of the conclusions of this thesis as done before in § 12.1, in the following paragraphs we outline some experimental ideas that could be carried out in the future, based on the knowledge generated by the research results of this thesis.

Polariton OPO phenomena: quantized rotation and OPO ignition in micropillars

Given the large-enough dimensions of the pillar where the experiments were performed and the availability to carry on polariton OPO excitation, interesting experiments could be performed in the near future joining the experienced gained in the last two Chapters 5 and 6. These experiments would deepen into the fundamental phenomena of polariton quantized rotation. One of the main difficulties in the experiments described in Chapter 5 was to find the proper location of the sample (single-QW one, § 3.1) and the optimum OPO excitation conditions where vortices could be imprinted in the OPO signal and last for long times (> 50 ps) in the MC avoiding the influence of the local supercurrents of the OPO signal on the vortex dynamics. We think that the 40 μm-$\varnothing$ pillar (on the etched multiple-QW sample, § 3.2) might offer a promising opportunity to create a stable OPO signal with less photonic disorder in the MC and reduced polariton currents than the situation that we observed with the sample used in Chapter 5. In such conditions, a quantized rotation memory could be probed by resonantly injecting in the OPO signal at the same position of the pillar two delayed vortices with certain angular momenta m_1 and m_2. The resulting quantized rotation of the fluid would be expected to be the addition of $m_1 + m_2$ phase dislocations, imprinted in the OPO polariton signal. Other different and interesting theoretical proposals for polariton vortex-based devices have been brought forward recently [422].

Interfering in momentum space two spatially separated polariton condensates

Further investigation in the results compiled in Chapter 7 is still being carried on by our group. Thanks to our collaboration with Prof. P. Savvidis, we are envisaging new sample scenarios where new momentum space interferometry experiments could be accomplished. The next proposed samples to be studied consist on etched patterns containing two parallel, near (separated by ~ 10 μm), twin ridges. Each ridge would be excited by a single, pulsed beam. The beams impinging on each ridge might be spatially shifted from each other along the x axis of the ridges by a distance similar to the one used in the discussed experiment (that is to say similar to d). This way, the independency in the creation process of a pair of polariton WPs from different ridge-structures, propagating in the same direction (ψ_j^A and ψ_j^B, where $j = 1, 2$ indicating the same direction of propagation $\pm k_x$), would not be questioned anymore. Another improvement to be considered in future experiments is to excite the mentioned ridges with two pulsed beams arising from two

different pulsed-laser sources. Nevertheless, the difficulty of having two pulsed lasers and the needed investment makes this idea become a hardly realizable proposal.

The optical spin Hall effect and the spin textures in a polariton circuit

The observation and the study of the fundamental phenomena studied in Chapter 8 are the base for the realization of an all-optical polariton spin filter (to appear soon, in collaboration with Prof. Savvidis group). The working principle of the spin filter relies on the previously and vastly explored polariton transistor switch mechanisms (Chapters 9 and 10), together with the physics discussed in this Chapter. We would like to mention that both time- and polarization-resolved experiments have been also performed in the MC ridges, but, hitherto, no fair theoretical explanation has been found for the unexpected results that we have found (we do not observe the polariton spin precession along their propagation). Therefore we omitted the inclusion and experimental discussion of such experiments. During the execution of these time-resolved experiments, we complementarily tried to observe the theoretical results reported by M. Y. Petrov and A. V. Kavokin in Ref. [395]; this work address the polariton spin transport in 1D channels. Nevertheless, in such proposal, the scheme of excitation is resonant and such choice is crucial to obtain the theoretically heralded stationary spin domain in the channel. For the sake of simplicity, our first attempt was to mimic the experimental conditions under non-resonant excitation, which unfortunately faded any satisfactory result. Future experiments on this topic should consider the pure resonant excitation as described in the cited work.

On the route of polariton-based, all-optical, ultrafast devices (I): a polariton transistor switch

The optimization of individual condensate transistor elements, as we reported in Chapter 9, was an essential step towards developing information processing devices with the present scheme. In the future, an important feature to be achieved is the cascadability and fan-out of multiple elements for the construction of extended circuits. Such a feat was recently achieved by D. Ballarini and coworkers in polariton-based systems with coherent, resonant excitation [39]. We must keep in mind that this configuration excitation offers a very complex interconnection of consecutive cascaded polariton signals: the working principle of their device consist on exciting the MC with particular angular and spectral tunings of each resonant laser that triggers the polariton signal in a cascaded scheme. In the present form of this resonant excitation scheme, a future electronic polariton-injection is not compatible. Achieving the fan-out of polariton devices working with incoherently generated polariton condensates, as we study in this Chapter, would be particularly promising since it would open up new routes towards electrically injected devices and, consequently, hybrid electro-optical processing systems. So far, it must be emphasized that the present scheme of a polariton transistor switch in our ridges does not offer the possibility to cascade the ON-state signal. Our future effort will be put in studying new theoretical proposals for devising polariton gates with more attractive and functional designs [302]. Let us finally mention that, in order to

account for the relaxation phenomena occurring at C without the presence of the exciton reservoir (described in § 9.3.1.3), a phonon-scattering theory is being implemented by Dr. Tim Liew to understand such experimental phenomenon.

Concerning the operation speed of the polariton transistor switch studied in Chapter 10, the possible "polariton applications" will not attract special interest unless our efforts are put in entering the THz range for the gating-response. To do so, the gating mechanism must be based on a system whose total lifetime is below 10 ps. This implies that non-resonantly photo-generated excitons do not constitute a suitable agent to gate the polariton flow. By the way, it is worth to remark that other recent experimental polariton devices such as the "double-barrier resonant tunneling diode" and the "Mach–Zehnder interferometer" [44, 45] are also based on the presence of excitons to rule the switching process, rendering comparable operation-speeds to ours.

On the route of polariton-based, all-optical, ultrafast devices (II): conceiving logical gates

The main drawback of the work reported in Chapter 11 is, again, the lack of a scheme for output-signal cascading. Added to this complication, we were not able to conceive and implement the indispensable NOT-type logic operation (negation operation with a single input) in order to fulfill the *Universal logic* condition of the "Keyes-list" (see the introduction of Chapter 11). The future experiments aim to conceptualize a polariton device performing both AND- and NOT-operations in a MC structure where the output-input signals can be cascaded between consecutive polariton devices.

In the following lines, some future and general perspectives of the research on polaritons are discussed. From our point of view, we consider which are the main difficulties to be overcome in short term to hold the polariton research in a sustainable, optimum regime. The main challenges to be addressed could be itemized in the three following topics:

(i) the seek of efficient **electrically-excited** polaritons in the MC,

(ii) the need for easier/accesible MC growth techniques and methods, or equivalently, **new (organic) materials** for MC samples (compatible with electrical excitation) and consequently:

(iii) the working **temperature** for polariton condensation or lasing.

Regarding the first point, one could argue that such goal has been already demonstrated in the recent works of Bhattacharya and coworkers [24, 25]. They claimed to have implemented a "*room temperature electrically pumped inversionless polariton lasing*" in a *GaN* MC diode, solving in one go the mentioned points (i) and (iii). There are two opposed points of view in the community

against and for these results (see for example Refs. [423, 424] for a positive report on the work; a critical reply to the Letter of Ref. [25] is expected to appear soon). The truth is that a deep inspection in their MC structure reveals that, somehow, Bhattacharya and coworkers were able to grow a $p-i-n$ diode junction in a perpendicular direction to the DBRs of the MC (in a usual situation, the QW is a parallel plane to the DBRs). They obtain a cavity-photon lifetime of 0.387 ps in such MC but contradictory values of the cavity linewidth γ_c are reported in the Letter and the supplementary report, where the peak of the cavity spectrum is only three times bigger that the noise fluctuations. They show a different threshold for the linewidth and the nonlinear PL emission as function of the current injection, which can not be reconciled with a correct threshold for condensation of polaritons. Authors claim to observe non negligible values of visibility of the polariton interference patterns (~ 0.3 for a complete overlapping between the interfered images) below the threshold, this is not compatible with the results reported, for example, in Ref. [21]. These results reported in Refs. [24, 25] must be reproduced and ratified by other laboratories.

Other studies on polariton phenomena are trying to exploit their pure quantum properties by devising MC samples where the "single-polariton" emission could be realized and manipulated for quantum information purposes. It is fair to point out that this quantum information research line in polariton-based systems is still very young and accounts just a few experimental results [425].

The second mentioned point, the lack of easier/accesible MC growth techniques, is the reason why nowadays the research breakthrough successes are mainly concentrated in those groups, working on III-V and II-IV semiconductor compounds, with exclusive access to clean rooms mastered in MBE tehcniques. In this case, these research groups are able to envisage, from a privileged situation, new samples and polariton devices, to the detriment of those researchers who do not have such direct access to new MC samples. This fact, somehow, conditions the expansion of the field as compared to other relatively new physics fields (graphene-based physics and QD fluorescence bioimaging, for example). The way to avoid this research bottleneck is to conceive new materials (if any), presumably made with organic compounds, which, in principle are cheaper and accesible to get MC structures working in the SCR [231, 426]. In these cases, as no crystal growth is involved [427], the approach reduces the complexity of experiments to investigate BEC physics and establish promising ways for a new generation of opto-electronic devices, taking advantage of the processability and flexibility of polymers as active media of the polariton condensation. Still great strides must be done in this direction in order to obtain reliable platforms of organic compounds where polariton condensation is easily achievable and manipulable (see Ref. [423] for a review of this topic).

Concerning the last point, while it is true that the main advantage of polaritons is their relatively high temperature for condensation when compared to atomic systems, still any "feasible" polariton chip or transistor must work (at least) at a higher temperature than 77 K to be relevant for technological purposes. This is where ZnO-based MCs enter the scene [187–191] (for the sake

of simplicity, we do not discuss here GaN-based MCs, which also yield polariton condensation at room temperature). The main drawback in ZnO systems is the low Q factor of their MCs due to the dense presence of impurities in the DBRs. This reduces the photon lifetime and therefore the possibility to enter the SCR. Following the approach developed in GaN-based systems, ZnO-based planar cavities have been fabricated with a bottom epitaxial mirror, an epitaxial ZnO active layer, and a final top dielectric DBR [187, 428–430]. VCSEL [428] and polariton lasers [187, 429] were fabricated from such structures, despite a low Q $(200 - 600)$ and remarkable presence of defects. Polycrystalline ZnO could serve as alternative to increase the cavity Q up to 1000, sacrificing the crystalline quality of the active material. This achievement has permitted the observation of polariton lasing up to 250 K [188]. Other types of MCs are merging the good crystalline properties of bulk ZnO substrates (reduced presence of defects) with the large Qs of dielectric DBRs (up to $\sim$4000). As a result, polariton condensates in ZnO can be created in a broad range of temperatures up to 300 K [191].

Many more fascinating results are expected to arrive in polariton physics. The fundamental phenomena of polaritons studied in $GaAs$ semiconductor MCs will surely bring exciting results at the frontiers of research, cross-talking with fluid dynamics, thermodynamics, magnetism, CQED, and even astrophysics. The future applications of polariton condensates will depend on bringing their working regimes to room temperature in novel materials (presumably organic ones) and, of course, using electrical injection.

This thesis tried to be a tiny input in both fundamental phenomena and applications areas.

Appendix A

Polariton condensation in a quasi-1D microcavity ridge

In Chapters 6, 7 and 11 we have used an excitation regime where lasers has been tuned to the bare exciton level in order to create polariton condensates. In our sample not all cavity QWs are degenerate, thus one gets additional bright states at the exciton energies between the two UPB and LPB. These are exactly the two bands centered at 1.545 and 1.547 eV that we already discussed in Fig. 3.10(b). As a result, the mirror reflectivity is not anymore 0.9999 percent. This means that one can reasonably inject light at the energy shown by the dashed, red arrow considering also the linewidth of the two lines. We wanted to uniformly populate all the QW states and therefore we chose to pump in the middle of the two bands.

In this Appendix we spectrally analyze the polariton condensation as function of the pump power under pulsed excitation at the bare exciton level. The time-integrated experiments show the polariton PL in both real and momentum space in the quasi-1D MC ridge, previously described in § 3.2. Figure A.1 shows energy-resolved distributions of polaritons in real and momentum space for different excitation powers. The emission in real space below threshold for condensation is depicted in Fig. A.1(a): it is centered at the position of the laser impinging on the sample ($x = 0$); the corresponding dispersion relation is shown in Fig. A.1(b), where several polariton sub-bands are observed, originating from the 1D confinement. The emission spans a large energy and k_x range. As the pump power is increased to threshold ($P_{th} = 2.77$ mW), polaritons move away from $x = 0$ [Fig. A.1(c)] and the emission slightly blueshifts and narrows in energy [Fig. A.1(d)]: narrow spots are observed in the dispersion at $|k_x| \sim 1$ μm^{-1} (moving, non dispersive condensates) coexisting with a dispersive, thermal population. At even higher pump powers, twice the threshold for condensation, the condensates travel even higher distances away from $x = 0$ [Fig. A.1(e)], the energy of the emission becomes narrower and in the dispersion, close to $|k_x| \sim 1$ μm^{-1}, emission from two confined sub-bands is observed [Fig. A.1(f)].

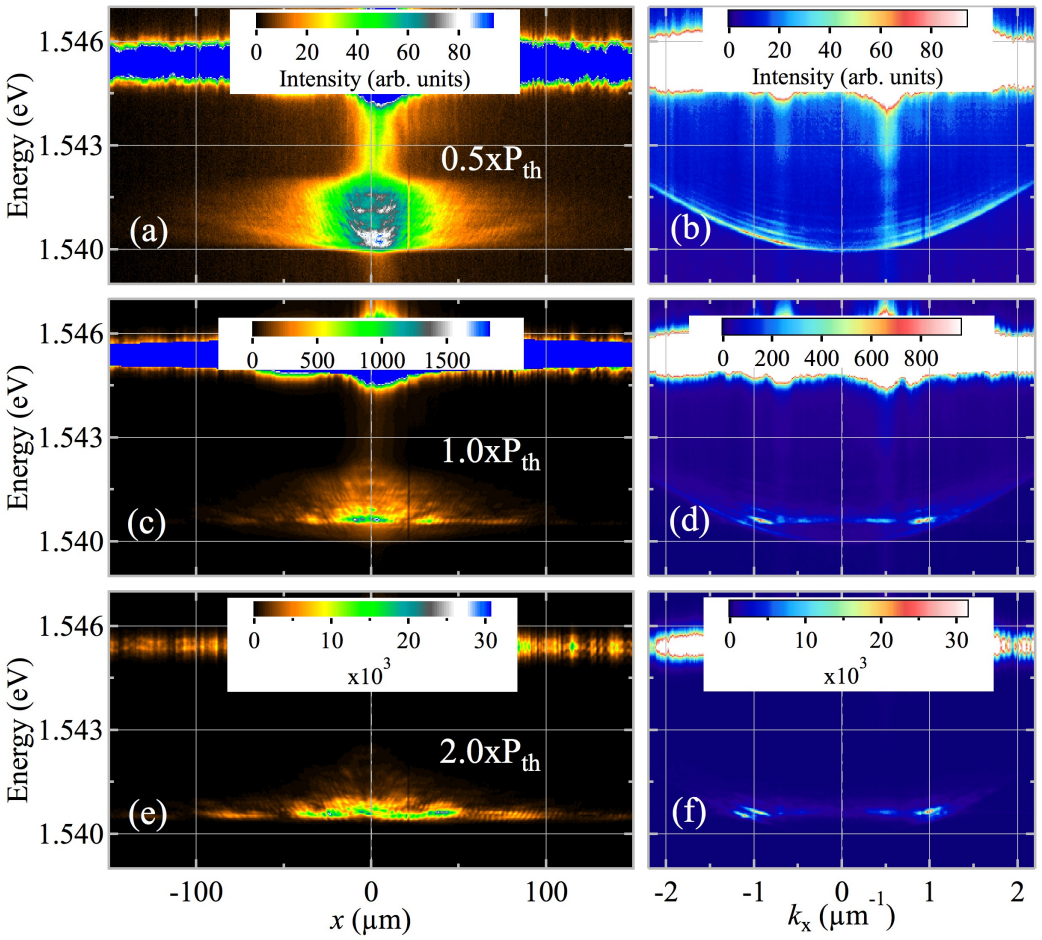

FIGURE A.1: Time-integrated dispersion relations of the ridge, under pulsed excitation at the exciton energy (laser straight light is observed at $\sim$ 1.545 eV). Left panels compile the emission (Energy vs. x position along the ridge) for three different excitation powers: (a), $0.5 \times P_{th}$, (c), $1.0 \times P_{th}$ and (e), $2.0 \times P_{th}$. The corresponding dispersion relations (Energy vs. k_x) are compiled in panels (b), (d) and (f), respectively.

The formation of condensed states is demonstrated by the power dependence of the emission intensity and the energy linewidth, summarized in Fig. A.2. A clear decrease of the linewidth (blue diamonds) is obtained at threshold. The typical non-linear behavior of the emission intensity (red circles) as a function of pump power (P_{pump}) is also observed.

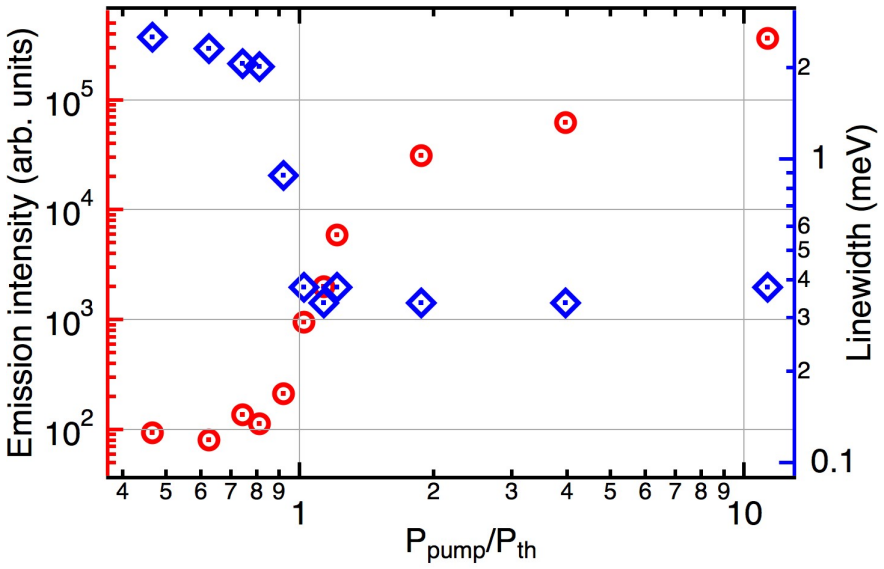

FIGURE A.2: Pump power (P_{pump}) dependence of the emission intensity showing the polariton condensation at the power threshold (P_{th}) through the non-linear increase of the intensity and the narrowing of the momentum distribution linewidth. Left axis (red circles): polariton emission intensity vs. normalized pump power. Right axis (blue diamonds): polariton energy linewidth vs. normalized pump power.

Appendix B

Polariton energy relaxation under excitation at the bare exciton level

We address in this Appendix the energy relaxation dynamics of the excitons created by the pulse excitation at the bare exciton level with a single pulse. This excitation scheme gives rise to the formation of two polariton wave packets (WPs) propagating towards the left/right hand side of the excitation spot.Further details on the polariton condensation under this excitation scheme is addressed in Appendix A.

We include here, in Fig. B.1, time-resolved dispersion relations showing the process of polariton WPs formation. Figure B.1(a) shows the arrival of the laser beam at the ridge (1.546 eV). After 16 ps, the emission from excitons at $k_x \sim 0$ and 1.546 eV, together with its relaxation towards polaritons at the lower branch, is observed in Fig. B.1(b). Further relaxation is shown in Fig. B.1(c) where a population of propagating polaritons at aprox.1.541 eV with $|k_x| \leq 2\ \mu\text{m}^{-1}$ is observed. At even longer times after the excitation, Figs. B.1(d,e) illustrate the formation of propagating polariton WPs, with a narrow energy band-width, at $|k_x| \sim 1.6\ \mu\text{m}^{-1}$, and the decrease of the excitonic emission.

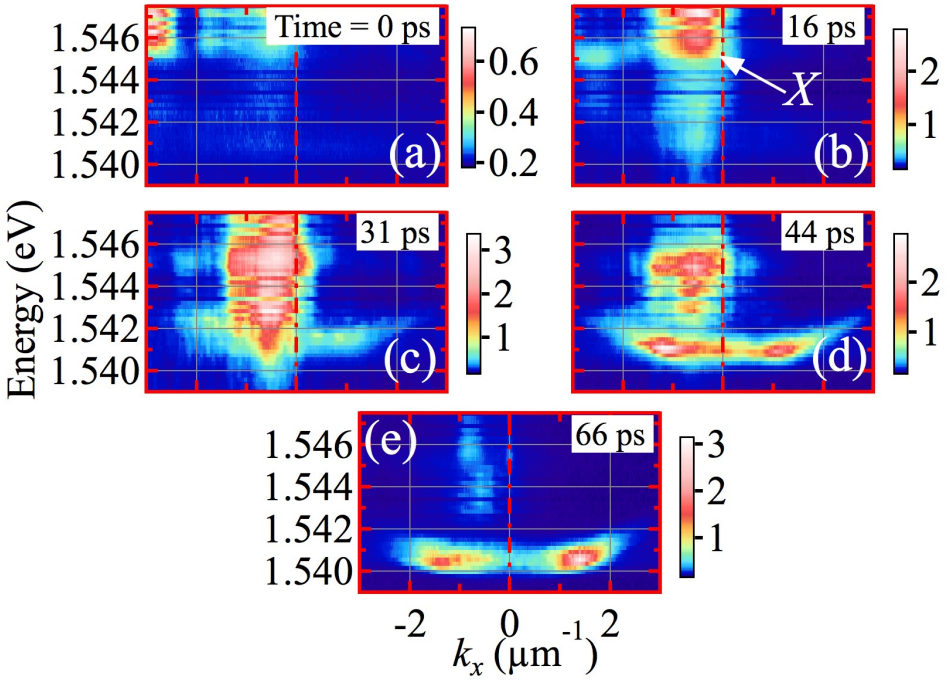

FIGURE B.1: Time-resolved dispersion relations of the emission in the ridge, under pulsed excitation at the exciton energy. (a), Arrival of the laser beam to the ridge at 1.546 eV. (b), Appearance of emission from excitons close to $k_x = 0$ at 1.546 eV together with its relaxation towards polaritons at the lower branch. (c), Further relaxation and increased emission from polaritons close to $k_x = 0$, together with a weaker one of $|k_x| \leq 2\ \mu\text{m}^{-1}$ propagating polaritons. (d), and (e), Increased emission of propagating polariton wave-packets, with a narrow energy band width, at $|k_x| \sim 2\ \mu\text{m}^{-1}$.

Appendix C

Analysis of the polariton momentum space distribution under local emission filtering in real space

In this appendix we include some supplemental results, related to Chapter 7, where we studied the momentum space distribution of condensed polaritons and their spectral emission at different positions along the ridge under the two beam excitation conditions, described in § 7.1. These experiments show in a systematic way how the local polariton dynamics is affected in the presence of a repulsive potential formed by A and B pump spots.

Time-integrated emission in real and momentum space at different x values are shown in Fig. C.1. The full, not-filtered, spectrally-resolved polariton PL in real space is shown in Fig. C.1(a): A and B pump spots are located at $x = -45$ and $+55$ μm, respectively. The polariton condensate extends along the full length of the ridge ($\sim$ 300 μm) and its emission is remarkably intense at the pump spot positions. The presence of the subbands structure in the dispersion relation of the ridge yields a polariton spectral FWHM above condensation of $\sim$ 0.25 meV, centered at 1.5407 eV. The intensity of the scattered laser light, tuned at 1.545 eV, is saturated in the shown false, color scale. The boxed areas in different positions of real space in Fig. C.1(a) correspond to the regions where we filtered the polariton PL in order to observe its local distribution in momentum space. The corresponding dispersion relation is displayed in Fig. C.1(i). A clear emission from ballistic condensates is observed at $k_x = \pm 1$ μm^{-1}, together with some emission at $k_x = 0$ and a thermal population of uncondensed polaritons that lies at higher energies ($\sim$ 1.541 eV) between $1 < |k_x| < 2$ μm^{-1}

In Fig. C.1(b) we filter the real space emission around $x = 0$, between the exciton reservoirs, the corresponding momentum space distribution of this polariton population reveals that

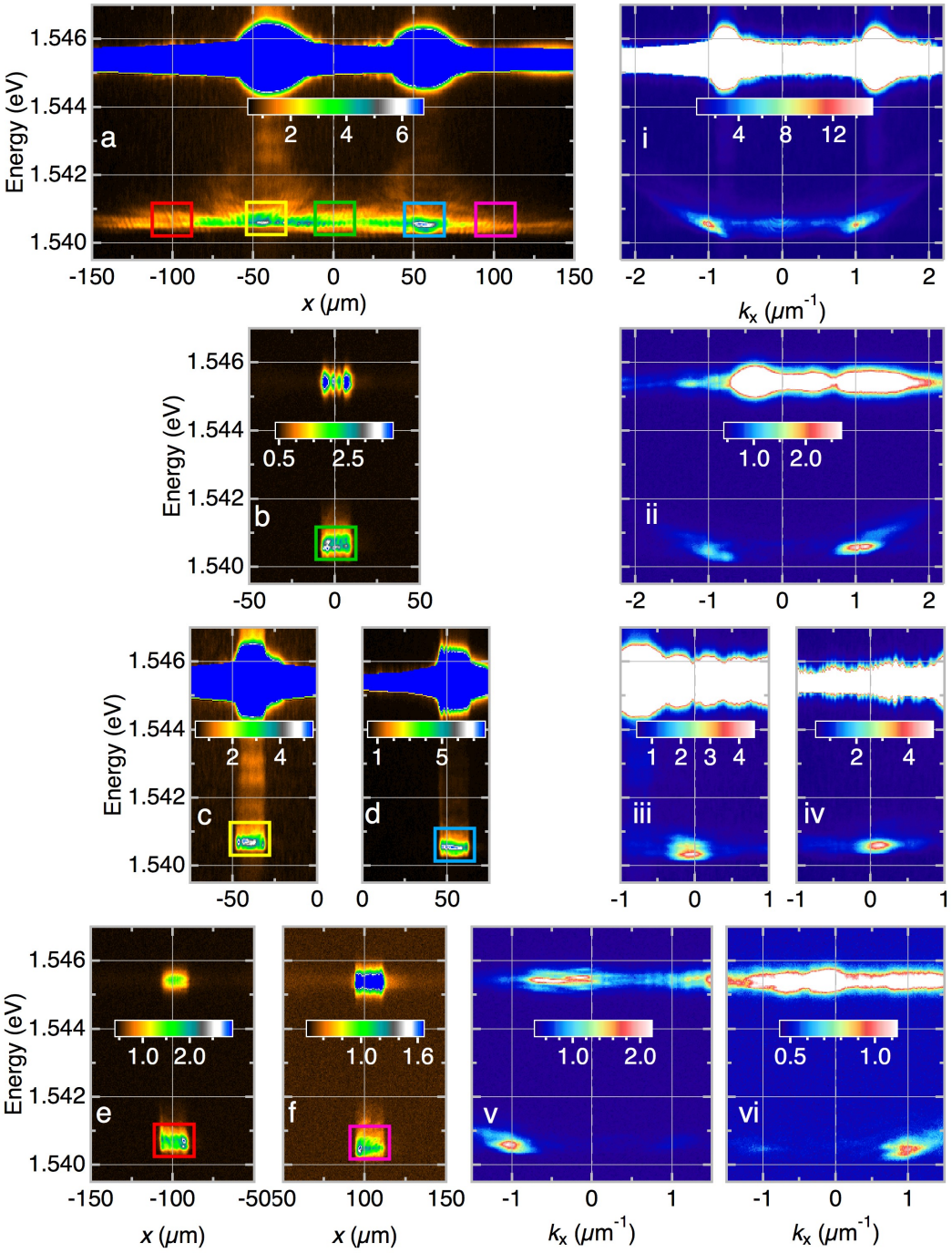

FIGURE C.1: Time-integrated spectra in real and momentum space of the emission in the ridge under two pulsed excitation laser beams at the exciton energy (1.545 eV), the laser spots are placed at $x = -45$ and 55 μm, respectively. (a) Energy vs. real space (x) distribution of polaritons with a narrow energy linewidth at 1.5405 eV, spatially extending from -150 to $+150$ μm. (i) Corresponding energy vs. momentum space (k_x) distribution: the polariton emission spans $|k_x| \sim 1.2$ μm^{-1}. (b) Energy vs. x polariton emission at $x = 0$. (ii), Corresponding energy vs. k_x polariton emission showing that, at $x = 0$, polaritons move with $k_x \sim \pm 1.2$ μm^{-1}. (c)/(d) Energy vs. x polariton emission at the two spot locations, $x = -45$ and 55 μm, respectively. (iii)/(iv), Corresponding energy vs. k_x distribution of polaritons demonstrating that they remain at rest, $k_x \sim 0$. (e)/(f) Energy vs. x polariton emission at $x = -100$ μm and $+100$ μm, respectively. (v)/(vi), Corresponding energy vs. k_x polariton emission, showing its flow at $k_x \sim -1.2$ μm^{-1} and $+1.2$ μm^{-1}, respectively.

are moving with an in-plane wave vector $k_x = \pm 1$ μm^{-1}, see Fig. C.1(ii). When we filter the PL at the pump spot positions, $x = -45$ and $+55$ μm, see Figs. C.1(c,d), respectively, the reciprocal distribution in momentum space, Figs. C.1(iii,iv) shows that polaritons are stopped, their emission originates from $k_x \simeq 0$.

Finally, in Figs. C.1(e,f) we filter the external regions of the polariton PL, located at $x = \mp 100$ μm, where polaritons move away from the exciton potentials, A and B, respectively. We observe that in the momentum space distribution, Figs. C.1(v,vi), polaritons propagate leftwards/rightwards ($k_x = \mp 1$ m^{-1}) since that is the favored direction of propagation in presence of the repulsive potential. Some weak PL arising from backscattered polaritons is observed at $k_x = \pm 1$ m^{-1}, further discussion on this effect is addressed in Appendix D.

Appendix D

Direct observation of backscattered polariton condensates

Effects of inter-particle interactions on the propagation of a polariton condensate are discussed in a quasi-1D semiconductor ridge MC, by time-resolved experiments in both real- [Fig. D.1(a)] and momentum-space [Fig. D.1(e)]. By performing emission filtering in real- [Fig. D.1(b)] and momentum-space [Figs. D.1(g,h)], we extract the polariton signal backscattered by the imperfections of the structure. Similar results have been previously addressed by D. Tanese and coworkers [61]. They observed a strong suppression of the backscattering produced by the imperfections of the structure when increasing the condensate density. This suppression occurred in the supersonic regime and is simultaneous to the onset of parametric instabilities which enable the "hopping" of the condensate through the disorder. We want to emphasize that the "unintended" interference effects of backscattering that we observe in real space in this case arise from a different situation to that described in Chapter 7, where the real space interferences were produced by the mutual overlap between two counter-propagating bullets, created on purpose to observe interference effects in momentum space.

In these experiments we excite in the central region of the ridge (150 μm away from the lateral edges) with a pulsed laser tuned to the bare exciton level, imitating the excitation conditions as those used in Chapter 7. The pulsed laser excites an exciton reservoir that creates a ballistically ejected polariton condensate. The filtering techniques, described in § 4.2.2, are used in both real and momentum spaces in order to extract the backscattered population in one of the sides of the polariton propagation.

Figure D.1(a) shows left- and rightwards propagating polaritons moving at ~ 1 μm/ps; conspicuous, vertical interference fringes (with a period $\Delta x = 2.4$ μm) manifest the presence of a backscattered polariton population, due to the spatial overlapping of counter-propagating condensates. The corresponding momentum space, Fig. D.1(e), displays a constant $|k_x|$ value of ~ 1.3

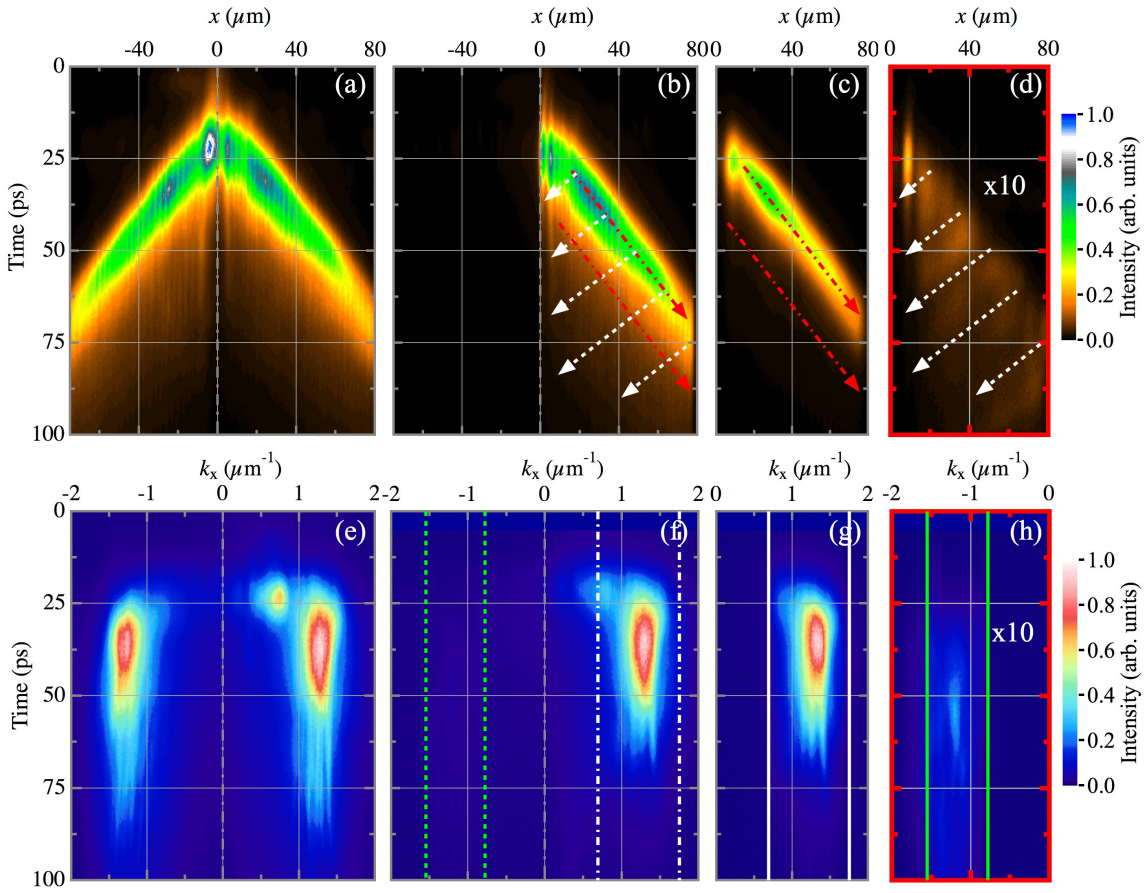

FIGURE D.1: Time-resolved real-/momentum-space distribution of the polariton wave trains emission under the following filtering conditions: (a)/(e) no-filtering, (b)/(f) filtered real-space for $x < 0$, (c)/(g) filtered real-space for $x < 0$ and restricted region $(k_x < 0.8)\&(k_x > 1.6)$ μm^{-1} in momentum-space and (d)/(h) filtered real-space for $x < 0$ and restricted region $(k_x > -1.6)\&(k_x < -0.8)$ μm^{-1} in momentum-space. Polariton emission in panels (d,h) is multiplied by a factor 10. Red, dot-dashed (white, dashed) arrows depict in real space the incident (backscattered) polariton population. In panel (f), green, dashed (white, dot-dashed) lines depict the region resolved in momentum space in panel (g) [(h)], $(k_x < 0.8)\&(k_x > 1.6)$ $[(k_x > -1.6)\&(k_x < -0.8)]$ μm^{-1}. Intensity is coded in a linear, normalized, false color scale.

μm^{-1}. The complete polariton distribution in momentum-/real-space is represented at a given time $t = 41$ ps in Figs. D.2(a)/(i). Real space filtering for $x < 0$ in Fig. D.1(b) [see also Fig. D.2(ii)] removes the main leftward propagating WP, as evidenced in Fig. D.1(f) [Fig. D.2(b)]. It must be noted that in Fig. D.1(b) the same conspicuous interference pattern in the PL profile of rightward propagating WP is observed, as in Fig. D.1(a). In Fig. D.2(b) [momentum-space restricted to $x > 0$ region], backscattered polaritons ($k_x < 0$) are barely visible, see dashed, green circle.

An iris in momentum space [white, full lines/circle in Fig. D.1(g)/D.2(c)] allows imaging the rightward propagating polaritons in $x > 0$ solely: now the interference fringes disappear in real space, see Figs. D.1(c) and D.2(iii), since the backscattered population has been totally removed.

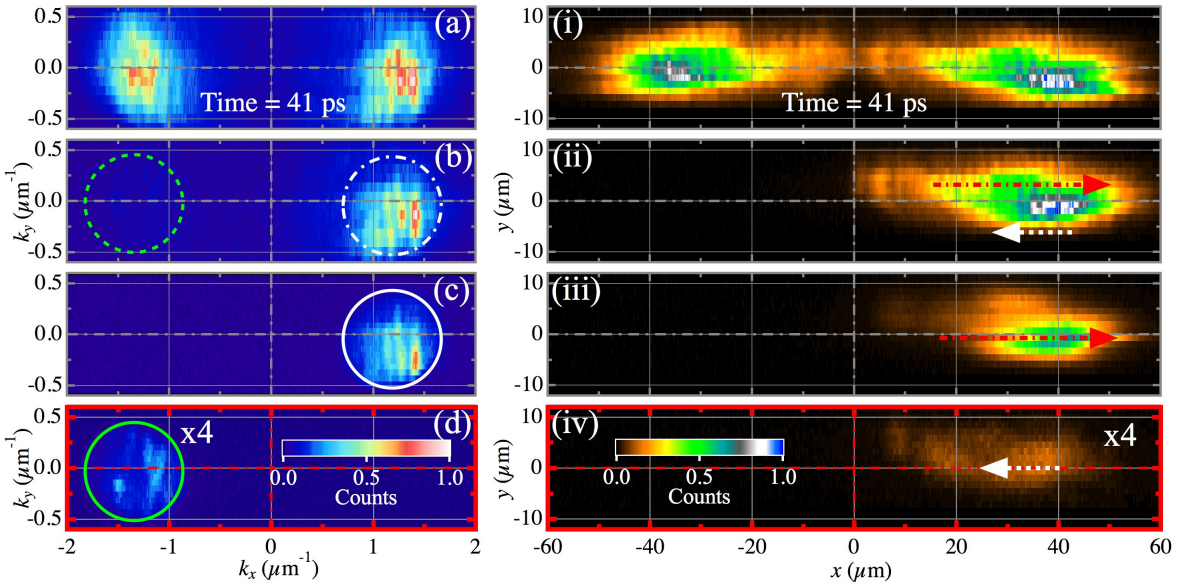

FIGURE D.2: Momentum/Real-space distribution of the polariton wave trains emission, 41 ps after the pulsed excitation, under the following filtering conditions: (a)/(i) no-filtering, (b)/(ii) filtered real-space for $x < 0$, (c)/(iii) filtered real- and momentum-space for $x < 0$ and $(k_x < 0.8)\&(k_x > 1.6)$ μm^{-1} and (d)/(iv) filtered real- and momentum-space for $x < 0$ and $(k_x > -1.6)\&(k_x < -0.8)$ μm^{-1}. Polariton emission in panels (d,h) is multiplied by a factor 4. Red, dot-dashed (white, dashed) arrows depict in real space the incident (backscattered) polariton population. In panel (b), green, dashed (white, dot-dashed) circles encloses the region resolved in momentum space in panel (c) [(d)], $(k_x < 0.8)\&(k_x > 1.6)$ $[(k_x > -1.6)\&(k_x < -0.8)]$ μm^{-1}. Intensity is coded in a linear, normalized, false color scale.

When the iris is located in the k_x value of the backscattered population [green, full lines/circle in Fig. D.1(h)/D.2(d)], we detect only the backscattered population, whose emission intensity is less than $\sim 1\%$ of the rightward propagating polariton WP, Figs. D.1(d) and D.2(iv).

In this way we are able to image the backscattered polariton population, responsible for a stunning effect of interferences in real space, and compare the backscattered PL intensity with that of the incoming polariton droplet. Further experiments on this phenomenon should address the interplay of the pump power excitation in order to corroborate the suppression of polariton backscattering [61], and therefore the decrease of the interference fringes visibility in real space or even their total disappearance.

Bibliography

[1] J. Bardeen and W. H. Brattain, *"The transistor, a semi-conductor triode"*, Physical Review **74**, 230 (1948).

[2] W. H. Brattain and J. Bardeen, *"Nature of the forward current in germanium point contacts"*, Physical Review **74**, 231 (1948).

[3] J. Gertner, *The Idea Factory: Bell Labs and the Great Age of American Innovation* (Penguin Group US, 2012).

[4] W. F. Brinkman, D. E. Haggan, and W. W. Troutman, *"A history of the invention of the transistor and where it will lead us"*, IEEE Journal of Solid-State Circuits **32**, 1858 (1997).

[5] T. Hiramoto, "Transistor evolution for CMOS extension and future information processing technologies", (2009) pp. 3–6.

[6] D. A. B. Miller, *"Are optical transistors the logical next step?"*, Nature Photonics **4**, 3 (2010).

[7] T. Baehr-Jones, T. Pinguet, P. Lo Guo-Qiang, S. Danziger, D. Prather, and M. Hochberg, *"Myths and rumours of silicon photonics"*, Nature Photonics **6**, 206 (2012).

[8] M. I. Nathan, *"Invention of the injection laser at IBM: personal recollections"*, Semiconductor Science and Technology **27**, 090202 (2012).

[9] H. Soda, K. Iga, C. Kitahara, and Y. Suematsu, *"GaInAsP/InP surface emitting injection lasers"*, Japanese Journal of Applied Physics **18**, 2329 (1979).

[10] H. Yokoyama, *"Physics and device applications of optical microcavities"*, Science **256**, 66 (1992).

[11] C. Weisbuch, M. Nishioka, A. Ishikawa, and Y. Arakawa, *"Observation of the coupled exciton-photon mode splitting in a semiconductor quantum microcavity"*, Physical Review Letters **69**, 3314 (1992).

[12] O. Penrose and L. Onsager, *"Bose-Einstein Condensation and Liquid Helium"*, Physical Review **104**, 576 (1956).

[13] M. H. Anderson, J. R. Ensher, M. R. Matthews, C. E. Wieman, and E. A. Cornell, *"Observation of Bose-Einstein Condensation in a Dilute Atomic Vapor"*, Science **269**, 198 (1995).

[14] K. B. Davis, M. O. Mewes, M. R. Andrews, N. J. van Druten, D. S. Durfee, D. M. Kurn, and W. Ketterle, *"Bose-Einstein Condensation in a Gas of Sodium Atoms"*, Physical Review Letters **75**, 3969 (1995).

[15] M. R. Andrews, C. G. Townsend, H. J. Miesner, D. S. Durfee, D. M. Kurn, and W. Ketterle, *"Observation of Interference Between Two Bose Condensates"*, Science **275**, 637 (1997).

[16] B. P. Anderson and M. A. Kasevich, *"Macroscopic quantum interference from atomic tunnel arrays"*, Science **282**, 1686 (1998).

[17] F. S. Cataliotti, S. Burger, C. Fort, P. Maddaloni, F. Minardi, A. Trombettoni, A. Smerzi, and M. Inguscio, *"Josephson Junction Arrays with Bose-Einstein Condensates"*, Science **293**, 843 (2001).

[18] S. Gupta, K. Dieckmann, Z. Hadzibabic, and D. E. Pritchard, *"Contrast Interferometry using Bose-Einstein Condensates to Measure h/m and α"*, Physical Review Letters **89**, 140401 (2002).

[19] Y.-J. Wang, D. Z. Anderson, V. M. Bright, E. A. Cornell, Q. Diot, T. Kishimoto, M. Prentiss, R. A. Saravanan, S. R. Segal, and S. Wu, *"Atom Michelson Interferometer on a Chip Using a Bose-Einstein Condensate"*, Physical Review Letters **94**, 090405 (2005).

[20] H. Deng, G. Weihs, C. Santori, J. Bloch, and Y. Yamamoto, *"Condensation of Semiconductor Microcavity Exciton Polaritons"*, Science **298**, 199 (2002).

[21] J. Kasprzak, M. Richard, S. Kundermann, A. Baas, P. Jeambrun, J. M. J. Keeling, F. M. Marchetti, M. H. Szymanska, R. Andre, J. L. Staehli, V. Savona, P. B. Littlewood, B. Deveaud, and L. S. Dang, *"Bose-Einstein condensation of exciton polaritons"*, Nature **443**, 409 (2006).

[22] R. Balili, V. Hartwell, D. Snoke, L. Pfeiffer, and K. West, *"Bose-Einstein Condensation of Microcavity Polaritons in a Trap"*, Science **316**, 1007 (2007).

[23] S. Christopoulos, G. B. H. von Högersthal, A. J. D. Grundy, P. G. Lagoudakis, A. V. Kavokin, J. J. Baumberg, G. Christmann, R. Butté, E. Feltin, J. F. Carlin, and N. Grandjean, *"Room-Temperature Polariton Lasing in Semiconductor Microcavities"*, Physical Review Letters **98**, 126405 (2007).

[24] P. Bhattacharya, B. Xiao, A. Das, S. Bhowmick, and J. Heo, *"Solid state electrically injected exciton-polariton laser"*, Physical Review Letters **110**, 206403 (2013).

[25] P. Bhattacharya, T. Frost, S. Deshpande, M. Z. Baten, A. Hazari, and A. Das, *"Room temperature electrically injected polariton laser"*, Physical Review Letters **112**, 236802 (2014).

[26] A. Amo, D. Sanvitto, F. P. Laussy, D. Ballarini, E. d. Valle, M. D. Martin, A. Lemaitre, J. Bloch, D. N. Krizhanovskii, M. S. Skolnick, C. Tejedor, and L. Viña, *"Collective fluid dynamics of a polariton condensate in a semiconductor microcavity"*, Nature **457**, 291 (2009).

[27] A. Amo, J. Lefrere, S. Pigeon, C. Adrados, C. Ciuti, I. Carusotto, R. Houdre, E. Giacobino, and A. Bramati, *"Superfluidity of polaritons in semiconductor microcavities"*, Nature Physics **5**, 805 (2009).

[28] D. Sanvitto, F. M. Marchetti, M. H. Szymanska, G. Tosi, M. Baudisch, F. P. Laussy, D. N. Krizhanovskii, M. S. Skolnick, L. Marrucci, A. Lemaître, J. Bloch, C. Tejedor, and L. Viña, *"Persistent currents and quantized vortices in a polariton superfluid"*, Nature Physics **6**, 527 (2010).

[29] M. Saba, C. Ciuti, J. Bloch, V. Thierry-Mieg, R. Andre, L. S. Dang, S. Kundermann, A. Mura, G. Bongiovanni, J. L. Staehli, and B. Deveaud, *"High-temperature ultrafast polariton parametric amplification in semiconductor microcavities"*, Nature **414**, 731 (2001).

[30] D. Bajoni, E. Semenova, A. Lemaître, S. Bouchoule, E. Wertz, P. Senellart, S. Barbay, R. Kuszelewicz, and J. Bloch, *"Optical Bistability in a GaAs-Based Polariton Diode"*, Physical Review Letters **101**, 266402 (2008).

[31] T. C. H. Liew, A. V. Kavokin, and I. A. Shelykh, *"Optical Circuits Based on Polariton Neurons in Semiconductor Microcavities"*, Physical Review Letters **101**, 016402 (2008).

[32] I. A. Shelykh, G. Pavlovic, D. D. Solnyshkov, and G. Malpuech, *"Proposal for a Mesoscopic Optical Berry-Phase Interferometer"*, Physical Review Letters **102**, 046407 (2009).

[33] A. Amo, T. C. H. Liew, C. Adrados, R. Houdre, E. Giacobino, A. V. Kavokin, and A. Bramati, *"Exciton-polariton spin switches"*, Nature Photonics **4**, 361 (2010).

[34] T. K. Paraïso, M. Wouters, Y. Léger, F. Morier-Genoud, and B. Deveaud-Plédran, *"Multistability of a coherent spin ensemble in a semiconductor microcavity"*, Nature Materials **9**, 655 (2010).

[35] T. C. H. Liew, A. V. Kavokin, T. Ostatnický, M. Kaliteevski, I. A. Shelykh, and R. A. Abram, *"Exciton-polariton integrated circuits"*, Physical Review B **82**, 033302 (2010).

[36] E. Wertz, L. Ferrier, D. D. Solnyshkov, R. Johne, D. Sanvitto, A. Lemaitre, I. Sagnes, R. Grousson, A. V. Kavokin, P. Senellart, G. Malpuech, and J. Bloch, *"Spontaneous formation and optical manipulation of extended polariton condensates"*, Nature Physics **6**, 860 (2010).

[37] T. C. H. Liew, I. A. Shelykh, and G. Malpuech, *"Polaritonic devices"*, Physica E: Low-dimensional Systems and Nanostructures **43**, 1543 (2011).

[38] M. Sich, D. N. Krizhanovskii, M. S. Skolnick, A. V. Gorbach, R. Hartley, D. V. Skryabin, E. A. Cerda-Mendez, K. Biermann, R. Hey, and P. V. Santos, *"Observation of bright polariton solitons in a semiconductor microcavity"*, Nature Photonics **6**, 50 (2012).

[39] D. Ballarini, M. De Giorgi, E. Cancellieri, R. Houdré, E. Giacobino, R. Cingolani, A. Bramati, G. Gigli, and D. Sanvitto, *"All-optical polariton transistor"*, Nature Communications **4**, 1778 (2013).

[40] E. Wertz, A. Amo, D. D. Solnyshkov, L. Ferrier, T. C. H. Liew, D. Sanvitto, P. Senellart, I. Sagnes, A. Lemaître, A. V. Kavokin, G. Malpuech, and J. Bloch, *"Propagation and Amplification Dynamics of 1D Polariton Condensates"*, Physical Review Letters **109**, 216404 (2012).

[41] G. Tosi, G. Christmann, N. G. Berloff, P. Tsotsis, T. Gao, Z. Hatzopoulos, P. G. Savvidis, and J. J. Baumberg, *"Sculpting oscillators with light within a nonlinear quantum fluid"*, Nature Physics **8**, 190 (2012).

[42] G. Tosi, G. Christmann, N. G. Berloff, P. Tsotsis, T. Gao, Z. Hatzopoulos, P. G. Savvidis, and J. J. Baumberg, *"Geometrically locked vortex lattices in semiconductor quantum fluids"*, Nature Communications **3**, 1243 (2012).

[43] T. Gao, P. S. Eldridge, T. C. H. Liew, S. I. Tsintzos, G. Stavrinidis, G. Deligeorgis, Z. Hatzopoulos, and P. G. Savvidis, *"Polariton condensate transistor switch"*, Physical Review B **85**, 235102 (2012).

[44] H. S. Nguyen, D. Vishnevsky, C. Sturm, D. Tanese, D. Solnyshkov, E. Galopin, A. Lemaître, I. Sagnes, A. Amo, G. Malpuech, and J. Bloch, *"Realization of a Double-Barrier Resonant Tunneling Diode for Cavity Polaritons"*, Physical Review Letters **110**, 236601 (2013).

[45] C. Sturm, D. Tanese, H. S. Nguyen, H. Flayac, E. Galopin, A. Lemaître, I. Sagnes, D. Solnyshkov, A. Amo, G. Malpuech, and J. Bloch, *"All-optical phase modulation in a cavity-polariton Mach–Zehnder interferometer"*, Nature Communications **5**, 3278 (2014).

[46] C. Antón, T. C. H. Liew, G. Tosi, M. D. Martín, T. Gao, Z. Hatzopoulos, P. S. Eldridge, P. G. Savvidis, and L. Viña, *"Dynamics of a polariton condensate transistor switch"*, Applied Physics Letters **101**, 261116 (2012).

[47] C. Antón, T. C. H. Liew, J. Cuadra, M. D. Martín, P. S. Eldridge, Z. Hatzopoulos, G. Stavrinidis, P. G. Savvidis, and L. Viña, *"Quantum reflections and shunting of polariton condensate wave trains: Implementation of a logic AND gate"*, Physical Review B **88**, 245307 (2013).

[48] C. Antón, T. C. H. Liew, D. Sarkar, M. D. Martín, Z. Hatzopoulos, P. S. Eldridge, P. G. Savvidis, and L. Viña, *"Operation speed of polariton condensate switches gated by excitons"*, Physical Review B **89**, 235312 (2014).

[49] G. Tosi, D. Sanvitto, M. Baudisch, E. Karimi, B. Piccirillo, L. Marrucci, A. Lemaître, J. Bloch, and L. Viña, *"Vortex stability and permanent flow in nonequilibrium polariton condensates"*, Journal of Applied Physics **109**, 102406 (2011).

[50] G. Tosi, F. M. Marchetti, D. Sanvitto, C. Antón, M. H. Szymanska, A. Berceanu, C. Tejedor, L. Marrucci, A. Lemaître, J. Bloch, and L. Viña, *"Onset and Dynamics of Vortex-Antivortex Pairs in Polariton Optical Parametric Oscillator Superfluids"*, Physical Review Letters **107**, 036401 (2011).

[51] C. Antón, G. Tosi, M. D. Martín, L. Viña, A. Lemaître, and J. Bloch, *"Role of supercurrents on vortices formation in polariton condensates"*, Optics Express **20**, 16366 (2012).

[52] P. G. Savvidis, J. J. Baumberg, R. M. Stevenson, M. S. Skolnick, D. M. Whittaker, and J. S. Roberts, *"Angle-resonant stimulated polariton amplifier"*, Physical Review Letters **84**, 1547 (2000).

[53] P. G. Savvidis, J. J. Baumberg, R. M. Stevenson, M. S. Skolnick, D. M. Whittaker, and J. S. Roberts, *"Asymmetric angular emission in semiconductor microcavities"*, Physical Review B **62**, R13278 (2000).

[54] J. J. Baumberg, P. G. Savvidis, R. M. Stevenson, A. I. Tartakovskii, M. S. Skolnick, D. M. Whittaker, and J. S. Roberts, *"Parametric oscillation in a vertical microcavity: A polariton condensate or micro-optical parametric oscillation"*, Physical Review B **62**, R16247 (2000).

[55] C. Antón, D. Solnyshkov, G. Tosi, M. D. Martín, Z. Hatzopoulos, G. Deligeorgis, P. G. Savvidis, G. Malpuech, and L. Viña, *"Ignition and formation dynamics of a polariton condensate on a semiconductor microcavity pillar"*, Physical Review B **90**, 155311 (2014).

[56] P. W. Anderson, *Basic Notions of Condensed Matter Physics* edited by C. Menlo Park, (Benjamin, 1984).

[57] C. Antón, G. Tosi, M. D. Martín, Z. Hatzopoulos, G. Konstantinidis, P. S. Eldridge, P. G. Savvidis, C. Tejedor, and L. Viña, *"Quantum coherence in momentum space of light-matter condensates"*, Physical Review B **90**, 081407 (2014).

[58] C. Antón, S. Morina, T. Gao, P. S. Eldridge, T. C. H. Liew, M. D. Martín, Z. Hatzopoulos, P. G. Savvidis, I. A. Shelykh, and L. Viña, *"Optical control of spin textures in quasi-one-dimensional polariton condensates"*, Physical Review B **91**, 075305 (2015).

[59] H. Flayac, D. D. Solnyshkov, and G. Malpuech, *"Bloch oscillations of exciton-polaritons and photons for the generation of an alternating terahertz spin signal"*, Physical Review B **84**, 125314 (2011).

[60] H. Flayac and I. G. Savenko, *"An exciton-polariton mediated all-optical router"*, Applied Physics Letters **103**, 201105 (2013).

[61] D. Tanese, D. D. Solnyshkov, A. Amo, L. Ferrier, E. Bernet-Rollande, E. Wertz, I. Sagnes, A. Lemaître, P. Senellart, G. Malpuech, and J. Bloch, *"Backscattering Suppression in Supersonic 1D Polariton Condensates"*, Physical Review Letters **108**, 036405 (2012).

[62] C. Antón, T. C. H. Liew, G. Tosi, M. D. Martín, T. Gao, Z. Hatzopoulos, P. S. Eldridge, P. G. Savvidis, and L. Viña, *"Energy relaxation of exciton-polariton condensates in quasi-one-dimensional microcavities"*, Physical Review B **88**, 035313 (2013).

[63] C. Antón and J. L. Brun, *"Isochronous oscillations: Potentials derived from a parabola by shearing"*, American Journal of Physics **76**, 537 (2008).

[64] J. Steinhauer, R. Ozeri, N. Katz, and N. Davidson, *"Excitation Spectrum of a Bose-Einstein Condensate"*, Physical Review Letters **88**, 120407 (2002).

[65] I. Bloch, T. W. Hansch, and T. Esslinger, *"Measurement of the spatial coherence of a trapped Bose gas at the phase transition"*, Nature **403**, 166 (2000).

[66] J. R. Abo-Shaeer, C. Raman, J. M. Vogels, and W. Ketterle, *"Observation of Vortex Lattices in Bose-Einstein Condensates"*, Science **292**, 476 (2001).

[67] P. Yu and M. Cardona, *Fundamentals of Semiconductors: Physics and Materials Properties* Graduate Texts in Physics (Springer, 2010).

[68] J. Schulman and Y.-C. Chang, *"New method for calculating electronic properties of superlattices using complex band structures"*, Physical Review B **24**, 4445 (1981).

[69] J. Schulman and Y.-C. Chang, *"Band mixing in semiconductor superlattices"*, Physical Review B **31**, 2056 (1985).

[70] M. Jaros, K. Wong, and M. Gell, *"Electronic structure of GaAs-$Ga_{1-x}Al_xAs$ quantum well and sawtooth superlattices"*, Physical Review B **31**, 1205 (1985).

[71] D. Smith and C. Mailhiot, *"Theory of semiconductor superlattice electronic structure"*, Reviews of Modern Physics **62**, 173 (1990).

[72] P. Voisin, G. Bastard, and M. Voos, *"Optical selection rules in superlattices in the envelope-function approximation"*, Physical Review B **29**, 935 (1984).

[73] L. Andreani, A. Pasquarello, and F. Bassani, *"Hole subbands in strained GaAs-$Ga_{1-x}Al_xAs$ quantum wells: Exact solution of the effective-mass equation"*, Physical Review B **36**, 5887 (1987).

[74] G. Bastard, *Wave mechanics applied to semiconductor heterostructures* (Les Éditions de Physique, 1988).

[75] A. Kavokin, J. Baumberg, G. Malpuech, and F. Laussy, *Microcavities* (Oxford University Press, 2007).

[76] N. F. Mott, *"Metal-insulator transition"*, Reviews of Modern Physics **40**, 677 (1968).

[77] J. Jackson, *Classical Electrodynamics* (Wiley, 1999).

[78] R. Boyd, *Nonlinear Optics* (Academic Press, 2008).

[79] K. J. Vahala, *"Optical microcavities"*, Nature **424**, 839 (2003).

[80] M. Göppl, A. Fragner, M. Baur, R. Bianchetti, S. Filipp, J. M. Fink, P. J. Leek, G. Puebla, L. Steffen, and A. Wallraff, *"Coplanar waveguide resonators for circuit quantum electrodynamics"*, Journal of Applied Physics **104**, 113904 (2008).

[81] A. I. Tartakovskii, V. D. Kulakovskii, A. Forchel, and J. P. Reithmaier, *"Exciton-photon coupling in photonic wires"*, Physical Review B **57**, R6807 (1998).

[82] J. J. Hopfield, *"Theory of the contribution of excitons to the complex dielectric constant of crystals"*, Physical Review **112**, 1555 (1958).

[83] H. Haug and S. Koch, *Quantum Theory of the Optical and Electronic Properties of Semiconductors* (World Scientific, 2009).

[84] L. C. Andreani, F. Tassone, and F. Bassani, *"Radiative lifetime of free excitons in quantum wells"*, Solid State Communications **77**, 641 (1991).

[85] E. L. Ivchenko, *"Exchange interaction and scattering of light with reversal of the hole angular momentum at an acceptor in quantum-well structures"*, Soviet physics. Solid state **34**, 254 (1992).

[86] M. Raizen, R. Thompson, R. Brecha, H. Kimble, and H. Carmichael, *"Normal-mode splitting and linewidth averaging for two-state atoms in an optical cavity"*, Physical Review Letters **63**, 240 (1989).

[87] Y. Zhu, D. Gauthier, S. Morin, Q. Wu, H. Carmichael, and T. Mossberg, *"Vacuum Rabi splitting as a feature of linear-dispersion theory: Analysis and experimental observations"*, Physical Review Letters **64**, 2499 (1990).

[88] B. Gayral, J. M. Gérard, B. Legrand, E. Costard, and V. Thierry-Mieg, *"Optical study of GaAs/AlAs pillar microcavities with elliptical cross section"*, Applied Physics Letters **72**, 1421 (1998).

[89] F. Boeuf, R. André, R. Romestain, L. Si Dang, E. Péronne, J. F. Lampin, D. Hulin, and A. Alexandrou, *"Evidence of polariton stimulation in semiconductor microcavities"*, Physical Review B **62**, R2279 (2000).

[90] T. Tawara, H. Gotoh, T. Akasaka, N. Kobayashi, and T. Saitoh, *"Cavity polaritons in InGaN microcavities at room temperature"*, Physical Review Letters **92**, 256402 (2004).

[91] V. Savona, L. C. Andreani, P. Schwendimann, and A. Quattropani, *"Quantum well excitons in semiconductor microcavities: Unified treatment of weak and strong coupling regimes"*, Solid State Communications **93**, 733 (1995).

[92] B. Deveaud, F. Clérot, N. Roy, K. Satzke, B. Sermage, and D. S. Katzer, *"Enhanced radiative recombination of free excitons in GaAs quantum wells"*, Physical Review Letters **67**, 2355 (1991).

[93] R. Houdré, R. Stanley, U. Oesterle, M. Ilegems, and C. Weisbuch, *"Room-temperature cavity polaritons in a semiconductor microcavity"*, Physical Review B **49**, 16761 (1994).

[94] S. Jorda, *"Theory of Rabi splitting in cavity-embedded quantum wells"*, Physical Review B **50**, 18690 (1994).

[95] S. Jorda, *"Dispersion of exciton polaritons in cavity-embedded quantum wells"*, Physical Review B **51**, 10185 (1995).

[96] V. Savona, C. Piermarocchi, A. Quattropani, P. Schwendimann, and F. Tassone, *"Optical properties of microcavity polaritons"*, Phase Transitions **68**, 169 (1999).

[97] L. Novotny, *"Strong coupling, energy splitting, and level crossings: A classical perspective"*, American Journal of Physics **78**, 1199 (2010).

[98] T. B. Norris, J. K. Rhee, C. Y. Sung, Y. Arakawa, M. Nishioka, and C. Weisbuch, *"Time-resolved vacuum Rabi oscillations in a semiconductor quantum microcavity"*, Physical Review B **50**, 14663 (1994).

[99] Y. Kaluzny, P. Goy, M. Gross, J. M. Raimond, and S. Haroche, *"Observation of Self-Induced Rabi Oscillations in Two-Level Atoms Excited Inside a Resonant Cavity: The Ringing Regime of Superradiance"*, Physical Review Letters **51**, 1175 (1983).

[100] E. T. Jaynes and F. W. Cummings, *"Comparison of quantum and semiclassical radiation theories with application to the beam maser"*, Proceedings of the IEEE **51**, 89 (1963).

[101] R. J. Thompson, G. Rempe, and H. J. Kimble, *"Observation of normal-mode splitting for an atom in an optical cavity"*, Physical Review Letters **68**, 1132 (1992).

[102] A. Wallraff, D. I. Schuster, A. Blais, L. Frunzio, R. S. Huang, J. Majer, S. Kumar, S. M. Girvin, and R. J. Schoelkopf, *"Strong coupling of a single photon to a superconducting qubit using circuit quantum electrodynamics"*, Nature **431**, 162 (2004).

[103] K. W. Böer, *Survey of Semiconductor Physics: Barriers, Junctions, Surfaces, and Devices* (Van Nostrand Reinhold, 1992).

[104] R. Winkler, *Spin-orbit Coupling Effects in Two-Dimensional Electron and Hole Systems* Physics and Astronomy Online Library No. 191 (Springer, 2003).

[105] W. W. Chow and S. W. Koch, *Semiconductor-Laser Fundamentals: Physics of the Gain Materials* (Springer, 1999).

[106] F. Meier and B. P. Zakharchenya, *Optical Orientation* (Elsevier Science, 2012).

[107] Ė. I. Rashba and M. D. Sturge, *Excitons* (North-Holland Publishing Company, 1982).

[108] R. Streater and A. Wightman, *PCT, Spin and Statistics, and All That* Landmarks in Physics (Princeton University Press, 1964).

[109] A. J. Leggett, *"Quantum liquids"*, Science **319**, 1203 (2008).

[110] A. Einstein, *"Quantentheorie des einatomigen idealen Gases. Zweite Abhandlung."*, Sitz. ber. Preuss. Akad. Wiss. , 3 (1925).

[111] L. P. Pitaevskii and S. Stringari, *Bose-Einstein Condensation* (Oxford University Press, 2003).

[112] A. Imamoglu, R. J. Ram, S. Pau, and Y. Yamamoto, *"Nonequilibrium condensates and lasers without inversion: Exciton-polariton lasers"*, Physical Review A **53**, 4250 (1996).

[113] R. M. Stevenson, V. N. Astratov, M. S. Skolnick, D. M. Whittaker, M. Emam-Ismail, A. I. Tartakovskii, P. G. Savvidis, J. J. Baumberg, and J. S. Roberts, *"Continuous wave observation of massive polariton redistribution by stimulated scattering in semiconductor microcavities"*, Physical Review Letters **85**, 3680 (2000).

[114] G. Christmann, R. Butte, E. Feltin, J.-F. Carlin, and N. Grandjean, *"Room temperature polariton lasing in a GaN/AlGaN multiple quantum well microcavity"*, Applied Physics Letters **93**, 051102 (2008).

[115] J. M. Blatt, K. W. Böer, and W. Brandt, *"Bose-Einstein Condensation of Excitons"*, Physical Review **126**, 1691 (1962).

[116] S. Moskalenko, *"Reversible optico-hydrodynamic phenomena in a nonideal exciton gas"*, Fiz. Tverd. Tela **4**, 276 (1962).

[117] L. Keldysh and A. Kozlov, *"Collective properties of excitons in semiconductors"*, Soviet Physics JETP **27** (1968).

[118] D. Hulin, A. Mysyrowicz, and C. B. àla Guillaume, *"Evidence for Bose-Einstein Statistics in an Exciton Gas"*, Physical Review Letters **45**, 1970 (1980).

[119] L. L. Chase, N. Peyghambarian, G. Grynberg, and A. Mysyrowicz, *"Evidence for Bose-Einstein Condensation of Biexcitons in CuCl"*, Physical Review Letters **42**, 1231 (1979).

[120] M. Combescot, O. Betbeder-Matibet, and R. Combescot, *"Bose-Einstein Condensation in Semiconductors: The Key Role of Dark Excitons"*, Physical Review Letters **99**, 176403 (2007).

[121] L. V. Butov, A. L. Ivanov, A. Imamoglu, P. B. Littlewood, A. A. Shashkin, V. T. Dolgopolov, K. L. Campman, and A. C. Gossard, *"Stimulated Scattering of Indirect Excitons in Coupled Quantum Wells: Signature of a Degenerate Bose-Gas of Excitons"*, Physical Review Letters **86**, 5608 (2001).

[122] L. V. Butov, A. C. Gossard, and D. S. Chemla, *"Macroscopically ordered state in an exciton system"*, Nature **418**, 751 (2002).

[123] L. V. Butov, C. W. Lai, A. L. Ivanov, A. C. Gossard, and D. S. Chemla, *"Towards Bose-Einstein condensation of excitons in potential traps"*, Nature **417**, 47 (2002).

[124] A. A. High, J. R. Leonard, A. T. Hammack, M. M. Fogler, L. V. Butov, A. V. Kavokin, K. L. Campman, and A. C. Gossard, *"Spontaneous coherence in a cold exciton gas"*, Nature **483**, 584 (2012).

[125] H. Deng, H. Haug, and Y. Yamamoto, *"Exciton-polariton Bose-Einstein condensation"*, Reviews of Modern Physics **82**, 1489 (2010).

[126] M. Planck, *"Ueber das Gesetz der Energieverteilung im Normalspectrum"*, Annalen der Physik **309**, 553 (1901).

[127] J. Klaers, F. Vewinger, and M. Weitz, *"Thermalization of a two-dimensional photonic gas in a white wall photon box"*, Nature Physics **6**, 512 (2010).

[128] J. Klaers, J. Schmitt, F. Vewinger, and M. Weitz, *"Bose-Einstein condensation of photons in an optical microcavity"*, Nature **468**, 545 (2010).

[129] N. N. Bogoliubov, *"On the theory of superfluidity"*, Journal of Physics **11**, 23 (1947).

[130] L. D. Landau and E. M. Lifshitz, *Quantum Mechanics* (Pergamon, Oxford, 1987).

[131] T. D. Lee, K. Huang, and C. N. Yang, *"Eigenvalues and Eigenfunctions of a Bose System of Hard Spheres and Its Low-Temperature Properties"*, Physical Review **106**, 1135 (1957).

[132] T. D. Lee and C. N. Yang, *"Many-body problem in quantum mechanics and quantum statistical mechanics"*, Physical Review **105**, 1119 (1957).

[133] P. Kapitza, *"Viscosity of Liquid Helium below the λ-Point"*, Nature **141**, 74 (1938).

[134] J. F. Allen and A. D. Misener, *"Flow of liquid Helium II"*, Nature **141**, 75 (1938).

[135] L. Landau, *"Theory of the Superfluidity of Helium II"*, Physical Review **60**, 356 (1941).

[136] L. D. Landau, *"The theory of Superfluity of Helium III"*, Journal of Physics USSR **5**, 71 (1941).

[137] A. Weiner, *Ultrafast Optics* (John Wiley & Sons, 2011).

[138] F. P. Laussy, E. del Valle, and C. Tejedor, *"Luminescence spectra of quantum dots in microcavities. I. Bosons"*, Physical Review B **79**, 235325 (2009).

[139] F. Manni, K. G. Lagoudakis, R. André, M. Wouters, and B. Deveaud, *"Penrose-Onsager Criterion Validation in a One-Dimensional Polariton Condensate"*, Physical Review Letters **109**, 150409 (2012).

[140] F. Dalfovo, S. Giorgini, L. P. Pitaevskii, and S. Stringari, *"Theory of Bose-Einstein condensation in trapped gases"*, Reviews of Modern Physics **71**, 463 (1999).

[141] N. D. Mermin and H. Wagner, *"Absence of Ferromagnetism or Antiferromagnetism in One- or Two-Dimensional Isotropic Heisenberg Models"*, Physical Review Letters **17**, 1133 (1966).

[142] P. C. Hohenberg, *"Existence of long-range order in one and two dimensions"*, Physical Review **158**, 383 (1967).

[143] V. L. Berezinskii, *"Destruction of Long-range Order in One-dimensional and Two-dimensional Systems Possessing a Continuous Symmetry Group. II. Quantum Systems"*, Soviet Journal of Experimental and Theoretical Physics **34**, 610 (1972).

[144] J. M. Kosterlitz and D. J. Thouless, *"Ordering, metastability and phase transitions in two-dimensional systems"*, Journal of Physics C: Solid State Physics **6**, 1181 (1973).

[145] Z. Hadzibabic, P. Kruger, M. Cheneau, B. Battelier, and J. Dalibard, *"Berezinskii-Kosterlitz-Thouless crossover in a trapped atomic gas"*, Nature **441**, 1118 (2006).

[146] E. Gross, *"Structure of a quantized vortex in boson systems"*, Il Nuovo Cimento Series 10 **20**, 454 (1961).

[147] L. P. Pitaevskii, *"Vortex lines in an imperfect Bose gas"*, Soviet Physics JETP-USSR **13**, 451 (1961).

[148] L. Onsager, *"Statistical hydrodynamics"*, Nuovo Cimento **6**, 279 (1949).

[149] R. Feynman, "Chapter II Application of quantum mechanics to liquid helium", in *Progress in Low Temperature Physics* Vol. 1 edited by C. Gorter, (Elsevier, 1955) pp. 17–53.

[150] J. F. Nye and M. V. Berry, *"Dislocations in wave trains"*, Proceedings of the Royal Society of London A: Mathematical, Physical and Engineering Sciences **336**, 165 (1974).

[151] K. Staliunas and V. Morcillo, *Transverse Patterns in Nonlinear Optical Resonators* Springer Tracts in Modern Physics (Springer, 2003).

[152] A. S. Desyatnikov, Y. S. Kivshar, and L. Torner, *Optical vortices and vortex solitons* edited by E. Wolf, Vol. 47 (Elsevier, 2005) pp. 291–391.

[153] R. E. Packard and T. M. Sanders, *"Observations on Single Vortex Lines in Rotating Superfluid Helium"*, Physical Review A **6**, 799 (1972).

[154] E. J. Yarmchuk, M. J. V. Gordon, and R. E. Packard, *"Observation of stationary vortex arrays in rotating superfluid helium"*, Physical Review Letters **43**, 214 (1979).

[155] K. W. Madison, F. Chevy, W. Wohlleben, and J. Dalibard, *"Vortex Formation in a Stirred Bose-Einstein Condensate"*, Physical Review Letters **84**, 806 (2000).

[156] A. A. Abrikosov, *"On the magnetic properties of superconductors of the second group"*, Soviet Physics JETP **5**, 1174 (1957).

[157] S. Moskalenko and D. Snoke, *Bose-Einstein Condensation of Excitons and Biexcitons: And Coherent Nonlinear Optics with Excitons* (Cambridge University Press, 2005).

[158] J. P. Eisenstein and A. H. MacDonald, *"Bose-Einstein condensation of excitons in bilayer electron systems"*, Nature **432**, 691 (2004).

[159] D. Sanvitto, S. Pigeon, A. Amo, D. Ballarini, M. De Giorgi, I. Carusotto, R. Hivet, F. Pisanello, V. G. Sala, P. S. S. Guimaraes, R. Houdre, E. Giacobino, C. Ciuti, A. Bramati, and G. Gigli, *"All-optical control of the quantum flow of a polariton condensate"*, Nature Photonics **5**, 610 (2011).

[160] G. Christmann, G. Tosi, N. G. Berloff, P. Tsotsis, P. S. Eldridge, Z. Hatzopoulos, P. G. Savvidis, and J. J. Baumberg, *"Polariton ring condensates and sunflower ripples in an expanding quantum liquid"*, Physical Review B **85**, 235303 (2012).

[161] L. S. Dang, D. Heger, R. André, F. Bœuf, and R. Romestain, *"Stimulation of polariton photoluminescence in semiconductor microcavity"*, Physical Review Letters **81**, 3920 (1998).

[162] M. Richard, J. Kasprzak, R. Romestain, R. André, and L. S. Dang, *"Spontaneous Coherent Phase Transition of Polaritons in CdTe Microcavities"*, Physical Review Letters **94**, 187401 (2005).

[163] J. Kasprzak, D. D. Solnyshkov, R. André, L. S. Dang, and G. Malpuech, *"Formation of an exciton polariton condensate: Thermodynamic versus kinetic regimes"*, Physical Review Letters **101**, 146404 (2008).

[164] A. P. D. Love, D. N. Krizhanovskii, D. M. Whittaker, R. Bouchekioua, D. Sanvitto, S. A. Rizeiqi, R. Bradley, M. S. Skolnick, P. R. Eastham, R. André, and L. S. Dang, *"Intrinsic decoherence mechanisms in the microcavity polariton condensate"*, Physical Review Letters **101**, 067404 (2008).

[165] E. Wertz, L. Ferrier, D. D. Solnyshkov, P. Senellart, D. Bajoni, A. Miard, A. Lemaitre, G. Malpuech, and J. Bloch, *"Spontaneous formation of a polariton condensate in a planar GaAs microcavity"*, Applied Physics Letters **95**, 051108 (2009).

[166] M. Aßmann, J.-S. Tempel, F. Veit, M. Bayer, A. Rahimi-Iman, A. Löffler, S. Höfling, S. Reitzenstein, L. Worschech, and A. Forchel, *"From polariton condensates to highly photonic quantum degenerate states of bosonic matter"*, Proceedings of the National Academy of Sciences **108**, 1804 (2011).

[167] R. Spano, J. Cuadra, C. Lingg, D. Sanvitto, M. D. Martin, P. R. Eastham, M. van der Poel, J. M. Hvam, and L. Viña, *"Build up of off-diagonal long-range order in microcavity exciton-polaritons across the parametric threshold"*, Optics Express **21**, 10792 (2013).

[168] R. Spano, J. Cuadra, G. Tosi, C. Antón, C. A. Lingg, D. Sanvitto, M. D. Martín, L. Viña, P. R. Eastham, M. van der Poel, and J. M. Hvam, *"Coherence properties of exciton polariton OPO condensates in one and two dimensions"*, New Journal of Physics **14**, 075018 (2012).

[169] K. G. Lagoudakis, M. Wouters, M. Richard, A. Baas, I. Carusotto, R. Andre, L. S. Dang, and B. Deveaud-Pledran, *"Quantized vortices in an exciton-polariton condensate"*, Nature Physics **4**, 706 (2008).

[170] K. G. Lagoudakis, T. Ostatnický, A. V. Kavokin, Y. G. Rubo, R. André, and B. Deveaud-Plédran, *"Observation of half-quantum vortices in an exciton-polariton condensate"*, Science **326**, 974 (2009).

[171] G. Roumpos, M. D. Fraser, A. Loffler, S. Hofling, A. Forchel, and Y. Yamamoto, *"Single vortex-antivortex pair in an exciton-polariton condensate"*, Nature Physics **7**, 129 (2011).

[172] G. Roumpos, M. Lohse, W. H. Nitsche, J. Keeling, M. H. Szymańska, P. B. Littlewood, A. Löffler, S. Höfling, L. Worschech, A. Forchel, and Y. Yamamoto, *"Power-law decay of the*

spatial correlation function in exciton-polariton condensates", Proceedings of the National Academy of Sciences **109**, 6467 (2012).

[173] G. Nardin, G. Grosso, Y. Leger, B. Pięt̨ka, F. Morier-Genoud, and B. Deveaud-Pledran, *"Hydrodynamic nucleation of quantized vortex pairs in a polariton quantum fluid"*, Nature Physics **7**, 635 (2011).

[174] G. Grosso, G. Nardin, F. Morier-Genoud, Y. Léger, and B. Deveaud-Plédran, *"Soliton instabilities and vortex street formation in a polariton quantum fluid"*, Physical Review Letters **107**, 245301 (2011).

[175] A. Amo, S. Pigeon, D. Sanvitto, V. G. Sala, R. Hivet, I. Carusotto, F. Pisanello, G. Leménager, R. Houdré, E. Giacobino, C. Ciuti, and A. Bramati, *"Polariton superfluids reveal quantum hydrodynamic solitons"*, Science **332**, 1167 (2011).

[176] R. Hivet, H. Flayac, D. D. Solnyshkov, D. Tanese, T. Boulier, D. Andreoli, E. Giacobino, J. Bloch, A. Bramati, G. Malpuech, and A. Amo, *"Half-solitons in a polariton quantum fluid behave like magnetic monopoles"*, Nature Physics **8**, 724 (2012).

[177] L. V. Butov and A. V. Kavokin, *"The behaviour of exciton-polaritons"*, Nature Photonics **6**, 2 (2012).

[178] B. Deveaud-Pledran, *"The behaviour of exciton-polaritons"*, Nature Photonics **6**, 205 (2012).

[179] M. Umlauff, J. Hoffmann, H. Kalt, W. Langbein, J. M. Hvam, M. Scholl, J. Söllner, M. Heuken, B. Jobst, and D. Hommel, *"Direct observation of free-exciton thermalization in quantum-well structures"*, Physical Review B **57**, 1390 (1998).

[180] A. I. Tartakovskii, M. Emam-Ismail, R. M. Stevenson, M. S. Skolnick, V. N. Astratov, D. M. Whittaker, J. J. Baumberg, and J. S. Roberts, *"Relaxation bottleneck and its suppression in semiconductor microcavities"*, Physical Review B **62**, R2283 (2000).

[181] M. Müller, J. Bleuse, and R. André, *"Dynamics of the cavity polariton in CdTe-based semiconductor microcavities: Evidence for a relaxation edge"*, Physical Review B **62**, 16886 (2000).

[182] F. Tassone, C. Piermarocchi, V. Savona, A. Quattropani, and P. Schwendimann, *"Bottleneck effects in the relaxation and photoluminescence of microcavity polaritons"*, Physical Review B **56**, 7554 (1997).

[183] D. Porras, C. Ciuti, J. J. Baumberg, and C. Tejedor, *"Polariton dynamics and Bose-Einstein condensation in semiconductor microcavities"*, Physical Review B **66**, 085304 (2002).

[184] G. Malpuech, Y. G. Rubo, F. P. Laussy, P. Bigenwald, and A. V. Kavokin, *"Polariton laser: thermodynamics and quantum kinetic theory"*, Semiconductor Science and Technology **18**, S395 (2003).

[185] M. Richard, J. Kasprzak, R. André, R. Romestain, L. S. Dang, G. Malpuech, and A. Kavokin, *"Experimental evidence for nonequilibrium Bose condensation of exciton polaritons"*, Physical Review B **72**, 201301 (2005).

[186] A. Baas, K. G. Lagoudakis, M. Richard, R. André, L. S. Dang, and B. Deveaud-Plédran, *"Synchronized and desynchronized phases of exciton-polariton condensates in the presence of disorder"*, Physical Review Letters **100**, 170401 (2008).

[187] T. Guillet, M. Mexis, J. Levrat, G. Rossbach, C. Brimont, T. Bretagnon, B. Gil, R. Butté, N. Grandjean, L. Orosz, F. Réveret, J. Leymarie, J. Zúñiga-Pérez, M. Leroux, F. Semond, and S. Bouchoule, *"Polariton lasing in a hybrid bulk ZnO microcavity"*, Applied Physics Letters **99**, 161104 (2011).

[188] H. Franke, C. Sturm, R. Schmidt-Grund, G. Wagner, and M. Grundmann, *"Ballistic propagation of exciton–polariton condensates in a ZnO-based microcavity"*, New Journal of Physics **14**, 013037 (2012).

[189] W. Xie, H. Dong, S. Zhang, L. Sun, W. Zhou, Y. Ling, J. Lu, X. Shen, and Z. Chen, *"Room-temperature polariton parametric scattering driven by a one-dimensional polariton condensate"*, Physical Review Letters **108**, 166401 (2012).

[190] A. Das, J. Heo, A. Bayraktaroglu, W. Guo, T.-K. Ng, J. Phillips, B. S. Ooi, and P. Bhattacharya, *"Room temperature strong coupling effects from single ZnO nanowire microcavity"*, Optics Express **20**, 11830 (2012).

[191] F. Li, L. Orosz, O. Kamoun, S. Bouchoule, C. Brimont, P. Disseix, T. Guillet, X. Lafosse, M. Leroux, J. Leymarie, M. Mexis, M. Mihailovic, G. Patriarche, F. Réveret, D. Solnyshkov, J. Zuniga-Perez, and G. Malpuech, *"From Excitonic to Photonic Polariton Condensate in a ZnO-Based Microcavity"*, Physical Review Letters **110**, 196406 (2013).

[192] D. Ballarini, D. Sanvitto, A. Amo, L. Viña, M. Wouters, I. Carusotto, A. Lemaitre, and J. Bloch, *"Observation of long-lived polariton states in semiconductor microcavities across the parametric threshold"*, Physical Review Letters **102**, 056402 (2009).

[193] M. Wouters and I. Carusotto, *"Goldstone mode of optical parametric oscillators in planar semiconductor microcavities in the strong-coupling regime"*, Physical Review A **76**, 043807 (2007).

[194] D. N. Krizhanovskii, D. M. Whittaker, R. A. Bradley, K. Guda, D. Sarkar, D. Sanvitto, L. Viña, E. Cerda, P. Santos, K. Biermann, R. Hey, and M. S. Skolnick, *"Effect of interactions on vortices in a nonequilibrium polariton condensate"*, Physical Review Letters **104**, 126402 (2010).

[195] I. Carusotto and C. Ciuti, *"Spontaneous microcavity-polariton coherence across the parametric threshold: Quantum Monte Carlo studies"*, Physical Review B **72**, 125335 (2005).

[196] I. Carusotto and C. Ciuti, *"Probing Microcavity Polariton Superfluidity through Resonant Rayleigh Scattering"*, Physical Review Letters **93**, 166401 (2004).

[197] J. Keeling and N. G. Berloff, *"Spontaneous rotating vortex lattices in a pumped decaying condensate"*, Physical Review Letters **100**, 250401 (2008).

[198] I. S. Aranson and L. Kramer, *"The world of the complex Ginzburg-Landau equation"*, Reviews of Modern Physics **74**, 99 (2002).

[199] J. Keeling and N. G. Berloff, *"Condensed-matter physics: Going with the flow"*, Nature **457**, 273 (2009).

[200] S. Pigeon, I. Carusotto, and C. Ciuti, *"Hydrodynamic nucleation of vortices and solitons in a resonantly excited polariton superfluid"*, Physical Review B **83**, 144513 (2011).

[201] C. Ciuti and I. Carusotto, *"Quantum fluid effects and parametric instabilities in microcavities"*, physica status solidi (b) **242**, 2224 (2005).

[202] G. E. Astrakharchik and L. P. Pitaevskii, *"Motion of a heavy impurity through a Bose-Einstein condensate"*, Physical Review A **70**, 013608 (2004).

[203] M. Wouters and I. Carusotto, *"Superfluidity and Critical Velocities in Nonequilibrium Bose-Einstein Condensates"*, Physical Review Letters **105**, 020602 (2010).

[204] E. Cancellieri, F. M. Marchetti, M. H. Szymańska, and C. Tejedor, *"Superflow of resonantly driven polaritons against a defect"*, Physical Review B **82**, 224512 (2010).

[205] A. C. Berceanu, E. Cancellieri, and F. M. Marchetti, *"Drag in a resonantly driven polariton fluid"*, Journal of Physics: Condensed Matter **24**, 235802 (2012).

[206] M. Wouters and I. Carusotto, *"Excitations in a Nonequilibrium Bose-Einstein Condensate of Exciton Polaritons"*, Physical Review Letters **99**, 140402 (2007).

[207] S. Utsunomiya, L. Tian, G. Roumpos, C. W. Lai, N. Kumada, T. Fujisawa, M. Kuwata-Gonokami, A. Loffler, S. Hofling, A. Forchel, and Y. Yamamoto, *"Observation of Bogoliubov excitations in exciton-polariton condensates"*, Nature Physics **4**, 700 (2008).

[208] C. Ryu, M. F. Andersen, P. Cladé, V. Natarajan, K. Helmerson, and W. D. Phillips, *"Observation of Persistent Flow of a Bose-Einstein Condensate in a Toroidal Trap"*, Physical Review Letters **99**, 260401 (2007).

[209] K. G. Lagoudakis, F. Manni, B. Pietka, M. Wouters, T. C. H. Liew, V. Savona, A. V. Kavokin, R. André, and B. Deveaud-Plédran, *"Probing the dynamics of spontaneous quantum vortices in polariton superfluids"*, Physical Review Letters **106**, 115301 (2011).

[210] L. Viña, R. André, V. Ciulin, J. D. Ganiere, and B. Deveaud, *"Oscillatory behaviour in the nonlinear emission of semiconductor microcavities"*, Semiconductor Science and Technology **19**, S333 (2004).

[211] I. A. Shelykh, L. Viña, A. V. Kavokin, N. G. Galkin, G. Malpuech, and R. André, *"Nonlinear coupling of polariton and dark exciton states in semiconductor microcavities"*, Solid State Communications **135**, 1 (2005).

[212] D. Read, T. C. H. Liew, Y. G. Rubo, and A. V. Kavokin, *"Stochastic polarization formation in exciton-polariton Bose-Einstein condensates"*, Physical Review B **80**, 195309 (2009).

[213] M. Wouters, *"Energy relaxation in the mean-field description of polariton condensates"*, New Journal of Physics **14**, 075020 (2012).

[214] D. D. Solnyshkov, H. Terças, K. Dini, and G. Malpuech, *"Hybrid Boltzmann–Gross-Pitaevskii theory of Bose-Einstein condensation and superfluidity in open driven-dissipative systems"*, Physical Review A **89**, 033626 (2014).

[215] L. M. Sieberer, S. D. Huber, E. Altman, and S. Diehl, *"Nonequilibrium functional renormalization for driven-dissipative Bose-Einstein condensation"*, Physical Review B **89**, 134310 (2014).

[216] M. Wouters, T. C. H. Liew, and V. Savona, *"Energy relaxation in one-dimensional polariton condensates"*, Physical Review B **82**, 245315 (2010).

[217] K. Huang, *Statistical mechanics* (Wiley, 1987).

[218] E. Cancellieri, F. M. Marchetti, M. H. Szymańska, D. Sanvitto, and C. Tejedor, *"Frictionless flow in a binary polariton superfluid"*, Physical Review Letters **108**, 065301 (2012).

[219] G. Khitrova, H. M. Gibbs, F. Jahnke, M. Kira, and S. W. Koch, *"Nonlinear optics of normal-mode-coupling semiconductor microcavities"*, Reviews of Modern Physics **71**, 1591 (1999).

[220] Y. Yamamoto, F. Matinaga, S. Machida, A. Karlsson, J. Jacobson, G. Björk, and T. Mukai, *"Quantum-Electrodynamic Effects In Semiconductor Microcavities - Microlasers And Coherent Exciton-Polariton Emission"*, Le Journal De Physique IV **3**, 39 (1993).

[221] I. Abram, S. Iung, R. Kuszelewicz, G. Le-Roux, C. Licoppe, J. L. Oudar, E. V. K. Rao, J. I. Bloch, R. Planel, and V. Thierry-Mieg, *"Nonguiding half-wave semiconductor microcavities displaying the exciton-photon mode splitting"*, Applied Physics Letters **65**, 2516 (1994).

[222] P. Kelkar, V. Kozlov, H. Jeon, A. V. Nurmikko, C. Chu, D. C. Grillo, J. Han, C. G. Hua, and R. L. Gunshor, *"Excitons in a II-VI semiconductor microcavity in the strong-coupling regime"*, Physical Review B **52**, R5491 (1995).

[223] Z. L. Zhang, M. Nishioka, C. Weisbuch, and Y. Arakawa, *"Demonstration of confined optical field effect in a vertical microcavity by examining the low temperature photon-exciton interaction in two kinds of quantum wells"*, Applied Physics Letters **64**, 1068 (1994).

[224] S. Long, B. Sermage, I. Abram, J. Bloch, R. Planel, and V. Thierry-Mieg, *"Time-resolved luminescence of excitons in a microcavity"*, Il Nuovo Cimento D **17**, 1601 (1995).

[225] T. A. Fisher, A. M. Afshar, D. M. Whittaker, M. S. Skolnick, J. S. Roberts, G. Hill, and M. A. Pate, *"Electric-field and temperature tuning of exciton-photon coupling in quantum microcavity structures"*, Physical Review B **51**, 2600 (1995).

[226] R. L. Greene, K. K. Bajaj, and D. E. Phelps, *"Energy levels of Wannier excitons in $GaAs-Ga_{1-x}Al_xAs$ quantum-well structures"*, Physical Review B **29**, 1807 (1984).

[227] T. R. Nelson, J. P. Prineas, G. Khitrova, H. M. Gibbs, J. D. Berger, E. K. Lindmark, J. Shin, H. Shin, Y. Lee, P. Tayebati, and L. Javniskis, *"Room-temperature normal-mode coupling in a semiconductor microcavity utilizing native-oxide $AlAl/GaAs$ mirrors"*, Applied Physics Letters **69**, 3031 (1996).

[228] R. André, D. Heger, L. S. Dang, and Y. Merle d'Aubigné, *"Spectroscopy of polaritons in $CdTe$-based microcavities"*, Journal of Crystal Growth **184–185**, 758 (1998).

[229] D. G. Lidzey, D. D. C. Bradley, M. S. Skolnick, T. Virgili, S. Walker, and D. M. Whittaker, *"Strong exciton-photon coupling in an organic semiconductor microcavity"*, Nature **395**, 53 (1998).

[230] S. Kena-Cohen and S. R. Forrest, *"Room-temperature polariton lasing in an organic single-crystal microcavity"*, Nature Photonics **4**, 371 (2010).

[231] D. M. Coles, N. Somaschi, P. Michetti, C. Clark, P. G. Lagoudakis, P. G. Savvidis, and D. G. Lidzey, *"Polariton-mediated energy transfer between organic dyes in a strongly coupled optical microcavity"*, Nature Materials **13**, 712 (2014).

[232] S. I. Tsintzos, N. T. Pelekanos, G. Konstantinidis, Z. Hatzopoulos, and P. G. Savvidis, *"A GaAs polariton light-emitting diode operating near room temperature"*, Nature **453**, 372 (2008).

[233] A. A. Khalifa, A. P. D. Love, D. N. Krizhanovskii, M. S. Skolnick, and J. S. Roberts, *"Electroluminescence emission from polariton states in GaAs-based semiconductor microcavities"*, Applied Physics Letters **92**, 061107 (2008).

[234] S. I. Tsintzos, P. G. Savvidis, G. Deligeorgis, Z. Hatzopoulos, and N. T. Pelekanos, *"Room temperature GaAs exciton-polariton light emitting diode"*, Applied Physics Letters **94**, 071109 (2009).

[235] P. Cristofolini, G. Christmann, S. I. Tsintzos, G. Deligeorgis, G. Konstantinidis, Z. Hatzopoulos, P. G. Savvidis, and J. J. Baumberg, *"Coupling quantum tunneling with cavity photons"*, Science **336**, 704 (2012).

[236] P. Tsotsis, S. I. Tsintzos, G. Christmann, P. G. Lagoudakis, O. Kyriienko, I. A. Shelykh, J. J. Baumberg, A. V. Kavokin, Z. Hatzopoulos, P. S. Eldridge, and P. G. Savvidis, *"Tuning the Energy of a Polariton Condensate via Bias-Controlled Rabi Splitting"*, Physical Review Applied **2**, 014002 (2014).

[237] C. Schneider, A. Rahimi-Iman, N. Y. Kim, J. Fischer, I. G. Savenko, M. Amthor, M. Lermer, A. Wolf, L. Worschech, V. D. Kulakovskii, I. A. Shelykh, M. Kamp, S. Reitzenstein, A. Forchel, Y. Yamamoto, and S. Hofling, *"An electrically pumped polariton laser"*, Nature **497**, 348 (2013).

[238] A. Cho and J. Arthur, *"Molecular beam epitaxy"*, Progress in Solid State Chemistry **10, Part 3**, 157 (1975).

[239] M. Perrin, J. Bloch, A. Lemaitre, and P. Senellart, *"Enhanced polariton relaxation by electron-polariton scattering"*, physica status solidi (c) **2**, 759 (2005).

[240] M. Perrin, P. Senellart, A. Lemaître, and J. Bloch, *"Polariton relaxation in semiconductor microcavities: Efficiency of electron-polariton scattering"*, Physical Review B **72**, 075340 (2005).

[241] D. Bajoni, M. Perrin, P. Senellart, A. Lemaître, B. Sermage, and J. Bloch, *"Dynamics of microcavity polaritons in the presence of an electron gas"*, Physical Review B **73**, 205344 (2006).

[242] P. Tsotsis, P. S. Eldridge, T. Gao, S. I. Tsintzos, Z. Hatzopoulos, and P. G. Savvidis, *"Lasing threshold doubling at the crossover from strong to weak coupling regime in GaAs microcavity"*, New Journal of Physics **14**, 023060 (2012).

[243] T. Lecomte, V. Ardizzone, M. Abbarchi, C. Diederichs, A. Miard, A. Lemaitre, I. Sagnes, P. Senellart, J. Bloch, C. Delalande, J. Tignon, and P. Roussignol, *"Optical parametric oscillation in one-dimensional microcavities"*, Physical Review B **87**, 155302 (2013).

[244] M. Z. Maialle, E. A. de Andrada e Silva, and L. J. Sham, *"Exciton spin dynamics in quantum wells"*, Physical Review B **47**, 15776 (1993).

[245] G. Panzarini, L. C. Andreani, A. Armitage, D. Baxter, M. S. Skolnick, V. N. Astratov, J. S. Roberts, A. V. Kavokin, M. R. Vladimirova, and M. A. Kaliteevski, *"Exciton-light coupling in single and coupled semiconductor microcavities: Polariton dispersion and polarization splitting"*, Physical Review B **59**, 5082 (1999).

[246] E. Kammann, T. C. H. Liew, H. Ohadi, P. Cilibrizzi, P. Tsotsis, Z. Hatzopoulos, P. G. Savvidis, A. V. Kavokin, and P. G. Lagoudakis, *"Nonlinear Optical Spin Hall Effect and Long-Range Spin Transport in Polariton Lasers"*, Physical Review Letters **109**, 036404 (2012).

[247] I. Savenko, T. Liew, and I. Shelykh, *"Stochastic Gross-Pitaevskii Equation for the Dynamical Thermalization of Bose-Einstein Condensates"*, Physical Review Letters **110**, 127402 (2013).

[248] M. Born and E. Wolf, *Principles of Optics: Electromagnetic Theory of Propagation, Interference and Diffraction of Light* (Cambridge University Press, 2000).

[249] T. Kreis, *"Digital holographic interference-phase measurement using the fourier-transform method"*, Journal of the Optical Society of America A **3**, 847 (1986).

[250] T. Kreis, *Holographic Interferometry-Principles and Methods* (Akademie Verlag, Berlin, 1996).

[251] S. O. Demokritov, V. E. Demidov, O. Dzyapko, G. A. Melkov, A. A. Serga, B. Hillebrands, and A. N. Slavin, *"Bose-Einstein condensation of quasi-equilibrium magnons at room temperature under pumping"*, Nature **443**, 430 (2006).

[252] T. Giamarchi, C. Ruegg, and O. Tchernyshyov, *"Bose-Einstein condensation in magnetic insulators"*, Nature Physics **4**, 198 (2008).

[253] M. Combescot, R. Combescot, M. Alloing, and F. Dubin, *"Optical signatures of a fully dark exciton condensate"*, Europhysics Letters **105**, 47011 (2014).

[254] I. Carusotto and C. Ciuti, *"Quantum fluids of light"*, Reviews of Modern Physics **85**, 299 (2013).

[255] F. Marchetti, M. Szymańska, C. Tejedor, and D. Whittaker, *"Spontaneous and triggered vortices in polariton optical-parametric-oscillator superfluids"*, Physical Review Letters **105**, 063902 (2010).

[256] M. Sich, F. Fras, J. K. Chana, M. S. Skolnick, D. N. Krizhanovskii, A. V. Gorbach, R. Hartley, D. V. Skryabin, S. S. Gavrilov, E. A. Cerda-Méndez, K. Biermann, R. Hey, and P. V. Santos, *"Effects of spin-dependent interactions on polarization of bright polariton solitons"*, Physical Review Letters **112**, 046403 (2014).

[257] G. Blatter, M. V. Feigel'man, V. B. Geshkenbein, A. I. Larkin, and V. M. Vinokur, *"Vortices in high-temperature superconductors"*, Reviews of Modern Physics **66**, 1125 (1994).

[258] A. L. Fetter, *"Quantum theory of superfluid vortices. ii. type-ii superconductors"*, Physical Review **163**, 390 (1967).

[259] A. L. Fetter, *"Quantum Theory of Superfluid Vortices. I. Liquid Helium II"*, Physical Review **162**, 143 (1967).

[260] A. L. Fetter, *"Rotating trapped Bose-Einstein condensates"*, Reviews of Modern Physics **81**, 647 (2009).

[261] M. Wouters and V. Savona, *"Superfluidity of a nonequilibrium Bose-Einstein condensate of polaritons"*, Physical Review B **81**, 054508 (2010).

[262] M. H. Szymanska, F. M. Marchetti, and D. Sanvitto, *"Propagating wave packets and quantized currents in coherently driven polariton superfluids"*, Physical Review Letters **105**, 236402 (2010).

[263] A. V. Gorbach, R. Hartley, and D. V. Skryabin, *"Vortex lattices in coherently pumped polariton microcavities"*, Physical Review Letters **104**, 213903 (2010).

[264] K. Guda, M. Sich, D. Sarkar, P. M. Walker, M. Durska, R. A. Bradley, D. M. Whittaker, M. S. Skolnick, E. A. Cerda-Méndez, P. V. Santos, K. Biermann, R. Hey, and D. N. Krizhanovskii, *"Spontaneous vortices in optically shaped potential profiles in semiconductor microcavities"*, Physical Review B **87**, 081309 (2013).

[265] G. Dasbach, M. Schwab, M. Bayer, D. Krizhanovskii, and A. Forchel, *"Tailoring the polariton dispersion by optical confinement: Access to a manifold of elastic polariton pair scattering channels"*, Physical Review B **66**, 201201 (2002).

[266] M. Abbarchi, V. Ardizzone, T. Lecomte, A. Lemaître, I. Sagnes, P. Senellart, J. Bloch, P. Roussignol, and J. Tignon, *"One-dimensional microcavity-based optical parametric oscillator: Generation of balanced twin beams in strong and weak coupling regime"*, Physical Review B **83**, 201310 (2011).

[267] J. Cuadra, D. Sarkar, L. Viña, J. M. Hvam, A. Nalitov, D. Solnyshkov, and G. Malpuech, *"Polarized emission in polariton condensates: Switching in a one-dimensional natural trap versus inversion in two dimensions"*, Physical Review B **88**, 235312 (2013).

[268] V. Ardizzone, M. Abbarchi, A. Lemaitre, I. Sagnes, P. Senellart, J. Bloch, C. Delalande, J. Tignon, and P. Roussignol, *"Bunching visibility of optical parametric emission in a semiconductor microcavity"*, Physical Review B **86**, 041301 (2012).

[269] O. El Daïf, A. Baas, T. Guillet, J.-P. Brantut, R. I. Kaitouni, J. L. Staehli, F. Morier-Genoud, and B. Deveaud, *"Polariton quantum boxes in semiconductor microcavities"*, Applied Physics Letters **88**, 061105 (2006).

[270] D. Bajoni, P. Senellart, E. Wertz, I. Sagnes, A. Miard, A. Lemaître, and J. Bloch, *"Polariton Laser Using Single Micropillar GaAs-GaAlAs Semiconductor Cavities"*, Physical Review Letters **100**, 047401 (2008).

[271] M. Maragkou, A. J. D. Grundy, E. Wertz, A. Lemaître, I. Sagnes, P. Senellart, J. Bloch, and P. G. Lagoudakis, *"Spontaneous nonground state polariton condensation in pillar microcavities"*, Physical Review B **81**, 081307 (2010).

[272] G. Nardin, T. K. Paraïso, R. Cerna, B. Pietka, Y. Léger, O. El Daif, F. Morier-Genoud, and B. Deveaud-Plédran, *"Probability density optical tomography of confined quasiparticles in a semiconductor microcavity"*, Applied Physics Letters **94**, 181103 (2009).

[273] G. Nardin, Y. Léger, B. Pietka, F. Morier-Genoud, and B. Deveaud-Plédran, *"Phase-resolved imaging of confined exciton-polariton wave functions in elliptical traps"*, Physical Review B **82**, 045304 (2010).

[274] G. Dasbach, M. Schwab, M. Bayer, and A. Forchel, *"Parametric polariton scattering in microresonators with three-dimensional optical confinement"*, Physical Review B **64**, 201309 (2001).

[275] D. Bajoni, E. Peter, P. Senellart, J. L. Smirr, I. Sagnes, A. Lemaître, and J. Bloch, *"Polariton parametric luminescence in a single micropillar"*, Applied Physics Letters **90**, 051107 (2007).

[276] L. Ferrier, S. Pigeon, E. Wertz, M. Bamba, P. Senellart, I. Sagnes, A. Lemaître, C. Ciuti, and J. Bloch, *"Polariton parametric oscillation in a single micropillar cavity"*, Applied Physics Letters **97**, 031105 (2010).

[277] V. K. Kalevich, M. M. Afanasiev, V. A. Lukoshkin, K. V. Kavokin, S. I. Tsintzos, P. G. Savvidis, and A. V. Kavokin, *"Ring-shaped polariton lasing in pillar microcavities"*, Journal of Applied Physics **115**, 094304 (2014).

[278] I. Carusotto, J. Schmiedmayer, and L. Viña, *"Focus on Bose condensation phenomena in atomic and solid state physics"*, New Journal of Physics **15**, 035010 (2013).

[279] D. S. Hall, M. R. Matthews, C. E. Wieman, and E. A. Cornell, *"Measurements of Relative Phase in Two-Component Bose-Einstein Condensates"*, Physical Review Letters **81**, 1543 (1998).

[280] T. Esslinger, I. Bloch, and T. W. Hänsch, *"Probing first-order spatial coherence of a Bose-Einstein condensate"*, Journal of Modern Optics **47**, 2725 (2000).

[281] I. Bloch, *"Ultracold quantum gases in optical lattices"*, Nature Physics **1**, 23 (2005).

[282] Z. Ficek and S. Swain, *Quantum Interference and Coherence: Theory and Experiments* Springer Series in Optical Sciences (Springer, 2005).

[283] A. Kavokin, *"Polaritons: The rise of the bosonic laser"*, Nature Photonics **7**, 591 (2013).

[284] L. Novotny and B. Hecht, *Principles of Nano-Optics* (Cambridge University Press, 2012).

[285] L. Mandel and E. Wolf, *Optical Coherence and Quantum Optics* (Cambridge University Press, 1995).

[286] G. J. Pryde, *"Optical quantum information: The quantum information cocoon"*, Nature Photonics **2**, 461 (2008).

[287] L. Pitaevskii and S. Stringari, *"Interference of Bose-Einstein Condensates in Momentum Space"*, Physical Review Letters **83**, 4237 (1999).

[288] M. Saba, T. A. Pasquini, C. Sanner, Y. Shin, W. Ketterle, and D. E. Pritchard, *"Light Scattering to Determine the Relative Phase of Two Bose-Einstein Condensates"*, Science **307**, 1945 (2005).

[289] Y. Shin, G.-B. Jo, M. Saba, T. A. Pasquini, W. Ketterle, and D. E. Pritchard, *"Optical Weak Link between Two Spatially Separated Bose-Einstein Condensates"*, Physical Review Letters **95**, 170402 (2005).

[290] Y. Castin and J. Dalibard, *"Relative phase of two Bose-Einstein condensates"*, Physical Review A **55**, 4330 (1997).

[291] A. Leggett, *Quantum Liquids: Bose Condensation And Cooper Pairing in Condensed-matter Systems* Oxford graduate texts in mathematics (Oxford University Press, 2006).

[292] A. I. Tartakovskii, V. D. Kulakovskii, D. N. Krizhanovskii, M. S. Skolnick, V. N. Astratov, A. Armitage, and J. S. Roberts, *"Nonlinearities in emission from the lower polariton branch of semiconductor microcavities"*, Physical Review B **60**, R11293 (1999).

[293] M. D. Martín, G. Aichmayr, L. Viña, and R. André, *"Polarization control of the nonlinear emission of semiconductor microcavities"*, Physical Review Letters **89**, 077402 (2002).

[294] Ł. Kłopotowski, M. D. Martín, A. Amo, L. Viña, I. A. Shelykh, M. M. Glazov, G. Malpuech, A. V. Kavokin, and R. André, *"Optical anisotropy and pinning of the linear polarization of light in semiconductor microcavities"*, Solid State Communications **139**, 511 (2006).

[295] P. G. Lagoudakis, P. G. Savvidis, J. J. Baumberg, D. M. Whittaker, P. R. Eastham, M. S. Skolnick, and J. S. Roberts, *"Stimulated spin dynamics of polaritons in semiconductor microcavities"*, Physical Review B **65**, 161310 (2002).

[296] C. Adrados, T. C. H. Liew, A. Amo, M. D. Martín, D. Sanvitto, C. Antón, E. Giacobino, A. Kavokin, A. Bramati, and L. Viña, *"Motion of spin polariton bullets in semiconductor microcavities"*, Physical Review Letters **107**, 146402 (2011).

[297] G. Grosso, S. Trebaol, M. Wouters, F. Morier-Genoud, M. T. Portella-Oberli, and B. Deveaud, *"Nonlinear relaxation and selective polychromatic lasing of confined polaritons"*, Physical Review B **90**, 045307 (2014).

[298] C. Leyder, T. C. H. Liew, A. V. Kavokin, I. A. Shelykh, M. Romanelli, J. P. Karr, E. Giacobino, and A. Bramati, *"Interference of coherent polariton beams in microcavities: Polarization-Controlled optical gates"*, Physical Review Letters **99**, 196402 (2007).

[299] R. Cerna, Y. Léger, T. K. Paraïso, M. Wouters, F. Morier-Genoud, M. T. Portella-Oberli, and B. Deveaud, *"Ultrafast tristable spin memory of a coherent polariton gas"*, Nature Communications **4**, 2008 (2013).

[300] I. A. Shelykh, T. C. H. Liew, and A. V. Kavokin, *"Spin rings in semiconductor microcavities"*, Physical Review Letters **100**, 116401 (2008).

[301] R. Johne, I. A. Shelykh, D. D. Solnyshkov, and G. Malpuech, *"Polaritonic analogue of Datta and Das spin transistor"*, Physical Review B **81**, 125327 (2010).

[302] T. Espinosa-Ortega and T. C. H. Liew, *"Complete architecture of integrated photonic circuits based on and and not logic gates of exciton polaritons in semiconductor microcavities"*, Physical Review B **87**, 195305 (2013).

[303] K. V. Kavokin, I. A. Shelykh, A. V. Kavokin, G. Malpuech, and P. Bigenwald, *"Quantum theory of spin dynamics of exciton-polaritons in microcavities"*, Physical Review Letters **92**, 017401 (2004).

[304] M. Vladimirova, S. Cronenberger, D. Scalbert, K. V. Kavokin, A. Miard, A. Lemaître, J. Bloch, D. Solnyshkov, G. Malpuech, and A. V. Kavokin, *"Polariton-polariton interaction constants in microcavities"*, Physical Review B **82**, 075301 (2010).

[305] E. del Valle, D. Sanvitto, A. Amo, F. P. Laussy, R. Andre, C. Tejedor, and L. Viña, *"Dynamics of the Formation and Decay of Coherence in a Polariton Condensate"*, Physical Review Letters **103**, 096404 (2009).

[306] S. S. Hodgman, R. G. Dall, A. G. Manning, K. G. H. Baldwin, and A. G. Truscott, *"Direct Measurement of Long-Range Third-Order Coherence in Bose-Einstein Condensates"*, Science **331**, 1046 (2011).

[307] D. Snoke, *"Spontaneous Bose Coherence of Excitons and Polaritons"*, Science **298**, 1368 (2002).

[308] A. Rahimi-Iman, A. V. Chernenko, J. Fischer, S. Brodbeck, M. Amthor, C. Schneider, A. Forchel, S. Höfling, S. Reitzenstein, and M. Kamp, *"Coherence signatures and density-dependent interaction in a dynamical exciton-polariton condensate"*, Physical Review B **86**, 155308 (2012).

[309] V. V. Belykh, N. N. Sibeldin, V. D. Kulakovskii, M. M. Glazov, M. A. Semina, C. Schneider, S. Höfling, M. Kamp, and A. Forchel, *"Coherence expansion and polariton condensate formation in a semiconductor microcavity"*, Physical Review Letters **110**, 137402 (2013).

[310] G. Christmann, G. Tosi, N. G. Berloff, P. Tsotsis, P. S. Eldridge, Z. Hatzopoulos, P. G. Savvidis, and J. J. Baumberg, *"Oscillatory solitons and time-resolved phase locking of two polariton condensates"*, New Journal of Physics **16**, 103039 (2014).

[311] H. Ohadi, R. L. Gregory, T. Freegarde, Y. G. Rubo, A. V. Kavokin, and P. G. Lagoudakis, *"Dissipative phase locking of exciton-polariton condensates"*, arXiv:1406.6377 [cond-mat.other] (2014).

[312] I. L. Aleiner, B. L. Altshuler, and Y. G. Rubo, *"Radiative coupling and weak lasing of exciton-polariton condensates"*, Physical Review B **85**, 121301 (2012).

[313] C. Leyder, M. Romanelli, J. P. Karr, E. Giacobino, T. C. H. Liew, M. M. Glazov, A. V. Kavokin, G. Malpuech, and A. Bramati, *"Observation of the optical spin Hall effect"*, Nature Physics **3**, 628 (2007).

[314] A. Kavokin, G. Malpuech, and M. Glazov, *"Optical Spin Hall Effect"*, Physical Review Letters **95**, 136601 (2005).

[315] M. Dyakonov and V. Perel, *"Current-induced spin orientation of electrons in semiconductors"*, Physics Letters A **35**, 459 (1971).

[316] J. Sinova, D. Culcer, Q. Niu, N. A. Sinitsyn, T. Jungwirth, and A. H. MacDonald, *"Universal Intrinsic Spin Hall Effect"*, Physical Review Letters **92**, 126603 (2004).

[317] W. Langbein and J. M. Hvam, *"Elastic scattering dynamics of cavity polaritons: Evidence for time-energy uncertainty and polariton localization"*, Physical Review Letters **88**, 047401 (2002).

[318] A. Amo, T. C. H. Liew, C. Adrados, E. Giacobino, A. V. Kavokin, and A. Bramati, *"Anisotropic optical spin Hall effect in semiconductor microcavities"*, Physical Review B **80**, 165325 (2009).

[319] M. Maragkou, C. E. Richards, T. Ostatnický, A. J. D. Grundy, J. Zajac, M. Hugues, W. Langbein, and P. G. Lagoudakis, *"Optical analogue of the spin Hall effect in a photonic cavity"*, Optics Letters **36**, 1095 (2011).

[320] W. Langbein, I. Shelykh, D. Solnyshkov, G. Malpuech, Y. Rubo, and A. Kavokin, *"Polarization beats in ballistic propagation of exciton-polaritons in microcavities"*, Physical Review B **75**, 075323 (2007).

[321] F. Manni, K. Lagoudakis, T. Paraïso, R. Cerna, Y. Léger, T. Liew, I. Shelykh, A. Kavokin, F. Morier-Genoud, and B. Deveaud-Plédran, *"Spin-to-orbital angular momentum conversion in semiconductor microcavities"*, Physical Review B **83**, 241307 (2011).

[322] F. Manni, Y. Léger, Y. G. Rubo, R. André, and B. Deveaud, *"Hyperbolic spin vortices and textures in exciton–polariton condensates"*, Nature Communications **4** (2013).

[323] V. G. Sala, D. D. Solnyshkov, I. Carusotto, T. Jacqmin, A. Lemaître, H. Terças, A. Nalitov, E. Abbarchi, M. Galopin, I. Sagnes, J. Bloch, G. Malpuech, and A. Amo, *"Engineering spin-orbit coupling for photons and polaritons in microstructures"*, arXiv:1406.4816 [cond-mat.mes-hall] (2014).

[324] T. C. H. Liew, A. V. Kavokin, and I. A. Shelykh, *"Excitation of vortices in semiconductor microcavities"*, Physical Review B **75**, 241301 (2007).

[325] H. Flayac, D. D. Solnyshkov, and G. Malpuech, *"Oblique half-solitons and their generation in exciton-polariton condensates"*, Physical Review B **83**, 193305 (2011).

[326] P. Cilibrizzi, H. Ohadi, T. Ostatnicky, A. Askitopoulos, W. Langbein, and P. Lagoudakis, *"Linear wave dynamics explains observations attributed to dark solitons in a polariton quantum fluid"*, Physical Review Letters **113**, 103901 (2014).

[327] O. A. Egorov and F. Lederer, *"Pseudospin-induced motion of cavity polariton soliton molecules"*, Optics Letters **39**, 4029 (2014).

[328] A. Werner, O. A. Egorov, and F. Lederer, *"Pseudospin dynamics of exciton-polariton patterns in a coherently driven semiconductor microcavity"*, Physical Review B **90**, 165308 (2014).

[329] O. A. Egorov, A. Werner, T. C. H. Liew, E. A. Ostrovskaya, and F. Lederer, *"Motion of patterns in polariton quantum fluids with spin-orbit interaction"*, Physical Review B **89**, 235302 (2014).

[330] H. Ohadi, E. Kammann, T. C. H. Liew, K. G. Lagoudakis, A. V. Kavokin, and P. G. Lagoudakis, *"Spontaneous symmetry breaking in a polariton and photon laser"*, Physical Review Letters **109**, 016404 (2012).

[331] G. Dasbach, C. Diederichs, J. Tignon, C. Ciuti, P. Roussignol, C. Delalande, M. Bayer, and A. Forchel, *"Polarization inversion via parametric scattering in quasi-one-dimensional microcavities"*, Physical Review B **71**, 161308 (2005).

[332] Y. O. Dudin and A. Kuzmich, *"Strongly Interacting Rydberg Excitations of a Cold Atomic Gas"*, Science **336**, 887 (2012).

[333] O. Firstenberg, T. Peyronel, Q.-Y. Liang, A. V. Gorshkov, M. D. Lukin, and V. Vuletic, *"Attractive photons in a quantum nonlinear medium"*, Nature **502**, 71 (2013).

[334] J. Pritchard, D. Maxwell, A. Gauguet, K. Weatherill, M. Jones, and C. Adams, *"Cooperative Atom-Light Interaction in a Blockaded Rydberg Ensemble"*, Physical Review Letters **105**, 193603 (2010).

[335] J. Volz, M. Scheucher, C. Junge, and A. Rauschenbeutel, *"Nonlinear π phase shift for single fibre-guided photons interacting with a single resonator-enhanced atom"*, Nature Photonics **8**, 965 (2014).

[336] H. Gorniaczyk, C. Tresp, J. Schmidt, H. Fedder, and S. Hofferberth, *"Single-Photon Transistor Mediated by Interstate Rydberg Interactions"*, Physical Review Letters **113**, 053601 (2014).

[337] D. Tiarks, S. Baur, K. Schneider, S. Dürr, and G. Rempe, *"Single-Photon Transistor Using a Förster Resonance"*, Physical Review Letters **113**, 053602 (2014).

[338] S. Baur, D. Tiarks, G. Rempe, and S. Dürr, *"Single-Photon Switch Based on Rydberg Blockade"*, Physical Review Letters **112**, 073901 (2014).

[339] A. Gaetan, Y. Miroshnychenko, T. Wilk, A. Chotia, M. Viteau, D. Comparat, P. Pillet, A. Browaeys, and P. Grangier, *"Observation of collective excitation of two individual atoms in the Rydberg blockade regime"*, Nature Physics **5**, 115 (2009).

[340] E. Urban, T. A. Johnson, T. Henage, L. Isenhower, D. D. Yavuz, T. G. Walker, and M. Saffman, *"Observation of Rydberg blockade between two atoms"*, Nature Physics **5**, 110 (2009).

[341] T. M. Weber, M. Honing, T. Niederprum, T. Manthey, O. Thomas, V. Guarrera, M. Fleischhauer, G. Barontini, and H. Ott, *"Mesoscopic rydberg-blockaded ensembles in the superatom regime and beyond"*, Nature Physics **11**, 157 (2015).

[342] R. Reimann, W. Alt, T. Kampschulte, T. Macha, L. Ratschbacher, N. Thau, S. Yoon, and D. Meschede, *"Cavity-Modified Collective Rayleigh Scattering of Two Atoms"*, Physical Review Letters **114**, 023601 (2015).

[343] B. Casabone, K. Friebe, B. Brandstätter, K. Schüppert, R. Blatt, and T. E. Northup, *"Enhanced quantum interface with collective ion-cavity coupling"*, Physical Review Letters **114**, 023602 (2015).

[344] P. Michler, A. Kiraz, C. Becher, W. V. Schoenfeld, P. M. Petroff, L. Zhang, E. Hu, and A. Imamoglu, *"A quantum dot single-photon turnstile device"*, Science **290**, 2282 (2000).

[345] N. Akopian, N. Lindner, E. Poem, Y. Berlatzky, J. Avron, D. Gershoni, B. Gerardot, and P. Petroff, *"Entangled photon pairs from semiconductor quantum dots"*, Physical Review Letters **96**, 130501 (2006).

[346] R. J. Young, R. M. Stevenson, P. Atkinson, K. Cooper, D. A. Ritchie, and A. J. Shields, *"Improved fidelity of triggered entangled photons from single quantum dots"*, New Journal of Physics **8**, 29 (2006).

[347] C. Santori, D. Fattal, J. Vuckovic, G. S. Solomon, and Y. Yamamoto, *"Indistinguishable photons from a single-photon device"*, Nature **419**, 594 (2002).

[348] S. Ates, S. Ulrich, S. Reitzenstein, A. Löffler, A. Forchel, and P. Michler, *"Post-selected indistinguishable photons from the resonance fluorescence of a single quantum dot in a microcavity"*, Physical Review Letters **103**, 167402 (2009).

[349] R. Stevenson, C. Salter, J. Nilsson, A. Bennett, M. Ward, I. Farrer, D. Ritchie, and A. Shields, *"Indistinguishable entangled photons generated by a light-emitting diode"*, Physical Review Letters **108**, 040503 (2012).

[350] Y.-M. He, Y. He, Y.-J. Wei, D. Wu, M. Atature, C. Schneider, S. Hofling, M. Kamp, C.-Y. Lu, and J.-W. Pan, *"On-demand semiconductor single-photon source with near-unity indistinguishability"*, Nature Nanotechnology **8**, 213 (2013).

[351] O. Gazzano, S. Michaelis de Vasconcellos, C. Arnold, A. Nowak, E. Galopin, I. Sagnes, L. Lanco, A. Lemaître, and P. Senellart, *"Bright solid-state sources of indistinguishable single photons"*, Nature Communications **4**, 1425 (2013).

[352] M. Muller, S. Bounouar, K. D. Jons, M. Glassl, and P. Michler, *"On-demand generation of indistinguishable polarization-entangled photon pairs"*, Nature Photonics **8**, 224 (2014).

[353] V. Loo, C. Arnold, O. Gazzano, A. Lemaître, I. Sagnes, O. Krebs, P. Voisin, P. Senellart, and L. Lanco, *"Optical nonlinearity for few-photon pulses on a quantum dot-pillar cavity device"*, Physical Review Letters **109**, 166806 (2012).

[354] R. Bose, D. Sridharan, H. Kim, G. Solomon, and E. Waks, *"Low-photon-number optical switching with a single quantum dot coupled to a photonic crystal cavity"*, Physical Review Letters **108**, 227402 (2012).

[355] D. Englund, A. Majumdar, M. Bajcsy, A. Faraon, P. Petroff, and J. Vučković, *"Ultrafast photon-photon interaction in a strongly coupled quantum dot-cavity system"*, Physical Review Letters **108**, 093604 (2012).

[356] A. Reinhard, T. Volz, M. Winger, A. Badolato, K. J. Hennessy, E. L. Hu, and A. Imamoglu, *"Strongly correlated photons on a chip"*, Nature Photonics **6**, 93 (2012).

[357] H. Kim, R. Bose, T. C. Shen, G. S. Solomon, and E. Waks, *"A quantum logic gate between a solid-state quantum bit and a photon"*, Nature Photonics **7**, 373 (2013).

[358] S. Laurent, B. Eble, O. Krebs, A. Lemaître, B. Urbaszek, X. Marie, T. Amand, and P. Voisin, *"Electrical Control of Hole Spin Relaxation in Charge Tunable InAs/GaAs Quantum Dots"*, Physical Review Letters **94**, 147401 (2005).

[359] A. Greilich, D. R. Yakovlev, A. Shabaev, A. L. Efros, I. A. Yugova, R. Oulton, V. Stavarache, D. Reuter, A. Wieck, and M. Bayer, *"Mode locking of electron spin coherences in singly charged quantum dots"*, Science **313**, 341 (2006).

[360] X. Xu, B. Sun, P. R. Berman, D. G. Steel, A. S. Bracker, D. Gammon, and L. J. Sham, *"Coherent population trapping of an electron spin in a single negatively charged quantum dot"*, Nature Physics **4**, 692 (2008).

[361] A. Ramsay, S. Boyle, R. Kolodka, J. Oliveira, J. Skiba-Szymanska, H. Liu, M. Hopkinson, A. Fox, and M. Skolnick, *"Fast optical preparation, control, and readout of a single quantum dot spin"*, Physical Review Letters **100**, 197401 (2008).

[362] B. D. Gerardot, D. Brunner, P. A. Dalgarno, P. Ohberg, S. Seidl, M. Kroner, K. Karrai, N. G. Stoltz, P. M. Petroff, and R. J. Warburton, *"Optical pumping of a single hole spin in a quantum dot"*, Nature **451**, 441 (2008).

[363] K. De Greve, P. L. McMahon, D. Press, T. D. Ladd, D. Bisping, C. Schneider, M. Kamp, L. Worschech, S. Hofling, A. Forchel, and Y. Yamamoto, *"Ultrafast coherent control and suppressed nuclear feedback of a single quantum dot hole qubit"*, Nature Physics **7**, 872 (2011).

[364] D. Brunner, B. D. Gerardot, P. A. Dalgarno, G. Wüst, K. Karrai, N. G. Stoltz, P. M. Petroff, and R. J. Warburton, *"A coherent single-hole spin in a semiconductor"*, Science **325**, 70 (2009).

[365] D. Press, K. De Greve, P. L. McMahon, T. D. Ladd, B. Friess, C. Schneider, M. Kamp, S. Hofling, A. Forchel, and Y. Yamamoto, *"Ultrafast optical spin echo in a single quantum dot"*, Nature Photonics **4**, 367 (2010).

[366] K. De Greve, L. Yu, P. L. McMahon, J. S. Pelc, C. M. Natarajan, N. Y. Kim, E. Abe, S. Maier, C. Schneider, M. Kamp, S. Hofling, R. H. Hadfield, A. Forchel, M. M. Fejer, and Y. Yamamoto, *"Quantum-dot spin-photon entanglement via frequency downconversion to telecom wavelength"*, Nature **491**, 421 (2012).

[367] W. B. Gao, P. Fallahi, E. Togan, J. Miguel-Sanchez, and A. Imamoglu, *"Observation of entanglement between a quantum dot spin and a single photon"*, Nature **491**, 426 (2012).

[368] S. Strauf, N. G. Stoltz, M. T. Rakher, L. A. Coldren, P. M. Petroff, and D. Bouwmeester, *"High-frequency single-photon source with polarization control"*, Nature Photonics **1**, 704 (2007).

[369] J. Claudon, J. Bleuse, N. S. Malik, M. Bazin, P. Jaffrennou, N. Gregersen, C. Sauvan, P. Lalanne, and J.-M. Gerard, *"A highly efficient single-photon source based on a quantum dot in a photonic nanowire"*, Nature Photonics **4**, 174 (2010).

[370] M. Munsch, N. Malik, E. Dupuy, A. Delga, J. Bleuse, J.-M. Gérard, J. Claudon, N. Gregersen, and J. Mørk, *"Dielectric GaAs Antenna Ensuring an Efficient Broadband Coupling between an InAs Quantum Dot and a Gaussian Optical Beam"*, Physical Review Letters **110**, 177402 (2013).

[371] A. Laucht, S. Pütz, T. Günthner, N. Hauke, R. Saive, S. Frédérick, M. Bichler, M. C. Amann, A. Holleitner, M. Kaniber, and J. Finley, *"A waveguide-coupled on-chip single-photon source"*, Physical Review X **2**, 011014 (2012).

[372] O. Gazzano, M. Almeida, A. Nowak, S. Portalupi, A. Lemaître, I. Sagnes, A. White, and P. Senellart, *"Entangling quantum-logic gate operated with an ultrabright semiconductor single-photon source"*, Physical Review Letters **110**, 250501 (2013).

[373] C. Hu, W. Munro, and J. Rarity, *"Deterministic photon entangler using a charged quantum dot inside a microcavity"*, Physical Review B **78**, 125318 (2008).

[374] Y. Zhang, G. Jin, and Y.-Q. Ma, *"Phase effects on the exciton polariton amplifier"*, Applied Physics Letters **91**, 191112 (2007).

[375] D. Bajoni, E. Semenova, A. Lemaître, S. Barbay, R. Kuszelewicz, and J. Bloch, *"Phenomenological theory of bistability in polariton diodes"*, Applied Physics Letters **97**, 091107 (2010).

[376] I. Shelykh, K. V. Kavokin, A. V. Kavokin, G. Malpuech, P. Bigenwald, H. Deng, G. Weihs, and Y. Yamamoto, *"Semiconductor microcavity as a spin-dependent optoelectronic device"*, Physical Review B **70**, 035320 (2004).

[377] T. Espinosa-Ortega, T. C. H. Liew, and I. A. Shelykh, *"Optical diode based on exciton-polaritons"*, Applied Physics Letters **103**, 191110 (2013).

[378] D. W. Snoke, *"Excitonic circuits: New tools for manipulating photons"*, Photonics Spectra **40** (2006).

[379] A. A. High, E. E. Novitskaya, L. V. Butov, M. Hanson, and A. C. Gossard, *"Control of exciton fluxes in an excitonic integrated circuit"*, Science **321**, 229 (2008).

[380] S. Lazić, A. Violante, K. Cohen, R. Hey, R. Rapaport, and P. V. Santos, *"Scalable interconnections for remote indirect exciton systems based on acoustic transport"*, Physical Review B **89**, 085313 (2014).

[381] A. Violante, K. Cohen, S. L. R. Hey, R. Rapaport, and P. V. Santos, *"Dynamics of indirect exciton transport by moving acoustic fields"*, New Journal of Physics **16**, 033035 (2014).

[382] S. Büyükköse, A. Hernández-Mínguez, B. Vratzov, C. Somaschini, L. Geelhaar, H. Riechert, W. G. van der Wiel, and P. V. Santos, *"High-frequency acoustic charge transport in GaAs nanowires"*, Nanotechnology **25**, 135204 (2014).

[383] D. Tanese, H. Flayac, D. Solnyshkov, A. Amo, A. Lemaître, E. Galopin, R. Braive, P. Senellart, I. Sagnes, G. Malpuech, and J. Bloch, *"Polariton condensation in solitonic gap states in a one-dimensional periodic potential"*, Nature Communications **4**, 1749 (2013).

[384] D. Tanese, E. Gurevich, F. Baboux, T. Jacqmin, A. Lemaître, E. Galopin, I. Sagnes, A. Amo, J. Bloch, and E. Akkermans, *"Fractal Energy Spectrum of a Polariton Gas in a Fibonacci Quasiperiodic Potential"*, Physical Review Letters **112**, 146404 (2014).

[385] T. Jacqmin, I. Carusotto, I. Sagnes, M. Abbarchi, D. D. Solnyshkov, G. Malpuech, E. Galopin, A. Lemaître, J. Bloch, and A. Amo, *"Direct Observation of Dirac Cones and a Flatband in a Honeycomb Lattice for Polaritons"*, Physical Review Letters **112**, 116402 (2014).

[386] A. V. Nalitov, G. Malpuech, H. Terças, and D. D. Solnyshkov, *"Spin-Orbit Coupling and the Optical Spin Hall Effect in Photonic Graphene"*, Physical Review Letters **114**, 026803 (2015).

[387] A. Amo, S. Pigeon, C. Adrados, R. Houdre, E. Giacobino, C. Ciuti, and A. Bramati, *"Light engineering of the polariton landscape in semiconductor microcavities"*, Physical Review B **82**, 081301 (2010).

[388] P. Cristofolini, A. Dreismann, G. Christmann, G. Franchetti, N. G. Berloff, P. Tsotsis, Z. Hatzopoulos, P. G. Savvidis, and J. J. Baumberg, *"Optical superfluid phase transitions and trapping of polariton condensates"*, Physical Review Letters **110**, 186403 (2013).

[389] A. Askitopoulos, H. Ohadi, A. Kavokin, Z. Hatzopoulos, P. Savvidis, and P. Lagoudakis, *"Polariton condensation in an optically induced two-dimensional potential"*, Physical Review B **88**, 041308 (2013).

[390] A. Dreismann, P. Cristofolini, R. Balili, G. Christmann, F. Pinsker, N. G. Berloff, Z. Hatzopoulos, P. G. Savvidis, and J. J. Baumberg, *"Coupled counterrotating polariton condensates in optically defined annular potentials"*, Proceedings of the National Academy of Sciences **111**, 8770 (2014).

[391] R. Dall, M. D. Fraser, A. S. Desyatnikov, G. Li, S. Brodbeck, M. Kamp, C. Schneider, S. Höfling, and E. A. Ostrovskaya, *"Creation of Orbital Angular Momentum States with Chiral Polaritonic Lenses"*, Physical Review Letters **113**, 200404 (2014).

[392] M. De Giorgi, D. Ballarini, E. Cancellieri, F. M. Marchetti, M. H. Szymanska, C. Tejedor, R. Cingolani, E. Giacobino, A. Bramati, G. Gigli, and D. Sanvitto, *"Control and ultrafast dynamics of a two-fluid polariton switch"*, Physical Review Letters **109**, 266407 (2012).

[393] E. Cancellieri, A. Hayat, A. Steinberg, E. Giacobino, and A. Bramati, *"Ultrafast Stark-Induced Polaritonic Switches"*, Physical Review Letters **112**, 053601 (2014).

[394] I. A. Shelykh, R. Johne, D. D. Solnyshkov, and G. Malpuech, *"Optically and electrically controlled polariton spin transistor"*, Physical Review B **82**, 153303 (2010).

[395] M. Y. Petrov and A. V. Kavokin, *"Polariton transport in one-dimensional channels"*, Physical Review B **88**, 035308 (2013).

[396] F. Manni, K. G. Lagoudakis, T. C. H. Liew, R. André, and B. Deveaud-Plédran, *"Spontaneous pattern formation in a polariton condensate"*, Physical Review Letters **107**, 106401 (2011).

[397] M. Galbiati, L. Ferrier, D. D. Solnyshkov, D. Tanese, E. Wertz, A. Amo, M. Abbarchi, P. Senellart, I. Sagnes, A. Lemaître, E. Galopin, G. Malpuech, and J. Bloch, *"Polariton condensation in photonic molecules"*, Physical Review Letters **108**, 126403 (2012).

[398] A. Amo, D. Sanvitto, and L. Viña, *"Collective dynamics of excitons and polaritons in semiconductor nanostructures"*, Semiconductor Science and Technology **25**, 043001 (2010).

[399] A. Hayat, C. Lange, L. A. Rozema, A. Darabi, H. M. van Driel, A. M. Steinberg, B. Nelsen, D. W. Snoke, L. N. Pfeiffer, and K. W. West, *"Dynamic Stark Effect in Strongly Coupled Microcavity Exciton Polaritons"*, Physical Review Letters **109**, 033605 (2012).

[400] M. Wouters and V. Savona, *"Stochastic classical field model for polariton condensates"*, Physical Review B **79**, 165302 (2009).

[401] F. Manni, K. G. Lagoudakis, T. C. H. Liew, R. André, V. Savona, and B. Deveaud, *"Dissociation dynamics of singly charged vortices into half-quantum vortex pairs"*, Nature Communications **3**, 1309 (2012).

[402] R. Rojas, *Neural Networks* (Springer-Verlag, New York, 1996).

[403] V. Savona, C. Piermarocchi, A. Quattropani, F. Tassone, and P. Schwendimann, *"Microscopic theory of motional narrowing of microcavity polaritons in a disordered potential"*, Physical Review Letters **78**, 4470 (1997).

[404] R. W. Keyes, *"What makes a good computer device?"*, Science **230**, 138 (1985).

[405] M. Nielsen and I. Chuang, *Quantum Computation and Quantum Information: 10th Anniversary Edition* (Cambridge University Press, 2010).

[406] M. Fiorentino and F. N. C. Wong, *"Deterministic Controlled-NOT Gate For Single-Photon Two-Qubit Quantum Logic"*, Physical Review Letters **93**, 070502 (2004).

[407] J. L. O'Brien, G. J. Pryde, A. G. White, T. C. Ralph, and D. Branning, *"Demonstration of an all-optical quantum controlled-NOT gate"*, Nature **426**, 264 (2003).

[408] R. Okamoto, H. F. Hofmann, S. Takeuchi, and K. Sasaki, *"Demonstration of an Optical Quantum Controlled-NOT Gate without Path Interference"*, Physical Review Letters **95**, 210506 (2005).

[409] T. B. Pittman, M. J. Fitch, B. C. Jacobs, and J. D. Franson, *"Experimental controlled-NOT logic gate for single photons in the coincidence basis"*, Physical Review A **68**, 032316 (2003).

[410] N. Zheludev, *"The life and times of the LED — a 100-year history"*, Nature Photonics **1**, 189 (2007).

[411] T. D. Ladd, F. Jelezko, R. Laflamme, Y. Nakamura, C. Monroe, and J. L. O´ Brien, *"Quantum computers"*, Nature **464**, 45 (2010).

[412] M. Steger, G. Liu, B. Nelsen, C. Gautham, D. W. Snoke, R. Balili, L. Pfeiffer, and K. West, *"Long-range ballistic motion and coherent flow of long-lifetime polaritons"*, Physical Review B **88**, 235314 (2013).

[413] D. Bajoni, E. Semenova, A. Lemaître, S. Bouchoule, E. Wertz, P. Senellart, and J. Bloch, *"Polariton light-emitting diode in a GaAs-based microcavity"*, Physical Review B **77**, 113303 (2008).

[414] S. De Liberato, C. Ciuti, and C. C. Phillips, *"Terahertz lasing from intersubband polariton-polariton scattering in asymmetric quantum wells"*, Physical Review B **87**, 241304 (2013).

[415] M. De Giorgi, D. Ballarini, P. Cazzato, G. Deligeorgis, S. I. Tsintzos, Z. Hatzopoulos, P. G. Savvidis, G. Gigli, F. P. Laussy, and D. Sanvitto, *"Relaxation oscillations in the formation of a polariton condensate"*, Physical Review Letters **112**, 113602 (2014).

[416] L. Dominici, D. Colas, S. Donati, J. P. Restrepo Cuartas, M. De Giorgi, D. Ballarini, G. Guirales, J. C. López Carreño, A. Bramati, G. Gigli, E. del Valle, F. P. Laussy, and D. Sanvitto, *"Ultrafast Control and Rabi Oscillations of Polaritons"*, Physical Review Letters **113**, 226401 (2014).

[417] G. Nardin, K. G. Lagoudakis, B. Pietka, F. Morier-Genoud, Y. Léger, and B. Deveaud-Plédran, *"Selective photoexcitation of confined exciton-polariton vortices"*, Physical Review B **82**, 073303 (2010).

[418] G. Grosso, G. Nardin, F. Morier-Genoud, Y. Léger, and B. Deveaud-Plédran, *"Dynamics of dark-soliton formation in a polariton quantum fluid"*, Physical Review B **86**, 020509 (2012).

[419] A. Bramati, M. Modugno, B. Deveaud, G. Nardin, G. Grosso, and Y. Léger, "Springer series in solid-state sciences", in *Physics of Quantum Fluids* Vol. 177 (Springer Berlin Heidelberg, 2013) pp. 99–126.

[420] O. A. Egorov, D. V. Skryabin, A. V. Yulin, and F. Lederer, *"Bright cavity polariton solitons"*, Physical Review Letters **102**, 153904 (2009) PMID: 19518634.

[421] G. Tosi, M. Baudisch, D. Sanvitto, L. Viña, A. Lemaître, J. Bloch, E. Karimi, B. Piccirillo, and L. Marrucci, *"Optical induced vortices and persistent currents in polariton condensates"*, Journal of Physics: Conference Series **210**, 012023 (2010).

[422] H. Sigurdsson, O. A. Egorov, X. Ma, I. A. Shelykh, and T. C. H. Liew, *"Information processing with topologically protected vortex memories in exciton-polariton condensates"*, Physical Review B **90**, 014504 (2014).

[423] P. Lagoudakis, *"Polariton condensates: Going soft"*, Nature Materials **13**, 227 (2014).

[424] P. G. Savvidis, *"Optoelectronics: A practical polariton laser"*, Nature Photonics **8**, 588 (2014).

[425] T. Boulier, M. Bamba, A. Amo, C. Adrados, A. Lemaitre, E. Galopin, I. Sagnes, J. Bloch, C. Ciuti, E. Giacobino, and A. Bramati, *"Polariton-generated intensity squeezing in semiconductor micropillars"*, Nature Communications **5** (2014).

[426] K. S. Daskalakis, S. A. Maier, R. Murray, and S. Kéna-Cohen, *"Nonlinear interactions in an organic polariton condensate"*, Nature Materials **13**, 271 (2014).

[427] J. D. Plumhof, T. Stöferle, L. Mai, U. Scherf, and R. F. Mahrt, *"Room-temperature Bose–Einstein condensation of cavity exciton–polaritons in a polymer"*, Nature Materials **13**, 247 (2014).

[428] S. Kalusniak, S. Sadofev, S. Halm, and F. Henneberger, *"Vertical cavity surface emitting laser action of an all monolithic ZnO-based microcavity"*, Applied Physics Letters **98**, (2011).

[429] L. Orosz, F. Réveret, F. Médard, P. Disseix, J. Leymarie, M. Mihailovic, D. Solnyshkov, G. Malpuech, J. Zuniga-Pérez, F. Semond, M. Leroux, S. Bouchoule, X. Lafosse, M. Mexis, C. Brimont, and T. Guillet, *"LO-phonon-assisted polariton lasing in a ZnO-based microcavity"*, Physical Review B **85**, 121201 (2012).

[430] T.-C. Lu, Y.-Y. Lai, Y.-P. Lan, S.-W. Huang, J.-R. Chen, Y.-C. Wu, W.-F. Hsieh, and H. Deng, *"Room temperature polariton lasing vs. photon lasing in a ZnO-based hybrid microcavity"*, Optics Express **20**, 5530 (2012).